UNIVERSITY OF SOUTHAMPTON

FACULTY OF ENGINEERING AND APPLIED SCIENCE

INSTITUTE OF SOUND AND VIBRATION RESEARCH

Doctor of Philosophy

WHEEL-RAIL NOISE: THEORETICAL MODELLING OF THE GENERATION OF VIBRATIONS

by David John Thompson

UNIVERSITY OF SOUTHAMPTON

ABSTRACT

FACULTY OF ENGINEERING AND APPLIED SCIENCE
INSTITUTE OF SOUND AND VIBRATION RESEARCH

Doctor of Philosophy

WHEEL-RAIL NOISE: THEORETICAL MODELLING OF THE GENERATION OF VIBRATIONS

by David John Thompson

The rolling of a wheel on a rail is an important source of noise from railways, particularly as the speeds of trains increase. This noise is known to emanate from the structural vibrations of the wheels and rails. A theoretical study is presented of the mechanisms which generate these wheel and rail vibrations.

Mathematical models of the vibrational response of a wheel and a rail are developed. These are then coupled in a linear frequency-domain model through a multi-degree-of-freedom contact zone, described by its receptances.

Excitation due to the surface roughness profiles of the wheel and rail is considered in detail. This generates a relative displacement input between the wheel and the rail in the vertical direction. The predicted responses of the wheel and rail generally correspond well to measured data, although some discrepancies are noted.

The effect of the rotation of the wheel is incorporated into the model, and is seen to improve the form of the response. Remaining discrepancies can be attributed to lack of precision in wheel modal data, and to systematic errors in the experimental results.

Parametric studies are presented of the overall model. They show, amongst other things, that, to reduce the wheel vibration, added wheel damping needs to be greater than would be expected from free wheel receptances. Reduction of noise from the rail is a less surmountable problem; very high levels of damping would be needed to reduce the radiating length significantly.

Alternative excitation mechanisms are discussed, such as the lateral movement of the contact, and absolute as well as relative force inputs.

CONTENTS

CONTENTS (Continued)

CONTENTS (Continued)

CONTENTS (Continued)

CONTENTS (Continued)

CONTENTS (Continued)

CONTENTS (Continued)

LIST OF SYMBOLS

a Distance from structural node point in rail to top of rail head (mm) (§5, p148)

a Distance from centroid of rail cross-section to its shear centre (Appendix D, pD6)

a,b Contact patch semi-axes, with a in the direction of travel (m) (§3, p45)

a_{nij},b_{nij} parts of receptance of rotating wheel (§4, p97)

A Beam cross-sectional area (m^2) (§3, p41)

A Second longitudinal wave of rail (§5, p126), also IV

A,B Functions of wheel/rail surface radii of curvature (Appendix E, pE2)

A_n,B_n Fourier series coefficients for rolling wheel vibration (§4, p96)

A_n,B_n Generalised coordinates relating to nth wavetype in right-hand and left-hand parts of periodic structure (Appendix F, pF7)

b Lateral offset to wheel-rail contact point from rail centre-line (mm) (§5, p161)

c Mean radius of contact patch $=\sqrt{(ab)}$ (§6, p195)

[c] Damping matrix (§4, p90)

c_{mn} Modal damping for (m,n)'th mode (§4, p90)

C Creep force damper (§3, p36)

C_{pq} Creep coefficients tabulated by Kalker (§3, p45)

C^*_{pq} Frequency-dependent creep coefficients (§6, p193)

c (Sub/superscript): refers to contact zone (relative motion between wheel and rail (§3, p34)

$d_\pm$ Modal denominator terms containing frequencies $\omega \pm n\Omega$ (§4, p92)

d_r Half effective radiating length of rail (§8, p271)

D Fourth lateral wave of rail (§5, p125), also IV

[D] Combined dynamic stiffness matrix = $(1+i\eta)[K] + \omega^2[M]$ (Appendix F, pF2)

e (Superscript) even wheel modes (§4, p91)

E Young's modulus (N/m^2) (§3, p41)

E^* Plain strain elastic modulus $E^*=E/(1-\nu^2)$ (§3, p42)

E(x) Integral of vibration-squared in beam over distance x from excitation point (§8, p269)

f_o Resonance frequency (Hz) (§3, p49)

f_L, f_U Lower and upper half-power point frequencies for wheel response (§3, p53)

f_{pq} Creep coefficients (Appendix E, pE5)

F Second vertical wave of rail (§5, p126), also III

{F} Absolute force input to wheel-rail interface (§6, p188)

{F} Force acting between adjacent periodic elements (Appendix F, pF1)

g aspect ratio of contact patch (=a/b) (§6, p204)

g_{ni}, h_{ni} components of vibration of rotating wheel (§4, p97)

G First longitudinal wave of rail (§5, p126), also II

G Shear modulus =E/2(1+ν)

H_j Relations between roughness and interaction force (§4, p96)

i $\sqrt{(-1)}$

i,j,k Indices for coordinates etc

I Second moment of area of beam cross-section (I_L for lateral rail vibrations, I_V for vertical, I_C equivalent value for cross receptance) (§3, p41)

I,II Division of wheel modeshape into two parts (§4, p91)

I_x Polar moment of area of beam in torsion (Appendix D, pD5)

J Torsion constant of beam in torsion (Appendix D, pD5)

[k] Stiffness matrix (§4, p90), [K] in Appendix F

k_{mn} Modal stiffness for (m,n)'th mode (§4, p90)

k_H Hertzian contact stiffness (§3, p35) (wheel and rail components k_{HW} and k_{HR})

k_T Transverse contact stiffness (§3, p36) (wheel and rail components k_{TW} and k_{TR})

k Wavenumber of rail vibration (radian/m) (§3, p41)

$\bar{k}$ Complex wavenumber of rail vibration (Appendix D, pD2)

k_R, k_I Real and imaginary parts of rail wavenumber (§5, p142)

k_n Wavenumber of nth mode of finite beam (Appendix D, pD5)

k Constant in C^*_{pq} approximations (Appendix E, pE7)

K Strain energy (§4, p90)

K Bulk modulus =E/3(1-2ν) (Appendix G, pG3)

L Length of finite beam (Appendix D, pD4)

L First lateral wave of rail (§5, p125), also I

L Wavelength of force fluctuation =2πV/ω (Appendix E, pE7)

L Length of periodic element (Appendix F, pF1)

L_1 Ratio E(∞)/E(2.25) for damped beam (§8, p269)

L_2 Ratio E(2.25)/w_o^2 for damped beam (§8, p269)

L (Sub/superscript): Lateral (§3, p36)

l Dummy index for n (§4, p97), and for 2 wheels (§6, p189)

m,n	Number of nodal circles/diameters in a wheel mode (§2, p13)
[m]	Mass matrix (§4, p90), also [M] in Appendix F
m_r	Modal mass of rth wheel mode (§2, p25), also m_{mn}
M,N	Lower and upper limits of modal sum (§2, p25)
n	Index of modes of finite beam (Appendix D, pD4)
N	Total number of nodal diameters, n, considered (§4, p99)
N	Number of coupling coordinates (§6, p185)
o	(Superscript) odd wheel modes (§4, p91)
p,q	Indices for creep coefficients (§3, p45) p,q =1 for longitudinal, 2 for lateral, 3 for spin
P	Force vector (§4, p91)
{P}	Mutual force vector acting on wheel and rail (§6, p185)
P_o	Static wheel load (§3, p42)
P_L,Pv	Interaction force (§3, p36)
{q}	Coordinates for periodic element (Appendix F, pF1)
q_r	Generalised coordinates of wheel motion (§4, p90)
Q_r	Generalised forces (§4, p90)
r	Index of wheel modes (§2, p25)
r	Roughness input (§3, p34), also r_i
r_R,r_W	Rail and wheel components of roughness (§3, p34)
(r,θ,z)	Polar coordinates for wheel (§4, p90)
(R,Ωt,Z)	Position of forcing point on wheel (§4, p90)
R_e	Effective radius of curvature at wheel-rail contact (§3, p42)
R'	Rail head radius of curvature (§3, p42), also R_{22} in §6
R''	Wheel radius (§3, p42), also R_{11} in §6
R_{12}	Radius of curvature of wheel surface (perpendicular to direction of travel) (§6, p195)
R_{21}	Radius of curvature of rail surface (parallel to direction of travel); always infinite (§6, p195)
R	(Sub/superscript): refers to rail (§3, p34)
R_y,R_w	Auto-correlation functions of y, w, etc (§4, p96)
R_{AB}	Cross-correlation functions (§4, p97)
R_{jk}	Mass residue term (§2, p25)
S_{jk}	Stiffness residue term (§2, p25)
S_P,S_y	Spectral densities of P, y, etc (§4, p94)
S_{AB}	Cross-spectral densities (§4, p97)
S(λ)	Part of C^*_{33} approximate formula (Appendix E, pE13)
t	Time (sec) (§3, p35)
T	Kinetic energy (§4, p90)
T	Second lateral wave of rail (§5, p125), also II

T_{mn} Complex forcing term in (m,n)'th mode (§4, p92)

$[]^T$ Transpose of a matrix

$T(\lambda)$ Part of C^*_{33} approximate formula (Appendix E, pE13)

u_X Vibration response at a general position X (§3, p37)

V Train speed (m/s) (§3, p37)

V First vertical wave of rail (§5, p126)

v (Sub/superscript): Vertical (§3, p36)

V^R_1, V^W_1 Longitudinal (z_1) velocities of wheel/rail (Appendix E, pE5)

V^R_2, V^W_2 Lateral (z_2) velocities of wheel/rail (Appendix E, pE6)

w Vibration displacement of wheel in rotating frame of reference (§3, p90)

w_n nth modeshape of finite beam (Appendix D, pD4)

W_n Anti-nodal amplitude nth modeshape of finite beam (Appendix D, pD4)

W Third lateral wave of rail (§5, p125), also III

w (Sub/superscript): refers to wheel (§3, p34)

x Position vector (§4, p90)

x Longitudinal coordinate for beam theory (Appendix D, pD1)

x,y,z Coordinates for rail response (§5, p121 (Figure 56))

x (Sub/superscript): Refers to general position (§3, p37)

y Vibration displacement of wheel in non-rotating frame of reference (§3, p93)

y_R, y_W, y_C Lateral vibration of rail, wheel and contact zone (§3,p36)

Y Lateral motion of contact point on wheel/rail (§6, p198)

z_R, z_W, z_C Vertical vibration of rail, wheel and contact zone (§3,p34)

$z_1 \ldots z_N$ Coupling coordinates (§6, p185), with superscripts C, R, W for contact rail and wheel vibration

$z_1 \ldots z_6$ ditto for 6 degrees of freedom (§6, p193; see Figure 103)

$\{z_o\}$ Absolute displacement input to wheel-rail interface (§6, p188)

α_{jk} Receptance (response at x_j due to force at x_k) (wheel: §2, p25, sum of wheel, rail and contact: §3, p37)

$[\alpha^C]$ Contact receptances (§3, p36)

$[\alpha^R]$ Rail receptances (§3, p36)

$[\alpha^W]$ Wheel receptances (§3, p36)

α, β Coefficients defining parabolic roughness (§6, p203)

α, β Coefficients used to define damping matrix from mass and stiffness, as used by NEWPAC program (Appendix G, pG2)

γ_1 Longitudinal creepage (§6, p195), also $\bar{\gamma}_1$ static component, $\Delta\gamma_1$ small variations.

γ_2 Lateral creepage (§6, p196), also $\bar{\gamma}_2$ static component, $\Delta\gamma_2$ small

variations.

Γ Factor in warping rigidity $E\Gamma$ for a beam in torsion-bending (Appendix D, pD6)

δ Dirac delta function (§4, p91)

Δ Decay of rail vibration with distance (dB/m) (§5, p142)

Δf Difference between frequency of peak response and natural frequency (§3, p52)

ε Lateral motion of crest of roughness (§6, p203)

ε_{ij} =1,-i or i depending on coordinate types of i and j (§4, p94)

ζ Equivalent damping ratio for wheel (§3, p52)

ζ_r Modal damping ratio for rth wheel mode (§2, p25), also ζ_{mn}

η_r Modal damping loss factor for rth wheel mode (§2, p26)

η Damping loss factor for rail and its supports (§5, p137)

θ Coordinate in azimuthal direction around wheel (§2, p16); in §4 this is in the frame of reference rotating with the wheel (§4, p91)

θ Function of radii of curvature of wheel/rail surfaces (Appendix E, pE2)

θ_o Coordinate in azimuthal direction around wheel in the non-rotating frame of reference $\theta_o=\theta-\Omega t$ (§4, p93)

θ_V Phase of vertical rail receptance (§3, p41)

θ_L Phase of lateral rail receptance (§3, p41)

θ_C Phase of cross rail receptance (§3, p42)

$\theta_W, \theta_R, \theta_C$ Twist rotations (z_4) of wheel, rail and contact (§6, p198)

$\varkappa$ Factor between Hertzian vertical contact stiffness and transverse stiffness (Appendix E, pE3)

λ Wavelength of roughness (§3, p38), also of rail vibration (§5, p142)

λ Non-dimensional wavelength of force fluctuation $=L/a=2\pi V/a\omega$ (Appendix E, pE11)

μ, σ Non-dimensional factors determining shape of contact patch (§6, p196; Table E1 contains values)

μ Propagation constant in periodic structure (Appendix F, pF2)

ν Poisson's ratio (§3, p42)

ξ Non-dimensional factor depending on shape of contact patch (§3, p42; Table E1 contains values)

ξ Longitudinal coordinate for beam relative to moving forcing point $\xi=x-Vt$ (Appendix D, pD12)

ρ Density (kg/m^3) (§3, p41)

τ Time delay (used in auto-correlation function) (§4, p96)

φ_r rth modeshape of wheel (§4, p90) (also φ_{mn})

χ Longitudinal motion of crest of roughness (§6, p204)

ψ_r Parts of (m,n)'th modeshape of wheel (§4, p91)

$\psi_{jn}, \bar{\psi}_{jn}$ Normalised displaced shapes ('waveshapes') of nth wavetype in right-hand and left-hand parts of periodic structure (Appendix F, pF7)

Ψ_{mn} Complex modeshape ($=\psi^{I}_{mn}+\psi^{II}_{mn}$) (§4, p93)

$_r\psi_j$ Amplitude of rth wheel mode at x_j (§2, p25)

ω Angular frequency (radian/s) (§2, p25)

ω_r rth wheel natural frequency (radian/s) (§2, p25), also ω_{mn}

ω_n nth natural frequency of finite beam (Appendix D, pD4)

ω_o Bounce resonance frequency of beam on elastic foundation (Appendix D, pD11)

ω_3 Spin creepage (§6, p196), also $\bar{\omega}_3$ static component, $\Delta\omega_3$ small variations.

Ω Angular velocity of wheel (radian/s) (§4, p90)

$\Omega^{R}_3, \Omega^{W}_3$ Spin (z_6) velocities of wheel and rail (Appendix E, pE6)

* Complex conjugate

{ } Vector

[ ] Matrix

COMMONLY USED ABBREVIATIONS

BR British Rail

cut-on Frequency above which structural waves of a particular type propagate

dB Decibels = 20 $\log_{10}$ (rms amplitude/reference amplitude)

dB(A) A-weighted decibels

FRF Frequency response function

Hz Hertz (cycles per second)

km/h kilometres per hour

m metres

masters Master degrees of freedom (in finite element solution)

NEWPAC The BR Research in-house finite element package

N Newtons

ORE Office for Research and Experiment of the International Union of Railways

rad/s Radians/s

rms Root-mean-squared average

s seconds

ACKNOWLEDGMENTS

I wish to express my gratitude to the British Railways Board, my employer between 1980 and 1990, for allowing me to carry out this research work, as an external student of the ISVR, and for giving complete financial support for it.

Many people have given me advice and encouragement for which I am very grateful, particularly Prof Bob White of ISVR as my supervisor, and many at British Rail Research, including Brian Hemsworth, Colin Stanworth, Charles Frederick and Chris Jones.

Finally I want to thank Claire, my wife, who has patiently put up with so much disruption at home.

CHAPTER 1

INTRODUCTION AND LITERATURE SURVEY

1.1 INTRODUCTION TO WHEEL-RAIL NOISE

1.1.1 General Background

Most people are familiar with railway noise, even if it is only to think of the "chuff-chuff of the engine" or the "clickety-clack of the coaches"! However in the last 20-30 years, technological advances have virtually eliminated these sounds from our mainline railways. On British Railways (BR), diesel and electric traction completely replaced steam in the 1960s, and it has to be admitted, even by those who still lament its passing, that this brought significant improvements to the environment as well as the quality of service. Furthermore the traditional fishplated rail joints have given way to continuously welded rail, giving a smoother and quieter ride.

Since then, following the lead of the Shinkansen in Japan, the railways have sought to increase the speed of trains considerably. Speeds of 200 km/h (125 mile/h) are now common on BR with the High Speed Train and with the most recent electric locomotives, and in other countries even higher speeds are achieved, notably with the Train à Grande Vitesse (TGV) in France, and the ICE prototype in Germany. New purpose-built high speed lines are being built across Europe, as the drive for higher and higher speeds continues.

However one penalty of increased speed is increased noise, and this has come at a time of increased awareness in the environment. The proposed high speed rail link between London and the Channel Tunnel has generated particular public interest in the noise issue [1-3].

1.1.2 Characteristics of Wheel-Rail Noise

When a train runs at high speed, the noise experienced by an observer beside the line tends to be dominated by a roaring noise, which is associated with the rolling of the steel wheel on the steel rail. This is usually referred to as "wheel-rail noise", or "rolling noise". By contrast, motive power noise is generally independent of speed, so that at high speeds it is masked by the rolling noise [4,5], whereas aerodynamic sources increase with speed at a greater rate and are likely to become important at very high speeds.

For a passenger inside the train, rolling noise need not be intrusive, as the modern design of vehicles allows for it largely to be excluded from the passenger areas, particularly where air-conditioning has allowed windows to be sealed. Similarly, driver's cabs can be designed to maintain an acceptable environment. However, wheel-rail noise can be a significant source for residents living adjacent to high speed lines, as well as for staff working next to running lines.

Early research into rolling noise tended to concentrate on prediction using empirical models [5,6]. Such prediction schemes have been used to assess the effects on the noise environment of new lines, revised traffic on existing lines, or to assess the suitability of plans for building development adjacent to existing lines.

Rolling noise has quite a broad frequency content, with the highest levels occurring in the range 800-2500 Hz. This coincides with the frequencies of greatest human response to noise, as indicated by the shape of the weighting networks (eg the A-weighting).

The casual observer may have noticed that rails tend to 'sing' as a train approaches or recedes, particularly on continuously welded rail. This tends to suggest that the rail is a source of noise. Additionally, close to a moving train, the noise reaches a peak as each wheel passes, so that much of the noise appears to originate in the vicinity of the wheels, suggesting that the wheels too are sources of noise.

1.1.3 Attempts at Control

Various attempts have been made in several countries to reduce wheel-rail noise but with only limited success. Treatments have been found which are successful in reducing the squeal noise which may be generated during curving or braking [7,8], notably the application of damping to the wheel surface, but such techniques have not been found to be particularly successful in controlling wheel-rail rolling noise.

Currently only two methods of direct noise control are employed by BR. The first is to grind the surface of the rail smooth regularly, using a dedicated train [9]. This is an expensive and temporary solution, usually applied at sites where "corrugations" have formed on the rail surface. It is not usually applied for noise reasons, but rather to maintain the structural integrity of track or vehicle components, which are more likely to fail when subject to the high levels of vibration induced by rail corrugations.

The second is that disc-braked vehicles have been found to be up to 10 dB quieter than the conventional cast-iron block tread-braked vehicles, so long as the track is not corrugated [10]. On corrugated track any advantage is lost, and the noise from both types of vehicle rises to around 10 dB higher than the tread-braked level. The use of disc-brakes can be expensive and so is not always favoured in vehicle design or procurement, although noise specifications often mean that new vehicles have to be designed with disc brakes, eg the Channel Tunnel international trains [3].

Although significant reductions in rolling noise have been achieved by the use of these two methods, these improvements have tended to be offset by the results of increased speeds.

As a last resort, additional reduction in noise at specific locations can be achieved by erecting noise barriers or artificial embankments at the lineside [11], by applying double glazing to properties, or by routing the line through cuttings or even tunnels. These measures are very expensive - at one stage the cost of the proposed 109 km high speed rail link from London to the Channel Tunnel was estimated to have been increased by 40% (from £1200M to £1700M) by the need to include a combination of such environmental protection measures, including placing one third of the line in tunnel [1,2]. Subsequent concessions have raised these costs yet further, and this has forced a delay in the submission of proposals to Parliament.

If the need for such expensive protection measures is to be minimised, further noise reduction at source is clearly desirable, including, if necessary, modifications to the design of wheels and track components. The lack of consistent noise reduction from ad hoc measures applied to the wheels and rails, leads to the conclusion that there is no short-cut solution to the problem.

It is thus essential to develop an accurate understanding of the mechanisms of generation of wheel-rail noise. Only from such a position of understanding, can economic control at source can be achieved. Such fundamental research work has been carried out in a number of countries, including the U.K., and will be summarised in the next section. However, as will be seen, many parts of the problem still remain to be solved [12,13].

1.2 REVIEW OF LITERATURE

1.2.1 Introduction: The Remington Model

Recently a survey of literature, and of work currently being carried out in different countries, was conducted for O.R.E. (the Office for Research and Experiments of the International Union of Railways (UIC)) [14]. It concluded that the work of Remington [15-21] presented the most comprehensive single model of wheel-rail noise, although it pointed out deficiencies and suggested how it might be improved by the inclusion of work from other sources. Similar conclusions were also reached by Remington in a recent review paper [12]. In order to discuss these deficiencies, the overall model will first be described, following which its individual components will be discussed with reference to wider literature.

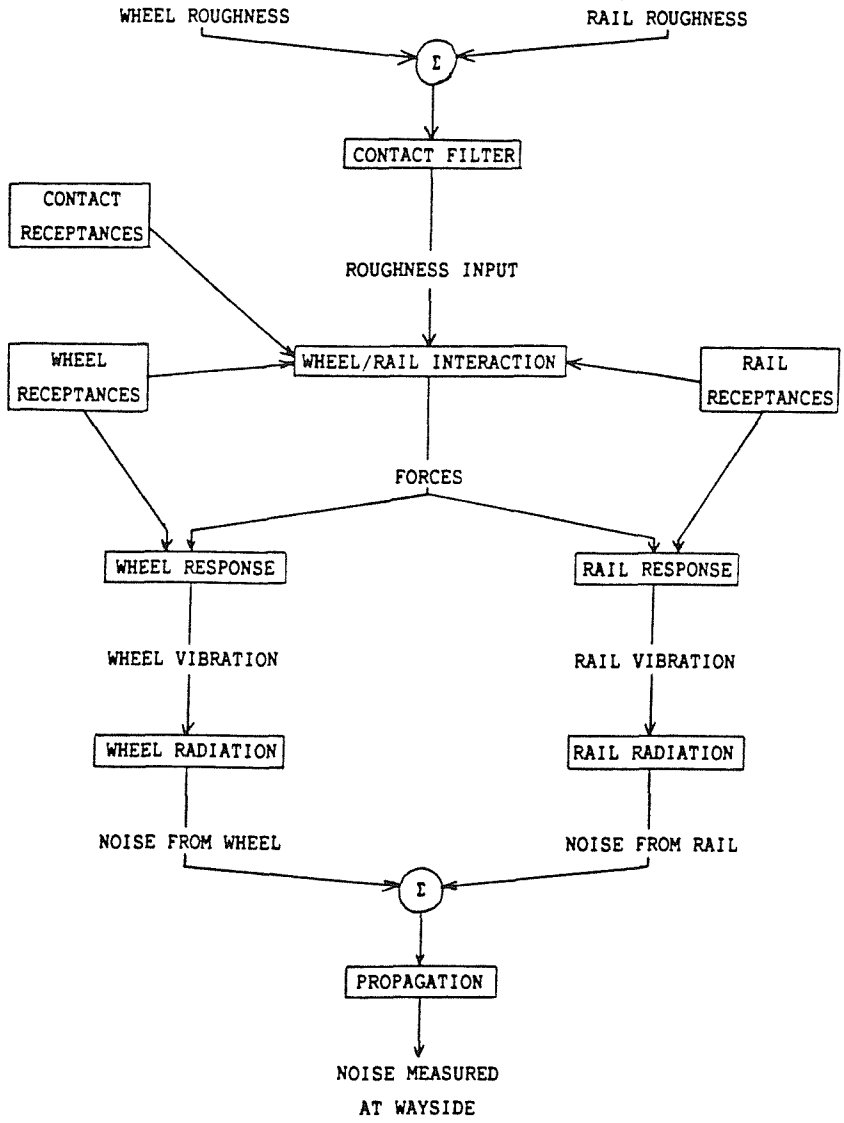

Figure 1 Framework for Theoretical Model of Wheel-Rail Noise

The framework for this model of wheel-rail rolling noise is summarised in Figure 1. It is based on the assumption that the major sources of noise are the structural vibrations of the wheel and rail. In turn it is assumed that small-scale undulations (roughnesses) on the wheel and rail surfaces generate these vibrations of the wheel and rail, at frequencies which correspond to the passage of the wheel-rail contact (at train speed) over the roughnesses of a particular wavelength (see also Lyon [22]).

These hypotheses were tested [18,21] by measuring the roughness profiles of wheels and rails, the vibrations of each and the resulting noise. These were compared with the point response and noise radiation characteristics of the wheels and the rails, with a certain amount of success, although the range of input conditions used was somewhat restricted. More recently an O.R.E. sponsored experiment [23] conducted similar measurements over a wide range of roughness conditions as well as speeds, and concluded that a simple linear relation, as predicted by the Remington model, was not to be found [24]. This experiment is described in Appendix A. It will be used to validate the current theoretical modelling.

Whilst Remington's model is comprehensive, in that it covers the whole noise generation process, this has been achieved at the expense of using over-simplified models of the various constituent parts, and thus having to be content with levels of agreement against experimental data which are less than may be desirable.

As well as the review papers mentioned [12,14], another useful source of literature is the series of four Railway Noise Workshops, papers from which have been published in Journal of Sound and Vibration [25-28]. At these, representatives from many railway establishments and research bodies working in the field of railway noise have been able to pool ideas and discuss their work.

1.2.2 Noise Radiation and Source Location

In locating the source, the basic question to be answered is whether the wheel or the rail generates most of the noise, or whether there is some other dominant source. Many attempts have been made to answer this simple question, with a great variety of results. The answers tend to mould the shape of research work, as, if one component is believed to be the most important, much effort is then expended in trying to reduce its contribution to the noise. Early results in the

U.S.A. tended to indicate that the rail was the major source [18] (but see also [29]), whilst in Europe it was believed that the wheel was dominant [6,30,31].

Remington's radiation models assumed uniform directivity and simple radiation efficiencies, which seemed to be validated by experiment. However, at times the level of agreement was not good enough when it is considered that the fine-tuning of the final results is critical to the conclusions drawn.

More elaborate mathematical models of the radiation from the wheel and the rail have been developed at BR Research [32,33], which have been used in conjunction with 1/3 octave data from the O.R.E. experiment mentioned above ([23] and Appendix A). Details of this sound radiation work are given in Appendix B. It was found that the rail was a significant source for all frequencies in the range considered (250-5000 Hz), but that the wheel was only a dominant source at high frequencies (for the particular wheel type considered this was 1250 Hz and above; for smaller wheels it is believed to be from 2000 Hz upwards).

Other papers have covered wheel-rail noise source location from an experimental point of view [34-37]. Whilst these appear somewhat contradictory, reinterpretation of the experimental data in the light of predicted behaviour, such as [33], leads one to the conclusion that most of them contain little data which contradict the predicted behaviour, and indeed many of the results are complementary. It is clear that great care is needed in the interpretation of the results of source location experiments. Often their assumptions, such as that the sound field is generated by an array of point sources, are not wholly valid.

Apart from the wheel and the rail, other sources may also be present, such as the bogie [38], the sleepers or even the vehicle body [39], but generally the major sources have been identified as in the wheel-rail region.

It is not intended to look in any more detail at the noise radiation and source location problem, as it is believed that this controversial issue is at last nearing resolution. Work will concentrate on predicting the vibration response from surface roughnessess (and any other input). It will be assumed that the vibrations of the wheel and the rail are both of importance (as shown in Appendix B), and that a

reduction in both is necessary for a significant reduction in noise. Some have asserted that the reduction of the vibration of one component (eg the wheel) will cause a reduction in the vibration of the other [40], while others have worked on the assumption that the opposite holds, so that both wheel and rail have to be treated for an adequate solution [13]. This question will have to be addressed by the present research.

1.2.3 Wheel Vibrational Response

Remington's early work [15] used a model for the wheel's vibrational response based on an equivalent mass or beam. Later work [20] used a more detailed prediction of the wheel impedance based on that of a ring. (Similar analytical models are found in [41-43]). Although point impedances were calculated, the lateral/vertical cross impedance was not estimated and had to be omitted from the model.

A more advanced model has been used by Irretier et al [44,45], based on the finite element method, using Mindlin's thick plate theory, and Haran and Finch [46] have recently published a multiple ring model of a wheel. Neither of these models focussed on the modes of interest in rolling noise, since they were both developed for use in studies into curve squeal. It has generally been found that only those modes which consist of nodal diameters but no nodal circles are of relevance in curve squeal, whereas in rolling noise it has been found that modes consisting of one nodal circle (together with various nodal diameters) are most prominant in the noise [47,33].

Recently Heiss [48] has completed a detailed finite element model, using 3-dimensional continuum elements, for the purpose of rolling noise research. This incorporated as many as 7000 degrees of freedom in 1/8 of a wheelset, and its results compared very well with experimental modal analysis.

Theoretical investigations of the modes of vibration of various wheel types have been carried out at BR Research using the in-house finite element package, "NEWPAC" [49-52]. In all cases the same basic idealisation was used which utilised the axisymmetry of the structure. The axle was ignored by imposing a clamped condition at the inner edge of the wheel hub.

Corresponding experimental investigations have been carried out at BR Research, consisting of measurements of natural frequencies, damping ratios and corresponding modeshapes of various wheel types [52-

54]. The level of agreement between them and the finite element predictions has not been as good as that obtained by Heiss, but is still reasonable. Measurements of rolling wheel vibration have been carried out in several countries, notably in the U.K.[47], and by Heiss [48].

Ferguson [55,56] has studied the effects of rolling theoretically by examining the vibration of a rolling disc excited by various types of force and moment at its contact with a plane. The frequency response at the contact point is modified from the static case by the splitting of the resonance frequencies by a factor which depends on the mode and the rotation speed. Honda et al [57] have also studied the forced response of a rotating disc and have included an analysis of the effects of slight imperfections in the axisymmetry of the disc.

1.2.4 Rail Vibrational Response

Remington modelled the rail response using a simple Euler-Bernoulli beam equation, which [14] considers inadequate. At low frequencies the restraint of the sleepers and ballast are ignored, whereas at high frequencies the model is insensitive to the force/response position.

A more comprehensive model of the rail response to vertical, lateral and longitudinal excitation has been developed by Grassie et al [58-60], in relation to rail corrugations. Validation experiments were also carried out on track with both wooden and concrete sleepers, over a frequency range from 50 Hz up to 1-2 kHz (depending on the case considered). For each excitation direction Grassie developed several models, and evaluated their relative merits. Each was based on a beam (Euler-Bernoulli or Timoshenko), on a one- or two-layer mass-spring foundation, representing the sleepers, ballast and railpads (which are inserted between the rail and concrete sleepers). For vertical vibration, the effects of discrete supports were also investigated using a transfer matrix technique, and found only to affect the receptance only at discrete frequencies (the "pinned-pinned" frequencies where the semi-wavelengths of bending waves correspond to the sleeper spacing).

Cox and Grassie [61,62] have further developed this vertical model by including the sleepers as Timoshenko beams, in place of the simple masses used in [58]. This provided a useful improvement in the lower part of the frequency range, particularly when considering the sleeper response.

Clark et al [63,64] have developed a model of the vertical vibration of the track, which included the discrete nature of the support of the rail. It is based on a modal sum for a finite length of track (20 sleepers). The rail itself was again represented by a Timoshenko beam, and the wheel as a mass. Forward motion of the vehicle was included in this work, which took account of non-linearities by using a time-stepping procedure.

Munjal and Heckl [65] produced a model of the vertical impedance of track, based on an Euler-Bernoulli beam and periodic structure theory. Unfortunately, comparison with measurements suggested that the model is not entirely appropriate, possibly because of the choice of parameters such as ballast stiffnesses. It is based on a wooden sleepered track, which is assumed to have a rigid connection to the rail in both vertical and rotational senses. Hence it is not readily applicable to concrete sleepered track, in which an elastic railpad is inserted between the sleeper and the rail. A similar effect for wooden sleepered track may occur due to localised flexibility of the sleeper.

Tassilly [66,67] has also modelled the track as a periodically supported Euler-Bernoulli beam, producing dispersion diagrams of wave-number against frequency, showing stop and pass bands. Ono and Yamada [68] have recently published a model of the vertical vibration of railway track, which includes the propagation of vibration into the roadbed. However the rail is once more modelled as an Euler-Bernoulli beam, and the wheel as a mass.

These models cannot readily be applied across the whole of the frequency range under consideration for noise generation (up to about 5000 Hz), since the assumptions of a rigid beam cross-section will break down. This has been shown by experiments carried out by BR Research in which a rail in situ was excited by a harmonic force and the amplitude and phase of the response were measured at many points [69-71]. It was found that the cross-section deformed significantly above about 1500 Hz for lateral excitation, and above 4000 Hz for vertical excitation.

Scholl [72,73] has investigated the deformation of the cross-section in terms of the nature of the waves propagating in a rail. This consisted of both experiments and theory, although the measurements were only on a short length, and neither theory nor experiment investigated the effect of sleepers.

1.2.5 Force Generation Mechanisms

Remington's linear roughness excitation model [18] has already been described (§1.2.1). This also forms the basis of Grassie's work [58-60], although he introduces a 'roughness' excitation for lateral and longitudinal excitations of the rail without any substantial justification.

The Hertzian contact between the wheel and rail is actually non-linear, as a result of the curved nature of the contacting surfaces [74], and takes the form of:

$$\text{force} \propto \text{separation}^{3/2}$$

This has been used by Clark et al [63,64] since a time-stepping model allows such non-linear effects to be included. However linearisation is preferable where the displacements are small enough to allow it, as linear models have many advantages.

For larger vibration amplitudes, the non-linearity in the contact spring becomes important, leading eventually to loss of contact. In studies of sliding between two bodies, Soom and Chen [75] have found this to lead to a change from a resonant response of the contact region (contact resonance) at low amplitudes, to a broad-band response at higher amplitudes which thus includes greater high frequency vibration.

Feldmann [76,77] has recently questioned the roughness displacement-input model, and has proposed an alternative based on a force-input due to an equivalent impulse. This was validated using a cylinder rolling on a beam, and has not been fully applied to the case of a full size railway.

It has been pointed out [78] that variations in material properties, such as modulus of elasticity, can act in the same way as a surface roughness to excite the wheel and rail. These effects are much more difficult to measure and so have not yet been investigated experimentally.

The response of the wheel to a moving load travelling around its perimeter has been considered by Munjal and Heckl [79] and its effect on noise generation has been shown to be negligable. It is to be expected that a similar result would hold for the response of a rail to a moving load, which will tend to produce predominantly low frequency vibrations.

Much work on rolling contact theory has been done by Kalker [eg 80,81], and this has been successfully applied to the quasi-static behaviour of a railway vehicle [82,83]. Lateral forces are generated by the lateral and spin creepages during rolling. It is generally felt that these creep forces, at high creepages, are responsible for a stick-slip mechanism which generates curve squeal [7,16,84].

In normal rolling the creep force has been modelled by Ferguson [56] as a damper coupling the wheel to the rail. Further work is required to investigate any contribution of creep forces to the excitation of the wheel and rail vibrations in normal rolling. The work of Knothe and Gross-Thebing [85,86] and Valdivia [87] is significant in developing the theory of high frequency creep coefficients, and this needs to be introduced into the Remington framework.

As well as excitation by surface roughness, other hypotheses have been put forward at various times for the origin of rolling noise, some of which are listed in [12]. Among these are aerodynamic sources, including aerodynamic excitation of the wheel, and air-pumping in the contact region, which are generally considered to be insignificant in a railway situation. In general aerodynamic sources have been shown to be important only at speeds greater than about 240 km/h [88,89] (although it should be remembered that if successful control measures for wheel-rail noise are found, this speed will be reduced).

1.3 APPROACH TO BE ADOPTED

Of existing models of rolling noise, that of Remington has been seen to offer most scope as a starting point for the current research.

Existing radiation models appear to be satisfactory (Appendix B) and confirm that the noise which is measured is produced by the vibrations of wheel and rail. Hence the work will concentrate on the mechanisms by which these vibrations are generated, with only minimal reference to noise radiation.

Into the framework of Figure 1, improved models of the wheel and rail response need to be introduced before changes to the wheel-rail interaction can be assessed accurately.

For the wheel, standard approaches are available using the finite element method, which are relatively successful. Nevertheless, every design of wheel is different, and so a detailed study is required of

the particular wheel on which experimental data (rolling vibration and noise) are available. This will be described in Chapter 2. For the rail, little account has yet been taken of the cross-sectional deformation, and so a totally new model is required, which will be described in Chapter 5.

These then need to be incorporated into the existing interaction model (Figure 1) to pinpoint its weaknesses, and as a starting point for the development of a more complete model of the interaction. This will be done initially in Chapter 3. As well as this simple roughness displacement-input model, account needs to be taken of wheel rotation (Chapter 4), creep forces, other details of the contact zone, and other methods of excitation (Chapter 6).

Finally in Chapter 7 these various elements will be brought together and the sensitivity of the total model to its various parameters will be assessed.

A frequency range of 100-5000 Hz has generally been adopted, although some results will be included beyond this range where interesting features are found there.

CHAPTER 2

THE FREQUENCY RESPONSE OF A WHEELSET

2.1 INTRODUCTION

2.1.1 The Modes of Vibration of a Wheelset

The modeshapes of a wheel are found to be similar in form to those of a flat circular plate. Out-of-plane modes can be categorised by the numbers of nodal diameters and nodal circles. Hence a mode can be labelled by the two numbers (n,m) where there are n nodal diameters (n=0,1,2,3...) and m nodal circles (m=0,1,2...) [90]. The number of nodal diameters, n, determines the distribution of vibration amplitude around the perimeter of the disc, whereas the number of nodal circles, m, determines the distribution along any radial line. Similar descriptions may be applied to in-plane (radial and circumferential) modes.

For a perfectly axisymmetric structure under point excitation, the positions of the node lines (nodal diameters) are determined in each case entirely by the choice of excitation point, this always being at an antinodal diameter. However, in the case of slight imperfections in the axisymmetry, two distinct modes of each type (except n=0 modes) would occur with slightly different natural frequencies. The nodes and antinodes would then be fixed in the structure at positions which are independent of the excitation point, with the node lines of one mode corresponding to the antinodal lines of its partner [57]. Results such as these have been found for a church bell which is also a nominally axisymmetric structure [91].

For a wheelset, the presence of an axle, coupling two nominally similar wheels, will result in a further doubling of the number of modes. For n>2 this coupling will probably not be very great - it is the n=0 and n=1 modes which will couple strongly with the longitudinal and flexural motions, respectively, of the axle. If the two wheels are identical, the modes will be symmetric and anti-symmetric about the axle centre. However where there are differences between the two wheels, it is expected that the modes will tend to reflect a slight dominance of one wheel or of the other, yet still with strong coupling between the two.

The wheelset studied is a "Commonwealth" type, since such a wheel was fitted to a laboratory coach at BR Research [92] and used for

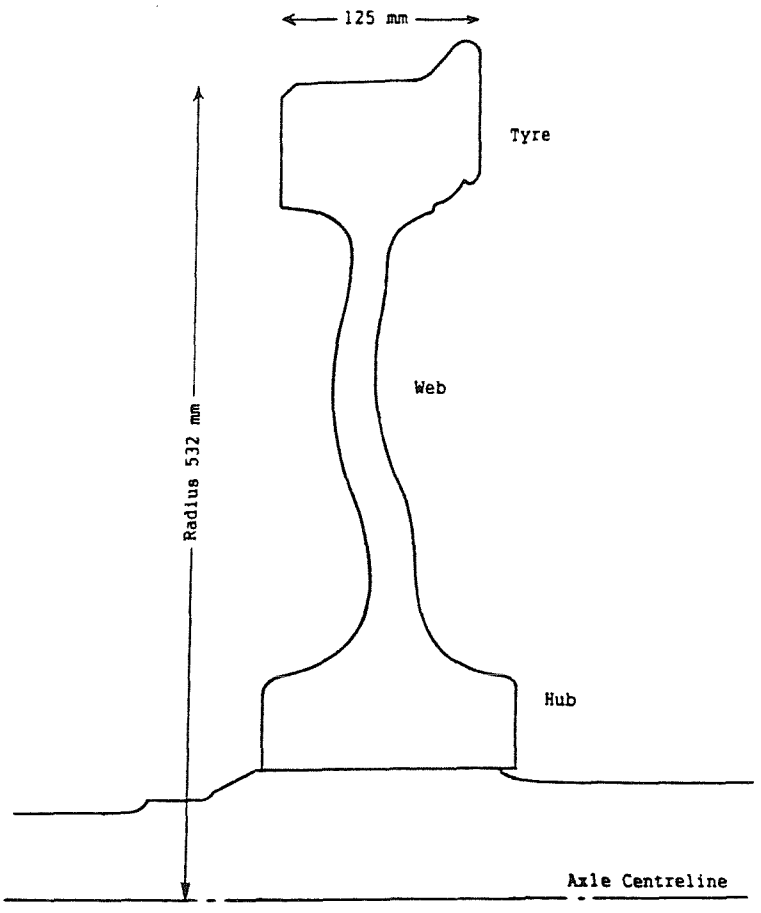

Figure 2 Commonwealth Wheel Cross-section

rolling vibration measurements [47,13]. The cross-section is shown in Figure 2. The nominal diameter of 1.06 m (42 inches) is larger than wheels fitted to many modern coaches which are typically 0.91 m (36 inches) or less. The curved web found on this and many other railway wheels leads to a coupling of radial and axial motions. This manifests itself in the appearance of two distinct groups of modes both exhibiting axial motion with a single nodal circle (m=1). One set is predominantly radial, whilst the other set is predominantly axial (one-nodal-circle), but both sets contain both types of motion to differing degrees [49,93]. This can be seen in the examples of modeshapes for a Commonwealth wheel which are shown in Figure 3, taken from [49]. For the straight-webbed BT10 wheelset no such coupling was evident either in a finite element study [49] or experimentally [54].

The order of these two sets of modes has been found to depend on the radius of the wheel - for larger wheels, such as the Commonwealth type, the set of predominantly radial modes is the higher of the two,

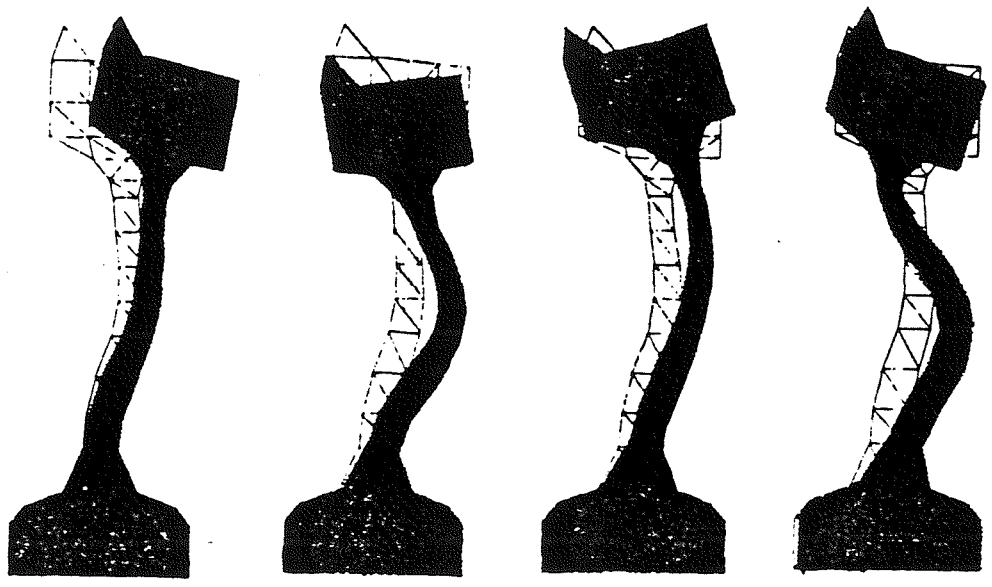

NODAL DIAMETERS	0-NODAL-CIRCLE	1-NODAL-CIRCLE	RADIAL	2-NODAL-CIRCLE
2	294	1390	2025	2765
3	760	1880	2560	3310
4	1375	2440	3060	3940
5	2090	3095	3690	4660
6	2860	3855	4360	
7	3670	4430		
8	4510			

NOTES

1. All frequencies in Hz.
2. Natural frequencies from measurements (Appendix C)
3. Modeshapes of 2 nodal diameter modes from finite element analysis in Ref [49]

Figure 3 Modeshapes and Natural Frequencies for a Commonwealth Wheel

whereas for smaller wheels, such as the 0.84 m diameter wheel fitted to class 150 Sprinters, it is the lower [51].

2.1.2 Summary of this Chapter

The aim of the theoretical work is to predict the frequency response functions (FRFs) of a wheelset. The FRF is the response level due to a unit force input, as a function of excitation frequency. It is known as "receptance", "mobility" or "accelerance" depending on whether the response is expressed as displacement, velocity or acceleration.

The objective is to produce a theoretical model, validated by measured data, which will then be used in the theoretical framework for

noise generation (Figure 1) in conjunction with an equivalent model for the rail response. Validation measurements have been carried out and are described in Appendix C. The measured natural frequencies from Appendix C are listed in Figure 3.

Finite element analysis will be used as the basis of this model. Such analyses of wheelsets are quite common at BR Research and elsewhere, although they are usually limited to finding the normal modes rather than to producing FRFs.

2.2 THEORETICAL MODELS

2.2.1 Finite Element Predictions using Axisymmetric Elements

The "NEWPAC" finite element package [94] includes "harmonic" elements. These elements allow the cross-section of an axisymmetric body to be input, the normal modes then being forced to have a specified sinusoidal variation in the azimuthal direction (cos $n\theta$). Lee [49] used these to model a Commonwealth and a BT10 wheel. Both wheels were assumed to be rigidly constrained at the inner edge of the hub. This idealisation would be expected to be reasonable except for the modes in the zeroth and first harmonics of the structure (ie n=0 and 1). In these, the axle needs to be included explicitly, since its extension and flexure respectively will play a part in such modes of the wheel. (Torsion cannot be included in this axisymmetric model).

Figure 4 shows a comparison between the natural frequencies predicted by Lee for the Commonwealth wheel for n>2 and the measurements of Appendix C. The results show a large degree of similarity, with the deviation being less than 5% below 3500 Hz, rising to 10% by 5000 Hz. The predicted frequencies are higher in each case. This effect was also found for a different wheel design [50] and numerical experiments showed that the principal reasons for it are (i) a lack of refinement in the idealisation, particularly in the wheel web where the structure is only one element thick, and (ii) in the choice of "master" degrees of freedom, particularly in the rim region, where additional masters are necessary to represent cross-sectional deformation. By modifying both of these features, the modes with 6 nodal diameters could be brought within 3% of the measured results.

Lee's idealisation was the starting point for the current work. It appears that Lee's wheel idealisation does not need further development for the n>2 modes, because of the reasonable agreement between its results and the experimental results. In order to extend

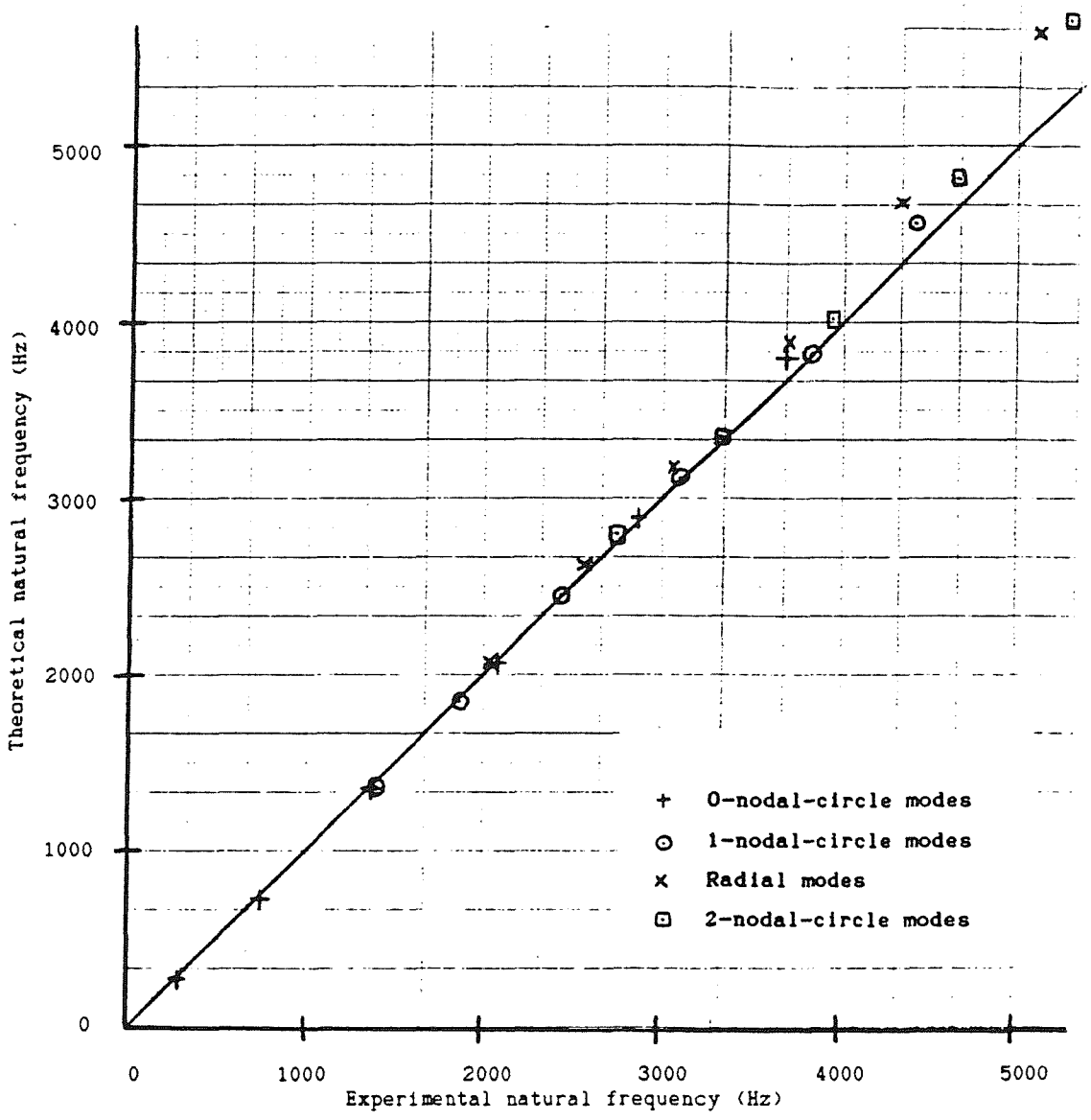

Figure 4 Comparison of Natural Frequencies Predicted by the Axisymmetric Finite Element Model with Experimental Results

it for n=0 and 1, the axle has also been modelled by axisymmetric elements, as shown in Figure 5. Structural symmetry at the centre of the axle is employed to reduce the size of the idealisation.

The "NEWPAC" program employs Guyan reduction [95] to reduce the size of the mass and stiffness matrices before calculating natural frequencies and modeshapes. For this method, "master" degrees-of-freedom must be specified, which need to be relatively evenly distributed throughout the structure, particularly concentrating on areas of high mass. The master degrees-of-freedom employed are shown in Figure 5.

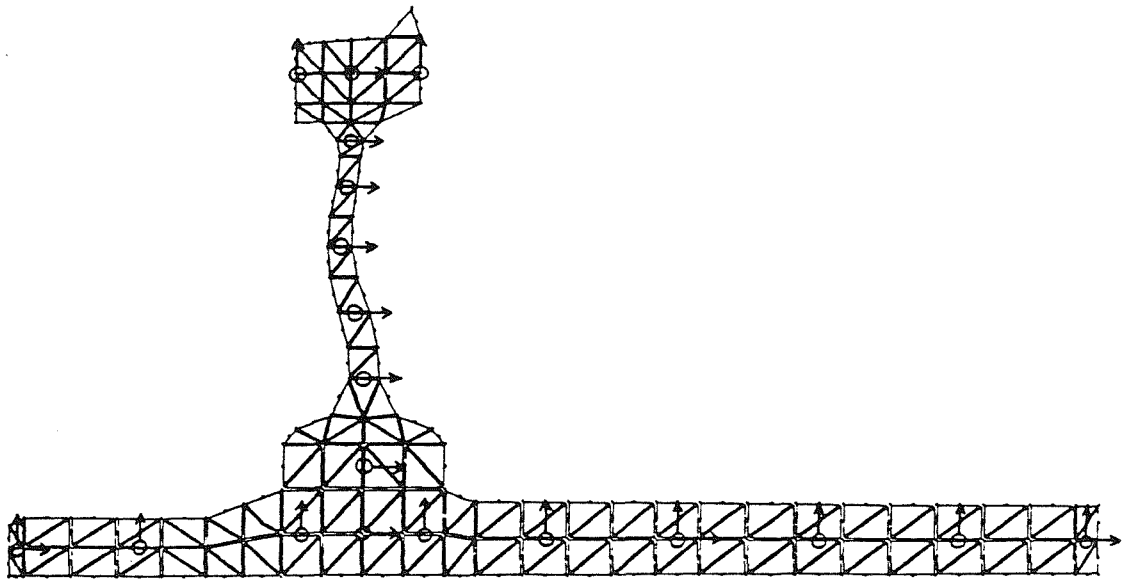

Figure 5 Finite Element Idealisation using Axisymmetric Elements showing Master Degrees of Freedom (O→)

Using this idealisation, predictions were also carried out for the n=2 and n=6 modes, and the natural frequencies were compared with those of Lee, as a check. The first three modes in each case were found to agree to within 1%, although for higher order modes, with more nodal circles, the increased flexibility at the hub caused a slight reduction in their natural frequencies.

The idealisation described so far has free axle ends. However the measurements in Appendix C were made on a wheelset with its axle ends supported in bearings in the axleboxes, which are themselves supported. This arrangement is more typical of a wheelset in situ under a vehicle. Two alternative idealisations were therefore used to evaluate the effects of the axleboxes. The first consisted of solid axleboxes rigidly attached to the ends of the axle. These are by necessity cylindrical, whereas in practice the axleboxes are of a more complex shape, and are not solid, but built-up containing the bearings. The second consisted of a fixed constraint applied to the bearing surface.

The resulting natural frequencies predicted by each of the three idealisations are listed in Table 1, together with a description of the modeshape applying to the first idealisation. Because of coupling between the wheel and axle modes, the modeshapes are not always very clear, so the descriptions are meant only as a general guide. The

Table 1 Natural frequencies from axisymmetric finite element models

(a) Harmonic 0

Without axle [49]	Symmetric at axle centre			Antisymmetric at axle centre			Description
	a	b	c	a	b	c	
187	179	179	185	282	266	184	Dishing
-	784	688	1735	-	-	-	Axle extension
1193	1272	1243	1151	1229	1221	1073	1-nodal-circle
2333	2399	2384	2427	2251	2206	2290	2-nodal-circle
-	-	-	-	2496	2426	1337	Axle mode
-	-	-	-	-	-	2593	Axle mode
2777	2939	2861	3061	3002	2866	3299	Radial wheel mode

(b) Harmonic 1

Without axle [49]	Symmetric at axle centre			Antisymmetric at axle centre			Description
	a	b	c	a	b	c	
-	53.6	51.7	95.9	-	-	-	Axle mode, 2 nodes
-	-	-	-	98.8	98.6	112	Axle mode, 3 nodes
135	257	236	235	485	372	384	1-nodal-diameter (wheel in opposition to axle)
-	700	539	543	-	-	-	Axle mode, 4 nodes
-	-	-	-	1025	892	867	Axle mode, 5 nodes
947	1153	1089	1040	1198	1187	1176	Radial wheel mode
1566	1565	1578	1630	1777	1853	1961	1-nodal-circle
-	1979	2034	2144	-	-	-	Axle mode
2460	2406	2349	3213	2349	2297	2638	2-nodal-circle
-	-	-	-	2658	2658	3564	Axle mode

KEY:-
a = with free axle ends
b = with solid axleboxes attached to axle ends
c = with axle ends rigidly constrained
All frequencies in Hz.

left-most column gives the equivalent natural frequencies found without the axle where appropriate. The degree to which the choice of model of the axle end affects the natural frequencies depends on the amount of motion of the axle end in a particular mode. Thus no effect is expected on the n>2 modes of the wheel.

Comparing the experimental axle bending modes (Table C2) with the equivalent predicted natural frequencies (Table 1(b)) shows generally good agreement. Figure 6 shows this comparison for each of the three idealisations. Three experimental modes are unresolved here: the 290 Hz, 1280 Hz and 2750 Hz modes have no obvious theoretical counterparts, although the latter is plotted against the 2-nodal-circle predicted mode. Conversely the one-nodal-diameter/antisymmetric mode

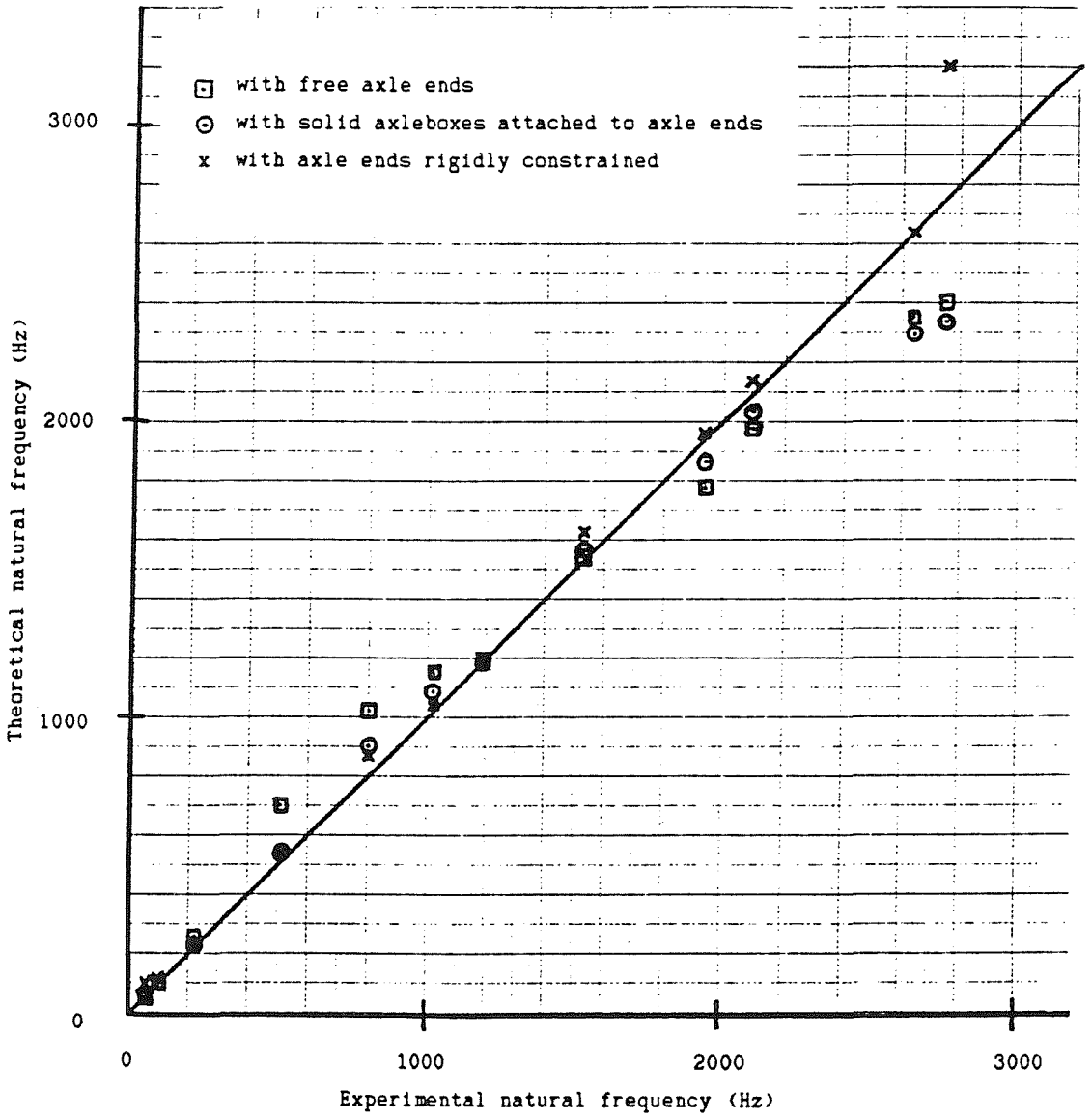

Figure 6 Comparison of Axle Mode Natural Frequencies Predicted by the Axisymmetric Finite Element Model with Measured Results (Appendix C)

has no experimental counterpart. The peaks at 1280 Hz and 2750 Hz were actually both quite sharp, and may correspond to wheel modes (n>2).

The first two models (free axles and added axleboxes) give much better agreement with the first two experimental modes than the third model (constrained axle end). In the mid frequencies the second and third models give the best agreement with the experimental results, and at high frequencies the third model alone gives good agreement. This suggests that the model should be chosen depending on the frequency range of interest. In fact the axlebox appears to be adding mass at lower frequencies, and constraint at higher frequencies.

2.2.2 Finite Element Predictions using Plate and Beam Elements

An alternative idealisation has been developed using plate and beam elements, to avoid the restrictions imposed by the axisymmetric assumptions about the structure and the constraints. For example this idealisation could be used to study the effect of adding radial stiffeners to a wheel. Another advantage of this type of idealisation is that realistic modal masses are calculated by the "NEWPAC" program for these element types, whereas this is not the case for the harmonic elements. This means that the modal parameters can be used in a modal sum to predict FRFs.

The idealisation which has been used is shown in Figure 7. The line elements in this figure (the axle and the rim) are beams, which include provision for torsion, extension and bending, including shear deformation and rotational inertia. The beams representing the rim are elements known as "referred beams" in which the beam axis is remote from the points to which it is connected. The links at either end of the beam element are taken as being rigid.

The quadrilateral elements (on the wheel web) are thin plates. The plate elements representing the hub are very thick and so the thin plate theory will not strictly be correct. However the motion in these parts of the wheelset will in any case not be very great on account of the hub thickness. The triangular elements connecting the hub to the axle are also plate elements. Their function is simply to prevent relative motion between the axle centreline and its outer surface, as the axle beams are represented only by their centreline. These elements have no mass as the mass of this region is already included in the structure by the axle beams.

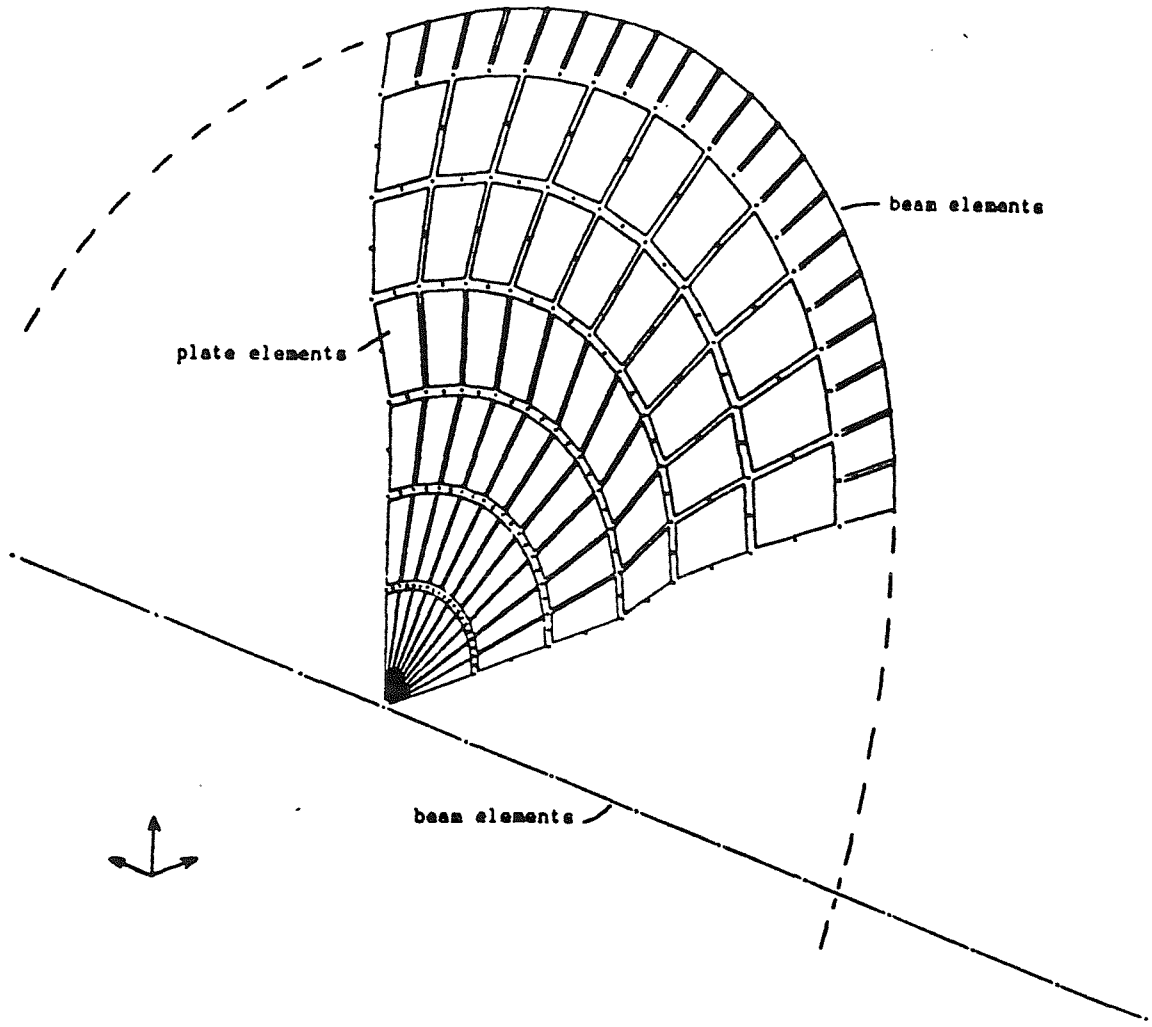

Figure 7 Finite Element Idealisation of 1/8 of a Wheelset using Plate and Beam Elements

It was found to be necessary to adjust slightly some of the parameters input for the beams representing the rim. Since the beam is connected to a plate along one edge by a rigid link the beams turned out to be too stiff using the values for moment of area and shear area derived directly from the beam geometry. These parameters were adjusted until a reasonable agreement was found with the harmonic model in terms of the natural frequencies of modes up to 4000 Hz. The resulting parameters were:

- the moment of area referring to lateral bending of the rim was reduced by 10%,

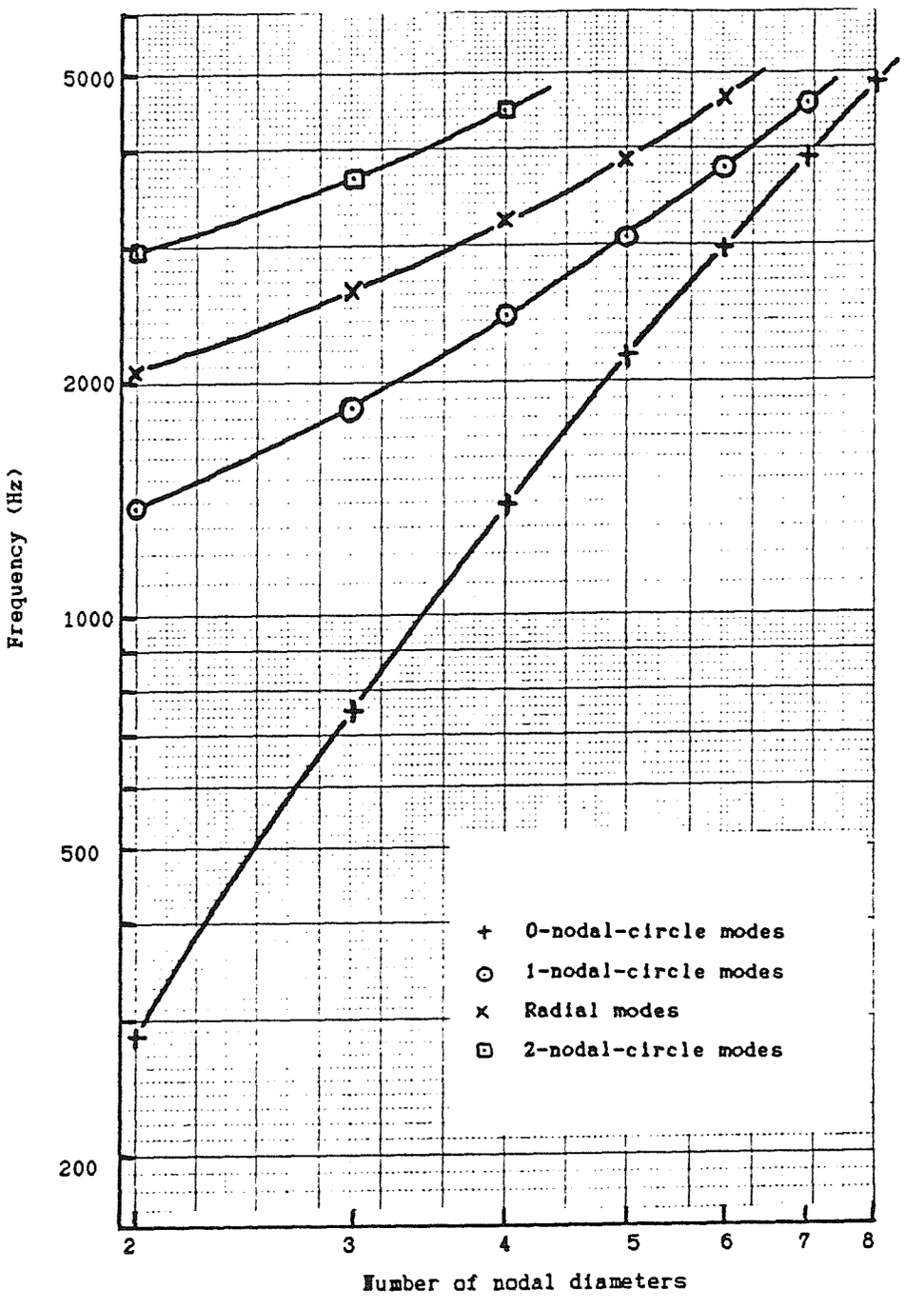

Figure 8 Natural Frequencies Predicted by the Plate/Beam Finite Element Model

- the shear coefficient (the proportion of the cross-sectional area which is effective in shear) referring to the same direction was reduced to 2/3 (instead of 5/6 which is used normally for rectangular beam cross-sections - see for example [96]).

These values appear to be justified when it is considered that wheel rim cross-section is not rectangular and its major axis is inclined at about 15° to the radial direction. By eliminating the corners, which would not be particularly effective in shear, this results in a shear coefficient of around 2/3.

With these values, the natural frequencies, which are shown in Figure 8, were mostly brought within 5% of the axisymmetric results. Exceptions were the two-nodal-circle modes, where insufficient detail in the web leads to an increase in their natural frequencies.

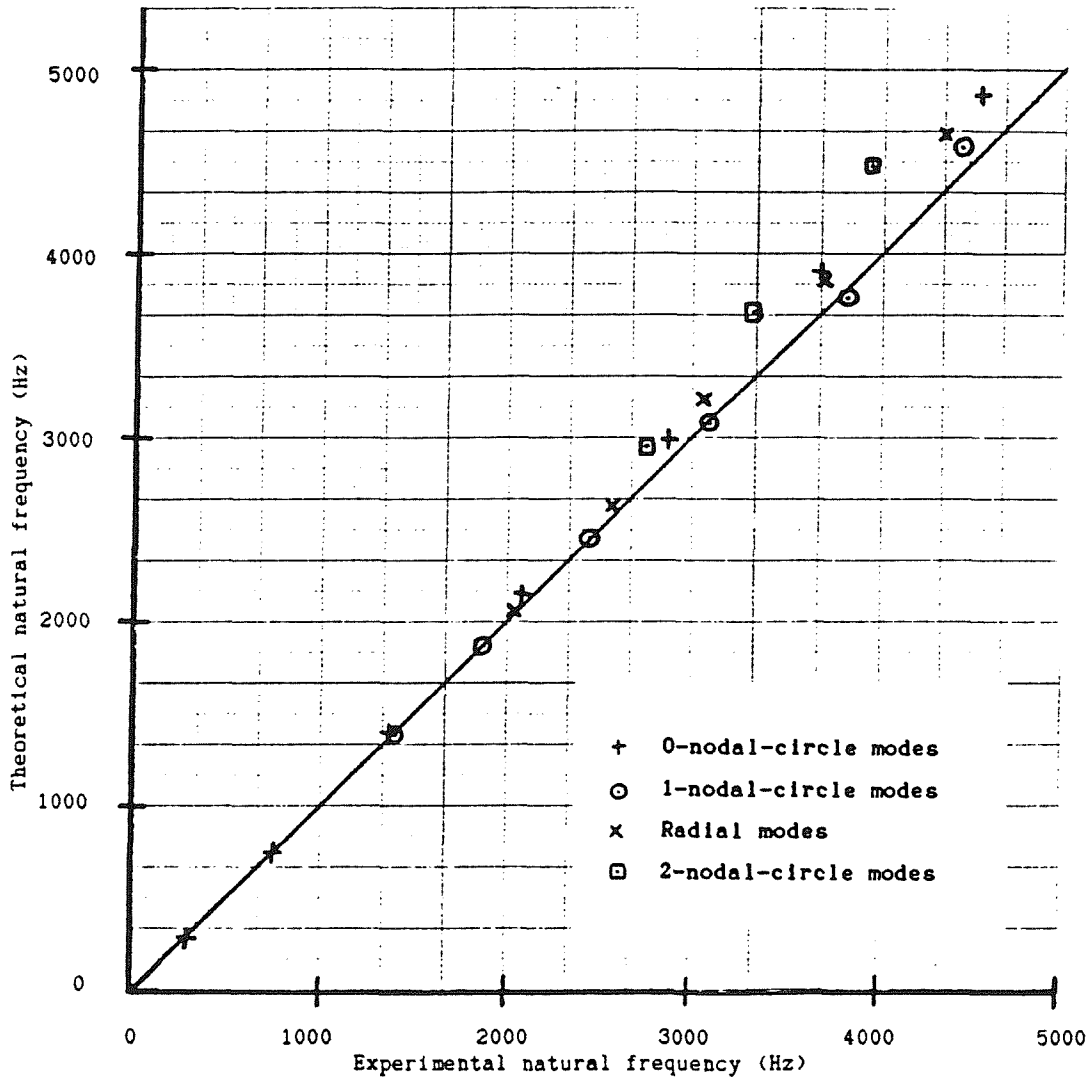

Figure 9 Comparison of Natural Frequencies Predicted by the Plate/Beam Finite Element Model with Measured Results (Appendix C)

The agreement with the experimental results is shown in Figure 9. It is not quite so good as was the case with the axisymmetric idealisation, particularly for 2-nodal-circle modes, but is still within 12% below 5000 Hz.

2.2.3 Modal Sum Calculations

By modelling a structure as a multi-degree-of-freedom system, its FRFs can be derived in terms of its natural frequencies and their corresponding modeshapes and damping loss factors. (See for example Ewins [97]).

The receptance $\alpha_{jk}(\omega)$, representing the response at the point x_j to a unit force applied at x_k, at the frequency ω, can be written as:-

$$\alpha_{jk}(\omega) = \sum_{r=1}^{\infty} \frac{{}_r\psi_j \; {}_r\psi_k}{m_r(\omega_r{}^2-\omega^2+2i\zeta_r\omega_r\omega)} \qquad \ldots(1)$$

where ${}_r\psi_j$ is the modeshape factor of the rth mode at x_j (in the direction of the response), and ${}_r\psi_k$ is the modeshape factor of the rth mode at x_k (in the direction of the force),

m_r is the modal mass for the rth mode (which depends on the normalisation used for the modeshapes),

ω_r is the rth natural frequency,

and ζ_r is the damping ratio for the rth mode.

In practice, the modal sum involves an approximation in the selection of a finite set of normal modes. The modes with frequencies lower than ω_M are then included in a mass residue term, R_{jk} and those above ω_N are included by a stiffness residue term, S_{jk}. For example,

$$R_{jk}(\omega) = \sum_{r=1}^{M-1} \frac{{}_r\psi_j \; {}_r\psi_k}{m_r} = \frac{1}{M_R} \qquad \text{for } \omega >> \omega_{M-1} \qquad \ldots(2)$$

where M_R represents the residual mass. Hence,

$$\alpha_{jk}(\omega) = \sum_{r=M}^{N} \frac{{}_r\psi_j \; {}_r\psi_k}{m_r(\omega_r{}^2-\omega^2+2i\zeta_r\omega_r\omega)} - \frac{R_{jk}(\omega)}{\omega^2} + S_{jk}(\omega) \qquad \ldots(3)$$

where $S_{jk}(\omega)$ is the stiffness residue. M and N are chosen so that the frequency range of interest lies within the range ω_M to ω_N.

For lightly damped structures, the viscous and hysteretic damping approximations give virtually the same FRFs, since the damping only

affects a narrow band of frequency around each resonance, the width of which is proportional to the damping. They are then related by:-

$$\text{loss factor } \eta_r \simeq 2 \times \text{damping ratio } \zeta_r \qquad \ldots(4)$$

In the case of general damping, the modeshape factors, ${}_r\psi_j$ and ${}_r\psi_k$, may be complex numbers (representing the flow of energy from one part of the structure to another where the damping is heavier). However if the damping is equally spread out through the structure, it can be approximated as "proportional" damping, in which the damping matrix is proportional to a linear combination of the stiffness and mass matrices. In this case the modeshapes are real, and they and the natural frequencies are equal to those which would apply for zero damping.

The "NEWPAC" program calculates the undamped natural frequencies and modeshapes. Thus an estimate of the FRFs can be derived from these parameters, on the assumption of proportional damping, and by assuming a value for the modal damping ratios or loss factors, which cannot be predicted by this analysis of the undamped structure.

In practice the wheel and axle are likely to be well approximated by proportional damping with the exception of the bearings, where localised damping may be present. Hence for wheel modes (n>2) the above assumptions should be valid, but difficulties may occur for the axle-dominated modes (n=0 or 1 on the wheel).

A computer program has been specially written to calculate the axial and radial point and cross FRFs of a wheelset from a list of modal properties. The input data for each mode consist of the natural frequency, the radial, axial and twist components of the modeshape (ie ${}_r\psi_j$ etc), the modal mass, and the damping ratio. (The twist component is used to modify the radial and axial components to make them correspond to the running surface, which is not at a calculation point (node) of the finite element idealisation). Other parameters such as the mass residue, and the frequency range over which calculations are to be made, can also be input.

The FRF is then calculated from equation (3) above for various frequencies in the range selected. The frequency increment between successive calculations is varied to ensure that sufficient resolution is obtained at the resonances and anti-resonances without wasting computing time on the intermediate points. This is regulated by

specifying the maximum difference between successive results in dB (the default value is 10 dB).

The modal parameters predicted by the "NEWPAC" program for the first 56 normal modes (all modes up to 5000 Hz) using the plate/beam idealisation were used to predict the various accelerances. The rigid body modes have been included into the mass residues, but no stiffness residue term was included. The only parameter which cannot be predicted by the finite element idealisation is the modal damping ratio. For this a nominal value of .0001 has been used, to prevent the curves from tending to infinity at the resonances.

The results for the lateral and vertical point accelerances and the cross accelerance based on the plate/beam model are shown in Figures 10-12.

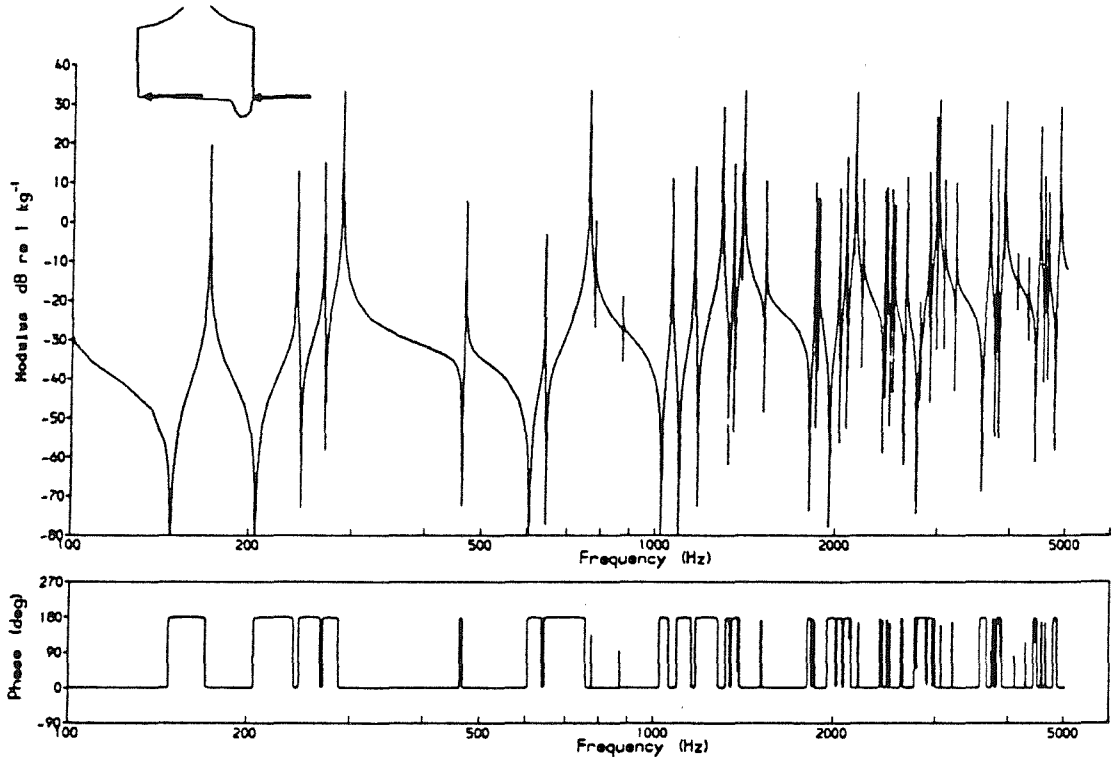

Figure 10 Lateral Point Accelerance from Plate/Beam Model with Nominal Damping

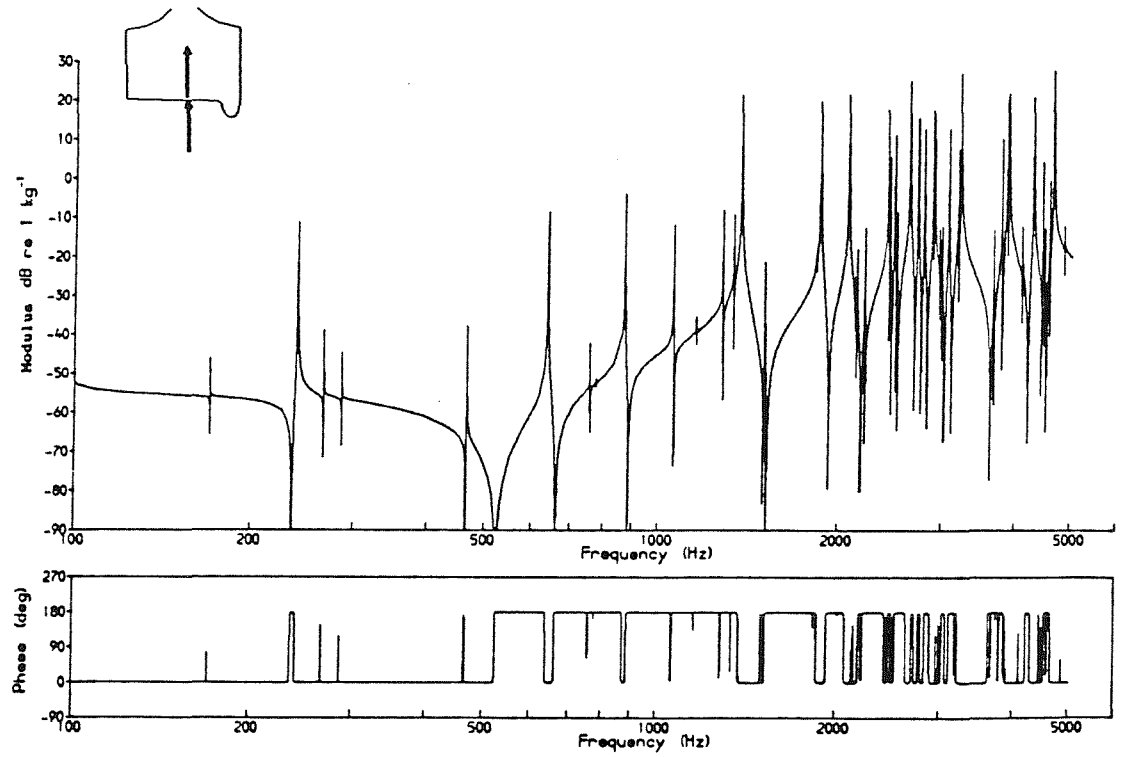

Figure 11 Vertical Point Accelerance from Plate/Beam Model with Nominal Damping

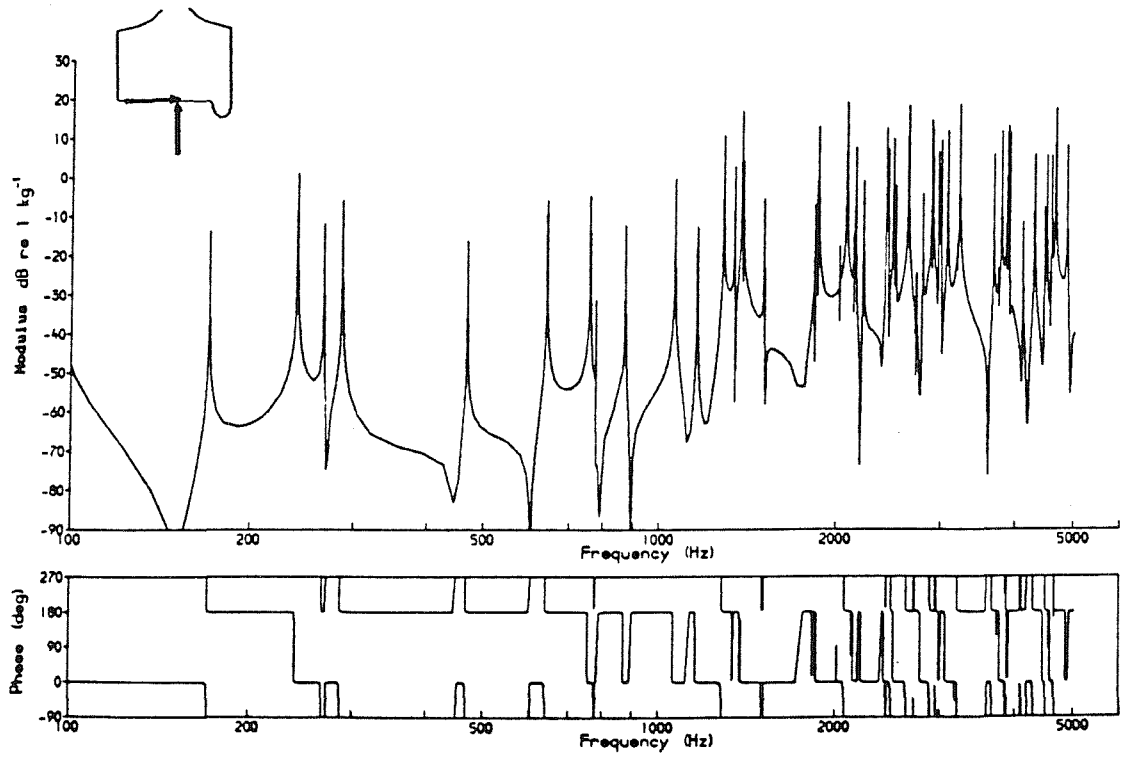

Figure 12 Cross Accelerance from Plate/Beam Model with Nominal Damping

2.3 DISCUSSION

2.3.1 Comparison of Modal Sum Predictions with Experimental Results

A direct comparison of predicted FRFs (Figures 10-12) with measured FRFs (Appendix C: Figures C3-6) shows the predictions to be much more peaky. This is due to the assumption of a constant modal damping of .0001. Clearly many of the modes have much higher damping than this, particularly the modes involving axle vibration. However the sharper peaks in the experimental data (which are the wheel modes) have been curtailed by the fixed frequency resolution of the analysis (bias errors).

In order to ascertain modal parameters which more closely represent the experimental results, and to verify the modal sum technique, the damping and the natural frequencies have been optimised manually relative to the experimental results.

Figures 13-15 show the modified results of the modal sum predictions. The wheel modes have been given damping ratios in the range .0001 to .0005, in line with those measured by Perry [53], but

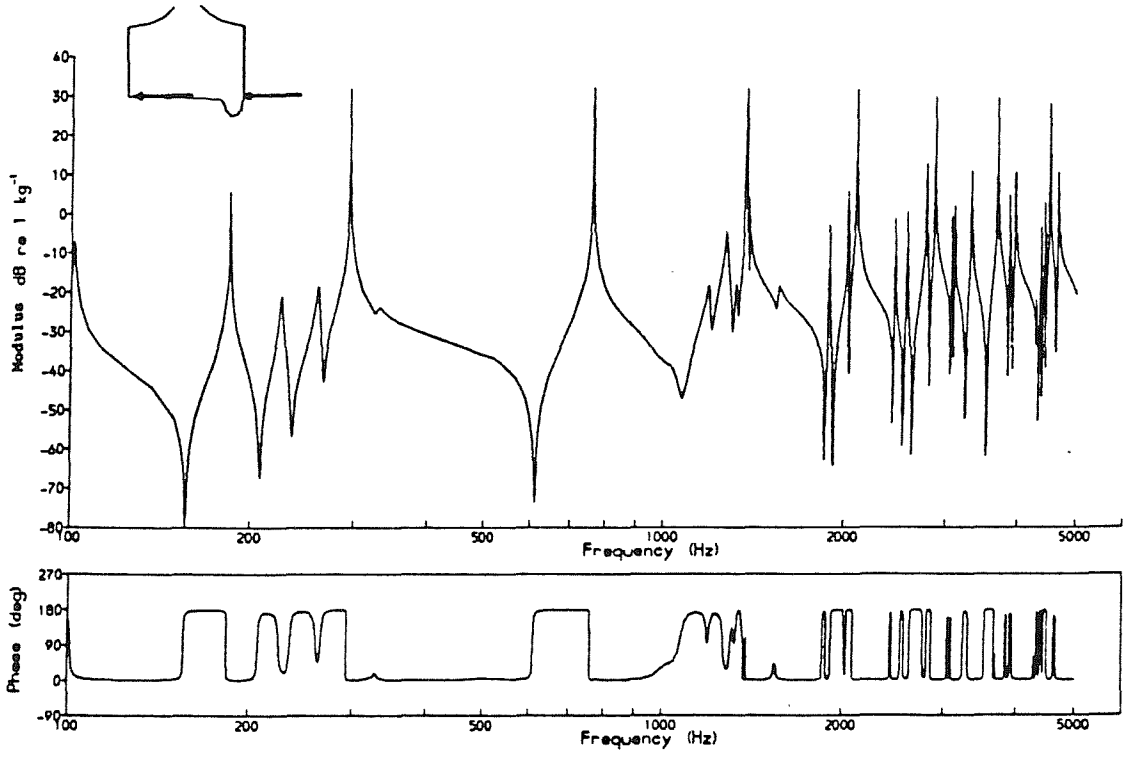

Figure 13 Lateral Point Accelerance from Plate/Beam Model with Adjusted Parameters

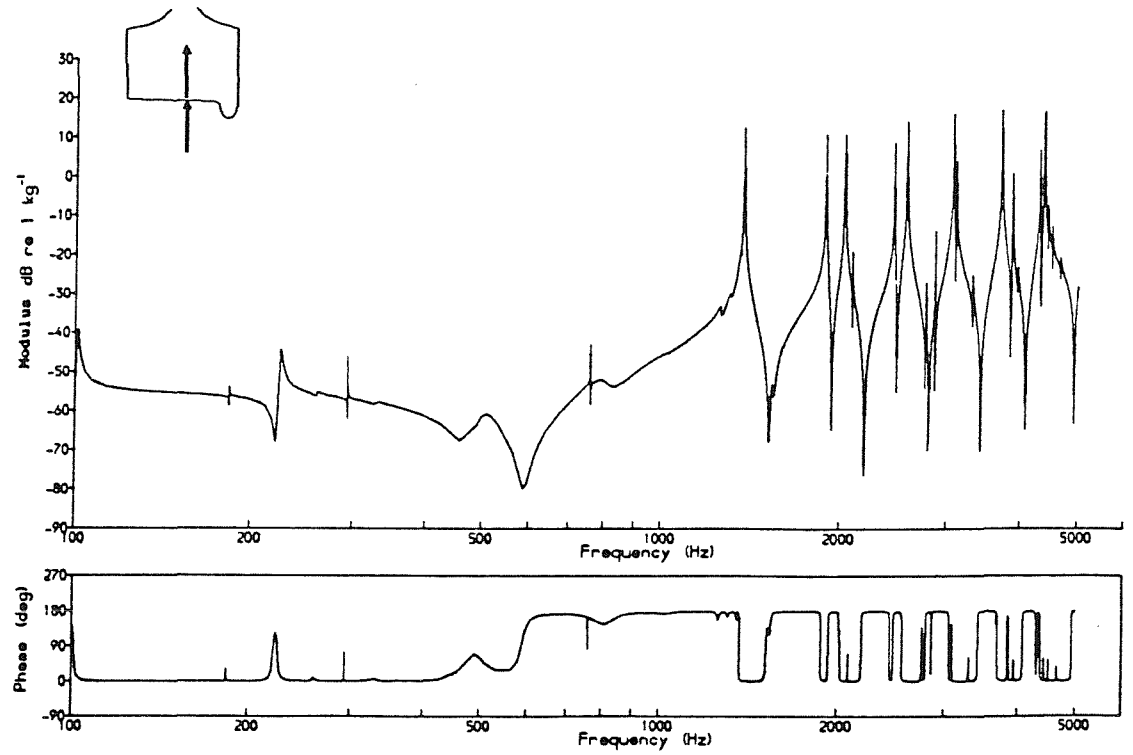

Figure 14 Vertical Point Accelerance from Plate/Beam Model with Adjusted Parameters

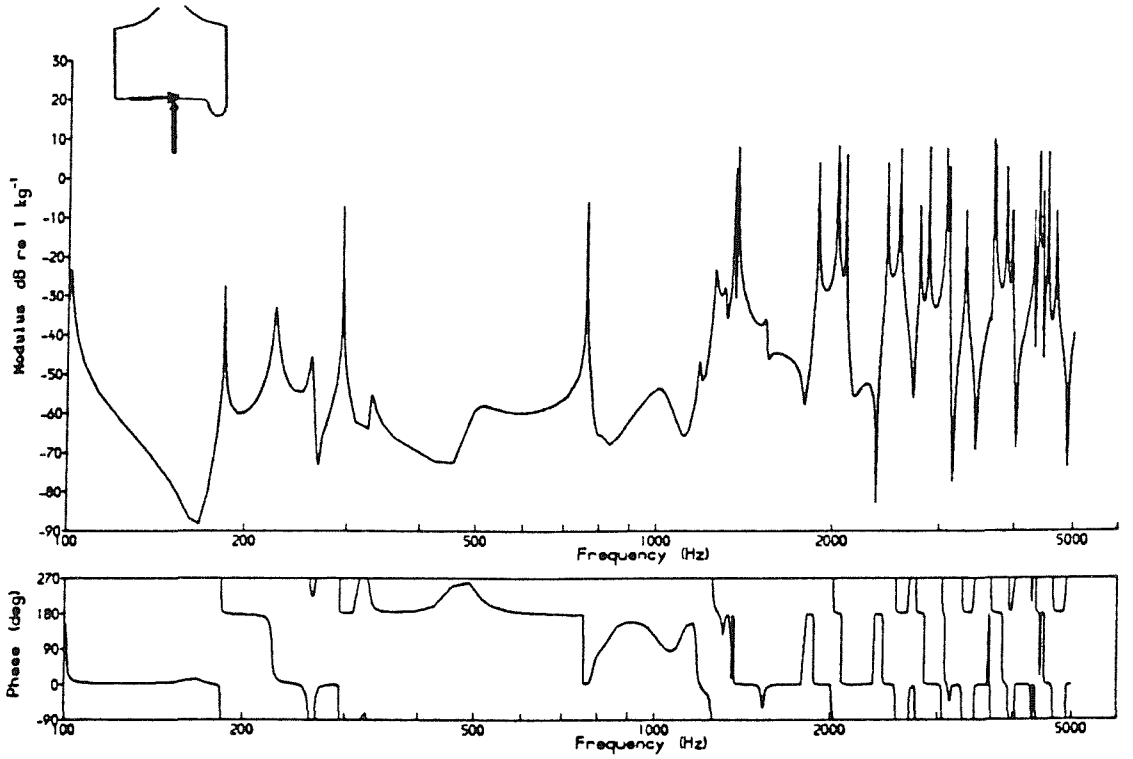

Figure 15 Cross Accelerance from Plate/Beam Model with Adjusted Parameters

based on an average for each mode type. Thus .00012 has been used for all the nodal-diameter-only modes, .00028 for all the one-nodal-circle modes, etc. These values of damping give sharper peaks than the current experimental data, but as explained above, this is due to a limitation of the experimental data. The modes involving axle vibration have been given damping ratios in the range .001 to .1, chosen to give closest agreement with the experimental results, in terms of the shape of the resonance peaks.

For simplicity the axle modes (n=0 and 1) above 1600 Hz were omitted from the modal sum at this stage. This omission seemed to have little effect on the FRFs, and was done as these modes could not be identified so easily as lower order axle modes.

2.3.2 Effectiveness of Prediction Technique

It has been shown that it is possible to give a good representation of the FRFs using the modal sum calculation technique, using resonance parameters from finite element analysis and measured modal damping. However it is clear that significant differences at a particular frequency are possible with only small changes in modal parameters (particularly near resonances if the resonance frequencies differ), so care must be taken in this respect.

These differences will have resulted in part from inaccuracies and over-simplification in the finite element model, but the cone angle of the wheel (1:20) will also have affected the measured results, as the radial measurements were not truly radial.

The cross accelerance is particularly sensitive to changes in modal amplitudes, as their sign is also important, ie the relative directions of the two components. Large differences off-resonance can be produced by a change in sign of a mode, due to changes in the positions of anti-resonances.

The mass residues included in the modal sums were based on the masses active in rigid body modes of the wheelset. These seem to be about right for the two point accelerances, but for the cross accelerance better agreement with experiment was found with zero mass residue. This can be explained by the effect of cone angle on the first axle mode (at 55 Hz), which is not plotted.

Although high frequency axle modes appear to have little effect on the modal sum, at low frequencies axle modes contribute signifi-

cantly to the frequency response. To illustrate this, Figure 16 shows the axial accelerance with all the axle modes omitted. Comparing this with Figure 13 reveals large differences, particularly below 300 Hz, but with differences as much as 20 dB in the range 300-1400 Hz.

The axle modes, which are quite heavily damped in comparison with the wheel modes, tend to raise and move the anti-resonances, so they may have an effect even where their peak may be hardly discernable in the FRF.

In order to predict for a different wheel design, it would be necessary either to base damping estimates on those used for the Commonwealth-type wheelset, or to take measurements. So long as the design were not too dissimilar, the former approach would probably be sufficient.

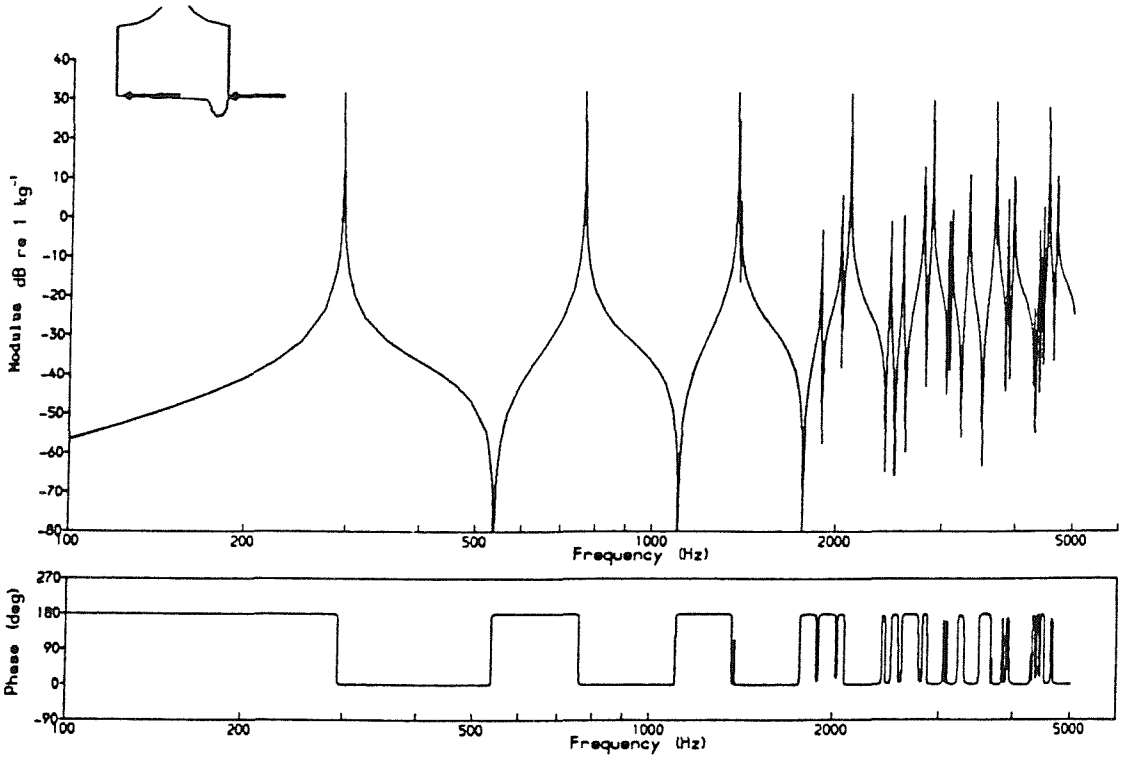

Figure 16 Lateral Point Accelerance from Plate/Beam Model without Axle Modes

2.4 CONCLUSIONS

The vibration behaviour of a Commonwealth-type wheelset has been studied theoretically and the results have been compared with measurements.

Two different finite element idealisations were used to predict the natural frequencies and modeshapes, with a good level of agreement being found between them as well as with measured natural frequencies.

A modal sum technique has been used to predict the frequency response functions (radial, axial and cross), starting from the modal parameters derived from the finite element predictions. The modal damping had to be based on measurements, but it is envisaged that predictions for a different wheel type could be based on these same values of damping.

For frequencies below about 1600 Hz, it has been found to be essential to include into the modal sum modes of vibration involving the axle. This is despite the fact that their damping is high and their amplitudes are relatively low.

The cross accelerance has been found to be more difficult to predict accurately than the point accelerances. This is due to the need to include the sign of the relevant modeshape parameters as well as their amplitudes. Particular difficulties are caused by modes which have nodal circles near the excitation point, as the relative accuracy of their modeshape parameters is reduced.

CHAPTER 3

INITIAL IMPLEMENTATION OF THE INTERACTION MODEL

3.1 REMINGTON'S MODEL FOR ROLLING NOISE GENERATION

Equipped with a model of the wheel frequency response, it is now possible to implement, and make an initial assessment of the wheel-rail interaction model of Remington [15,18,20,21].

Figure 1 showed a block diagram of this overall model for wheel-rail rolling noise generation. The source of the noise is assumed to be the combined surface roughnesses of the wheel and the rail. These are assumed to generate interaction forces in the contact patch and hence cause vibrations in the wheel and rail, which then radiate noise. Only the generation of vibrations is studied here, not the radiation.

In this chapter, the mathematical formulation of the wheel-rail interaction model is given. Although based on Remington's model it uses a modified notation (in particular, receptances are used in place of impedances for the various system components), and it includes some refinements.

The dependence on its various input parameters is then studied in some detail, and comparisons are made with the experimental results which are presented in Appendix A.

3.1.1 Formulation

Figure 17 shows the wheel-rail contact region schematically. A surface roughness irregularity, r, consisting of wheel and rail components (r_W and r_R), introduces a relative displacement between the wheel and the rail. This displacement must be taken up by the flexibility of the wheel, the flexibility of the rail and the compliance of the Hertzian contact spring between them. This gives an equation for the vertical displacements (following the sign convention of Figure 17):-

$$z_R = z_W - z_C + r \qquad \ldots(5)$$

where z_R and z_W are the vertical displacements (downwards) of the rail and the wheel respectively, and z_C is the vertical compression of the contact spring. In Figure 17 this contact spring, k_H, is shown in two

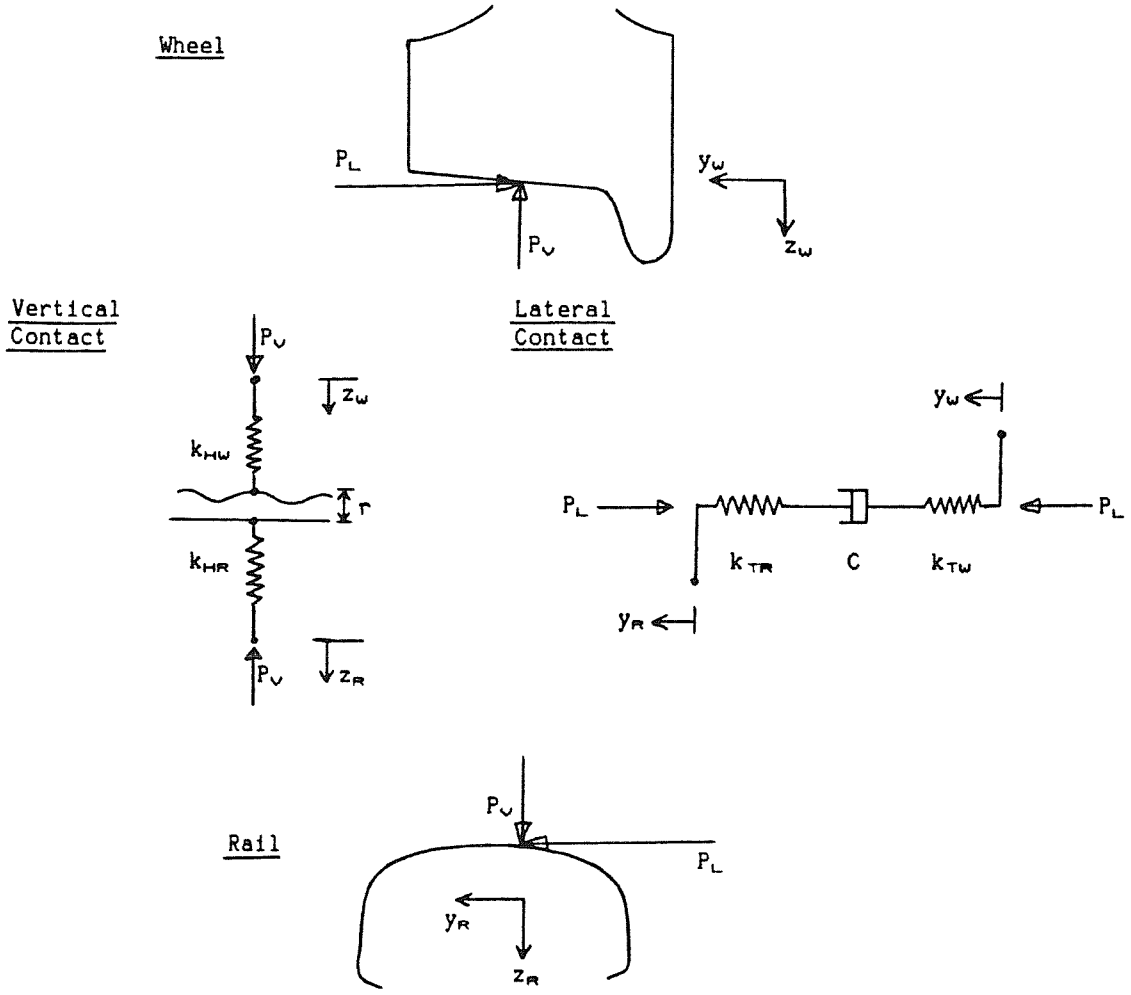

Figure 17 Schematic Diagram of Wheel-Rail Contact Region

parts, k_{HW} in the wheel and k_{HR} in the rail, although only their combined effect will be considered here. This gives z_C as:-

$$z_C = \frac{P_V}{k_H} = P_V \left(\frac{1}{k_{HW}} + \frac{1}{k_{HR}} \right) \qquad \ldots(6)$$

where P_V is the vertical contact force. The Hertzian contact spring is actually non-linear, but k_H is a linear approximation for it, valid for small deflections. Hysteretic damping could also be included into these spring elements by making k_H a complex quantity, although in practice this effect will be very small.

Whilst the above equations have been formulated in the time domain, where $z=z(t)$ etc, since the model is linear, they can also be taken to apply in the frequency domain where $z=z(\omega)$ etc, by Fourier transformation. Each term is then a complex function of ω, including phase information as well as amplitude.

A similar equation can be written for the lateral displacements, except that no roughness input is present in this direction:-

$$y_R = y_W - y_C \qquad \ldots(7)$$

where y_R and y_W are the lateral displacements of the rail and the wheel respectively, and y_C is the relative lateral motion in the contact region. For the particular arrangement shown in Figure 17, this is given by:-

$$y_C = P_L \left(\frac{1}{k_{TW}} + \frac{1}{i\omega C} + \frac{1}{k_{TR}} \right) \qquad \ldots(8)$$

where P_L is the lateral contact force, k_{TW} and k_{TR} are the transverse contact stiffness components of the wheel and rail, which again can be combined into a single stiffness k_T, and C is the viscous damping equivalent to the creep force. Compared with the vertical vibration, C is an additional term representing the lateral creep force acting on the wheel and rail, which is proportional to their relative velocity (hence the use of a damper, cf Ferguson [56]).

It should be noted that the cone angle of the wheel could be included by taking 'vertical' to refer to the direction normal to the wheel surface, and 'lateral' to refer to that tangential to it.

At a given frequency the displacements can be written in terms of the vertical and lateral contact forces and the relevant receptances. Taking account of the sign conventions shown in Figure 17 this gives:-

$$\begin{aligned} z_R &= P_V\,\alpha^R_{VV} + P_L\,\alpha^R_{VL} & \qquad y_R &= P_V\,\alpha^R_{LV} + P_L\,\alpha^R_{LL} \\ z_W &= -P_V\,\alpha^W_{VV} - P_L\,\alpha^W_{VL} & \qquad y_W &= -P_V\,\alpha^W_{LV} - P_L\,\alpha^W_{LL} \\ z_C &= P_V\,\alpha^C_{VV} + P_L\,\alpha^C_{VL} & \qquad y_C &= P_V\,\alpha^C_{LV} + P_L\,\alpha^C_{LL} \end{aligned} \qquad \ldots(9)$$

where the α's are receptances of the rail (R), the wheel (W) and the wheel-rail contact zone (C). Note that, by reciprocity, it is expected that $\alpha_{VL}=\alpha_{LV}$ in each case.

3.1.2 Force Equations

Substituting equations (9) into equations (5) and (7), gives two equations for the two contact forces:-

$$P_V\,(\alpha^R_{VV} + \alpha^W_{VV} + \alpha^C_{VV}) + P_L\,(\alpha^R_{VL} + \alpha^W_{VL} + \alpha^C_{VL}) = r$$

$$P_V\,(\alpha^R_{VL} + \alpha^W_{VL} + \alpha^C_{VL}) + P_L\,(\alpha^R_{LL} + \alpha^W_{LL} + \alpha^C_{LL}) = 0 \qquad \ldots(10)$$

These can be expressed more simply by defining the three bracketed terms as combined receptances of the whole system:-

$$\begin{aligned} \alpha_{VV} &= \alpha^R_{VV} + \alpha^W_{VV} + \alpha^C_{VV} \\ \alpha_{VL} &= \alpha^R_{VL} + \alpha^W_{VL} + \alpha^C_{VL} \\ \alpha_{LL} &= \alpha^R_{LL} + \alpha^W_{LL} + \alpha^C_{LL} \end{aligned} \qquad \ldots(11)$$

which allows the forces to be expressed as:-

$$P_V = \frac{\alpha_{LL}\, r}{\alpha_{VV}\,\alpha_{LL} - \alpha_{VL}\,\alpha_{VL}} \qquad P_L = \frac{\alpha_{VL}\, r}{\alpha_{VL}\,\alpha_{VL} - \alpha_{VV}\,\alpha_{LL}} \qquad \ldots(12)$$

3.1.3 Response Equations

The contact forces can be used to calculate the response displacement (or velocity or acceleration) either at the contact point, or, by using transfer receptances, at any remote point, such as the position of an accelerometer in the measurements. For example, at a point (and in a specified direction) X on the wheel, the transfer receptance is the response at X to a force at another point, in this case the contact point. Two such transfer receptances are required, to give the response due to a unit vertical force, α^W_{XV}, and due to a unit lateral force, α^W_{XL}. Noting that the forces acting on the wheel are $-P_V$ and $-P_L$, the response, u_{WX}, at X is given by:-

$$u_{WX} = -\,P_V\,\alpha^W_{XV} - P_L\,\alpha^W_{XL} \qquad \ldots(13)$$

For the response at the contact point, this is the same as the equation already derived (equations (9)). Eliminating the forces, using equations (12), gives:-

$$\frac{u_{WX}}{r} = \frac{-\,\alpha^W_{XV}\,\alpha_{LL} + \alpha^W_{XL}\,\alpha_{VL}}{\alpha_{VV}\,\alpha_{LL} - \alpha_{VL}\,\alpha_{VL}} \qquad \ldots(14)$$

Similarly for the rail:-

$$\frac{u_{RX}}{r} = \frac{\alpha^R_{XV}\,\alpha_{LL} - \alpha^R_{XL}\,\alpha_{VL}}{\alpha_{VV}\,\alpha_{LL} - \alpha_{VL}\,\alpha_{VL}} \qquad \ldots(15)$$

3.1.4 Excitation by the Roughness Profile

In the above analysis, a roughness, r, has been introduced which has been taken as a function of frequency, ω. The excitation process is generally assumed to be linear, so that for a given wavelength, the result is a displacement input at the passing frequency. Hence a wavelength λ is equivalent to an excitation frequency of,

$$\omega = \frac{2\pi V}{\lambda} \qquad \ldots(16)$$

A combination of a frequency range of 250-5000 Hz, and a speed range of 40-160 km/h (as used in Appendix A), yields an overall roughness wavelength range of 200-2 mm.

This implies that taking the spectrum of the roughness profile, as measured, should produce the required input. In practice, however, some modification to the measured roughness profiles is required, before they can be converted into spectra. (The experimental results described in Appendix A contain some of these modifications).

1) A method of combining the surface roughnesses of the wheel, r_W, and the rail, r_R, has to be devised. It is usual to assume that the two surfaces are random and uncorrelated, and hence their spectra can be added (in an energy sum) [20]. This would appear reasonable: although the wheel roughness is periodic, with the circumference of the wheel (or at least pseudo-periodic as a different rolling line is probably taken on each revolution), the rail roughness is a random phenomenon, independent of the wheel radius.

2) It may be noted that the roughness may contain features, such as 'pits' in the surface, which the wheel-rail geometry cannot fully sense - the wheel radius is relatively large and so does not allow the contact point to follow the profile in the same way that a pointed measuring sensor would. Two methods can be used to overcome this difficulty. The first is to use a measuring sensor which has a relatively large radius, and thus partially emulates the profile sensed by the wheel-rail contact, by not following every detail of the surface. The second is to measure using a pointed sensor, but then to correct the profile mathematically during analysis. However it is important to note that a

frequency domain correction cannot be used, as pits need to be treated differently from asperities.

3) The wheel-rail contact does not exist merely at a point, but rather covers an area (the contact patch). This means that roughness features which are shorter than the contact patch will not be fully sensed. Remington [20] applied a frequency domain 'contact filter' to correct for this effect.

4) Variations in the roughness profile across the surfaces need to be taken into account. Remington [20] used a correlation function to quantify this effect, although its value had to be assumed due to lack of data. No account is taken of this effect in Appendix A.

Such questions concerning the analysis of roughness data have largely been avoided in the current study, by concentrating on predictions of the vibration due to a hypothetical unit roughness input, ie the transfer function from roughness to vibration. In that way, roughness analysis has been separated into an issue relating to experimental validation of the model rather than being part of the model itself.

3.1.5 Remington's Approximations

Remington's model implemented the above general derivation, but used a number of approximations, which will be set out in this section. As will be seen, the work described in the current chapter improves on a number of these assumptions.

The FRFs of the wheel (actually expressed as impedances rather than receptances) were derived analytically from the equations of motion for a ring. For the axial modes, the equations of Love for out-of-plane vibration of a free ring were used. In the case of the radial modes, Love's equations for in-plane vibration of a free ring were modified by the inclusion of a stiffness to represent the wheel web. This gave a reasonable representation of the axial and radial FRFs [20]. The wheel cross receptance, however, was omitted due to lack of data: no measurements of cross receptance were taken, and the ring equations used assume that there is no coupling between axial and radial motion and hence that the cross receptance is zero.

For the rail, the vertical and lateral receptances were modelled using Euler's equations for an infinite beam. The rail cross recept-

ance was measured in one-third octave bands, and these measurements were used as empirical data, although they were measured on a different rail section from that modelled.

For the wheel-rail contact zone, the vertical receptance was represented by a simple spring stiffness representing a linearised Hertzian contact spring. The contact lateral receptance was taken as zero (a rigid connection), as was the contact cross receptance (indicating no lateral relative motion resulting from the vertical contact force and vice versa).

Finally, the whole model was implemented only in one-third octave frequency bands.

3.2 IMPLEMENTATION OF THE THEORETICAL MODEL

Computer programs have been written to calculate the various parts of the theoretical model described in §3.1. The first program, which calculates the wheel receptances, has already been described in §2.2.3.

These wheel receptances are passed to a second program which calculates the rail receptances at the same frequencies. It then couples the wheel and the rail together, to calculate the dynamic contact forces, and, from these, the wheel and rail displacements at the contact point.

A third program calculates the wheel response at a point remote from the contact zone, starting from the dynamic contact forces calculated above.

3.2.1 Wheel Receptances

The theoretical model used to calculate the wheel receptances has been described in detail in §2. In the notation of §3.1, the responses at a point X (in a particular direction), to unit vertical and lateral forces at the contact point are given by

$$\alpha^{W}_{XV} = \sum_{r} \frac{{}_{r}\psi_{X}\ {}_{r}\psi_{V}}{m_{r}(\omega_{r}^{2}-\omega^{2}+2i\zeta_{r}\omega_{r}\omega)}$$

and ...(17)

$$\alpha^{W}_{XL} = \sum_{r} \frac{{}_{r}\psi_{X}\ {}_{r}\psi_{L}}{m_{r}(\omega_{r}^{2}-\omega^{2}+2i\zeta_{r}\omega_{r}\omega)}$$

where $_r\psi_X$ is the modal amplitude of the rth mode at the point X (in the direction required for the response), and $_r\psi_V$ and $_r\psi_L$ are the modal amplitudes of the rth mode at the contact point in the vertical and lateral directions (other parameters as in §2).

The parameters $_r\psi_V$, $_r\psi_L$, $_r\psi_X$, m_r and ω_r can all be derived directly from the finite element analysis. The modal damping, ζ_r, however, cannot be predicted reliably, so values derived from measurements were used for this. The natural frequencies, ω_r, used in the modal sum were actually those found experimentally, in order to give results more easily comparable with the experiments.

3.2.2 Rail Receptances

In the current chapter the rail receptances are based on the simple Euler beam equations, as used by Remington (a review of simple beam theories is given in Appendix D). The Euler beam receptance has a phase of -135°, but in order to investigate the effects of varying the phase of the rail receptances, it can be specified independently in the program. The magnitude remains as for an Euler beam, ie

$$\alpha^R_{LL} = \frac{\sqrt{2}}{4EI_L\ k_L^3}\ e^{i\theta_L} \qquad \ldots(18a)$$

$$\alpha^R_{VV} = \frac{\sqrt{2}}{4EI_V\ k_V^3}\ e^{i\theta_V} \qquad \ldots(18b)$$

where $k_L = \left(\frac{\rho A\omega^2}{EI_L}\right)^{1/4}$ and $k_V = \left(\frac{\rho A\omega^2}{EI_V}\right)^{1/4}$ are the wavenumbers of lateral and vertical bending waves,

E is Young's modulus, ρ is the density,

I_V and I_L are the second moments of area of the cross-section,

A is the cross-sectional area,

and θ_L and θ_V are the phases of the lateral and vertical receptances (in radians).

For the cross receptance the simple beam bending equations offer no solution. The actual cross receptance is expected to depend on the degree of asymmetry in the rail section, its support, and the position of the contact point. However the program is arranged so that values can be input following the same format as for the vertical and lateral receptances, ie via an equivalent EI, ρA and phase, and the same form of equation as above is used:-

$$\alpha^{R}_{VL} = \frac{\sqrt{2}}{4EIc\ kc^3}\, e^{i\theta c} \qquad \ldots(18c)$$

Although these rail receptances are over-simplified, they will be used in this chapter to study a range of values of rail receptance parameters within which practical values may be expected to lie.

Initially the rail receptances have been calculated using the parameters listed in Table 2. The phases have been set to -90° as this appears to fit experimental results, such as those of Remington [20], more closely than the value of -135° derived from beam theory. The cross receptance has been taken simply to be 10 dB lower than the vertical receptance, which is approximately the case in the experimental results of Remington. Because of the sign convention used here, this has the opposite phase to the vertical receptance.

These rail receptances are shown in Figures 18-20 together with the corresponding wheel receptances.

3.2.3 Contact Receptances

For the wheel-rail contact, the vertical receptance is defined, in the same way as by Remington, by a simple spring representing the Hertzian contact stiffness (k_H), which has by necessity been linearised. Additionally, allowance has been made in the program to add a damper (viscous or hysteretic) in series or in parallel with this stiffness, although this has no physical justification.

The contact vertical receptance may be calculated using the following equation, (see Appendix E for more details):

$$\alpha^{C}_{VV} = \frac{1}{k_H} = \frac{\xi}{2}\left(\frac{2}{3\ E^{*2}\ R_e\ P_o}\right)^{1/3} \qquad \ldots(19)$$

where E^* is the plain strain elastic modulus, $E^*=E/(1-\nu^2)$, E being Young's modulus and ν Poisson's ratio,

R_e is an effective radius of curvature, given by $1/R_e=1/2R'+1/2R''$ where R' is the rail head radius of curvature, and R'' is the wheel radius,

ξ depends only on the ratio of the radii R' and R'', and hence the shape of the contact patch - a table of ξ is given in Appendix E,

and P_o is the static wheel load.

Table 2 Parameters Used in Baseline Study

Rail

EI_L = 0.97 MNm², phase -90°, typical of BR flat bottomed rail

EI_V = 4.84 MNm², phase -90°, typical of BR flat bottomed rail

ρA = 56 kg/m, typical of BR flat bottomed rail

EI_C = 484 MNm², phase +90°, to give 10 dB lower than the vertical receptance

Contact

R' = 0.3 m (typical for a new BR type 113A rail and similar to the value used by Remington)

R" = 0.53 m (radius of a Commonwealth wheel)

ξ = 1.96, derived from the table in Appendix E

P_o = 50 kN (1/8 of nominal weight of the test vehicle)

a = 6.12 mm (from equations in Appendix E)

b = 4.19 mm (from equations in Appendix E)

C_{22} = 1.67 (interpolated from the table given in [80], but related to E rather than G)

V = 44.4 m/s (160 km/h)

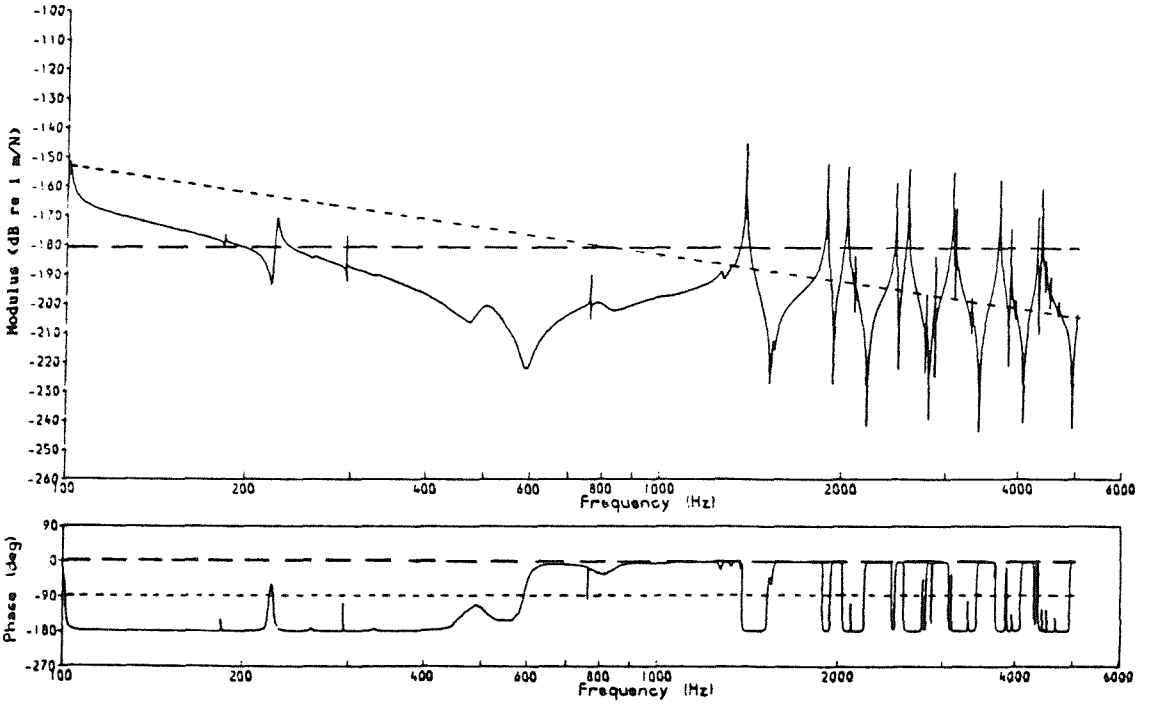

Figure 18 Vertical Point Receptances (——— Wheel, ····· Rail, — — Contact Spring)

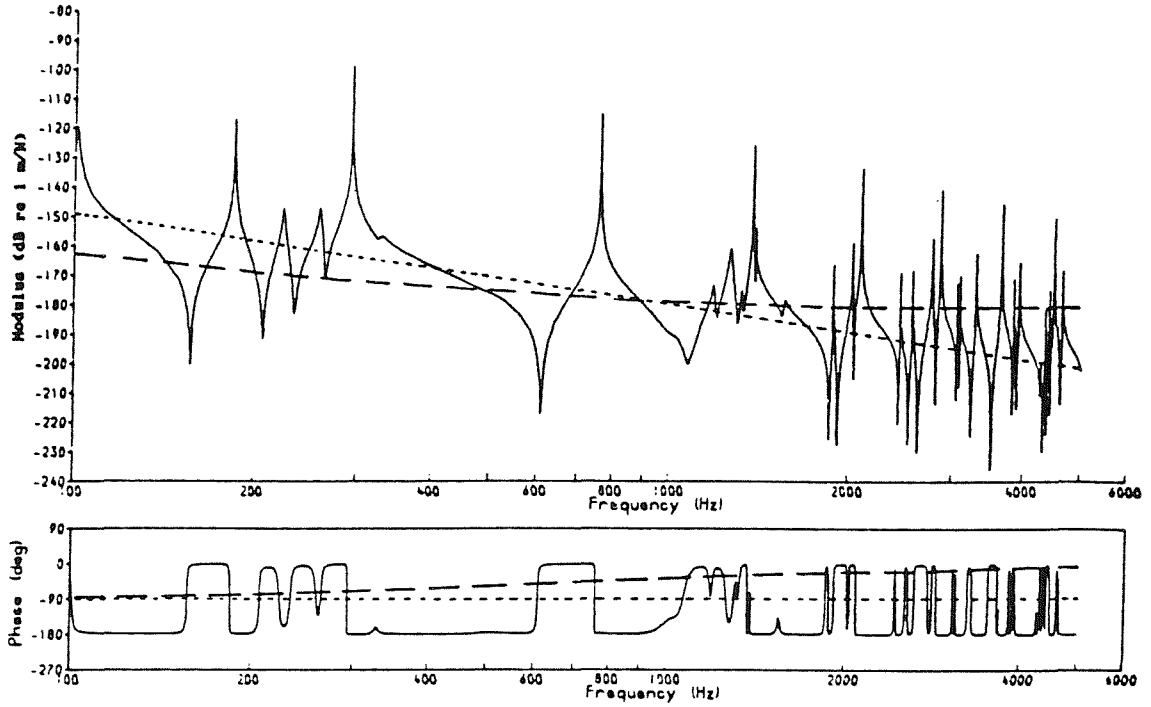

Figure 19 Lateral Point Receptances (——— Wheel, ····· Rail, — — Contact (spring and damper in series for 160 km/h))

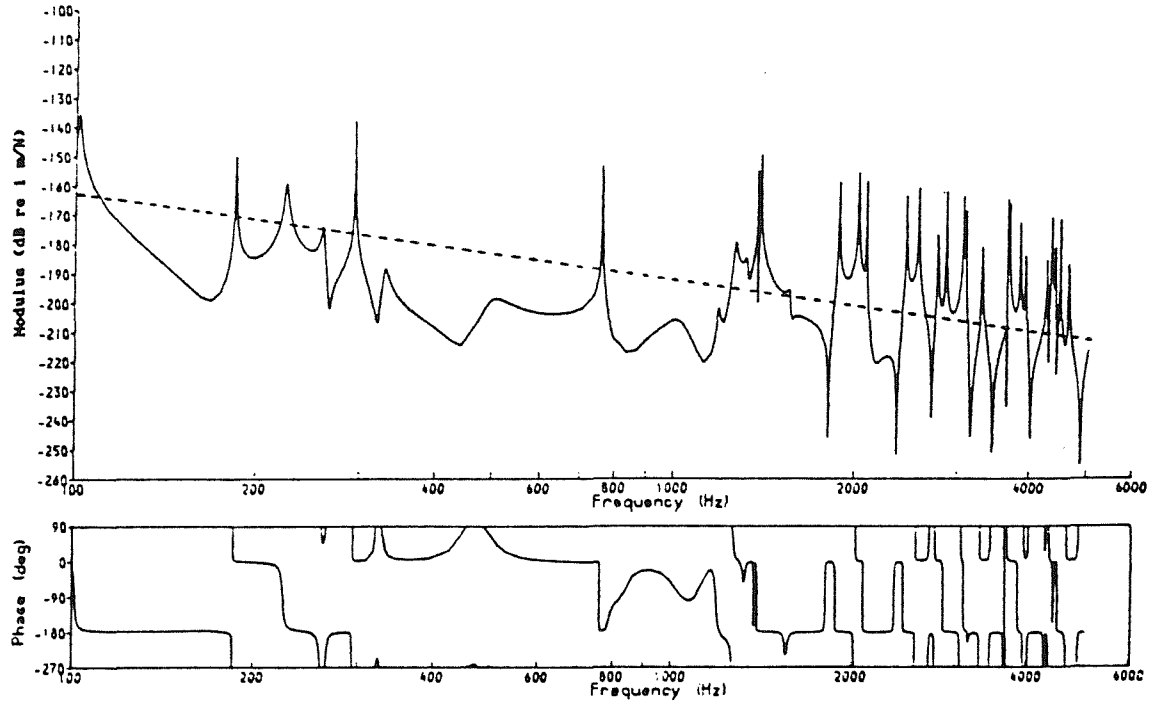

Figure 20 Cross Receptances (——— Wheel, ····· Rail)

The value of k_H is taken as 1.16 GN/m, which is derived from the values in Table 2. The resulting receptance is shown in Figure 18.

For this initial study, the contact lateral receptance has been modelled by a spring and a damper in series, as shown in Figure 17. A more detailed model will be developed later (in §6). The spring represents the Hertzian contact stiffness (generally assumed to be similar in magnitude to the vertical, following work by Mindlin [98] - see Appendix E for more details). The damper represents the linearised lateral creep force between the wheel and the rail, which is proportional to the velocity of sliding. This is based on quasi-static work carried out by Kalker [80], which has not actually been validated over the frequency range used here. The damping, which has been used by Ferguson [56], is given by:-

$$C = \frac{E\ ab\ C_{22}}{V} \qquad \ldots(20)$$

where a and b are the major and minor semi-axis lengths of the contact patch, assumed to be elliptical. Expressions for a and b are given in Appendix E.

C_{22} is a creep coefficient tabulated by Kalker, and dependent on the ratio of a to b, and on Poisson's ratio, v.†

and V is the forward velocity of rolling.

Putting the creep damper and contact spring in series gives

$$\alpha c_{LL} = \frac{1}{k_H} + \frac{1}{i\omega C} \qquad \ldots(21)$$

(as in equation (8)). This means that the creep damper is dominant at lower frequencies, and the contact spring is dominant at higher frequencies, whereas a parallel model would reverse this. The series model appears more realistic when it is considered as the speed $V \to 0$, the receptance should tend to $1/k_H$, whereas for $V \to \infty$, it should tend to 0. These conditions are satisfied by the series model but not by the parallel model (see also Ferguson [56]).

The lateral contact stiffness has been set at 1.16 GN/m (equal to the vertical stiffness), but in series with a damper of 0.2 MNs/m.

†: the shear modulus G is often used in place of E in equation (20), in which case C_{22} is altered by a factor depending on v).

These are derived from the parameters in Table 2. The resulting receptance is shown in Figure 19.

The contact cross receptance, ie the lateral response to a varying vertical force, or vice versa, has been ignored in this chapter, as it was by Remington, ie $\alpha^{C}_{VL} = 0$.

3.3 PREDICTED RESULTS

The programs have been run initially for a reasonably typical set of parameters, the results of which will be examined in some detail. This will be followed by a study of the effects of varying some of these parameters, to establish the sensitivity of the model to such variations. Hence these initial predictions can be considered as a 'baseline' for the parameter studies.

Although an actual roughness spectrum could have been used as the input to the programs, all of the results will be calculated using a roughness input spectrum of unit amplitude for all frequencies. This yields a transfer function from roughness to vibration, u_X/r, which is given in non-dimensional form; hence the units used will be dB re 1 m/m. This form of presentation means, therefore, that the results are independent of the analysis of the surface roughnesses, such as contact filtering, considered in Appendix A. It should not be forgotten, however, that the roughness input, r, is the roughness experienced by the wheel-rail contact, and not necessarily that measured directly.

3.3.1 Rail Vibration

The results for the vibration (displacement) of the rail, for a unit roughness input and for a single speed (ie 160 km/h), are given in Figure 21. These results are compared with measurements, (from Appendix A) in terms of one-third octave spectra in Figure 22.

The vertical vibration contains marked similarities between predicted and experimental results. At higher frequencies, both experimental and predicted results fall from around 0 dB to around -20 dB, although the measured results fall a little more sharply.

At low frequencies the experimental results drop from 0 dB to about -10 dB whereas the predicted results remain at 0 dB. This is likely to be an effect of the decay of the vibration with distance from the excitation point. Experiments have shown that the decay with distance from the excitation point is quite large for frequencies below

(a) Vertical Rail Vibration Displacement for a Unit Roughness Input

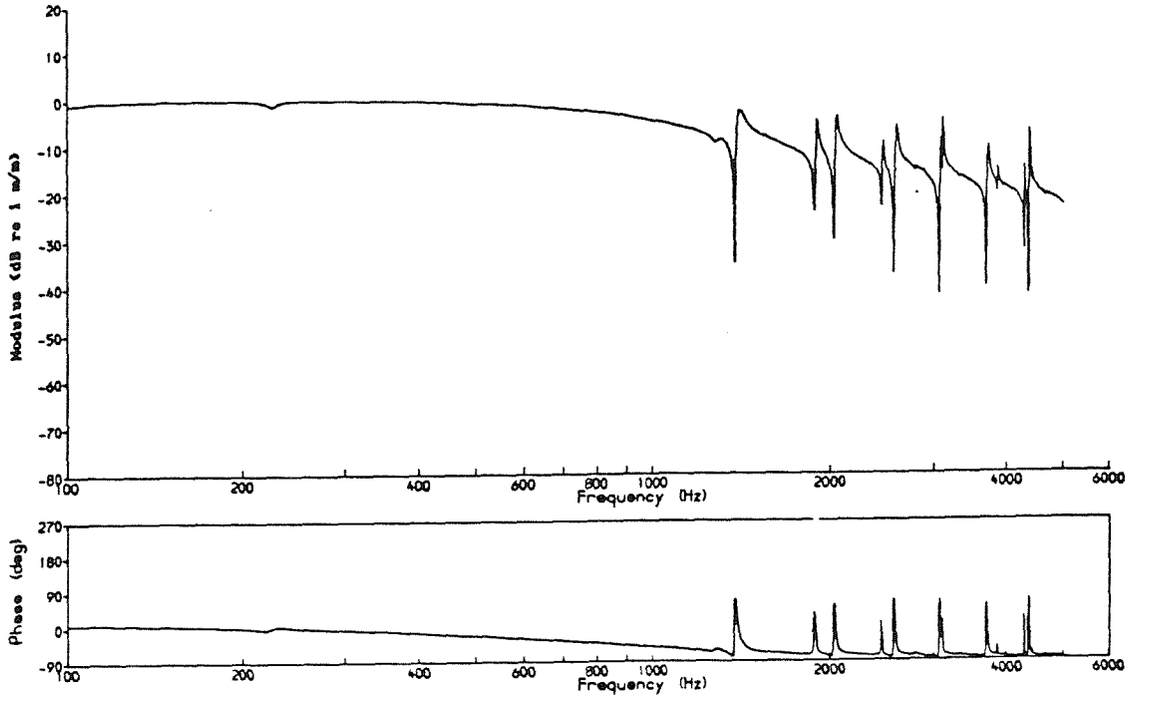

(b) Lateral Rail Vibration Displacement for a Unit Roughness Input

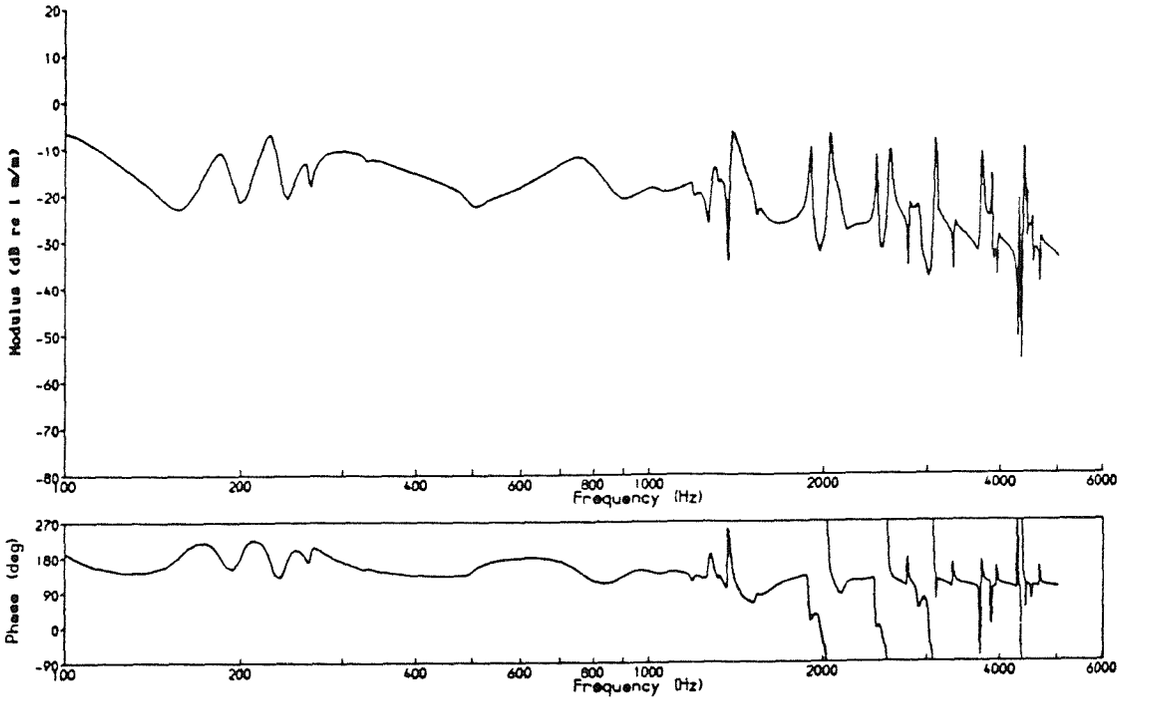

Figure 21 Baseline Predictions: Rail Vibration

(a) Vertical Rail Vibration Displacement for a Unit Roughness Input

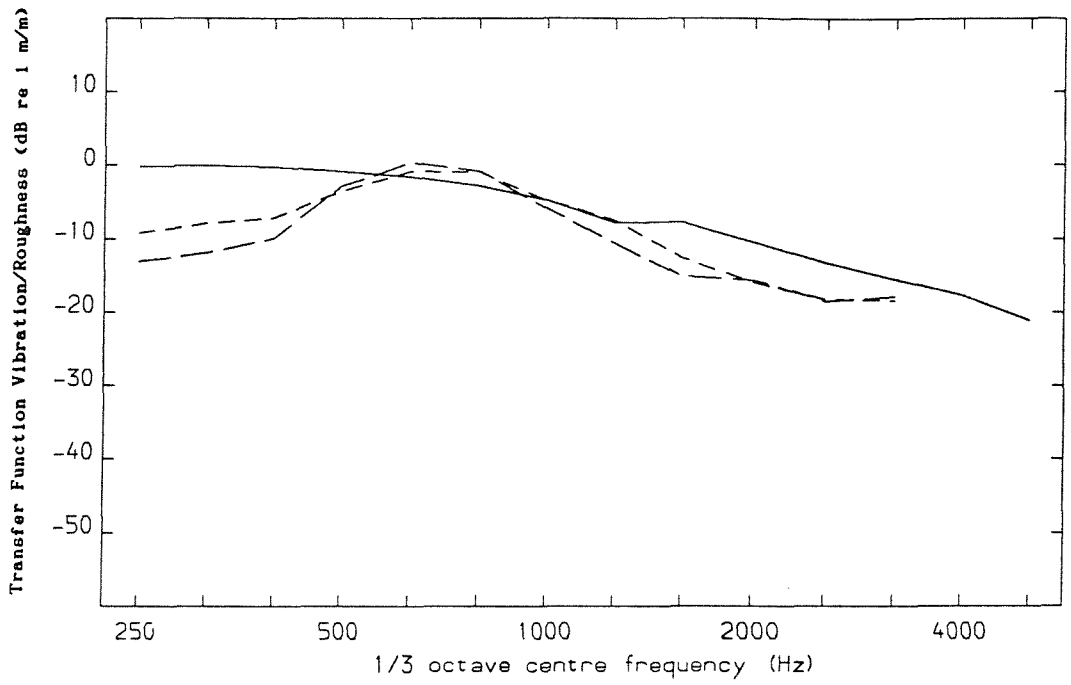

(b) Lateral Rail Vibration Displacement for a Unit Roughness Input

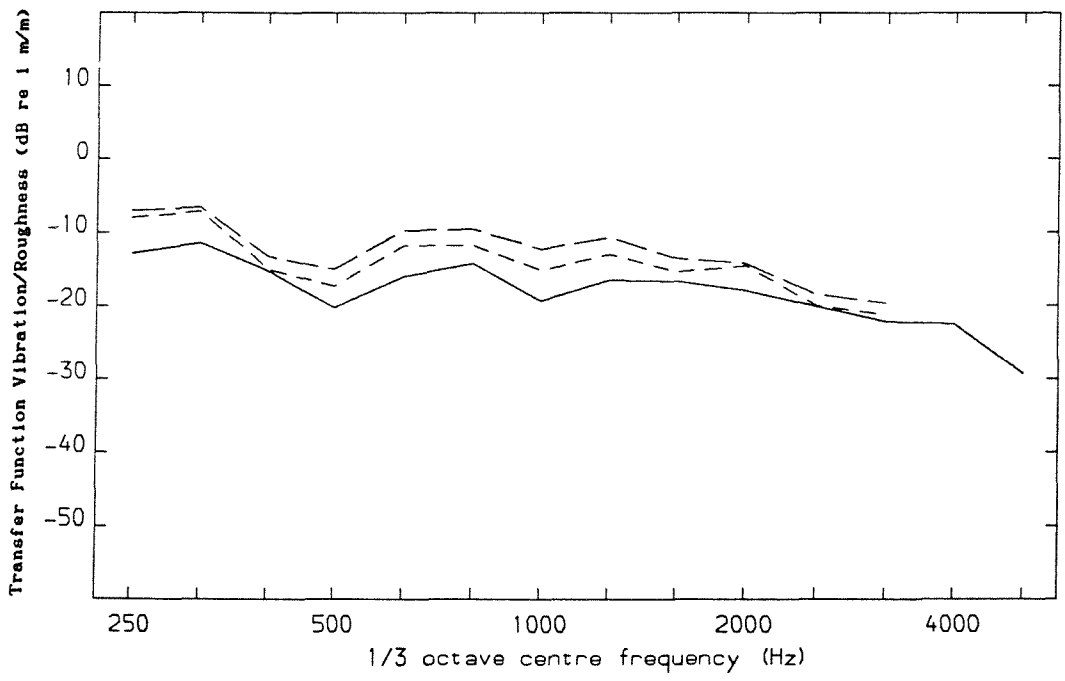

Figure 22 Comparison of Predictions (———) with Measurements at 160 km/h (— — Smooth Wheel, - - - Rough Wheel) from Appendix A

about 500 Hz [70] due to the effects of the support which introduces a 'blocked' frequency band at low frequencies. For these lower frequencies, the rail vibration amplitude at the contact point will be larger than the measurements indicate, since the experimental analysis (Appendix A) uses an average (over a finite time) as the train passes the measurement position. Correcting the measurements for this effect to give the vibration at the contact point would, therefore, give results which should lie nearer to 0 dB for these frequencies.

The effect of the decay of vibration with distance will be considered theoretically in §5. Unfortunately no measurements of this decay with distance were carried out at the test sites used in the rolling tests. Nevertheless, after taking this effect into account in a qualitative fashion, it would seem that the agreement, for the vertical rail vibration, between predictions and measurements is reasonable at these lower frequencies.

Decay with distance is unlikely to be a significant effect for the lateral vibration as it was found that only frequencies below about 200 Hz were blocked in this way. Analysis of the vibration of a rolling wheel has shown that the amplitude of vibration is not noticeably different as the measuring point passes the contact region [47], and thus no correction will be needed to the wheel vibration measurements either.

Comparing the predicted lateral vibration of the rail with measurements in Figure 22b, the predicted results are slightly lower in level than those which were measured, but the shape is quite similar.

3.3.2 Wheel Vibration

Figure 23 shows results for the vibration of the wheel, and comparisons of one-third octave spectra with measurements are shown in Figure 24. In comparison with the measurements, the predictions for the vertical responses are too low at low frequencies, and are too high at higher frequencies. The lateral responses are considerably over-predicted at high frequencies.

In both the measured and predicted results the vertical vibration is well below 0 dB for low frequencies and rises sharply at around 1.25 kHz. Peaks in the vertical response correspond to the wheel's resonances in both cases. However, numerical results have revealed a subtle difference: the peak frequencies in Figure 23 are actually slightly higher than the corresponding resonance frequencies, f_o, input

(a) Vertical Wheel Vibration Displacement for a Unit Roughness Input

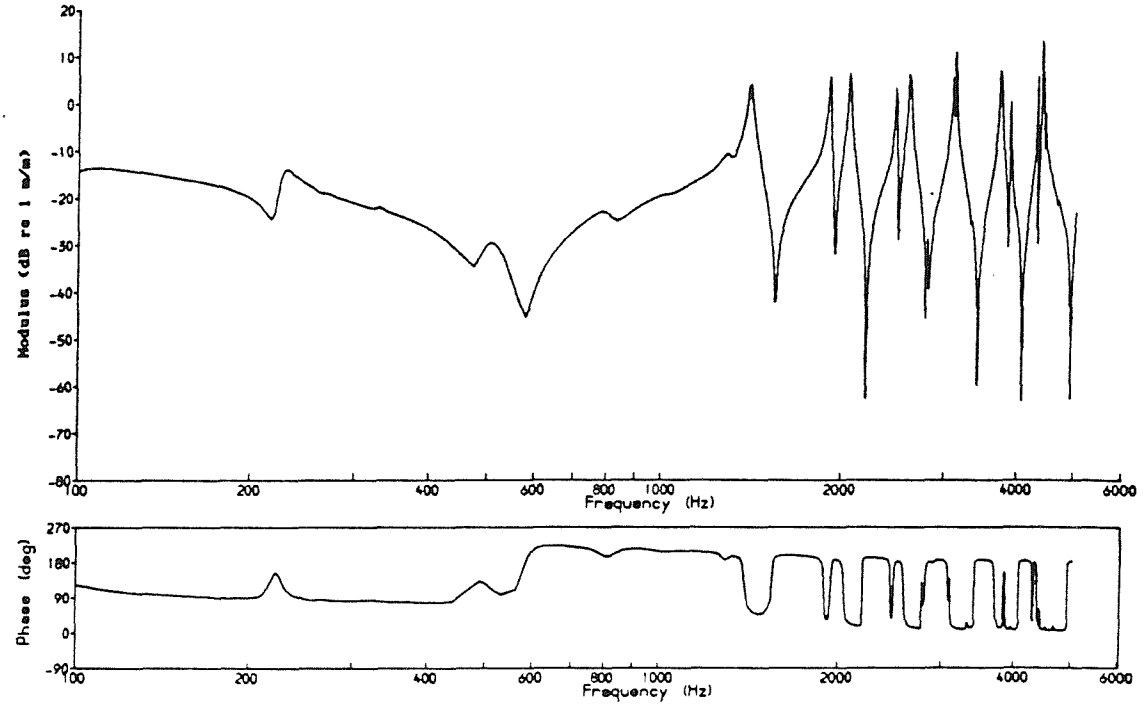

(b) Lateral Wheel Vibration Displacement for a Unit Roughness Input

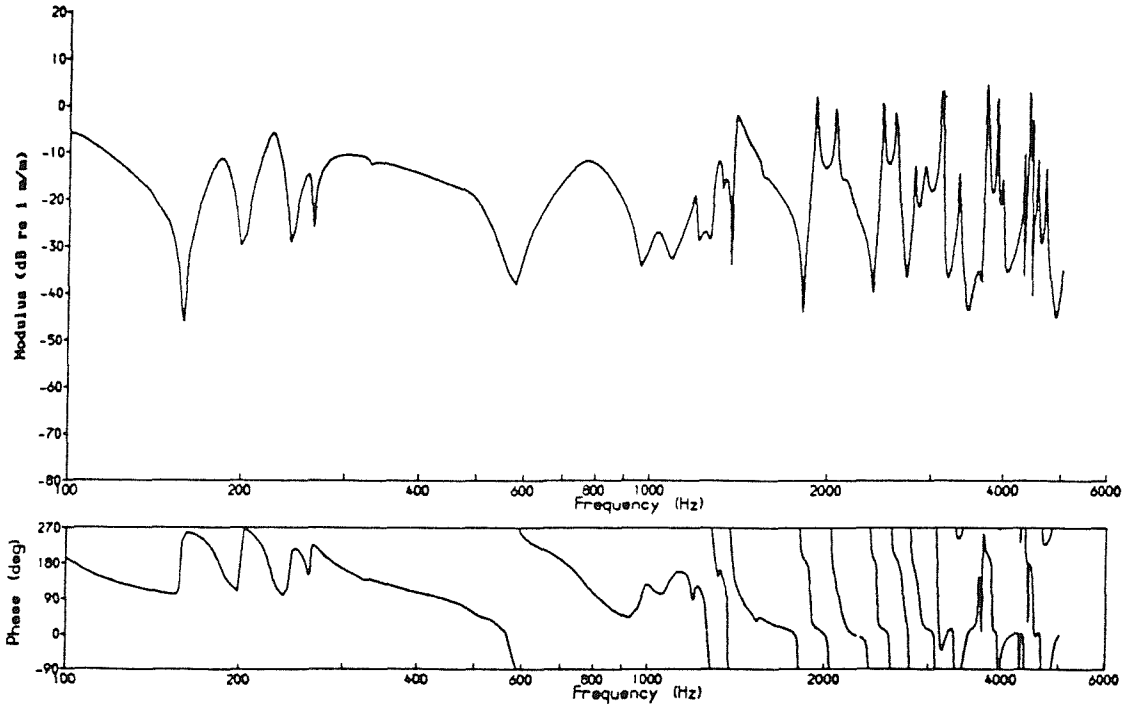

Figure 23 Baseline Predictions: Wheel Vibration

(a) Vertical Wheel Vibration Displacement for a Unit Roughness Input

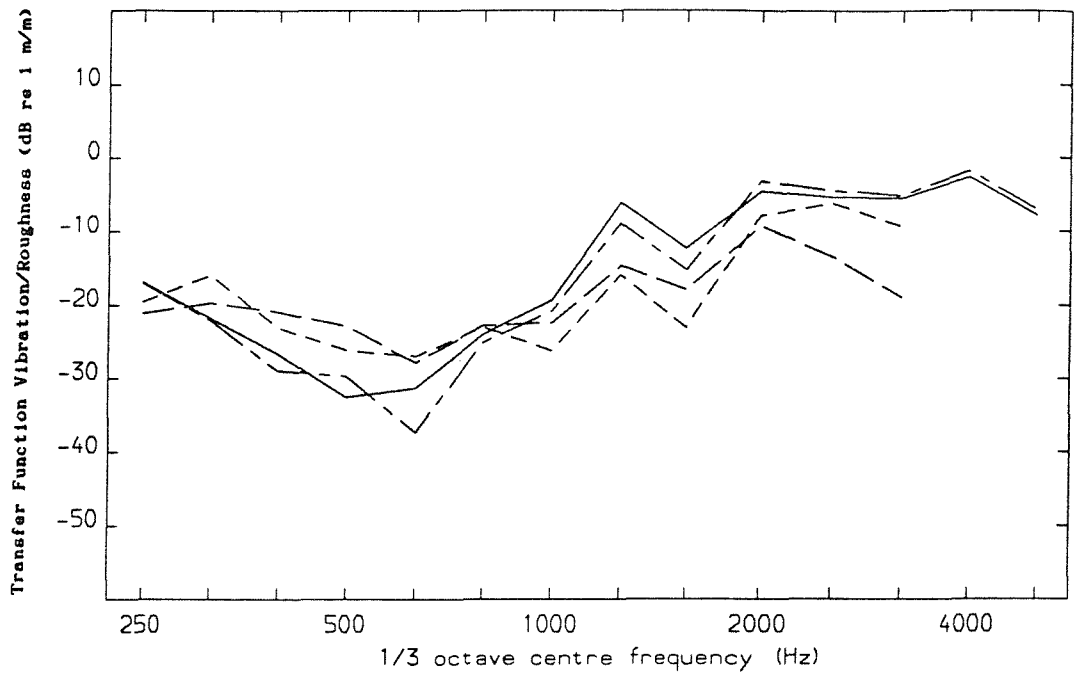

(b) Lateral Wheel Vibration Displacement for a Unit Roughness Input

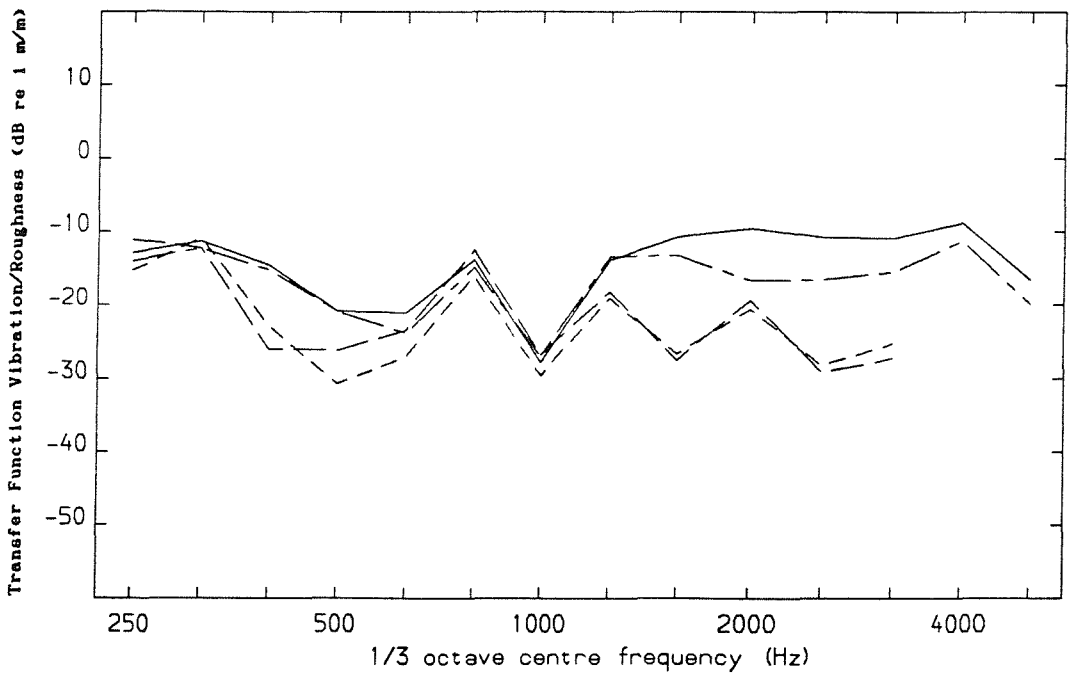

Figure 24 Comparison of Predictions (——— Contact Point, —·—· Tyre Accelerometer Positions) with Measurements at 160 km/h (— — Smooth Wheel, - - - Rough Wheel) from Appendix A

to the predictions. By contrast, the rail response has minima at f_o, and slight peaks at frequencies just above those in the wheel response.

Table 3 lists the differences between the peak frequencies and f_o for the wheel. The one-nodal-circle modes have a frequency difference of 7-16 Hz, and the radial modes have a greater difference of 19-23 Hz. The value quoted for the frequency difference, Δf, is subject to a tolerance of several Hz, also listed, due to the spacing of the calculation points in the frequency domain. The frequency difference seen here is a feature of coupled systems, in this case the contact spring adding a stiffness loading to the wheel, which raises the natural frequencies of the combined system relative to those of the wheel. Conversely, a mass loading would lower them. Whilst this effect may be expected from the coupled model, it is not observed to the same degree in practice. In Appendix A, the peaks in Figure A7 correspond to the resonance frequencies of the wheel in question, to within the bandwidth of the analysis (ie 10 Hz).

Table 3 Details of Peaks in the Baseline Predictions of Vertical Wheel Vibration (Figures 23 & 25)

(a) One-nodal-circle modes

n	f_o	Δf	tol	amp	b/w	ζ	web
2	1390	16	4	4	23	80	13
3	1880	14	3	6	11	30	18
4	2440	11	2	5	9	20	18
5	3095	10	2	12	6	10	18
6	3855	7	2	1	6	8	14

(b) Radial modes

n	f_o	Δf	tol	amp	b/w	ζ	web
2	2025	19	3	6	16	40	13
3	2560	23	4	9	14	30	13
4	3060	21	2	7	12	20	13
5	3690	23	6	8	18	20	8
6	4360	20	2	13	9	10	9

KEY

n number of nodal diameters in mode
f_o natural frequency input to the prediction (Hz)
Δf difference between peak frequency and f_o (Hz)
tol tolerance in estimate of Δf (Hz)
amp amplitude of vertical response at the spectral peak (dB re 1 m/m)
b/w 3 dB-down bandwidth of peak (Hz)
ζ equivalent damping ratio derived from b/w ($\times 10^{-4}$)
web amplitude of response at web axial accelerometer position (dB re 1 m/m)

An estimate of the apparent damping of the peaks in the spectrum has been calculated using the 3 dB-down (half-power) points. The damping ratio, ζ, of a resonance of a structure can be estimated from the half-power points of its receptance using [97]:-

$$\zeta = (f_U - f_L) / 2f_o \qquad \ldots(22)$$

where f_U and f_L are the frequencies of the upper and lower half-power points and f_o is the resonance frequency. In the present case the apparent damping has been calculated using the above formula but with the peak frequency instead of the resonance frequency. The results are included in Table 3, and imply a 'rolling damping' in the range .001-.008, which is significantly greater than the modal damping of about .0003. It should be borne in mind, however, that apart from the creep force term, the model does not distinguish between the cases of a rolling wheel and a static wheel sat on the rail.

The predicted lateral vibration of the wheel at the contact point (Figure 23b) appears to be non-resonant, at least at low frequencies. By contrast the measured spectra (Figure A6b) clearly show resonant behaviour, with peaks at 290, 760, 1370, 2080, 2850, 3660 and 4490 Hz, which correspond to 0-nodal-circle modes with 2, 3, 4... nodal diameters. These are the modes which are dominant in the axial point receptance. Although Figure 23b contains various peaks at higher frequencies, these do not correspond to the 0-nodal-circle set of modes. The general form of the lateral response appears to follow the wheel cross receptance rather than the lateral point receptance.

In practice the measuring positions are remote from the contact patch (as shown in Figure A1), and this effect can be allowed for. Figure 25 shows the predictions for two accelerometer positions (channels 2 and 6 as used in Figure A6) as well as for the contact point. These accelerometers measure axial vibration at the centre of the web and at the centre of the tyre respectively. Figure 25 is plotted to a linear frequency scale for more ready comparison with Figure A6. In addition, the 1/3 octave results for the accelerometer positions closest to the contact (channels 5 and 6: tyre radial and axial) are shown in Figure 24. These positions, therefore, correspond to the positions used for the measurements shown in Figure 24.

Clearly the form of the predictions for the tyre axial accelerometer position is little different to those of the contact point. The

(a) Wheel Vibration Displacement for a Unit Roughness Input

——— Vertical at Contact Point

····· Web Axial Accelerometer Position

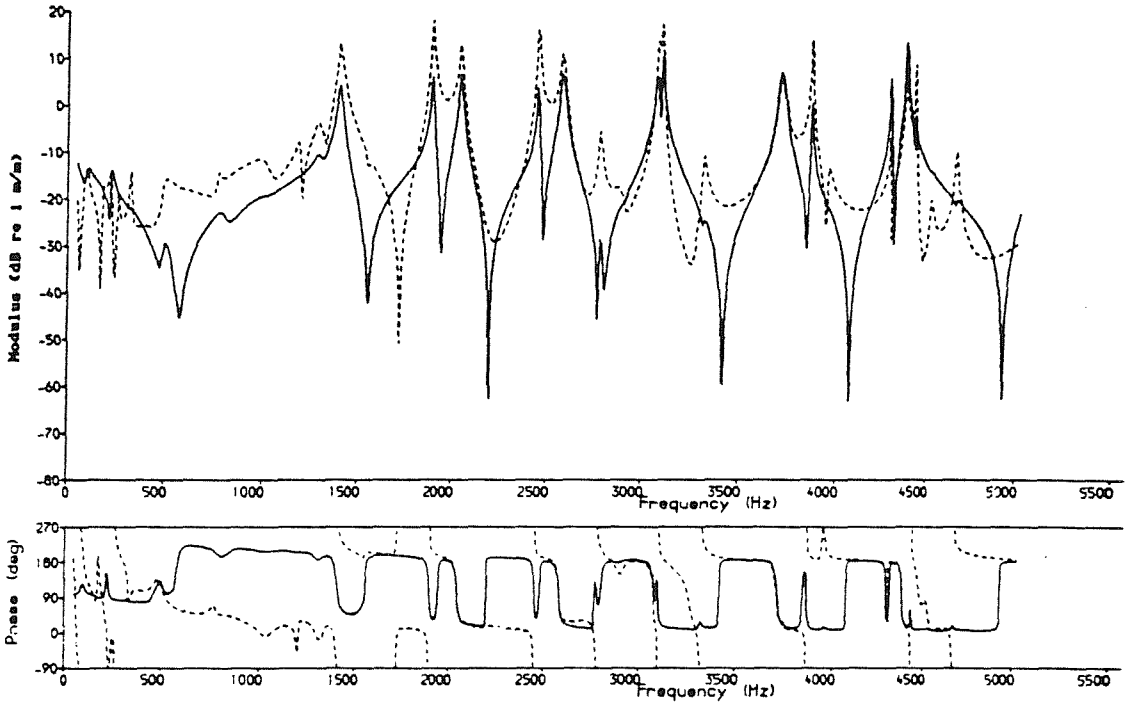

(b) Wheel Vibration Displacement for a Unit Roughness Input

——— Lateral at Contact Point

····· Tyre Axial Accelerometer Position

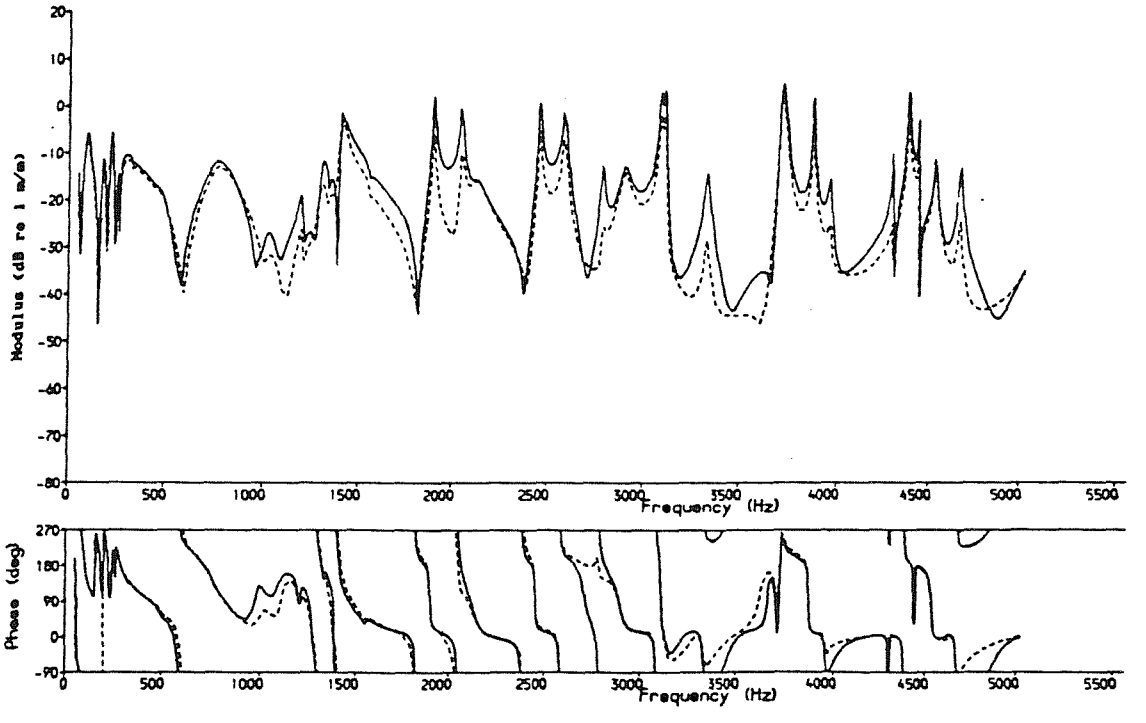

Figure 25 Wheel Vibration: Comparison of Vibration at Contact Point and at Accelerometer Positions

1/3 octave levels are reduced at higher frequencies, but the predictions still appear to be inadequate. The tyre radial position gives similar results to the vertical vibration at the contact, with slight differences in the magnitudes of the various contributing modes.

The predicted vibration at the web axial accelerometer position contains the same resonance peaks as the predicted vertical vibration at the contact point, although the various peaks appear at different amplitudes (see Table 3). The differences between the resonance frequencies and the resultant peak frequencies are the same in both spectra for all modes.

These peaks correspond closely to the peaks in the experimental results of Figure A6a. The precise frequencies are not identical, partly because of the differences (Δf) discussed above, but also because the wheel is not identical to that on which measurements have been taken (Appendix C), and on which the resonance frequencies of the predicted response are based in §2.

Noise radiation from the wheel [33] has been found to be predominantly due to modes with a high axial amplitude on the web - the 1-nodal-circle and radial modes. These have relatively low axial vibration on the tyre, but relatively large radial components and correspond to all the peaks listed in Table 3. Thus it should be borne in mind that the vertical vibration at the contact, through its connection with high axial vibration of the web, is more important to noise radiation from the wheel than the lateral vibration at the contact.

3.4 PARAMETER STUDIES

This section considers the effects of varying the values of the parameters input to the model. Due to the large number of parameters, multiple combinations of parameter variations cannot be considered, but an idea of the effect of each variable should still be obtained. If the model were reliable, such an analysis would allow identification of preferred parameters which should be altered in the wheel-rail system in attempts to reduce noise.

However even though the model does not appear entirely reliable at this stage, such an analysis allows determination of: (1) whether the initial choice of parameters was correct, or whether a better set can be envisaged (in which case they must be justified physically), (2) whether the choice of parameters is critical, or whether similar results are obtained with a different set of parameters, (3) an

increased understanding of the mechanisms of the model, hopefully allowing improvements to be suggested.

3.4.1 Effects of Cross Receptances

Remington omitted the wheel cross receptance, but included the rail cross receptance. In this section, both are suppressed, simultaneously and in turn, in order to study their contributions.

First, both cross receptances are suppressed (set to zero) simultaneously. This results in a solution for the vertical interaction alone, the results of which are shown in Figure 26, superimposed on the baseline solution of §3.3. Since there is little difference between the two results, it is clear that the baseline solution is dependent mainly on the vertical interaction of the wheel and the rail. It seems therefore that the lateral interaction has very little influence on the response at the contact region in the vertical direction.

Details of the peaks in the spectrum of vertical wheel vibration found in this case are given in Table 4. The results are similar to those for the baseline case although not identical.

Table 4 Details of peaks in predicted vertical wheel vibration for vertical interaction alone - no cross receptances (Figure 26)

(a) One-nodal-circle Modes

n	f_o	Δf	tol	amp
2	1390	20	4	6
3	1880	12	2	9
4	2440	7	2	9
5	3095	8	2	13
6	3855	3	1	6

(b) Radial Modes

n	f_o	Δf	tol	amp
2	2025	17	2	10
3	2560	19	4	12
4	3060	17	3	12
5	3690	19	4	14
6	4360	18	2	15

KEY

n number of nodal diameters in mode
f_o natural frequency input to the prediction (Hz)
Δf difference between peak frequency and f_o (Hz)
tol tolerance in estimate of Δf (Hz)
amp amplitude of vertical response at the spectral peak (dB re 1 m/m)

(a) Vertical Rail Vibration Displacement for a Unit Roughness Input

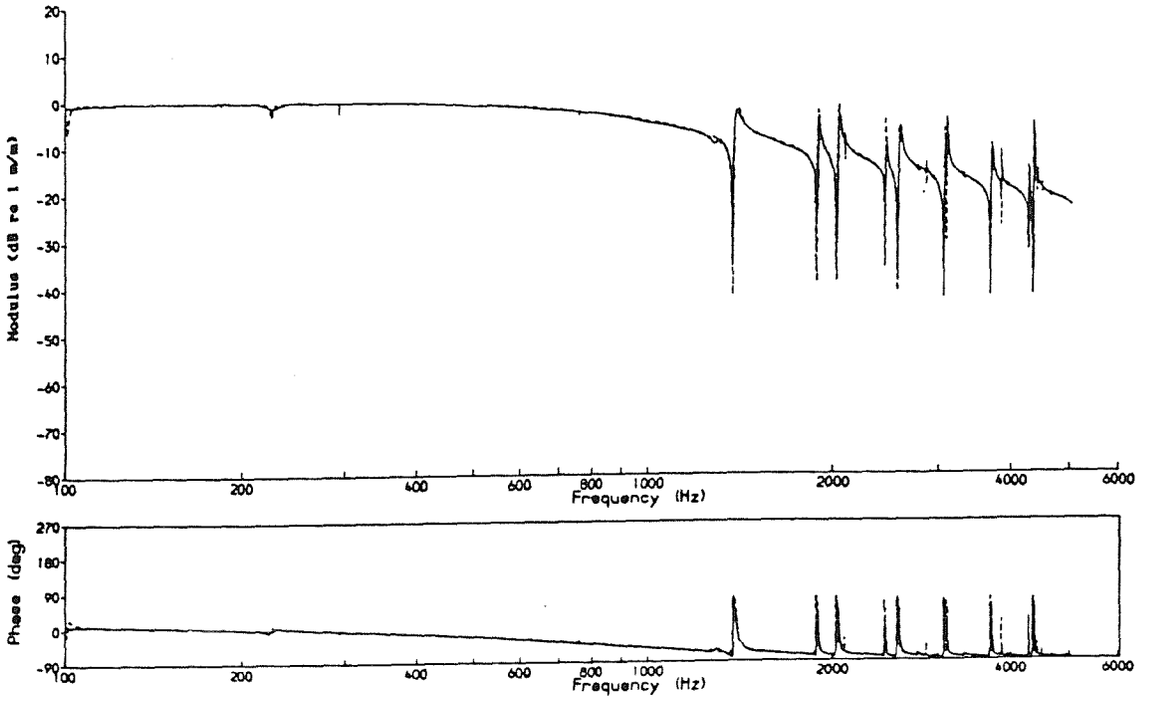

(b) Vertical Wheel Vibration Displacement for a Unit Roughness Input

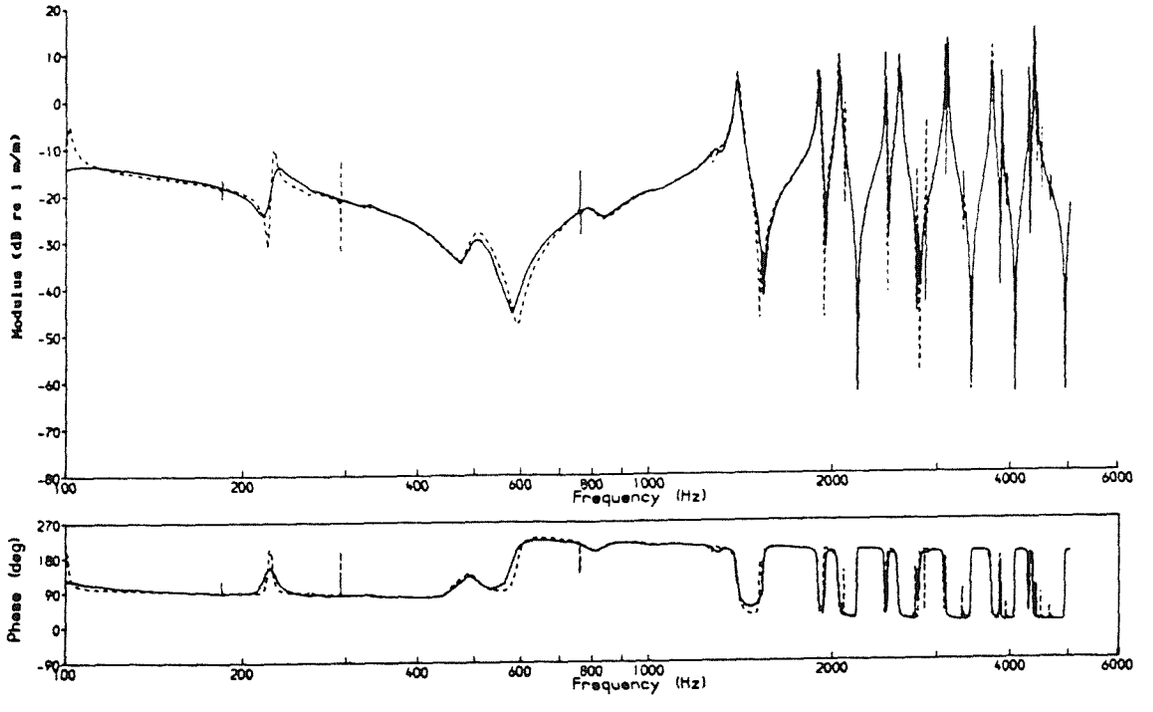

Figure 26 Predicted Vertical Vibration with and without Cross Receptances: ——— Baseline, ····· Vertical Interaction Alone

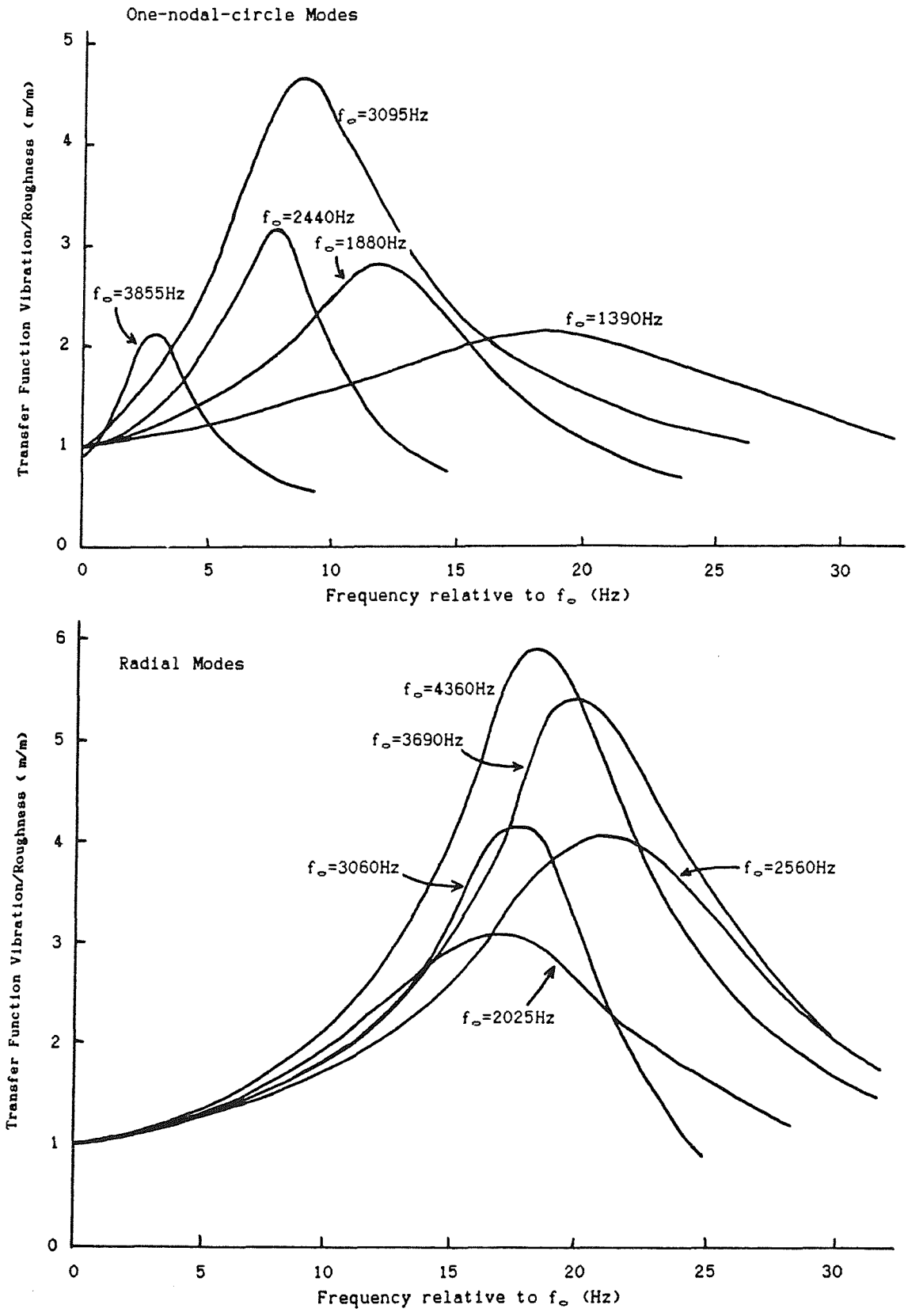

Figure 27 Details of Peaks in the Vertical Response
(for Vertical Interaction Alone)

Figure 27 shows the parts of the vertical wheel response spectrum around the peak frequency for the various peaks. It can be seen that the form is similar in each case, with the curve passing close to 1 at the corresponding resonance frequency, f_o, and rising to a maximum in the region up to about 20 Hz above this frequency. Each has a similar shape, which is considerably more rounded than the peaks in the wheel receptance. This is due to the apparent damping introduced by the coupling to the rail, as noted in Table 3.

It is worthwhile considering this simplified model in detail, for it will help in understanding of the nature of the vertical responses in the overall model. Figure 27 will help in this. The equations in §3.1 reduce to:-

$$\frac{z_R}{r} = \frac{\alpha^R_{vv}}{(\alpha^W_{vv} + \alpha^R_{vv} + \alpha^C_{vv})}$$

$$\frac{z_W}{r} = \frac{-\alpha^W_{vv}}{(\alpha^W_{vv} + \alpha^R_{vv} + \alpha^C_{vv})} \qquad \ldots(23)$$

At each frequency, the roughness generates rail vibration, wheel vibration, and relative motion within the Hertzian contact spring, the proportions depending on the relations between the three (complex) receptances. The three extreme possibilities are shown in Figure 28. At frequencies below 500 Hz, the rail receptance is dominant,

$$|\alpha^R_{vv}| \gg |\alpha^W_{vv} + \alpha^C_{vv}| \qquad \ldots(24a)$$

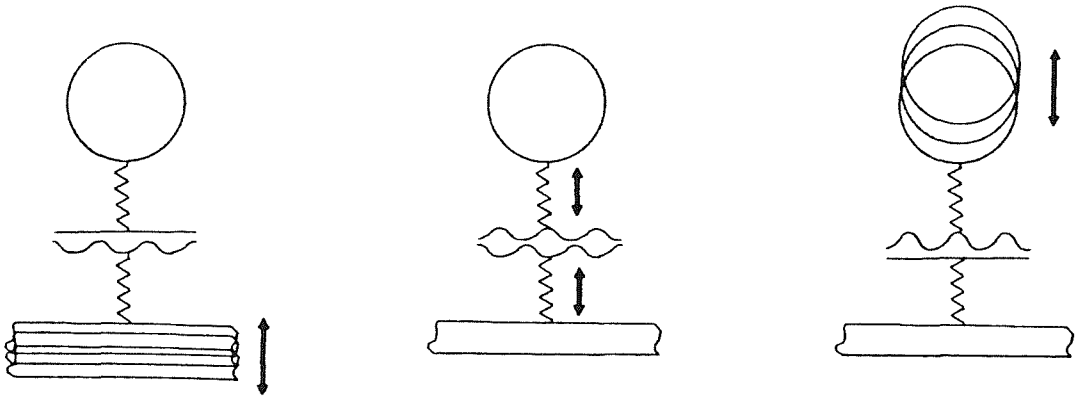

Case I
Rail Vibrates

Case II
Contact Zone Vibrates

Case III
Wheel Vibrates

Figure 28 Extreme Cases of Roughness-generated Vibration

and so $z_R/r \approx 1$ (case I) as seen in Figure 26 whereas $z_W/r \approx \alpha^W_{vv}/\alpha^R_{vv}$. This applies regardless of small variations which may be applied to α^R_{vv}, α^W_{vv} or α^C_{vv}.

At higher frequencies (above about 1200 Hz) the picture is not so simple and two regimes need to be considered.

First, away from wheel resonances, α^C_{vv} has the greatest magnitude, its importance increasing as frequency increases, and the roughness increasingly excites the contact spring (case II). Thus in general z_R/r falls at high frequencies.

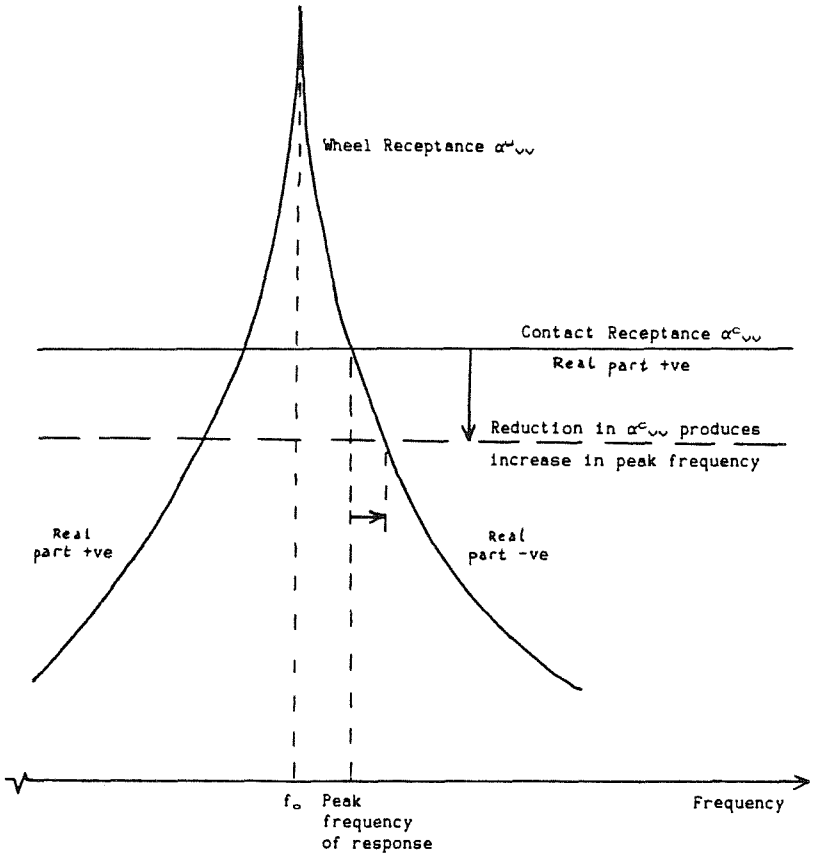

Figure 29 Schematic Diagram of Region Around a Wheel Resonance

Secondly, consider the neighbourhood of a wheel resonance. The various receptances in this region are shown schematically in Figure 29. At the resonance frequency, f_o,

$$|\alpha^W_{vv}| \gg |\alpha^R_{vv} + \alpha^C_{vv}| \qquad \ldots(24b)$$

and so $z_W/r \approx 1$ (case III) as found in Figure 27, whereas $z_R/r \approx \alpha^R_{vv}/\alpha^W_{vv}$. However because of the phases of α^R_{vv}, α^W_{vv} and α^C_{vv}, above f_o

$$|\alpha^W_{vv}| > |\alpha^W_{vv} + \alpha^R_{vv} + \alpha^C_{vv}| \qquad \ldots(25a)$$

which results in $|z_w/r| > 1$, whereas below f_o,

$$|\alpha^W_{vv}| < |\alpha^W_{vv} + \alpha^R_{vv} + \alpha^C_{vv}| \qquad \ldots(25b)$$

which results in $|z_w/r| < 1$. From this it is clear that the peak frequency of the wheel response occurs above f_o, as seen in Figure 27, when $|\alpha^W_{vv}+\alpha^R_{vv}+\alpha^C_{vv}|$ is a minimum ie $|\alpha^W_{vv}|$ and $|\alpha^R_{vv} + \alpha^C_{vv}|$ cross each other with roughly opposite phases.

From this discussion it is apparent that the prediction of peaks in the vertical wheel response slightly above the resonance frequencies is a feature of the vertical interaction between the wheel and the rail. No indications have been found yet of how to bring the predictions more into line with the experimental results, but it is clear that only changes in vertical receptance parameters are likely to have any significant effect.

When one of the cross receptances is suppressed, leaving the other, the vertical responses are not significantly affected, as would be expected from above, but the lateral responses are affected. Figure 30 shows the results for a zero wheel cross receptance, as in Remington's work. This results in a reduction in the predicted lateral wheel response particularly at high frequencies, with smaller changes in the rail vibration.

Figure 31 shows the results with the rail cross receptance suppressed, and also with its sign reversed. Apart from the phase of the response, the sign makes only a small difference, whereas a zero cross receptance leads to lower predicted lateral responses on both the wheel and the rail, and in fact both become similar in shape, although the rail has a lower response level, particularly at high frequencies.

Clearly both cross receptances contribute to the solution for the lateral responses and should not be omitted, but the contribution of that of the rail appears to be greater.

3.4.2 Effects of Rail Parameters

The predictions have been run using various values of rail vertical receptance. Figure 32 shows the results for levels of ±5 dB from the baseline. At low frequencies the rail vertical vibration is unaffected, whereas at high frequencies it is increased as the receptance is increased. In contrast, the wheel vertical response is reduced at low frequencies as the rail receptance is increased, but is

(a) Lateral Rail Vibration Displacement for a Unit Roughness Input

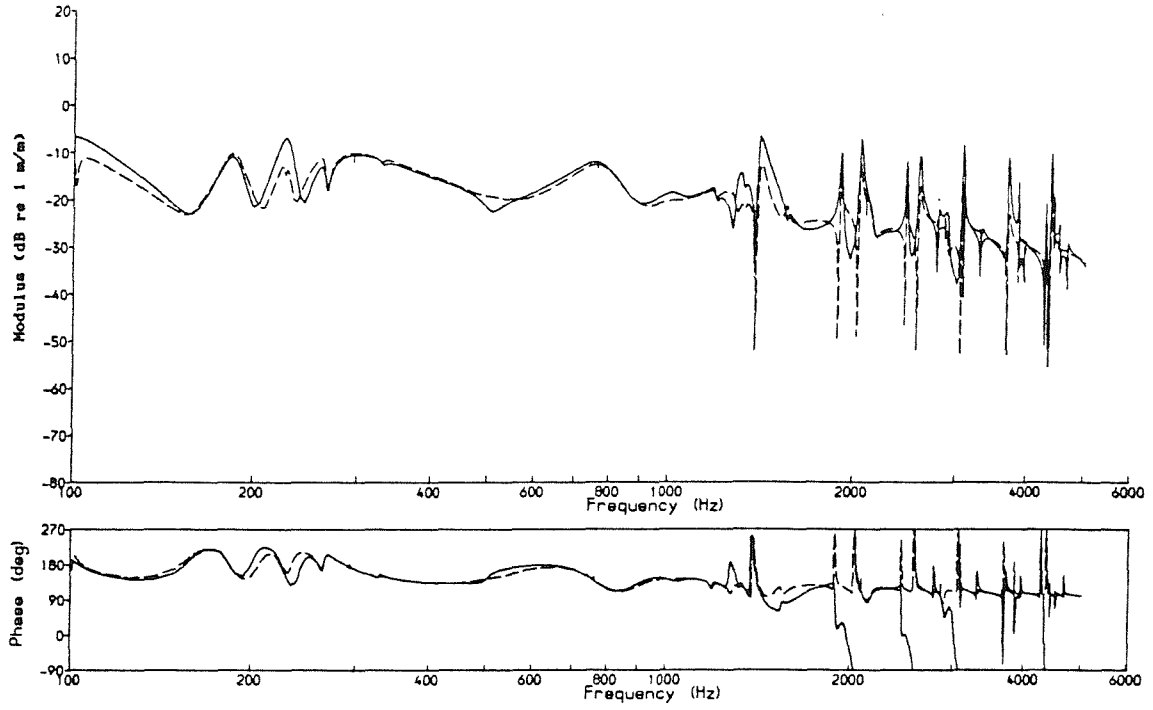

(b) Lateral Wheel Vibration Displacement for a Unit Roughness Input

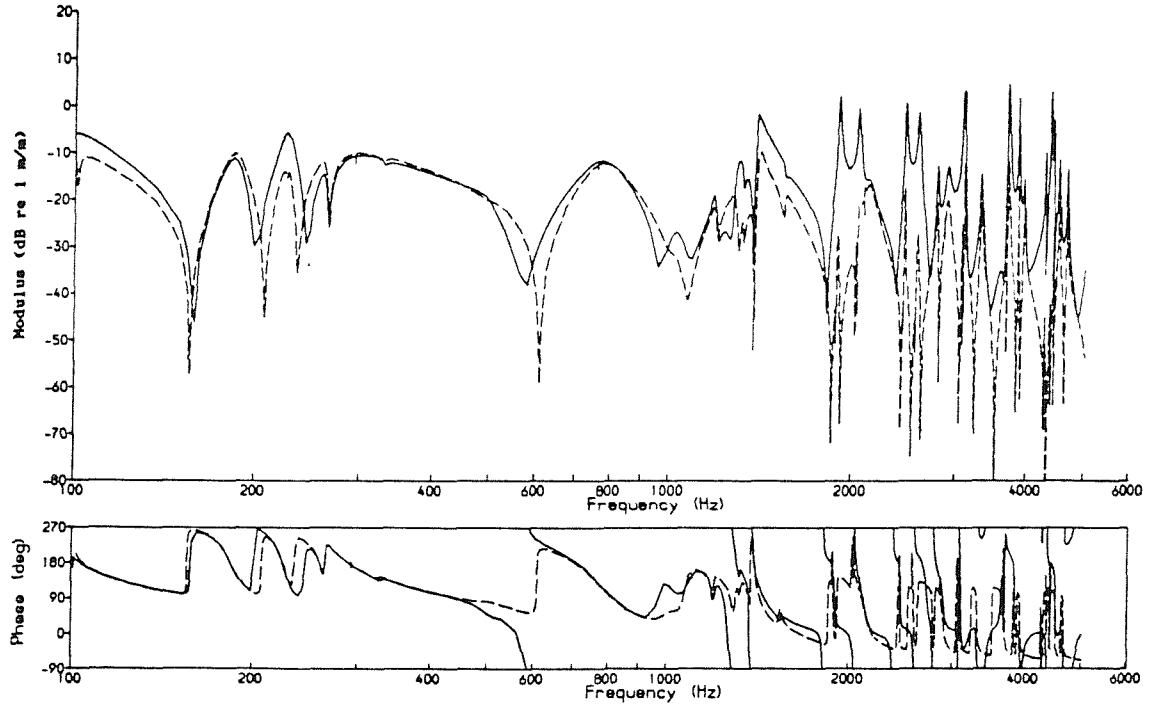

Figure 30 Predicted Lateral Vibration with and without Wheel Cross Receptance: ——— Baseline, ····· Wheel Cross Receptance Zero

(a) Lateral Rail Vibration Displacement for a Unit Roughness Input

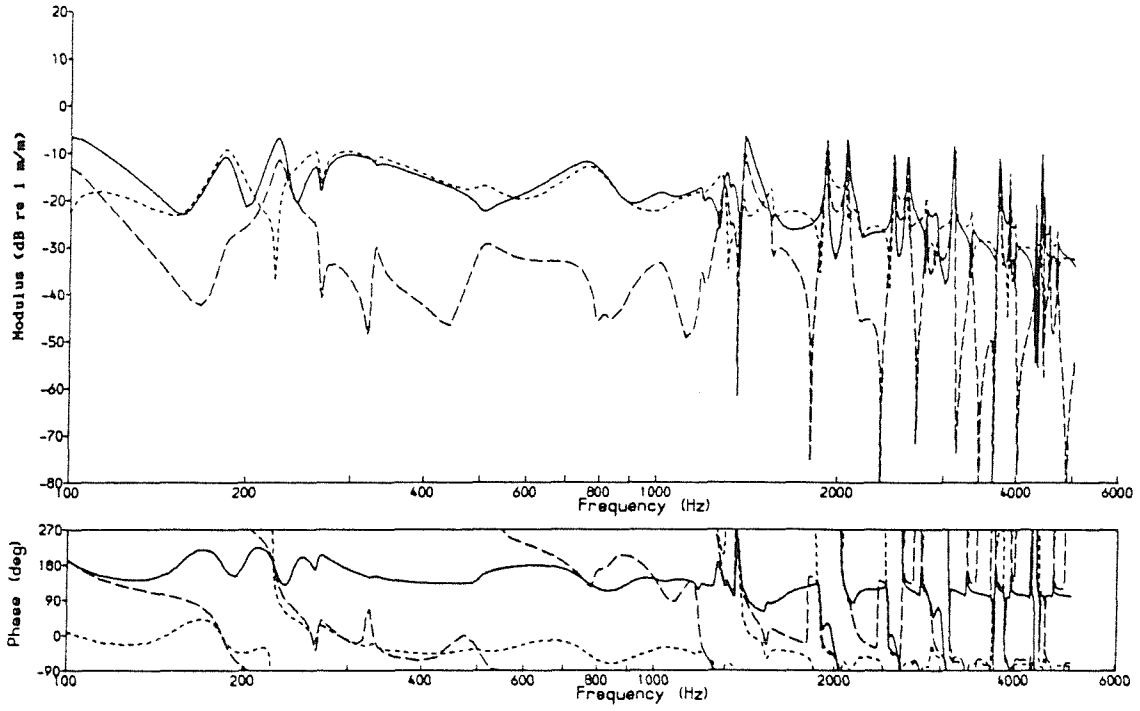

(b) Lateral Wheel Vibration Displacement for a Unit Roughness Input

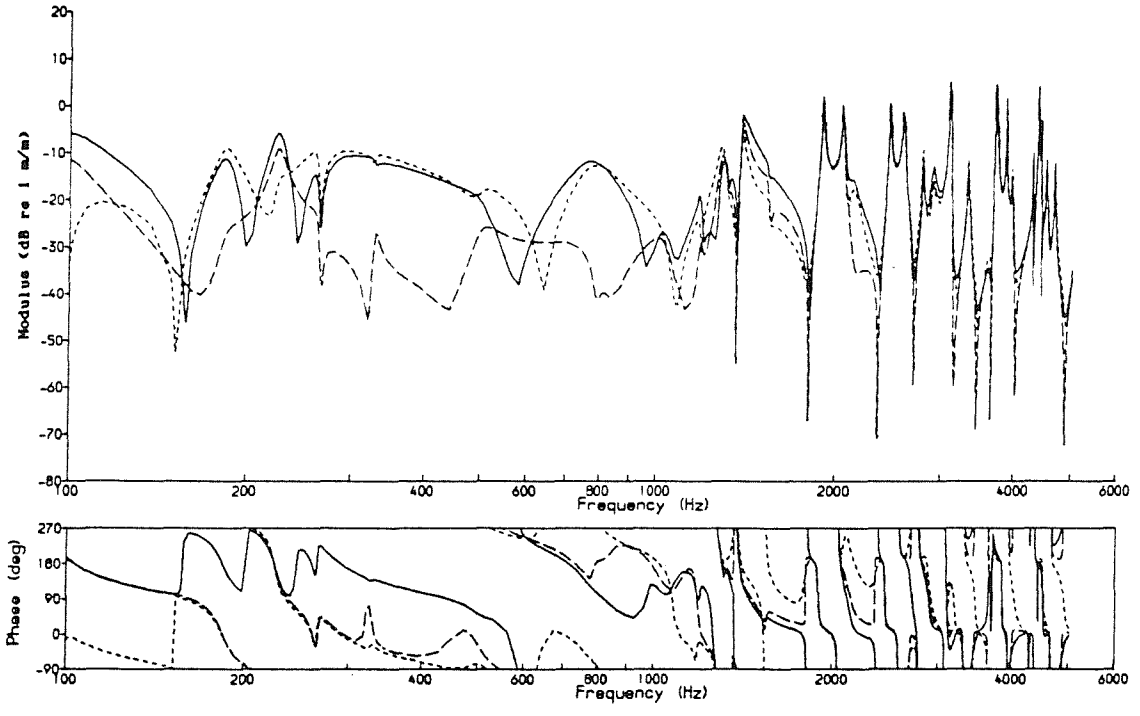

Figure 31 Predicted Lateral Vibration with various Rail Cross Receptances: ——— Baseline, – – – Zero, ····· Negative

(a) Vertical Rail Vibration Displacement for a Unit Roughness Input

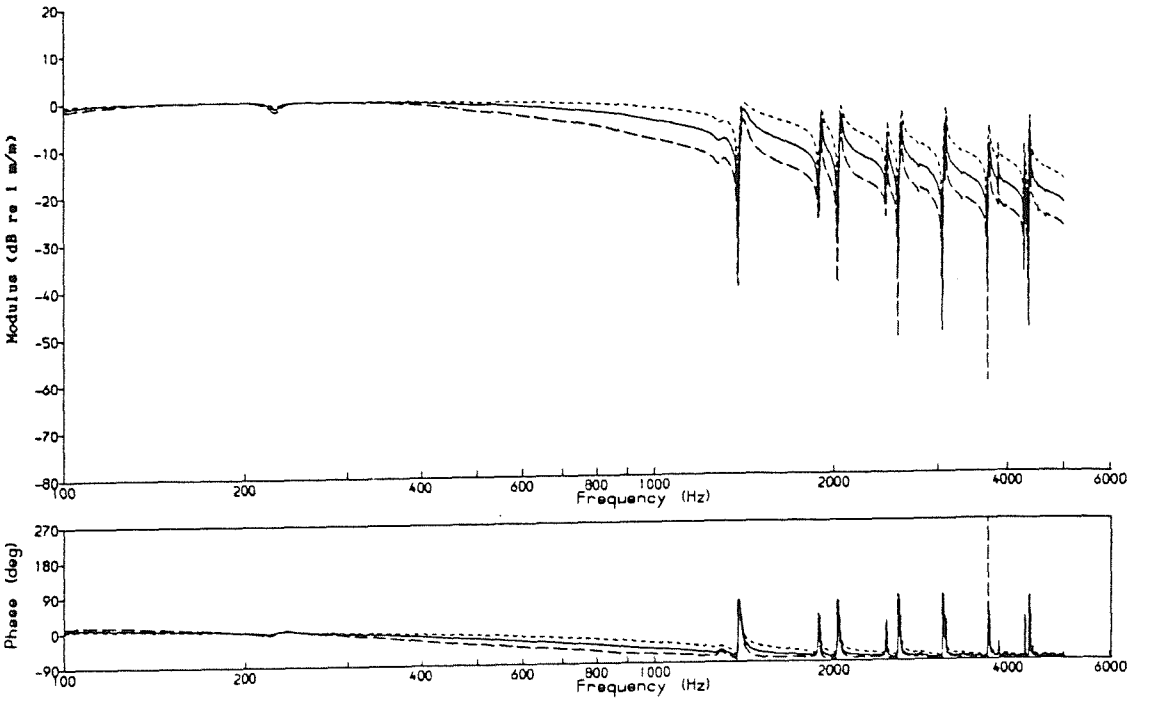

(b) Vertical Wheel Vibration Displacement for a Unit Roughness Input

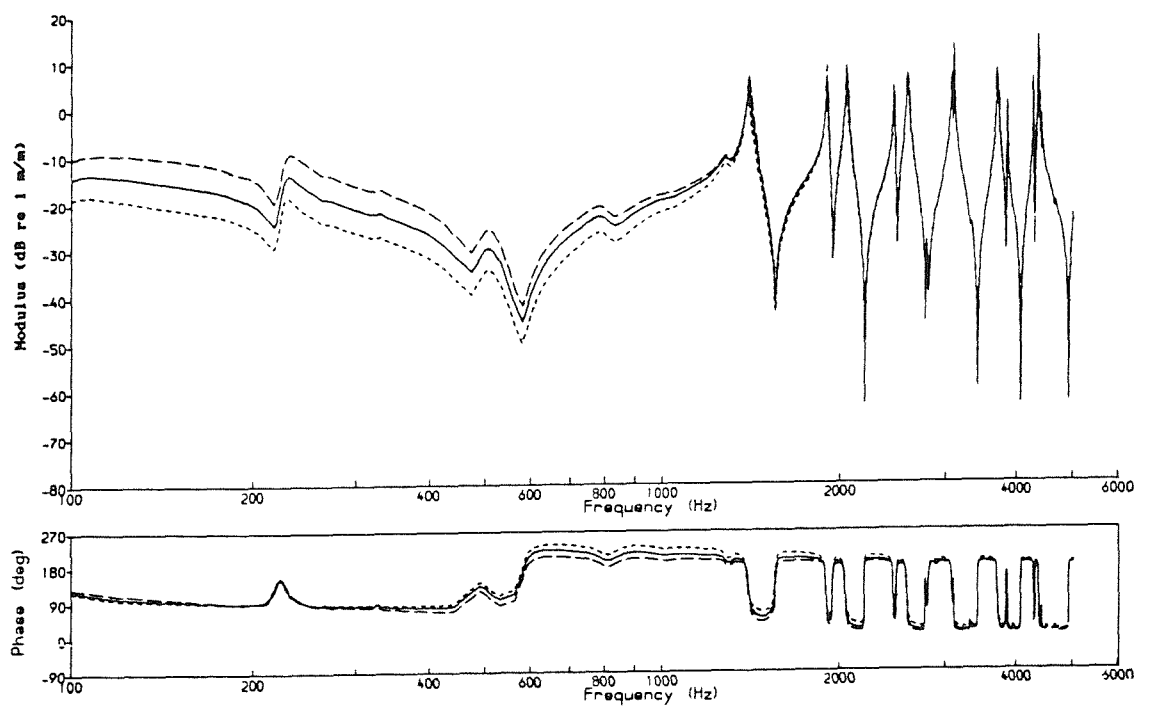

Figure 32 Predicted Vertical Vibration for Various Levels of Rail Vertical Receptance: ——— Baseline, – – – Baseline -5 dB, ····· Baseline +5 dB

unaffected at high frequencies. These effects can be understood in the light of the discussion of §3.4.1. The lateral vibrations of both the wheel and the rail follow the same trend as the wheel vertical response, and are not shown.

The phase of the rail receptance was set to -90° in the baseline analysis, but in practice the phase varies with frequency within a broad range, so the effect of changing the phase of the rail vertical receptance to -135° or -45° has been studied. This produces the results shown in Figure 33.

The main effect is in the region of 500-1000 Hz, which is where the predicted rail and contact receptances have similar magnitudes. If the phase of α^{R}_{vv} is -135°, its real part is negative, so that it appears masslike, and this forms a damped 'resonant circuit' in combination with the stiffness of the contact spring. This results in amplification of the input to greater than 0 dB ($|z_R/r|>1$) and is generally referred to as the 'contact resonance'. However if the phase is -45°, the real part is positive, which adds to the spring of the coupling, and the damping introduced by the imaginary part ensures that the response is attenuated, as if by a vibration isolator. The lateral responses are affected in precisely the same way as the vertical responses in the region of 500-1000 Hz, and so are not shown.

In practice the frequency dependence of the phase of the vertical rail receptance is unlikely to have a significant effect on the amplitudes of the response, its effect being restricted to this part of the frequency range, and is therefore not a particularly critical parameter.

The cross receptance has already been considered in §3.4.1, where it was found that the vertical responses were unaffected, but that the lateral responses were significantly affected, by omitting this term (Figure 31). Additionally, the effect of a ±5 dB change is considered here. The corresponding lateral responses are shown in Figure 34. Generally these are altered by ±5 dB. For the rail, the exception to this is at the peaks and troughs, where the wheel receptances have more effect. For the wheel, the response is affected less at the higher frequencies.

The level of rail cross receptance and the level of the lateral rail response appear to be directly related. Since the lateral responses appeared to be around 5 dB too low (Figure 22b), this

(a) Vertical Rail Vibration Displacement for a Unit Roughness Input

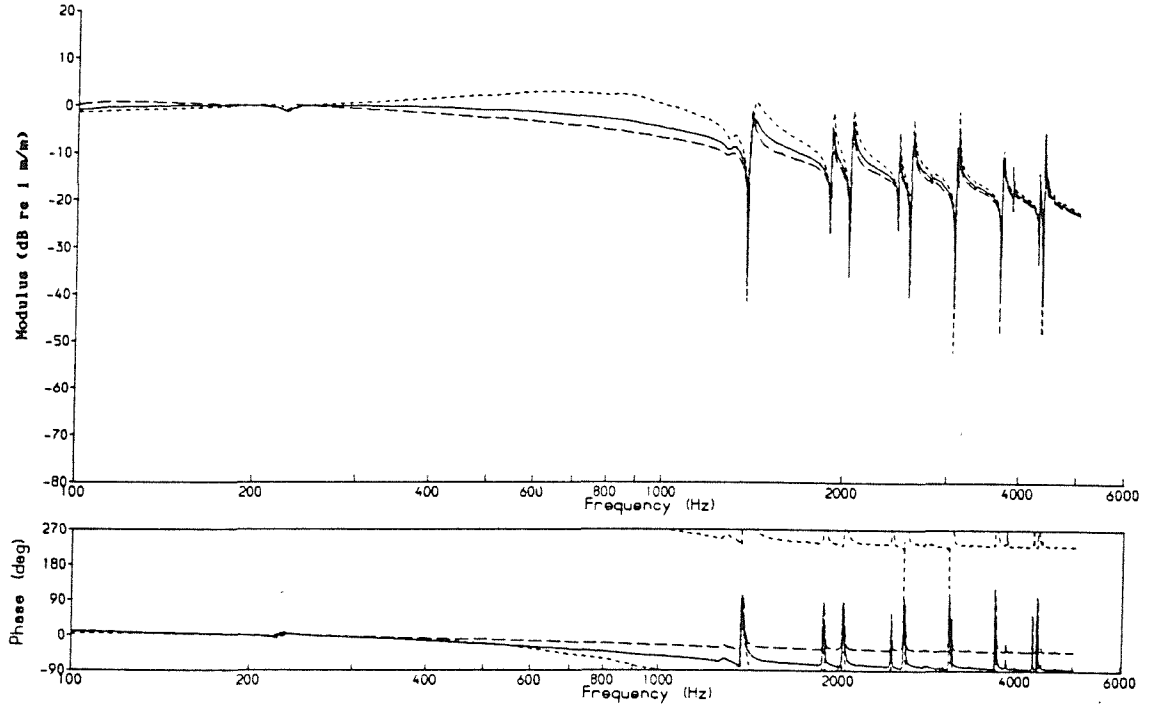

(b) Vertical Wheel Vibration Displacement for a Unit Roughness Input

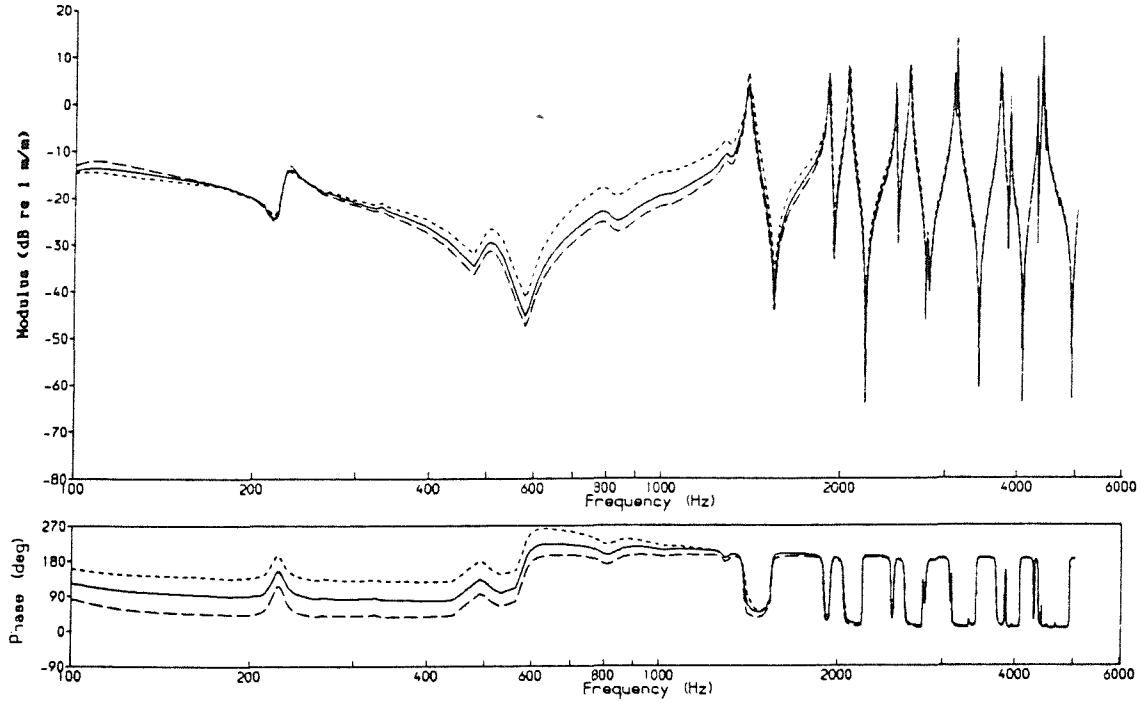

Figure 33 Predicted Vertical Vibration for Various Phases of Rail Vertical Receptance: ——— Baseline (-90°), - - - -45°, ····· -135°

(a) Lateral Rail Vibration Displacement for a Unit Roughness Input

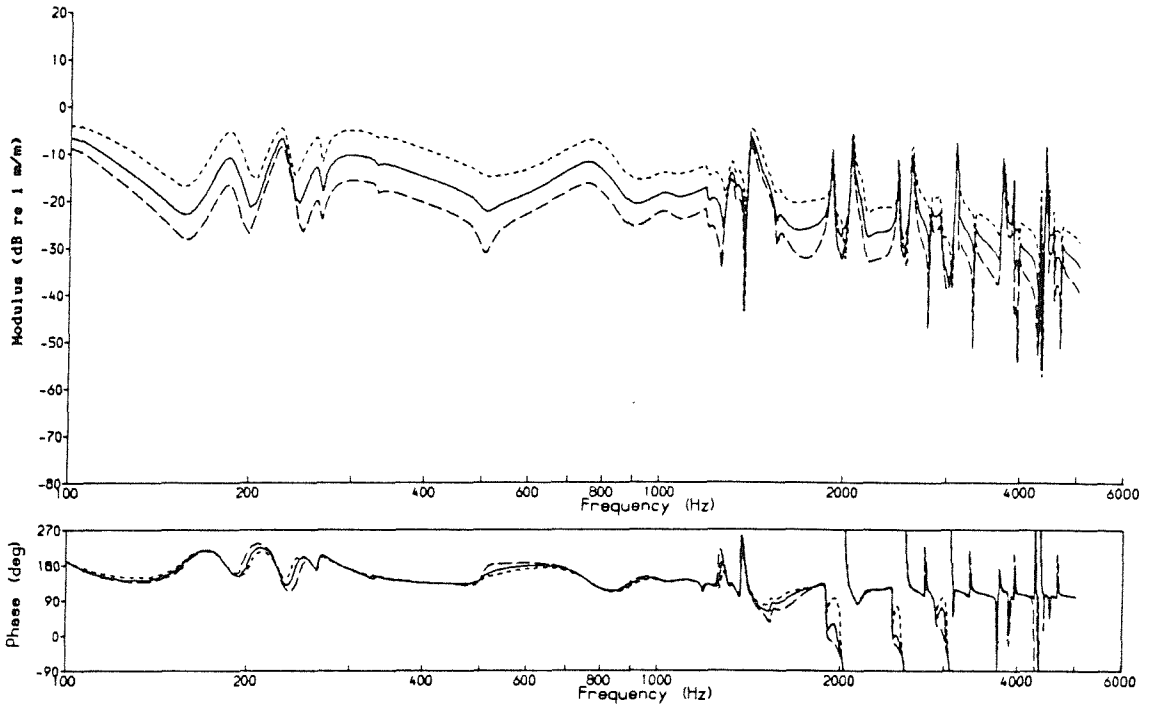

(b) Lateral Wheel Vibration Displacement for a Unit Roughness Input

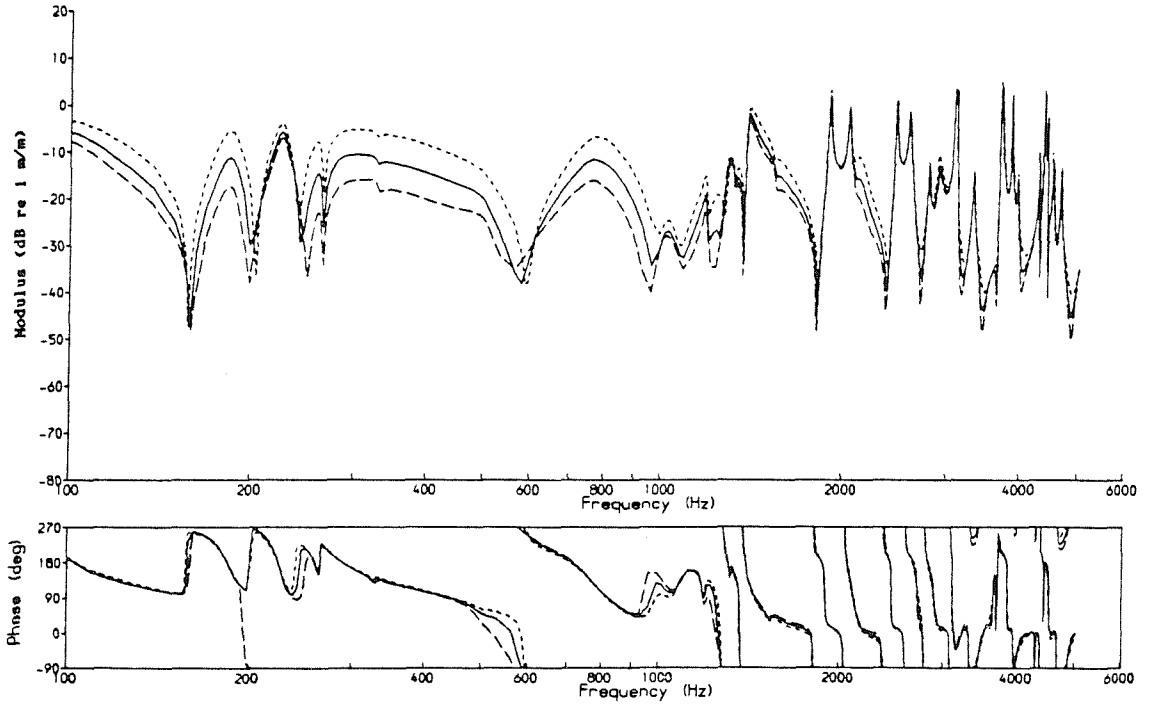

Figure 34 Predicted Lateral Vibration for Various Levels of Rail Cross Receptance: ——— Baseline, – – – Baseline -5 dB, ····· Baseline +5 dB

suggests that the rail cross receptance should perhaps have been set slightly higher. The shape of the response may be expected to be determined by detail variations in the cross receptance.

The effects on the lateral response of altering the rail lateral receptance by ±5 dB are shown in Figure 35, there being no significant change to the vertical responses. The changes are much less than those due to the cross receptance (Figure 34). When the lateral receptance is increased there is a slight reduction in both the wheel and rail lateral responses. This is rather surprising as the opposite might have been expected. However the secondary nature of this effect is consistent with the hypothesis that the rail cross receptance has a direct effect on the lateral responses.

Similarly, changing the phase of the lateral receptance produces only small changes to the lateral responses.

3.4.3 Effects of Contact Parameters

Changing the contact vertical receptance by ±5 dB affects the vertical responses as shown in Figure 36, the lateral responses following the same trends as the vertical wheel response. This parameter has an effect only at higher frequencies, since at lower frequencies the rail vertical receptance dominates (see §3.4.1). The results for the vertical wheel response contrast with Figure 31b in which the effect of changing the rail receptance was limited to the lower frequencies.

It should be noted that the precise frequencies of the peaks in the wheel response are altered - they are raised for a decrease in contact receptance, ie an increase in stiffness, and vice versa. This happens because the cross-over of the wheel and contact receptances above f_o, which roughly becomes the peak frequency of the response, is raised when the contact receptance is lowered. This can be seen from Figure 29. The peak frequencies are listed in Table 5, which are subject to a similar tolerance as before (not quoted). The peak amplitudes can also be seen to be affected - they are reduced for a decrease in receptance or raised for an increase.

Figure 37 contains the results of altering the rail and contact vertical receptances simultaneously. For the wheel response, this combines the low frequency effects of altering the rail receptance (Figure 32) and the high frequency effect of the contact receptance (Figure 36), and once more the peak frequencies are affected. The

(a) Lateral Rail Vibration Displacement for a Unit Roughness Input

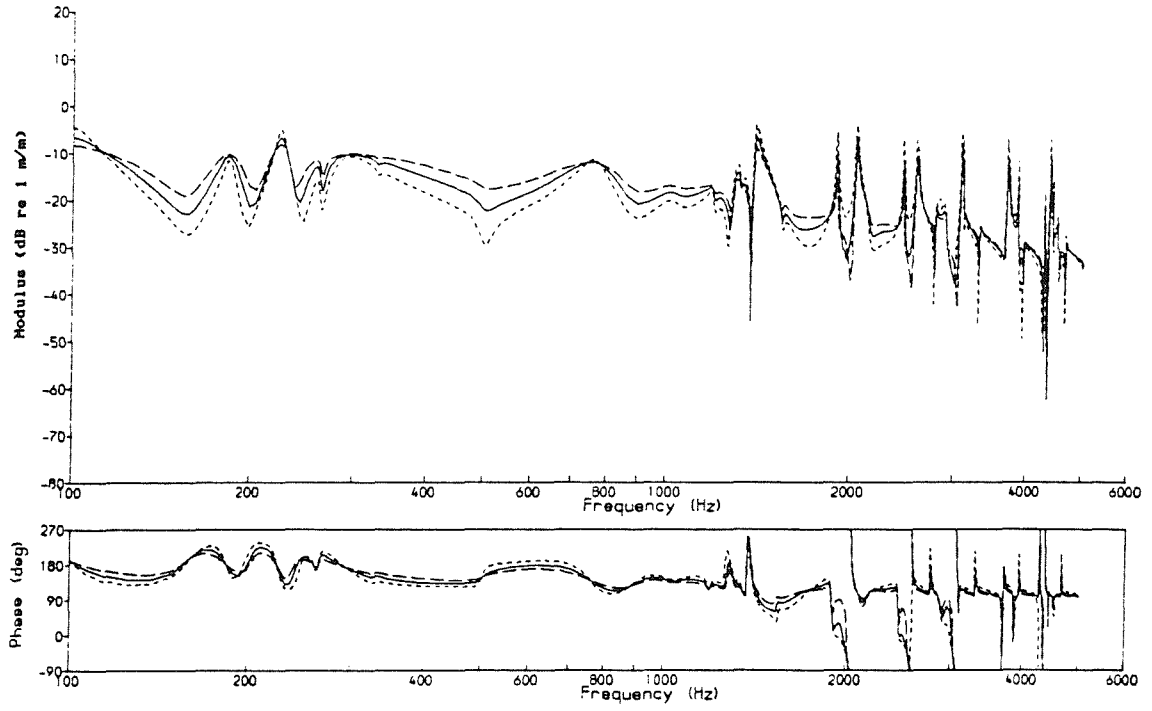

(b) Lateral Wheel Vibration Displacement for a Unit Roughness Input

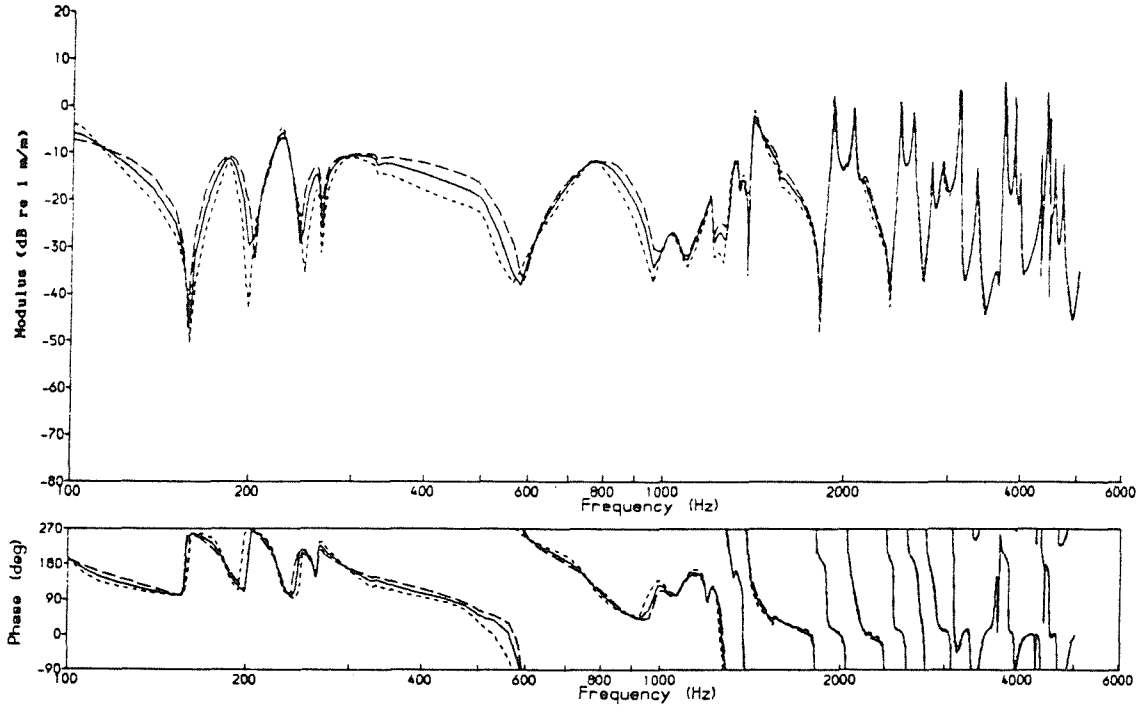

Figure 35 Predicted Lateral Vibration for Various Levels of Rail Lateral Receptance: ——— Baseline, – – – Baseline -5 dB, ····· Baseline +5 dB

(a) Vertical Rail Vibration Displacement for a Unit Roughness Input

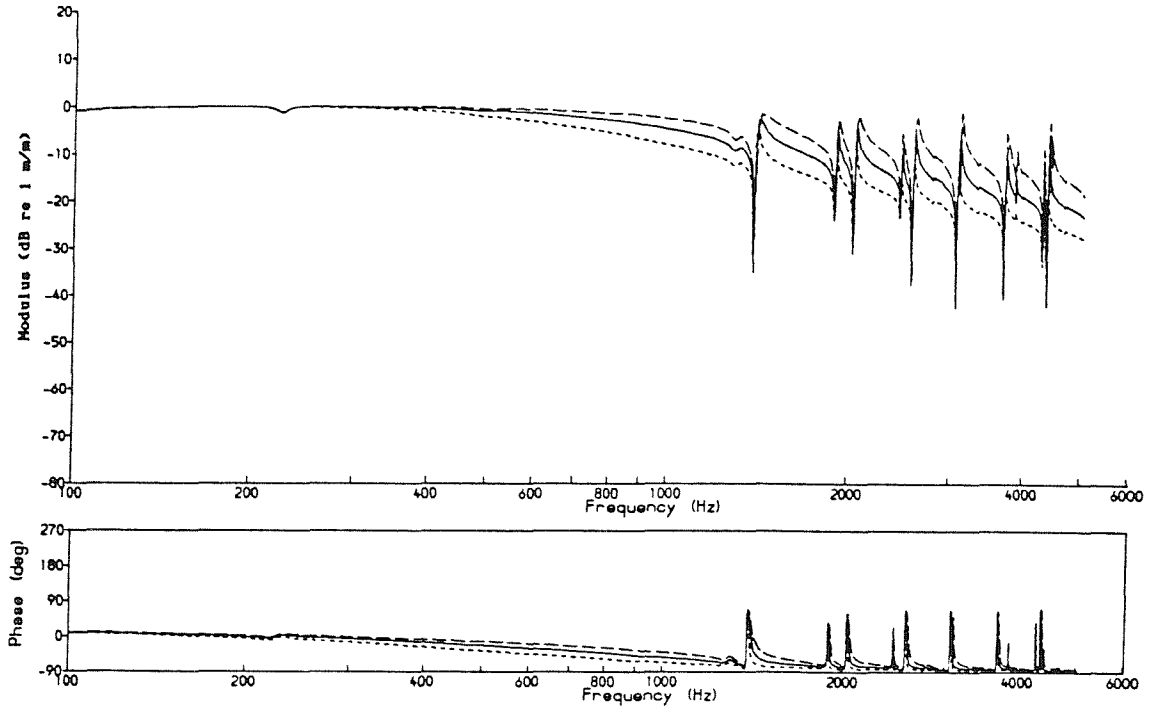

(b) Vertical Wheel Vibration Displacement for a Unit Roughness Input

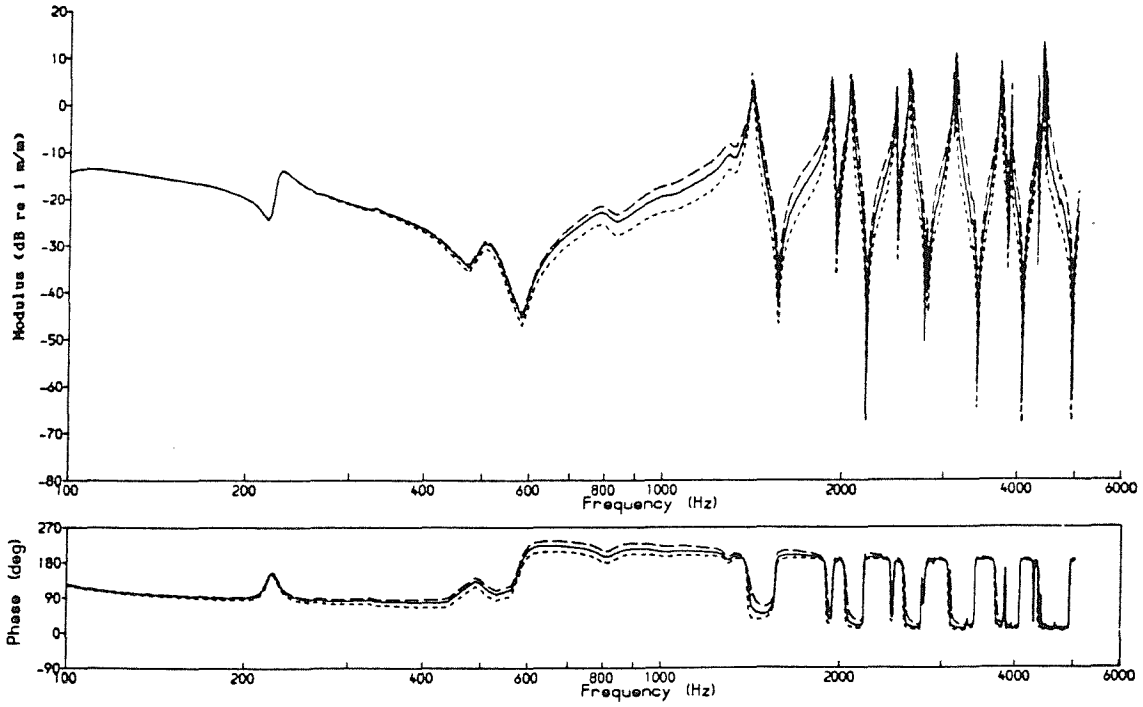

Figure 36 Predicted Vertical Vibration for Various Levels of Contact Vertical Receptance: ——— Baseline, – – – Baseline -5 dB, ····· Baseline +5 dB

(a) Vertical Rail Vibration Displacement for a Unit Roughness Input

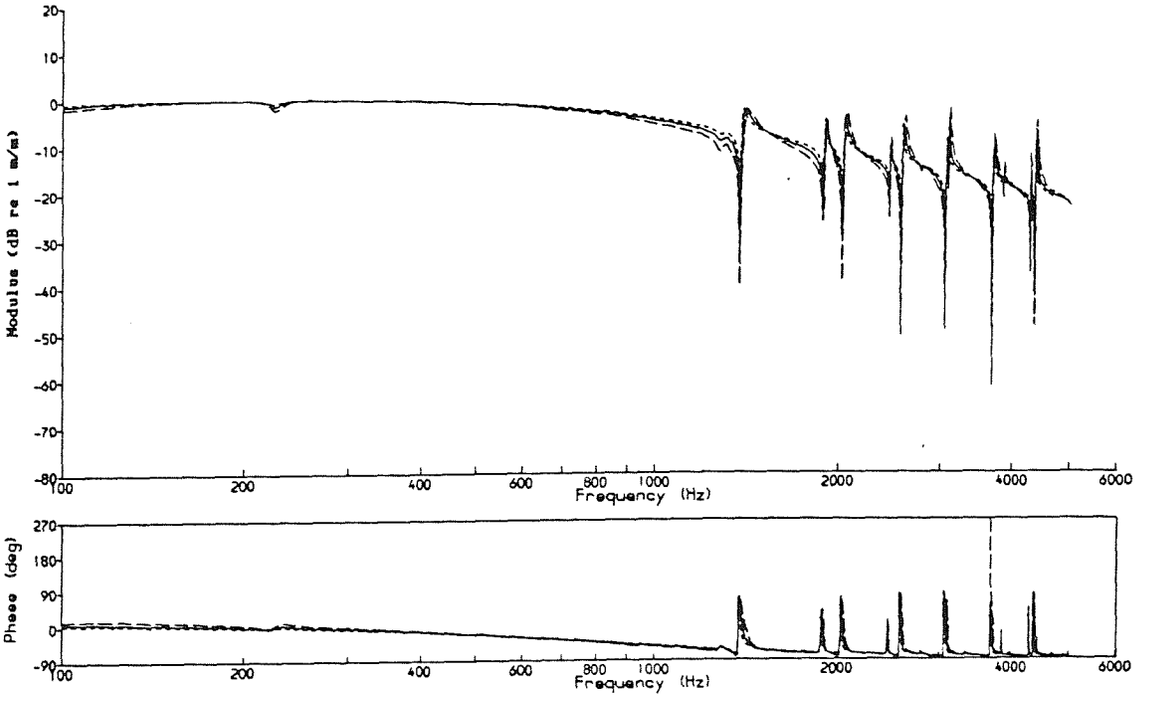

(b) Vertical Wheel Vibration Displacement for a Unit Roughness Input

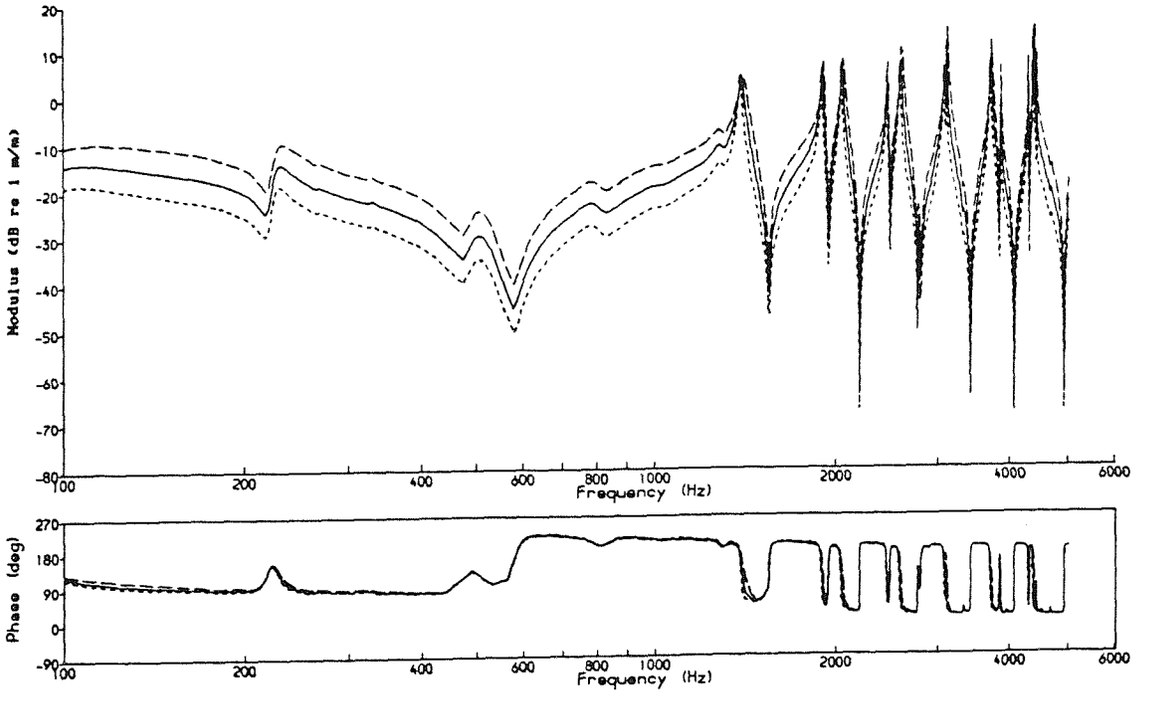

Figure 37 Predicted Vertical Vibration: Effect of Varying Rail and Contact Receptances Together: ——— Baseline, – – – Baseline -5 dB, ····· Baseline +5 dB

Table 5 Results on Peaks in Predicted Vertical Wheel Vibration of Varying the Amplitude of the Vertical Contact Receptance (Figure 36)

(a) 1-nodal-circle modes		Baseline		Vertical contact receptance			
				−5 dB		+5 dB	
n	f_o	Δf	amp	Δf	amp	Δf	amp
2	1390	16	4	16	2	10	7
3	1880	14	6	18	4	10	7
4	2440	11	5	15	4	7	4
5	3095	10	12	22	11	6	5
6	3855	7	1	9	6	5	−4

(b) Radial modes		Baseline		Vertical contact receptance			
				−5 dB		+5 dB	
n	f_o	Δf	amp	Δf	amp	Δf	amp
2	2025	19	6	27	5	13	6
3	2560	23	9	35	8	15	8
4	3060	21	7	24	4	13	7
5	3690	23	8	39	9	7	6
6	4360	20	13	35	12	12	11

KEY
n number of nodal diameters in mode
f_o natural frequency input to the prediction (Hz)
Δf difference between peak frequency and f_o (Hz)
amp amplitude of vertical response at the spectral peak (dB re 1 m/m)

Table 6 Results on Peaks in Predicted Vertical Wheel Vibration of Varying the Amplitudes of Vertical Contact Receptance and Vertical Rail Receptance Together (Figure 37)

(a) 1-nodal-circle modes		Baseline		Vertical contact & rail receptances			
				−5 dB		+5 dB	
n	f_o	Δf	amp	Δf	amp	Δf	amp
2	1390	16	4	24	4	8	4
3	1880	14	6	22	7	10	5
4	2440	11	5	15	6	7	2
5	3095	10	12	22	15	6	4
6	3855	7	1	9	7	5	−4

(b) Radial modes		Baseline		Vertical contact & rail receptances			
				−5 dB		+5 dB	
n	f_o	Δf	amp	Δf	amp	Δf	amp
2	2025	19	6	31	8	13	5
3	2560	23	9	39	11	15	6
4	3060	21	7	25	5	13	6
5	3690	23	8	39	12	7	5
6	4360	20	13	37	15	12	10

KEY
n number of nodal diameters in mode
f_o natural frequency input to the prediction (Hz)
Δf difference between peak frequency and f_o (Hz)
amp amplitude of vertical response at the spectral peak (dB re 1 m/m)

results are tabulated in Table 6. However in this case the rail response is not significantly affected, as the two effects of Figures 31 and 36 cancel out.

Changing the phase of the vertical contact receptance to -10° or -20° produced little effect, but changing it to -90° resulted in the peak frequencies being lowered to correspond almost exactly to the resonance frequencies as shown in Figure 38 and listed in Table 7. Also the amplitudes are reduced to just below 0 dB. However, such a large deviation from the theoretical phase of 0° does not appear to be physically justifiable.

The contact lateral receptance affects only the lateral responses. Figure 39 shows the effect of altering the creep damper according to the train speed. If the lateral contact stiffness is omitted, leaving only the creep damper, the effects seen in Figure 39 are carried over to the higher part of the frequency range as well. These changes have only a slight effect on the responses, however, and are clearly not responsible for the differences observed in Appendix A between the various speeds. In particular the speed effect observed in the experimental data was strongest in the vertical rail vibration which is unaffected by the contact lateral receptance.

Table 7 Results on Peaks in Predicted Wheel Vibration of Varying the Phase of the Vertical Contact Receptance (Figure 38)

(a) 1-nodal-circle modes

		Baseline		Vertical contact receptance phase -10°		-20°		-90°	
n	f_o	Δf	amp	Δf	amp	Δf	amp	Δf	amp
2	1390	16	4	12	3	10	2	-2	0
3	1880	14	6	14	4	12	2	1	-2
4	2440	11	5	11	3	9	2	1	-2
5	3095	10	12	10	7	10	4	6	-4
6	3855	7	1	7	-1	7	-2	5	-7

(b) Radial modes

		Baseline		Vertical contact receptance phase -10°		-20°		-90°	
n	f_o	Δf	amp	Δf	amp	Δf	amp	Δf	amp
2	2025	19	6	17	4	17	2	5	-2
3	2560	23	9	19	6	19	4	3	-1
4	3060	21	7	19	5	17	3	1	-1
5	3690	23	8	19	5	19	3	-5	-1
6	4360	20	13	18	8	18	5	2	-1

KEY

n number of nodal diameters in mode
f_o natural frequency input to the prediction (Hz)
Δf difference between peak frequency and f_o (Hz)
amp amplitude of vertical response at the spectral peak (dB re 1 m/m)

(a) Vertical Rail Vibration Displacement for a Unit Roughness Input

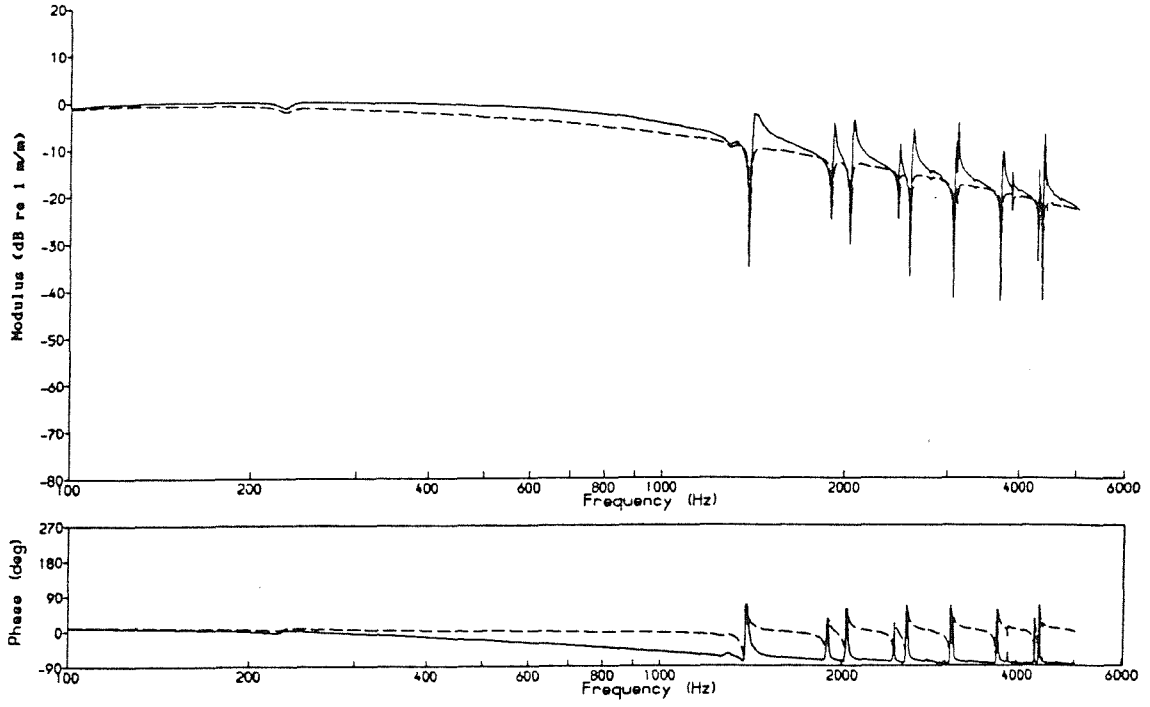

(b) Vertical Wheel Vibration Displacement for a Unit Roughness Input

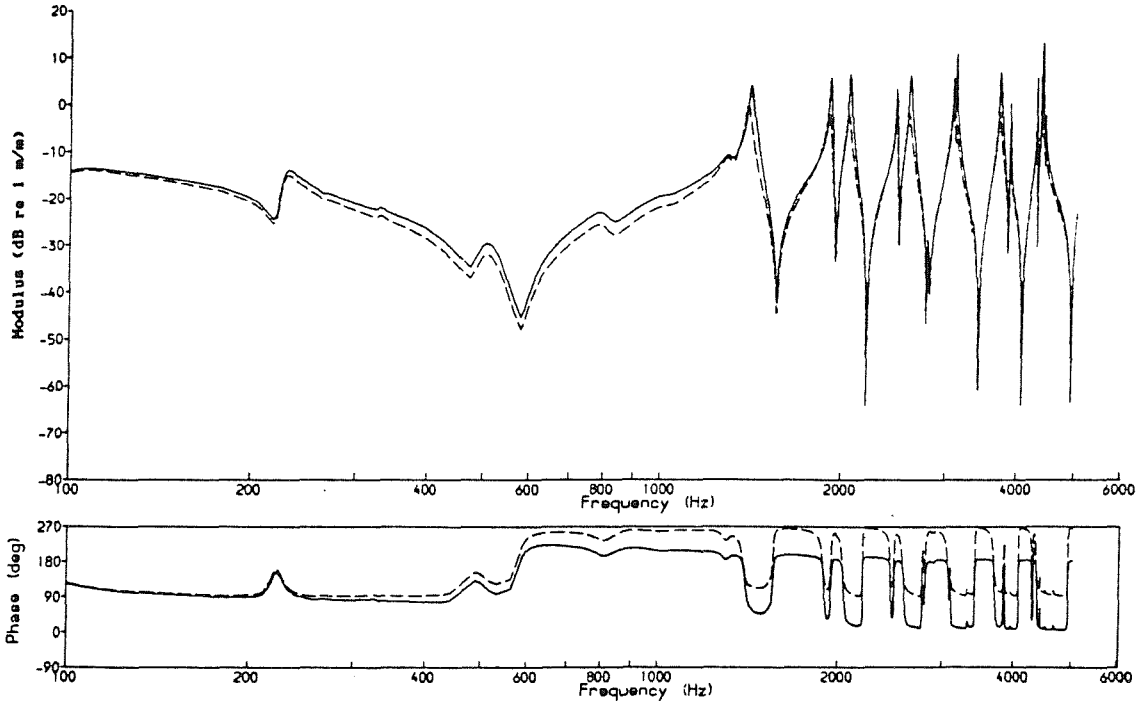

Figure 38 Predicted Vertical Vibration for Various Phases of Contact Vertical Receptance: ——— Baseline (0°), – – – 90°

(a) Lateral Rail Vibration Displacement for a Unit Roughness Input

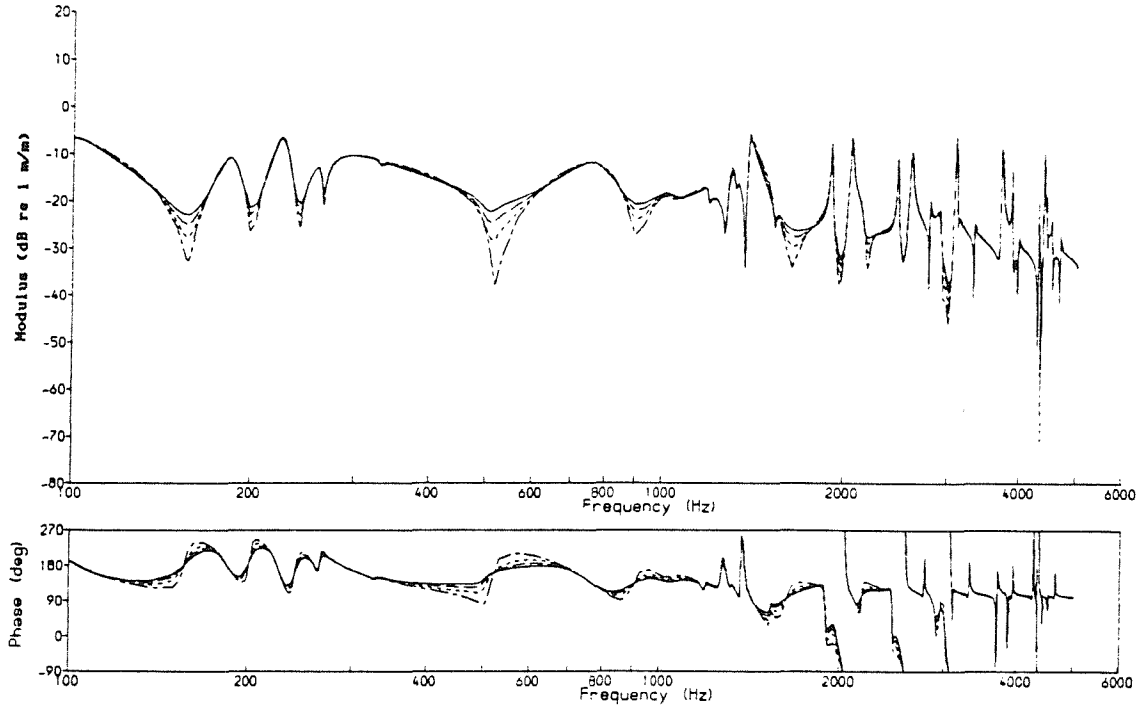

(b) Lateral Wheel Vibration Displacement for a Unit Roughness Input

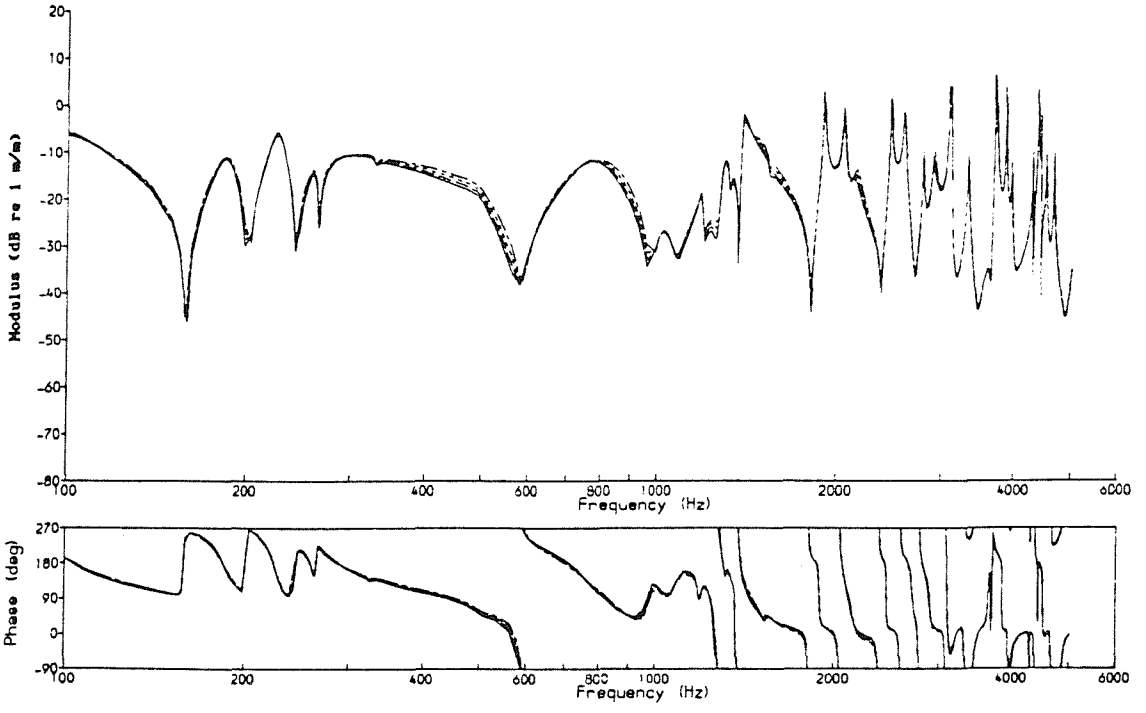

Figure 39 Predicted Lateral Vibration: Speed Effect of Creep Damper in Lateral Contact Receptance: ——— Baseline (160 km/h), – – – 120 km/h, ····· 80 km/h, —·—· 40 km/h

Figure 40 compares the lateral predictions for the creep damper with and without the contact stiffness, and a rigid lateral connection (specified by an infinite stiffness). The latter, which corresponds to the parameters used by Remington, gives wheel and rail lateral responses which are identical to each other, with greater dips in the rail response than previously. However it would seem that the creep damper used in the baseline predictions is not greatly different from a rigid connection.

Figure 41 compares a very soft connection with the baseline. This consists of a damper of value C=1 Ns/m (used for convenience as zero would render the receptance infinite). This value corresponds to a receptance greater than -90 dB for all frequencies, which is much higher than either the wheel or the rail, and so it should be a reasonable simulation of an infinitely soft connection.

In this case the response is much different from the baseline case, with very large wheel response at the 0-nodal-circle modes of vibration of the wheel. This appears a more reasonable result than that produced by the relatively stiff creep damper formulation, although the peaks are now much sharper than in the experimental results (Figure A6).

Also shown in Figure 41 are results produced by replacing the creep force damper by a hysteretic damper of 7×10^6 N/m (ie a receptance level of -137 dB re 1 m/N (cf Figure 19)). This is a fairly soft connection for the frequency range under consideration, but has a similar receptance level to the creep damper at low frequencies (where the creep force equations have been validated [80]). This gives similar results to the soft connection at frequencies above about 500 Hz.

The use of a soft lateral connection appeared to be a way of rectifying the predictions of lateral wheel response, but in practice the 0-nodal-circle modes are either too sharp or not present. There appears to be no straightforward compromise giving a damped (broadened) peak as found experimentally.

(a) Lateral Rail Vibration Displacement for a Unit Roughness Input

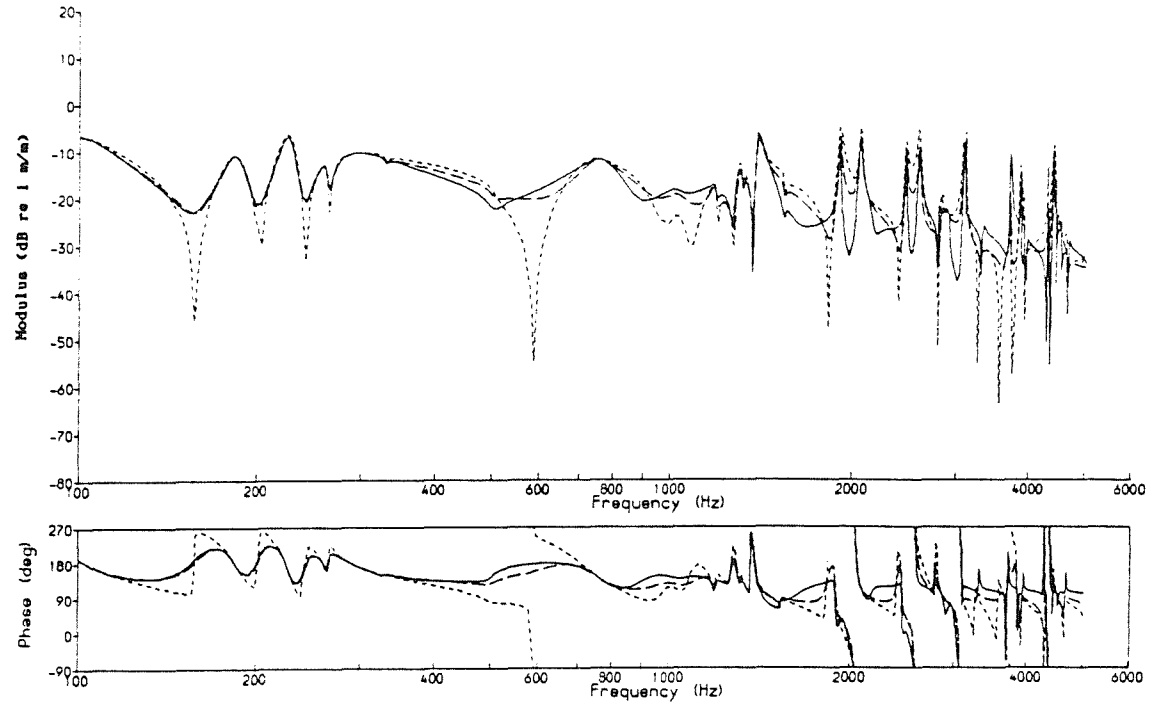

(b) Lateral Wheel Vibration Displacement for a Unit Roughness Input

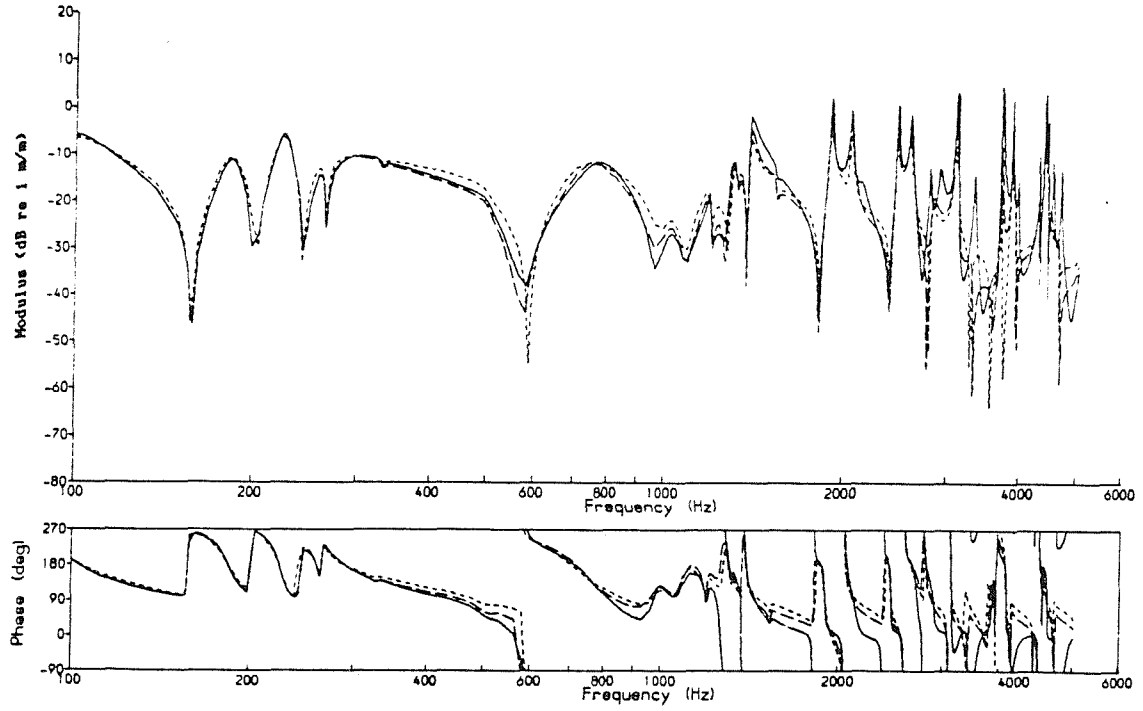

Figure 40 Predicted Lateral Vibration for Various Contact Lateral Receptances: ——— Baseline, – – – Creep Damper only, ····· Rigid Lateral Connection

(a) Lateral Rail Vibration Displacement for a Unit Roughness Input

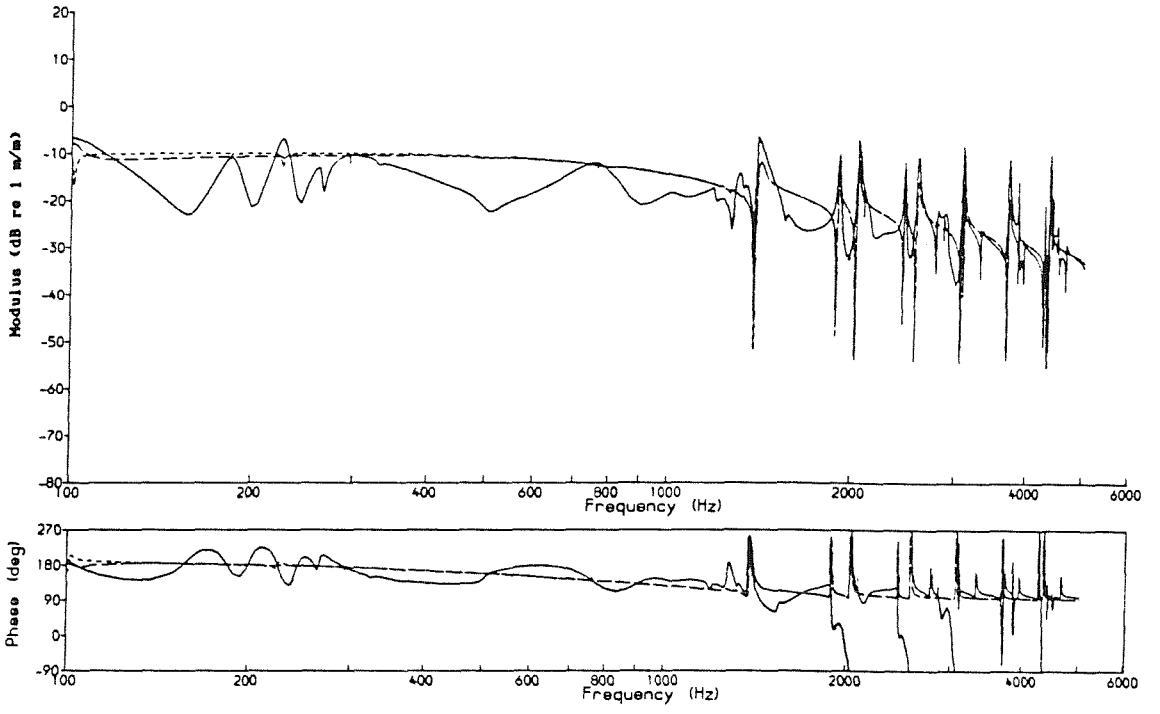

(b) Lateral Wheel Vibration Displacement for a Unit Roughness Input

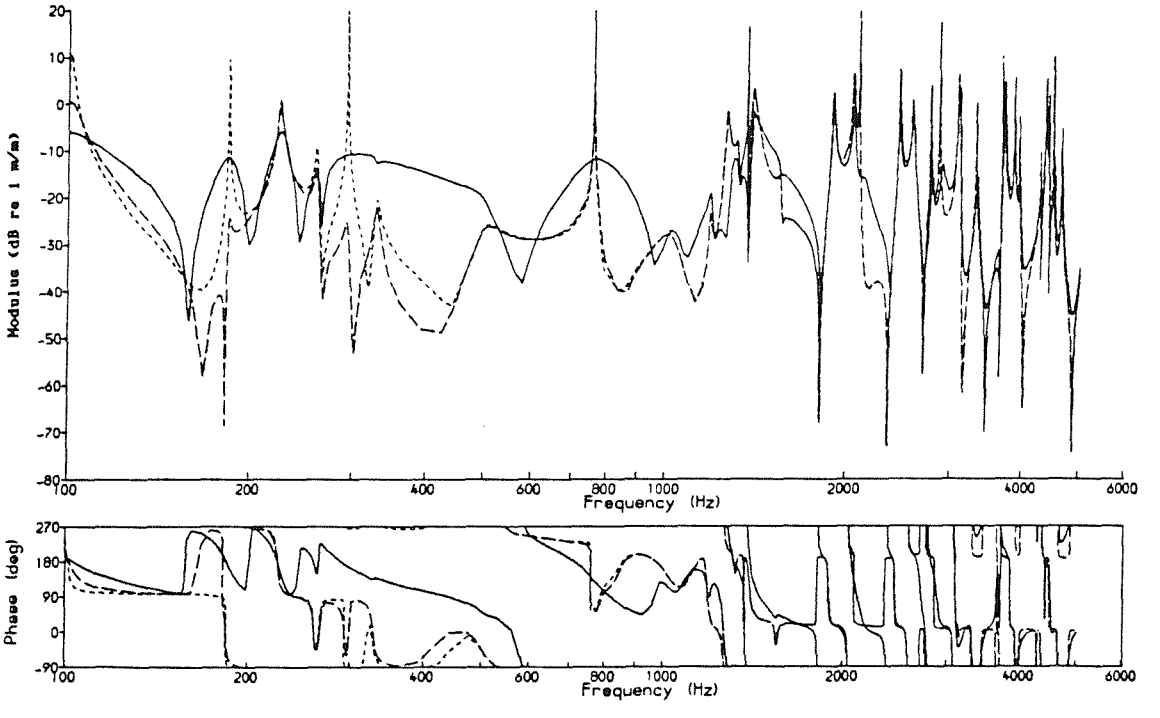

Figure 41 Predicted Lateral Vibration for Various Soft Contact Lateral Receptances: ——— Baseline, – – – Hysteretic Damper (7×10⁶ N/m), ····· Very Soft Connection (C=1 Ns/m)

3.4.4 Effects of Wheel Parameters

The rail and contact receptances are based on fairly simple models and have therefore been varied with relative ease. By contrast the wheel receptances, based on the model of §2, have already been established with more confidence, but are more difficult to vary. However the effects of two changes in parameters will be looked at: the inclusion of the cone angle of the wheel and the effects of changes to the modal damping.

The analysis so far has ignored the cone angle of the wheel - the angle at which the running surface is inclined to the horizontal. The modal parameters, $_r\psi_j$ etc, can be rotated through this angle to derive normal (~vertical) and tangential (~lateral) point receptances, which are shown in Figure 42, using the cone angle of a newly profiled wheel which is 1:20, or 2.9°. The normal receptance contains larger components of the 0-nodal-circle modes than the vertical receptance, particularly noticeable at 290 and 760 Hz, and thus looks more like the measurement in Figure C4 which was taken at an angle to the vertical.

Using these rotated receptances (and the corresponding cross receptance), predictions of the normal and tangential vibrations were produced, which were then re-rotated to give results for the vertical and lateral vibration. The vertical vibration was virtually unchanged, whereas the lateral vibration, shown in Figure 43, was affected by a small amount. However the 0-nodal-circle modes still do not appear in the wheel lateral response as they did in the experimental results (Figure A6).

The wheel damping can be varied by altering the modal damping ratios input to the modal sum program. The baseline damping varies from one mode to another, in the range .0001-.0005 for the wheel modes and up to .1 for axle modes. Rather than try to increase the damping of all modes in the same proportion, a minimum damping ratio first of .001, then .003, and finally .01 was imposed on the modes. (Thus, for the case of a minimum of .001, damping is introduced into all modes with damping less than this, whereas modes with greater damping are unaltered). Each increase in damping corresponds approximately to a 10 dB decrease in amplitudes at the peaks of the wheel receptances.

Such changes in modal damping could be achieved by the introduction of damping treatments to the wheel. As an example of the likely level of damping which may be achieved, the following damping ratios

(a) Tangential Wheel Receptance

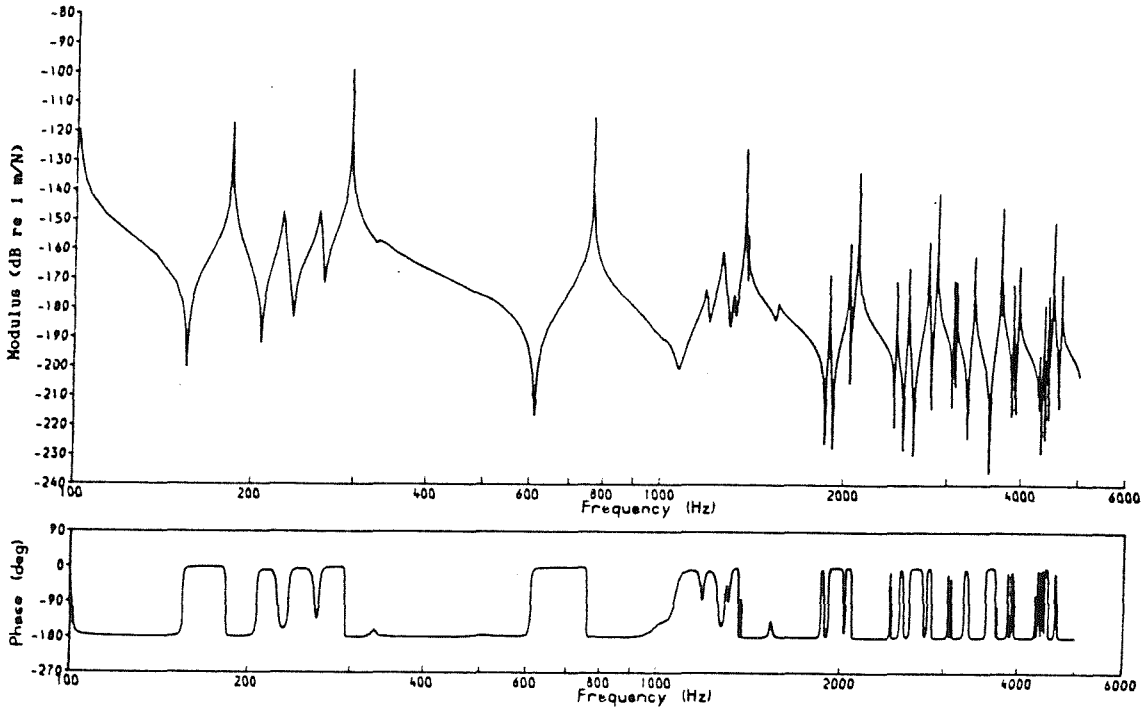

(b) Normal Wheel Receptance

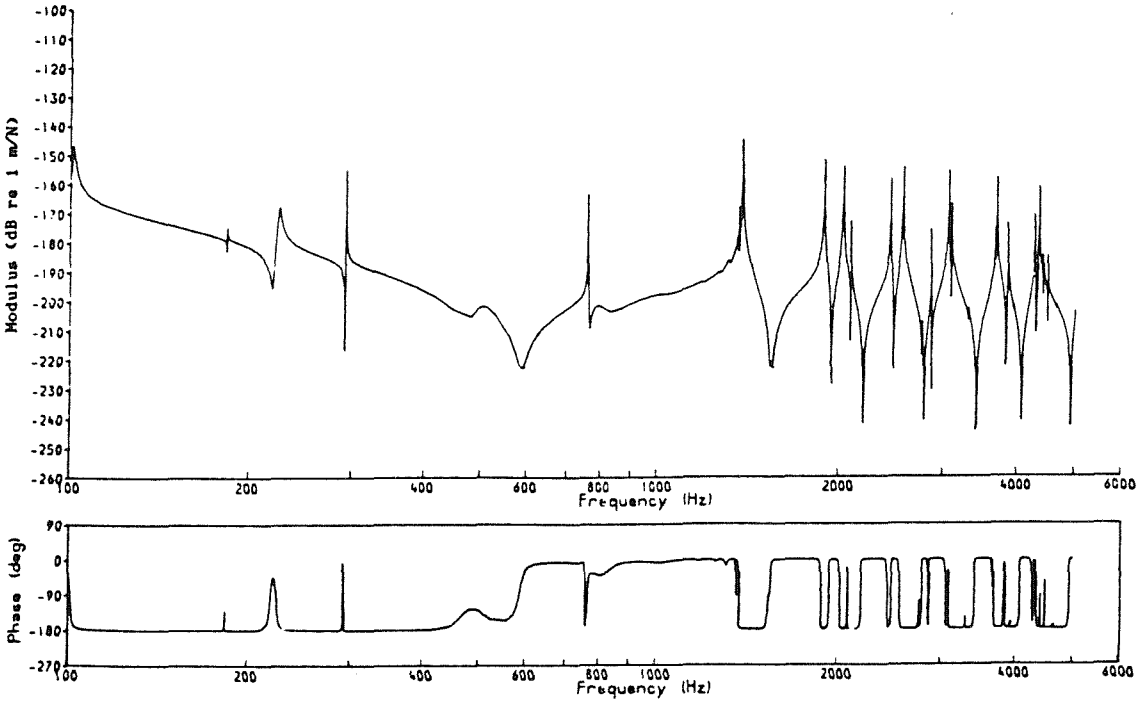

Figure 42 Predicted Point Receptances of the Wheel Allowing for Cone Angle of 2.9°

(a) Lateral Rail Vibration Displacement for a Unit Roughness Input

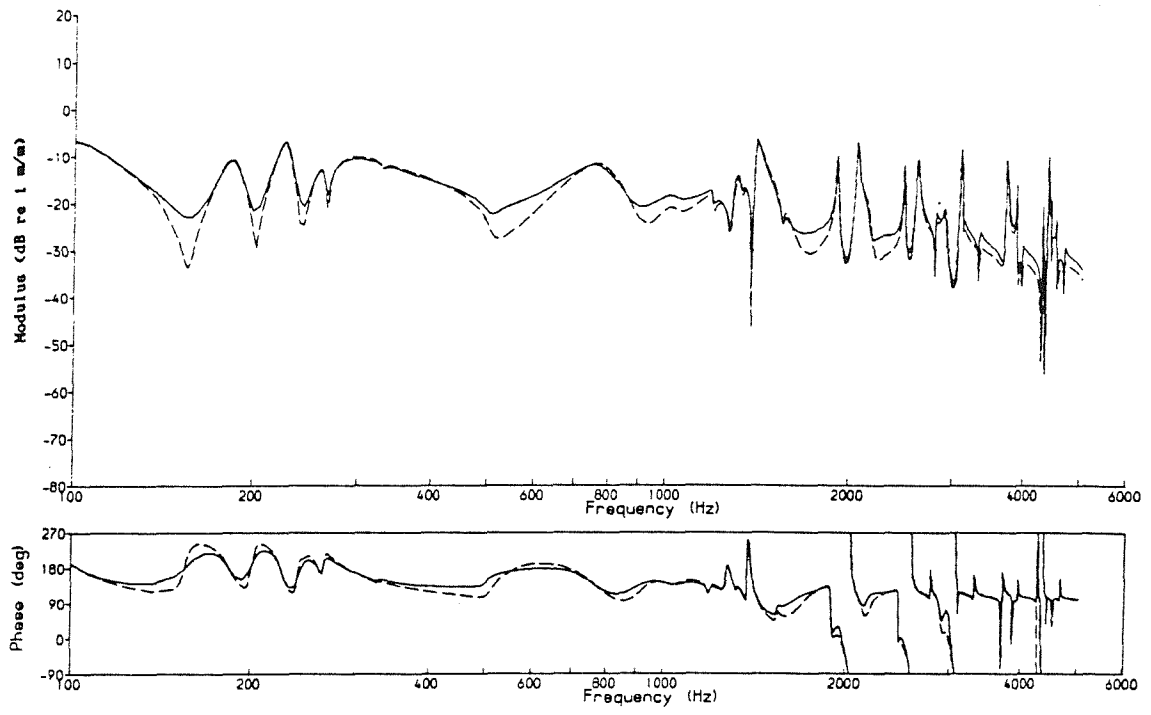

(b) Lateral Wheel Vibration Displacement for a Unit Roughness Input

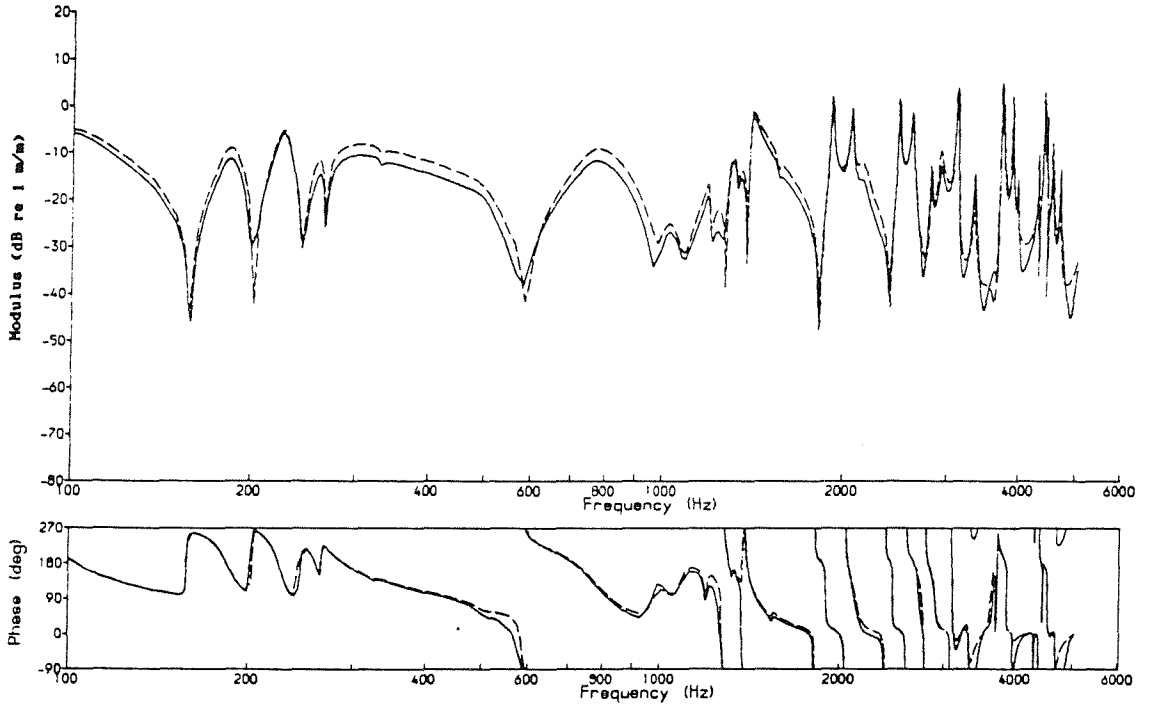

Figure 43 Predicted Lateral Vibration: ——— Baseline,
– – – Allowing for Cone Angle 2.9°

are taken from some preliminary tests which have been carried out at BR Research, using a 1/5 scale (brass) wheel [99]:

- Untreated wheel: .0003-.001
- Ring (friction) damper: .001-.004
- Unconstrained layer damping treatment: .002-.005
- Constrained layer damping treatment: .005-.01

Thus levels of between .003 and .01 should be achievable by constrained layer damping treatments of full size wheels; higher levels may be difficult to achieve.

The resulting wheel and rail vertical vibrations are shown in Figure 44, again to a linear frequency scale. The .001 damping gives very little change in peak levels of the wheel vibration, with up to 5 dB reduction at high frequencies. The higher values of damping produce more significant reductions in modal response.

The reductions achieved relative to the baseline case are shown in Figure 45 in 1/3 octave form, including results for a further increase in wheel damping (.03). From this figure it is clear that a 10 dB increase in damping does not give a full 10 dB reduction in the response. Overall, it can be seen that the first 10 dB increase in damping produces virtually no improvement, and each subsequent 10 dB of damping only produces about 3 dB improvement in the 1/3 octave response levels. For the lateral vibration of the wheel the effect is slightly greater.

Thus it would seem that a significant amount of damping needs to be added to the wheel before any reduction in vibration ensues. This corresponds to the so-called 'rolling damping' of the combined system being higher than the damping of the wheel alone, as was seen in §3.3.2 in terms of the bandwidth of the spectral peaks†.

The vertical rail response is virtually unaffected by the introduction of wheel damping. However, contrary to expectation, the lateral rail vibration is reduced slightly (by up to 5 dB for the highest level of wheel damping).

†: It should be noted that in the current model, the vertical interaction is independent of rolling velocity, and therefore applies equally for a stationary system. Thus the apparent damping of the model derives from the wheel sitting on the track rather than the actual rolling process. Any additional effect of the rolling process is not seen in this model.

(a) Vertical Rail Vibration Displacement for a Unit Roughness Input

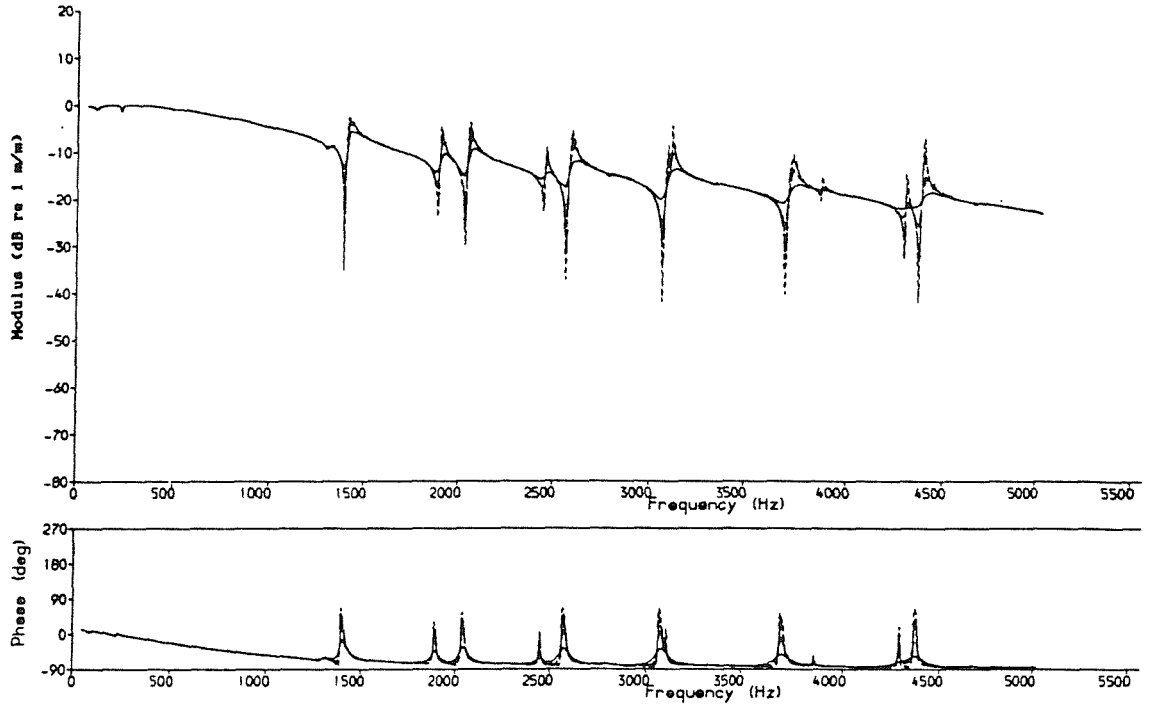

(b) Vertical Wheel Vibration Displacement for a Unit Roughness Input

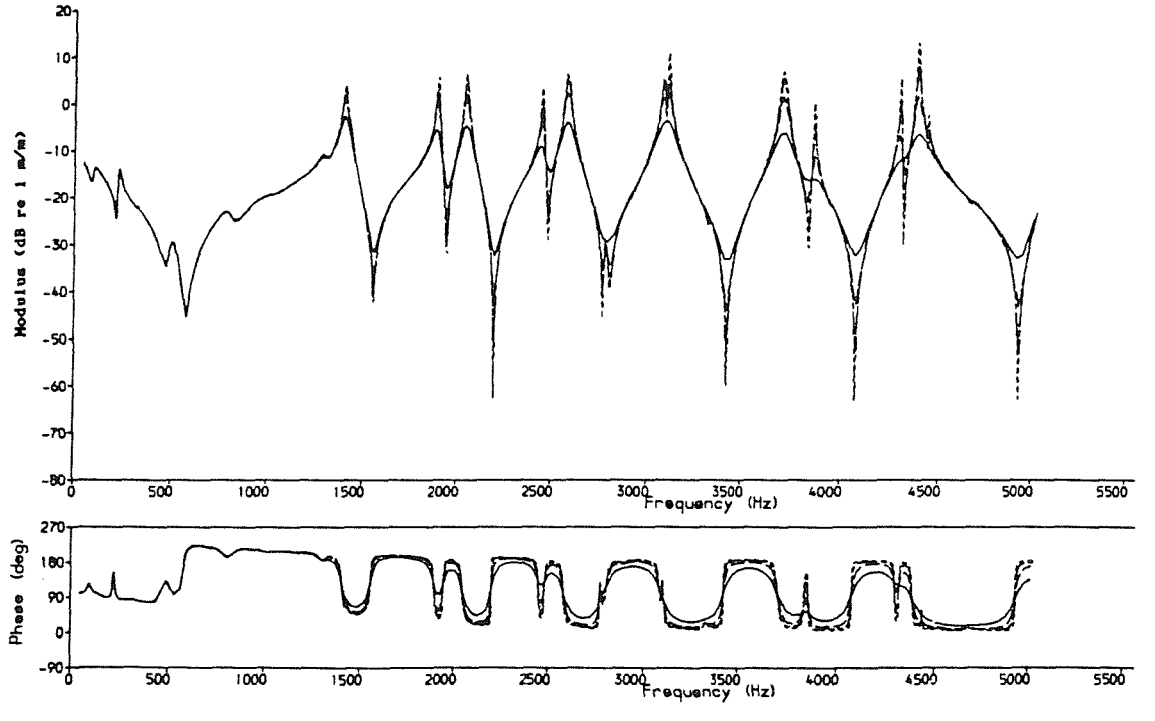

Figure 44 Predicted Vertical Vibration for Various Levels of Wheel Damping: ——— Baseline, —·—· minimum .001, – – – minimum .003 ····· minimum .01

(a) Vertical Rail Vibration

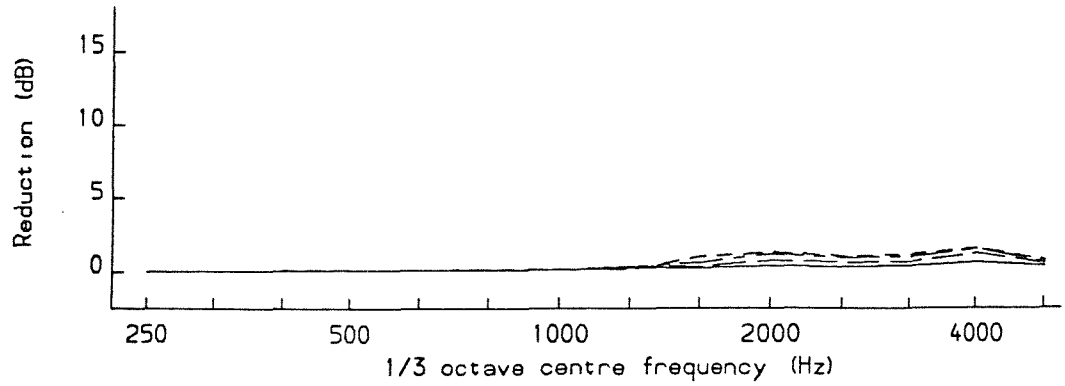

(b) Vertical Wheel Vibration

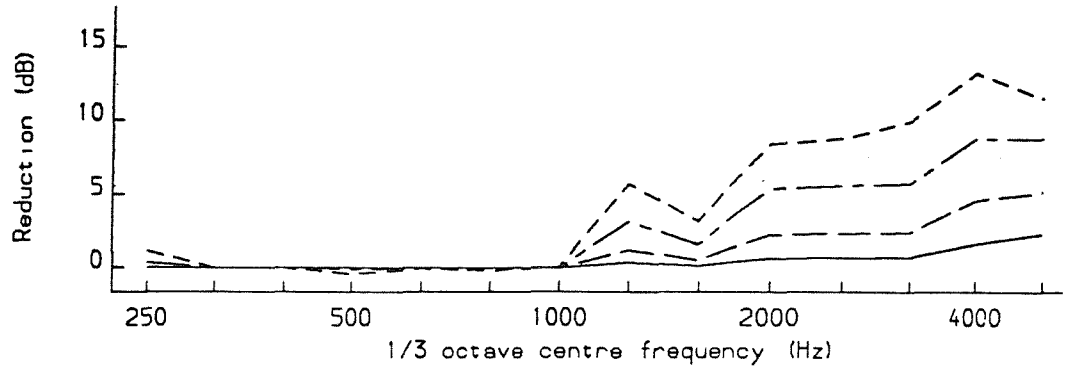

(c) Lateral Rail Vibration

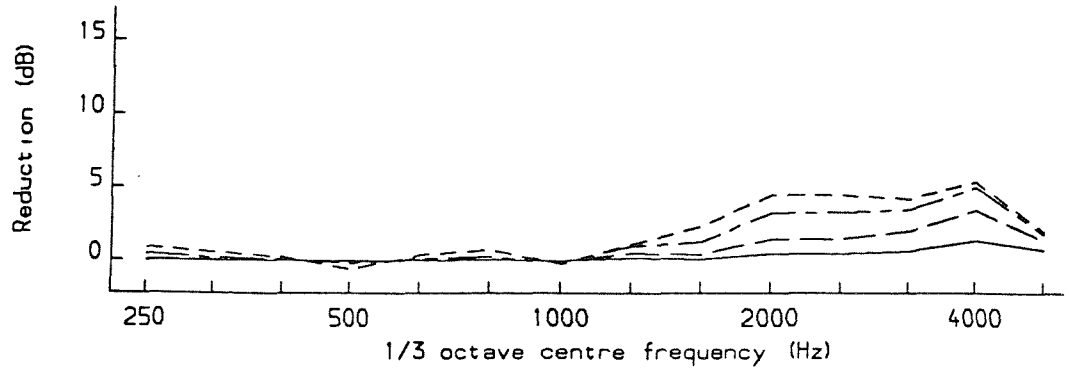

(d) Lateral Wheel Vibration

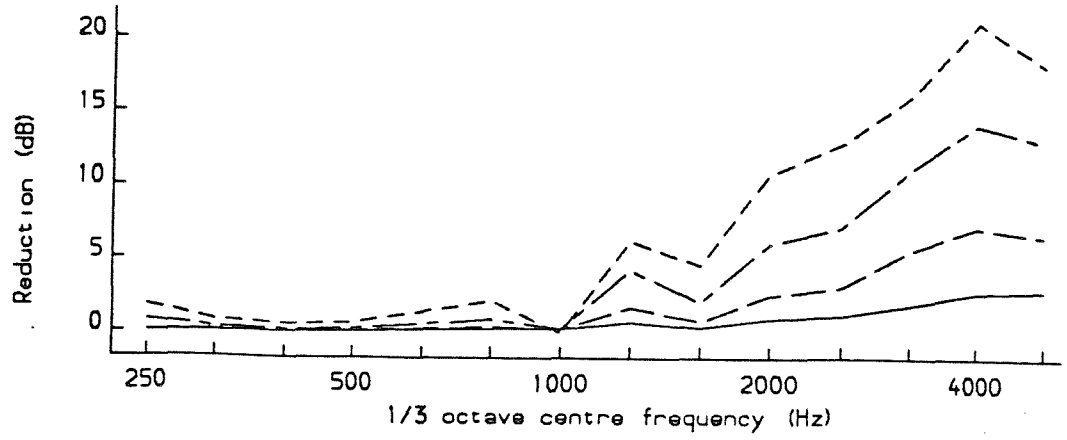

Figure 45 Predicted Reductions in 1/3 Octave Spectra for Various Levels of Wheel Damping: ——— minimum .001, — — minimum .003, —·—· minimum .01, ····· minimum .03

3.5 CONCLUSIONS

An initial development of Remington's model for the generation of wheel and rail vibration from surface roughness has been investigated. This retains the 2 coupling degrees of freedom (vertical and lateral), and the simple beam representation of the rail. The wheel, however, has been modelled using finite elements, and in the contact zone improvements have been made to the lateral wheel-rail connection.

This model has been investigated in detail, and has been shown to be partially successful, but not completely. Consequently, it needs further development before it can be fully applied to the study of potential noise reduction measures. Subsequent chapters will cover various aspects of this development.

Relative to the roughness level, the system is excited to vibration levels which are comparable to those measured. This confirms the importance of the roughness as a source of vibration, and hence noise. At low frequencies the rail vertical vibration corresponds to the level of the roughness input, the wheel vibration being much lower. The wheel vertical vibration rises sharply at around 1.25 kHz, whereas the rail vibration gradually decreases as frequency increases. The experimental data also contain these features.

An essential feature of the model which has emerged is that the roughness excites the system principally through the vertical interaction of the wheel and the rail. This has been seen particularly in the comparison of the baseline predictions with those for the vertical interaction alone, but it was also seen throughout the remaining analysis, as whenever lateral or cross receptances were varied, the effect on the vertical vibrations was minimal. Furthermore, the cross receptances appeared to have a greater effect on the lateral responses than the lateral receptances. Unfortunately they are more difficult to model accurately.

The close frequency spacing used appears to have been vital in resolving the subtleties of the interaction, as are the phases of the various receptances.

Peaks in the lateral vibration of the wheel web corresponded roughly to the resonance frequencies of modes known to be important in noise radiation, as seen in measured spectra. The breadth of the peaks was roughly consistent with measured results, and suggests that the damping of the wheel-rail coupled system is greater than the damping of

the free wheel. Inaccuracies in the wheel damping estimates are therefore unlikely to be critical. Furthermore, it appears that added wheel damping would have to be quite large to have any significant effect; the full benefit of added damping was not seen in the wheel response.

The precise frequencies of the peaks in the wheel web lateral and tyre vertical vibration were found to be slightly too high in relation to the corresponding resonance frequencies; no reasonable choice of parameters reduced them significantly.

The lateral vibration of the wheel tyre did not show the 0-nodal-circle axial modes of vibration found to predominate in experimental data at this position, unless the lateral contact receptance was very soft (which is not physically justifiable), in which case the peaks were too sharp in comparison with measured results.

Although the wheel receptances used did not correspond precisely to those measured (Appendix C), particularly in the case of the cross receptance, this is unlikely to have a fundamental effect on the responses. The rail has been modelled using a very simple receptance and many effects have been ignored, yet, as will be seen, the receptance of a rail is markedly unresonant in nature, and its receptance is likely to be covered by the range of levels and phases considered.

In the contact region, the non-linear contact spring and creep forces have been approximated by linear expressions, and the cross contact receptance (lateral displacement resulting from vertical forces and vice versa) has been ignored. Inclusion of the latter, and of further linking coordinates which are possible, up to 6 for a complete point connection (3 translations and 3 rotations) provide potential for improvement of the model.

A speed effect found in the experimental data, particularly the vertical vibration of the rail, has not been reproduced in the predictions. Although Remington's linear model contained no provision for a speed effect, the creep force damper introduced one possibility for speed dependence whilst maintaining an essentially linear model. However this had no significant effect on the vertical vibration. It appears that only changes in vertical response parameters are likely to have any significant effect.

It should be remembered that the experimental data may still contain anomalies, particularly the rail data, which are transient in

nature. The roughness measurements, too, have not been validated completely, although in comparison with other systems, the rail roughness system used appeared to give reasonable results down to the imposed wavelength limit of 14 mm [100]. Errors in roughness measurements could be responsible for some of the speed effects seen in Appendix A, but not all of them, since the results for each measurement position are different in this respect.

CHAPTER 4

A THEORY FOR THE VIBRATION OF A ROLLING WHEEL

4.1 INTRODUCTION

The model of the wheel-rail interaction studied in §3 represents the wheel and rail by their static receptances. In practice, however, the wheel rotates and moves along the rail. Whilst the response of the rail is unlikely to be affected greatly by the motion of the forcing point, since the train velocity is much less than the wave velocity (see Appendix D), the wheel response is modal, and the effect of the rotation of the forcing point around its periphery needs to be considered.

Ferguson [55,56] considered theoretically the free and forced out-of-plane response of a rotating thin disc. Structural effects of rotation, such as centrifugal stiffening and Coriolis forces, were neglected, an assumption which is reasonable for relatively low rotational speeds (including those typical of a railway wheel). This allowed the rotating disc to be modelled as a stationary disc which is subject to a force which rotates around its periphery.

He also studied the effects of the in-plane loading on the natural frequencies of such a disc. He found these to be negligible for realistic loading - they only make a significant difference as the magnitude of the load approaches the buckling load of the disc, so these effects will also be ignored here.

This chapter considers first the response of a wheel to a rotating harmonic force, following Ferguson's analysis but extending it to include in-plane as well as out-of-plane motion. It then proceeds to consider the response to random forcing, and in particular the forcing generated by the wheel-rail interaction, as presented in §3. The mathematical derivation is based on the general multi-degree-of-freedom case, but the results are restricted (for now) to the 2 coupling coordinates used in §3.

4.2 RESPONSE OF A WHEEL TO A HARMONIC ROTATING FORCE

4.2.1 Equations of Motion

Consider a wheel which is subject to a harmonic force, the point of application of which is rotating around the wheel at a constant

(a) Frame of Reference Stationary with Respect to Forcing Point

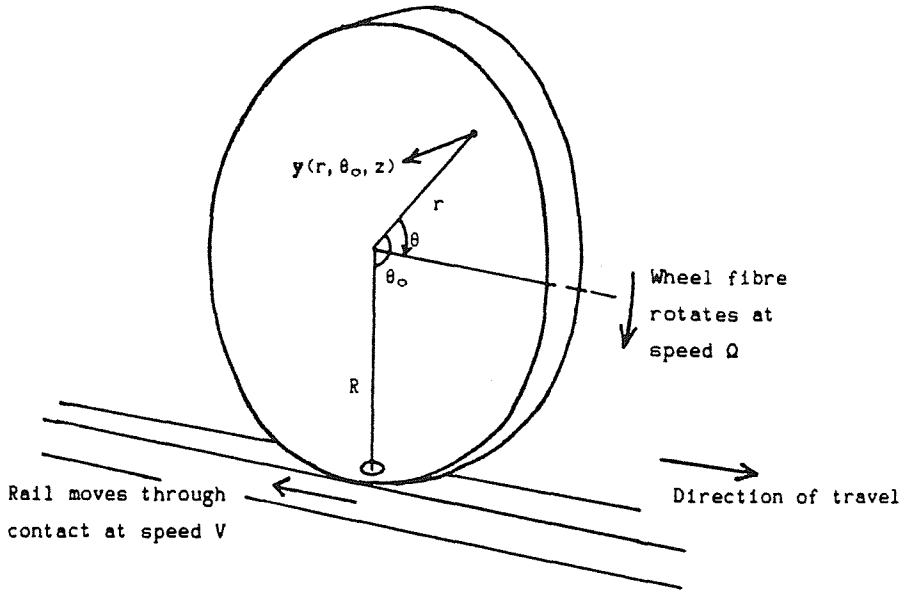

(b) Frame of Reference Moving with the Wheel

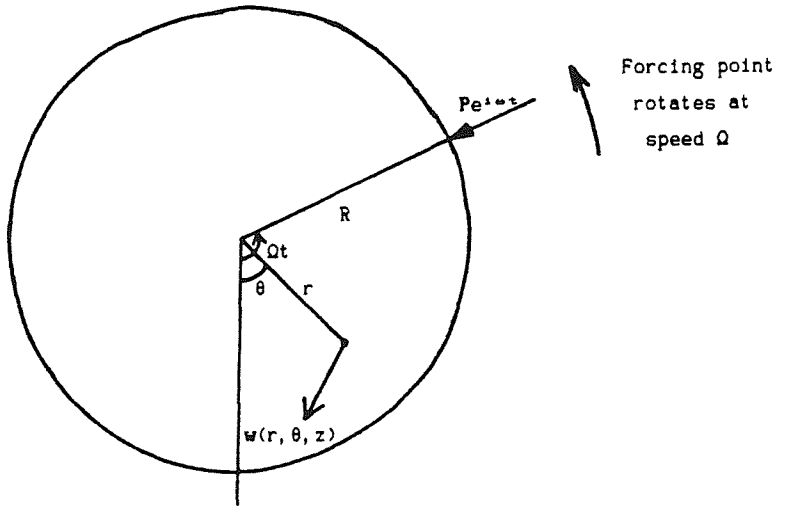

Figure 46 Coordinate Systems for a Rotating Wheel

rotational velocity, Ω (Figure 46). This problem has time-varying boundary conditions, and so cannot be solved using the standard techniques of modal analysis. Ferguson [56] used the Assumed Modes Method [101], which is an approximate method for solving the forced response of continuous systems by using a set of trial functions for the modes (eg based on the modes of a similar problem with an analytical solution) and expressing the vibration as a sum of these trial functions.

The eigenvalues and modeshapes have already been found for the current problem, ie for a non-rotating wheel (§2), as was also the case

for Ferguson's thin disc. Thus an approximate solution for the response of the wheel to a force rotating around its periphery (representing the rotating wheel) can be derived by using these calculated modes as the trial functions, ie by expressing the vibration displacement, w, (at the point, x, and time, t), in terms of the first N (known) normal modes of the static wheel, $\boldsymbol{\varphi}_r(\mathbf{x})$ as,

$$\mathbf{w}(\mathbf{x},t) = \sum_{r=1}^{N} \boldsymbol{\varphi}_r(\mathbf{x})\, q_r(t) \qquad \ldots(26)$$

where q_r are the (unknown) generalised coordinates, which are functions only of time. It should be noted that w, x and $\boldsymbol{\varphi}_r$ (in bold type) are vectors. The method proceeds by formulating instantaneous kinetic and strain energy terms, T and K, and extracting from them N-dimensional mass and stiffness matrices [m] and [k]. Since $\boldsymbol{\varphi}_r$ are eigenvectors of the free vibration problem, the corresponding mass and stiffness matrices are diagonal. The damping matrix [c] can also be formulated using the Rayleigh dissipation function, and, assuming that the modal dampings are uncoupled, this too is diagonal.

These are substituted into the form of Lagrange's equations including damping [101], in which Q_r are generalised forces corresponding to the modeshapes $\boldsymbol{\varphi}_r$:-

$$[m]\,\{\ddot{q}(t)\} + [c]\,\{\dot{q}(t)\} + [k]\,\{q(t)\} = \{Q(t)\} \qquad \ldots(27a)$$

Since [m], [k] and [c] are diagonal, the matrix equations (27a) can be resolved into n uncoupled equations:-

$$m_r\,\ddot{q}_r(t) + c_r\,\dot{q}_r(t) + k_r\,q_r(t) = Q_r(t) \qquad \ldots(27b)$$

4.2.2 Derivation of Generalised Forces

This result appears fairly standard, since the equations (27) are already uncoupled by the choice of normal modes. However it should be noted that the generalised forces are dependent on the time-varying boundary conditions. The force acting is a rotating harmonic force (or moment) of amplitude P acting at the point $(r,\theta,z)=(R,\Omega t,Z)$. In practice the force between a circular wheel and a rail (both with a finite radius of curvature) acts over a finite contact area, which is roughly an ellipse and is typically 10-15 mm across. However this distribution of the force will be ignored for the purpose of the

current analysis, since it is small in relation to the wheel as a whole (see Ferguson [56]).

The force is taken as $P\delta(r,\theta,z|R,\Omega t,Z)e^{i\omega t}$ where δ is the Dirac delta function in 3 dimensions, which satisfies

$$\delta(r,\theta,z|R,\Omega t,Z) = \frac{\delta(r-R)\ \delta(\theta-\Omega t)\ \delta(z-Z)}{r} \qquad \ldots(28)$$

In order to derive the corresponding generalised forces it is convenient to classify the modes using two subscripts (m,n) instead of one (r), with n corresponding to the number of nodal diameters in the modeshape. However it should be noted that for n>0, these subscripts are not sufficient to define the mode completely. For each (m,n) two independent modes exist, with nodal diameters and anti-nodal diameters transposed, both having the same natural frequency, ω_{mn}, and basic modeshape. For convenience these can be specified as having even (cosine) and odd (sine) angular distribution. Any alternative modal description can then be expressed as a linear combination of these two distributions.

In fact the deformation vector consists of up to 6 coordinates (3 translations and 3 rotations). Whilst 3 of these (the axial and radial translations, and one rotation - which will be labelled as "type I") follow a cosine distribution, the other 3 (circumferential translation, and rotations about the radial and axial axes - labelled as "type II") will follow a sine distribution, and vice versa. Thus the full mode-shapes must be written as:-

$$\text{Even modes:}\quad \overset{e}{\varphi}_{mn}(r,\theta,z) = \overset{I}{\psi}_{mn}(r,z)\cos n\theta + \overset{II}{\psi}_{mn}(r,z)\sin n\theta \qquad \ldots(29)$$

$$\text{Odd modes:}\quad \overset{o}{\varphi}_{mn}(r,\theta,z) = \overset{I}{\psi}_{mn}(r,z)\sin n\theta - \overset{II}{\psi}_{mn}(r,z)\cos n\theta$$

where ψ^{I}_{mn} is the part of the (m,n)th modeshape consisting of type I coordinates, and ψ^{II}_{mn} is the part consisting of type II coordinates. The origin of θ, which determines the positions of the nodal diameters of these modes, is the position of the force at time t=0, and thus depends on the (arbitrary) time origin. For the modes where n=0, the modeshapes do not vary in the θ direction, since cos $n\theta$ = 1 and sin $n\theta$ = 0, so that only one of the two modes is required.

The generalised coordinates, q_r, are now relabelled using q^e_{mn} for the even modes, and q^o_{mn} for the odd modes. For even modes, the equation of motion, (27b), can be written as,

$$m_{mn}\,\ddot{q}^e_{mn}(t) + c_{mn}\,\dot{q}^e_{mn}(t) + k_{mn}\,q^e_{mn}(t) = Q^e_{mn}(t)$$

$$= \iiint_V [P\delta(r,\theta,z|R,\Omega t,Z)e^{i\omega t}]\cdot\phi^e_{mn}(r,\theta,z)\,dV$$

$$= \{P^I\cdot\psi^I_{mn}(R,Z)\cos n\Omega t + P^{II}\cdot\psi^{II}_{mn}(R,Z)\sin n\Omega t\}\,e^{i\omega t} \quad ...(30a)$$

where $\cdot$ represents the vector dot product, and the force vector P has been split into type I and type II components, P^I and P^{II}. Similarly, for odd modes,

$$m_{mn}\,\ddot{q}^o_{mn}(t) + c_{mn}\,\dot{q}^o_{mn}(t) + k_{mn}\,q^o_{mn}(t)$$

$$= \{P^I\cdot\psi^I_{mn}(R,Z)\sin n\Omega t - P^{II}\cdot\psi^{II}_{mn}(R,Z)\cos n\Omega t\}\,e^{i\omega t} \quad ...(30b)$$

4.2.3 Solution of the Equations of Motion

Equations (30) each contain two time-dependent functions on the right-hand side. However their solution is relatively straightforward when use is made of the following identities:-

$$\begin{aligned} e^{i\omega t}\cos n\Omega t &= (e^{i(\omega+n\Omega)t} + e^{i(\omega-n\Omega)t})/2 \\ e^{i\omega t}\sin n\Omega t &= (e^{i(\omega+n\Omega)t} - e^{i(\omega-n\Omega)t})/2i \end{aligned} \quad ...(31)$$

Using the dummy variables, x and $\bar{\omega}$, the equation

$$m_{mn}\,\ddot{x}(t) + c_{mn}\,\dot{x}(t) + k_{mn}\,x(t) = A\,e^{i\bar{\omega}t} \quad ...(32)$$

has the solution:-

$$x(t) = \frac{A\,e^{i\bar{\omega}t}}{k_{mn} - m_{mn}\bar{\omega}^2 + ic_{mn}\bar{\omega}} = \frac{A\,e^{i\bar{\omega}t}}{m_{mn}(\omega_{mn}^2 - \bar{\omega}^2 + 2i\zeta_{mn}\bar{\omega}\omega_{mn})} \quad ...(33)$$

where $\omega_{mn}^2 = k_{mn}/m_{mn}$ and $\zeta_{mn} = c_{mn}/2\omega_{mn}m_{mn}$. Use will also be made of the substitutions:-

$$\begin{aligned} d_\pm &= 2m_{mn}\,(\omega_{mn}^2 - (\omega\pm n\Omega)^2 + 2i\zeta_{mn}(\omega\pm n\Omega)\omega_{mn}) \\ T_{mn} &= P^I\cdot\psi^I_{mn}(R,Z) - iP^{II}\cdot\psi^{II}_{mn}(R,Z) \end{aligned} \quad ...(34)$$

Substituting $\bar{\omega}=\omega\pm n\Omega$ in (33), and adding a combination of these results, yields the solutions to equations (30):-

$$q^{e}_{mn} = T_{mn}\frac{e^{i(\omega+n\Omega)t}}{d_+} + T^{*}_{mn}\frac{e^{i(\omega-n\Omega)t}}{d_-} \qquad \ldots(35)$$

$$q^{o}_{mn} = -iT_{mn}\frac{e^{i(\omega+n\Omega)t}}{d_+} + iT^{*}_{mn}\frac{e^{i(\omega-n\Omega)t}}{d_-}$$

where * denotes the complex conjugate

Substituting these into equation (26) and allowing for equation (29), the vibration displacement at (x,t), as viewed by an observer fixed in relation to the wheel, can be derived as

$$w(r,\theta,z,t) = \sum_{m,n}\left\{\Psi_{mn}(r,z)T_{mn}\frac{e^{i((\omega+n\Omega)t-n\theta)}}{d_+} + \Psi^{*}_{mn}(r,z)T^{*}_{mn}\frac{e^{i((\omega-n\Omega)t+n\theta)}}{d_-}\right\} \qquad \ldots(36)$$

where $\Psi_{mn} = \psi^{I}_{mn} + i\psi^{II}_{mn}$. This consists of two waves for each (m,n) which are rotating in opposite directions, and <u>at different frequencies</u>, $\omega\pm n\Omega$.

4.2.4 <u>Response in Non-rotating Frame</u>

Next a Galilean transformation is applied, into a frame of reference in which the point of application of the force is stationary and the wheel is rotating. The coordinates are (r,θ_o,z) where $\theta_o=\theta-\Omega t$ (see Figure 46) and the notation for the displacement is changed from $w(r,\theta,z)$ to $y(r,\theta_o,z)$. From equation (36), the solution is:-

$$y(r,\theta_o,z,t) = e^{i\omega t}\sum_{m,n}\left\{\Psi_{mn}(r,z)T_{mn}\frac{e^{-in\theta_o}}{d_+} + \Psi^{*}_{mn}(r,z)T^{*}_{mn}\frac{e^{in\theta_o}}{d_-}\right\} \qquad \ldots(37)$$

Viewed from this frame of reference, the two rotating waves both occur at a single frequency - the excitation frequency, ω. Hence equation (37) can be rewritten in terms of a receptance matrix, α_{ij},

$$y_i(r,\theta_o,z,t) = \sum_j \alpha_{ij}(r,\theta_o,z,R,Z,\omega)\,P_j\,e^{i\omega t} \qquad \ldots(38)$$

where y_i, P_j, ψ_{mni} and ψ_{mnj} are components of the respective vectors. The receptances are given by

$$\alpha_{ij}(\omega) = \sum_{m,n} \frac{\psi_{mni}(r,z)\ \psi_{mnj}(R,Z)}{2m_{mn}} \left\{ \frac{\varepsilon_{ij}\ e^{-in\theta_o}}{d_+} + \frac{\varepsilon^*_{ij}\ e^{in\theta_o}}{d_-} \right\} \quad \ldots(39)$$

$$\text{where } \varepsilon_{ij} = \begin{cases} 1 \text{ if } i \text{ and } j \text{ are both of type I or both of type II} \\ -i \text{ if } i \text{ is of type I and } j \text{ is of type II} \\ i \text{ if } i \text{ is of type II and } j \text{ is of type I} \end{cases}$$

It should be noted that the receptance α_{ij} has two resonant peaks for each natural frequency of the wheel ω_{mn} (for $n>0$), at $\omega=\omega_{mn}\pm n\Omega$ (when $d_\pm \to 0$). The predominant response at these frequencies consists of only one of the two terms in equation (39), ie a single rotating wave rather than a fixed modeshape. In the frame of reference rotating with the wheel (equation (36)), however, resonance in both of these waves appears at the natural frequency of the wheel, ω_{mn}, but results from forces at different frequencies, $\omega_{mn}\pm n\Omega$.

Applying these results to the wheel studied in §2 and §3 (a Commonwealth-type), the receptances in the frame of reference which is stationary with respect to the forcing point are given in Figure 47. These are based on a rotation speed, Ω, equivalent to 160 km/h (44.4 m/s). The modal parameters (ψ_{mni}, m_{mn} etc) are derived from the finite element model of the wheel (§2), although the natural frequencies, ω_{mn}, and damping ratios, ζ_{mn}, have been chosen to correspond to experimental results, as used in §3. The splitting in the resonance frequencies, which depends on the speed, can be clearly seen in comparison with Figures 18 and 19.

4.3 RESPONSE TO RANDOM FORCES

The analysis so far has been based on a harmonic force $Pe^{i\omega t}$, as used by Ferguson [56]. However the rolling wheel is actually excited by a broad-band random force, specified by its spectral density $Sp(\omega)$. Since P is a vector, the force actually consists of a series of random force components (eg vertical, lateral), P_j, with corresponding spectral densities $S_{P_j}(\omega)$.

The calculation of the response of a rotating wheel to random forces, particularly as viewed from a rotating frame, is much more complex than was the case for a static wheel. This arises because the

(a) Lateral Wheel Receptance

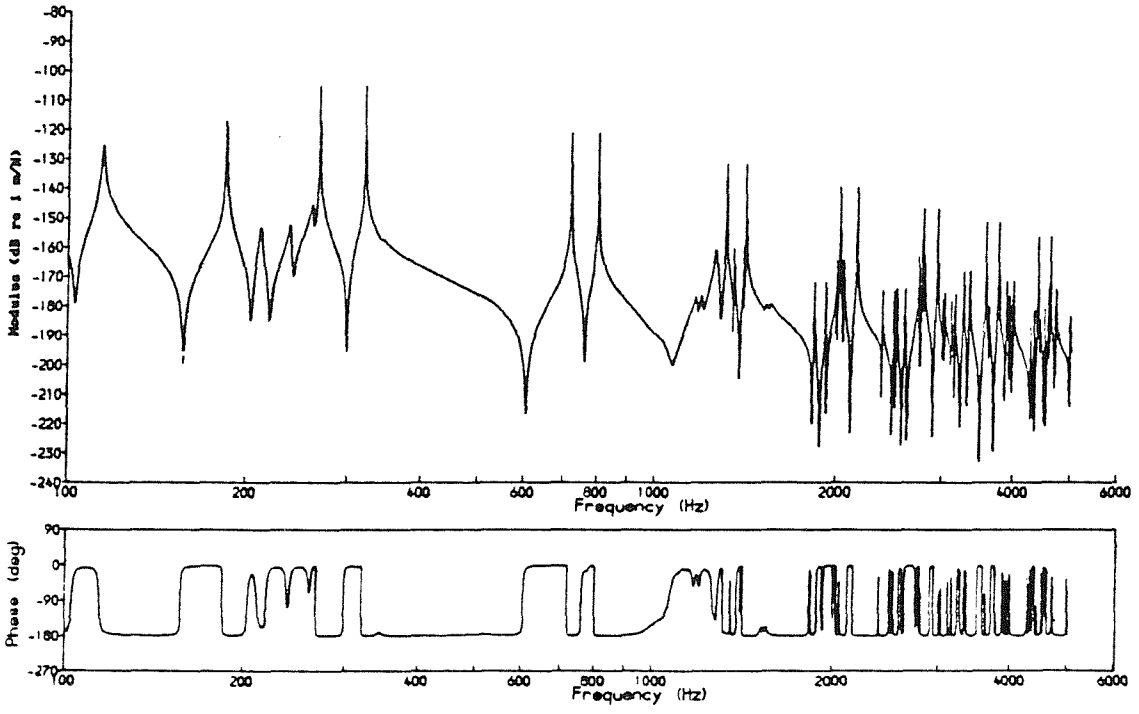

(b) Vertical Wheel Receptance

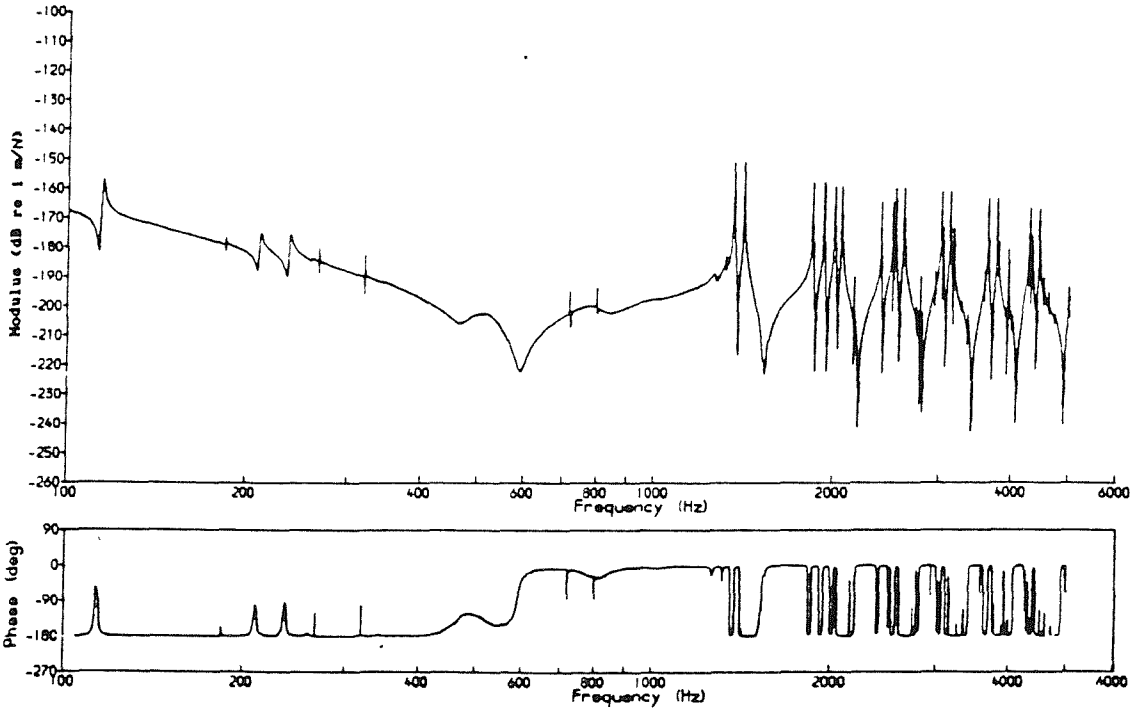

Figure 47 Predicted Receptances of a Wheel Rotating at 160 km/h

response at a particular frequency is the result of forces acting at more than one frequency, so that a simple transfer function between force and response is no longer appropriate. Instead the spectral densities of the reponse need to be studied. This will be done first for a non-rotating frame (stationary with respect to the forcing point) and then for a frame of reference rotating with the wheel.

4.3.1 Response in Non-rotating Frame

From linear system theory [102], equation (38) can be re-expressed (for a single force P_j) as:-

$$S_{y_i}(\omega) = \left|\alpha_{ij}(r,\theta_o,z,R,Z,\omega)\right|^2 S_{P_j}(\omega) \qquad ...(40)$$

where $S_{y_i}(\omega)$ is the spectral density corresponding to $y_i(r,\theta_o,z)$, the displacement in the frame stationary with respect to the excitation point. For multiple force components, it will be assumed initially that, since they are all generated by the same roughness $r(\omega)$, all are perfectly correlated, so that:-

$$P_j\, e^{i\omega t} = H_j(\omega)\, r(\omega)\, e^{i\omega t} \qquad ...(41)$$

for some set of functions $H_j(\omega)$. Hence in terms of spectral densities

$$S_{y_i}(\omega) = \left|\sum_j H_j(\omega)\, \alpha_{ij}(r,\theta_o,z,\omega,R,Z)\right|^2 S_r(\omega) \qquad ...(42)$$

The objective is to calculate first the spectral density of the response in the non-rotating frame, $S_{y_i}(\omega)$. In order to do this, its auto-correlation function denoted by $R_{y_i}(\tau)$ is considered:-

$$R_{y_i}(r,\theta_o,z,\tau) = \int_{-\infty}^{\infty} y_i(r,\theta_o,z,t)\, y_i(r,\theta_o,z,t+\tau)\, dt \qquad ...(43)$$

Without making any assumptions about the vibration, it is possible to decompose y_i at any particular time, t, into sinusoidal spatial components in the θ_o direction, using a Fourier series:-

$$y_i(r,\theta_o,z,t) = \sum_n \left(A_n(r,z,t)\cos n\theta_o + B_n(r,z,t)\sin n\theta_o\right) \qquad ...(44)$$

where A_n and B_n are unknown variables. Substituting this into equation (43) gives,

$$R_{y_i}(\tau) = \sum_n \sum_\ell \{R_{A_nA_\ell}(\tau) \cos n\theta_o \cos \ell\theta_o + R_{A_nB_\ell}(\tau) \cos n\theta_o \sin \ell\theta_o + R_{B_nA_\ell}(\tau) \sin n\theta_o \cos \ell\theta_o + R_{B_nB_\ell}(\tau) \sin n\theta_o \sin \ell\theta_o\} \quad ...(45)$$

where

$$R_{A_nA_\ell}(r,z,\tau) = \int_{-\infty}^{\infty} A_n(r,z,t)\, A_\ell(r,z,t+\tau)\, dt \quad ...(46)$$

etc. Taking Fourier transforms,

$$S_{y_i}(\omega) = \sum_n \sum_\ell \{S_{A_nA_\ell}(\omega) \cos n\theta_o \cos \ell\theta_o + S_{A_nB_\ell}(\omega) \cos n\theta_o \sin \ell\theta_o + S_{B_nA_\ell}(\omega) \sin n\theta_o \cos \ell\theta_o + S_{B_nB_\ell}(\omega) \sin n\theta_o \sin \ell\theta_o\} \quad ...(47)$$

The $S_{A_nA_\ell}(\omega)$ etc. which are the Fourier transforms of $R_{A_nA_\ell}(\tau)$ etc, are unknowns but they can be identified from consideration of α_{ij} as follows: Referring to equation (39), it is possible to write

$$\sum_j \alpha_{ij}(r,\theta,z,R,Z,\omega)\, H_j(\omega) = \sum_j H_j(\omega) \sum_n (a_{nij}\cos n\theta_o + b_{nij}\sin n\theta_o) \quad ...(48)$$

where a_{nij} and b_{nij} are defined by:-

$$a_{nij} = \sum_m \frac{\psi_{mni}(r,z)\, \psi_{mnj}(R,Z)}{2m_{mn}} \left\{ \frac{\varepsilon_{ij}}{d_+} + \frac{\varepsilon^*_{ij}}{d_-} \right\} \quad ...(49)$$

$$b_{nij} = \sum_m \frac{\psi_{mni}(r,z)\, \psi_{mnj}(R,Z)}{2im_{mn}} \left\{ \frac{\varepsilon_{ij}}{d_+} - \frac{\varepsilon^*_{ij}}{d_-} \right\}$$

From these, define g_{ni} and h_{ni} as:-

$$g_{ni} = \sum_j H_j(\omega)\, a_{nij}(\omega) \quad \text{and} \quad h_{ni} = \sum_j H_j(\omega)\, b_{nij}(\omega) \quad ...(50)$$

to give equation (48) in the form:-

$$\sum_j \alpha_{ij}(r,\theta,z,R,Z,\omega)\, H_j(\omega) = \sum_n (g_{ni} \cos n\theta_o + h_{ni} \sin n\theta_o) \quad ...(51)$$

Substituting this into (40) gives

$$S_{y_i}(\omega) = \left| \sum_n (g_{ni}\cos n\theta_o + h_{ni}\sin n\theta_o) \right|^2 S_r(\omega) \quad \ldots(52)$$

$$\Rightarrow S_{y_i}(\omega) = S_r(\omega) \sum_n \sum_\ell \left\{ g^*_{ni} g_{\ell i} \cos n\theta_o \cos \ell\theta_o + g^*_{ni} h_{\ell i} \cos n\theta_o \sin \ell\theta_o \right.$$

$$\left. + h^*_{ni} g_{\ell i} \sin n\theta_o \cos \ell\theta_o + h^*_{ni} h_{\ell i} \sin n\theta_o \sin \ell\theta_o \right\} \quad \ldots(53)$$

From this, comparing equations (47,53), it is possible to identify,

$$\begin{aligned} S_{A_nA_\ell}(\omega) &= g^*_{ni}(\omega)\, g_{\ell i}(\omega)\, S_r(\omega) \\ S_{A_nB_\ell}(\omega) &= g^*_{ni}(\omega)\, h_{\ell i}(\omega)\, S_r(\omega) \\ S_{B_nA_\ell}(\omega) &= h^*_{ni}(\omega)\, g_{\ell i}(\omega)\, S_r(\omega) \\ S_{B_nB_\ell}(\omega) &= h^*_{ni}(\omega)\, h_{\ell i}(\omega)\, S_r(\omega) \end{aligned} \quad \ldots(54)$$

in which g_{ni} and h_{ni} are known transfer functions defined by equations (50) and (49), and hence, from equation (47), the response $S_{y_i}(\omega)$ is known.

4.3.2 Response in Rotating Frame

Considering now the response in the rotating frame, $w_i(r,\theta,z,t)$ it is possible to write, by introducing $\theta=\theta_o+\Omega t$ into equation (44):-

$$w_i(r,\theta,z,t) = \sum_n (A_n(r,z,t)\cos n(\theta-\Omega t) + B_n(r,z,t)\sin n(\theta-\Omega t)) \quad \ldots(55)$$

Hence the auto-correlation function,

$$R_{w_i}(\tau) = \int_{-\infty}^{\infty} \left\{ \sum_n (A_n(t)\cos n(\theta-\Omega t) + B_n(t)\sin n(\theta-\Omega t)) \right\}$$

$$\times \left\{ \sum_\ell (A_\ell(t+\tau)\cos \ell(\theta-\Omega t) + B_\ell(t+\tau)\sin \ell(\theta-\Omega t)) \right\} dt \quad \ldots(56)$$

which can be expanded using trigonometrical identities to give:-

$$R_{w_i}(\tau) =$$

$$\frac{1}{2}\sum_n\sum_\ell \left\{ \int_{-\infty}^{\infty} A_n(t)A_\ell(t+\tau)[\cos((n-\ell)(\theta-\Omega t)+\ell\Omega\tau) + \cos((n+\ell)(\theta-\Omega t)-\ell\Omega\tau)]dt \right.$$

$$- \int_{-\infty}^{\infty} A_n(t)B_\ell(t+\tau)[\sin((n-\ell)(\theta-\Omega t)+\ell\Omega\tau) - \sin((n+\ell)(\theta-\Omega t)-\ell\Omega\tau)]dt$$

$$+ \int_{-\infty}^{\infty} B_n(t)A_\ell(t+\tau)[\sin((n-\ell)(\theta-\Omega t)+\ell\Omega\tau) + \sin((n+\ell)(\theta-\Omega t)-\ell\Omega\tau)]dt$$

$$\left. + \int_{-\infty}^{\infty} B_n(t)B_\ell(t+\tau)[\cos((n-\ell)(\theta-\Omega t)+\ell\Omega\tau) - \cos((n+\ell)(\theta-\Omega t)-\ell\Omega\tau)]dt \right\}$$

...(57)

Because the time origin is arbitrary, and hence the position $\theta=\theta_o+\Omega t$ is arbitrary, the result should be independent of θ. It is possible, therefore, without loss of generality, to integrate over θ from 0 to 2π, which causes all the terms to cancel, except for $n=\ell$ and $n=-\ell$, the latter only being valid for $n=0$. Thus, noting that $B_0=0$,

$$R_{w_i}(\tau) = \int_{-\infty}^{\infty} A_0(t)A_0(t+\tau)\,dt$$

$$+ \frac{1}{2}\sum_{n=1}^{N} \left\{ \cos n\Omega t \int_{-\infty}^{\infty} [A_n(t)A_n(t+\tau) + B_n(t)B_n(t+\tau)]\,dt \right.$$

$$\left. + \sin n\Omega t \int_{-\infty}^{\infty} [B_n(t)A_n(t+\tau) - A_n(t)B_n(t+\tau)]\,dt \right\} \quad ...(58)$$

$$= R_{A_0A_0}(\tau) + \frac{1}{2}\sum_{n=1}^{N} \left\{ \cos n\Omega t\,(R_{A_nA_n}(\tau) + R_{B_nB_n}(\tau)) \right.$$

$$\left. + \sin n\Omega t\,(R_{B_nA_n}(\tau) - R_{A_nB_n}(\tau)) \right\} \quad ...(59)$$

where N is the total number of n's considered, ie the maximum number of nodal diameters in wheel modes included in the sum. Hence taking Fourier transforms

$$S_{w_i}(\omega) = \int_{-\infty}^{\infty} e^{-i\omega\tau} R_{A_0A_0}(\tau)\,d\tau$$

$$+ \frac{1}{2}\int_{-\infty}^{\infty} e^{-i\omega\tau} \sum_{n=1}^{N} \left\{ \cos n\Omega\tau\,(R_{A_nA_n}(\tau) + R_{B_nB_n}(\tau)) \right.$$

$$\left. + \sin n\Omega\tau\,(R_{B_nA_n}(\tau) - R_{A_nB_n}(\tau)) \right\} d\tau \quad ...(60)$$

$$= S_{A_0A_0}(\omega) + \frac{1}{4}\sum_{n=1}^{N}\int_{-\infty}^{\infty}\Big\{ (e^{-i(\omega-n\Omega)\tau} + e^{-i(\omega+n\Omega)\tau})\,(R_{A_nA_n}(\tau) + R_{B_nB_n}(\tau)) - i\,(e^{-i(\omega-n\Omega)\tau} - e^{-i(\omega+n\Omega)\tau})\,(R_{B_nA_n}(\tau) - R_{A_nB_n}(\tau))\Big\}\,d\tau \quad ...(61)$$

$$= S_{A_0A_0}(\omega) + \frac{1}{4}\sum_{n=1}^{N}\Big\{S_{A_nA_n}(\omega-n\Omega) + S_{A_nA_n}(\omega+n\Omega) + S_{B_nB_n}(\omega-n\Omega) + S_{B_nB_n}(\omega+n\Omega) - iS_{B_nA_n}(\omega-n\Omega) + iS_{B_nA_n}(\omega+n\Omega) + iS_{A_nB_n}(\omega-n\Omega) - iS_{A_nB_n}(\omega+n\Omega)\Big\} \quad ...(62)$$

Substituting from equations (54),

$$S_{w_i}(\omega) = g_{0i}^{*}(\omega)\, g_{0i}(\omega)\, S_r(\omega) + \frac{1}{4}\sum_{n=1}^{N}\Big\{((g_{ni}^{*}g_{ni} + h_{ni}^{*}h_{ni} + ig_{ni}^{*}h_{ni} - ih_{ni}^{*}g_{ni})\,S_r)\Big|_{(\omega-n\Omega)} + ((g_{ni}^{*}g_{ni} + h_{ni}^{*}h_{ni} + ig_{ni}^{*}h_{ni} - ih_{ni}^{*}g_{ni})\,S_r)\Big|_{(\omega+n\Omega)}\Big\} \quad ...(63)$$

$$= |g_{0i}(\omega)|^2\, S_r(\omega) + \frac{1}{4}\sum_{n=1}^{N}\Big\{ \big|g_{ni}(\omega-n\Omega) + i\,h_{ni}(\omega-n\Omega)\big|^2\, S_r(\omega-n\Omega) + \big|g_{ni}(\omega+n\Omega) - i\,h_{ni}(\omega+\Omega)\big|^2\, S_r(\omega+n\Omega)\Big\} \quad ...(64)$$

It may be noted, from equations (49,50,34), that

$$g_{ni}(\omega-n\Omega) + ih_{ni}(\omega-n\Omega) = \sum_j H_j(\omega-n\Omega)\,(a_{nij}(\omega-n\Omega) + ib_{nij}(\omega-n\Omega))$$

$$= \sum_j H_j(\omega-n\Omega)\sum_m \frac{\psi_{mni}(r,z)\,\psi_{mnj}(R,Z)\,\varepsilon_{ij}}{m_{mn}\,(\omega_{mn}^2 - \omega^2 + 2i\zeta_{mn}\omega_{mn}\omega)} \quad ...(65a)$$

since the terms involving $(\omega-2n\Omega)$ cancel out, whereas

$$g_{ni}(\omega+n\Omega) - ih_{ni}(\omega+n\Omega) = \sum_j H_j(\omega+n\Omega)\,(a_{nij}(\omega+n\Omega) - ib_{nij}(\omega+n\Omega))$$

$$= \sum_j H_j(\omega+n\Omega)\sum_m \frac{\psi_{mni}(r,z)\,\psi_{mnj}(R,Z)\,\varepsilon_{ij}^{*}}{m_{mn}\,(\omega_{mn}^2 - \omega^2 + 2i\zeta_{mn}\omega_{mn}\omega)} \quad ...(65b)$$

since the terms involving $(\omega+2n\Omega)$ cancel out. Thus, finally, substituting equations (65) into (64) and incorporating the n=0 term into the summation by splitting it into two identical terms,

$$S_{w_i}(\omega) = \sum_{n=0}^{N} \left\{ \left| \sum_j H_j(\omega-n\Omega) \sum_m \frac{\varepsilon_{ij}\, \psi_{mni}(r,z)\, \psi_{mnj}(R,Z)}{2m_{mn}(\omega_{mn}^2-\omega^2+2i\zeta_{mn}\omega_{mn}\omega)} \right|^2 S_r(\omega-n\Omega) \right.$$

$$\left. + \left| \sum_j H_j(\omega+n\Omega) \sum_m \frac{\varepsilon^*_{ij}\, \psi_{mni}(r,z)\, \psi_{mnj}(R,Z)}{2m_{mn}(\omega_{mn}^2-\omega^2+2i\zeta_{mn}\omega_{mn}\omega)} \right|^2 S_r(\omega+n\Omega) \right\} \quad \ldots(66)$$

Since this formulation is an expression for the spectral density of the vibration, it may be noted that, unlike §3, it contains information only about the modulus of the response and not the phase.

4.3.3 Excitation by Several Forces

The above derivation is based on the assumption that the force components P_j are all perfectly correlated, since each is taken to be a direct function of the roughness input (equation (41)). For completeness, this section considers the possibility that the various force components are uncorrelated or partially correlated. In place of equation (40), the following applies:-

$$S_{y_i}(\omega) = \sum_j \sum_k \alpha^*_{ij}(\omega)\, \alpha_{ik}(\omega)\, S_{P_jP_k}(\omega) \quad \ldots(67)$$

where α_{ij} is given in equation (39), and $S_{P_jP_k}(\omega)$ is the cross spectral density between the two force components P_j and P_k. If j=k, $S_{P_jP_k}=S_{P_j}$, the spectral density of P_j. Substituting for α_{ij} in terms of a_{nij} and b_{nij}, from equations (49), gives

$$S_{y_i}(\omega) = \sum_n \sum_\ell \sum_j \sum_k \{a^*_{nij}a_{\ell ik} \cos n\theta_o \cos \ell\theta_o + a^*_{nij}b_{\ell ik} \cos n\theta_o \sin \ell\theta_o$$

$$+ b^*_{nij}a_{\ell ik} \sin n\theta_o \cos \ell\theta_o + b^*_{nij}b_{\ell ik} \sin n\theta_o \sin \ell\theta_o\}\, S_{P_jP_k}(\omega) \quad \ldots(68)$$

Comparing equations (68) and (47) it is possible to identify

$$S_{A_nA_\ell}(\omega) = \sum_j \sum_k a^*_{nij}\, a_{\ell ik}\, S_{P_jP_k}(\omega) \qquad \text{etc} \quad \ldots(69)$$

in place of equations (54). These can be substituted into equation (61), which is independent of the details of the forces since it is

derived from the Fourier series representation, equation (44). This gives

$$S_{w_i}(\omega) = \sum_j \sum_k a0^*_{ik}\, a0_{ik}\, S_{P_jP_k}(\omega)$$

$$+ \frac{1}{4} \sum_{n=1}^{N} \left\{ \sum_j \sum_k \left[(a_{nij}+ib_{nij})^* (a_{nik}+ib_{nik})\, S_{P_jP_k} \right]\Big|_{(\omega-n\Omega)} \right.$$

$$\left. + \sum_j \sum_k \left[(a_{nij}-ib_{nij})^* (a_{nik}-ib_{nik})\, S_{P_jP_k} \right]\Big|_{(\omega+n\Omega)} \right\} \qquad \ldots(70)$$

In the same way as for g_{ni} and h_{ni} in §4.3.2, use can be made of equations (49) to substitute for a_{nij} and b_{nij}. This gives

$$a_{nij}(\omega-n\Omega) + ib_{nij}(\omega-n\Omega) = \sum_m \frac{\varepsilon_{ij}\, \psi_{mni}(r,z)\, \psi_{mnj}(R,Z)}{m_{mn}(\omega_{mn}^2-\omega^2+2i\zeta_{mn}\omega_{mn}\omega)} \qquad \ldots(71)$$

as the terms containing $(\omega-2n\Omega)$ cancel out, whereas

$$a_{nij}(\omega+n\Omega) - ib_{nij}(\omega+n\Omega) = \sum_m \frac{\varepsilon^*_{ij}\, \psi_{mni}(r,z)\, \psi_{mnj}(R,Z)}{m_{mn}(\omega_{mn}^2-\omega^2+2i\zeta_{mn}\omega_{mn}\omega)} \qquad \ldots(72)$$

since the terms involving $(\omega+2n\Omega)$ cancel out. Thus, finally, substituting these terms into equation (70) and including n=0 into the sum,

$$S_{w_i}(\omega) = \sum_{n=0}^{N} \sum_j \sum_k \left\{ \sum_m \frac{\psi_{mni}(r,z)\, \psi_{mnj}(R,Z)}{2m_{mn}(\omega_{mn}^2-\omega^2+2i\zeta_{mn}\omega_{mn}\omega)} \right\}^*$$

$$\times \left\{ \sum_m \frac{\psi_{mni}(r,z)\, \psi_{mnk}(R,Z)}{2m_{mn}(\omega_{mn}^2-\omega^2+2i\zeta_{mn}\omega_{mn}\omega)} \right\}$$

$$\times \left\{ \varepsilon^*_{ij}\varepsilon_{ik} S_{P_jP_k}(\omega-n\Omega) + \varepsilon_{ij}\varepsilon^*_{ik} S_{P_jP_k}(\omega+n\Omega) \right\} \qquad \ldots(73)$$

For the particular case covered in §4.3.2 where P_j and P_k depend on a single roughness input, and hence are perfectly correlated, this can be shown to reduce to equation (66), by substituting

$$S_{P_jP_k}(\omega) = H^*_j(\omega)\, H_k(\omega)\, S_r(\omega) \qquad \ldots(74)$$

4.3.4 Discussion of the Form of the Response

The nature of the response of a wheel while rolling has been the subject of discussion for some time [47]. The fact that the modes of

vibration are each defined by a number of nodal diameters, has led to various hypotheses about what happens to the nodal diameters - whether they move with the wheel or remain fixed in relation to the excitation point.

However it should be remembered that for each natural frequency ω_{mn} for $n>0$, there are actually two independent modes (as described in §4.2.2). Whilst they are normally represented in terms of cosine and sine components, an equally valid representation is in terms of two contra-rotating waves. These two forms are interchangable:-

$$A_1 e^{in\theta} + A_2 e^{-in\theta} = B_1 \cos n\theta + B_2 \sin n\theta \qquad ...(75)$$

for some choice of the constants A_i and B_i.

Normally resonance might be considered to occur when the wavelength of the two contra-rotating waves is such that they interfere to give a stationary pattern. However for a rotating wheel, the two resonant waves are <u>independent</u> (they are excited by forces at different frequencies, or by roughnesses of different wavelengths) and thus resonance can occur in each separately.

For a rotating wheel, the wave representation is therefore the more appropriate. With random forces, as considered here, the two waves are excited by forces at different frequencies (equations (66) and (73)). This means that the two waves will be uncorrelated, since force components at different frequencies cannot have a fixed phase relationship, and this should show itself in measured results so long as a sufficiently long time average is taken. More rigorously, this is shown by equations (66) and (73), since these contain sums of energy (modulus-squared) terms.

The result is that the two waves cannot add together into a <u>fixed</u> modal pattern, along the lines of equation (75), since the coefficients A_1 and A_2 are independent random variables. Thus THERE ARE NO NODE LINES, fixed either in space or in the wheel, but a random combination of the two contra-rotating waves, or equivalently, a random combination of the cosine and sine modes.

This has been borne out by experimental evidence at BR Research [47]. The results of Heiss [48] also seem to support the model. He found a modulated signal but no fixed pattern of node lines - modulation occurred with a non-integer number of nodes per wheel

revolution. This is indicative of variations in the force, and thus is an instantaneous minimum rather than the presence of constant node lines.

4.3.5 Limitations

It should be pointed out that the above analysis is based on the assumption that the wheel is perfectly symmetrical. Asymmetry tends to introduce a split in the natural frequencies, ω_{mn}, into two close frequencies, ω^1_{mn} and ω^2_{mn}, and with it a preferential location of the nodal diameters (see §2.1.1). This in turn will lead to a break-down of the above analysis.

Nevertheless, practical frequency splits are small, of the order of 1-2 Hz. Although a free wheel is sufficiently lightly damped for these two frequencies to be separable, coupling with the rail introduces an effective damping which is much larger than the static damping, as seen in §3. It is conceivable that, since this will cause the two peaks to coalesce, it may allow the above results to be used. Unfortunately the mathematics are too complex to allow this to be examined here.

A further complication is that the wheel roughness is not strictly a random phenomenon, but is quasi-periodic. (It is not strictly periodic since on each revolution a different sensing line may be encountered.) This implies that, if the excitation is principally due to the wheel roughness rather than the rail roughness, the response should consist of discrete frequencies, $M\Omega$, for integer values of M.

Apart from its discrete spectrum, however, the result should have a very similar form to that obtained already, since for a given frequency of response, $\omega=M\Omega$, the frequencies of excitation, $\omega\pm n\Omega$ all belong to the set of frequencies excited.

This effect will not be considered further, as generally the rail roughness is the dominant of the two, and so random effects prevail. In any case, unless the bandwidth of the analysis of the results is smaller than Ω, such discrete frequencies will not be observed.

4.4 RESPONSE DUE TO WHEEL-RAIL INTERACTION

4.4.1 Application of the Theory of Interaction to a Rotating Wheel

The frequency domain model for wheel-rail interaction used in §3 can be used to derive the dynamic contact forces (vertical and lateral) for the present case of a rotating wheel, by replacing the static wheel receptances, used in §3, by those derived in §4.2 for a rotating wheel as viewed from a non-rotating frame (equation (39)). These receptances, which were plotted in Figure 47, represent the response of the wheel as viewed by an observer located in the contact patch.

In order to compare the predicted response with that measured during the running tests by an accelerometer attached to the wheel, it is necessary to use these forces to predict the response at a point corresponding to the accelerometer position which is rotating with the wheel. To do this the expression given in equation (66) is used, since both lateral and vertical forces are assumed to be derived directly from the roughness, and thus are perfectly correlated.

It should be noted that the forces (P_j) are required at various frequencies at once, unlike for the static wheel, where all calculations are performed at single frequencies. Thus data for a significant range of frequencies need to be held in the computer simultaneously. This range is $\pm n\Omega$, where the largest n under consideration, in the frequency range up to 6 kHz, is actually 9. Some interpolation between calculation points is generally required.

The formulation of §3 uses only 2 coupling coordinates between the wheel and rail, and hence forces in only two degrees of freedom. The transfer functions, $H_j(\omega)$, contained in equation (66) are relations between the dynamic forces, P_j (or P_V and P_L) and the surface roughness, r, as defined in equations (41). From §3.1.2, these can be identified as

$$H_V(\omega) = \frac{\alpha_{LL}}{\alpha_{VV}\,\alpha_{LL} - \alpha_{VL}\,\alpha_{VL}}$$

$$H_L(\omega) = \frac{\alpha_{VL}}{\alpha_{VL}\,\alpha_{VL} - \alpha_{VV}\,\alpha_{LL}} \qquad \ldots(76)$$

The sum over j in equation (66) is, in this case, over j=1,2 corresponding to V and L. It should be noted that all the terms for a

given number of nodal diameters, n, are added first, using complex addition, but that the sum over n is an energy sum (adding modulus-squared terms).

This model has been incorporated into the computer programs described in §3, and these have been re-run for the rotating wheel using the 'baseline' parameters of §3 (listed in Table 2).

As before, the results are derived and presented for a unit roughness spectrum, although an actual roughness spectrum could be input to the programs. In comparing predictions with experimental results it should be borne in mind that the roughness spectrum should be modified to correspond to that sensed by the wheel-rail contact, a discussed in §3.1.4.

4.4.2 Web Vibration Results

In terms of the radiation of sound by the wheel, the most important motion is the vibration of the web (see Appendix B). The predictions for the static wheel in §3 gave reasonably good results for the web vibration, although there were some systematic discrepancies with measured results.

Figure 48 shows the predicted axial vibration of the wheel at an accelerometer position on the centre of the web for 3 speeds for a unit roughness. The results are in dB re 1 m/m (ie non-dimensional units) as before. Each of these is similar to that predicted for a static wheel in §3 (Figure 25) with a single peak corresponding to each 1-nodal-circle and radial wheel mode. The main difference which can be observed is that the troughs in the response disappear. This is a consequence of the energy sum of the various terms in equation (66) which eliminates the possibility of cancellation and hence anti-resonances.

This form of response shows a much better resemblance to measured results, shown in Figure A6, than the previous results. However, the effects of measurement noise and the limits to the dynamic range of the equipment, which will have similar effects, should not be forgotten. (Note that the overall shape of the measured spectrum in Figure A6 is determined by the roughness spectrum, and also that it is presented in the form of a velocity spectrum).

As before, in the region above 1300 Hz the web response rises sharply, with the main peaks corresponding closely to the two sets of

(a) 40 km/h

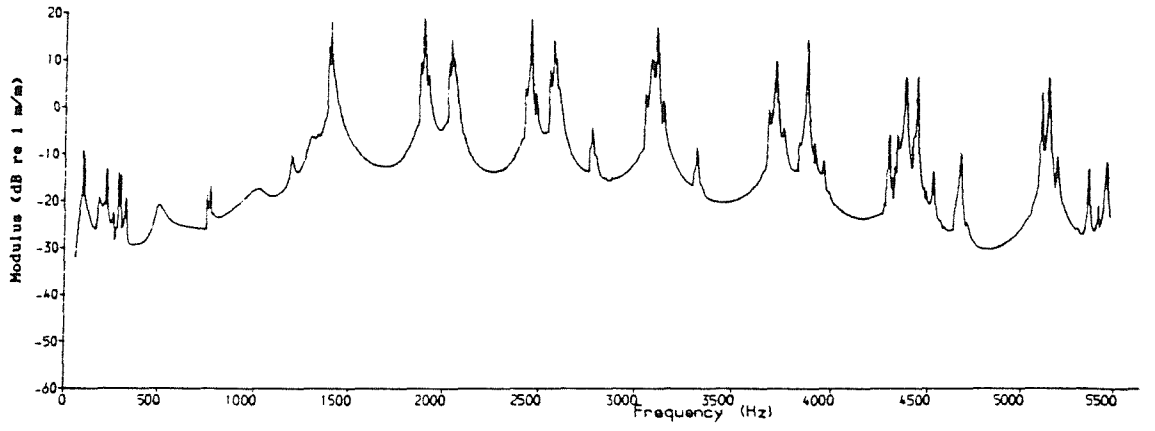

(b) 80 km/h

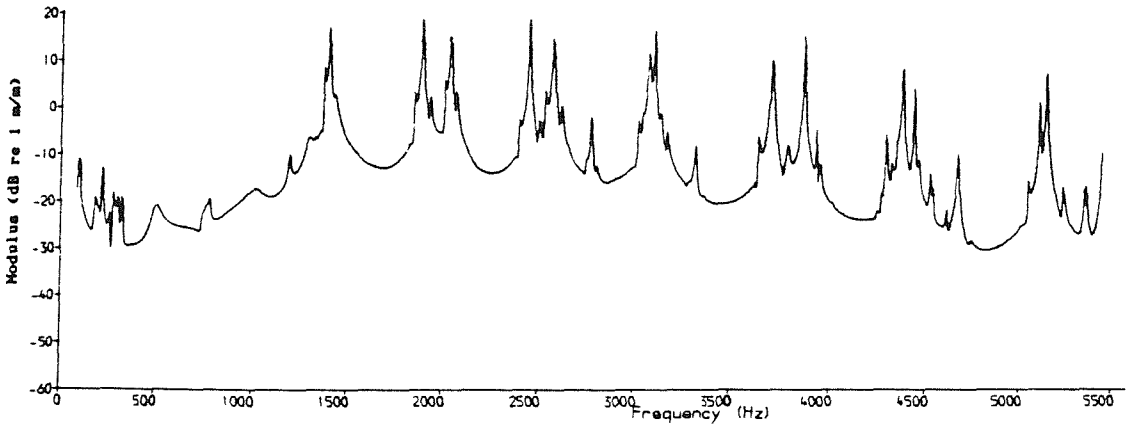

(c) 160 km/h

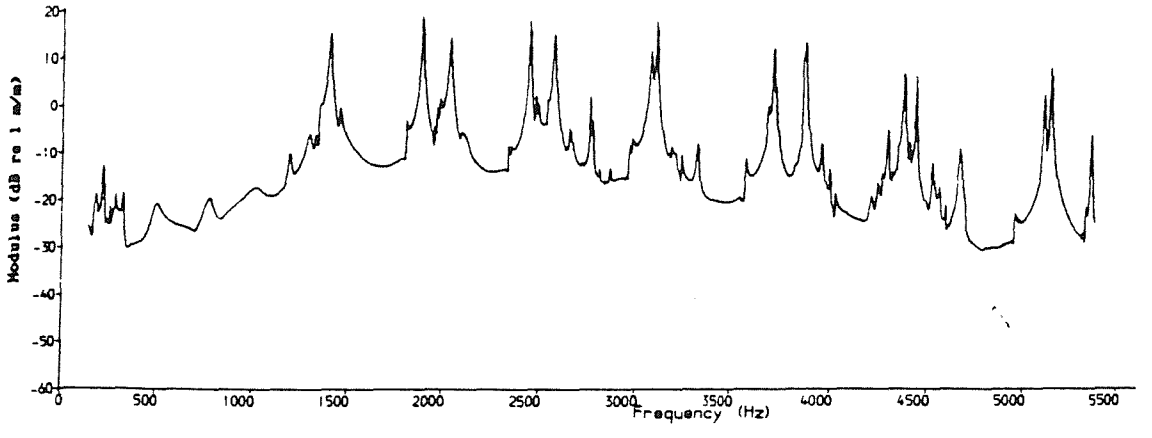

Figure 48 Predicted Wheel Web Axial Vibration
(Displacement for a Unit Roughness Input)

modes of vibration which have a single nodal circle along with several nodal diameters ("one-nodal-circle" and "radial" modes), which are the modes responsible for the main noise radiation from the wheel [33,48]. These modes each exhibit a single peak in the response, as expected from the theory, since they are observed in a frame of reference which is rotating with the wheel.

There is essentially no difference between the results for the three speeds presented, apart from some secondary changes in the spectrum shape at lower amplitudes. The experimental results in Figure A6 contain large differences in level between the various speeds, but this is because these results do not take account of the differences in excitation at the various speeds, due to the dependence on speed of the frequency base of the roughness spectrum. Even so, in Appendix A, when such allowance was made for these differences in input using one-third octave data, there was a small residual speed effect. It, therefore, now appears that this cannot be attributed to the effects of wheel rotation.

4.4.3 Determination of Peak Frequencies

The main discrepancy between predicted and measured web vibration noted in §3 is not readily observable from the figures. This was that the peaks in the predicted web vibration were found to occur at frequencies which were up to 20 Hz above the corresponding resonance frequencies of the wheel, which had been input to the program. This resulted from the coupling of the wheel with the rail and the contact spring, in the vertical direction. The measured results however had no discernible frequency shift of the peaks from the natural frequencies. The measured data were analysed to a resolution of 10 Hz, so small shifts would not be detected.

Figures 49 and 50 show details of the peaks in the web vibration curves (Figure 48), with the frequency referenced to the resonance frequency, f_o. Roughly comparable figures were given in §3 (Figure 27), although they were for the vertical vibration at the contact point, and therefore passed through 1 at the frequency f_o. The vertical scale is linear, again non-dimensionalised by the use of a unit roughness.

The frequency spacing is determined by the wheel receptance program, and in particular the requirement that the receptances are calculated at points sufficiently close together to give no more than a

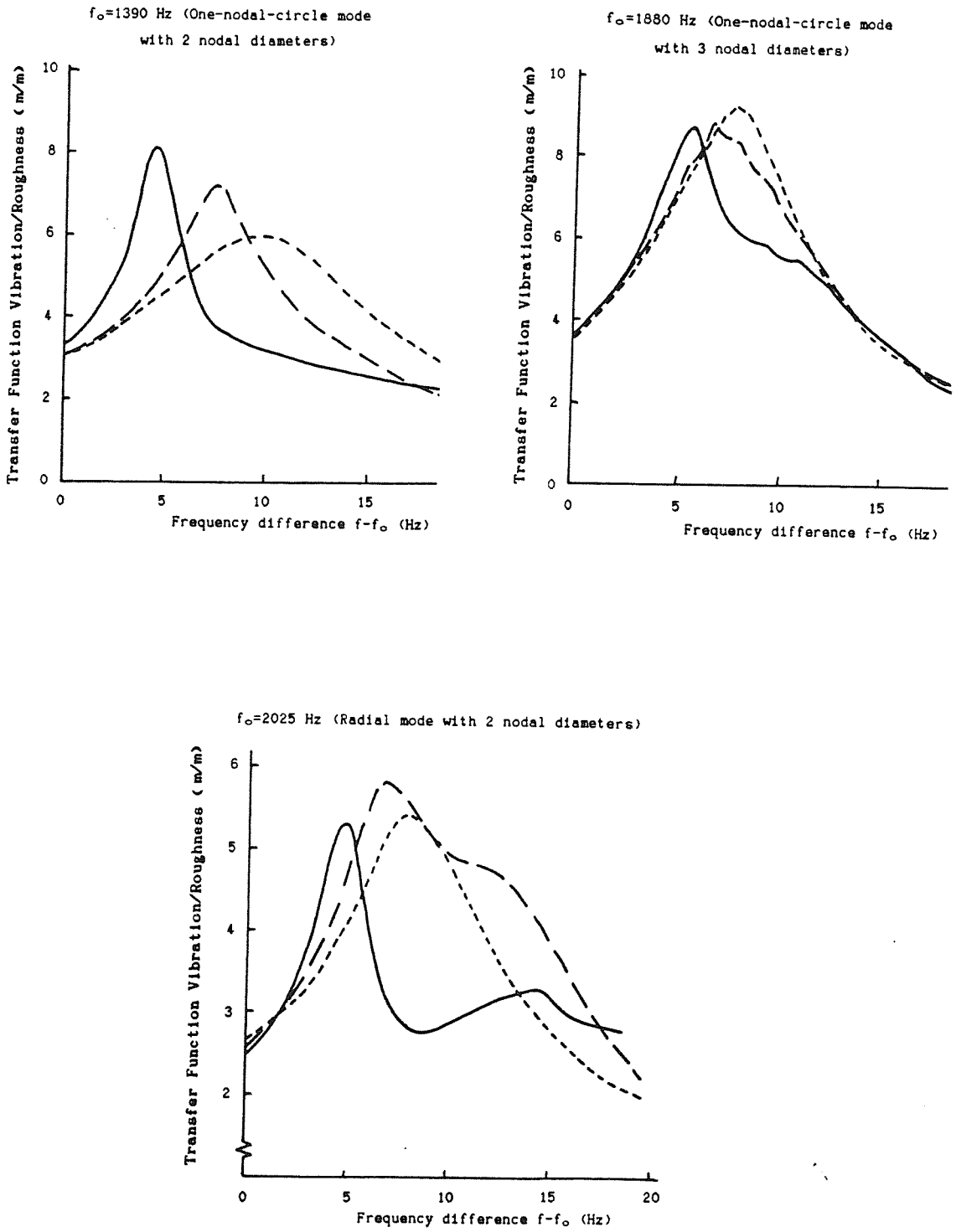

Figure 49 Details of Peaks in the Web Axial Response

(——— 40 km/h, — — 80 km/h, - - - - - 160 km/h)

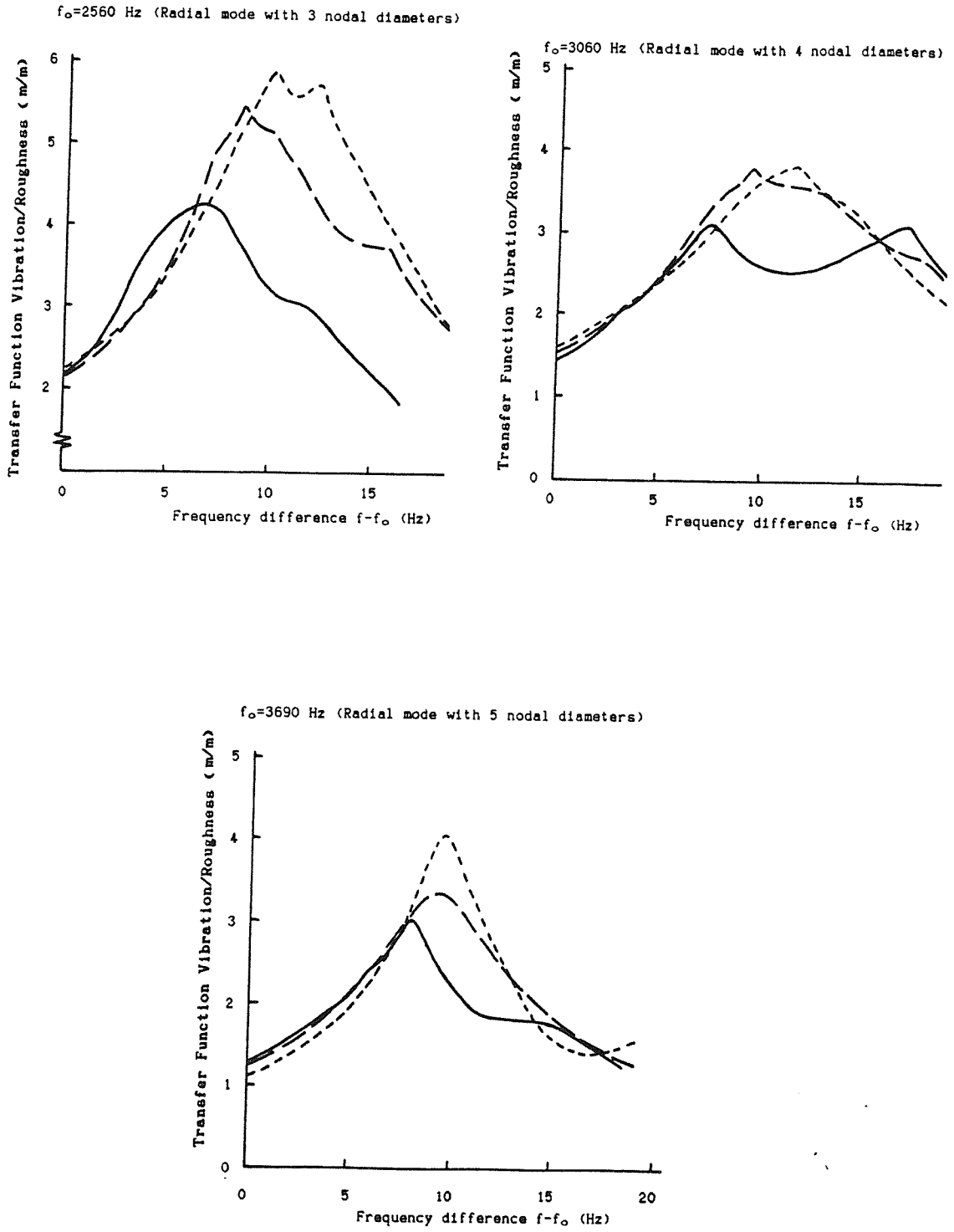

Figure 50 Details of Peaks in the Web Axial Response

(——— 40 km/h, — — 80 km/h, - - - - - 160 km/h)

specified step between adjacent points. Close to resonances this gives a very close spacing, but away from resonances the spacing is broader. Because the response relies on an interpolation of the forces between calculation frequencies, the exact details of the response are sensitive to the frequency resolution used, and a finer step than previously (3 dB instead of 10 dB) has been used.

Figures 49 and 50 indicate that, when wheel rotation is taken into account, the maximum response amplitude occurs at a frequency which is greater than the wheel resonance frequency, as for the static wheel, but the difference is now much less. Table 8 lists these differences in frequency, Δf, from which it can be seen that the peak is less than 10 Hz above the resonance frequency in almost all cases, which is about half of the Δf obtained using the model of a static wheel.

Table 8 Peak Frequencies in Web Axial Response for Various Speeds

(a) One-nodal-circle modes

		Baseline		160 km/h		80 km/h		40 km/h	
n	f_o	Δf	tol	Δf	tol	Δf	tol	Δf	tol
2	1390	16	4	10	1	8	½	4	½
3	1880	14	3	8	1	6	½	5	2
4	2440	11	2	5	5	5	2	3	½
5	3095	10	2	4	2	5	4	6	6
6	3855	7	2	2	1	3	1	2	2

(b) Radial modes

		Baseline		160 km/h		80 km/h		40 km/h	
n	f_o	Δf	tol	Δf	tol	Δf	tol	Δf	tol
2	2025	19	3	8	1	7	1	5	2
3	2560	23	4	10	½	9	½	6	2
4	3060	21	2	11	1	9	½	7	1
								17	0
5	3690	23	6	10	½	10	2	8	1
6	4360	20	2	9	3	10	1	10	3

KEY

n number of nodal diameters
f_o natural frequency (Hz)
Δf difference between peak frequency and f_o (Hz)
tol tolerance in estimate of Δf (Hz)

It may be noted that this difference in frequency (Δf) is speed-dependent, generally increasing slightly as the speed increases. Also the peaks in Figures 49 and 50 are no longer the typical shape of a resonance, as was the case in §3. In some cases there is a double peak, and in other cases the peak appears to project from a broad plateau in the curve.

The smaller frequency difference (Δf) obtained currently will be explained with the help of Figure 51, which shows diagrammatically the wheel receptance as viewed from the non-rotating frame of reference (ie as in Figure 47), in the region of a wheel resonance. The rotation has the effect of splitting the peak at ω_{mn} (shown dotted, cf Figure 29) into two peaks, at $\omega_{mn} \pm n\Omega$, between which is an anti-resonance. Each of these peaks has an amplitude which is half that of the original single peak (ie 6 dB lower).

The peak response occurs when the combined receptance of the contact and the rail (in practice dominated by the contact) crosses the wheel receptance with approximately opposite phase (§3), which occurs just above ω_{mn} for a static wheel (Figure 29). Since the wheel

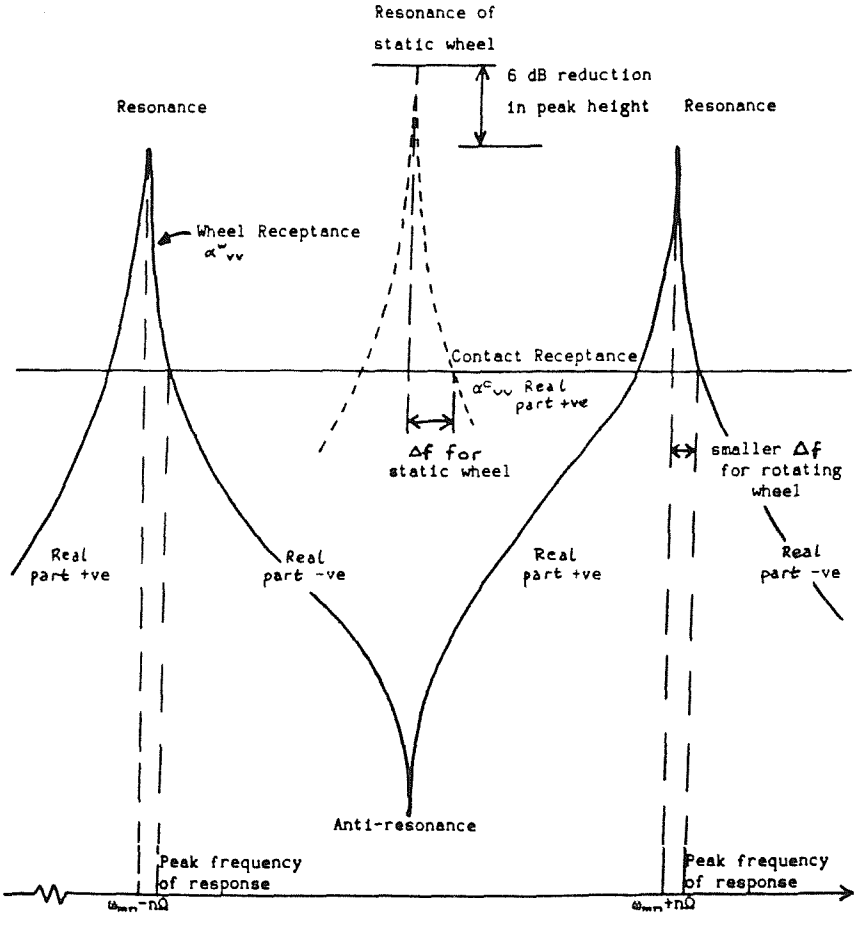

Figure 51 Schematic Diagram of the Region Around a Wheel Resonance when Wheel Rotation is Taken into Account

resonance has been split into two, there are now two such crossings for each ω_{mn}. Therefore two peaks occur in the response (in the non-rotating frame), and due to the fact that the peak amplitudes of the wheel receptance are 6 dB lower than for Ω=0, the peaks in the response occur much closer to the two resonance frequencies, $\omega_{mn} \pm n\Omega$, as shown in Figure 51.

Because of their close proximity to a wheel resonance, these two peak responses each consist predominantly of the response in a single resonance, the other terms being very small in comparison. As may be seen from equation (37), this means that each will consist of a single wave, one rotating in each direction. When viewed from the frame of reference which is rotating with the wheel, both waves correspond to a common resonance frequency, ω_{mn} (equation (36)). Thus the final response, as seen by an accelerometer attached to the wheel, is expected to contain two peaks both slightly above ω_{mn}, which will appear essentially as a single peak close to ω_{mn}, as was the case for a static wheel, but the difference in frequency from ω_{mn} will now be smaller. The double peaks seen occasionally in Figures 49 and 50 can be interpreted as the appearance of the two wave components at slightly different peak frequencies.

The inclusion of wheel rotation into the model of wheel-rail interaction has thus resolved the problem of the differences in the frequencies of the peak response relative to the resonance frequencies. The remaining difference of up to about 10 Hz could not be detected by measurements with a bandwidth of only 10 Hz, and in any case is so small that secondary effects could be significant, eg temperature variations between static resonance measurements and rolling tests, or the centrifugal effects of rolling.

4.4.4 Tyre Vibration Results

Unlike the web vibration, the axial tyre vibration was not predicted adequately previously (§3), as the experimental results contain a strong response in the 0-nodal-circle modes (at around 290, 760, 1390, 2070 Hz etc), which did not appear at all in the predictions. After including wheel rotation the results are improved, but are still not adequate. These are shown in Figure 52, for the same three speeds as Figure 48. The corresponding static predictions and measured results are given in Figures 25 and A6 respectively.

(a) 40 km/h

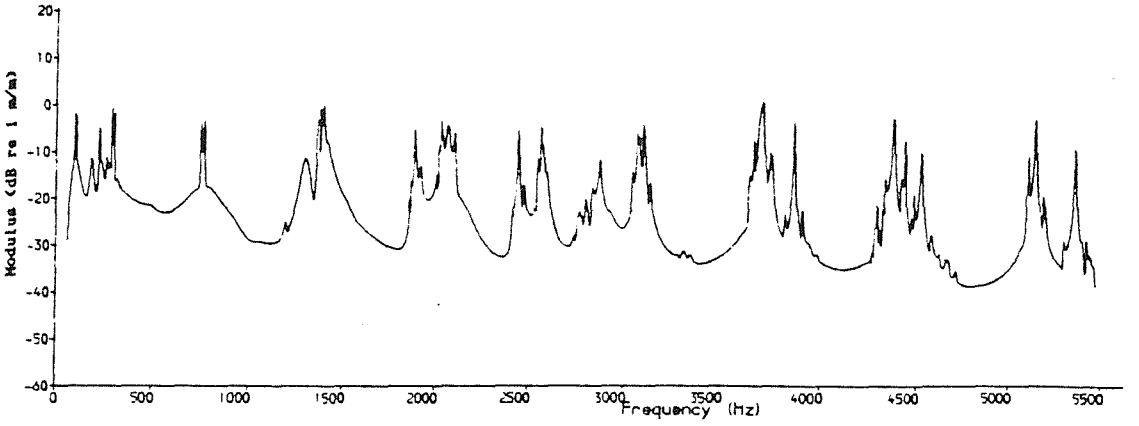

(b) 80 km/h

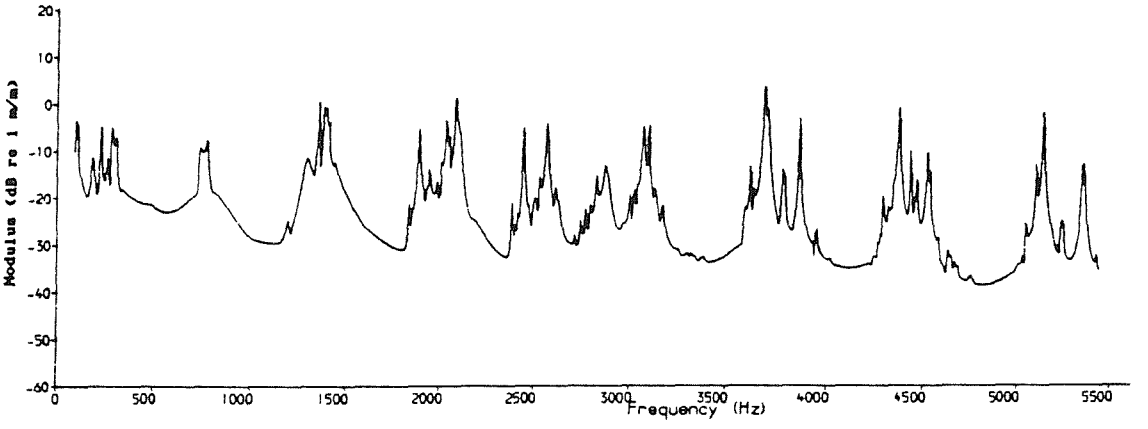

(c) 160 km/h

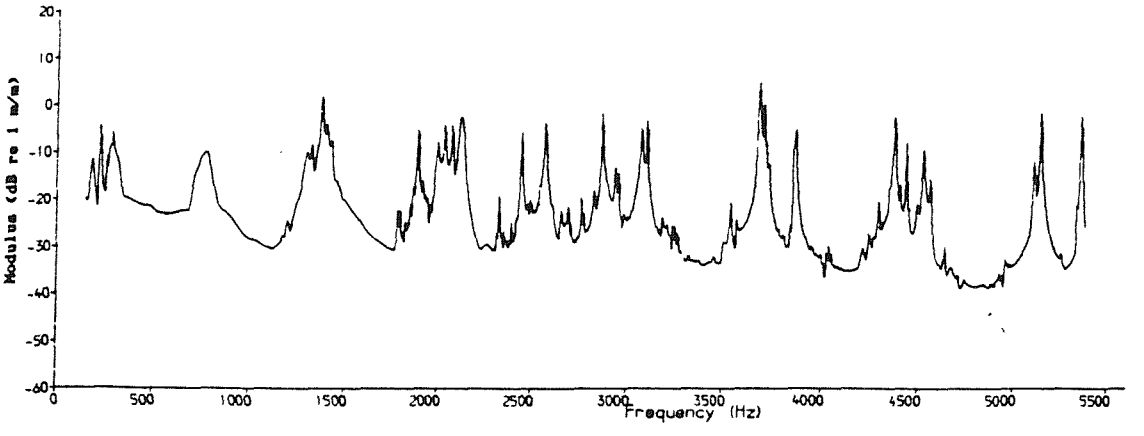

Figure 52 Predicted Wheel Tyre Axial Vibration
(Displacement for a Unit Roughness Input)

At 40 km/h, double peaks can be seen in the tyre response at around 290 Hz and 760 Hz (corresponding to the 2 and 3 nodal diameter 0-nodal-circle modes). At higher speeds these merge to become a broad hump in the response. These features are not seen in the measured results, which rather contain a stronger single peak at each of these frequencies, for all speeds (although the frequency resolution of the measured data is limited to about 10 Hz). This reinforces the inadequacy of the modelling of the lateral responses found in §3.

4.4.5 Other Results

Figures 53 and 54 show the vertical and lateral response at the contact, ie in the frame of reference which is not rotating for 40 and 160 km/h. The vertical response, which corresponds closely to the axial vibration of the web since the same modes are dominant in each case, contains pairs of peaks corresponding to the single peaks in the rotating frame (Figure 48) with a separation which depends on the speed, as expected. However it is interesting to note that the two peaks do not always have the same magnitude as each other, so that in the rotating frame the components of the two contra-rotating waves will not necessarily be equal. The shape of the roughness spectrum will also influence their relative magnitude.

There is no sign in the lateral response at the contact of the split peaks around 290 Hz and 760 Hz seen in Figure 52, nor of a corresponding single peak which might have been expected. It would appear that, in the non-rotating frame, the two components cancel each other out at the contact. This means that the predicted lateral response around these frequencies has a stationary pattern with a minimum at the excitation point. This type of behaviour is not observed experimentally in either [47] or [48].

Such motion is unrestrained by this 2-degree-of-freedom model at the contact patch, as no coupling has been included between the spin coordinates (the rotations about a vertical axis). In practice such a coupling will exist, and this may alter the response.

Whatever the cause of this spurious effect, it seems that the inclusion of wheel rotation, by itself, has not resolved the outstanding deficiency of the modelling of the lateral response of the wheel tyre. Thus, as concluded in §3, it appears that the modelling of the contact zone, particularly for the lateral response, requires further development.

(a) Vertical Wheel Vibration Displacement for a Unit Roughness Input

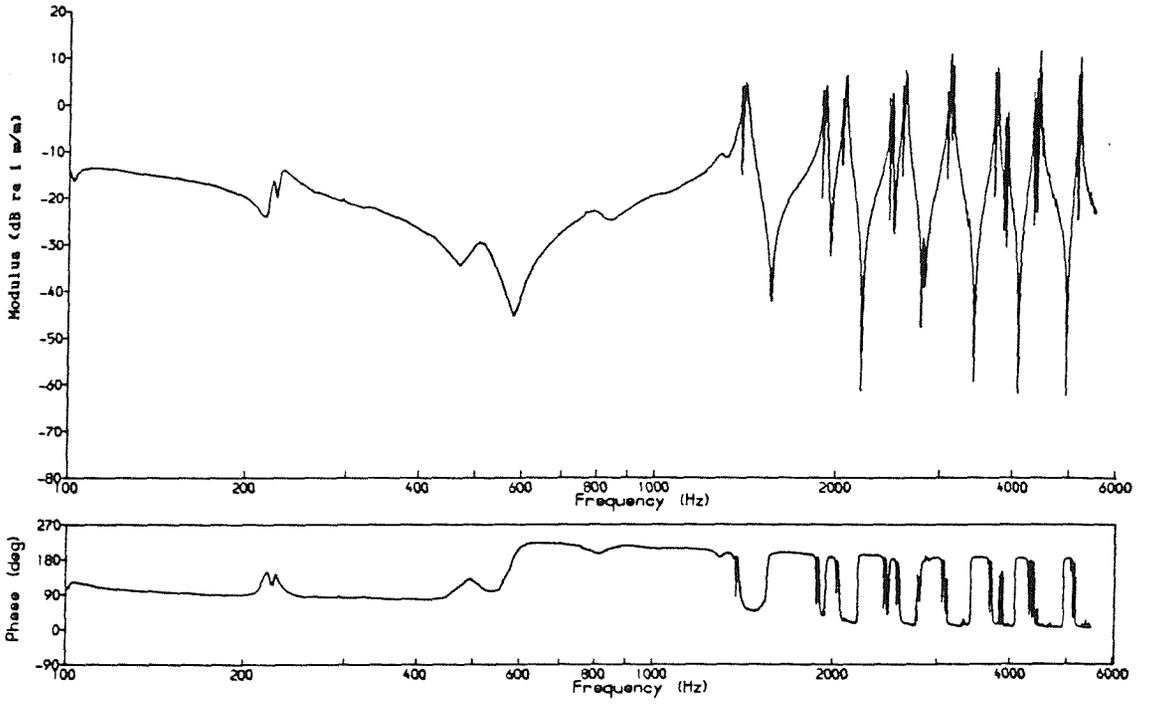

(b) Lateral Wheel Vibration Displacement for a Unit Roughness Input

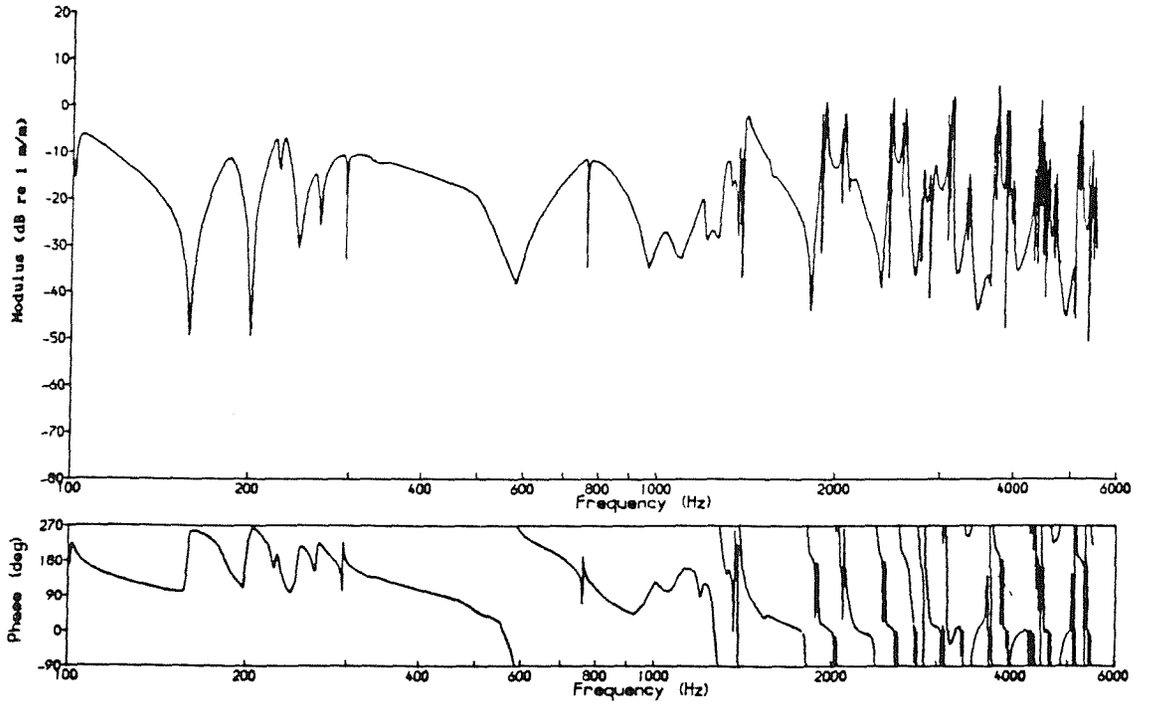

Figure 53 Predicted Wheel Vibration at Wheel-Rail Contact - 40 km/h

(a) Vertical Wheel Vibration Displacement for a Unit Roughness Input

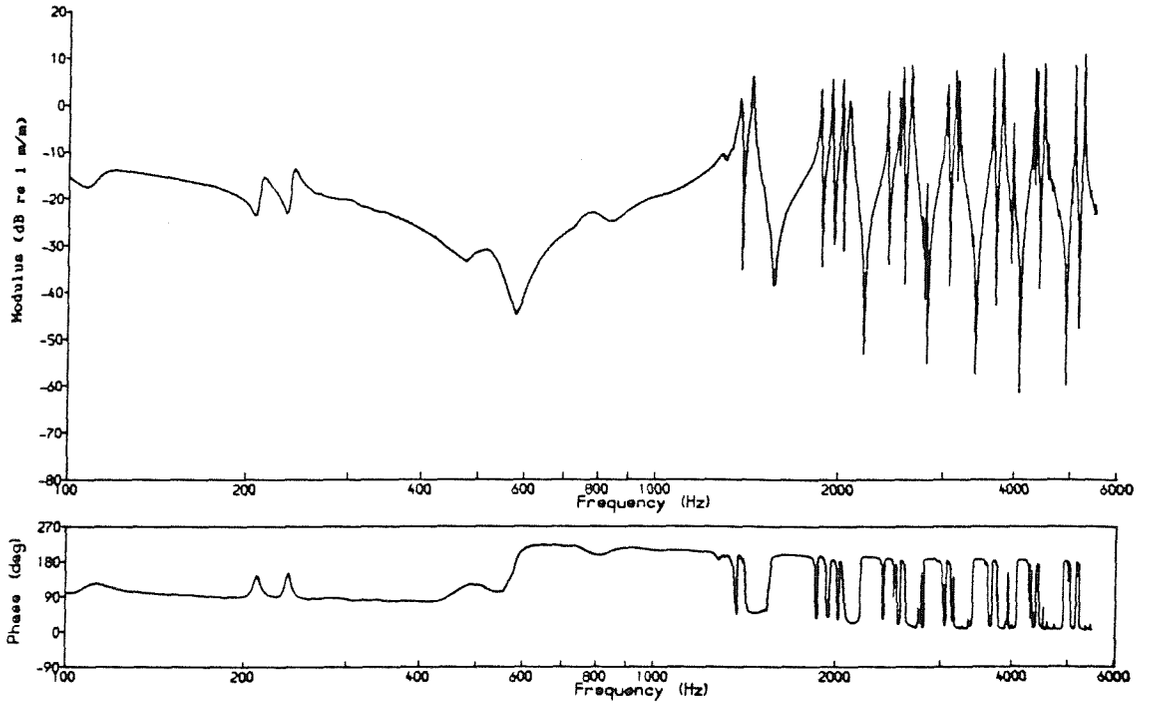

(b) Lateral Wheel Vibration Displacement for a Unit Roughness Input

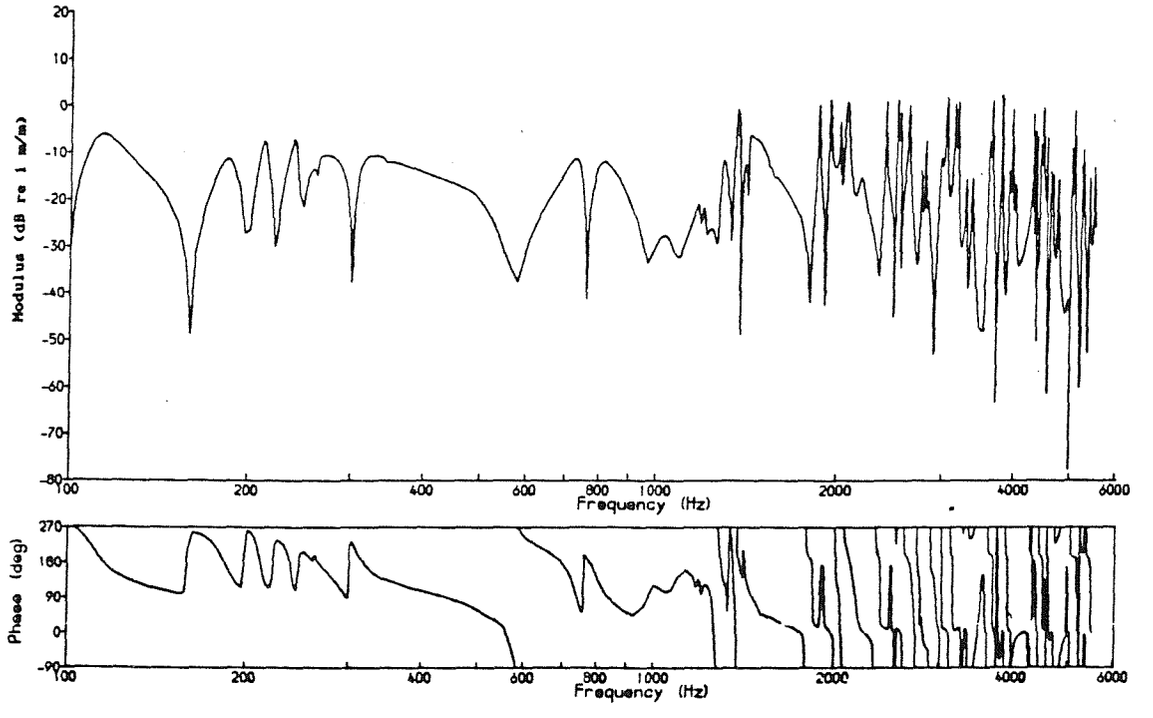

Figure 54 Predicted Wheel Vibration at Wheel-Rail Contact - 160 km/h

4.5 CONCLUSIONS

The effects of rotation have been included into the model for wheel-rail noise generation. Whilst the mathematical derivation has been presented for the general multi-degree-of-freedom case, results have been given using the same approximations as in §3 (eg 2 degrees of freedom at the contact, simple beam model for the rail receptances).

It has been found that this gives an improved representation of the wheel web response, containing no anti-resonance dips. The major peaks in this motion, the most important acoustically, appear as single peaks, and are located closer to the corresponding resonance frequencies than was the case for the model based on a static wheel. This has resolved this apparent deficiency of the model of interaction found in §3.

In a non-rotating frame these single peaks each split into two, separated by $2n\Omega$, where n is the number of nodal diameters and Ω is the rotational speed. These two peaks correspond to two contra-rotating waves. In the frame rotating with the wheel, however, these two waves appear at the same frequency. Since the two waves are excited by different frequencies at the contact patch, their phases are randomly related, and the final 'modeshape' of the wheel vibration, when viewed from either a rotating or non-rotating frame, should contain no distinct node lines, a feature which is confirmed in practice.

No significant speed effect has been found in the predicted response to a unit roughness, whereas the measurements in Appendix A contained a slight speed effect (even after the effects of roughness were removed). The rotation, therefore, cannot explain this phenomenon.

The inclusion of rotation does not appear to have improved the lateral response of the wheel tyre, which was not modelled realistically in §3. It has changed the nature of the response, however: at low speeds split peaks appear in the response in the rotating frame, corresponding to the 2 and 3 nodal diameter modes, not seen in measurements. There is no corresponding peak in the response in the non-rotating frame, indicating that the contact is at a node of this vibration pattern. In practice, the wheel and rail will be coupled via the spin coordinate (rotation about the vertical axis), and this coupling may have an influence on such lateral motion.

CHAPTER 5

THE VIBRATION BEHAVIOUR OF A RAIL

5.1 INTRODUCTION

The work so far, and in particular the initial assessment of the wheel-rail interaction model carried out in §3, has used a simple beam theory to represent the rail, as used by Remington [15,20]. The focus is now turned to the development of a more realistic model for rail response, which will subsequently be combined with the wheel.

A review of literature related to rail vibration was given in §1.2.4. Most existing models are limited in validity at the higher end of the frequency range under consideration here, due to the break-down of the assumptions of a rigid beam cross-section. This has been shown by experiments carried out at BR Research in which a rail was excited in situ by a harmonic force, the magnitude and phase of the response being measured at many points [69,70]. It was found that the cross-section deforms significantly above about 1500 Hz for lateral excitation, and above 4000 Hz for vertical excitation.

Whilst some account can be taken of the deformation of the rail cross-section, such as by Scholl [72,73], none of the work to date provides a means of calculating the point frequency response of the rail taking into account these deformations, and so a new method is required.

A finite element model of a length of rail is presented first, which allows the cross-sectional deformations to be studied, but not the point receptances. This is then followed by a model of an infinite rail, which makes use of periodic structure theory. Finally the effects of the sleepers and railpads are considered by using an equivalent continuous system.

For this work a standard BR flat-bottomed rail section (type 113A), shown in Figure 55, will be studied. Although the frequency range of interest is generally 100-5000 Hz, results up to slightly higher frequencies will be included, as significant features occur just above the 5000 Hz limit.

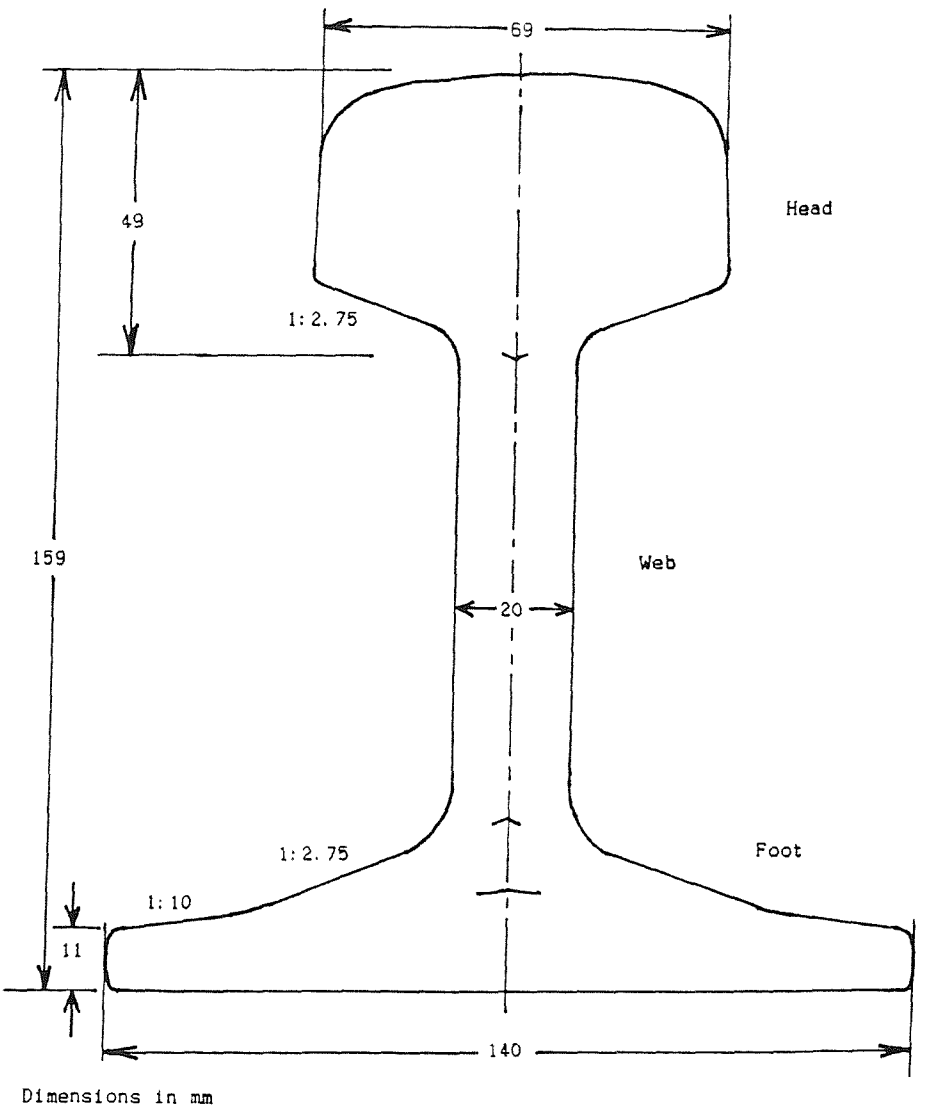

Figure 55 Cross-section of Type 113A Flat-bottom Rail

5.2 FINITE ELEMENT ANALYSIS

5.2.1 Finite Element Grid for a Length of Rail

A finite element idealisation of a 0.54 m length of rail has been produced, as shown in Figure 56. This length corresponds to half that used in experimental work which will be used to validate the idealisation, as described in §5.2.3 below.

In modelling this length of rail, full use has been made of structural symmetry. Symmetry at the mid-point of the length allows half of the length to be neglected, and the plane of symmetry of the cross-section has also been utilised to allow half the width to be neglected. A symmetric boundary condition in this plane gives the

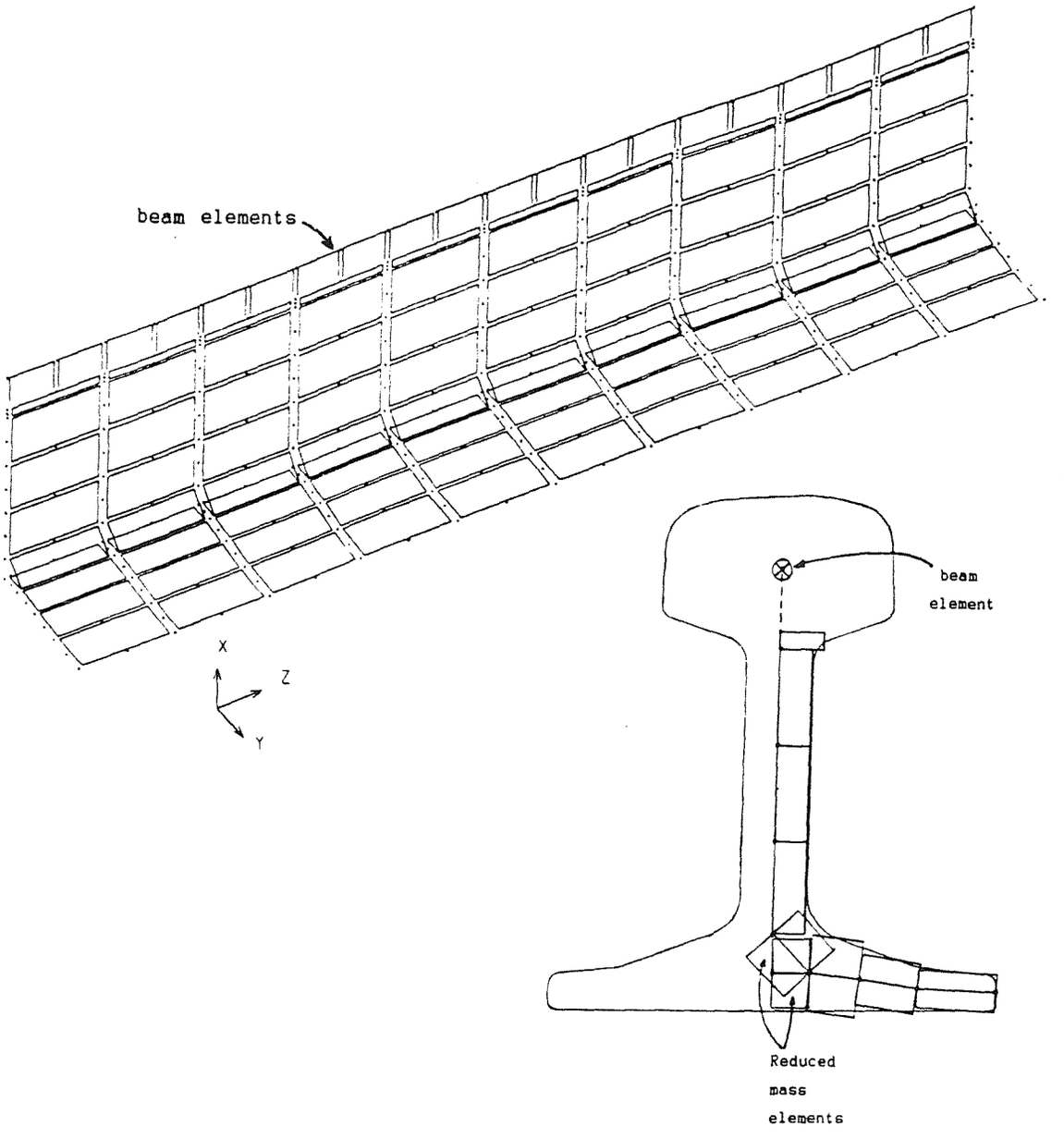

Figure 56 Finite Element Idealisation of Length of Rail

vertical and longitudinal modes; an anti-symmetric boundary condition gives the lateral and torsional modes.

The BR Research in-house finite element package "NEWPAC" [94] has been used (as for the wheel in §2). This provides a wide range of elements such as plates and beams, although it has no facilities for 3-dimensional 'brick' elements.

The rail head is represented by Timoshenko beam elements. Their axis has been offset from the point of connection to the rest of the structure, so that the axis is at the centroid of the rail head, whereas it is connected to the web elements at the base of the head.

The remaining elements are thin plates of various sizes, as determined by the cross-sectional geometry of the rail (they are shown in Figure 56 superimposed on the rail section). The elements in the web are located along the plane of symmetry, and hence are given a reduced thickness parameter (depending on the symmetry condition).

The region at the base of the web and the centre of the foot, with its generous radii, is too thick to be represented simply by perpendicular plates, and so it has been formed of a triangle of plates. These elements had a slightly reduced density to compensate for their increased thickness, so that the mass of the region was correctly represented. Several alternative idealisations of this region were considered, such as a simple perpendicular join of the web and foot plate elements, or various shapes of triangle, and also various thicknesses of plate element. That shown in Figure 56 was chosen as it was found to give the best agreement between measured and predicted natural frequencies in §5.2.3 below.

The structure is mounted on soft springs, to ensure that the rigid body modes have some inherent stiffness. The values of spring stiffness were very low, giving rigid body modes below 1 Hz, and thus will not affect the structural modes significantly.

The finite element program requires 'master' degrees-of-freedom to be specified, to reduce the size of the matrices to managable proportions. In total over 100 'masters' were specified, spread evenly throughout the structure, and these should be adequate for the number of modes which are to be calculated in each run. The masters are located at plate mid-side nodes; this is generally recommended in preference to the corner nodes since a greater proportion of the mass of these elements is located at the mid-side nodes.

5.2.2 Predictions of Frequency-Wavenumber Relations

The modes of vibration of the free-free 1.08 m length, which will form the basis of validation of the idealisation, will be seen to be quite complicated. It is therefore instructive first to study the hypothetical system which has symmetric or anti-symmetric boundary conditions at both ends of the 0.54 m idealisation. These are the generalisations of the simply supported boundary conditions for a simple beam (see Appendix D); all the near-field (decaying) waves resulting from the free boundary are eliminated. With these boundary conditions, each natural frequency corresponds to a point on the

frequency-wavenumber relation for a rail of infinite extent, as with a simply supported beam, the wavelengths produced being integer fractions of 2.16 m. The resulting modeshapes will correspond to the cross-sectional deflections of the various wavetypes in an infinite rail.

A total of eight sets of boundary conditions (combinations of symmetry and anti-symmetry on 3 boundaries) are possible, of which 5 are actually required to cover all the possible modes.

The results have been calculated for natural frequencies up to 7 kHz and are shown for the lateral modes in Figure 57, as a graph of wavenumber against frequency. At low wavenumbers, these modes can be considered as (from top to bottom of Figure 57): lateral bending (designated 'L'), torsion ('T'), web bending ('W') and double bending of the web ('D'). General similarities can be seen at low frequencies between the lateral bending and torsion curves and those for a simple beam (Appendix D), but this breaks down at higher frequencies as deformation of the cross-section occurs.

Figure 58 shows, for each mode plotted in Figure 57, the cross-sectional deformation at the section of maximum deflection. Each row contains the results corresponding to a single line on Figure 57, whilst each column corresponds to a single value of wavenumber. The natural frequencies of each mode are also listed on this figure.

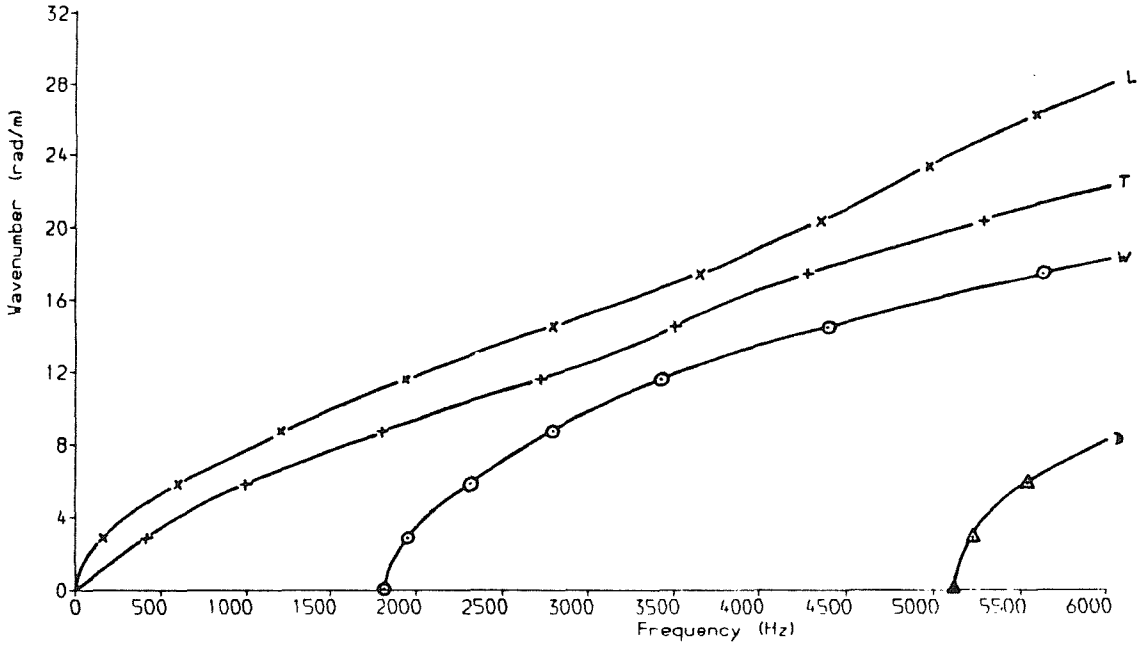

Figure 57 Natural Frequencies of Lateral Modes of Rail with Symmetry/Anti-Symmetry at Both Ends

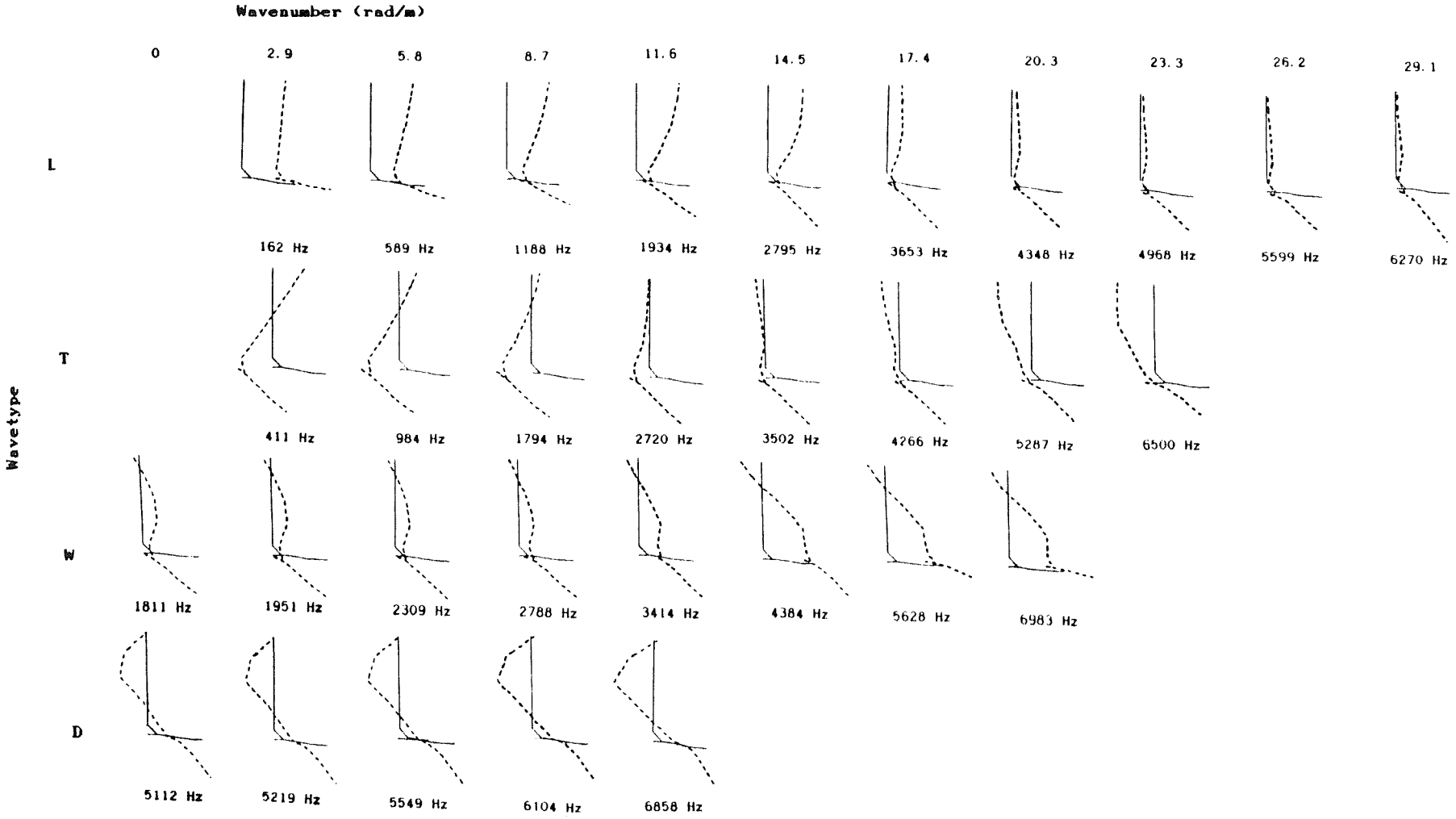

Figure 58 Displaced Shapes for Lateral Waves of Rail from Finite Element Model with Symmetry/Anti-Symmetry at Both Ends

The first row (L) shows the results for the first lateral mode, which is simple lateral bending at low frequencies. At higher wavenumbers this mode becomes rocking of the foot with very little motion of the head or web.

The second set of modes (T) is torsional at low frequencies. At higher wavenumbers it looks more like a bending mode, since the whole cross-section moves laterally in phase, but differs from the simple bending modes (L at low frequencies) by having significant deformation of the web. Clearly at higher wavenumbers, the descriptions "simple bending", "torsion" etc become inappropriate, although the reference letters will be retained for clarity.

The third set of modes (W) involve bending of the web, or equivalently torsion of both the foot and the head out of phase with each other. At higher wavenumbers the mode appears more torsional, yet again with significant deformation of the web. At these higher frequencies the foot bends in-plane, but does not appear to deflect vertically.

The fourth set of modes (D) is a double bending of the web, so that the foot and head are again each in torsion, but this time in phase with each other. The cross-sectional shape of this mode is

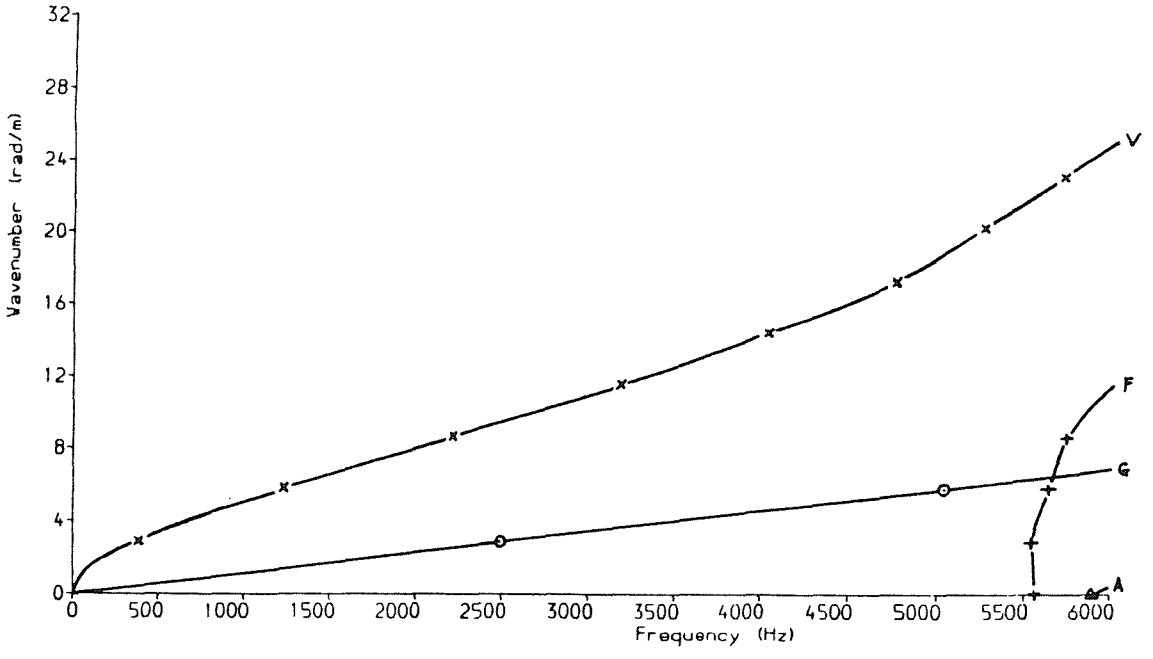

Figure 59 Natural Frequencies of Vertical and Longitudinal Modes of Rail with Symmetry/Anti-Symmetry at Both Ends

reasonably constant over the frequency range considered since only relatively low wavenumbers are represented.

The results for the vertical and longitudinal modes are shown in a similar manner in Figures 59 and 60. The vertical modes are, at low wavenumber, vertical bending (designated 'V') and flapping of the foot out of phase with the head ('F'). At high wavenumbers, the V mode becomes dominated by flapping of the foot (which in this case is in phase with the head).

The longitudinal modes consist of simple longitudinal motion (designated 'G') and an "anti-longitudinal" motion in which the head and foot move in opposite directions on the shear stiffness of the web ('A'). Both modes also contain some vertical motion, particularly of the foot, as is shown in Figure 60. Two views are shown of each longitudinal mode: the vertical motion is at a node when the longitudinal motion is at an antinode and vice versa. Both are shown at their antinodal positions.

At zero wavenumber and frequency, four rigid-body modes occur (lateral, vertical, longitudinal and torsional). Their natural frequencies are essentially zero, in practice depending on the suspension stiffness. Because of the arbitrary nature of the suspension springs, these modes have not been plotted in Figures 58 and 60.

It should be noted that using the current idealisation with 10 element bays covering 0.54 m and one set of master degrees-of-freedom per element bay, accurate results can be expected only up to about the 10th mode of each set (ie for modes with a wavelength down to 0.216 m). For higher order modes more than half a wavelength falls within each element bay and the results will deteriorate. In order to test this, some additional results were calculated using a 10 bay idealisation of 0.27 m (thus giving twice the resolution), and these results are given in Table 9. These confirm the above expectations.

5.2.3 Results for Free-Free 1 m Length of Rail

By leaving one end of the idealisation free, but retaining the symmetric or anti-symmetric boundary conditions at the other end, a 1.08 m free-free length is represented. Measurements on such a length of rail (type 113A) have already been made at BR Research and can therefore be used to validate the finite element model.

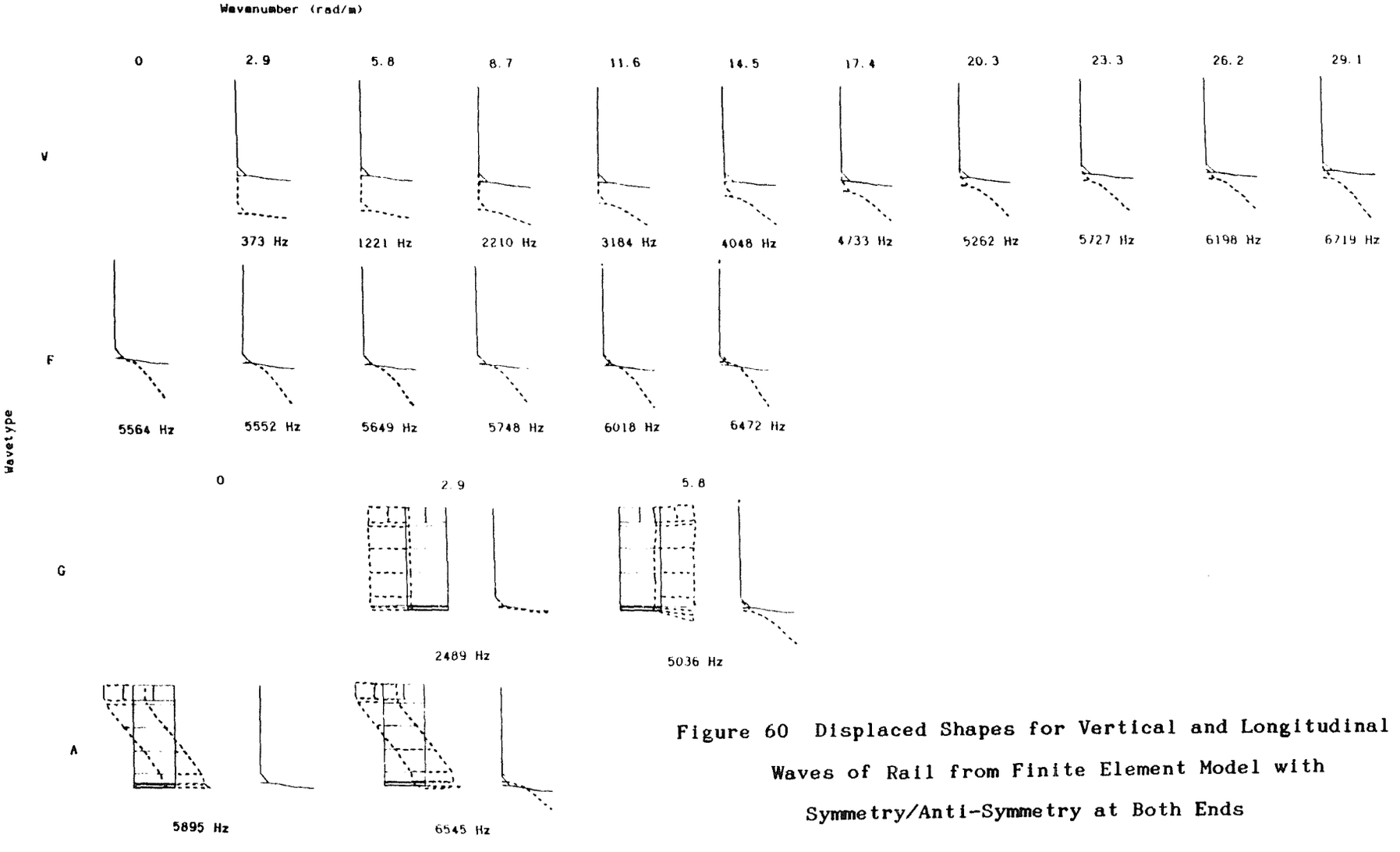

Figure 60 Displaced Shapes for Vertical and Longitudinal Waves of Rail from Finite Element Model with Symmetry/Anti-Symmetry at Both Ends

Table 9 Results of Using Twice as Many Finite Elements over a Given Length

N	L	(L)	%	T	(T)	%	W	(W)	%	D	(D)	%
0	-	-	-	-	-	-	1809	1811	-0.1	5071	5112	-0.8
2	589	589	0.0	995	984	1.1	2336	2309	1.2	5552	5549	0.1
4	1938	1934	0.2	2712	2720	-0.3	3433	3414	0.5	6934	6858	1.1
6	3670	3653	0.5	4244	4266	-0.5	5591	5628	-0.7			
8	4893	4968	-1.5	6554	6500	0.8						
10	6065	6270	-3.3									
12	7357	7802	-5.7									

N	V	(V)	%	F	(F)	%	G	(G)	%	A	(A)	%
0	-	-	-	5481	5564	-1.5	-	-	-	5843	5895	-0.9
2	1221	1221	0.0	5557	5649	-1.6	4995	5036	-0.8	7965	8102	-1.7
4	3171	3184	-0.4	5900	6018	-2.0						
6	4675	4733	-1.2	6998	7195	-2.7						
8	5595	5727	-2.3									
10	6469	6719	-3.7									
12	7528	8000	-5.9									

KEY:-
- N number of nodes in 1.08 m
- L first lateral mode set (lateral bending)
- T second lateral mode set (torsional)
- W third lateral mode set (web bending)
- D fourth lateral mode set (double web bending)
- V first vertical mode set
- F second vertical mode set (foot flapping)
- G first longitudinal mode set
- A second longitudinal mode set

All frequencies in Hz.
Modes in brackets are from the coarser F.E. grid.
% = (more accurate value/coarser value - 1)×100%

Experimental investigations were carried out into the natural frequencies and modes of vibration of this length of rail, originally to complement noise radiation work [103]. Measurements were taken of the natural frequencies of the length of rail, and some modeshapes were investigated in detail. This original work was limited to excitation of the rail at its centre, thus eliminating all odd modes of the rail (ie those with a node at the centre).

Recently further work has been carried out on the same piece of rail in connection with a project to study the effects of damping treatments attached to a rail [104]. This consisted of measurements of the natural frequencies and damping ratios, in connection with which the modeshapes of all of the modes up to 6 kHz were investigated in terms of the positions of their nodes along the head, and various other features to assist mode identification.

In modelling this case, symmetry or anti-symmetry of the cross-section is once again employed to reduce the size of the idealisation. This separates the lateral modes from the vertical and longitudinal modes. The experimental results were similarly separated by the use of lateral and vertical excitation at the head.

The modes were found to be much more complicated than those described in §5.2.2 above. This is partly due to end effects - near-field waves are generated at the ends, which are superimposed on the sinusoidal waveform. Also, coupling of the various possible wavetypes occurs, particularly for the case of lateral vibration. As a result the modes are difficult to interpret.

The predicted and measured frequencies up to 6 kHz are listed in Tables 10 and 11. They are matched with the most appropriate mode, although at high frequencies it is not possible to identify the measured modes sufficiently, due to coupling as described above.

The agreement between natural frequencies is generally very good. The vertical modes are slightly over-predicted at low frequencies (up to 4%), but most of the first 16 lateral modes are within 2% of the measured results. The double web bending modes (D), which are predicted above 5100 Hz, appear to occur in the measurements from around 4600 Hz which indicates that the predictions are about 10% too high. The second order vertical modes (F), which are predicted from 5400 Hz, are measured slightly above this, but agreement is within 3%. The longitudinal modes are over-predicted by 5% and 8%. These modes contain vertical motion, particularly of the foot, in both measurements and predictions.

The idealisation is obviously a compromise, particularly in the region at the base of the web and centre of the foot. The incorporation of a triangle of plates has made the vertical bending modes slightly too stiff at long wavelengths, but most other modes agree fairly well. The double web bending modes are inaccurate since

Table 10 Predicted and Measured Natural Frequencies of Lateral Modes for 1.08 m Length of Rail

Symmetric Modes					Anti-symmetric Modes				
Experiment			Finite Element		Experiment			Finite Element	
Number of nodes on head	freq Hz	% diff	freq Hz	mode shape	Number of nodes on head	freq Hz	% diff	freq Hz	mode shape
2	359	0.6	361	L2	1	396	-2.8	385	T1
2	838	-0.6	833	T2	3	888	1.4	901	L3
4	1583	0.4	1590	L4	3	1466	0.3	1470	T3
0	1786	1.1	1806	W0	1	1929	0.6	1940	W1
2	2270	0.0	2269	W2*	5	2360	2.4	2416	L5
2	2345	0.8	2364	T4*	3	2757	-0.7	2738	W3
6	3173	1.6	3225	W4	5	3226	1.5	3273	T5
6	3314	1.8	3374	L6	7	4090		3928	W5
6	3935	2.0	4012	T6		4656		4236	L7
	4638		4880	L8		4733		4830	T7
	4687		5017	W6				5189	D1
	4884		5106	D0				5540	L9
			5525	D2					

KEY:-

L first lateral mode set (lateral bending)
T second lateral mode set (torsional)
W third lateral mode set (web bending)
D fourth lateral mode set (double web bending)

} number refers to the number of nodes along the length

* coupled modes

$$\%\ \text{diff} = \frac{\text{Finite element} - \text{Experimental}}{\text{Experimental}} \times 100\%$$

they will depend very much on this region, and also on the refinement of the web idealisation, and the longitudinal modes are also too stiff. Using other idealisations, such as a straight perpendicular join of the web and foot, it was possible to predict the vertical bending modes more accurately at low frequencies, but the agreement was worse for other, higher order, modes. In particular the W modes had large discrepancies from the measurements in the position of their 'cut-on' frequency.

Table 11 Predicted and Measured Natural Frequencies of Vertical and Longitudinal Modes for 1.08 m Length of Rail

Symmetric Modes					Anti-symmetric Modes				
Experiment			Finite Element		Experiment			Finite Element	
Number of nodes on head	freq Hz	% diff	freq Hz	mode shape	Number of nodes on head	freq Hz	% diff	freq Hz	mode shape
2	770	3.9	800	V2	3	1733	2.0	1768	V3
4	2748	1.7	2795	V4	5	3686	1.0	3723	V5
6	4485	0.3	4499	V6	9	5060	-0.4	5038	V7
6	5443	-0.9	5392	F	5/7	5542	-1.5	5460	F
0/2	5740	-3.2	5559	F	3	5777	-1.9	5666	F
6	5690	-0.5	5661	V8	3	5946	0.5	5976	V9
4	5879	-0.2	5870	F					
	2372	5.2	2495	G1		4708	8.1	5091	G2

KEY:-

V first vertical mode set
F second vertical mode set (foot flapping)
G first longitudinal mode set

} number refers to the number of nodes along the length

$$\% \text{ diff} = \frac{\text{Finite element} - \text{Experimental}}{\text{Experimental}} \times 100\%$$

5.3 CALCULATION OF WAVENUMBERS AND RECEPTANCES FOR AN INFINITE BEAM

5.3.1 Discussion of Methods

At low frequencies, the wavenumber and receptance of a beam at a given frequency can be calculated analytically from the Euler-Bernoulli equations, as described in Appendix D. Analytical solutions are also possible for the Timoshenko beam equations, and for coupled bending and torsion of the type described briefly in Appendix D. Allowance can even be made for bending of the web and flanges of an I-beam using analytical techniques [105,106], although this has not been extended to the prediction of receptances.

The analytical techniques clearly become increasingly complex as additional degrees-of-freedom are added. Consequently they would be much too complicated to contemplate for the number of cross-sectional

degrees-of-freedom included in the finite element analysis in §5.2 above. A method is therefore sought into which a complicated cross-section can be input in detail, as in the finite element method.

The above finite element model, whilst predicting points on the frequency-wavenumber curves, is inadequate for the present purpose, as it can only predict the frequency for given wavenumbers, and not vice versa. Furthermore, it is not possible directly to predict near-field waves, or the receptances. Whilst it might be possible to consider a finite element model which was sufficiently long for end effects to be negligible, this would be extremely unwieldy. A better approach would be to take specific account of the constant cross-sectional shape and the infinite extent.

One such possibility would be the use of a 'finite strip' method. In such a model the cross-section is represented by 2-dimensional elements, and a wavenumber is imposed in the longitudinal direction. A membrane finite element analysis of a rail cross-section carried out previously [71] is a particular case of this, with zero wavenumber. For a given wavenumber, the various allowed frequencies can be calculated. The receptance can be calculated by Fourier transformation. Such a model was applied to a rail for static loading by the Track Unit, BR Research, but unfortunately it was not reported.

This method has the limitation, however, that once more it is the wavenumber which is specified, rather than the frequency. The latter would be preferable as a model is sought which can be linked to the wheel response model (§2) in the frequency domain. To overcome this an alternative method is employed, using periodic structure theory.

An infinite beam of constant cross-section, such as the rail, can be considered as a periodic structure of arbitrary period. Periodic structure theory [107-109] allows the motion of the infinite structure to be derived from the properties of a single element. This periodic element can be made up from finite elements, as in [110].

This is generally carried out by deriving the allowable wavenumbers at a particular frequency. Hence the motion of the infinite rail can be derived in the frequency domain from the properties of a short length. From the wavenumber solution at a given frequency, it is possible to proceed to derive the receptances as well, by a superposition of the various wavetypes.

A program has been specially written to carry out the various calculations, details of which are given in Appendix F, following the method of Mead [107]. The finite element program, NEWPAC [94], is used to derive the mass and stiffness matrices of the short length, and these are then extracted and passed to the periodic structure program.

As an initial test, the model has been used in conjunction with a finite element idealisation consisting of an undamped single beam element. Figure 61a shows the predicted wavenumbers, which compare well with analytical results (see Appendix D). The agreement is not so good for the torsional wave, but this can be explained by noting that the NEWPAC program does not allow any difference between the values of the moments of area used in stiffness and inertia (I_x and J). Figure 61b shows various receptances derived from the same beam model, which also agree well with the results of Appendix D.

5.3.2 Input Data for Rail Cross-Section

The rail cross-section has been modelled using the same set of finite elements as in §5.2 (see Figure 56), except that now only a single element bay is used. In order to eliminate internal coordinates, 4-noded plate quadrilateral elements have been substituted for the 8-noded elements used previously. Various element lengths, L, have been investigated, with 10 mm being adopted as generally satisfactory. It was found that 50 mm was too long, as deterioration occurred at higher frequencies, as the wavelengths approached 2L. Very short lengths, however, are more likely to be subject to rounding error. Symmetry of the cross-section has been utilised, so that only half of the cross-section is modelled (as in §5.2), with separate runs required for the lateral motion (anti-symmetric boundary condition) and the vertical/longitudinal motion (symmetric).

For lateral motion, the idealisation has a total of 37 degrees of freedom at each end of the periodic element, all of which have been defined as 'masters', except for the rotations about the longitudinal axis, z, of which only the head rotation was included (the coordinate system used for the rail is defined in Figure 56). This resulted in matrices of dimension 28 being used in the periodic structure program.

Investigations were carried out into the optimum number of such master degrees of freedom to be used, and it was found that it was not possible to eliminate any more than this without a deterioration in the results. In particular it was found to be essential that the rotations

(a) Dispersion Diagram

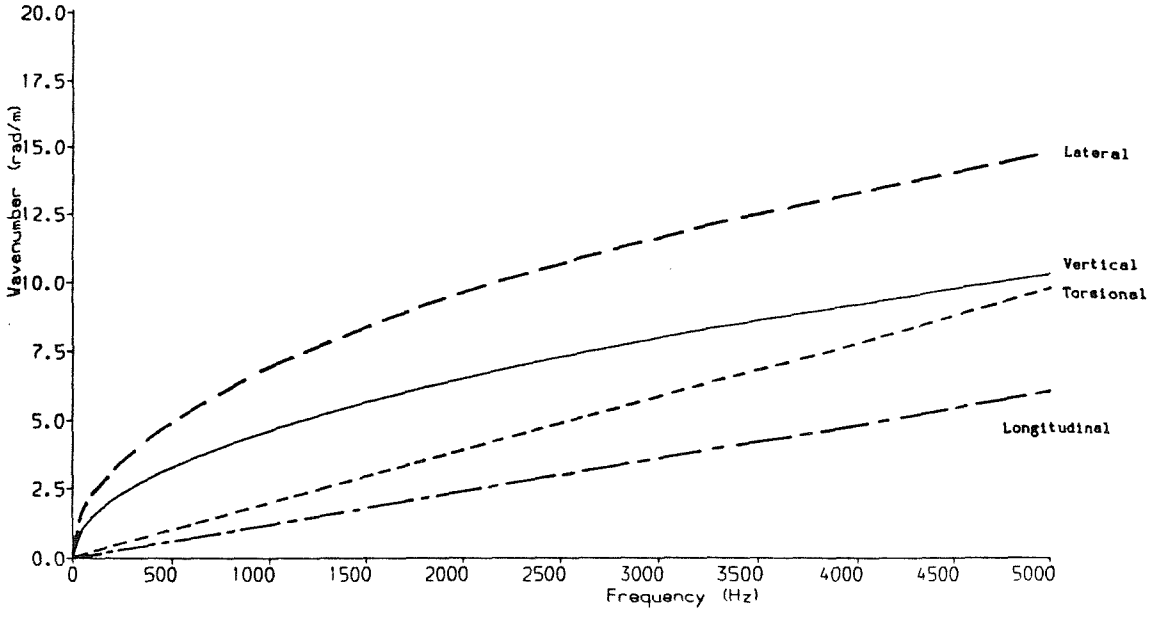

(b) Receptances

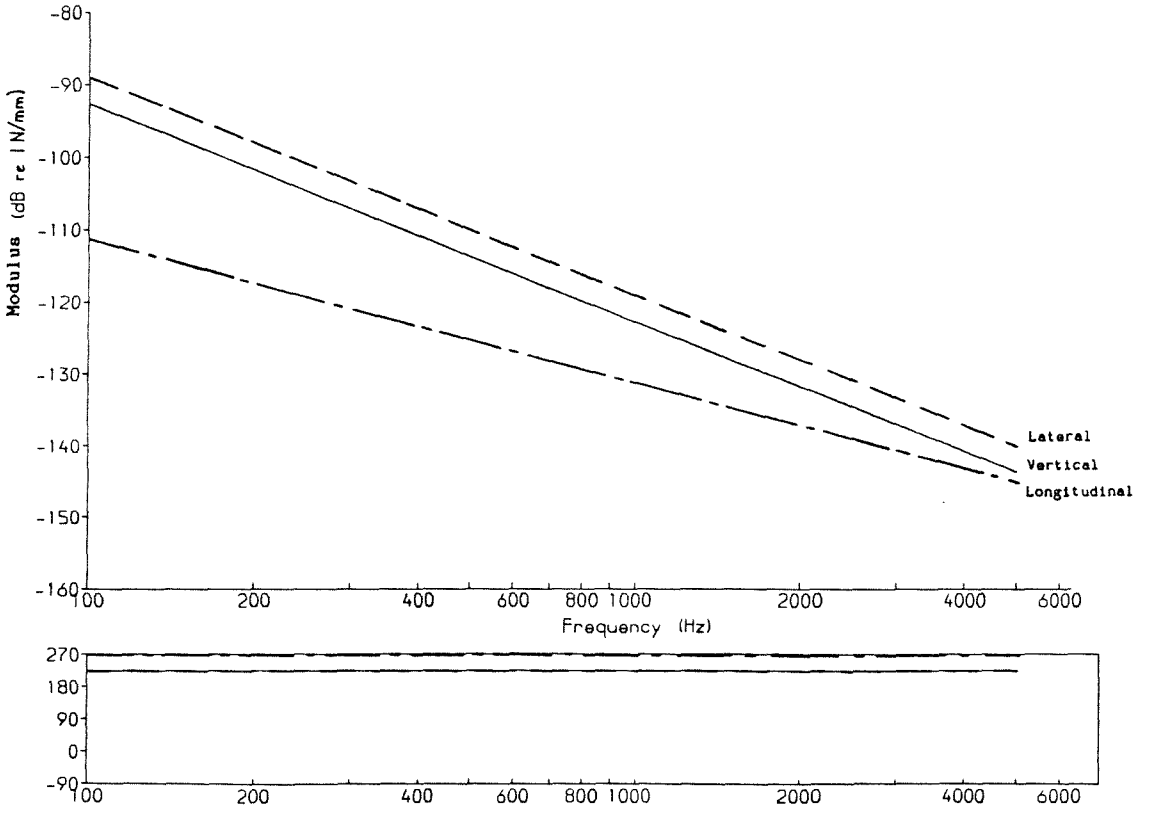

Figure 61 Predictions from Periodic Structure Model for Simple Beam Element

about the x and y (vertical and lateral) directions were included whenever displacements in the y and x directions respectively were included. If they were omitted, the structure would effectively be allowed to be pin-jointed. Thus the criteria for selecting masters seem to be much more stringent than for a standard finite element analysis (as used in §5.2).

To achieve smaller matrices, it should be possible to use fewer elements to model the cross-section, but it can be expected, once more, that almost all degrees of freedom should be retained as masters. If better finite elements were available, particularly to model the thick region at the base of the web more effectively, it might be possible to achieve reasonable results using fewer elements, and perhaps fewer degrees of freedom.

For vertical vibration, an initial total of 38 degrees of freedom has been reduced to 31, again by elimination only of the rotations about the z direction.

5.3.3 Model including Sleepers

The model described so far consists of a free infinite rail. In practice a rail is supported on resilient pads, concrete (or wooden) sleepers, and ballast. An attempt will be made to include these supports into the model, although avoiding the complication of the periodic nature of the support. Whilst it would be possible to use periodic structure theory to model the periodic support offered by the sleepers etc, for the current work the track model will be limited to the form already used, ie a continuous model. For this, the sleeper, pads and ballast are replaced by equivalent continuous layers of mass and stiffness, as shown in Figure 62, as also used by Grassie [58-60].

This has the additional advantage of being suitable for incorporation into the linear interaction model of §3, whereas a periodic support would lead to time-varying receptances which are incompatible with such an interaction model.

Appendix G considers a finite element model of a concrete sleeper on a foundation stiffness (representing the ballast), excited through a spring (representing the rail pad). It is shown that a simple mass-spring model of the pad-sleeper-ballast system is quite acceptable in terms of the receptance of the system as excited through the pad. This has the additional advantage that the symmetry of the rail cross-section can be maintained.

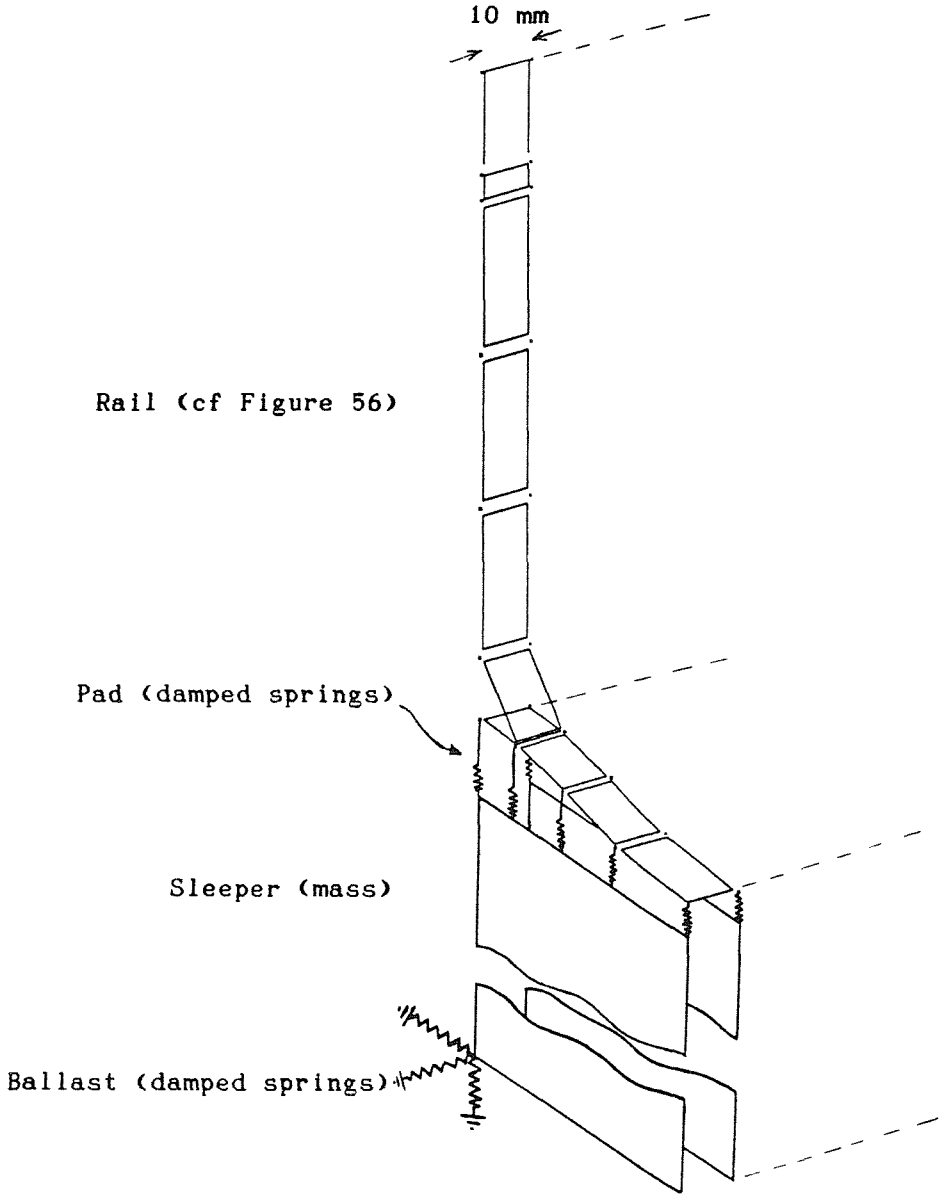

Figure 62 Finite Element Idealisation of Rail with Equivalent Continuous Support

Assuming a nominal sleeper spacing of 0.7 m, and a periodic element length of 10 mm (as above), the masses and stiffnesses used for a complete sleeper (as listed in Appendix G) should be factored by 1/70. These are then divided between the two ends of the periodic element, and again halved due to the use of symmetry of the rail cross-section. For the pad, the stiffness is further divided among 5 spring elements, attached to the 5 node points on the rail foot, in proportion to their spacing, as shown in Figure 62. Rotational stiffnesses are not included, since the array of stiffnesses takes care of this. Each spring is rigidly connected to the sleeper mass, which is at the height of the sleeper centroid.

It should be noted that the sleeper mass has three coordinates (for each of the two boundary conditions), but that these coordinates are not connected directly across the periodic element. Thus each sleeper mass is independent, and waves cannot propagate through the sleeper layer. This results in spurious waves with a wavelength equal to 4 times the periodic element length, which may be ignored. If the model were to be used for a slab track, some account may be necessary of the bending stiffness and corresponding waves in the concrete slab.

Also neglected here is the coupling between rails through the sleepers. This is considered briefly in Appendix G, from which it appears to be a justifiable approximation at most frequencies. However at some frequencies, particularly around 350 and 700 Hz for vertical vibration, the transmission of force from one rail to the other can be as much as -5 dB, ie more than half the input force amplitude.

In Appendix G viscous damping is used, as required by the NEWPAC finite element program [94], but in the periodic structure model structural damping is used. For the rail a loss factor of 0.0005 is used, which has been chosen to correspond to measurements of the damping ratio of a free length of rail which were in the region of 2 to 5×10^{-4} [104], ie loss factors of twice this: 4 to 10×10^{-4}. For the ballast, a loss factor of 0.5 is used, which corresponds roughly to the level of damping used in Appendix G at the bounce mode at 90 Hz, which had a damping ratio of 0.24. For the pad, a loss factor of 0.5 is also used. A value of 0.3 would give damping approximately equivalent to that used in Appendix G for frequencies around 500 Hz, where the vertical rail-on-pad resonance occurs (as $\eta \sim \omega C/K$). However 0.5 corresponds more closely with Grassie's model [58] at this frequency.

5.4 RESULTS OF PERIODIC STRUCTURE MODEL

5.4.1 Wavenumbers and Eigenvectors for Free Rail

The predicted wavenumbers for lateral waves in the free rail, are given in Figure 63. These are based on a 10 mm element length, and are for zero damping. Each wave type is labelled by a Roman numeral. The real parts of the wavenumbers are shown as solid lines, and the imaginary parts as dotted lines. Real wavenumbers (such as in Figure 63a) represent propagating waves, and imaginary wavenumbers represent near-field waves. Figure 63b also contains regions of complex wavenumber (labelled a, b, c) which have both real and imaginary parts. These are near-field waves (decaying rapidly with distance due to their imaginary

(a)

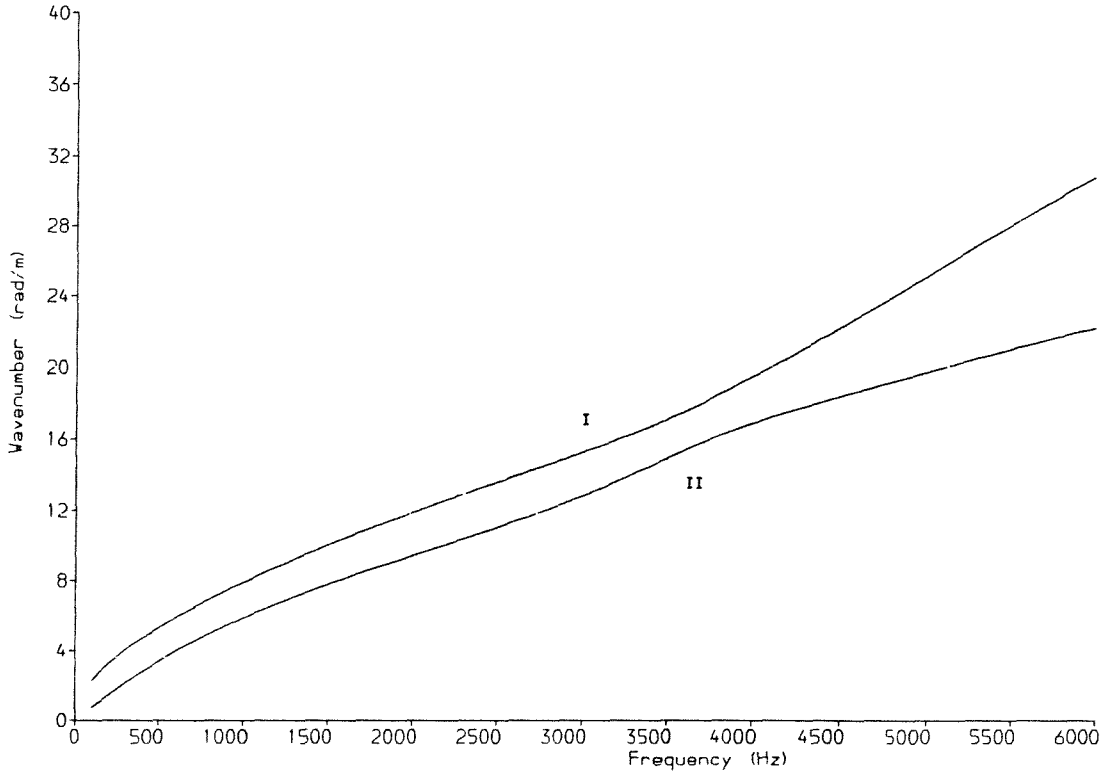

(b)

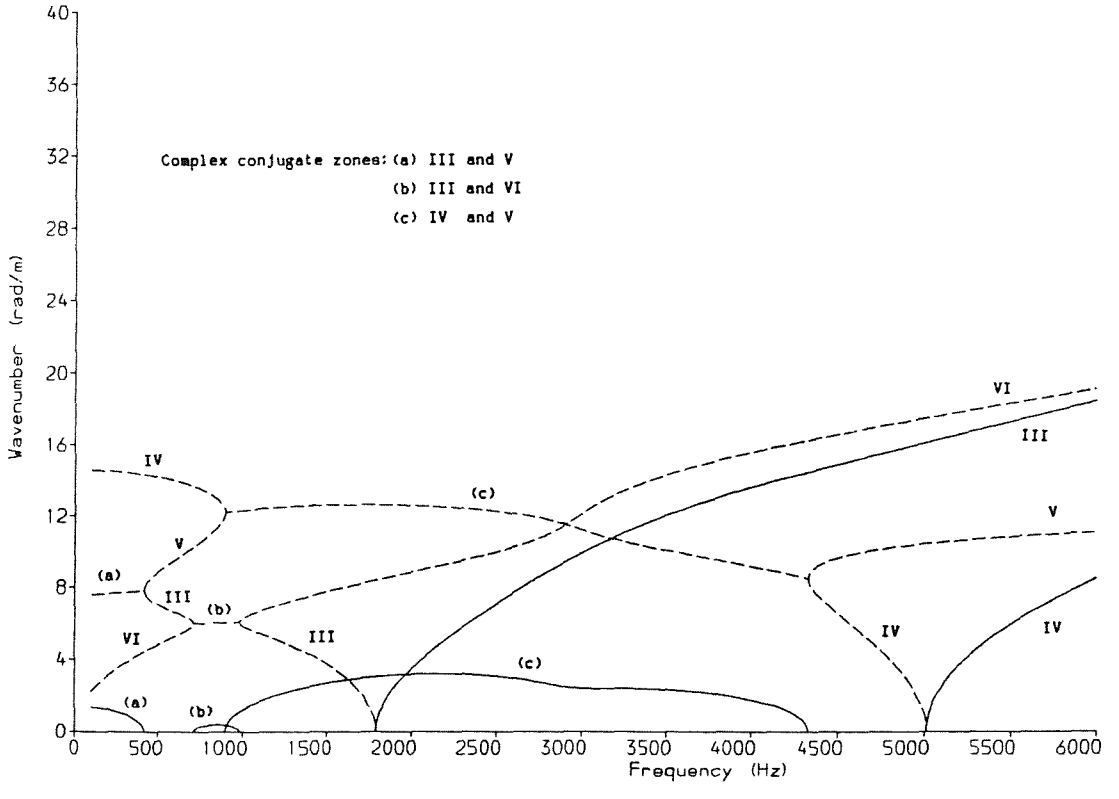

Figure 63 Wavenumbers of Lateral Waves from 10 mm Model of Free Rail
(——— Real Part, – – – Imaginary Part)

parts) but with a spatial harmonic component (due to their real part). They should not be confused with propagating waves which have zero (or very small) imaginary part. In the absence of damping, the complex wavenumbers occur in conjugate pairs, so that one of the pair has a positive real part, and the other has a negative real part (not shown). These conjugate regions occur where two imaginary wavenumber curves cross each other: for example region (a) corresponds to the crossover of waves III and V.

The real wavenumbers may be compared directly with the results of the finite element work of §5.2 (Figure 57). The agreement is very good, with the largest deviation occurring with the first bending wave (L, ie I in Figure 63a), and then only by 4% at 5000 Hz. When account is taken of the deterioration of the finite element results for the larger wavenumbers (Table 9), this error is further reduced. The W and D waves (III and IV in Figure 63b) both 'cut-on' (ie change from imaginary to real wavenumbers) at the correct frequency in comparison with the results in Figure 57 (within 2%).

Near-field waves exist with higher wavenumbers than those shown (a total of 28 wavenumbers are produced (at each frequency) by this 28 degree-of-freedom system), but these will contribute little to the

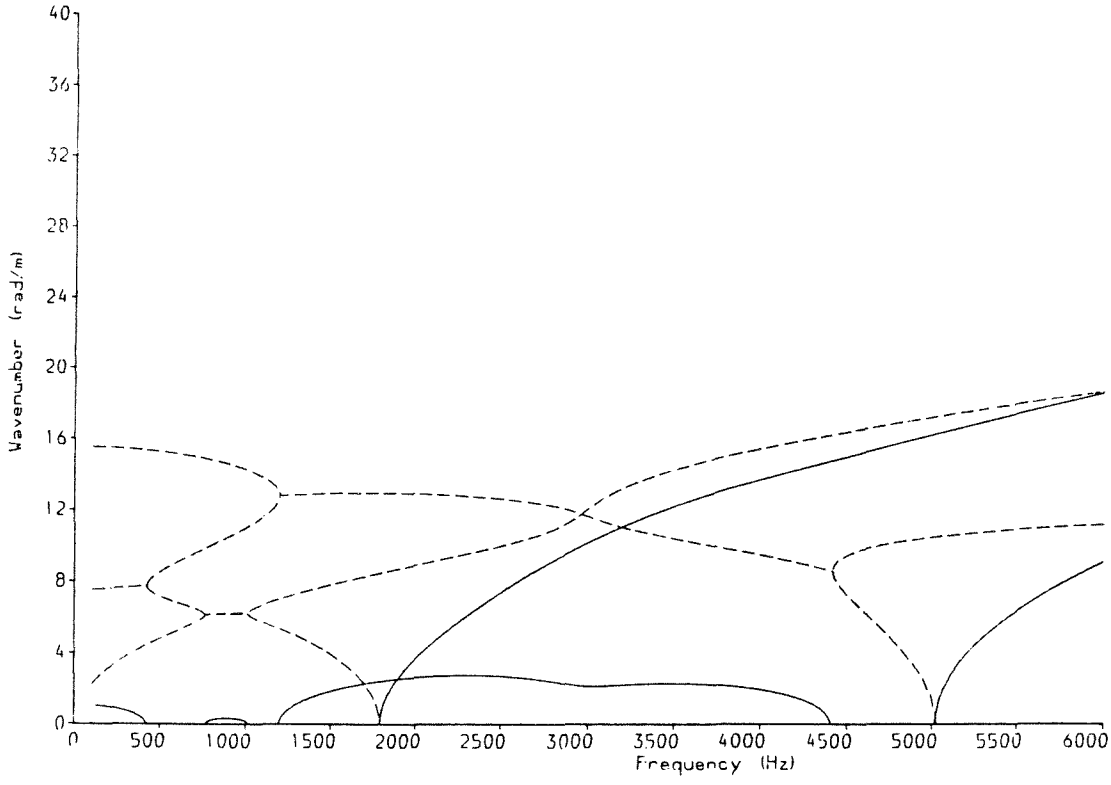

Figure 64 Wavenumbers of Lateral Waves from 20 mm Model of Free Rail
(——— Real Part, – – – Imaginary Part)

vibration of the rail as their magnitude is negligible after one or two element lengths, L. It should be remembered, of course, that in calculating the receptances, all waves contribute - it may be noted (see Appendix D) that for an Euler-Bernoulli beam the near-field waves contribute as much to the receptance as the propagating waves. For the 28 degree-of-freedom model, however, the contribution is found to decrease somewhat as the (imaginary) wavenumbers increase.

Figure 64 shows the results equivalent to Figure 63b for a 20 mm element length. It can be seen that, although the propagating waves are unchanged (including the first two waves (I & II), given in Figure 63a, but not shown here) the near-field waves are affected slightly by the element length, particularly for higher wavenumbers. In particular the regions of complex conjugate behaviour are slightly altered - see especially the start of region (c). However these details are of little consequence to the overall rail vibration.

Figure 65 shows the results for the vertical and longitudinal waves, which may be compared with Figure 59. Agreement is again favourable. The A wave (ie wave IV) 'cuts on' at 5704 Hz, which is within 3% of the previous value. However the F wave (ie wave III) 'cuts on' significantly lower (5081 Hz against 5564 Hz, a difference of 9%). This is likely to be an effect of having used 4-noded elements rather than 8-noded ones, so that less accuracy is achievable.

It may be noted that the longitudinal (G) and foot-flapping (F) waves (labelled II and III) exhibit coupling in the region 5000-5500 Hz, with their curves not crossing each other. This is a feature which could not have been deduced from the coarser finite element results in Figure 59. It is, nevertheless, consistent with the vertical component which was noted in the longitudinal waves in Figure 60, as a result of asymmetry in the cross-section.

Figure 66 shows the lateral wavenumbers (equivalent to Figure 63b) for a fairly high level of damping (η=.01). It can be seen that the clear division into real, imaginary and complex conjugate zones has been lost, and the corners of the various graphs have been rounded. Moreover, the propagating waves have a non-zero imaginary part, indicating that the damping has introduced a decay with distance. This decay, Δ in dB/m, can be calculated using ([111], cf Appendix D):-

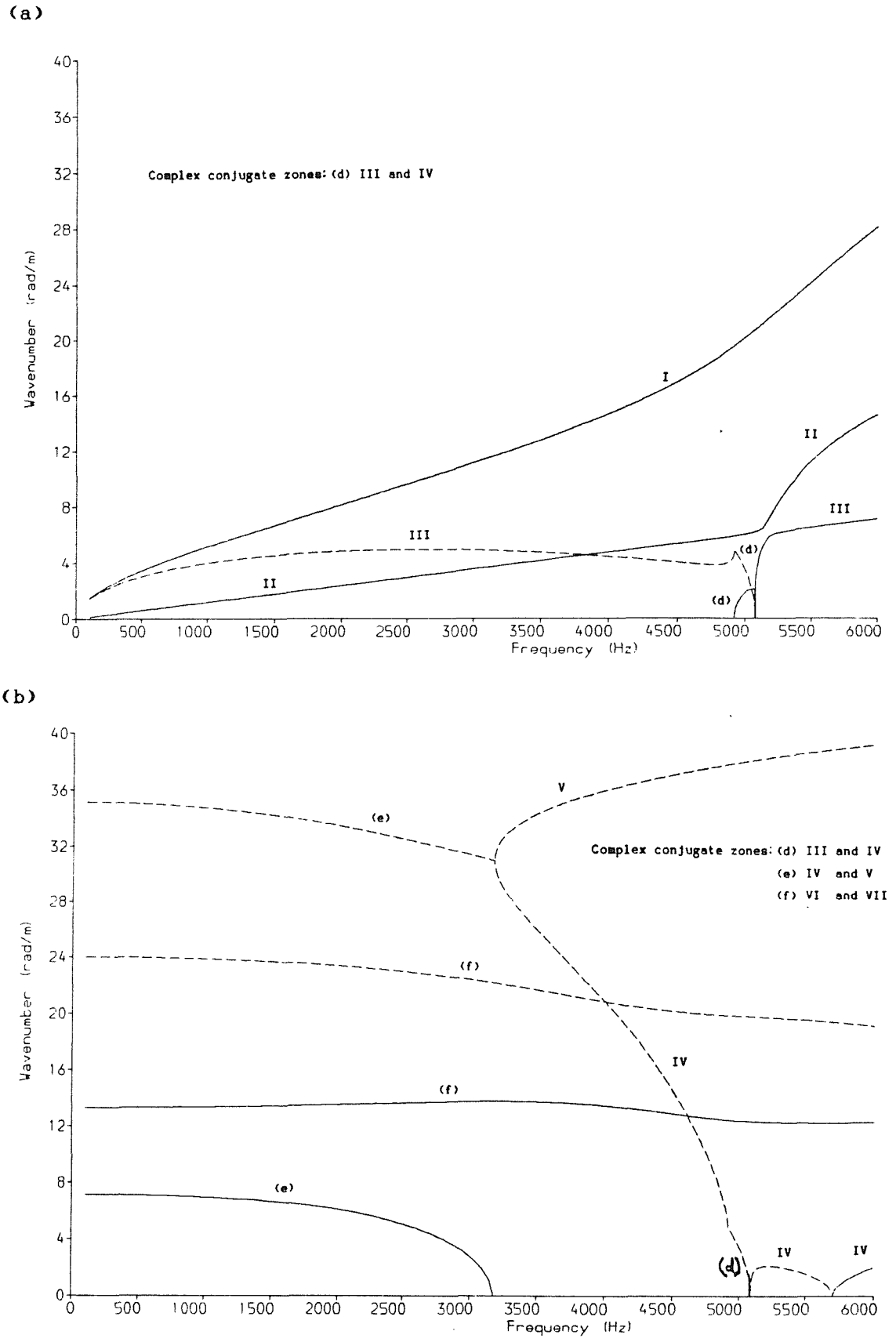

Figure 65 Wavenumbers of Vertical/Longitudinal Waves from 10 mm Model of Free Rail (——— Real Part, – – – Imaginary Part)

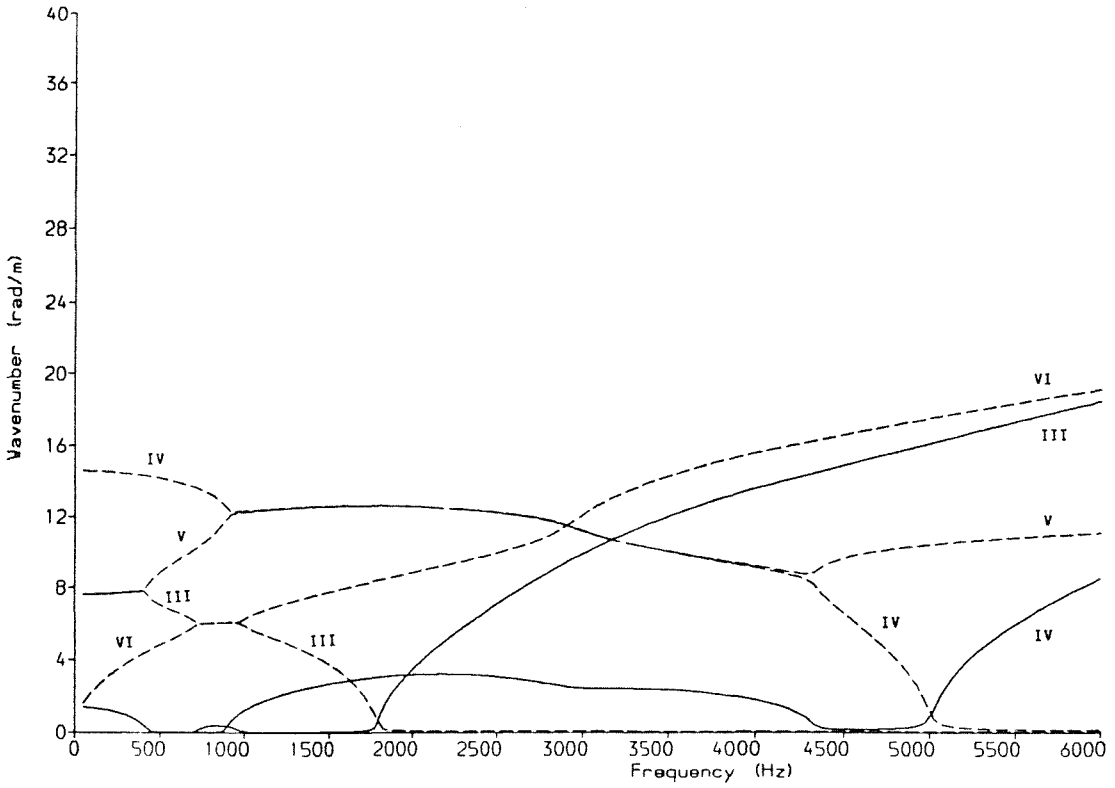

Figure 66 Wavenumbers of Lateral Waves of Free Rail (corresponding to Figure 63b) with Damping Loss Factor η=0.01
(——— Real Part, – – – Imaginary Part)

$$\Delta = 20 \log_{10} (e^{k_I}) = 8.686\ k_I \qquad \ldots(77)$$

where k_I is the imaginary part of the wavenumber. This is presented in Figure 67a for the various lateral waves. The 'cut-on' of the W and D waves (III and IV) can be clearly seen here, as, in each case, Δ is very high below the 'cut-on' frequency. Also a general increase can be seen in the decay as the frequency increases. This is due to the reduction of the wavelengths as frequency increases, η being closely related to the decay per wavelength. If λ is the wavelength, the decay per wavelength is given by

$$\Delta\lambda = 8.686\ k_I \frac{2\pi}{k_R} = 54.6 \frac{k_I}{k_R} \qquad \ldots(78)$$

(a) Decay Rate dB/m

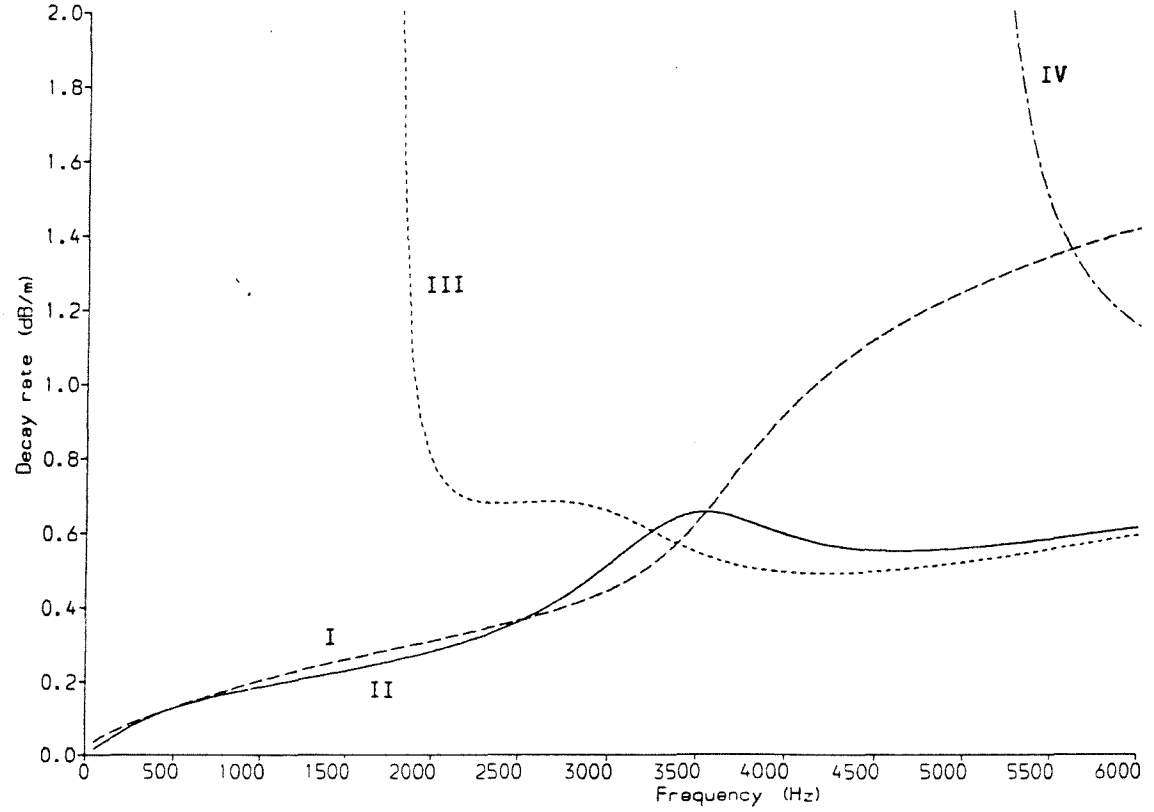

(b) Imaginary Part/Real Part of Wavenumber

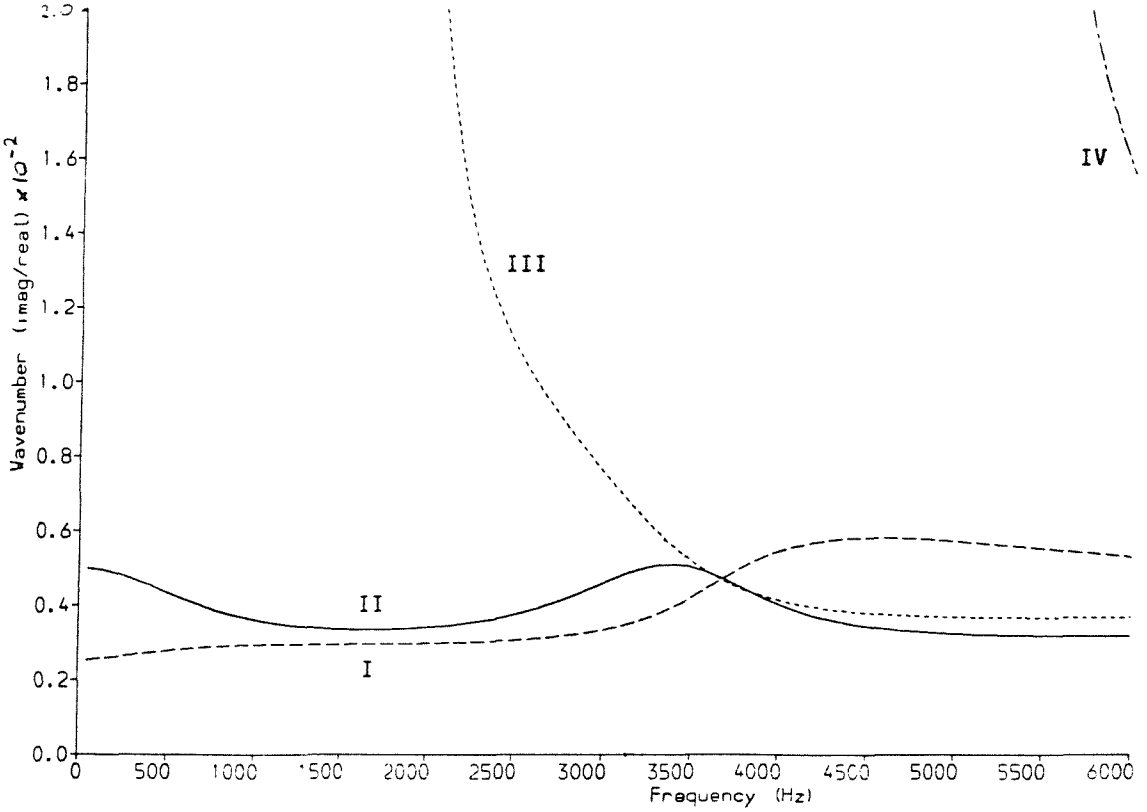

Figure 67 Decay Rates of Lateral Waves of Free Rail for Damping Loss Factor η=0.01

(a) Decay Rate dB/m

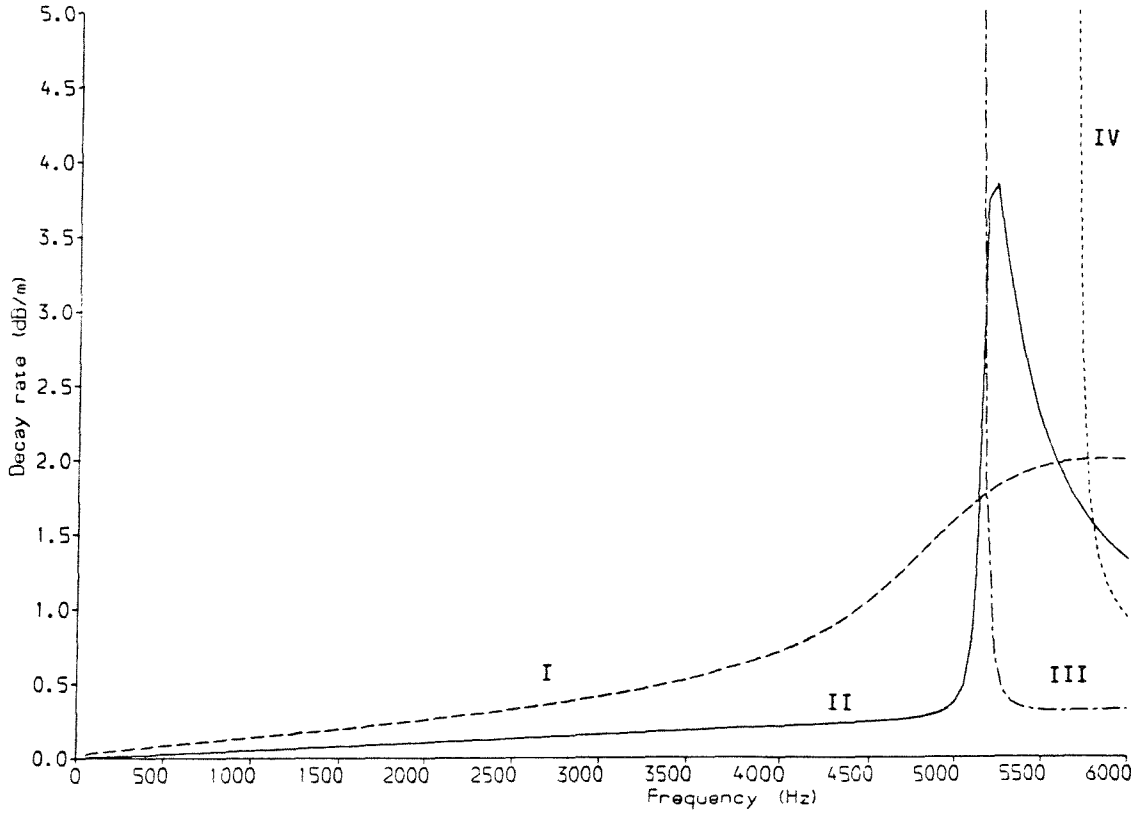

(b) Imaginary Part/Real Part of Wavenumber

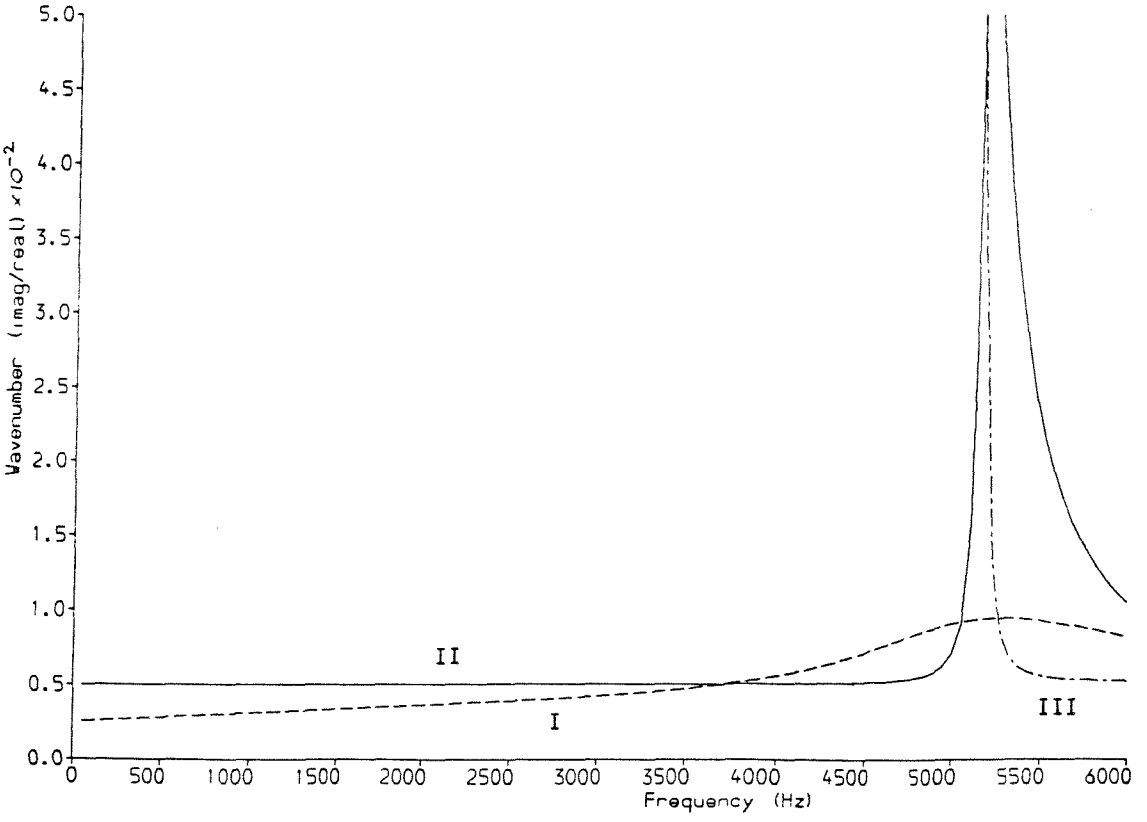

Figure 68 Decay Rates of Vertical/Longitudinal Waves of Free Rail for Damping Loss Factor η=0.01

where k_R is the real part of the wavenumber. This ratio of the imaginary part to the real part of the wavenumbers (k_I/k_R) is shown in Figure 67b for the above results. For a pure bending wave this ratio should be $\eta/4$ (see Appendix D), whereas for a pure torsional wave it should be $\eta/2$. The L and T waves tend to these limits as the frequency tends to zero, but vary significantly from them at higher frequencies, as the nature of the various waves alters. At the higher frequencies the T wave appears most like lateral bending (see Figure 58) and this corresponds to it having the lowest value of k_I/k_R.

The equivalent results for the vertical and longitudinal waves are shown in Figure 68. At low frequencies, the V wave has $k_I/k_R \sim \eta/4$, as expected for a bending wave, whereas the G wave has $k_I/k_R \sim \eta/2$, as expected for a longitudinal wave. The 'cut-on' of the F and A waves can be seen above 5000 Hz.

Figures 69-73 show the cross-sectional deformed shapes corresponding to the real parts of the eigenvectors for the first few propagating waves, in the absence of damping. The results are shown at selected frequencies, which are the nominal one-third octave centre frequencies, between 100 Hz and 5000 Hz. Changes can be seen in these

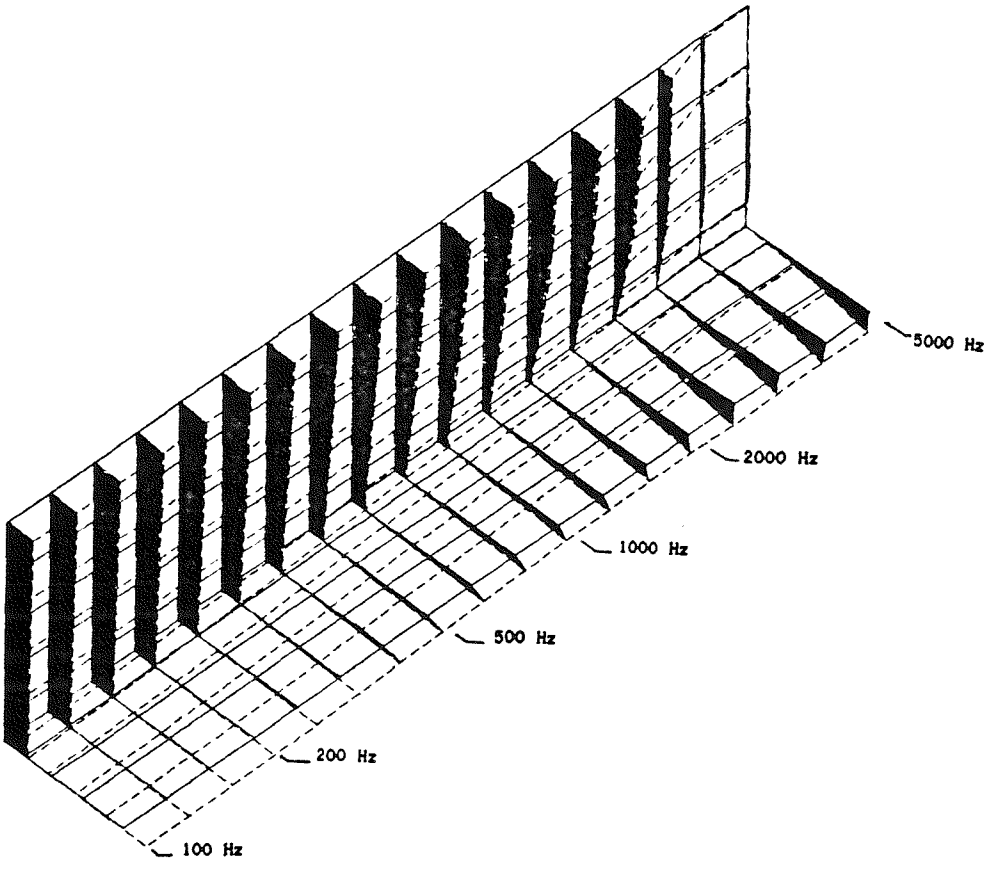

Figure 69 Displaced Shape (Real Part) of First Lateral Wave of Free Rail at 1/3 Octave Band Centre Frequencies

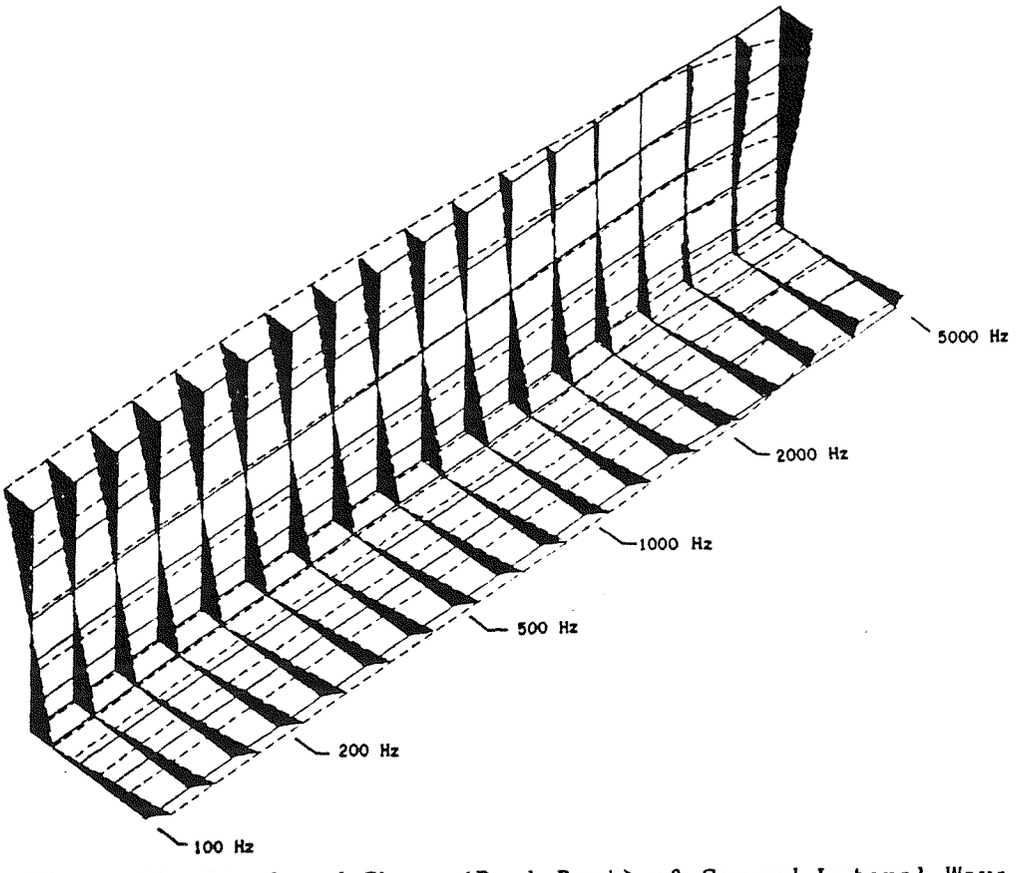

Figure 70 Displaced Shape (Real Part) of Second Lateral Wave of Free Rail at 1/3 Octave Band Centre Frequencies

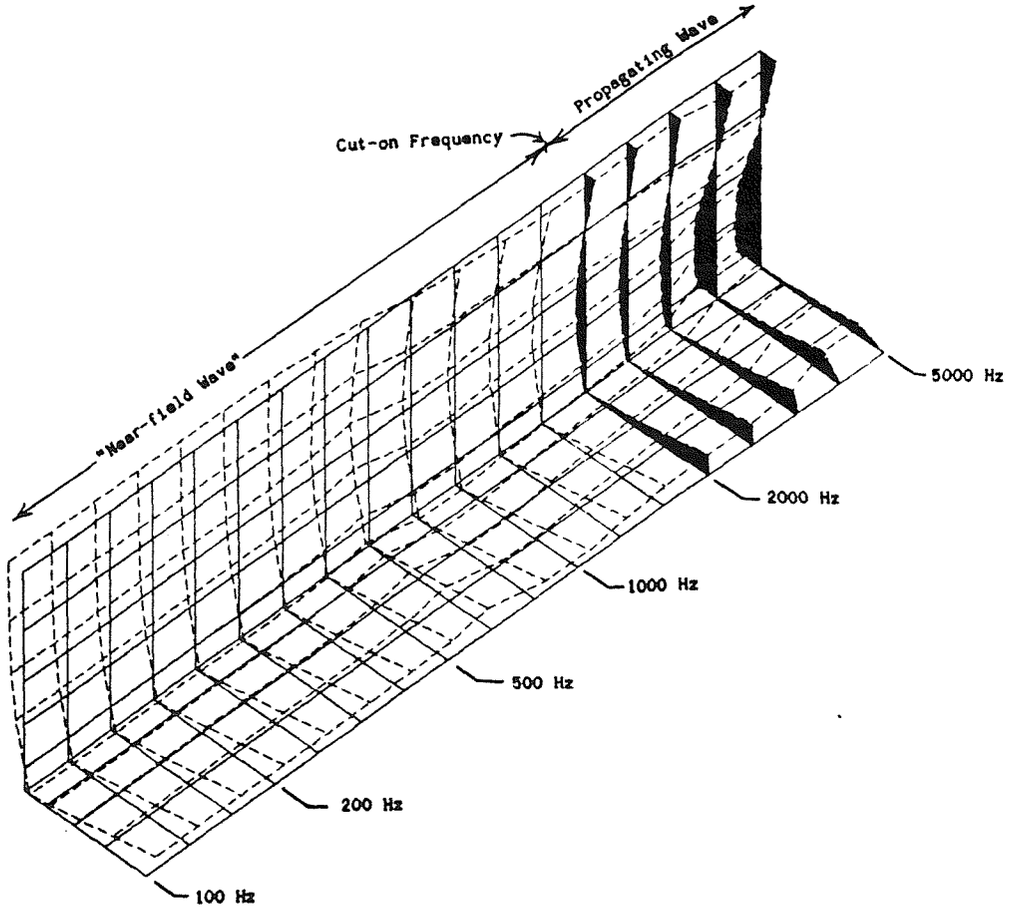

Figure 71 Displaced Shape (Real Part) of Third Lateral Wave of Free Rail at 1/3 Octave Band Centre Frequencies

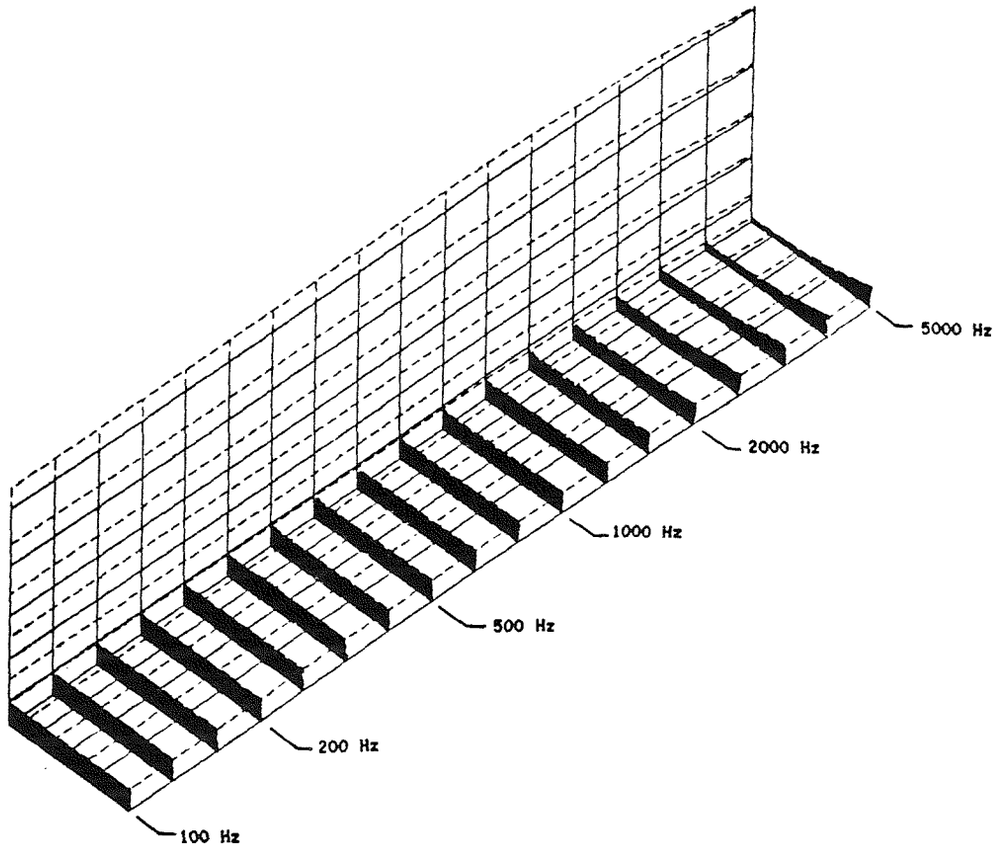

Figure 72 Displaced Shape (Real Part) of First Vertical Wave of Free Rail at 1/3 Octave Band Centre Frequencies

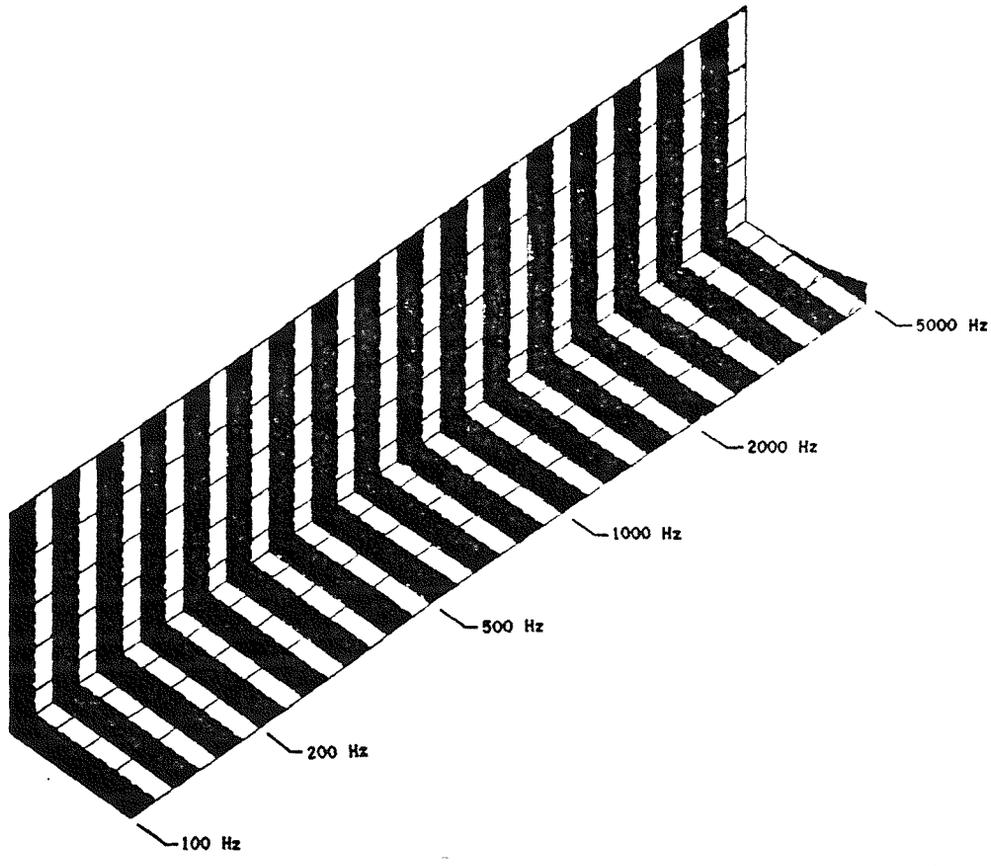

Figure 73 Displaced Shape (Real Part) of First Longitudinal Wave of Free Rail at 1/3 Octave Band Centre Frequencies

shapes as frequency increases, due to coupling of the various motions. The results correspond closely to those given in Figures 58 and 60 from the direct finite element model, although the latter are spaced according to constant increments in wavenumber, rather than by frequency.

In Figure 73, a change can be seen in the longitudinal wave at around 5000 Hz due to coupling with the foot-flapping wave. This change appears abrupt, and appears to occur slightly below the 'cut-on' frequency of the foot-flapping wave. However the figure shows only the real parts of the waveshapes, not the imaginary parts. These are significant in this region due to the coupling, since the longitudinal and vertical motions occur 90° out of phase with each other.

5.4.2 Receptances for Free Rail

Figure 74 shows the lateral receptance at the top of the rail head, for zero damping. Since this is not a node point on the structure, it was estimated by calculating first the receptances at the nearest node point (the bottom of the head): denoting these by α_{LL} for the lateral receptance, α_{TT} for the torsional receptance, α_{LT} for the lateral/torsional cross receptance, and the distance from this node point to the top of the head (40 mm) by a, the receptance at the top of the head α_{HH}, is given by

$$\alpha_{HH} = \alpha_{LL} + 2a\,\alpha_{LT} + a^2\,\alpha_{TT} \qquad \ldots(79)$$

assuming that the head moves rigidly, which is valid as a first-order approximation (at least within the frequency range of interest).

This result is compared with predictions from the simple Euler-Bernoulli beam, from Appendix D and also shown in Figure 61. The latter was used in §3 to represent the rail. It should also be noted that the phase is always greater than -135°, a consequence of the addition of torsion to the lateral bending. (In §3 -90° was used as it is closer to experimental results).

Two resonance peaks can be observed in Figure 74, which correspond to the 'cut-on' frequencies of the W and D waves. These are analogous to the resonance peak which may be observed for a beam on elastic foundation at the foundation-bounce frequency (see Appendix D). At 'cut-on' the wavenumber is zero, which means that the rail moves in phase along its length. Due to the absence of damping, the receptances

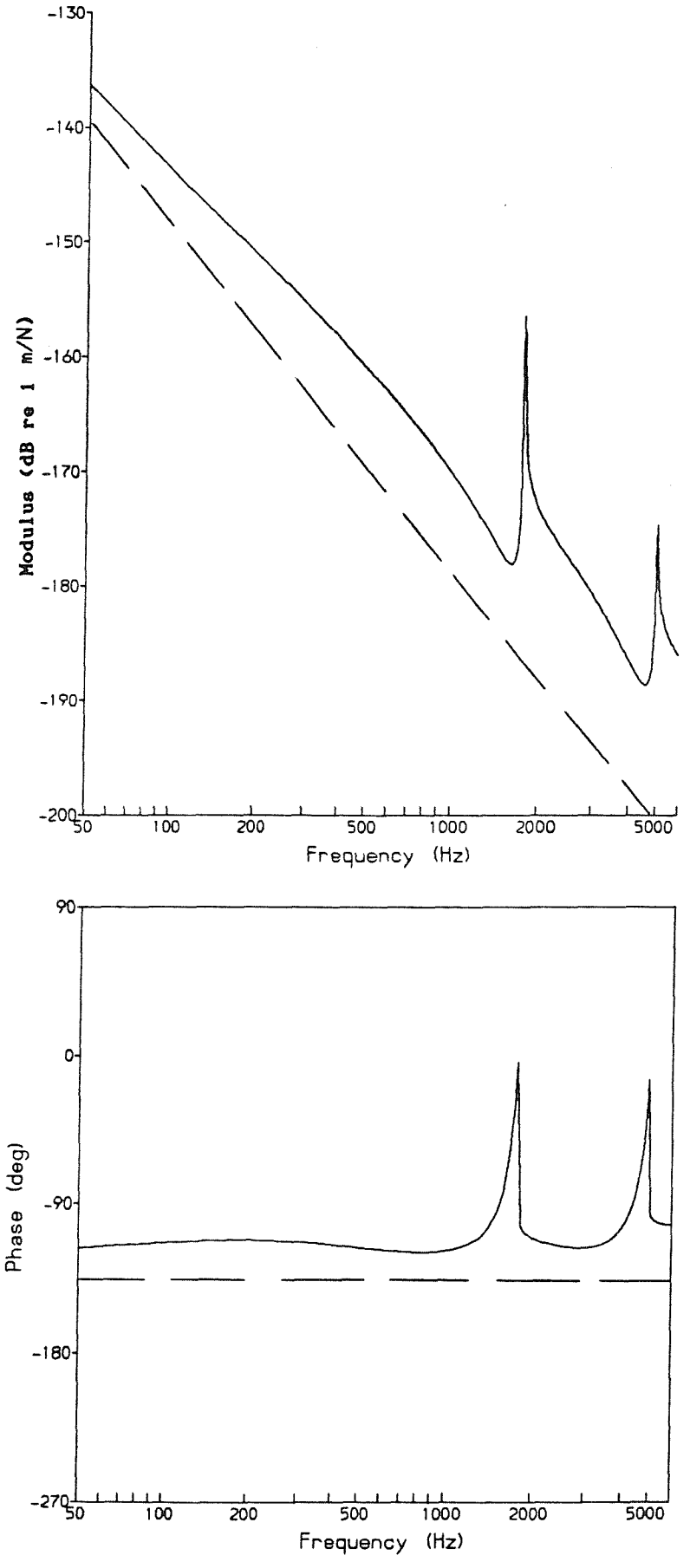

Figure 74 Lateral Receptance of Free Rail (——— from Periodic Structure Theory, — — from Simple Beam Theory (Figure 61))

tend to infinity at these cut-on frequencies, although by avoiding these frequencies in the calculation, the peaks have been truncated.

Figure 75 shows the vertical receptance, for zero damping, which is again compared with the Euler-Bernoulli beam result from Figure 61 (as used in §3). No correction is required here to represent the receptance at the top of the rail head, apart from any effect of the compression of the head, which may be ignored in the frequency range under consideration. The difference between the current prediction and the simple theory is smaller in this case, major differences being restricted to high frequencies.

Figure 76 shows the corresponding longitudinal receptance, with the equivalent simple beam result from Figure 61. The longitudinal receptance contains the same correction as the lateral receptance (equation (79)), but with a=-40 mm to take account of the sign convention.

In both of these figures, resonance peaks can be observed corresponding to the 'cut-on' of the F and A waves in the region 5-6 kHz. As for the lateral motion, the receptance of the undamped rail is infinite at these frequencies, but the peaks are truncated by avoiding these frequencies in the calculation.

Transfer receptances can also be calculated to predict the response at various distances along the rail. Figure 77a shows the magnitude of the rail head lateral response at 0, 2.4 and 4.8 m from the force, for a damping of η=.01 (actually in the form of mobilities to accommodate the curves more easily). Zones of lower response can be observed, notably at around 50 Hz at 2.4 m and at 400 Hz at 4.8 m. These occur because the lateral force excites two waves, types L and T (more at higher frequencies), which have different wavespeeds (see Figure 62). Thus at particular combinations of distance and frequency, it is possible for them to cancel out on the head. This occurs when $(k_1-k_2)x=\pi, 3\pi, 5\pi...$ where k_1 and k_2 are the wavenumbers of the two waves, and x is the longitudinal distance. This effect is not influenced by the introduction of damping - the influence of the damping is limited to a small reduction of the higher frequency components, and the reduction of the resonance peaks at the cut-on frequencies.

Figure 77b shows the corresponding results for the lateral response of the foot. Here the two waves (L and T) are out of phase at the excitation point, giving a much lower response than on the head,

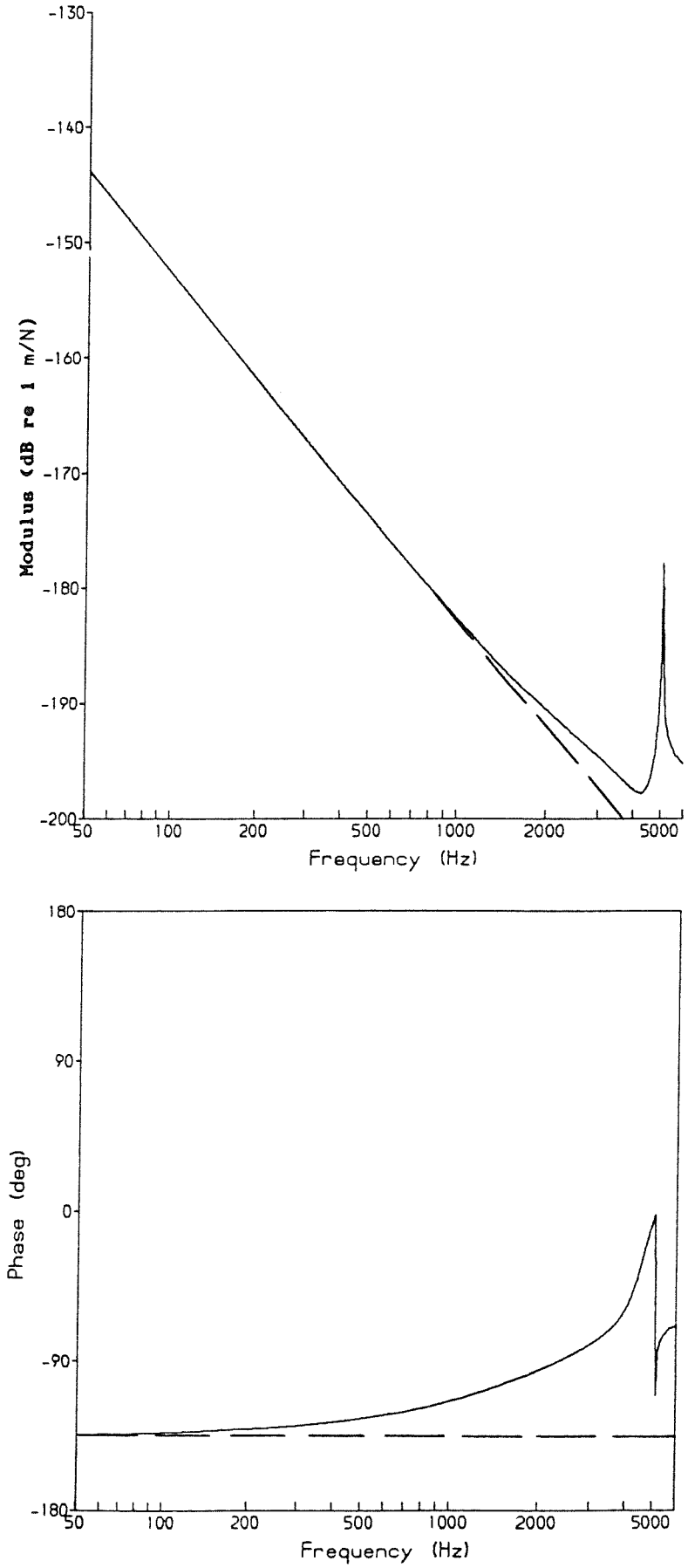

Figure 75 Vertical Receptance of Free Rail (——— from Periodic Structure Theory, — — from Simple Beam Theory (Figure 61))

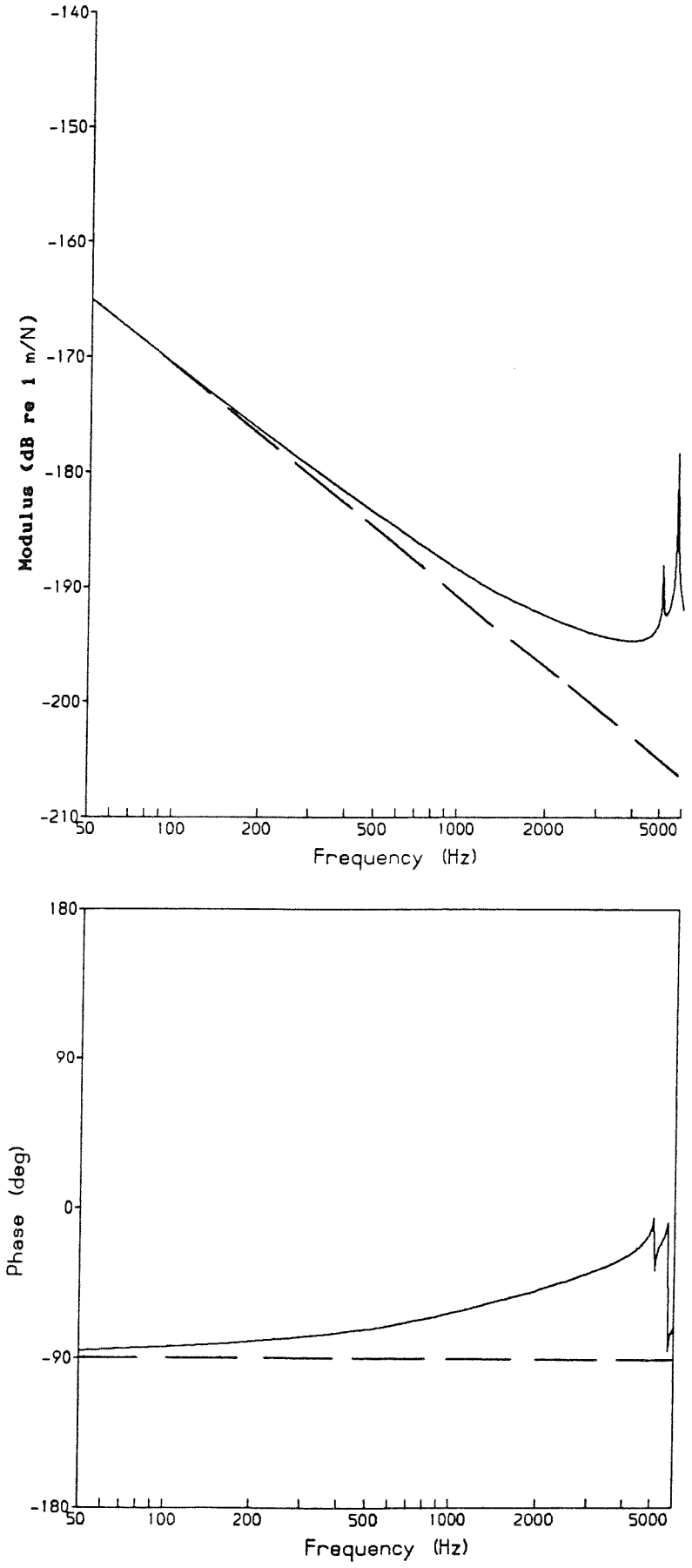

Figure 76 Longitudinal Receptance of Free Rail (——— from Periodic Structure Theory, — — from Simple Beam Theory (Figure 61))

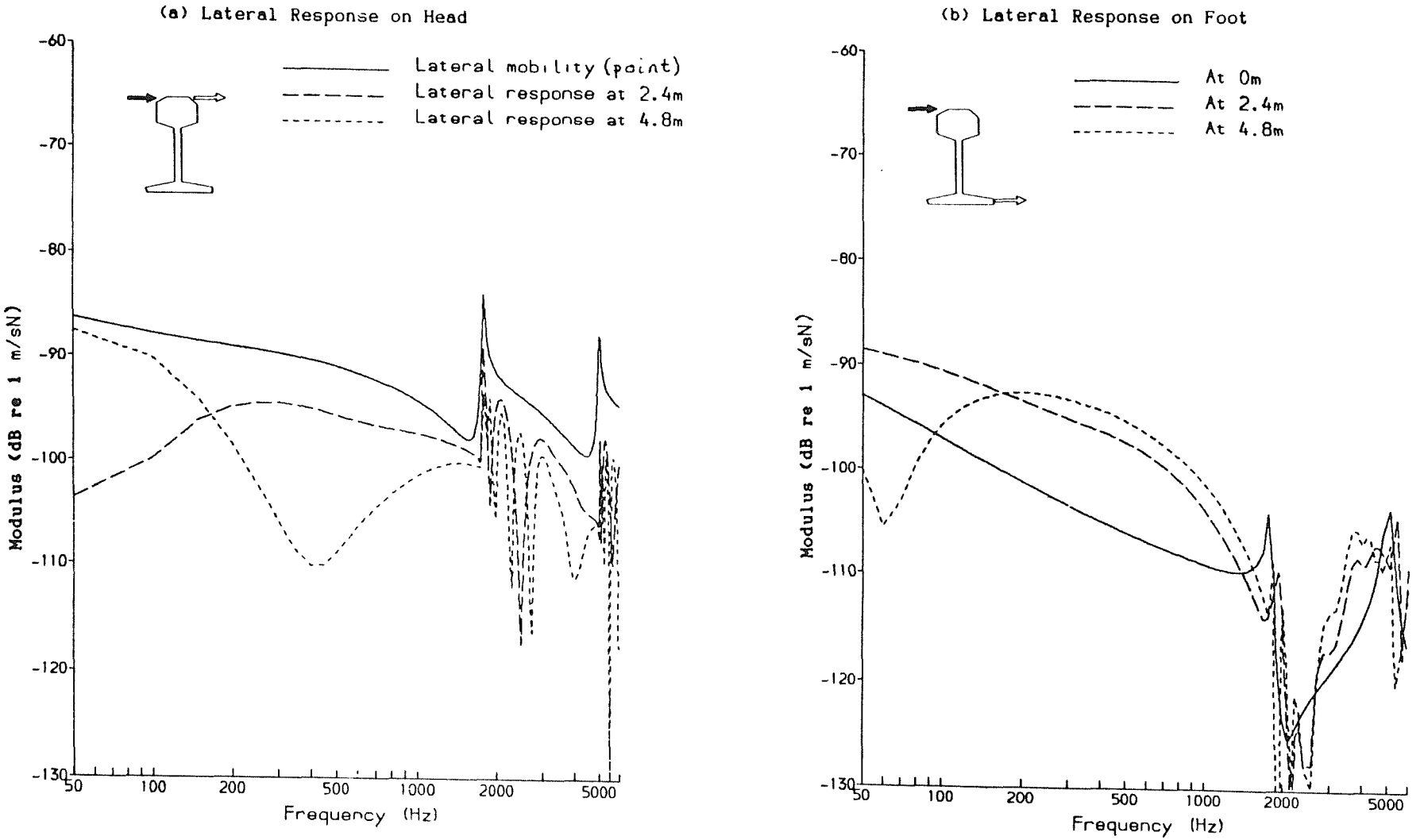

Figure 77 Transfer Mobilities: Response to Lateral Force Applied to Head for Free Rail

but at 2.4 and 4.8 m the foot response has a maximum at those frequencies at which cancellation occurred on the head.

Although this effect is due to interference of two wave types, in the rail response due to a moving train, it would appear like a 'standing' wave pattern moving with the train.

No such interference occurs for the vertical motion of the head, as can be seen in Figure 78a, as only one wave (V) is excited by a force in this direction below 5 kHz. However for frequencies above about 1 kHz, the vertical response of the foot is progressively greater than that of the head, as shown in Figure 78b. This results from the dominance of motion of the foot in the displaced shape of the V wave at these higher frequencies (see Figures 60 and 72).

5.4.3 Inclusion of Supports - Results for Lateral Motion

Including the supports, Figure 79 shows the lateral receptance at the rail head, which is compared with the previous results from Figure 74. As before this includes the effect of the distance between the rail head and the structural node point (see equation (79)). The main effect of the inclusion of the sub-layers is at low frequencies, where the receptance is reduced and the phase is significantly altered.

Three well-damped resonances can be seen, at around 80 Hz, 150 Hz and 350 Hz. At 80 Hz the whole track bounces on the lateral stiffness of the ballast, whereas at 150 Hz the rail vibrates laterally on the stiffness of the pad. This can be identified as the 'cut-on' of the lateral bending waves. The 350 Hz peak can similarly be identified as the cut-on of the torsional waves. These cut-on peaks are well damped due to the influence of the high loss factor of the pad. The web bending (W) wave cut-on peak (at 1800 Hz) appears to have been damped appreciably compared with the free rail case, but for the D wave (5000 Hz) its effect is much smaller.

In Figure 80 the effect of distance is shown for the rail head and foot vibration, which may be compared with Figure 77 for the free rail. There is a much greater decay with distance at low frequencies, below the wave cut-on. At higher frequencies the effects noted previously are repeated. Once more the foot response at the excitation point is consistently lower than the head response, but at some distance/frequency combinations it is greater.

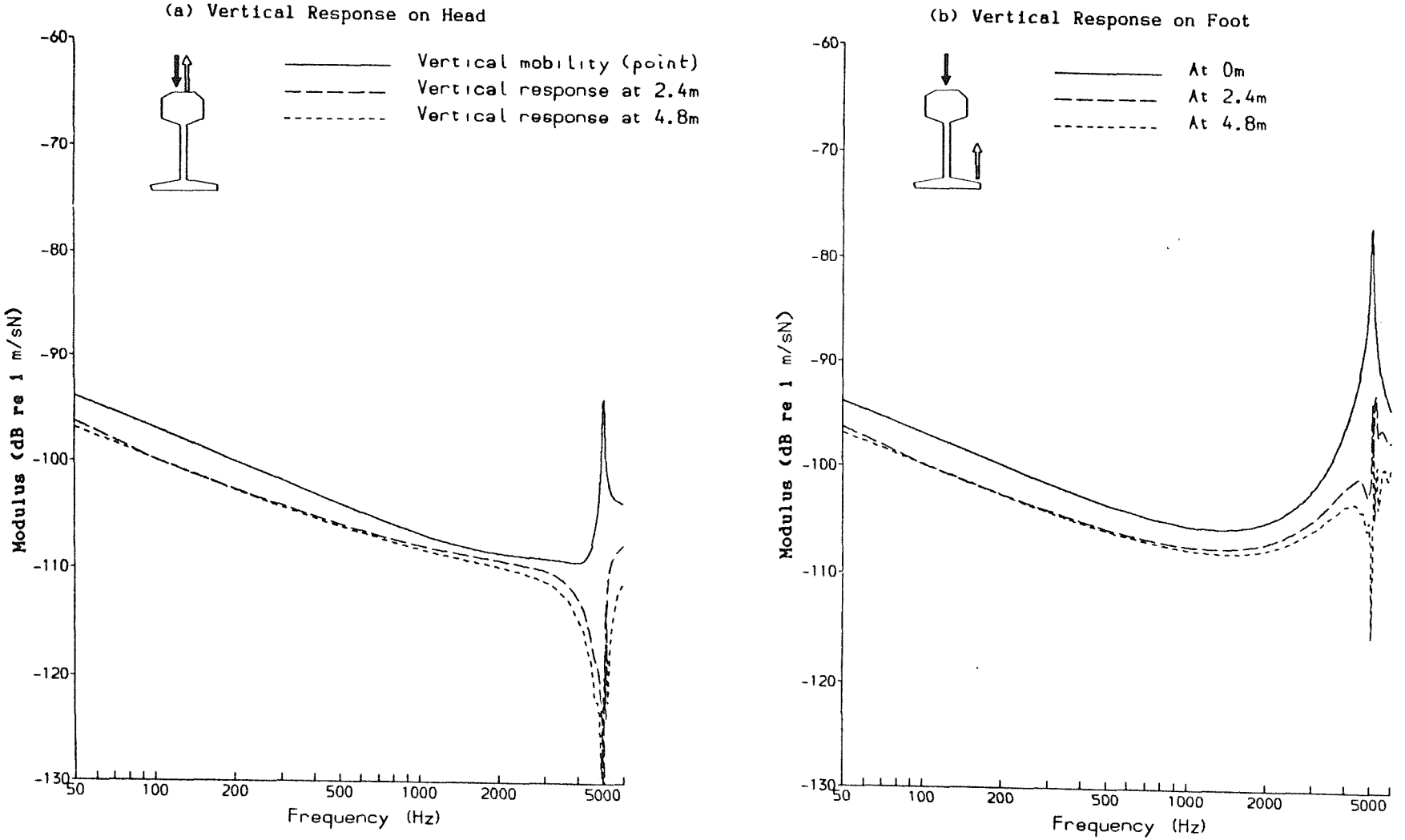

Figure 78 Transfer Mobilities: Response to Vertical Force Applied to Head for Free Rail

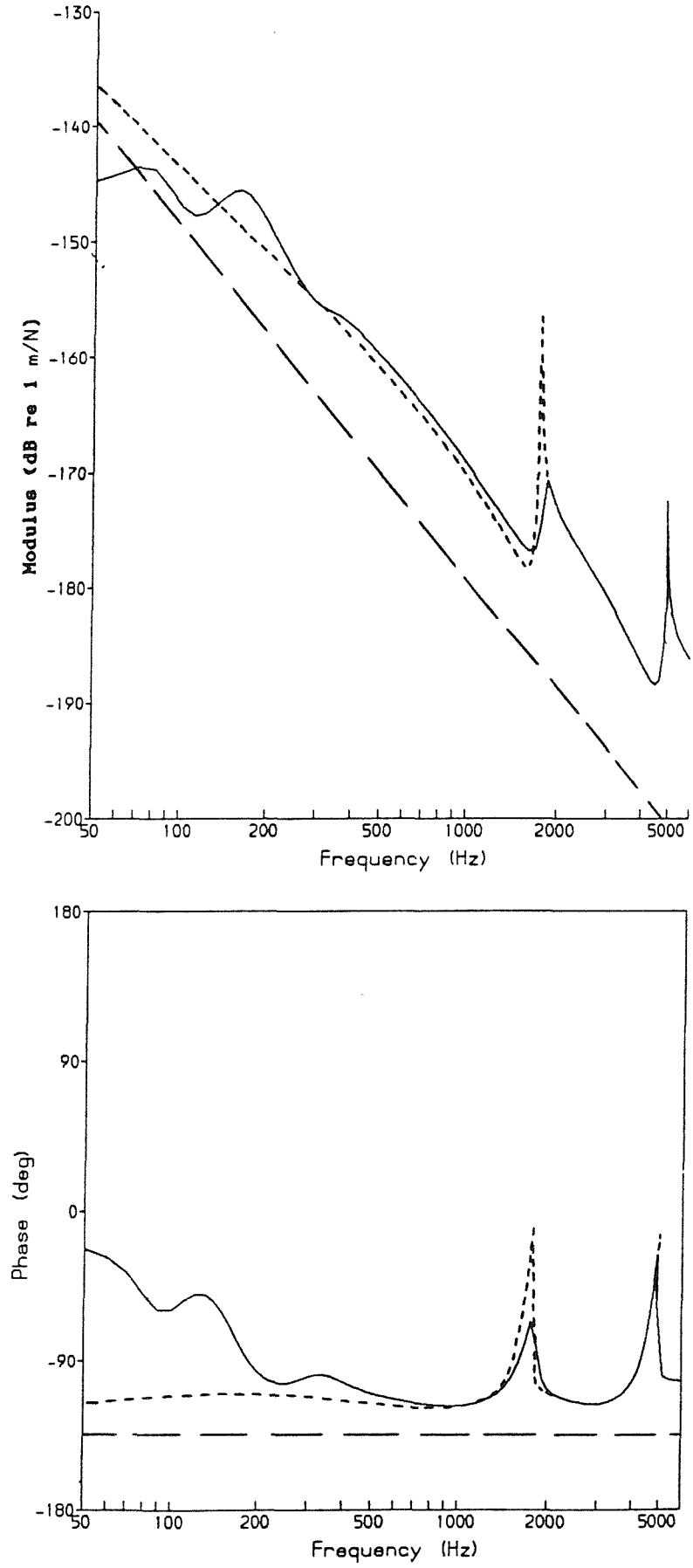

Figure 79 Lateral Rail Head Receptance (——— Supported Rail, ····· Free Rail (Figure 74), — — from Simple Beam Theory (Figure 61))

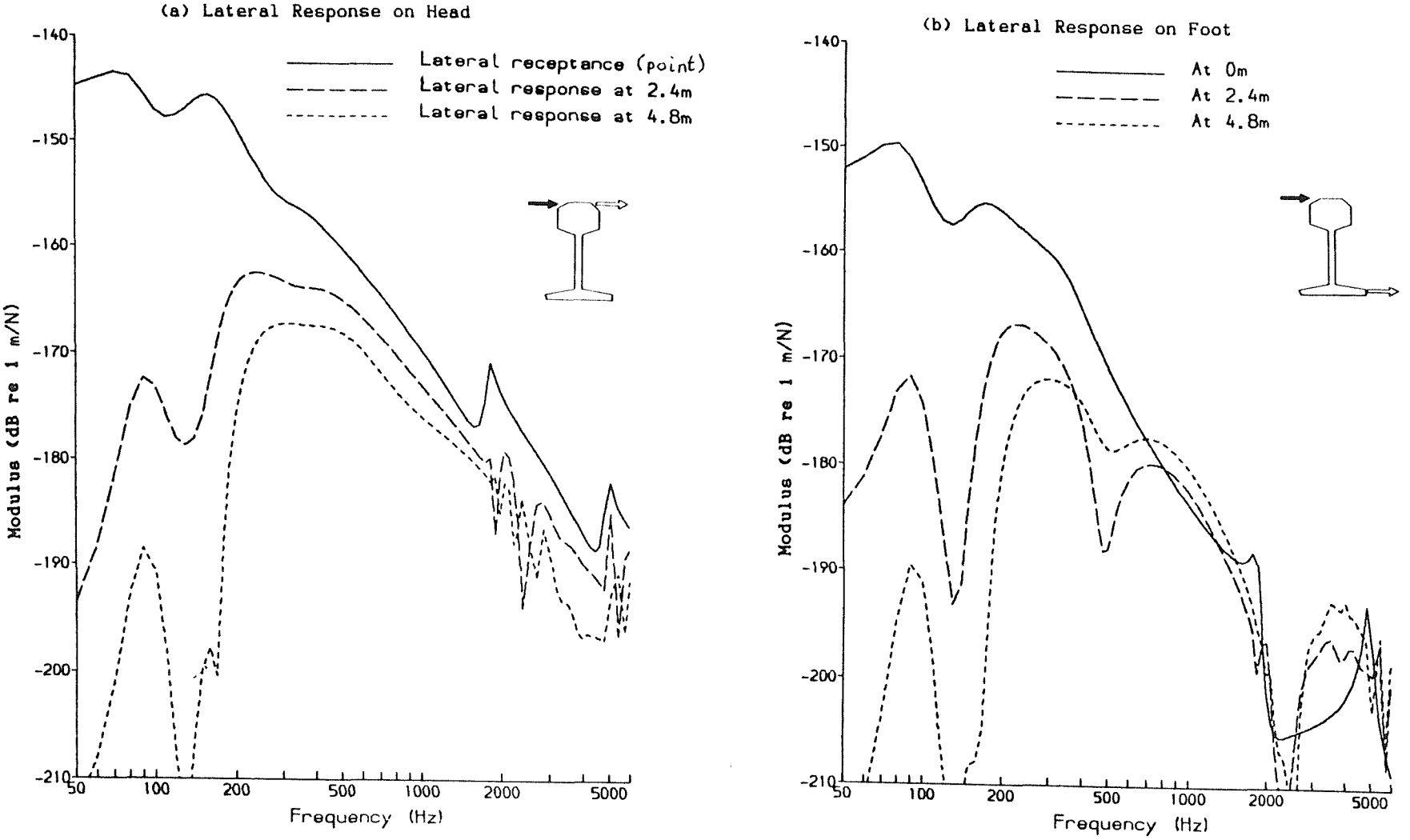

Figure 80 Transfer Receptances: Response to Lateral Force Applied to Head for Supported Rail

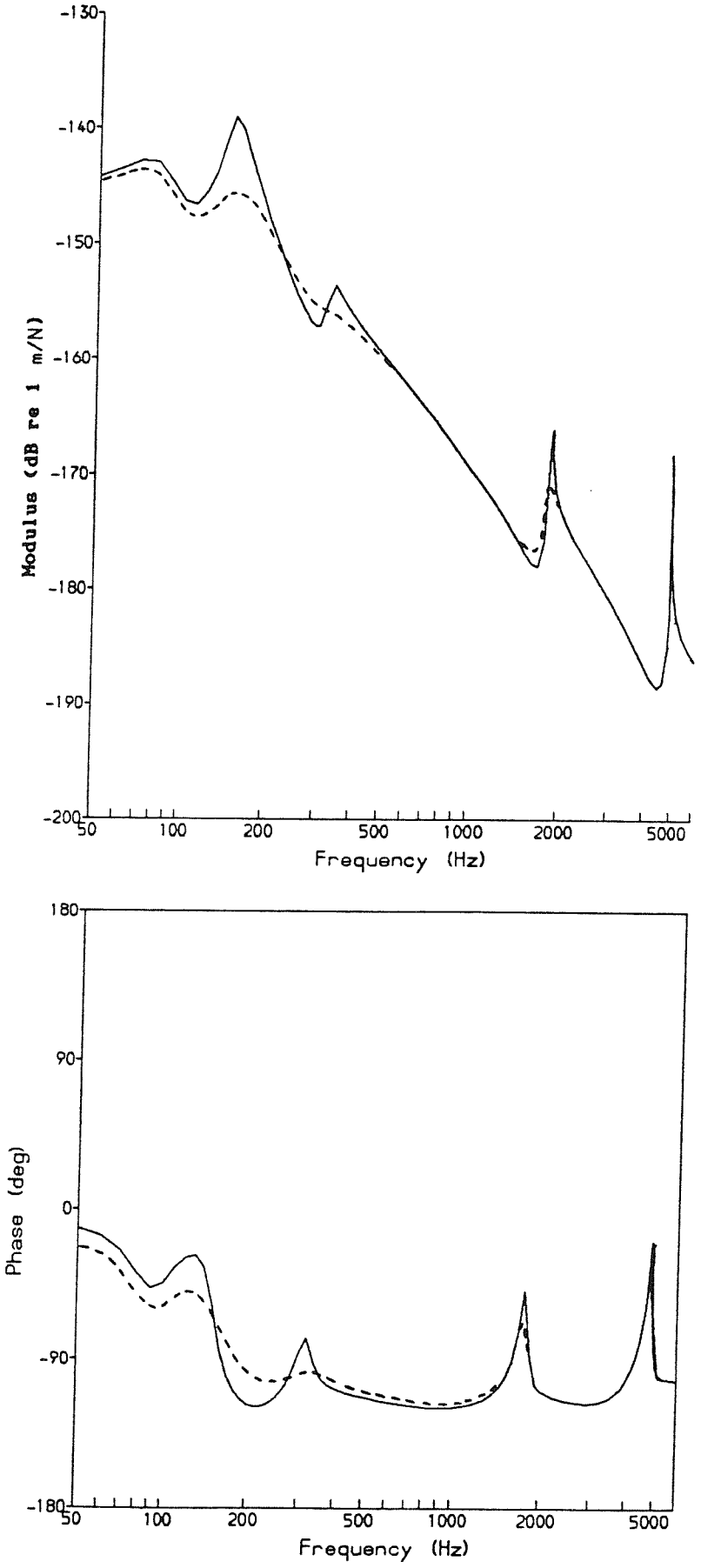

Figure 81 Effect of Pad Damping Loss Factor on Lateral Receptance
(——— η=0.1, — — η=0.5 (Figure 79))

In Figure 81 results for a lower value of pad damping loss factor (0.1) are presented along with the results for η=0.5 from Figure 79. The peak at 80 Hz is little altered (consistent with the dominance of the ballast stiffness at this frequency), but those at 150 Hz, 350 Hz and 1800 Hz are much sharper for the lower loss factor (indicating the dominance of the pad).

The wavenumbers of the first few waves are presented in Figure 82. The main effects of the inclusion of the sub-layers, as with the receptances, are concentrated at low frequencies. Larger imaginary parts can be seen for the lateral and torsional waves below their respective cut-on frequencies. Figure 83 shows the decay with distance of the various waves (Δ in dB/m) and the ratio k_I/k_R, as in Figure 67. The high decay with distance at low frequencies is seen again here. At higher frequencies the decay rates are in the region 0.2 to 2 dB/m, which is much higher than the rail damping loss factor of 0.0005 would produce. Thus it can be seen that the pad damping introduces a significant decay with distance. This varies from one wave type to another, and with frequency, depending on the importance of motion of the rail foot in the various waves.

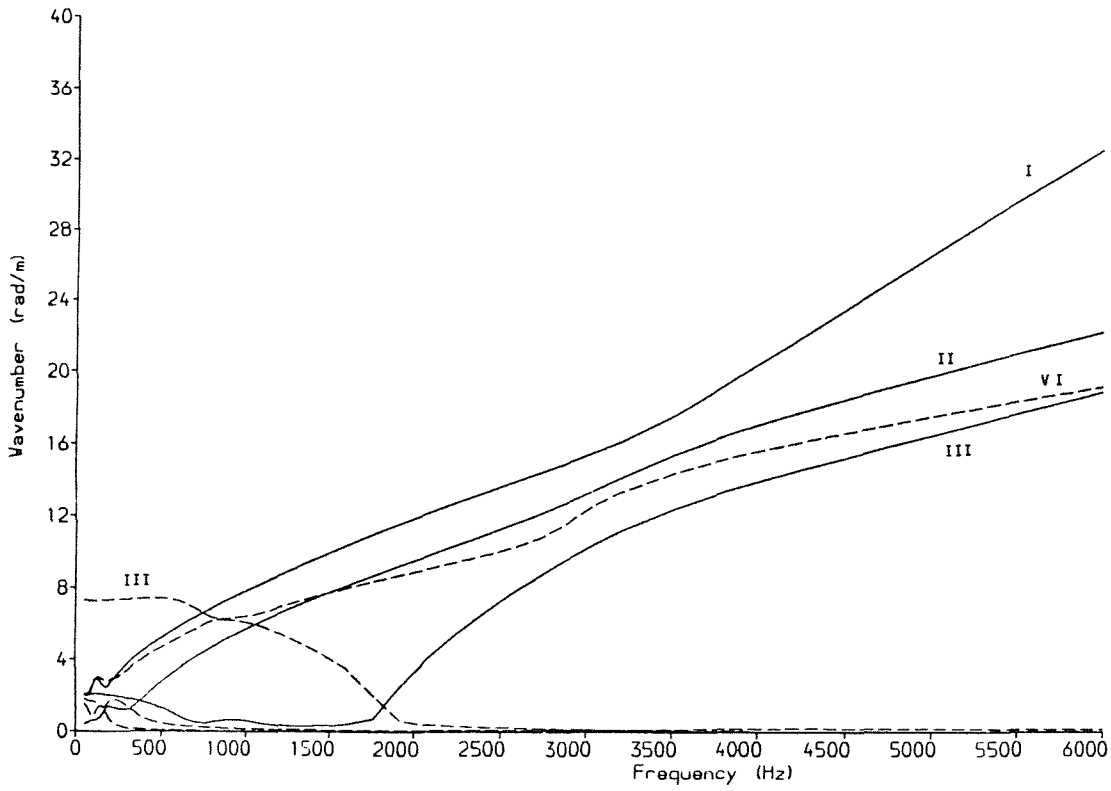

Figure 82 Wavenumbers of Lateral Waves for Supported Rail
(——— Real Part, — — Imaginary Part)

(a) Decay Rate dB/m

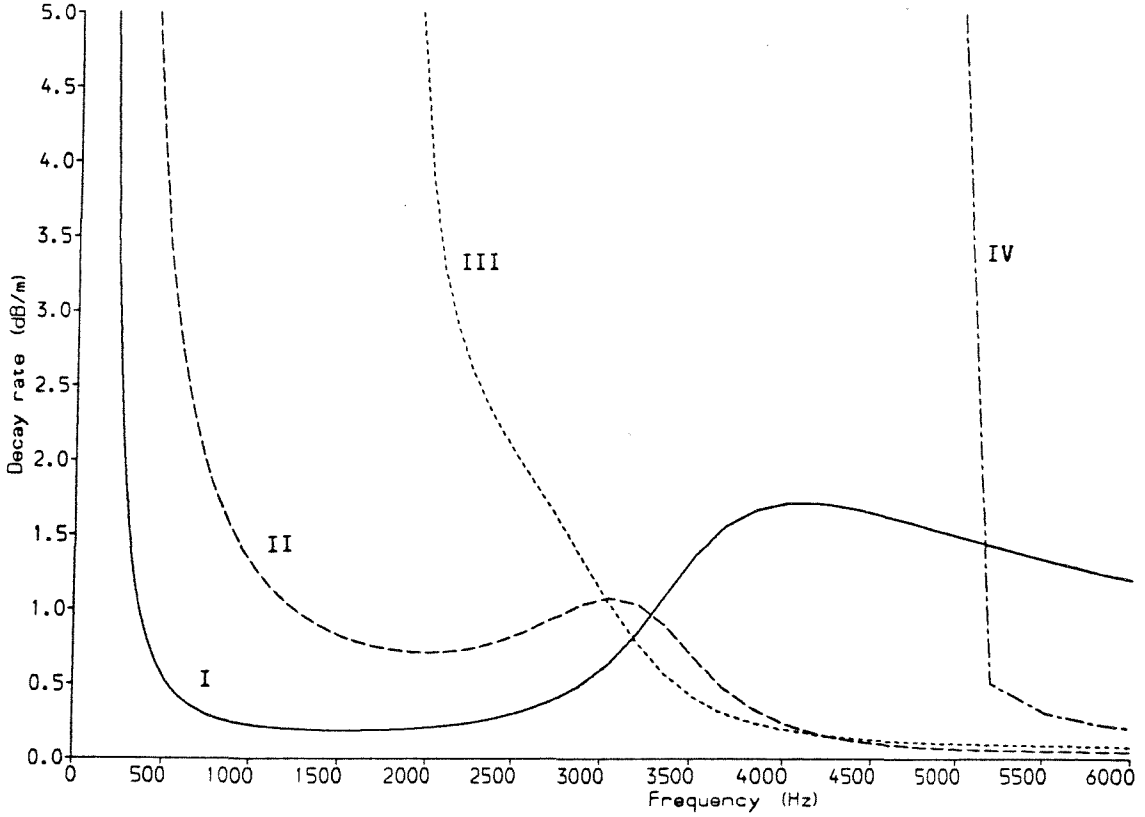

(b) Imaginary Part/Real Part of Wavenumber

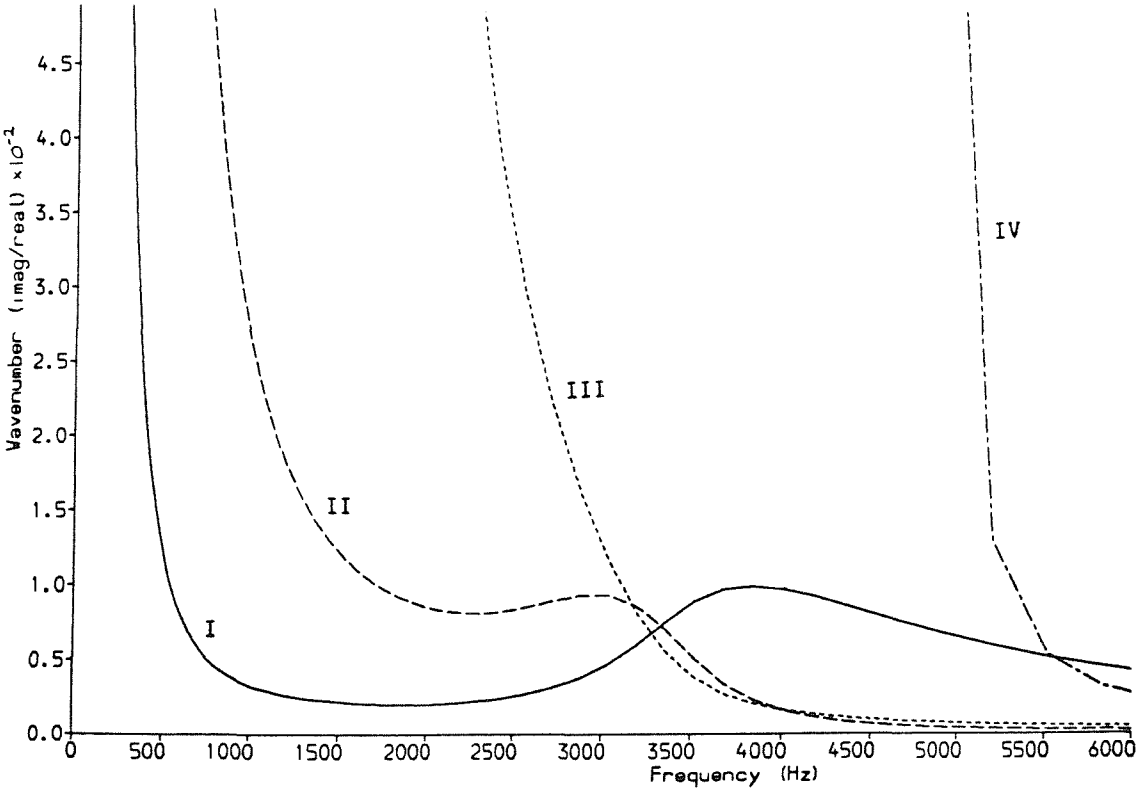

Figure 83 Decay Rates of Lateral Waves for Supported Rail

5.4.4 Inclusion of Supports - Results for Vertical/Longitudinal Motion

Figure 84 shows the vertical receptance, along with the previous results from Figure 75. Again the receptance is reduced relative to that of the free rail at low frequencies and the phase is significantly altered. This time two well damped resonances can be seen, at 80 Hz and 450 Hz. As for lateral motion, the first corresponds to a mode of the whole track on the stiffness of the ballast, whereas the second corresponds to the resonance of the rail on the pad stiffness, and hence to the 'cut-on' of vertical bending waves.

The effect of a lateral offset on the forcing (and response) point is illustrated in Figure 85. Denoting the receptances at the centre of the rail head by α_{VV} for the vertical receptance, and α_{TT} for the torsional receptance (the vertical/torsional cross receptance is zero), the receptance at a point offset by a distance b from the centre, $\alpha_{VV'}$, is given by (cf equation (79)):-

$$\alpha_{VV'} = \alpha_{VV} + b^2 \alpha_{TT} \qquad \ldots(80)$$

The result is that the receptance is raised, particularly at higher frequencies. Of the offsets used, 30 mm corresponds to excitation near the edge of the rail head, and 15 mm to a point midway between the centre and the edge.

The vertical/lateral cross receptance is zero at the centreline due to the symmetry of the rail (apart from the effect of the asymmetry of the sleepers). However by offsetting the position of the vertical force, as for Figure 85, a cross receptance is also introduced, given by $b\alpha_{LT}$, where α_{LT} is here the lateral/torsional cross receptance at the top of the head. The result is shown in Figure 86 for the same values of b as in Figure 85 above.

Figure 87 shows the longitudinal receptance along with the previous results. The amplitude is altered a little at low frequencies, with the phase also showing up some differences in behaviour. At high frequencies the higher of the two sharp peaks above 5000 Hz (the cut-on of the anti-longitudinal wave, A) is suppressed. It would seem that this wave, as well as being damped by the pad, has a higher cut-on frequency due to the additional influence of the stiffness of the pad. The F wave has also had its cut-on frequency raised slightly.

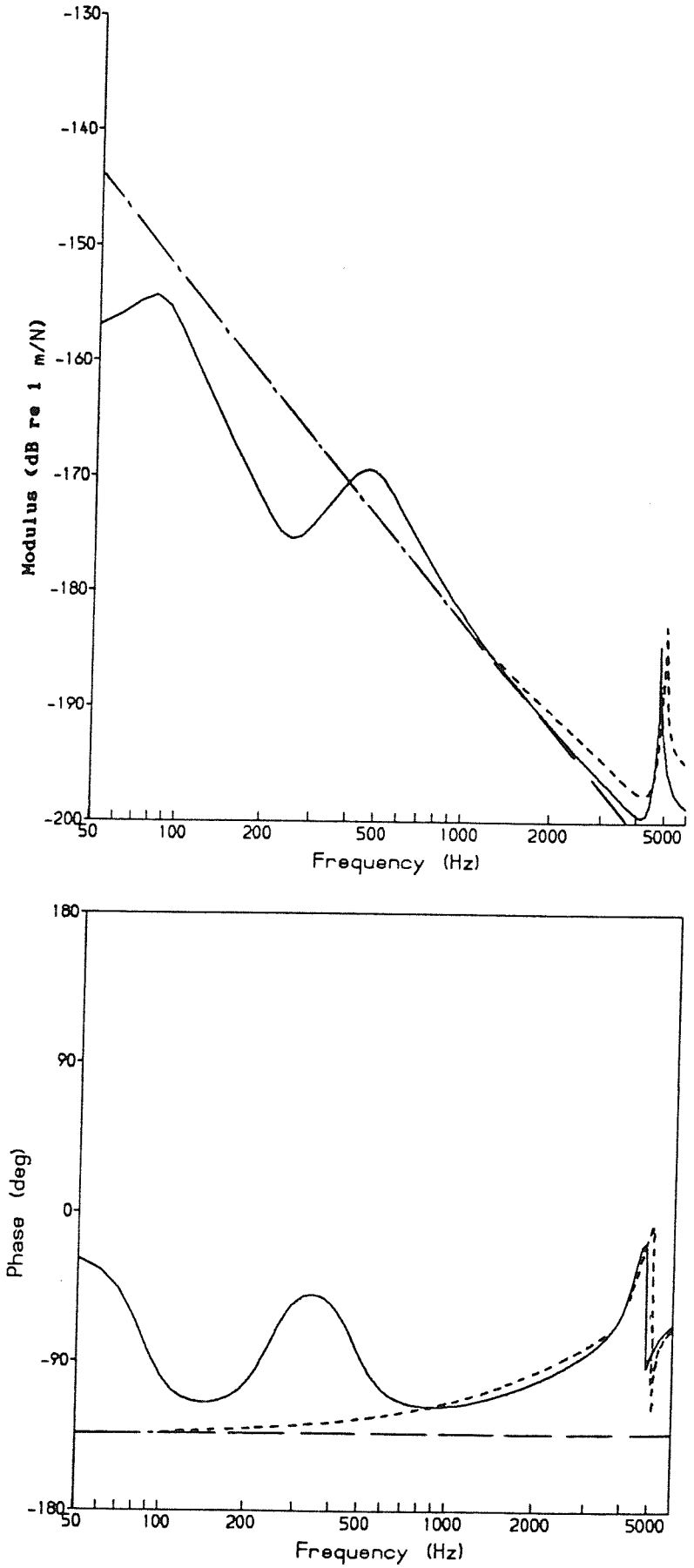

Figure 84 Vertical Rail Head Receptance (——— Supported Rail, ····· Free Rail (Figure 75), — — From Simple Beam Theory (Figure 61))

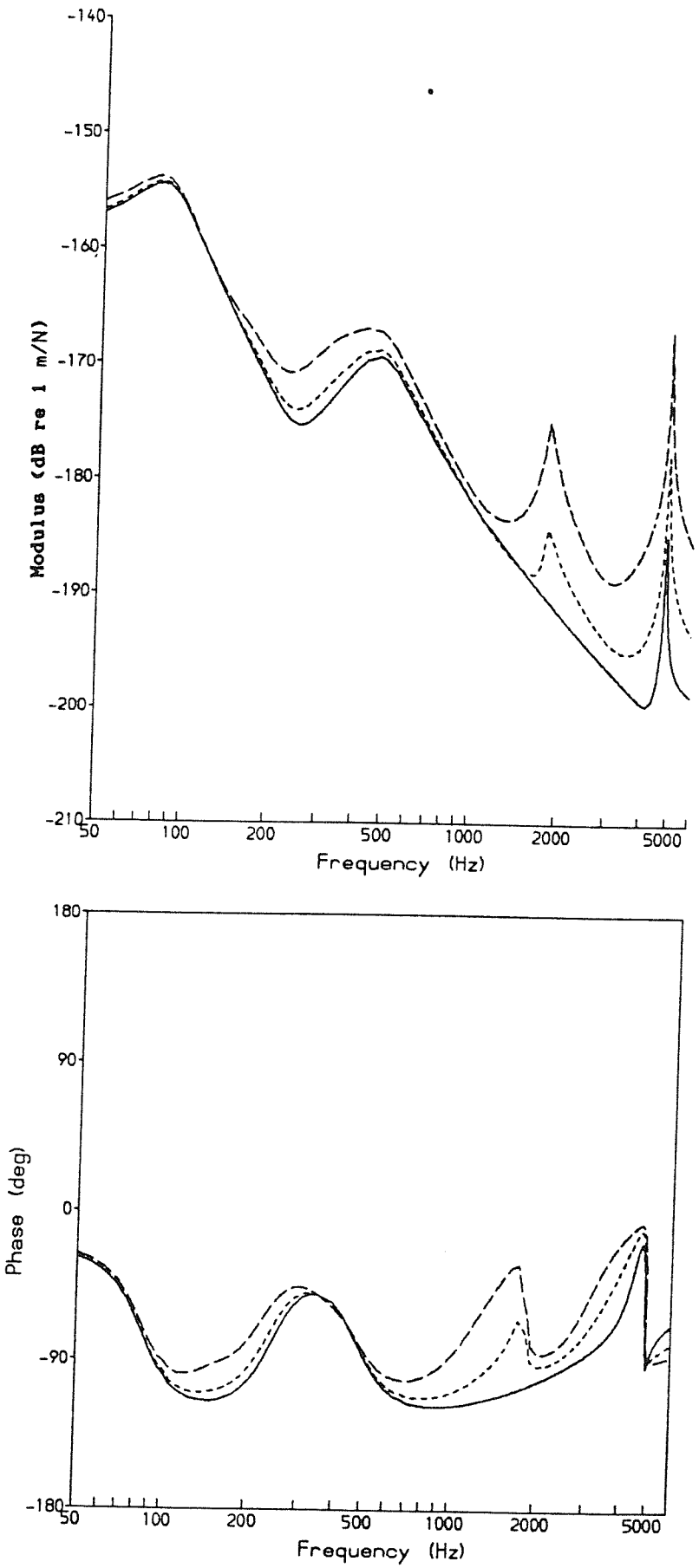

Figure 85 Effect of Lateral Position on Vertical Receptance
(——— No offset, ····· Offset = 15 mm, — — Offset = 30 mm)

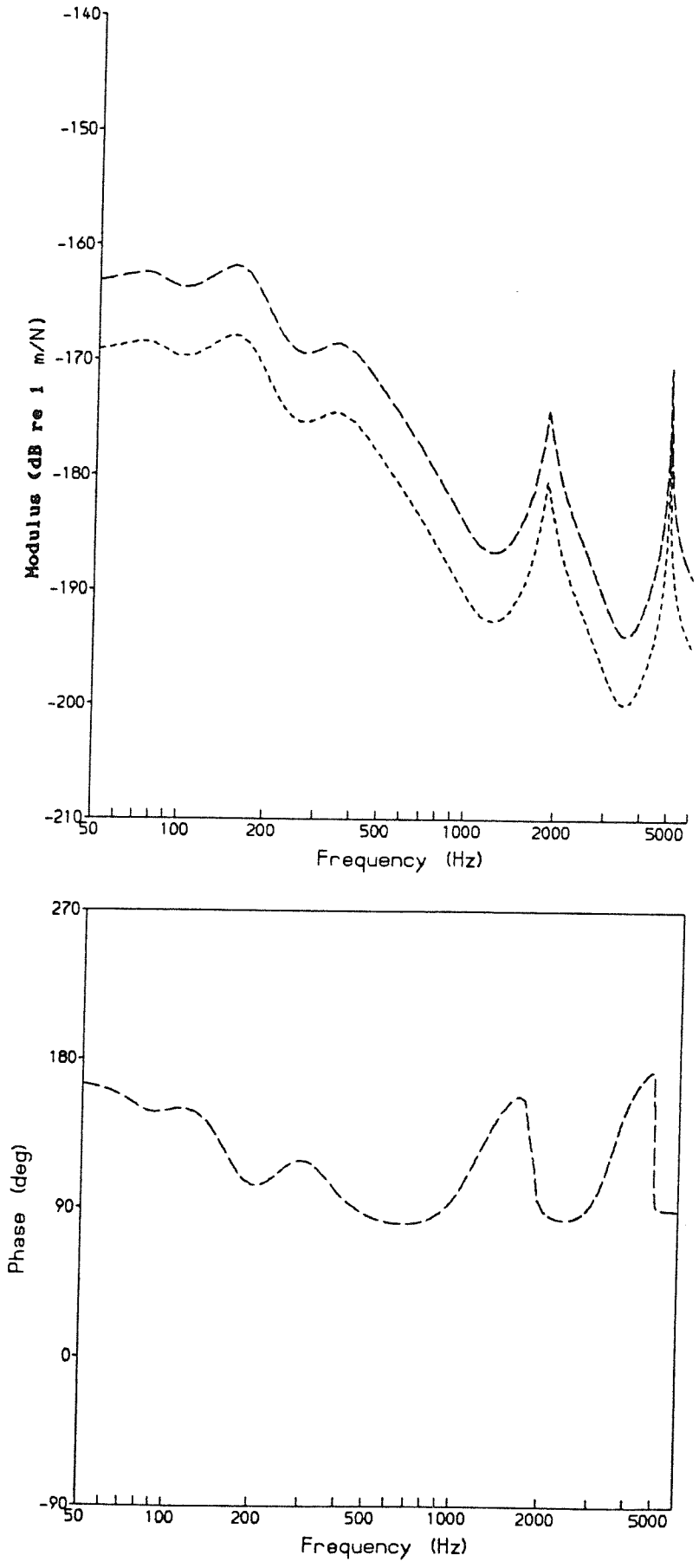

Figure 86 Effect of Lateral Position on Cross Receptance

(····· Offset = 15 mm, — — Offset = 30 mm)

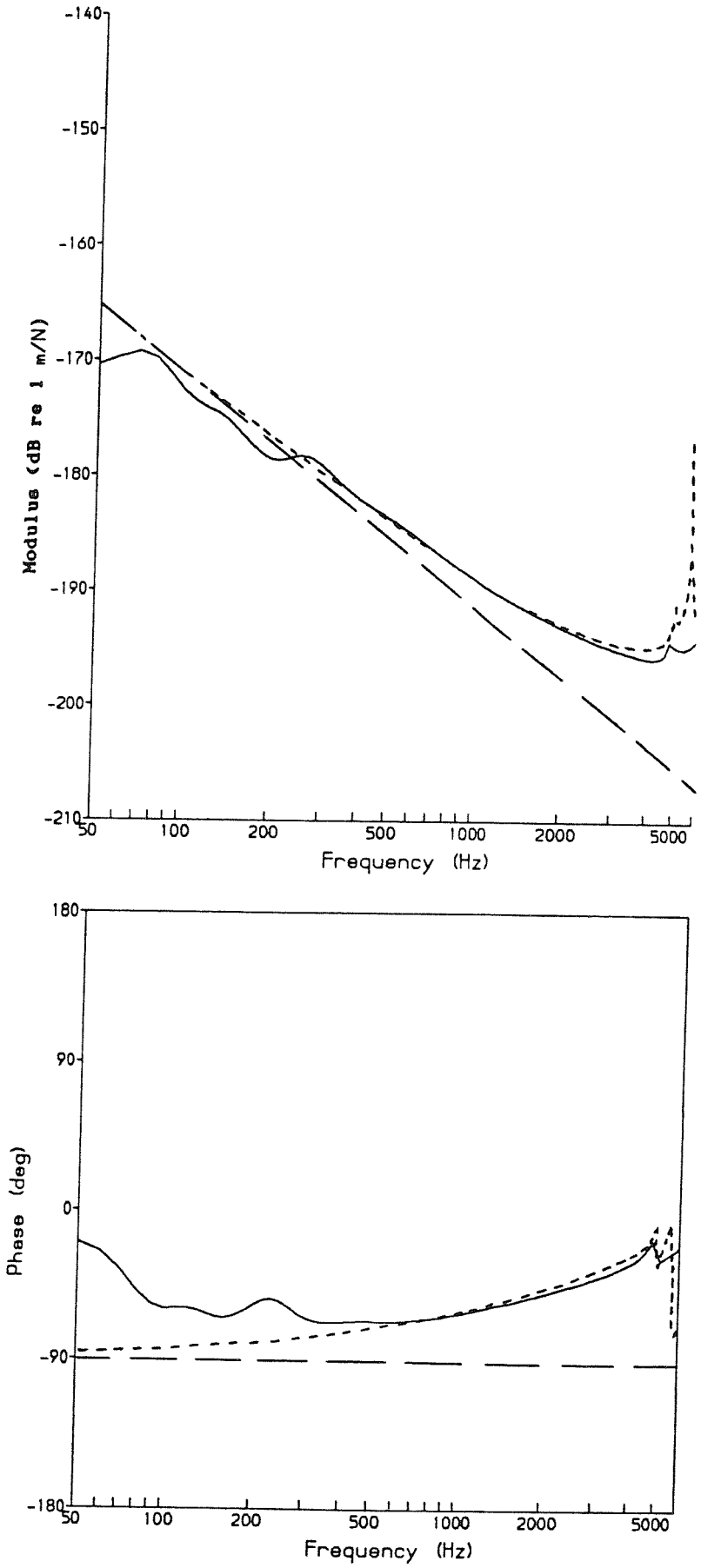

Figure 87. Longitudinal Rail Head Receptance (——— Supported Rail, ····· Free Rail (Figure 76), — — From Simple Beam Theory (Figure 61))

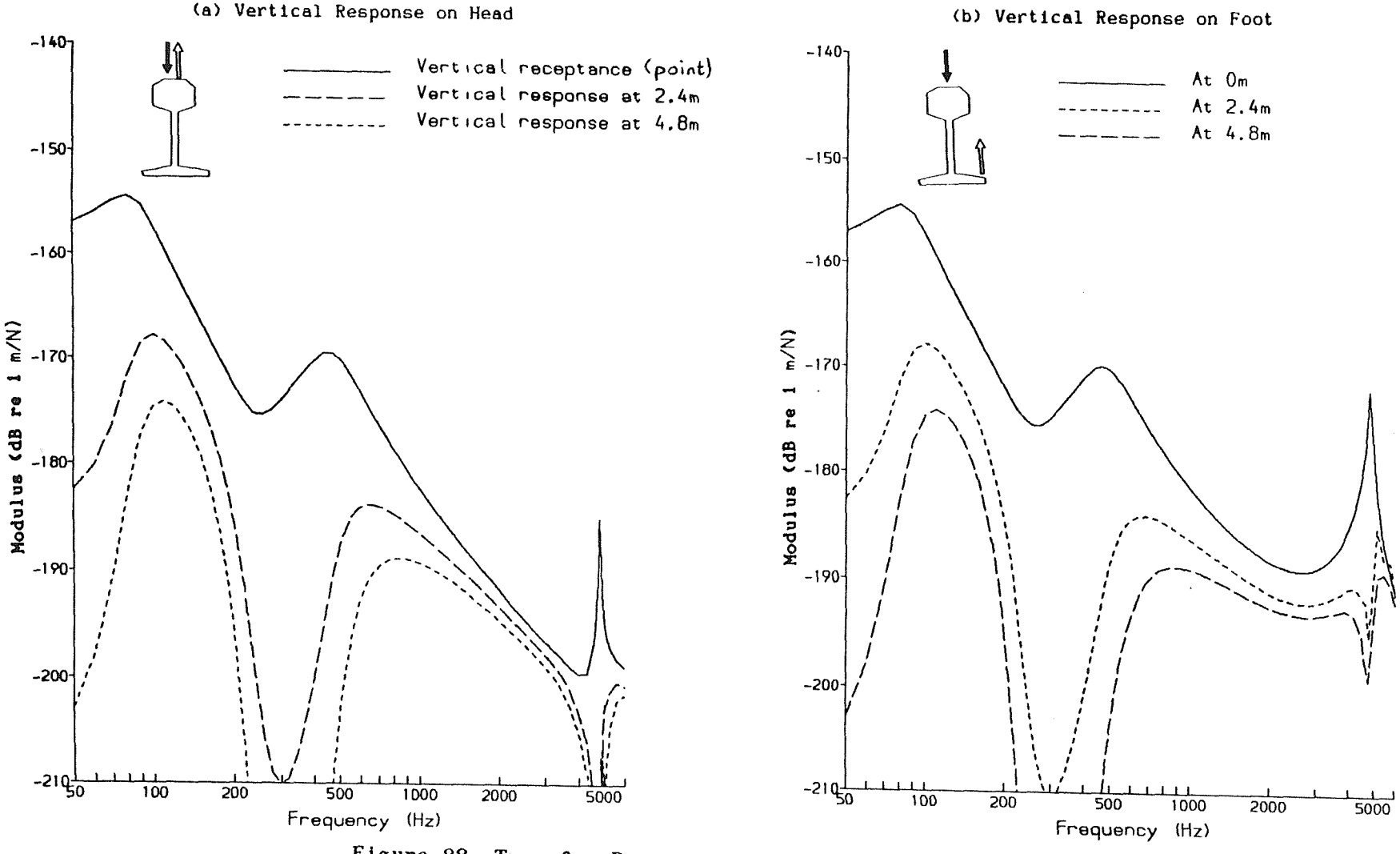

Figure 88 Transfer Receptances: Response to Vertical Force Applied to Head for Supported Rail

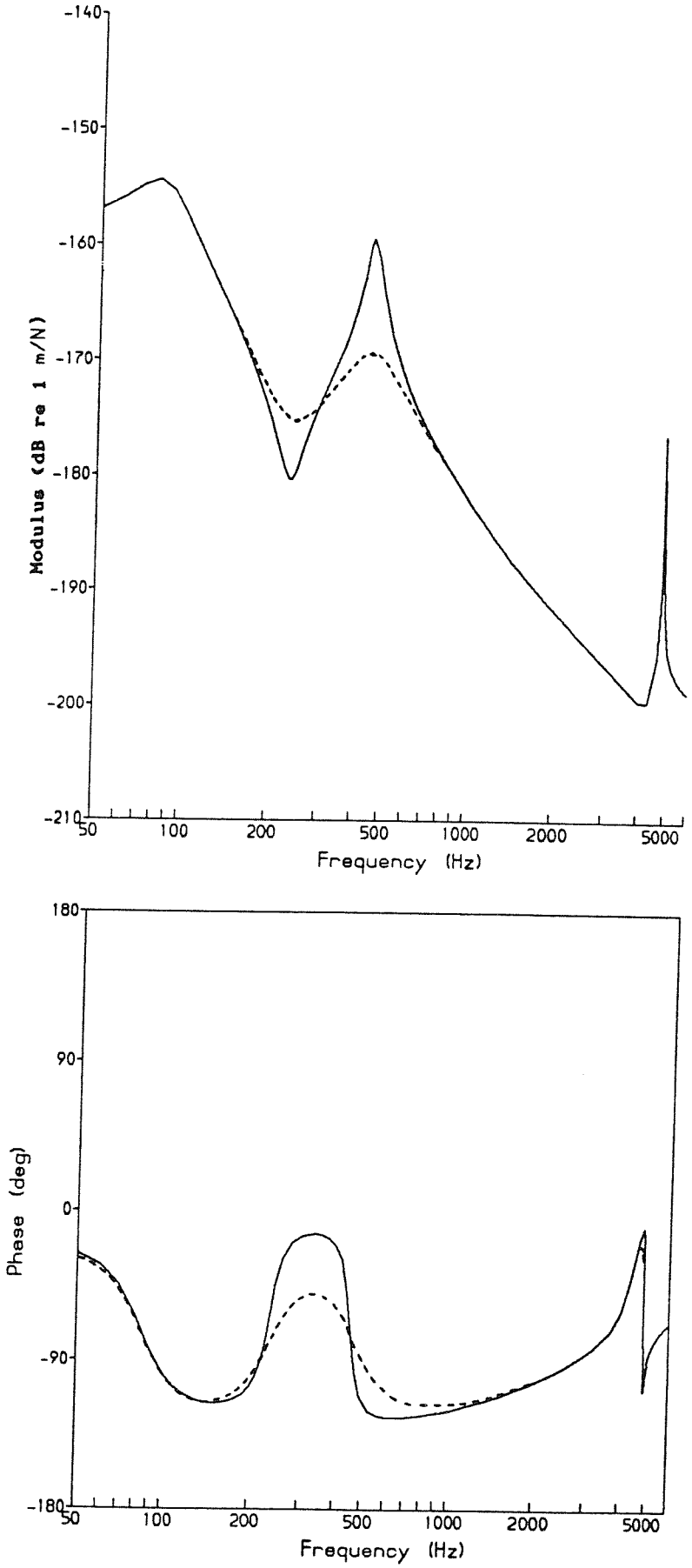

Figure 89 Effect of Pad Damping Loss Factor on Vertical Receptance

(——— η=0.1, — — η=0.5 (Figure 84))

Figure 88 shows the effect of distance on the vertical response, which may be compared with Figure 84. As for the lateral response, the main effect of the sub-layers is to introduce a greater decay at low frequencies.

Figure 89 shows the effect on the vertical receptances of altering the pad damping loss factor (from 0.5 to 0.1). The effect is strongest around the 450 Hz resonance (the vertical wave cut-on), indicating the dominance of the pad in this mode. Additionally, for a different value of pad stiffness, the frequency at which this peak occurs can be found to be altered accordingly. The pad damping also affects the magnitude of the response at the F wave cut-on, as might be expected, since this wave contains significant foot motion.

The wavenumbers of various vertical and longitudinal waves are shown in Figure 90. These results are similar to those for the free rail (Figure 65) except at low frequencies, where a significant imaginary part can be seen for the vertical bending wave, as well as features in the real part. Figure 91 shows the decay rates and the ratios k_I/k_R for these waves. Once more, large decays can be seen at low frequencies, below cut-on, particularly for vertical bending. At

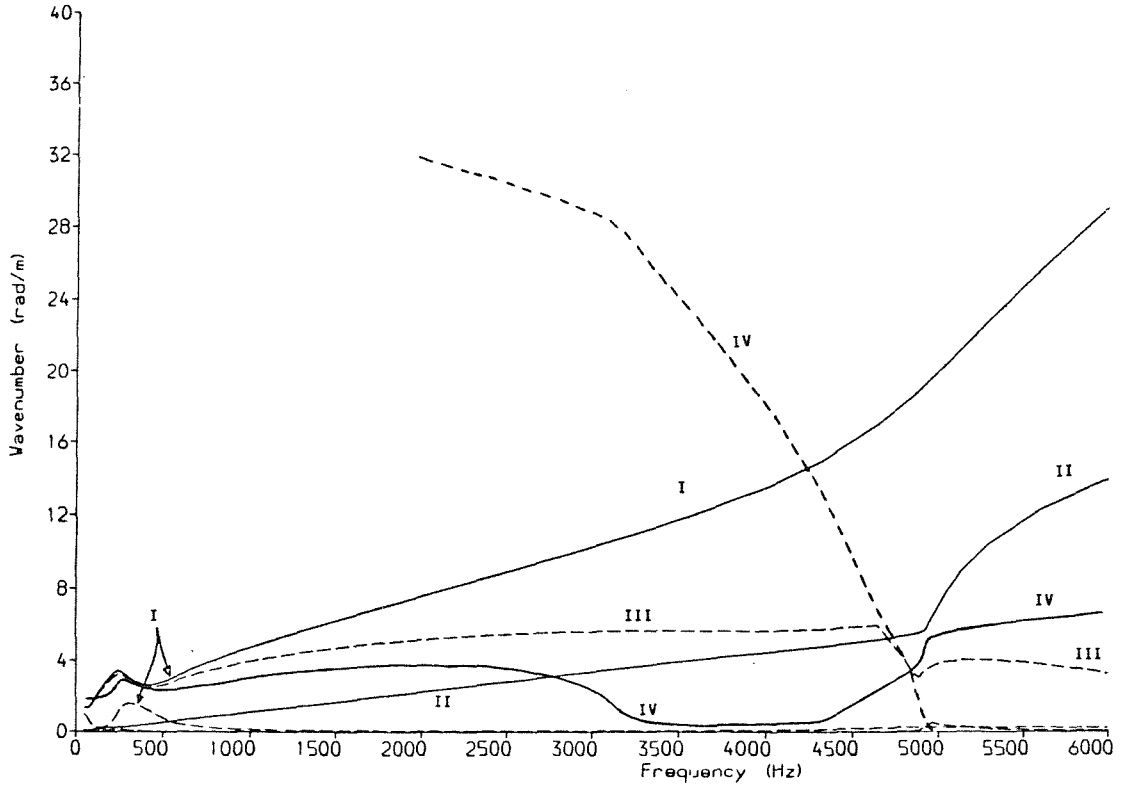

Figure 90 Wavenumbers of Vertical/Longitudinal Waves for Supported Rail (——— Real Part, — — Imaginary Part)

(a) Decay Rate dB/m

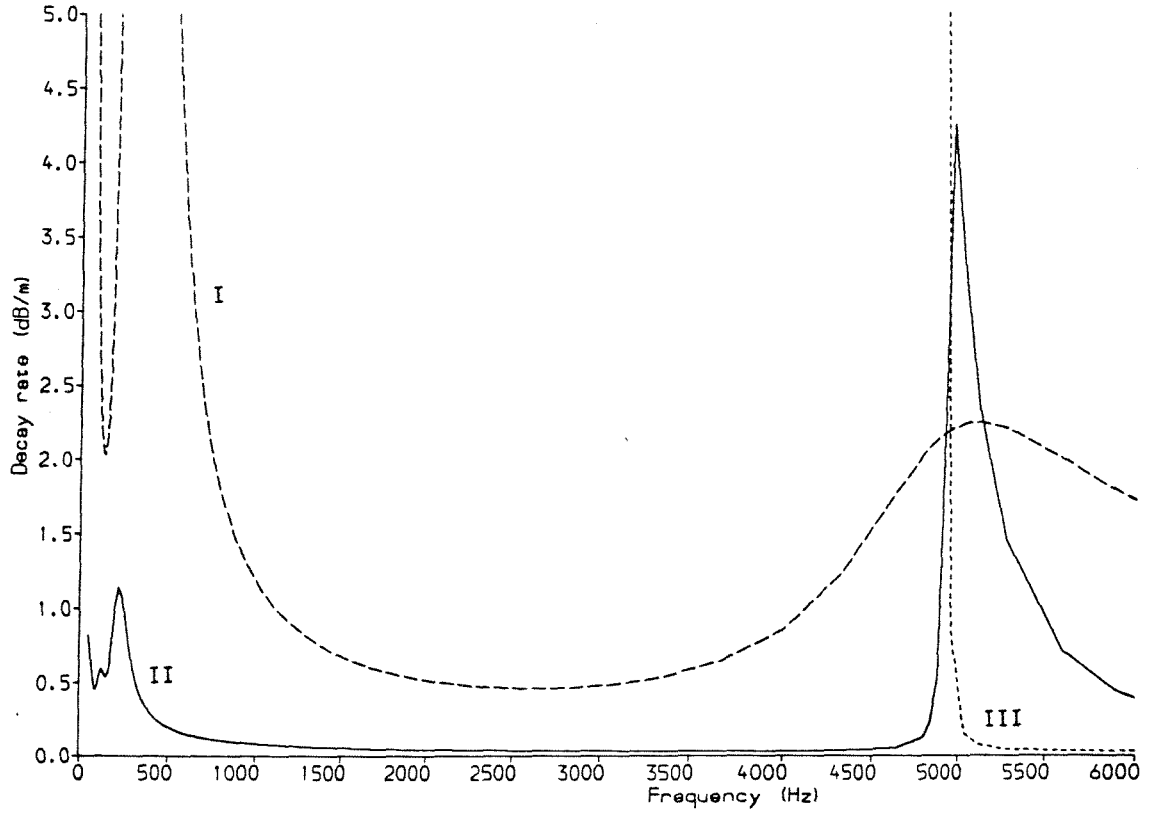

(b) Imaginary Part/Real Part of Wavenumber

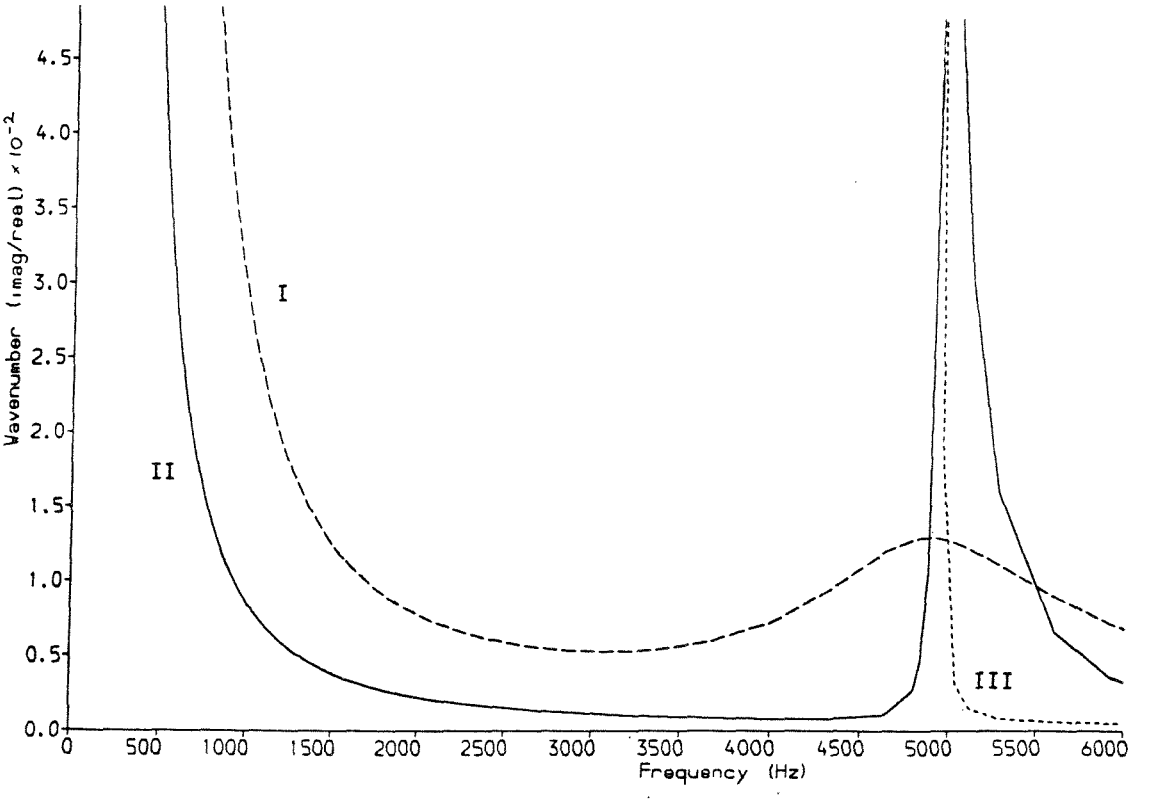

Figure 91 Decay Rates of Vertical/Longitudinal Waves for Supported Rail

higher frequencies a significant decay due to the influence of the pad damping can be seen. The longitudinal motion has the lowest decay rate, generally below 0.1 dB/m, although it is greater at low frequencies and close to 5000 Hz.

5.5 DISCUSSION

5.5.1 Comparison with Experimental Results

A number of experimental results of rail FRF's measured in situ, from various sources, are available in the literature. No new measurements have been made for this study.

Detailed receptances are available from Grassie [58-60], although only for frequencies up to 1-2 kHz. These cover track with wooden sleepers as well as concrete sleepers, but only the latter are included here. Narrow-band impedances have been measured by van Ruiten [112,37], although they are for a smaller rail section (42 kg/m rather than 56 kg/m). Results from Remington [20] include one-third octave impedances for a 60 kg/m rail, and equivalent results for the vertical impedance can be found in Munjal and Heckl [65]. Other results of Remington used a lighter (50 kg/m) rail section. In each case these impedance results have been converted to receptances for comparison with the predictions.

Figure 92 compares results for the lateral receptances. The agreement is generally good. The low frequency results agree well with Grassie's measurements. Peaks in Grassie's data at 360 Hz and 700 Hz correspond to an effect of sleeper periodicity (the "pinned-pinned mode"). The peak in the lateral response at around 2 kHz is mirrored in van Ruiten's results (the slightly higher frequency presumably being a consequence of the smaller cross-section).

Figure 93 gives the comparisons for vertical receptances. The results agree well with those of Grassie, although using a stiffer ballast (as used by Grassie in his model) gives a higher bounce frequency as seen in the experimental results, and closer agreement. A single "pinned-pinned" frequency can be seen at 760 Hz. Remington's and Munjal's results are higher in the region 600-1500 Hz, but this is probably an effect of the sleeper periodicity. The peak corresponding to the cut-on frequency of the vertical bending waves depends on the pad stiffness, and hence is likely to vary among the experimental results.

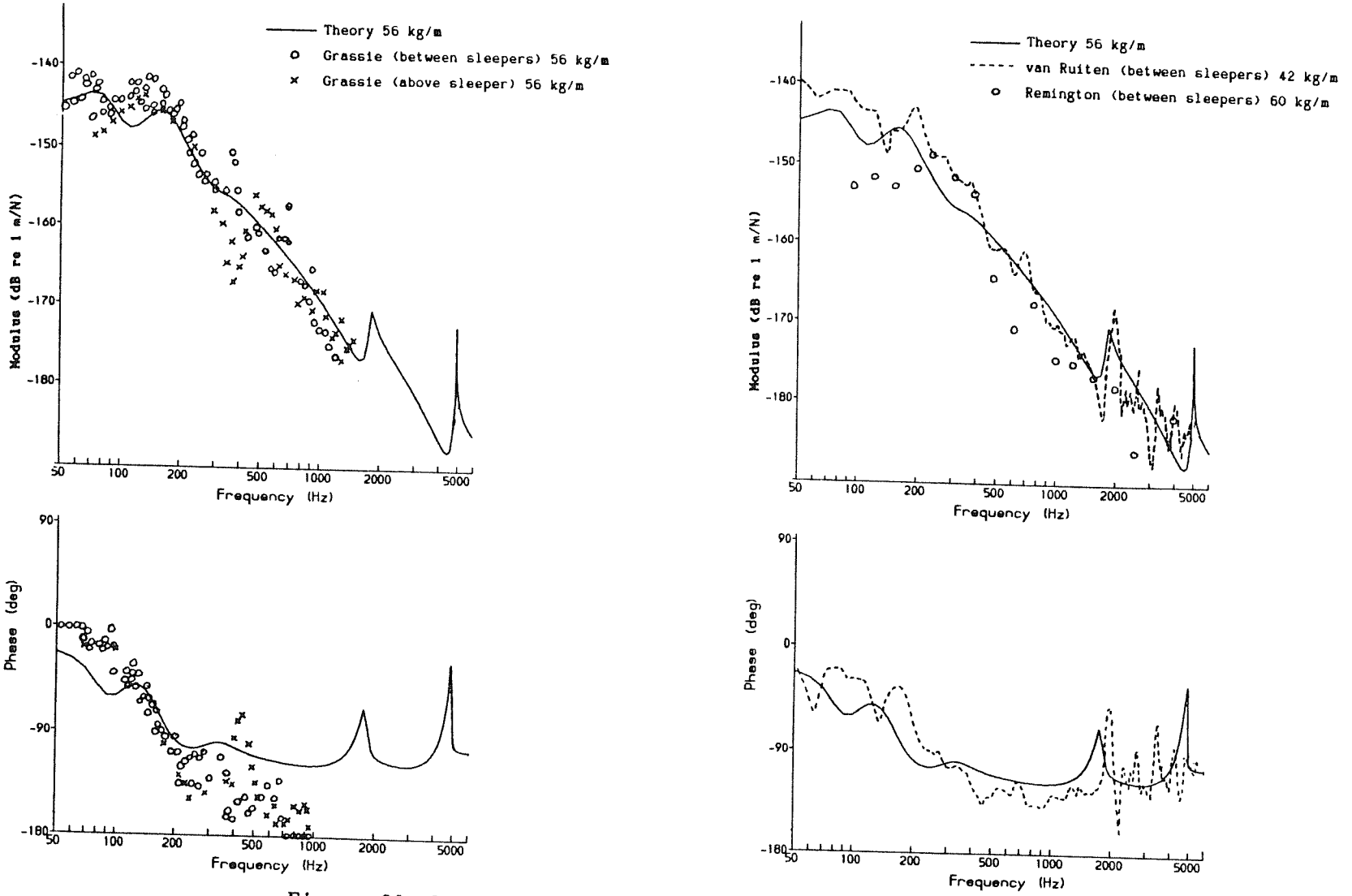

Figure 92 Lateral Rail Head Receptance: Comparison with Experimental Results

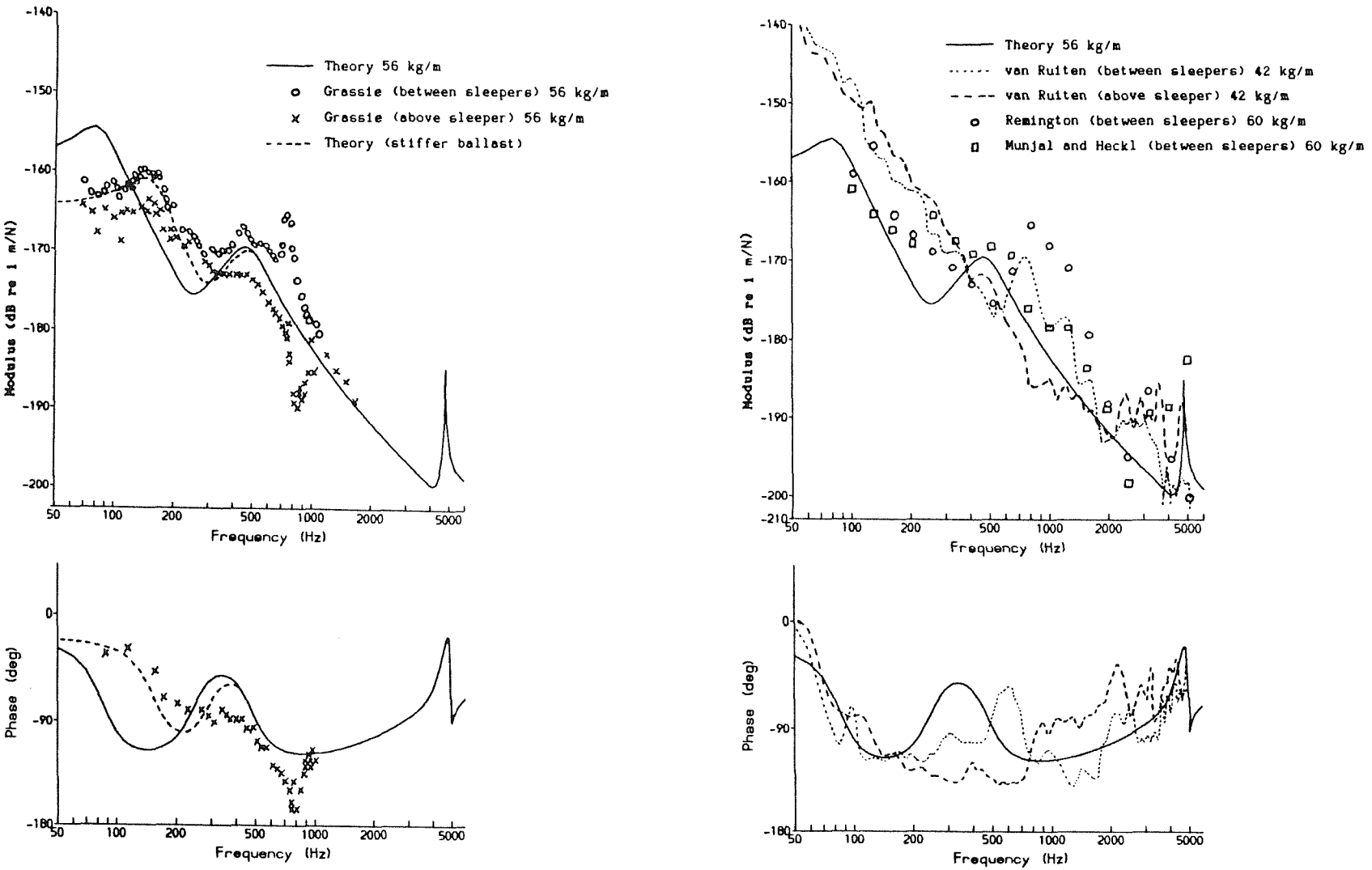

Figure 93 Vertical Rail Head Receptance: Comparison with Experimental Results

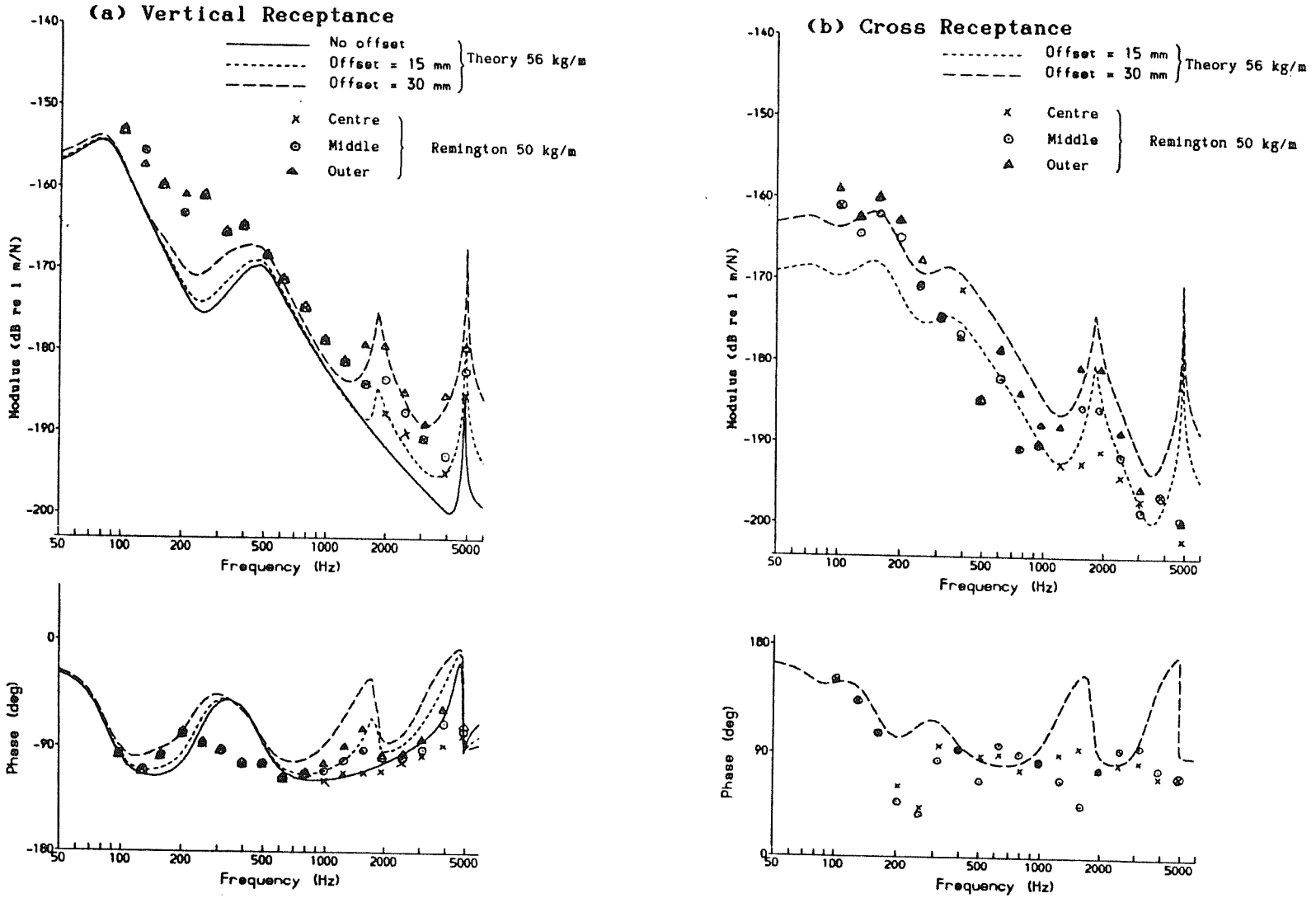

Figure 94 Effect of Lateral Position: Comparison with Experimental Results

Figure 94 compares the results at various lateral positions, with experimental results given by Remington on a 50 kg/m rail section. The three positions (0, 15 and 30 mm) correspond closely to those used by Remington. Similar trends can be seen in the vertical receptances, particularly at higher frequencies. At low frequencies the agreement could be closer for a different choice of ballast and pad stiffnesses. Although the predictions for the cross receptances contain the correct trends at high frequencies, the measurements contain a non-zero cross receptance at the centre-line, which is ruled out in the theory. This could be an effect of asymmetry in the support (sleepers) which is ignored in the model.

Figure 95 compares the longitudinal prediction with the measurements of Grassie. Amplitude agreement is good, although the

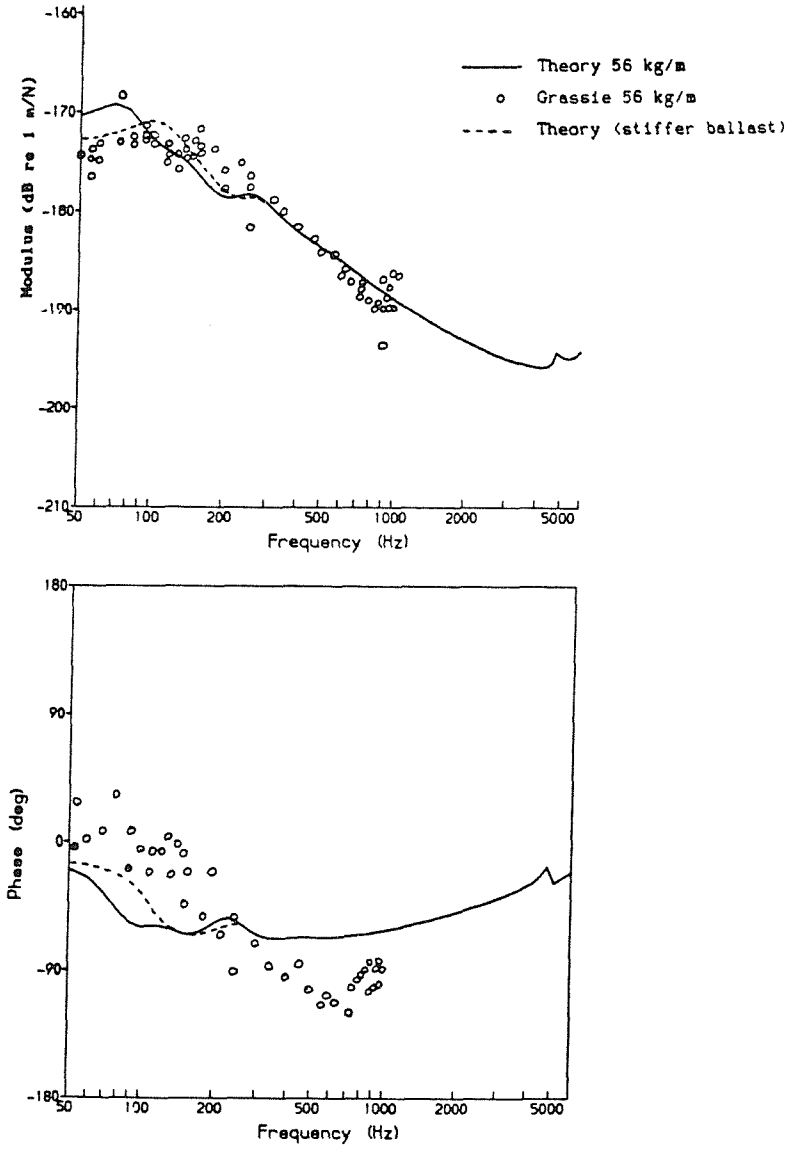

Figure 95 Longitudinal Rail Head Receptance: Comparison with Experimental Results

phase agrees less well. Again a stiffer ballast may be more appropriate to model this site.

A dispersion diagram has been derived from experimental results [70] and this is shown in Figure 96. These results are based on measurements of the response of a section of rail in situ, to vertical and lateral sinusoidal excitation at 1/3 octave band centre frequencies. The response was measured at over 20 cross-sections, spaced at intervals of half a sleeper-spacing, with 10 accelerometers placed on each cross-section. The deformation at each cross-section was resolved into various components (lateral, vertical, torsional, web bending etc), and from their phases the wavespeeds were deduced. Although a limited number of frequencies were studied, and not all wavetypes could be detected at each frequency, the results agree very well with the predictions of §5.4, superimposed here, for those waves for which experimental data are available.

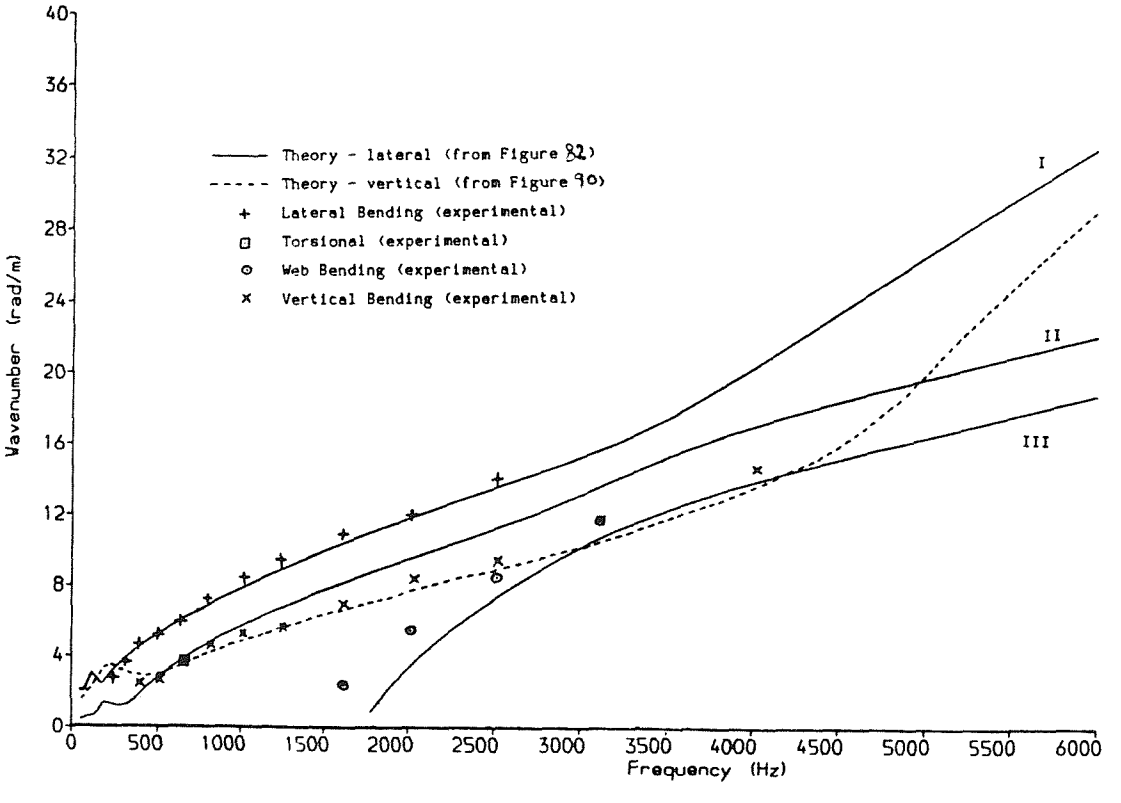

Figure 96 Dispersion Diagram: Comparison with Experimental Results

5.5.2 Effects of Spatial Averaging on Measured Rail Vibration

In the analysis of measured rail vibration from a train pass-by, it is necessary to take an average over a finite length of time, in order to derive frequency components (see Appendix A). As noted in §3.3.1, due to the motion of the train during the analysis time, this measurement does not correspond exactly to the vibration opposite the wheel-rail contact point, which is the parameter which is predicted in the interaction modelling.

In an attempt to quantify this effect, the theoretical model has been used to predict the average vibration over a given length. The measurements in Appendix A use an analysis 'length' of 4.45 m, within which two wheels (approximately 2.5 m apart) pass the measurement position. The average vibration which would be registered due to one of the wheels can, therefore, be calculated from the average response over (roughly) 1 m on one side of the excitation point and 3.5 m on the other side. The effect of the two wheels is then produced by doubling the result (adding 3 dB), making the assumption that the two wheels act as incoherent sources.

The difference between the spatially averaged result and the point response, is given in Figure 97, in 1/3 octave bands, showing the effect on the lateral and vertical receptances at the rail head. In the bands 250-500 Hz, the vertical vibration is attenuated by the spatial average by around 5 dB, whereas in the range 1.25-3.15 kHz it is actually amplified by about 2 dB (because of the addition of the results from two wheels). For the lateral vibration the effect lies between 0 and -3 dB over the entire frequency range shown. These results are roughly in accord with the assumptions made in §3 (see in particular Figure 22 and the corresponding discussion).

5.5.3 Effects of Additional Rail Damping

In §3 it was seen that the introduction of damping to the wheel reduced the modal response, and, whilst not producing as much benefit as might be expected from results for a free wheel, a reduction in 1/3 octave spectra of wheel vibration, and (to a lesser extent) rail vibration was predicted by the model.

For the rail, the effect of added damping is not so simple. The effect on the point receptances is negligible, as seen in Figure 98 which shows the lateral and vertical receptances for a loss factor of 0.5 for the rail, in place of the nominal value of 0.0005 (retaining a

(a) Head Vertical

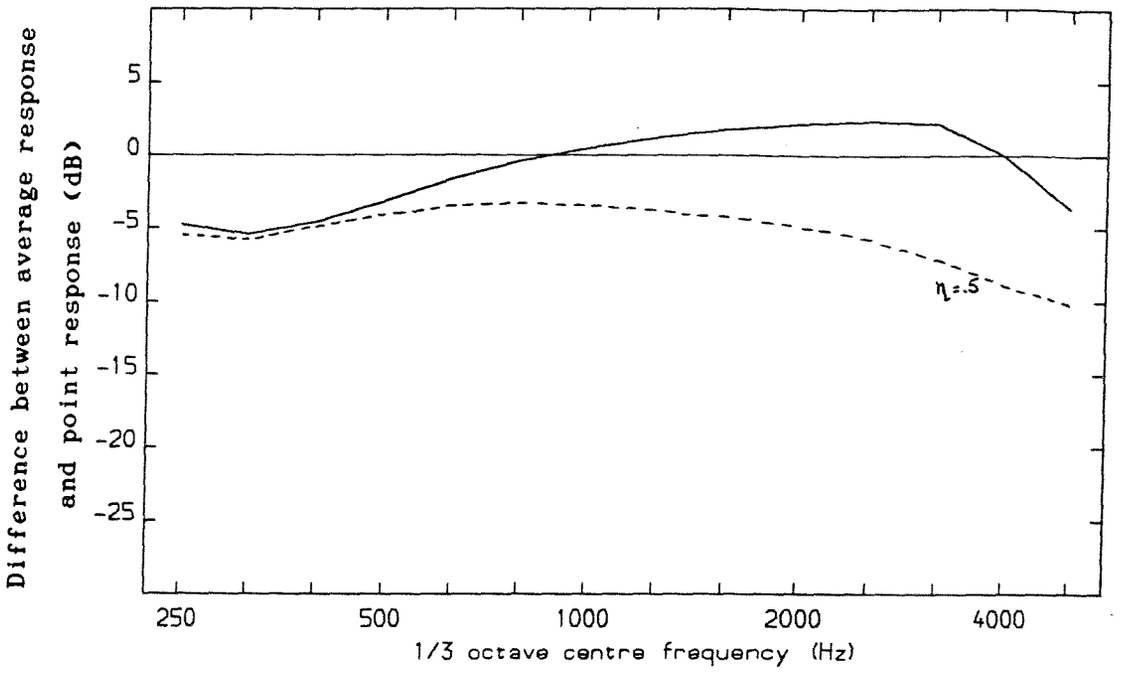

(b) Head Lateral

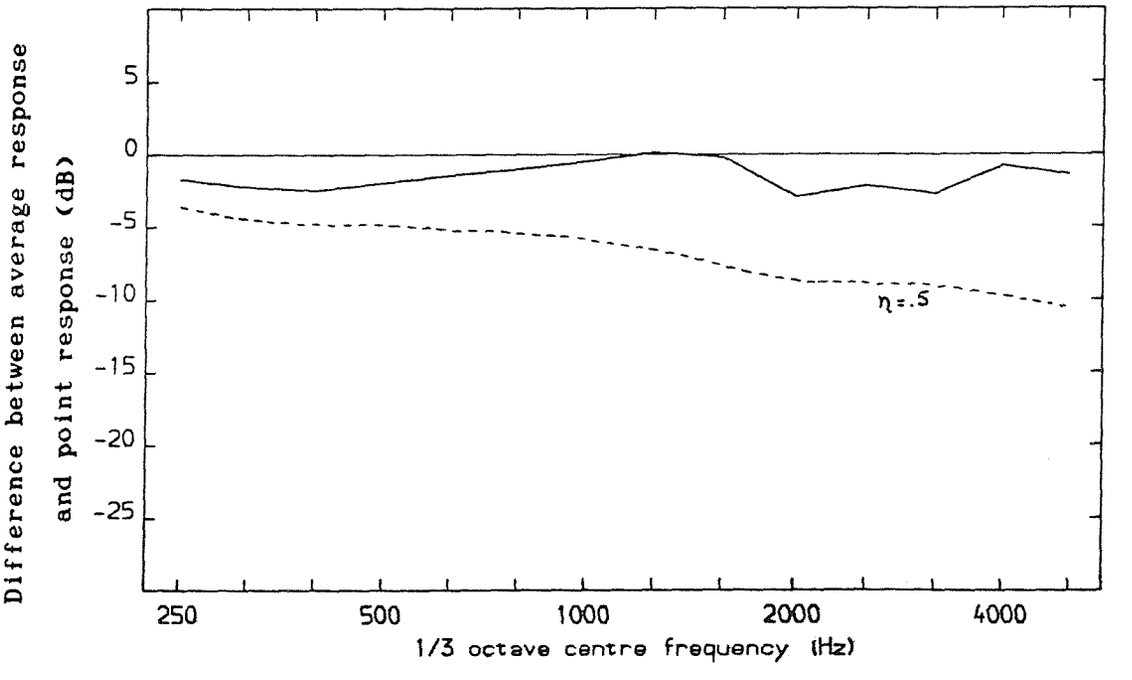

Figure 97 Effect of 4.5 m Spatial Average on Rail Vibration

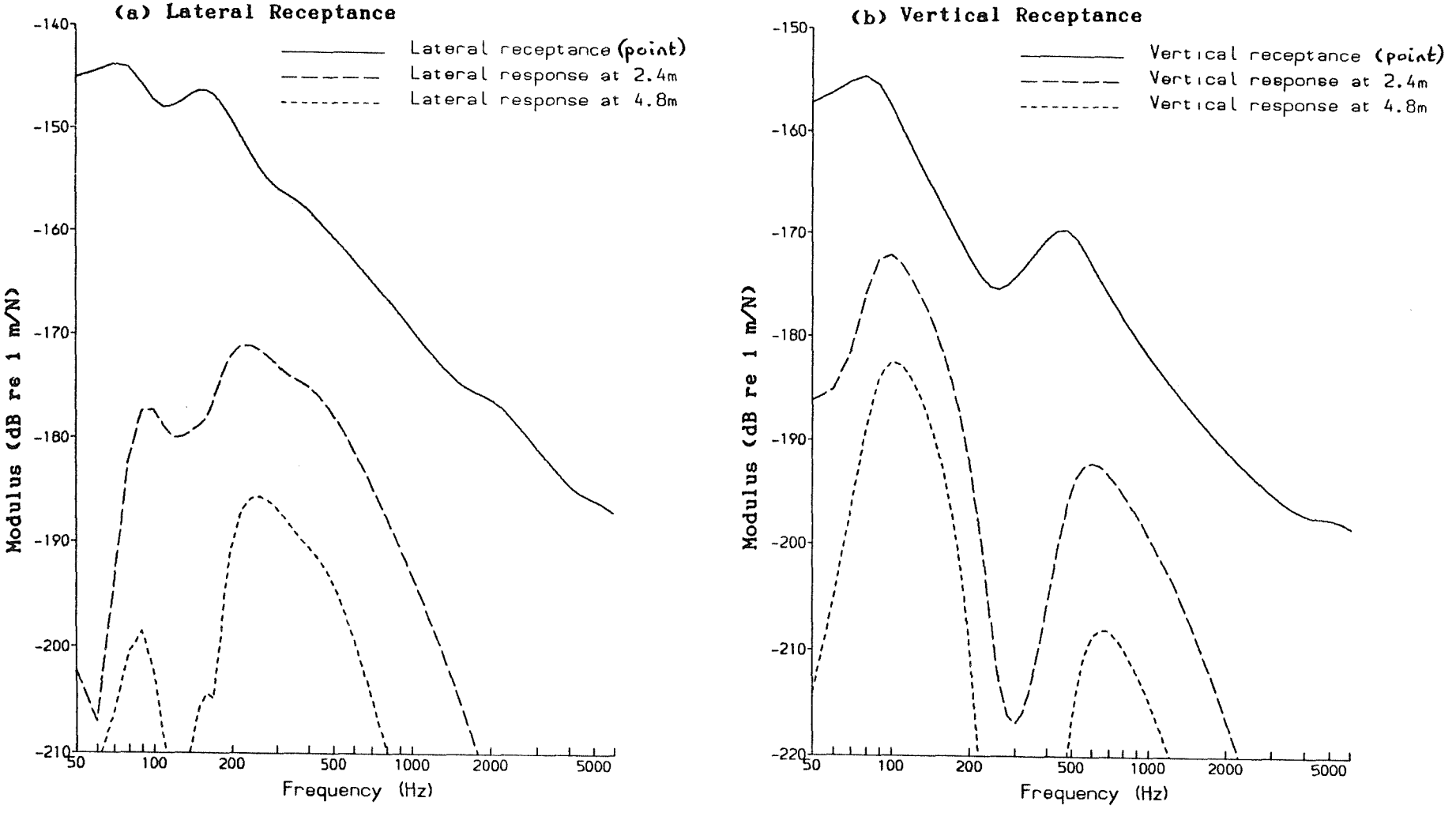

Figure 98 Rail Receptances for a Rail Damping Loss Factor of 0.5

loss factor of 0.5 for the pad and ballast layers). Comparing these results with those from Figures 79 and 84, the only effect is around the 'cut-on' frequencies of the higher order waves. This also means that introducing damping to the rail will not have any significant effect on the wheel response.

By contrast the response at a distance (eg 2.4 and 4.8 m) is much reduced by the damping, particularly at high frequencies. The decay of vibration with distance along the rail is thus very sensitive to the levels of damping in the rail, pad and ballast. The above results, for the average vibration over a length, will be affected by the decay of rail vibration with distance. Figure 97, therefore, also shows the equivalent results using a loss factor of 0.5 for the rail. The effect is now greatly increased at higher frequencies, where the damping introduces a significant decay with distance. Both the vertical and lateral results now lie between -3 and -10 dB.

Since the noise radiation from the rail is related to the effective radiating length, this suggests that there is a potential benefit in introducing damping to the rail. By increasing the decay with distance (Δ dB/m), the effective radiating length of the rail is reduced.

Although this appears promising as a source of noise reduction, it should be remembered that this level of damping (η=0.5) is very high, and would be extremely difficult to achieve. For example, experiments on a free length of rail have achieved loss factors of around 0.03, using a constrained layer damping treatment under the rail foot [104]. For more realistic levels of damping such as this, the decay with distance results will be much lower.

The effect of damping can be seen to increase with frequency; in addition the effectiveness of damping treatments increases with frequency, as the wavelength reduces. Thus it is easier to achieve a given loss factor at high frequencies than at low frequencies, and any benefit of added damping will tend to be limited to these higher frequencies.

It is worthwhile to ask what level of damping is introduced by the support (pads and ballast). This will give an indication of how much has to be added to achieve any additional benefit; the consequent damping should be substantially more than the equivalent result due to the support.

Comparing Figures 68 and 91 it can be deduced that, for the vertical waves in the supported rail, above about 2.5 kHz the damping is roughly equivalent to a loss factor of 0.01 in the unsupported rail. At lower frequencies it is equivalent to a higher rail loss factor. For the longitudinal waves the damping is much lower, and is equivalent to a rail loss factor of about 0.002. Similarly, for the lateral waves, comparing Figures 67 and 83, the supported rail appears to have similar decay rates to a free rail with a loss factor of 0.01 for 1-2.5 kHz; at higher frequencies the equivalent loss factor is lower than this.

Thus to reduce the radiation from lateral motion of the rail, above about 1 kHz, a loss factor of substantially more than 0.01 must be introduced. For vertical motion such a value would produce an improvement above about 2.5 kHz; a higher value would be needed to be effective for lower frequencies.

Experimental estimates of the decay with distance for this form of track [70] have suggested values in the range 0.5-2 dB/m. This indicates that a slightly higher damping is present than was included in the model which produced the predictions in Figures 83 and 91, and thus that the above values should perhaps be higher.

The sublayers of pad, sleeper and ballast affect the rail response substantially at low frequencies, but above about 1 kHz their effect is limited to the introduction of damping. More data are therefore required on the damping properties of railpads, in particular, which will be vary as a function of frequency. Grassie's assumption of a viscous damper [113] is not adequate to model these effects of damping over a broad range of frequencies. However, it should be noted that it is unlikely that much higher values of pad damping could be achieved than the value included in the model (η=0.5).

5.5.4 Effects not Considered

Asymmetry of the support has been ignored, and is expected to influence the cross receptance in particular. However an offset of 15 mm to the lateral position of the contact produces a level of cross receptance which is reasonably consistent with measured results.

The effect of the forward velocity of the forcing point has been ignored in this work. Its effect will be to modify the apparent wavespeeds of the various waves in the rail, as shown for an Euler-Bernoulli beam in Appendix D. However for realistic speeds of travel

these shifts are very small (also mentioned in [58]). It is therefore reasonable to ignore the effects of movement of the forcing point along the rail, apart from any effects arising from the periodic support.

The periodic nature of the support of the rail has not been taken into account. However the minimal effect on the rail of a continuous sublayer for frequencies above about 1 kHz, suggests that a periodic support would similarly have little influence here, although this conclusion depends on the values of pad stiffness. For a stiffer pad (or no pad), the frequency range of influence would increase.

Below 1 kHz the periodic nature of the support will introduce some modifications to the response. These have been studied by Grassie [58,59] using a simple beam. Isolated frequencies exist where a large response is predicted between sleepers, while the response over the sleepers is a minimum (known as "pinned-pinned resonances"). These can be seen in the experimental results in Figures 92 and 93. These frequencies correspond to wavelengths of two sleeper spans (about 1.4 m), and can be identified from Figures 63 and 65, for k~4.5.

Grassie predicted that these peaks would be quite sharp, ie only affecting a small part of the frequency spectrum. Two factors will mean in practice that these regions may be broader: (1) The sleeper spacing tends to be somewhat irregular, which broadens the frequency range of influence. (2) The connection to the sleeper is not at a point but is over a length of some 200 mm. Hence the coupling in at least the rotational coordinate should also be taken into account, so that the "pinning" effect of the sleeper will be less marked. Reference to the work of Tassilly [66,67], where such a longer connection is made, suggests that the pinned-pinned region (which is a blocked zone) is broader as a result.

Whilst it would be possible to include discrete supports into the current model by using 700 mm as the periodic length, and including many internal coordinates, a more managable alternative would be to use a second stage of periodicity. Mead [114] has developed a periodic structure model for infinite beam-like and plate-like structures with periodic additions. It is based on the receptances of the additions and of the beams at the connection points. Thus the receptances (displacement and rotational) of the free rail under the foot could be calculated using the current model, and then linked to the receptances of the pad-sleeper-ballast substructure, as calculated in Appendix G.

5.6 CONCLUSIONS

The vibration of an infinite rail beam has been successfully modelled using periodic structure theory, based on an arbitrary period length of 10 mm. Wavenumber results for propagating waves agree well with finite element predictions, and with limited results derived from experimental data. The rail idealisation, which was assembled from finite element matrices, appears to be reasonable. It is, however, somewhat limited by the elements used (4-noded plates), particularly for the transition between web and foot.

The cross-section was found to deform significantly above about 1500 Hz for lateral excitation, as found experimentally. For vertical motion the foot response is progressively greater than that of the head for frequencies above about 1 kHz. The simple beam equations used previously are thus deficient at these higher frequencies.

Receptances can be predicted, which agree closely with published experimental data. Strong resonance peaks are seen to occur at wave 'cut-on' frequencies (1.8 kHz and 5 kHz laterally, and 5.1 kHz vertically), although damping reduces these significantly. Overall the result of including the flexibility of the rail cross-section has been to increase the receptances particularly at high frequencies and to alter the phase.

For the purposes of predicting the rail response, the details of the sleepers can be ignored (for normal pad stiffness values), and can be replaced simply by an equivalent mass and spring. Above the bounce frequency at around 90 Hz the resilience of the pad dominates. For a stiffer pad, however, more details of the sleeper may be needed.

The inclusion of these sublayers leads to a reduction in the receptance at low frequencies, but has little effect on the receptances above about 1 kHz. However the damping of the railpad introduces a significant decay with distance along the rail, not seen for the free rail. More detailed measurements of damping loss factors of railpads, as a function of frequency are therefore required.

Adding damping to the rail, for example by a constrained layer treatment, has negligible effect on the point receptances, but should reduce the effective radiating length of the rail. However, to be effective, such damping should yield a loss factor for the treated rail

of substantially more than 0.01, and even then the effect will only be significant at high frequencies.

The main discrepancy with experimental results is at "pinned-pinned" frequencies, which the present continuous model cannot represent. However the large degree of isolation offered by the rail pads suggests that the effects of the periodic supports will be limited to the region below 1 kHz, where existing models are valid, so long as the pads are as soft as those included in the current model.

CHAPTER 6

THEORY OF WHEEL-RAIL CONTACT AND INTERACTION

6.1 THEORY OF WHEEL-RAIL INTERACTION

6.1.1 Derivation for Relative Displacement Inputs

Equations were presented in §3 for the excitation of a coupled wheel and rail by a roughness acting between them in the vertical direction, based on Remington's work. This roughness introduces a relative displacement, as shown in Figure 99. The wheel and rail were coupled in two coordinate directions - vertically and laterally, the wheel and rail being represented by point receptances in these two directions along with the corresponding cross receptances. The contact zone was similarly represented by receptances.

In this chapter, more general wheel-rail interaction equations will be derived, and alternative excitation mechanisms will be discussed. This begins by looking at the relative displacement input, but it may be noted that, as well as the vertical input due to the roughness, similar inputs in other directions might be envisaged (eg as used by Grassie [59]). In a later section a more rigorous derivation of the contact receptances will be given.

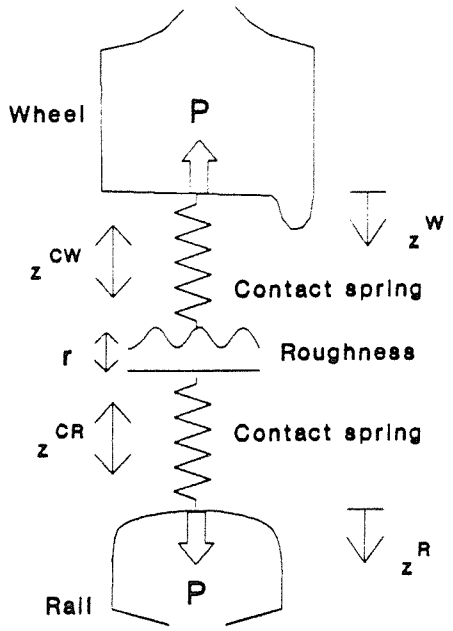

Figure 99 Schematic Diagram of Wheel-Rail Contact Region for Relative Displacement Input

To improve the representation of the wheel-rail interaction, coupling in further coordinate directions can be included - longitudinal (ie in the direction of motion), and rotational coordinates - up to a total of 6 for a point contact. Because of the distributed nature of the contact area, it may even be justified to include further coordinates, eg higher spatial derivatives of the displacements, although these will not be discussed here.

It will be assumed in this section that there are N coupling coordinates, $z_1 \ldots z_N$, with z^R_i used to represent the displacements of the rail, z^W_i for the wheel and z^C_i for the relative motion in the contact zone. The latter can be separated into two parts, z^{CW}_i for local deformations of the wheel, and z^{CR}_i for local deformations of the rail. Then, following the sign convention used in §3 (as shown in Figure 99),

$$z^R_i = z^W_i - z^{CW}_i - z^{CR}_i + r_i \qquad \ldots(81)$$

where r_i is the relative displacement input to the ith coordinate (eg roughness). The interaction force acting in the jth coordinate direction, P_j, results from the coupling (ie the force is transmitted by the contact springs etc) and the same force acts on both the wheel and the rail (in opposite directions). This means that the forces and displacements, at a particular frequency, ω, can be related by the receptances of the various subsystems,

$$\begin{aligned} z^R_i &= \sum_{j=1}^{N} \alpha^R_{ij} P_j \\ z^{CR}_i &= \sum_{j=1}^{N} \alpha^{CR}_{ij} P_j \\ z^{CW}_i &= \sum_{j=1}^{N} \alpha^{CW}_{ij} P_j \\ z^W_i &= \sum_{j=1}^{N} \alpha^W_{ij} (-P_j) \end{aligned} \qquad \ldots(82)$$

or in matrix form

$$\begin{aligned} \{z^R\} &= [\alpha^R] \{P\} \\ \{z^{CR}\} &= [\alpha^{CR}] \{P\} \\ \{z^{CW}\} &= [\alpha^{CW}] \{P\} \\ \{z^W\} &= - [\alpha^W] \{P\} \end{aligned} \qquad \ldots(83)$$

Note the negative signs for the wheel, since here the force acts in the opposite direction to the displacement. Hence from equation (81),

$$\{r\} = [\alpha^R + \alpha^{CR} + \alpha^{CW} + \alpha^W]\ \{P\} = [\alpha]\ \{P\} \qquad \ldots(84)$$

where $[\alpha]$ is the matrix of combined wheel, rail and contact zone receptances

$$\Rightarrow \quad \{P\} = [\alpha]^{-1}\ \{r\} \qquad \ldots(85)$$

Thus the response at a general point, X, on the wheel, can be calculated as

$$z^W_X = [\alpha^{WT}]\ \{-P\} = -[\alpha^{WT}]\ [\alpha]^{-1}\ \{r\} \qquad \ldots(86)$$

where α^{WT}_i is the transfer receptance of the wheel from the ith contact coordinate to the position X. A similar equation holds for a point on the rail (although with the opposite sign). These equations are the multi-degree-of-freedom generalisations of those given in §3.

6.1.2 Relative Force Excitation

In the above, the same mutual force $\{P\}$ acts on the wheel and the rail. Instead of the relative displacement input, an equivalent force excitation could be envisaged, equation (85) giving the equivalence.

However, if excitation is envisaged in one particular direction, for instance by a vertical force, the resulting force vector would be $\{P\}^T=(0,0,1,0,0,0)$. Consequently the wheel and rail have no interaction force in any other direction, ie they are decoupled in all but one coordinate.

The desired idealisation is, rather, that the interaction forces in the other directions should be unknowns, whereas the corresponding displacement inputs should be set to zero. Hence for this particular case, of a force input to P_3,

$$P_j = \begin{cases} 1 \text{ for } j=3 \\ \text{unknown for } j\neq 3 \end{cases} \qquad r_j = \begin{cases} \text{unknown for } j=3 \\ 0 \text{ for } j\neq 3 \end{cases}$$

In general, the force and displacement input vectors can be partitioned into known and unknown parts; let a indicate that the force is known (and the displacement is unknown) and b indicate that the

displacement is known (and the force unknown), with $\{P\}^T=\{P_a|P_b\}$, $\{r\}^T=\{r_a|r_b\}$. Thus equation (85) can be partitioned to give:-

$$\left[\begin{array}{c|c} I & 0 \\ \hline 0 & I \end{array}\right] \left\{\begin{array}{c} r_a \\ \hline r_b \end{array}\right\} = \left[\begin{array}{c|c} \alpha_{aa} & \alpha_{ab} \\ \hline \alpha_{ba} & \alpha_{bb} \end{array}\right] \left\{\begin{array}{c} P_a \\ \hline P_b \end{array}\right\} \qquad \ldots(87)$$

This can be rearranged to give

$$\left[\begin{array}{c|c} I & -\alpha_{ab} \\ \hline 0 & -\alpha_{bb} \end{array}\right] \left\{\begin{array}{c} r_a \\ \hline P_b \end{array}\right\} = \left[\begin{array}{c|c} \alpha_{aa} & 0 \\ \hline \alpha_{ba} & -I \end{array}\right] \left\{\begin{array}{c} P_a \\ \hline r_b \end{array}\right\} \qquad \ldots(88)$$

where the right-hand side is known, and hence the left-hand (unknown) vector can be found by inversion of the left-hand matrix. From this, the force vector $\{P\}$ can be reconstructed, and can then be used in equation (86).

6.1.3 External Force and Displacement Excitations

An alternative model has been put forward by Feldmann [77]. He introduced an external force excitation at the wheel-rail interface, as signified in Figure 100. This may alternatively be described [77] (by analogy with electrial circuit theory) as a series impedance model, in contrast to the above which is described as a parallel impedance model.

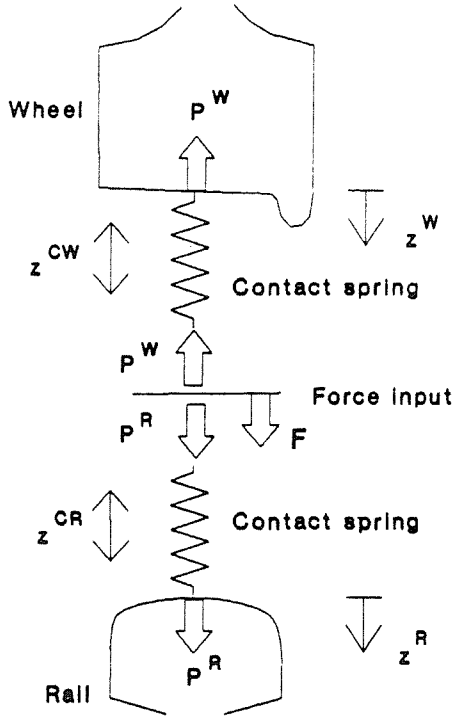

Figure 100 Schematic Diagram of Wheel-Rail Contact Region for Absolute Force Input

The force transmitted through the contact region to the structure will now be different for the wheel and the rail, denoted by P^W_j and P^R_j respectively, with:-

$$P^R_j = P^W_j + F_j \qquad \ldots(89)$$

Equations (83) become

$$\begin{aligned} \{z^R\} &= [\alpha^R]\{P^R\} \\ \{z^{CR}\} &= [\alpha^{CR}]\{P^R\} \\ \{z^{CW}\} &= [\alpha^{CW}]\{P^W\} \\ \{z^W\} &= -[\alpha^W]\{P^W\} \end{aligned} \qquad \ldots(90)$$

The external force $\{F\}$ can be introduced, whilst retaining the relative displacement excitation $\{r\}$ introduced in §6.1.1. Hence from equation (81),

$$\{r\} = \{z^R\} + \{z^{CR}\} + \{z^{CW}\} - \{z^W\} = [\alpha^R+\alpha^{CR}]\{P^R\} + [\alpha^{CW}+\alpha^W]\{P^W\} \qquad \ldots(91)$$

$$\Rightarrow \quad \{r\} = [\alpha^R+\alpha^{CR}]\{F\} + [\alpha]\{P^W\} = -[\alpha^W+\alpha^{CW}]\{F\} + [\alpha]\{P^R\} \qquad \ldots(92)$$

where $[\alpha] = [\alpha^R+\alpha^{CR}+\alpha^W+\alpha^{CW}]$ as before. Thus the response at a general point, X, on the wheel or the rail, can be calculated as

$$z^W_X = -\lfloor\alpha^{WT}\rfloor [\alpha]^{-1} (\{r\} - [\alpha^R+\alpha^{CR}]\{F\}) \qquad \ldots(93a)$$

$$z^R_X = \lfloor\alpha^{RT}\rfloor [\alpha]^{-1} (\{r\} + [\alpha^W+\alpha^{CW}]\{F\}) \qquad \ldots(93b)$$

For $\{r\}=0$, the displacement at the wheel-rail interface, $\{z_o\}$, can be calculated as

$$\{z_o\} = [\alpha^R+\alpha^{CR}]\,[\alpha]^{-1}[\alpha^W+\alpha^{CW}]\,\{F\} = [\alpha^W+\alpha^{CW}]\,[\alpha]^{-1}[\alpha^R+\alpha^{CR}]\,\{F\} \qquad \ldots(94)$$

This has the implication that, in the same way as the relative displacement input (§6.1.1) was equivalent to a mutual force excitation (§6.1.2), the external force excitation is equivalent to an absolute displacement input, in which the contact point experiences a specified absolute displacement $\{z_o\}$. A fuller discussion of the merits of these two representations of the interaction problem will be given in the next chapter, where results from the two models will be compared.

Nevertheless it must be pointed out that the absolute displacement/force input models do not appear to be consistent with Newton's third law, since $\{P^R\} \neq \{P^W\}$ yet there are no external influences acting on the wheel-rail system.

One problem with the above concerns the division of $[\alpha^C]$ into its two components. Feldmann [77] used the following, for his one-degree-of-freedom model:

$$\alpha^{CW} = \alpha^C \left\{ \frac{|\alpha^R|}{|\alpha^W|+|\alpha^R|} \right\} \qquad \alpha^{CR} = \alpha^C \left\{ \frac{|\alpha^W|}{|\alpha^W|+|\alpha^R|} \right\} \qquad \ldots(95)$$

in which $\alpha^{CR} = \alpha^{CW} = \alpha^C/2$ if $|\alpha^W| = |\alpha^R|$. It is claimed that this gives satisfactory behaviour as either $|\alpha^W|$ or $|\alpha^R|$ tend to 0. (For the relative displacement excitation (§6.1.1), this is not a problem as the two receptances only appear together).

6.1.4 Model including Two Wheels on an Axle

The model used so far has assumed that the wheel under study is excited in isolation from all other wheels. However in modelling the wheel receptances it has been found to be important to include modes of the wheelset in which the axle plays a major part (§2). These modes have equal magnitude of vibration on either wheel, and hence are affected by the wheel-rail contact at both ends of the wheelset. This means that studying the excitation of a single wheel in isolation is unlikely to be valid. Coupling of the two rails through the sleepers will not be considered, however, as they are somewhat isolated by the flexibility of the railpad (see Appendix G).

A further index, k=1,2, is now introduced to represent the two ends of the wheelset. Equations (81) and (89) become,

$$z^R_{ik} = z^W_{ik} - z^{CW}_{ik} - z^{CR}_{ik} + r_{ik} \qquad \ldots(96a)$$

$$P^R_{jk} = P^W_{jk} + F_{jk} \qquad \ldots(96b)$$

and equations (90) become

$$\begin{aligned} \{z^R\}_k &= [\alpha^R]_k \{P^R\}_k \\ \{z^{CR}\}_k &= [\alpha^{CR}]_k \{P^R\}_k \\ \{z^{CW}\}_k &= [\alpha^{CW}]_k \{P^W\}_k \\ \{z^W\}_k &= -\sum_{\ell=1}^{2} [\alpha^W]_{k\ell} \{P^W\}_\ell \end{aligned} \qquad \ldots(97)$$

where $[\alpha^W]_{k\ell}$ represents the set of receptances $\alpha^W_{i,jk\ell}$; if $k=\ell$ these are point receptances and if $k\neq\ell$ they are transfer receptances (from one wheel to the other). Hence from equations (96),

$$\{r\}_k = [\alpha^R+\alpha^{CR}]_k \{P^R\}_k + [\alpha^{CW}]_k \{P^W\}_k + \sum_{\ell=1}^{2} [\alpha^W]_{k\ell} \{P^W\}_\ell \quad ...(98)$$

$$\Rightarrow \quad \left[\begin{array}{c|c} [\alpha]_{11} & [\alpha^W]_{12} \\ \hline [\alpha^W]_{21} & [\alpha]_{22} \end{array}\right] \left\{\begin{array}{c} P^W_1 \\ \hline P^W_2 \end{array}\right\} = \left\{\begin{array}{c} r_1 \\ \hline r_2 \end{array}\right\} - \left[\begin{array}{c|c} [\alpha^R+\alpha^{CR}]_1 & 0 \\ \hline 0 & [\alpha^R+\alpha^{CR}]_2 \end{array}\right] \left\{\begin{array}{c} F_1 \\ \hline F_2 \end{array}\right\} \quad ...(99)$$

This equation may be inverted to yield the forces acting on the two wheels, $\{P^W_k\}$,

$$\left\{\begin{array}{c} P^W_1 \\ \hline P^W_2 \end{array}\right\} = \left[\begin{array}{c|c} [\alpha]_{11} & [\alpha^W]_{12} \\ \hline [\alpha^W]_{21} & [\alpha]_{22} \end{array}\right]^{-1} \left(\left\{\begin{array}{c} r_1 \\ \hline r_2 \end{array}\right\} - \left[\begin{array}{c|c} [\alpha^R+\alpha^{CR}]_1 & 0 \\ \hline 0 & [\alpha^R+\alpha^{CR}]_2 \end{array}\right] \left\{\begin{array}{c} F_1 \\ \hline F_2 \end{array}\right\} \right) \quad ...(100)$$

and hence the response, at a general point X on the wheelset, can be derived from the transfer receptances from the two contact points to X,

$$z^W_X = - \left[\alpha^{WT}_1 \mid \alpha^{WT}_2\right] \left\{\begin{array}{c} P^W_1 \\ \hline P^W_2 \end{array}\right\} \quad ...(101)$$

Similarly the forces on the rail can be derived from equation (98)

$$\left[\begin{array}{c|c} [\alpha]_{11} & [\alpha^W]_{12} \\ \hline [\alpha^W]_{21} & [\alpha]_{22} \end{array}\right] \left\{\begin{array}{c} P^R_1 \\ \hline P^R_2 \end{array}\right\} = \left\{\begin{array}{c} r_1 \\ \hline r_2 \end{array}\right\} - \left[\begin{array}{c|c} [\alpha^W+\alpha^{CW}]_{11} & [\alpha^W]_{12} \\ \hline [\alpha^W]_{21} & [\alpha^W+\alpha^{CW}]_{22} \end{array}\right] \left\{\begin{array}{c} F_1 \\ \hline F_2 \end{array}\right\} \quad ...(102)$$

which may similarly be inverted and hence the response at a general point X, on the kth rail

$$z^R_{Xk} = [\alpha^{RT}]_k \{P^R\}_k \quad ...(103)$$

In order to calculate the total response it should be noted that the displacement or force inputs at the two wheels/rails are most likely to be randomly related (incoherent). The response to $\{r\}_1$ and $\{F\}_1$ alone can be calculated by setting $\{r\}_2$ and $\{F\}_2$ to 0. (Note that this solution is different to the single wheel solution as a connection is still made to the second rail). The response to the second set of displacements/forces can be calculated in the same way. Using the principle of superposition, and the incoherence of the two sources, the two cases can be added energy-wise to give the overall level.

6.1.5 Consideration of the Effect of Multiple Wheels on a Rail

A train contains many wheelsets running on the same rails. The rail vibration at the contact point of any wheel is therefore composed of that excited by that wheel-rail interaction, and that transmitted along the rail from other wheel-rail contact points.

In order to consider the effect of multiple wheels running on the same rail, it is sufficient to consider the effect on one wheel-rail interaction of remotely-excited propagating waves in the rail. In particular, to what extent are the waves modified by the wheel-rail contact, producing transmitted and reflected waves, and to what extent is the vibration transmitted into the wheel? The effect of a train of wheelsets can then be derived from a sum of such cases.

Consider a rail with a source of vibrations located at $x<<0$, and a wheel coupled to it at $x=0$ which is assumed to be passive, ie no external forces or displacements act at $x=0$. This is shown in Figure 101. Then an incident wave $u_I(x,\omega)$ can be assumed to propagate from $x<<0$ in the positive x direction, generating interaction forces $\{P\}$ at $x=0$ as shown in Figure 101. The total motion of the rail, $u(x,\omega)$, can be decomposed into in the incident wave, $u_I(x,\omega)$, and a generated wave, $u_G(x,\omega)$ produced by the forces $\{P\}$. If $[\alpha^R]$ are the receptances of the rail at $x=0$, and $[\alpha']=[\alpha^W]+[\alpha^C]$ is the combined receptance of the wheel and contact spring at $x=0$, the forces $\{P\}$ can be derived from

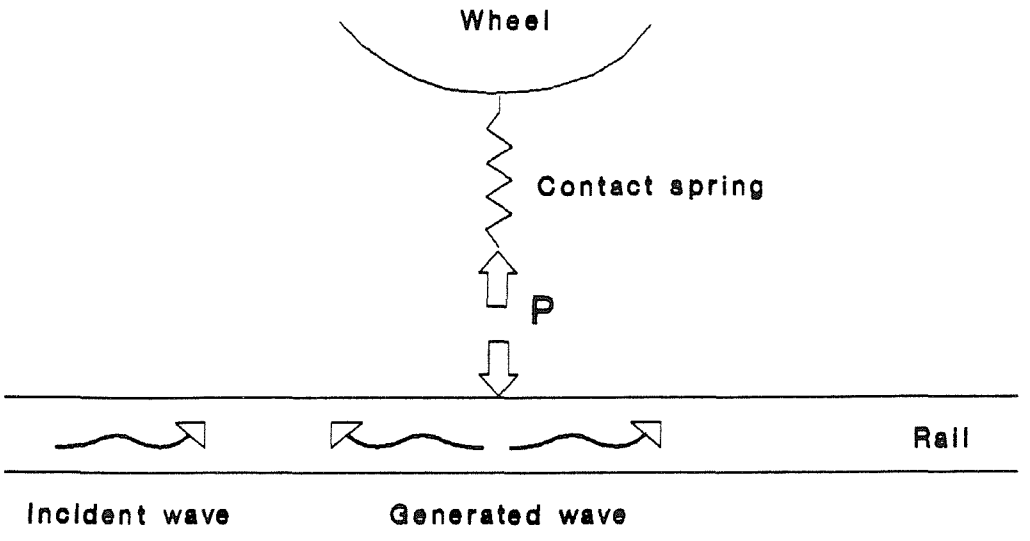

Figure 101 Effect of a Wheel on Wave Propagation in the Rail

$$\{u(0)\} = [\alpha'] \{P\} \quad \ldots(104a)$$

and $$\{u_G(0)\} = - [\alpha^R] \{P\} \quad \ldots(104b)$$

$$\Rightarrow \quad \{u_I(0)\} = \{u(0)\} - \{u_G(0)\} = ([\alpha'] + [\alpha^R]) \{P\} = [\alpha] \{P\} \quad \ldots(105)$$

$$\Rightarrow \quad \{P\} = [\alpha]^{-1} \{u_I(0)\} \quad \ldots(106)$$

which is identical in form to the relative displacement-input (equation (85), §6.1.1). Thus the vibration in the rail due to other wheels adds to the roughness displacement at x=0. (NB The rail receptances $[\alpha^R]$ will actually be modified slightly by the presence of the various other wheels resting on the rail).

It should be noted that, in general, there will be a phase difference between the roughness input and the secondary rail waves so that cancellation as well as reinforcement can occur, depending on the frequency. On average, however, the total vibration energy in the rail can be estimated from the sum of the energies of the vibration from each wheel-rail excitation.

The incident wave will consist of a sum of wavetypes at each frequency (see §5), which will all have a non-zero decay rate along the rail due to damping. Measurements of these decay rates [70] have shown that they are in the region of 0.5-2 dB/m, and predictions in §5 agree with this. For a train of bogied coaches where the wheels are arranged typically as shown in Figure 102, this means that the effect of one wheel on another can be ignored for wheels at opposite ends of a coach

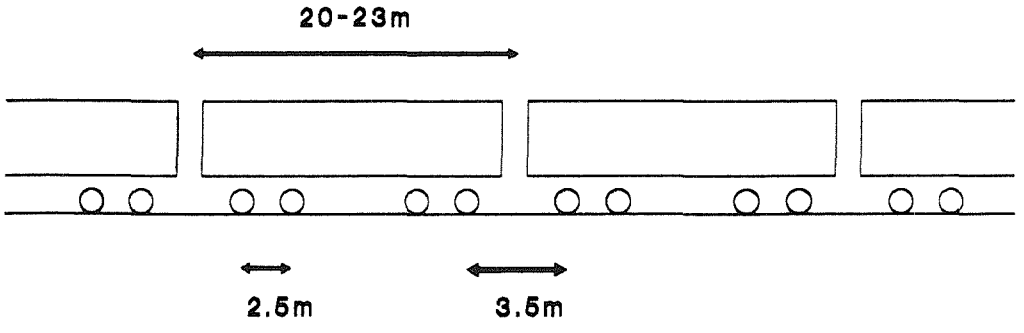

Figure 102 Typical Wheel Arrangement

(typically 15 m apart) as the amplitudes of the waves will mostly be more than 10 dB below that of the roughness amplitude. However, consideration perhaps needs to be given to the interaction of adjacent wheels in the same bogie or in a pair of adjacent bogies where a typical wheel separation is 2.5-3.5 m. The details will depend on the exact separations of the wheels in comparison to the (frequency-dependent) wavelengths of the various waves. No further work has been done on this effect here.

As noted above, this effect is not likely to affect the overall noise radiated by the rail, but may alter its detailed distribution in the vicinity of a train. It is therefore of a secondary nature.

6.2 RECEPTANCES OF THE CONTACT ZONE

The equations of wheel-rail interaction presented in §6.1 require receptance matrices for the wheel $[\alpha^W]$, the rail $[\alpha^R]$ and the contact zone $[\alpha^C]$. Models of the wheel and rail receptances have already been developed (in §2 and §5 respectively). For the contact zone these have not yet been fully developed, although an initial representation was given in §3. The next part of this chapter is concerned with the development of representations of these contact receptances.

Appendix E contains a review of the traditional contact theory of Hertz, and the theory of creep forces between rolling bodies developed by Kalker. It goes on to discuss the use of frequency-dependent creep coefficients for higher frequency phenomena, and develops approximate formulae for these coefficients. Interestingly it is found that the lateral frequency-dependent creep coefficient C^*_{22} is quite well represented by a lateral contact spring and a creep force damper in series, as used in §3. For the spin creep coefficient C^*_{33}, and the lateral-spin cross coefficient C^*_{23}, more complex approximations are necessary.

A coordinate system will be used which allows relative motion between the wheel and rail in 6 degrees of freedom at the contact patch: three translations, denoted by $z_1 \ldots z_3$ and three rotations, $z_4 \ldots z_6$, as shown in Figure 103, with the coordinate axes set parallel/perpendicular to the contact surface. The interaction forces can be resolved into these three coordinate directions, $P_1 \ldots P_3$, with corresponding moments, $P_4 \ldots P_6$. For a linearised set of equations of motion these can be expressed as a 6×6 matrix of receptances

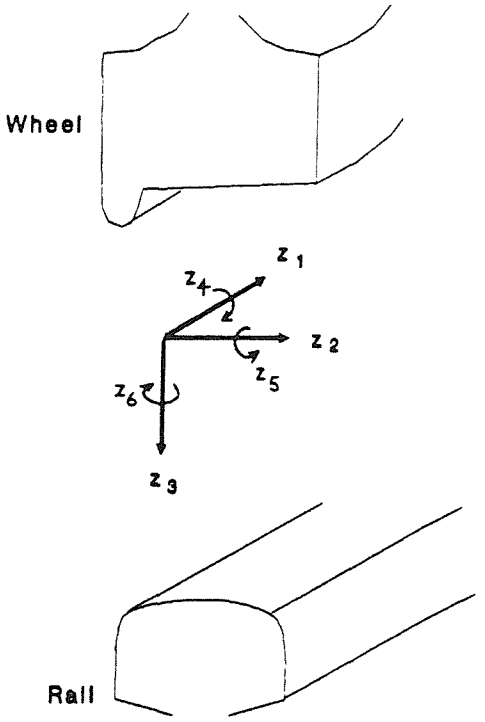

Figure 103 Coordinate System at Wheel-Rail Contact

$$[\alpha^C]\ \{P\} = \{z^C\} \qquad \ldots(107)$$

This section, therefore, aims to derive the 36 elements of the $[\alpha^C]$ matrix which has been used in the formulation of §6.1.

6.2.1 Vertical Displacement

The vertical displacement, z^C_3, (normal to the surface) is related simply to the vertical contact force, P_3, by the Hertzian contact spring, which has been given in linearised form in Appendix E. Thus, from equation (E3), the receptances are given by

$$\alpha^C_{33} = \frac{1}{k_H} = \frac{\xi}{2}\left(\frac{2}{3\ E^{*2}\ R_e\ P_o}\right)^{1/3} \qquad \ldots(108)$$

where E^* is the plain strain elastic modulus, and P_o is the static wheel load. ξ is a dimensionless quantity dependent on the radii of curvature (values of ξ are given in Table E1). R_e is an effective radius of curvature of the surfaces in contact, defined in Appendix E.

All other terms of this row of $[\alpha^C]$ are zero, $\alpha^C_{3j}=0$ $j\neq3$, as shown in Table 12 (third row).

Table 12 Receptance Matrix for Contact Zone

$$\begin{bmatrix} \frac{V}{i\omega Ec^2 C^*_{11}} & 0 & -\frac{2\bar{\gamma}_1 V}{3i\omega P_o} & 0 & 0 & 0 \\ 0 & \frac{VC^*_{33}}{i\omega Ec^2 S_1} & \frac{VS_4}{3i\omega P_o S_1} & 0 & 0 & -\frac{VC^*_{23}}{i\omega Ec^3 S_1} \\ 0 & 0 & \frac{\xi}{2}\left(\frac{2}{3E^{*2}R_e P_o}\right)^{1/3} & 0 & 0 & 0 \\ 0 & 0 & 0 & \frac{1}{P_o R'} & 0 & 0 \\ 0 & 0 & 0 & 0 & \frac{-1}{P_o R''} & 0 \\ 0 & \frac{VC^*_{23}}{i\omega Ec^3 S_1} & \frac{VS_5}{3i\omega P_o c S_1} & 0 & 0 & \frac{VC^*_{22}}{i\omega Ec^4 S_1} \end{bmatrix}$$

Key

$\bar{\gamma}_1$, $\bar{\gamma}_2$, $\bar{\omega}_3$ are steady-state components of the creepages in the z_1, z_2 and z_6 directions respectively.

$S_1 = C^*_{22} C^*_{33} + C^*_{23} C^*_{23}$

$S_4 = \bar{\omega}_3 c C^*_{23} C^*_{33} - \bar{\gamma}_2 (2C^*_{22} C^*_{33} + 3C^*_{23} C^*_{23})$

$S_5 = \bar{\gamma}_2 C^*_{22} C^*_{23} - \bar{\omega}_3 c (4C^*_{22} C^*_{33} + 3C^*_{23} C^*_{23})$

$$\frac{1}{R'} = \frac{1}{R_{12}} + \frac{1}{R_{22}} \qquad \frac{1}{R''} = \frac{1}{R_{11}} + \frac{1}{R_{21}}$$

6.2.2 Longitudinal Displacement

The longitudinal displacement is given in terms of the longitudinal creep force in Appendix E (§E.3.1), and approximations for the frequency-dependent creep coefficients are given in §E.4. Combining these results gives,

$$P_1 = E\,ab\,C^*_{11}\,\gamma_1 = E\,c^2\,C^*_{11}\,\frac{\dot{z}_{c_1}}{V} \qquad \ldots(109)$$

where $\dot{}$ denotes differentiation by time (ie velocity), a and b are the semi-axis lengths of the contact patch ($c=\sqrt{ab}$), V is the train speed and C^*_{11} is the frequency-dependent creep coefficient. It should be noted that c^2 depends on the normal load P_3. This means that if the creepage γ_1 is separated into a constant creepage $\bar{\gamma}_1$, superimposed on top of which are small harmonic variations $\Delta\gamma_1$, a harmonic increment of

vertical force will also enter equation (109). Thus taking increments, and ignoring the products of small quantities, gives

$$\Delta P_1 = E \frac{\delta(c^2)}{\delta P_3} C^*_{11} \bar{\gamma}_1 \Delta P_3 + E c^2 C^*_{11} \frac{\Delta \dot{z} C_1}{V} \qquad \ldots(110)$$

since from Appendix E (equations (E19,E22)) $\omega C/k_T$ and hence C^*_{11} are not dependent on P_3. Now from equations (E4):-

$$\frac{\delta(c^n)}{\delta P_3} = \frac{n}{3} P_3^{n/3-1} \mu\sigma \left(\frac{3 R_e}{2 E^*}\right)^{n/3} = \frac{nc^n}{3P_3} \simeq \frac{nc^n}{3P_o} \qquad \ldots(111)$$

Thus

$$\Delta P_1 = E c^2 C^*_{11} \left(\frac{2}{3P_o} \bar{\gamma}_1 \Delta P_3 + \frac{\Delta \dot{z} C_1}{V} \right) \qquad \ldots(112)$$

$$\Rightarrow \quad \Delta \dot{z} C_1 = \frac{V}{E c^2 C^*_{11}} \Delta P_1 - \frac{2 \bar{\gamma}_1 V}{3 P_o} \Delta P_3 \qquad \ldots(113)$$

from which the receptances shown in the first row of Table 12 can be derived.

It may be noted, from this, that an oscillating vertical load can excite longitudinal vibrations if a steady longitudinal creep is present, such as in traction or braking.

6.2.3 Lateral and Spin Displacements

The lateral and spin displacements are coupled, and so will be dealt with together. From Appendix E, combining the results of §E.3.2 and §E.4,

$$P_2 = Ec^2 (C^*_{22} \gamma_2 + c C^*_{23} \omega_3) = \frac{Ec^2}{V} \left(C^*_{22} \dot{z} C_2 + c C^*_{23} \dot{z} C_6 \right) \qquad \ldots(114)$$

and

$$P_6 = Ec^3 (-C^*_{23} \gamma_2 + c C^*_{33} \omega_3) = \frac{Ec^3}{V} \left(-C^*_{23} \dot{z} C_2 + c C^*_{33} \dot{z} C_6 \right) \qquad \ldots(115)$$

It should be noted once more that c depends on the normal load P_3. This means that if the creepages γ_2 and ω_3 are separated into a constant creepage $\bar{\gamma}_2$ and $\bar{\omega}_3$, superimposed on top of which are small harmonic variations $\Delta\gamma_2$ and $\Delta\omega_3$, harmonic increments of vertical force

will also enter equations (114,115). Thus taking increments and ignoring the products of small quantities gives

$$\Delta P_2 = \frac{Ec^2}{V}\left(C^*_{22}\,\Delta\dot{z}^C_2 + c\,C^*_{23}\,\Delta\dot{z}^C_6 \right) + E\left(C^*_{22}\,\bar{\gamma}_2\,\frac{\delta(c^2)}{\delta P_3} + C^*_{23}\,\bar{\omega}_3\,\frac{\delta(c^3)}{\delta P_3} \right)\Delta P_3 \qquad \ldots(116)$$

and

$$\Delta P_6 = \frac{Ec^3}{V}\left(-C^*_{23}\,\Delta\dot{z}^C_2 + c\,C^*_{33}\,\Delta\dot{z}^C_6 \right) + E\left(-C^*_{23}\,\bar{\gamma}_2\,\frac{\delta(c^3)}{\delta P_3} + C^*_{33}\,\bar{\omega}_3\,\frac{\delta(c^4)}{\delta P_3} \right)\Delta P_3 \qquad \ldots(117)$$

Substituting equation (111) into equation (116) and rearranging gives

$$C^*_{22}\,\Delta\dot{z}^C_2 + c\,C^*_{23}\,\Delta\dot{z}^C_6 = \frac{V}{Ec^2}\Delta P_2 - \left(C^*_{22}\,\bar{\gamma}_2\,\frac{2V}{3P_o} + C^*_{23}\,\bar{\omega}_3\,\frac{Vc}{P_o} \right)\Delta P_3 \qquad \ldots(118)$$

and similarly from equation (117)

$$-C^*_{23}\,\Delta\dot{z}^C_2 + c\,C^*_{33}\,\Delta\dot{z}^C_6 = \frac{V}{Ec^3}\Delta P_6 + \left(C^*_{23}\,\bar{\gamma}_2\,\frac{V}{P_o} - C^*_{33}\,\bar{\omega}_3\,\frac{4Vc}{3P_o} \right)\Delta P_3 \qquad \ldots(119)$$

Eliminating $\Delta\dot{z}^C_6$, from equations (118,119) gives

$$(C^*_{22}\,C^*_{33} + C^*_{23}\,C^*_{23})\,\Delta\dot{z}^C_2 = \frac{VC^*_{33}}{Ec^2}\Delta P_2 - \frac{VC^*_{23}}{Ec^3}\Delta P_6 - \frac{V\bar{\gamma}_2}{P_o}\left(\frac{2}{3}\,C^*_{22}\,C^*_{33} + C^*_{23}\,C^*_{23} \right)\Delta P_3 + \frac{V\bar{\omega}_3 c}{3P_o}\,C^*_{23}\,C^*_{33}\,\Delta P_3 \qquad \ldots(120)$$

from which the receptances given in the second row of Table 12 are derived. Similarly eliminating $\Delta\dot{z}^C_2$,

$$c\,(C^*_{23}\,C^*_{23} + C^*_{22}\,C^*_{33})\,\Delta\ddot{c}_6 = \frac{V\,C^*_{23}}{Ec^2}\,\Delta P_2 + \frac{V\,C^*_{22}}{Ec^3}\,\Delta P_6$$

$$- \frac{V\bar{\omega}_3 c}{P_o}\left(C^*_{23}\,C^*_{23} + \frac{4}{3}\,C^*_{22}\,C^*_{33}\right)\Delta P_3 + \frac{V\bar{\gamma}_2}{3P_o}\,C^*_{22}\,C^*_{23}\,\Delta P_3 \quad \ldots(121)$$

from which the receptances given in the sixth row of Table 12 are derived.

It may be noted that a steady lateral creepage, $\bar{\gamma}_2$, occurs when a wheelset is misaligned (yawed) or during curving, whereas a steady spin creepage, $\bar{\omega}_3$, occurs when a wheel is coned. All wheels are coned, to varying degrees - a new wheel profile is coned at 1:20, whereas on a worn profile the cone angle reduces. Thus in general the cross terms α^{C}_{23} and α^{C}_{63} are non-zero, a feature which was not taken into account earlier (§3).

6.2.4 Angular Coordinates

The two remaining coordinates to be considered are z^{C}_4 (rotation about the longitudinal axis) and z^{C}_5 (rotation about the lateral axis). Creep forces do not act in these coordinate directions, and so the only forces generated will be moments resulting from a movement in the position of the contact patch as the wheel and rail move relative to each other, ie due to geometric considerations. Nevertheless they can be expressed as receptances.

This arrangement is shown diagrammatically in Figure 104. For a rotation θ_W of the wheel, and/or θ_R of the rail, the contact point moves a distance Y on the rail and the wheel, where

$$Y = (\theta_W - \theta_R)\,\frac{R_{12}\,R_{22}}{R_{12} + R_{22}} \quad \ldots(122)$$

where R_{22} is the radius of curvature of the rail, and R_{12} is the radius of curvature of the wheel profile. In addition, for lateral displacements y_W of the wheel, and/or y_R of the rail, the contact point moves by Y_R on the rail and Y_W on the wheel, where

$$Y_R = (y_W - y_R)\,\frac{R_{22}}{R_{12} + R_{22}} \qquad Y_W = -(y_W - y_R)\,\frac{R_{12}}{R_{12} + R_{22}} \quad \ldots(123)$$

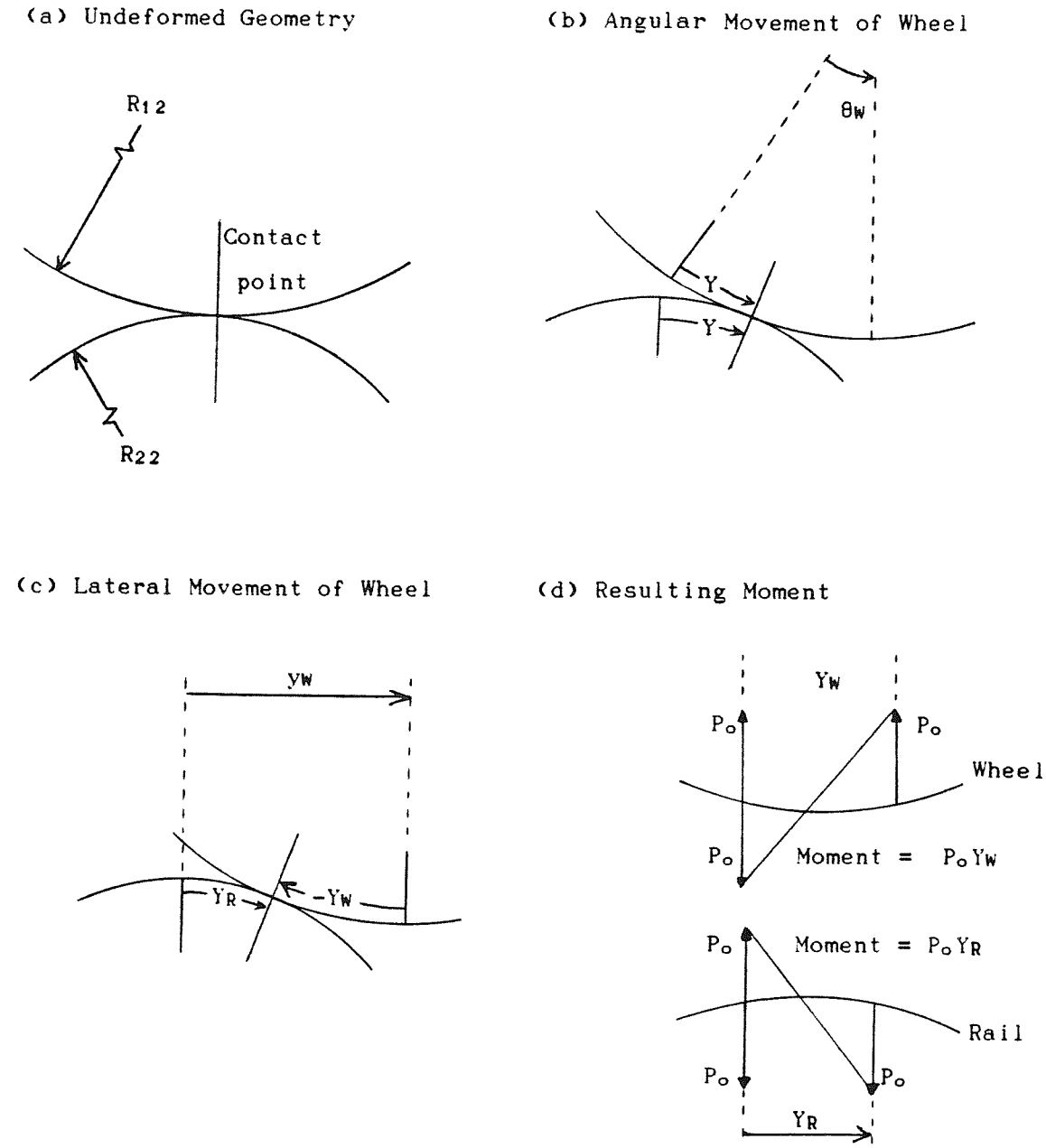

Figure 104 Generation of Twist (P_4) Moments by Relative Motion at the Contact

Thus the total moments acting are

$$P^R_4 = P_o \left\{ z^C_4 + \frac{z^C_2}{R_{12}} \right\} \frac{R_{12}\, R_{22}}{R_{12} + R_{22}} \qquad P^W_4 = P_o \left\{ z^C_4 - \frac{z^C_2}{R_{22}} \right\} \frac{R_{12}\, R_{22}}{R_{12} + R_{22}} \qquad \ldots(124)$$

making use of $z^C_2 = y_W - y_R$ and $z^C_4 = \theta_W - \theta_R$. These equations can be seen to consist of a receptance part (α^C_{44}), relating to z^C_4 which has an equal and opposite effect on the wheel and rail, and a term involving z^C_2 which is different for the wheel and rail. In the particular case $R_{12}=\infty$ (wheel surface not curved), this second term only acts on the wheel. Only the receptance part is given in Table 12.

Similar results hold for the other angular coordinate, from which

$$P^R_5 = - P_o \{ R_{11}\, z^C_5 - z^C_1 \} \qquad P^W_5 = - P_o\, R_{11}\, z^C_5 \qquad \ldots(125)$$

as one radius of curvature (R_{21}) will be infinite.

Figure 105 compares α^C_{44} and α^C_{55} with the corresponding wheel and rail receptances, from which it can be seen that the wheel-rail connection in these two coordinate directions is very soft, particularly so for the z_5 direction. This suggests that their inclusion or omission is unlikely to have a strong influence on the wheel-rail contact.

6.3 METHODS OF EXCITATION

In §6.1, equations for two types of excitation at the wheel-rail interface were derived:-

(i) relative displacement inputs {r} (shown in Figure 99), or equivalently mutual force inputs {P} (or combinations of them as in §6.1.2).

(ii) external force inputs {F} (shown in Figure 100), or equivalently absolute displacement inputs $\{z_o\}$.

Various inputs of both types are possible, and several will be discussed in this section. Excitation by the roughness profile (as a relative displacement input) was the basis of Remington's model [20], and was studied initally in §3. However several of the inputs which will be mentioned are based in some way on the surface profiles of the wheel and rail.

(a) Twist (z_4) Receptance

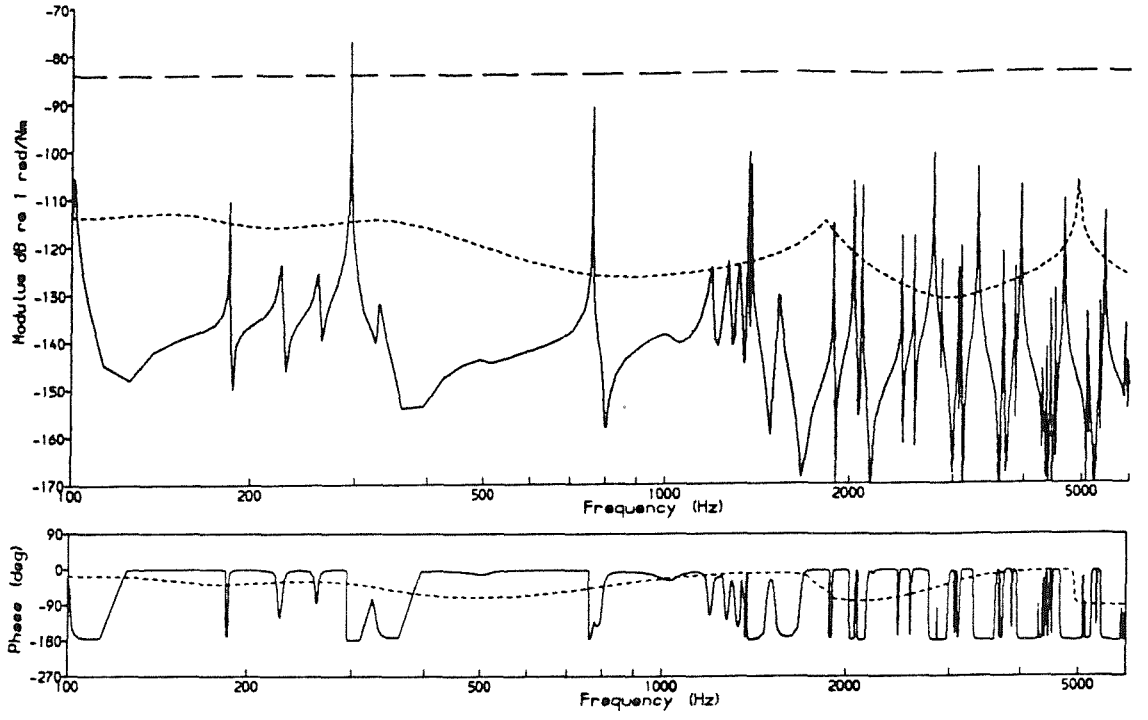

(b) Roll (z_5) Receptance

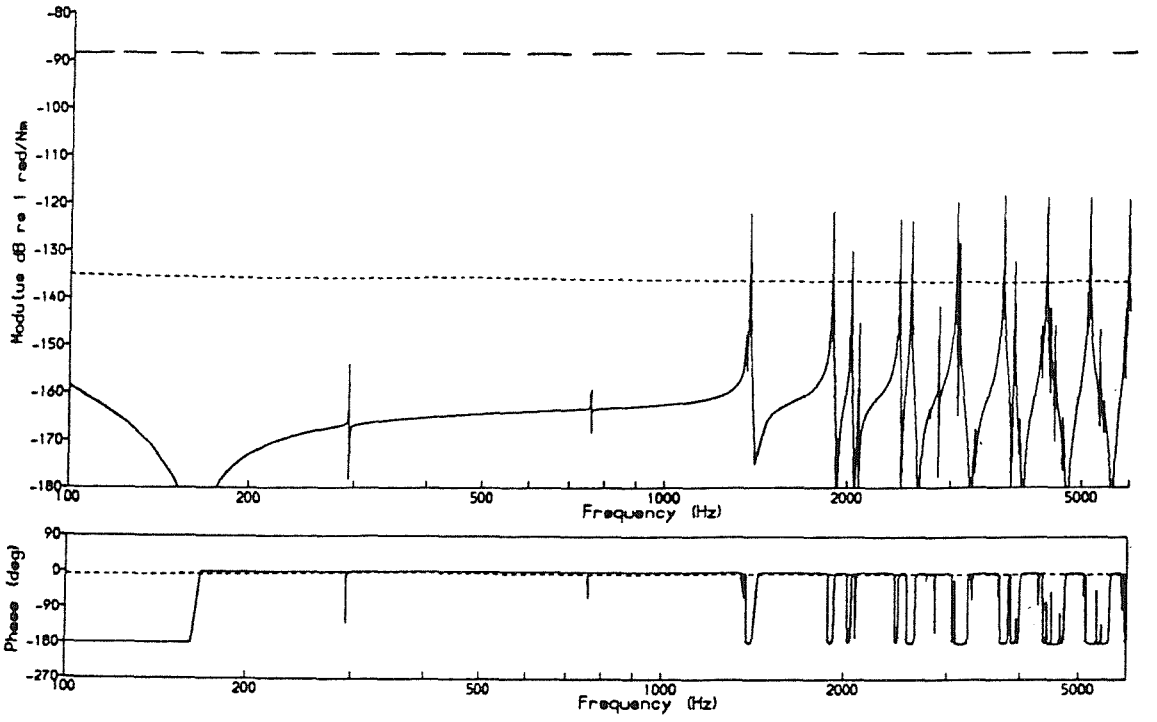

Figure 105 Point Receptances in Rotational Coordinates

(——— Wheel, ····· Rail, — — Contact)

This leads to a requirement for valid measurements of the surface profiles of wheels and rails. Although a number of roughness profile measuring devices are available, which use a variety of measuring techniques, the validity of their measurements has not been completely proven.

For the rail, an experiment was conducted recently to compare 7 roughness measuring devices [100]. While a good level of agreement was achieved for the amplitudes and wavelengths of rail corrugation, there was, unfortunately, little agreement between them for shorter wavelengths or for rails with smaller amplitudes of roughness. For the wheel, such a detailed comparison between different systems has not yet been made. A major problem, in both cases, lies in finding a reliable reference measurement.

There is clearly a need for further development and validation of roughness measuring capability, if complete validation of theoretical models is to be achieved, but this is, unfortunately, beyond the scope of this thesis.

6.3.1 Roughness Profile

It is generally held that variations in the vertical height of the roughness of either surface (wheel or rail) introduce a relative displacement input to the system, as shown in Figure 99. This has been considered already in §3 - see in particular §3.1.4 for a discussion of data analysis requirements for surface roughnesses, and Appendix A for details of the analysis carried out in conjunction with the experimental data which is used for validating the current theoretical modelling.

As mentioned in §3, questions concerning the analysis of roughness data have largely been avoided in the current study, by the use of predictions for a unit roughness input, ie predicting the transfer function between roughness and vibration.

It should be noted that Feldmann [77] assumed that, at low frequencies, the roughness provided an absolute displacement input $\{z_o\}$, rather than a relative input $\{r\}$ (see §6.1). At higher frequencies an alternative impact model was used (see below).

6.3.2 Changes in Lateral Position of Wheel-Rail Contact

The roughness profile of the wheel and rail is more than a variation in height along the length; there are also variations in

height in the lateral direction. Data on the extent of such variations are not nearly so common as measurements of the overall profile.

A simple model of this (used by Valdivia [87]) is to represent the surface r(x,y) (where x is in the direction of travel, and y is across the rail) by a parabola with coefficients varying with distance:-

$$r(x,y) = r(x) + y\,\alpha(x) + y^2\,\beta(x) \qquad \ldots(126)$$

Thus r(x) represents the height of the surface at the usual contact line (y=0), $\alpha(x)$ represents a slope at y=0, and $\beta(x)$ introduces the curvature. The peak position, ε, is given by,

$$\frac{\partial r(x,\varepsilon)}{\partial y} = 0 = \alpha(x) + 2\varepsilon\,\beta(x) \quad \Rightarrow \quad \varepsilon(x) = -\frac{\alpha(x)}{2\beta(x)} \qquad \ldots(127)$$

Referring to Figure 104 it may be seen that the movement of the contact point across the wheel-rail interface results in a restoring moment of εP_3, in the coordinate frame based at the usual interface. This moment acts with an equal magnitude but opposite sense on the two bodies (wheel and rail), and thus is a mutual force {P} rather than an external force {F}. If this roughness variation is on the rail, then neglecting the incremental part of P_3 (ΔP_3), this force input is given by

$$\bar{P}_4 = -\varepsilon\,P_o\,\frac{R_{12}}{R_{12}+R_{22}} = -\frac{\varepsilon}{R_{22}\,\alpha c_{44}} \qquad \ldots(128a)$$

or if the roughness variation is on the wheel

$$\bar{P}_4 = \varepsilon\,P_o\,\frac{R_{22}}{R_{12}+R_{22}} = \frac{\varepsilon}{R_{12}\,\alpha c_{44}} \qquad \ldots(128b)$$

In order to apply this force input in one coordinate (P_4) with the other force components unknown, the analysis of §6.1.2 should be used. Neglected in the above are any changes in the contact patch size and/or shape due to the lateral movement of the contact patch.

6.3.3 Other Variations in Contact Parameters

For completeness, three other forms of excitation are mentioned in this section, but will not be considered further, due to their complex nature.

(a) Longitudinal Changes in Contact Position

In a similar manner to the lateral movement of the contact patch considered above, the position of the contact patch may oscillate in the longitudinal direction, due to the gradient of the roughness profile. On a rising gradient the contact patch will move forwards; on a falling gradient it will move towards the rear. This results in a similar equation to above (assuming $R_{21}=\infty$),

$$\bar{P}_5 = - \chi P_o \qquad \ldots(129)$$

where for a roughness profile of $r(x) = r_o \sin\left(\frac{2\pi x}{\lambda}\right)$, the movement of the contact patch, χ, is given by,

$$\chi = \frac{2\pi}{\lambda} r_o R_{11} \cos\left(\frac{2\pi x}{\lambda}\right) \qquad \ldots(130)$$

The gradient of the roughness, χ, can be derived from above, or directly from the roughness profile. It should be noted that $2\pi/\lambda=\omega/V$, and hence the effect increases as frequency increases. However, when the wavelength approaches the length of the contact patch, or the curvature of the roughness approaches that of the wheel (R_{11}), the assumptions break down.

Because of the limits to the range of validity of the assumptions, such second-order effects as this are probably best investigated using a time domain model of the wheel-rail interaction.

(b) Variations in Contact Patch Size and Shape

As the roughness, $r(x,y)$, introduces variations in curvature in both x and y directions, this leads to changes in the size and shape of the contact patch, represented by the parameters $c=\sqrt{(ab)}$ and $g=a/b$. These in turn influence the creep forces. Unfortunately the resulting equations are complicated, and depend on the derivatives of the frequency-dependent creep coefficients $\frac{\delta C^*_{pq}}{\delta c}$ and $\frac{\delta C^*_{pq}}{\delta g}$. Since these coefficients are only defined by approximations in the current work, their derivatives will contain greater inaccuracies. Furthermore, data on the variations $r(x,y)$ are needed to assess the extent of the effect.

For more details of this effect, refer to Valdivia [87]. It may be noted that it will generate a relative (rather than an absolute) force input, since the variations in c and g influence the mutual forces $\{P\}$ acting on both the wheel and the rail.

(c) Parametric Excitation

It is possible that a completely smooth rail (or wheel) surface may contain variations in material properties, such as hardness or elasticity. In particular, corrugated rails have been found to contain variations in material properties, resulting from plastic deformation of the rail during corrugation formation. When corrugated rails are ground smooth, it is possible, if the grinding is not deep enough, that residual variations in material properties can be left.

The value of the Young's modulus of the surfaces, E, enters the equations for k_H, and C_{pq}, and hence is contained in most of the contact receptances αc_{ij} in Table 12. The resulting excitation equations are therefore difficult to derive. No attempt will be made to do so as, in addition, such variations in material properties are also very difficult to measure. Once more it is expected that a relative force/displacement input will ensue.

6.3.4 Feldmann's Impact Model

Feldmann [77] modelled a cylinder rolling on two parallel beams, and found that an external force input model gave a better representation of the vibration of the rolling body and track than a relative displacement input. At low frequencies, the roughness displacement was used as an absolute displacement input (as already mentioned). At high frequencies a different mechanism was used which is based on the assumption that impacts occur due to roughness asperities.

In order to calculate these impacts, the roughness profile was converted into an equivalent single (triangular) asperity, with height and gradient derived from the averages over a certain sample length. The time history of the impact force was then derived from impact theory, and converted into a frequency spectrum. The impact was calculated assuming that the two bodies acted as rigid masses, since it was found that inclusion of their flexibility into the impact equations led to a much poorer agreement with the final response.

The impact generated a broad-band excitation, so that the wavelength of the roughness no longer corresponded to the frequency of excitation according to $\omega=2\pi V/\lambda$ (equation (16)). Increasing the speed tended to increase the frequency of the peak force, but only in proportion to $V^{1/5}$.

For the wheel-rail case, it should be noted that the static load is much greater than for Feldmann's cylinder (which was only loaded by its self-weight). This has the effect of lengthening the contact patch, so that the impact geometry becomes much more complicated, and also reducing the likelihood of loss of contact.

Feldmann's calculation will not be repeated here, but the significance of relative and absolute force and displacement inputs will be studied in the next chapter, which should give some indication of their applicability to the wheel-rail case.

If the absolute input model appears unjustified, it would still be possible to use the impact theory of Feldmann by applying it to a relative force input in the vertical direction (whilst maintaining the displacement constraint in other degrees of freedom - see §6.1.2).

6.4 CONCLUSIONS

A general linear theory of wheel-rail interaction has been developed which allows for the inclusion of any number of coupling degrees of freedom. Excitation may be due to a relative displacement, a mutual force, an absolute displacement or an external force (or a combination of these). This allows the various excitation models, and in particular those of Remington and Feldmann, to be compared directly. Allowance has also been made for the effects of coupling through the axle to the other wheel.

In addition the relative motion in the contact region has been modelled using a receptance matrix. The components of this matrix have been developed for 6 degrees of freedom (3 translations and 3 rotations), whereas previous studies (including Remington [18,20] and in §3) used only 2. These receptances include the effects of the (linearised) Hertzian contact spring, and Kalker's creep force formulation including approximations for the frequency-dependence of the creep coefficients. The effects of steady creepages on the dynamic behaviour have also been included. These models are therefore very comprehensive in comparison with previous models of wheel-rail noise generation.

The application of Feldmann's impact theory to the wheel-rail case has been given initial consideration here, but it will require further work to consider fully its relevance to the wheel-rail case.

As well as direct roughness excitation, equations have been derived for the effect of the lateral movement of the contact patch as

a possible excitation mechanism. Other excitation mechanisms have been mentioned, but not considered in detail: parametric excitation due to variations in material properties, and the effects of the surface profiles on the contact patch size, shape and longitudinal position. In order to study such secondary mechanisms, it would be preferable to use a time domain model of the wheel-rail contact problem. In addition much more detailed data of wheel and rail profiles in 2 dimensions would be necessary.

The source of the excitation, in almost all cases considered, is the surface profile of the wheel and rail. Although measurements of these are available, further work is required in developing and validating the measurements of surface roughnesses, and the analytical modification of these measurements to provide the correct input to the theory.

CHAPTER 7

RESULTS USING THE FULL INTERACTION MODEL

7.1 INTRODUCTION

7.1.1 Developments of the Interaction Model Studied in §3

In §3, an initial investigation was presented of the wheel-rail interaction. Following the work of Remington [20], the coupling between the wheel and the rail consisted of two degrees of freedom (vertical and lateral), the excitation being a relative displacement input due to the surface roughness. Several refinements were included within the original Remington framework, such as more accurate wheel receptances, finer frequency resolution, and a representation of the lateral coupling, based on creep forces. This model was run for an extensive range of parameters, to investigate the relative importance of the various inputs.

However, in comparison with measured data, this basic interaction model was found to be only partially successful in predicting the vibration behaviour of the wheel and rail from the surface roughness. Therefore, several parts of the model have been substantially developed in subsequent chapters.

Consideration of the effects of wheel rotation, in §4, produced significant improvements to the form of the wheel response, especially for the axial response of the web. However, it did not appear to resolve all of the discrepancies with the measurements, particularly for the lateral wheel tyre vibration.

For the rail, the development of a periodic structure model, in §5, allowed much more detailed predictions of the receptances to be established. This model also enables more degrees of freedom (up to 6) at the contact to be considered, as well as effects such as the position of the contact point on the rail head to be assessed. Receptances for the rotational coordinates have not actually been presented or verified experimentally, but, nevertheless, they are available.

Similarly in §6, much more general interaction equations and contact receptacnes have been established. These also allow up to 6 degrees of freedom at the contact to be considered, as well as effects such as the influence of steady creepages. Equations for alternative

excitation models have also been formulated, which can be assessed alongside the roughness displacement-input model.

7.1.2 Purpose of this Chapter

This chapter will bring together these various developments. It will present results from the full interaction model, that is for up to 6 degrees of freedom at the contact, incorporating the more detailed rail response model, and the effects of wheel rotation as appropriate.

In order to take advantage of these developments, the wheel receptances, developed in §2 for 2 degrees of freedom, will also be required for up to 6 degrees of freedom. The modal parameters derived from the finite element model allow this, although the results should be treated more tentatively than those which have been confirmed experimentally (as is also the case with the rail). However, as long as the results are used to establish the relative importance of the various coordinates, these tentative results should provide a reasonable basis.

Because of the increasing complexity of the model, it will not be possible to assess as many parameter variations as in §3. However the changes produced by the various additional effects will be assessed, to enable determination of the extent to which the results of §3 remain valid.

As well as the consideration of these extra degrees of freedom, the chapter will also assess the relative importance of other terms, developed in §6, such as the presence of steady creepages, and the connection to the second wheel on an axle. Finally the various alternative forcing mechanisms will be looked at briefly.

Throughout this chapter, the results will be presented, as in §3, in the form of non-dimensional transfer functions from roughness to vibration displacement, ie in dB re 1 m/m. For rotational coordinates the transfer functions are in dB re 1 radian/m, whilst the displacement response to a force input will be in dB re 1 m/N.

7.1.3 Computer Programs

The computer programs used in §3 have been updated to incorporate all of the above features. A similar technique is used: a series of separate programs perform the various tasks, passing data between them in the form of files containing narrow-band spectra. The various programs are:-

- Wheel receptances: as in §2, except that the program reads 6 modal amplitudes and calculates the 21 terms in the upper triangle of the 6×6 receptance matrix, each as a modulus and phase. The effects of wheel rotation on the receptances (§4.2) are also included (by specifying a non-zero train speed). As before, the program selects the frequency spacing in order to ensure that sufficient resolution is achieved around wheel resonances, whilst not using excessive computing time elsewhere.

- Rail receptances: one of two programs is used:
  (a) Simple rail receptances, as used in §3, based on the Euler beam equations. Only the lateral, vertical and cross receptances are calculated.
  (b) Based on the periodic structure model (§5). Separate runs are carried out for the lateral and vertical/longitudinal vibrations. From the output files from these runs, the results are concatenated into a single receptance file containing the 21 terms in the upper triangle of the 6×6 receptance matrix, as for the wheel receptance.

  Both rail receptance programs determine their own frequency spacing.

- The wheel and rail are linked by a separate program, which includes the calculation of the contact receptances. The frequency points used are taken from the wheel receptance results, whilst the rail receptances are interpolated as necessary. This program calculates the contact forces, and the wheel and rail response at the wheel-rail interface. Although receptances for the full 6 degrees of freedom are read in, each degree of freedom may be included in, or excluded from, the interaction. The excitation, which may be in any degree of freedom, may be a relative displacement, relative force, absolute displacement, or absolute force or a combination of these.

- The response of the wheel at a point remote from the contact point, can be calculated using a separate wheel response program, as in §3. This also allows the effects of wheel rotation to be included, as in §4.

7.2 INCLUSION OF REVISED RAIL AND CONTACT MODELS

In the initial assessment of the wheel-rail interaction model in §3, simplified models of rail and contact receptances were used. More detailed receptances are now available for these components from the work of §5 and §6 respectively. Therefore, before proceeding in later sections to assess the effects of adding further linking coordinates at the wheel-rail contact, the effects of substituting these more detailed receptances for the simpler ones will be assessed here, using the two-degree-of-freedom model.

Unless otherwise indicated, the same parameters are used here as in the original baseline study of §3, which were listed in Table 2, the corresponding wheel, rail and contact receptances being shown in Figures 18-20.

7.2.1 Effects of Using Improved Contact Receptances

The improvements to the contact receptances, which were described in §6, will be assessed first. For a two-degree-of-freedom wheel-rail interaction, these changes affect only the lateral receptance and the vertical/lateral cross receptance.

The lateral receptance, α^{C}_{22}, was previously based on the creep force damper and Hertzian contact spring in series. In §6 these terms have been expressed, instead, by an approximation to the frequency-dependent creep coefficient, C^{*}_{22}. This has then been slightly modified by the inclusion of extra terms due to the coupling of the lateral and spin creepages (see Table 12).

The vertical/lateral cross receptances were previously set to zero, but in §6 it has been shown that α^{C}_{23} may be non-zero if a steady lateral or spin creep is present (see Table 12). By contrast α^{C}_{32} is always zero.

Results are presented first for the case of no steady creepages. The vertical responses are shown in Figure 106. Comparing them with the original baseline results, which were shown in Figure 21, they are not noticeably affected by using the modified lateral contact receptance, as would be expected from the study of §3. Figure 107 shows that there is also very little difference in the lateral responses (cf Figure 23). It should be remembered that the changes which have been made to the lateral contact receptance are quite small in relation to the dynamic range of the wheel and rail receptances (Figure 19). In

(a) Vertical Rail Vibration Displacement for a Unit Roughness Input

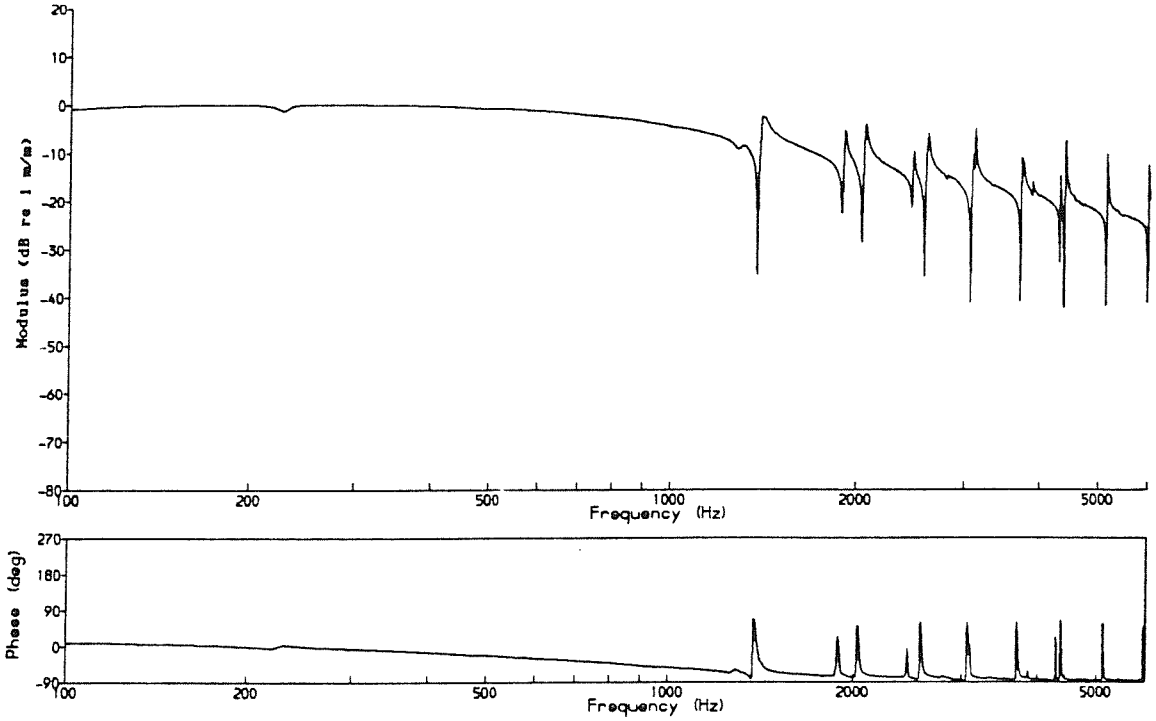

(b) Vertical Wheel Vibration Displacement for a Unit Roughness Input

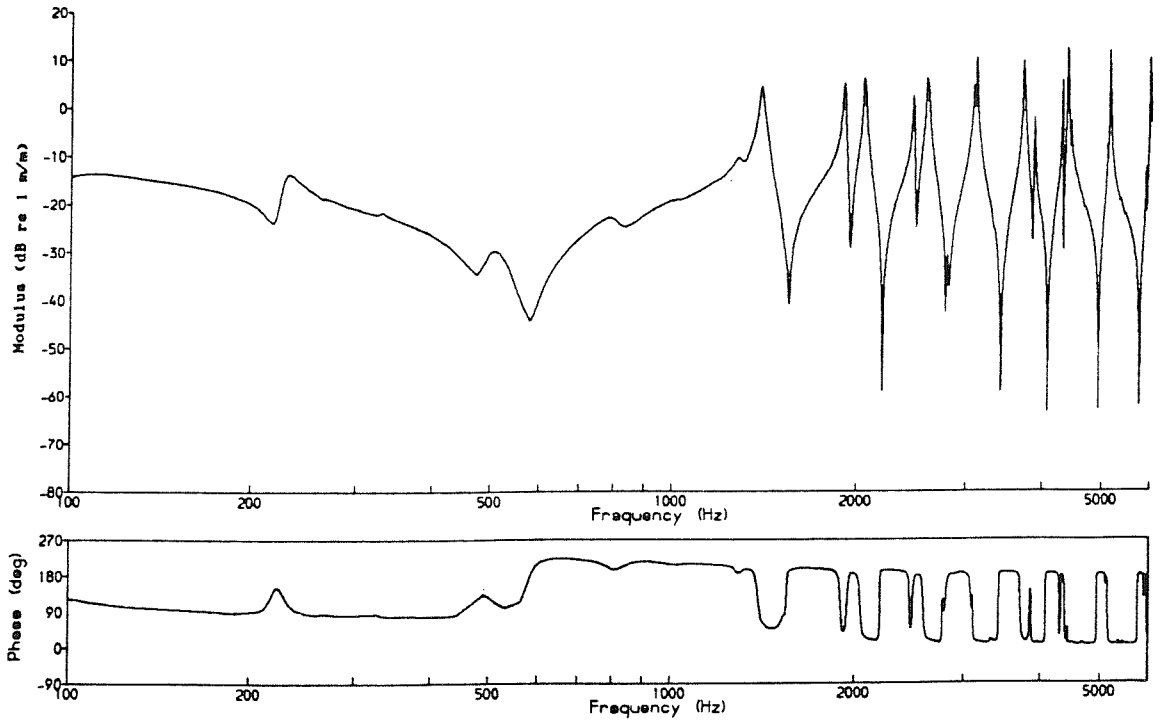

Figure 106 Vertical Responses using Revised Contact Equations with Simple Rail Model

(a) Lateral Rail Vibration Displacement for a Unit Roughness Input

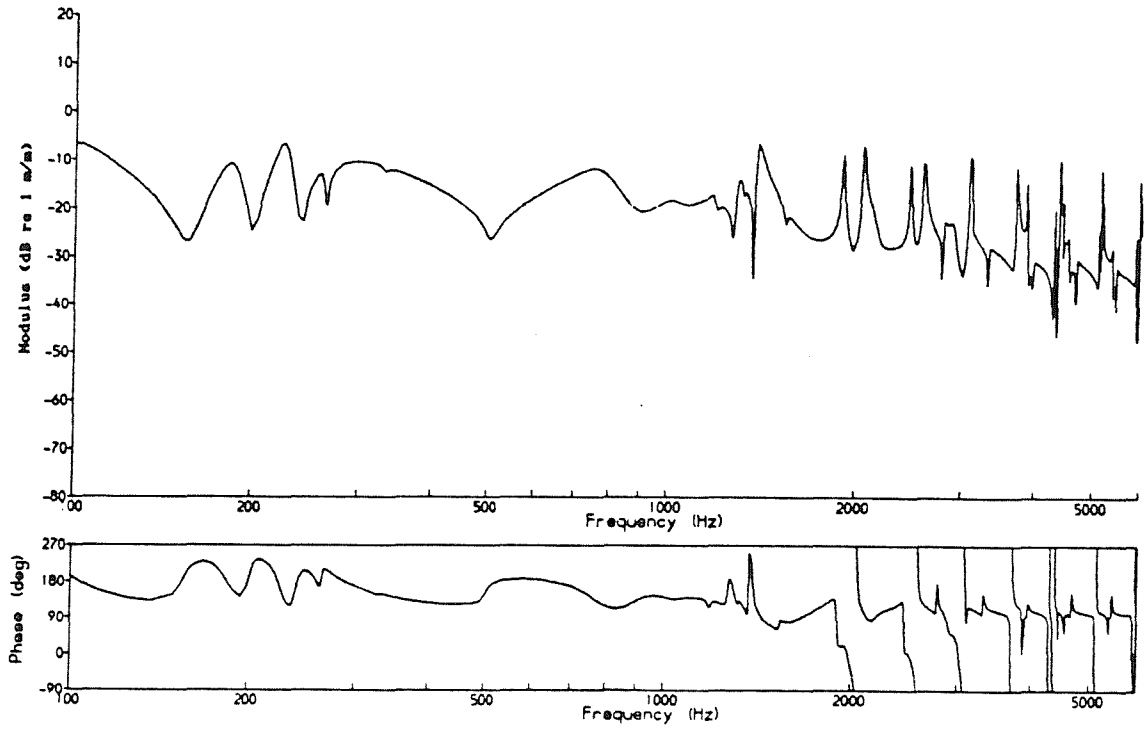

(b) Lateral Wheel Vibration Displacement for a Unit Roughness Input

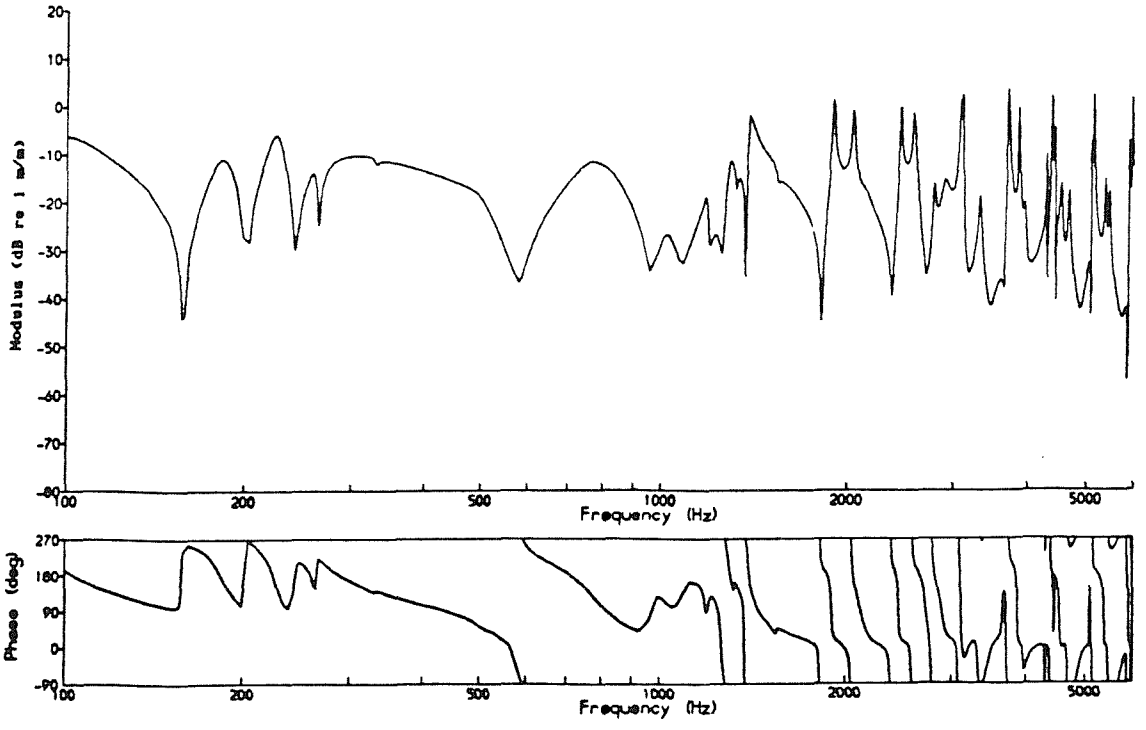

Figure 107 Lateral Responses using Revised Contact Equations with Simple Rail Model

§3.4.3 the lateral contact receptance was found to have a significant effect on the responses only when it was increased by a large amount.

The coning of the wheel introduces a steady spin creepage ($\bar{\omega}_3$). A value of approximately 0.1 rad/m is generated by a 1:20 coning of the surface of the (0.53 m radius) wheel. This value is independent of the train speed†. This level of creepage does not appear to introduce a marked change in the results of this two-degree-of-freedom model.

This is most clearly demonstrated by setting the wheel and rail cross receptances to zero. This has the effect of separating the component of the lateral response which is due solely to the αc_{23} term containing $\bar{\omega}_3$. These results are shown in Figure 108. Since they are less than -40 dB (relative to the roughness), compared to levels of typically up to -10 dB in Figure 107, it can be concluded that this term has little influence for practical levels of $\bar{\omega}_3$.

For the steady lateral creepage ($\bar{\gamma}_2$), a value of 0.001 (0.1%) could be considered as typical without being severe. Repeating the above analysis (ie with wheel and rail cross receptances set to zero) produces a similar picture to Figure 108, but 20-30 dB higher. Figure 109 shows the overall lateral responses (now including the cross receptances). For a positive creepage (ie the wheel moving outwards relative to the rail), the rail response is reduced slightly, whereas the wheel response is increased at most frequencies. A negative creepage (ie in the opposite direction) produces the opposite effect. The vertical responses (not shown) are virtually unaffected.

In conclusion, the αc_{23} term has little effect on the vertical or lateral responses for practical values of creepage. It does not excite the 0-nodal-circle modes (found in measured lateral wheel vibration), as might have been hoped.

7.2.2 Effects of Using Improved Rail Receptances

The improved rail model developed in §5, produced generally higher rail receptances at most frequencies. At higher frequencies, peaks appeared at the cut-on frequencies of various waves. By

†: The creepage is defined as the relative velocity divided by the train speed. This steady spin creepage ($\bar{\omega}_3$) derives simply from geometric considerations; the relative spin velocity is therefore directly proportional to the train speed, and hence the creepage is independent of the train speed.

(a) Lateral Rail Vibration Displacement for a Unit Roughness Input

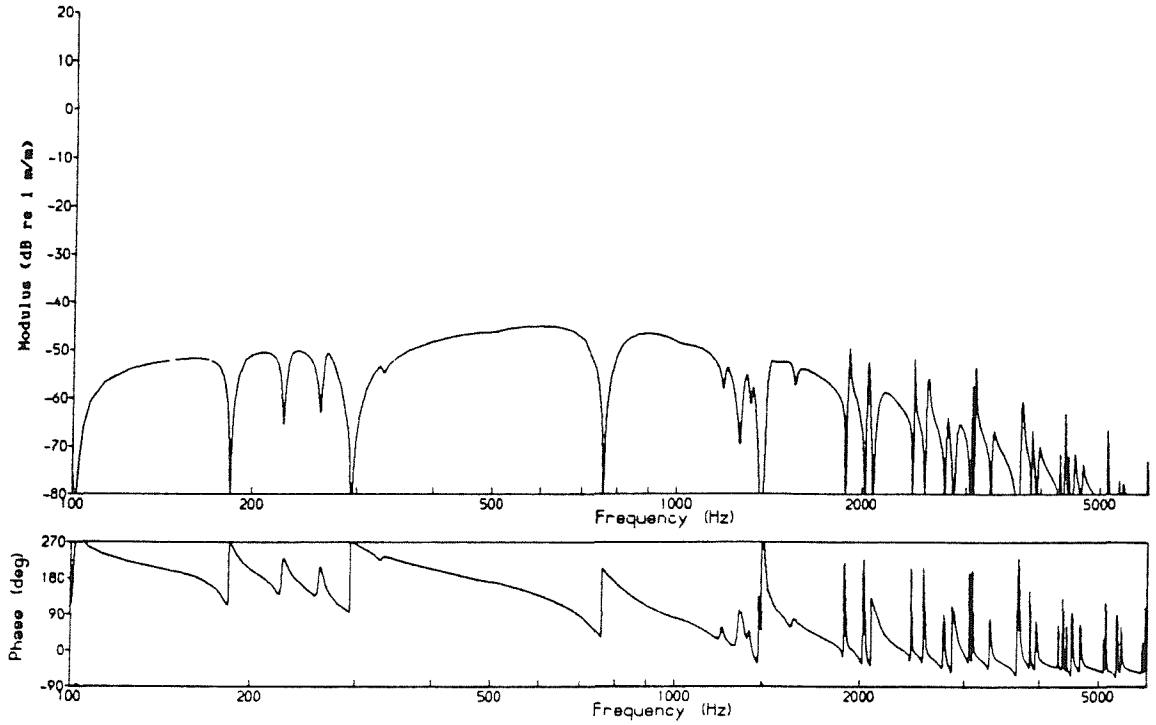

(b) Lateral Wheel Vibration Displacement for a Unit Roughness Input

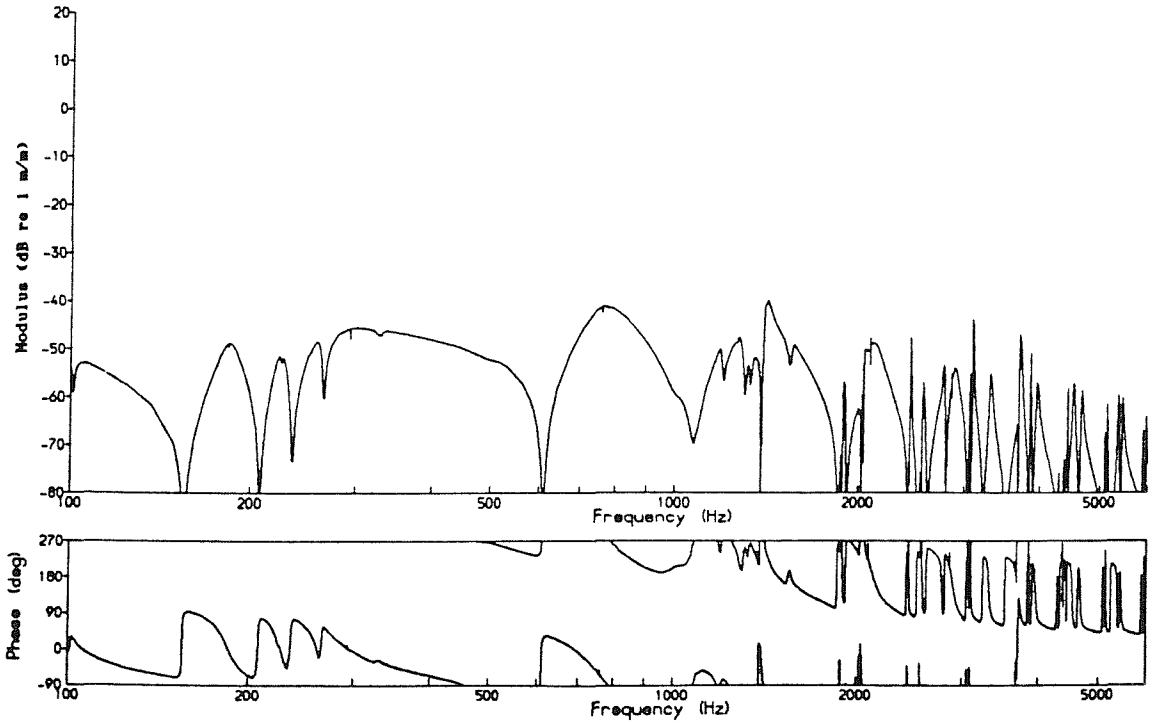

Figure 108 Lateral Responses with Simple Rail Model for Steady Spin Creep of 0.1 with Wheel and Rail Cross Receptances set to 0

(a) Lateral Rail Vibration Displacement for a Unit Roughness Input

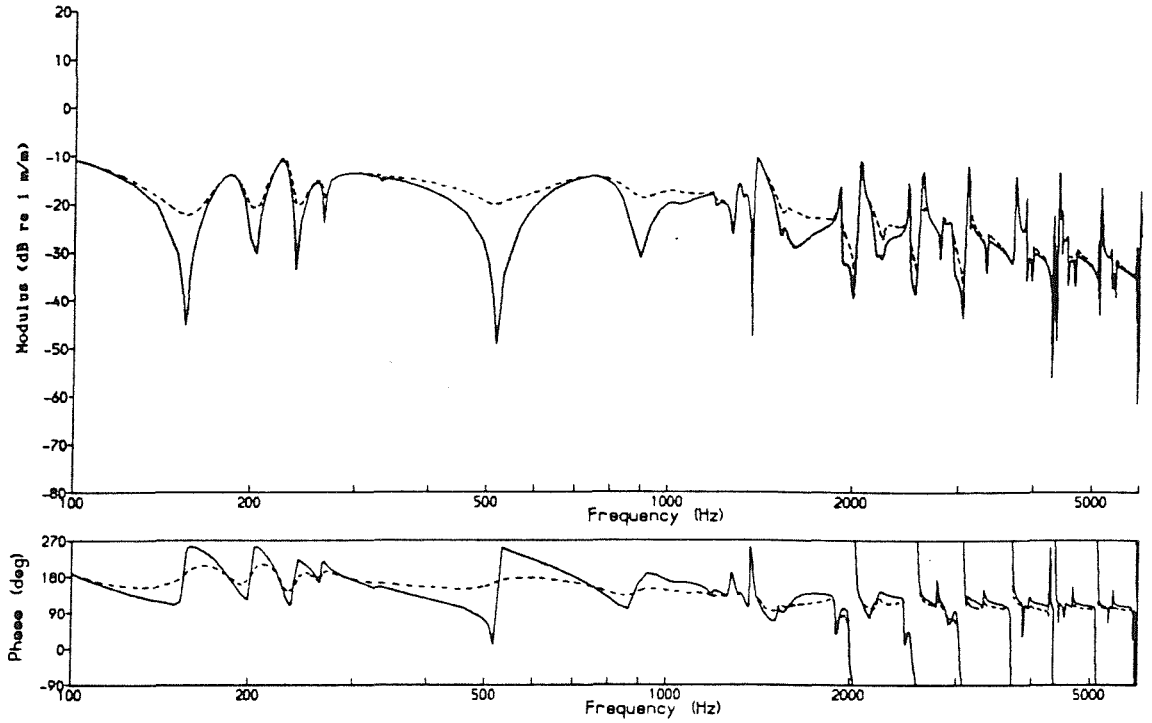

(b) Lateral Wheel Vibration Displacement for a Unit Roughness Input

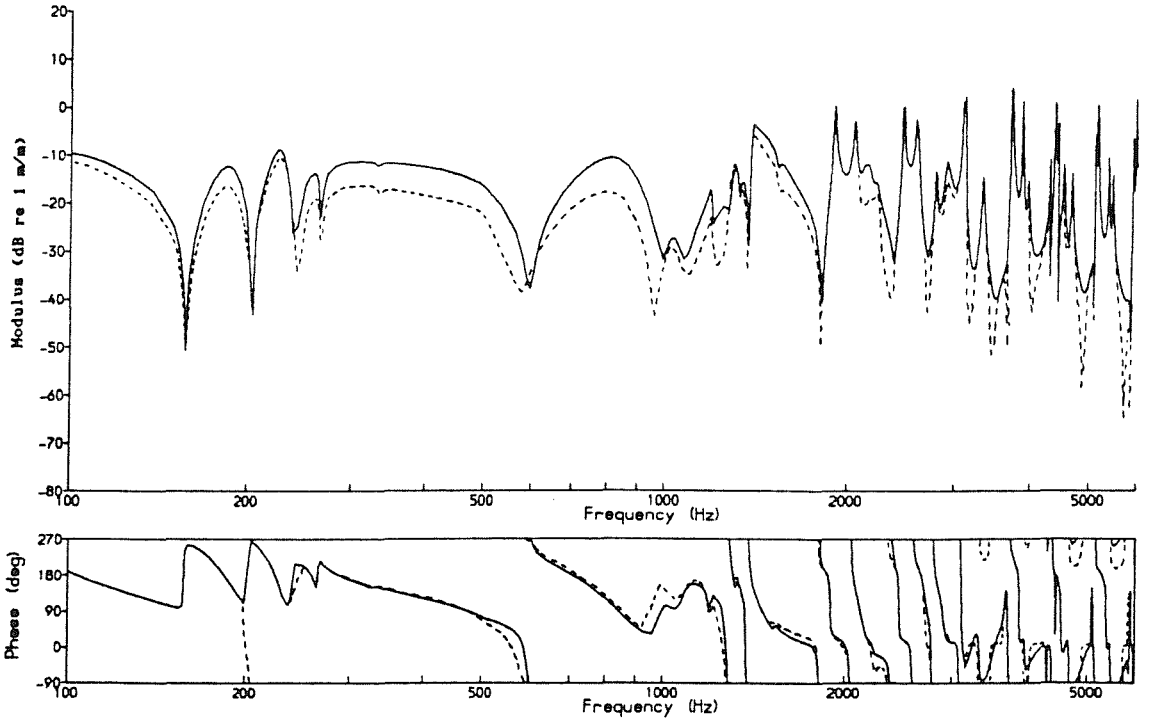

Figure 109 Lateral Responses with Simple Rail Model for Steady Lateral Creepage of .001 (——— positive, ····· negative)

contrast, at low frequencies the stiffness of the railpad and ballast reduced the receptances. However relative to the wheel receptances (Figures 18-20) these changes are relatively small, and are therefore not expected to affect the relative importance of the rail greatly. Lateral and vertical receptances were given in Figures 79 and 84 (with comparisons with the earlier simple beam theory results), and the cross receptance was shown in Figure 86. The latter, in particular is dependent on the lateral position of the contact point on the railhead (for a central position the model predicts a receptance of zero, although this neglects effects of asymetry in the supports).

Retaining the improved contact receptances used in the previous section, but replacing the simple rail receptances used there by these from §5, gives the results shown in Figures 110 and 111 for the vertical and lateral responses respectively. From a comparison of these results with the earlier results (Figures 106 and 107), they can be seen to be generally similar; at low frequencies the rail vibrates at an amplitude which is equivalent to almost all of the roughness input, whereas the wheel and contact play increasingly important roles at higher frequencies.

However some detail differences can be noted. The reduced rail receptance at low frequencies, due to the inclusion of ballast and railpad stiffnesses, results in a somewhat greater vertical wheel response below 300 Hz. Between 500 and 1000 Hz the phase of the vertical rail receptance lies between -135° and -90° (Figure 84), so that the resulting vibration is amplified a little in this region in comparison with the baseline result of -90° (cf Figure 33). The peak in the vertical rail receptance at around 5 kHz, due to the cut-on of the foot-flapping wave, can be detected in the vertical rail response, and the generally larger vertical rail receptance above 4 kHz (see Figure 84), raises the level of the rail response.

7.2.3 Dependence on Contact Patch Position and Shape

Due to the symmetry of the idealisation used in §5, the rail cross receptance has been set to zero for the above results. The lateral vibration will be affected by this omission, as shown by Figure 31. Both wheel and rail lateral responses are therefore somewhat lower in Figure 111 than in Figure 107, and are very similar to each other.

In order to introduce a cross receptance which is much closer to measured levels, an offset to the position of the contact point on the

(a) Vertical Rail Vibration Displacement for a Unit Roughness Input

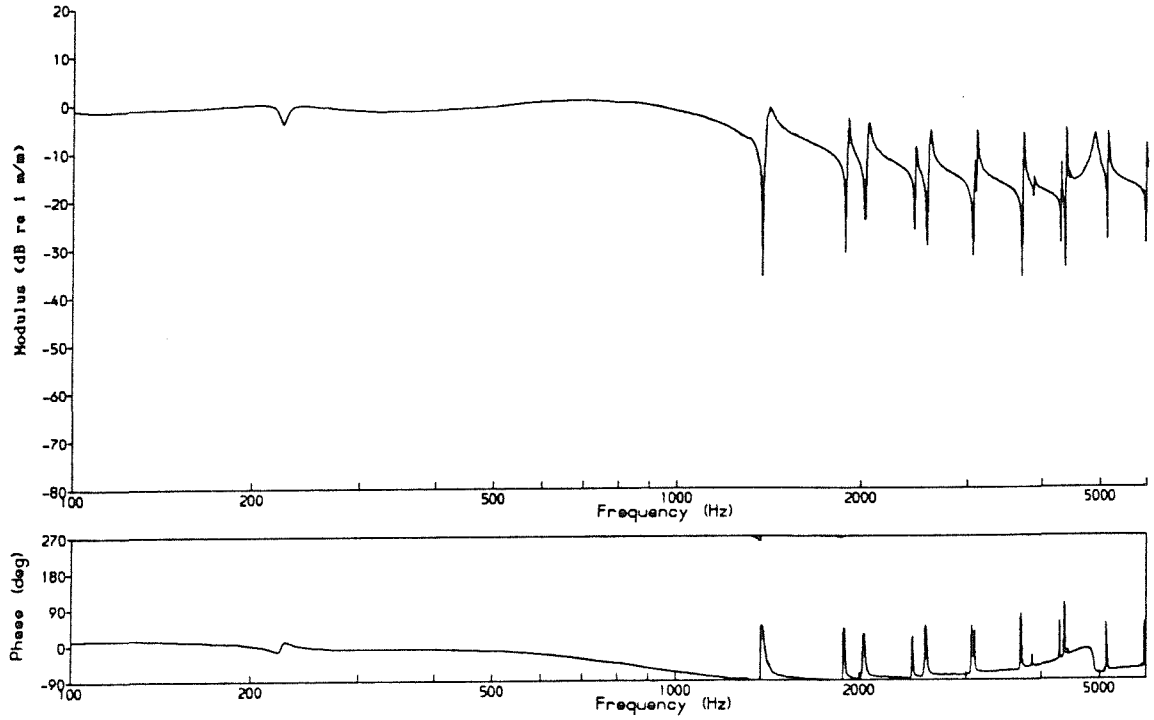

(b) Vertical Wheel Vibration Displacement for a Unit Roughness Input

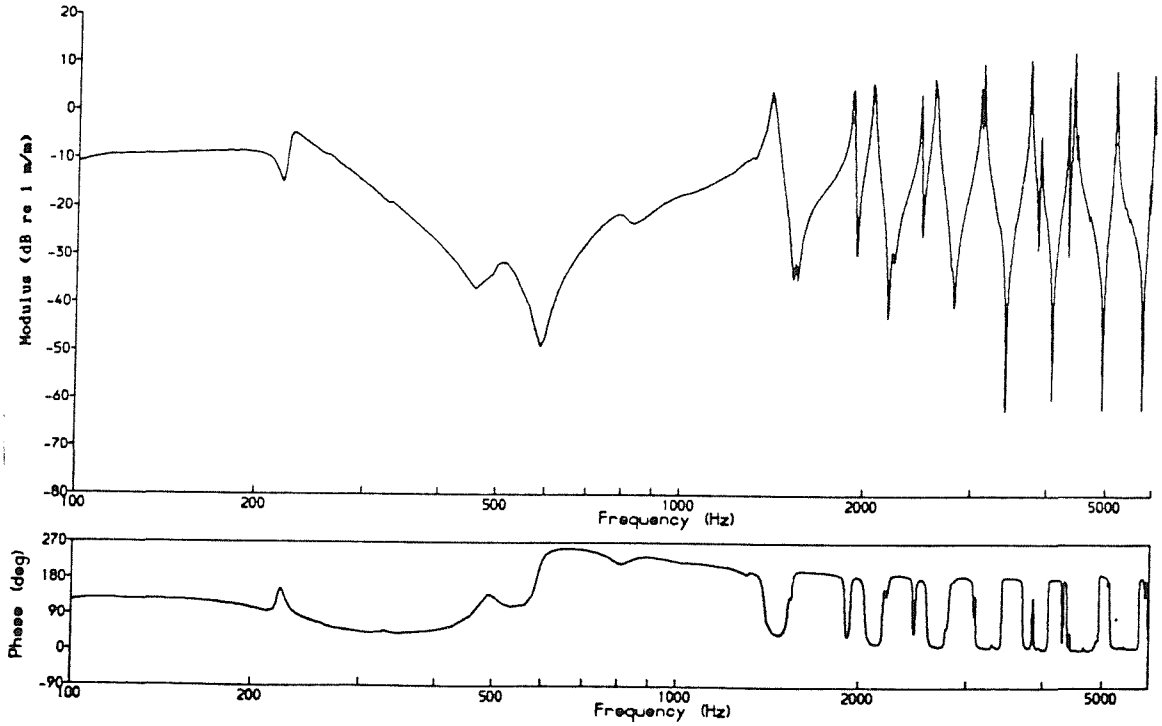

Figure 110 Vertical Responses using 2 Coupling Degrees of Freedom with Full Rail Model

(a) Lateral Rail Vibration Displacement for a Unit Roughness Input

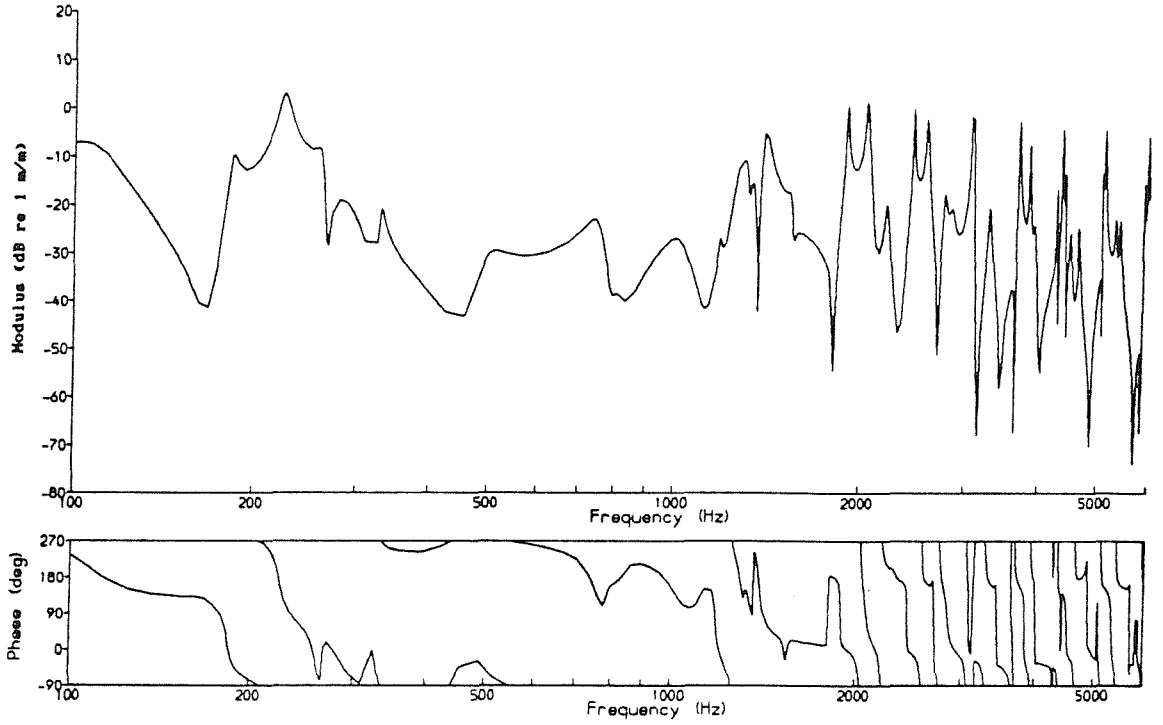

(b) Lateral Wheel Vibration Displacement for a Unit Roughness Input

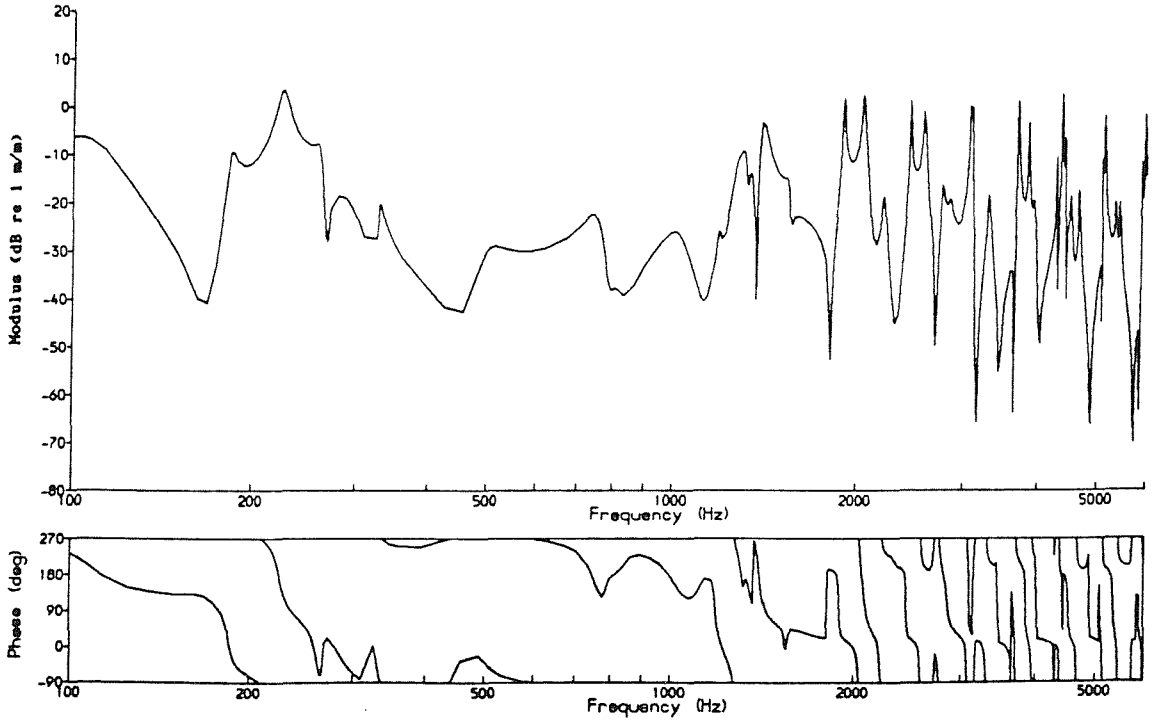

Figure 111 Lateral Responses using 2 Coupling Degrees of Freedom with Full Rail Model

rail is introduced (see §5.4.4). The vertical receptance is also raised slightly by this change. Figure 112 shows the vertical responses for an offset of 15 mm. The rail response is raised slightly at high frequencies due to the change in vertical receptance, but the wheel is little affected.

The main effect of these changes in the rail receptances is seen in the lateral responses, however, as shown in Figure 113. The rail lateral response is greater than that with no cross receptance (Figure 111). At high frequencies it is also greater than that predicted using the simpler rail model (Figure 107), since at these frequencies the rail cross receptance (like the other rail receptances) is larger in the current case than that derived from the Euler-Bernoulli beam equations.

The lateral wheel response is greater than in Figure 111 between 200 and 1000 Hz, and between 200 and 300 Hz it is also greater than that from the simple rail model (Figure 107). At higher frequencies the wheel response is little affected.

Also shown in Figures 112 and 113 is the effect of introducing a similar offset to the contact point on the wheel as well as on the rail. The effects are once more limited mainly to the lateral response, this time due to the influence on the wheel cross receptance. However, at the higher frequencies the appearance of an extra set of peaks in the wheel vertical response should be noted. These correspond to the 2-nodal-circle set of modes, which have a node in their radial component close to the usual contact position.

By varying the radii of the wheel and rail running surfaces (R_{12} and R_{22}), changes are produced in the creep coefficients, and hence the lateral contact receptance. Quite large variations in these radii have been studied, as listed in Table 13. However, none of these produced a noticeable change in the responses. This can be attributed to two factors: firstly only small relative changes in the contact receptances were produced by these parameter changes, and secondly, as already shown in §3, the response is not particularly sensitive to changes in the lateral contact receptance, anyway.

It should be remembered that, in practice, such changes in contact geometry may lead to vehicle instability, and hence increased noise through other means, such as flange contact etc.

(a) Vertical Rail Vibration Displacement for a Unit Roughness Input

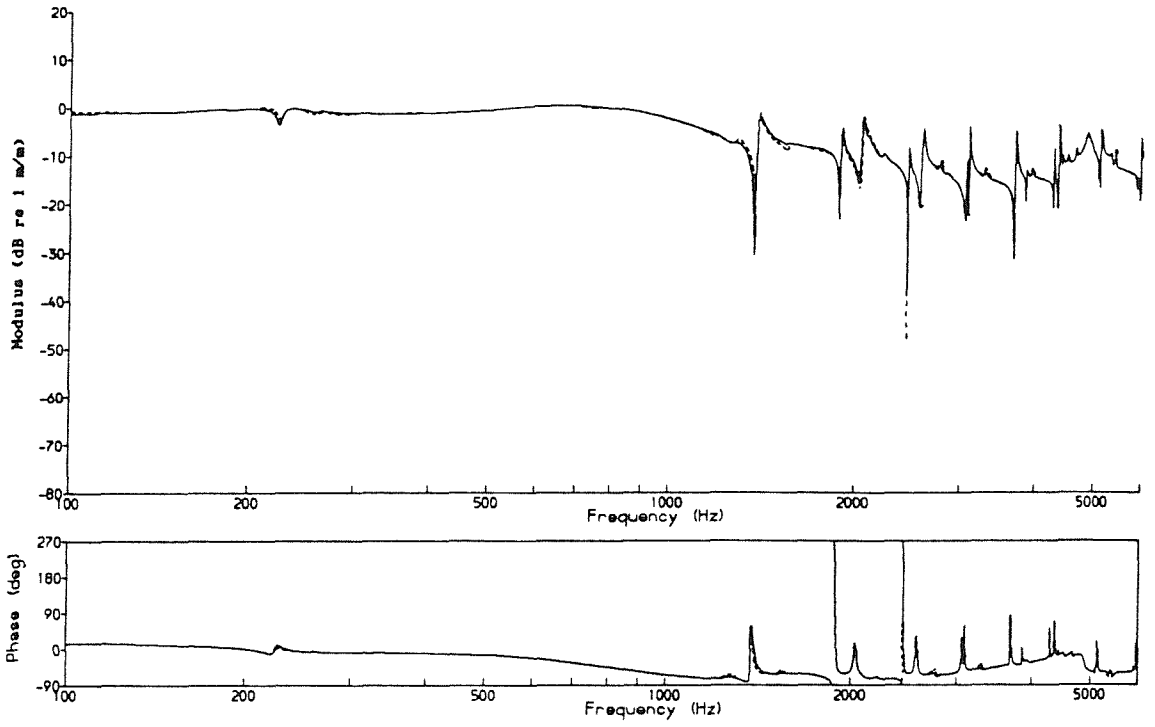

(b) Vertical Wheel Vibration Displacement for a Unit Roughness Input

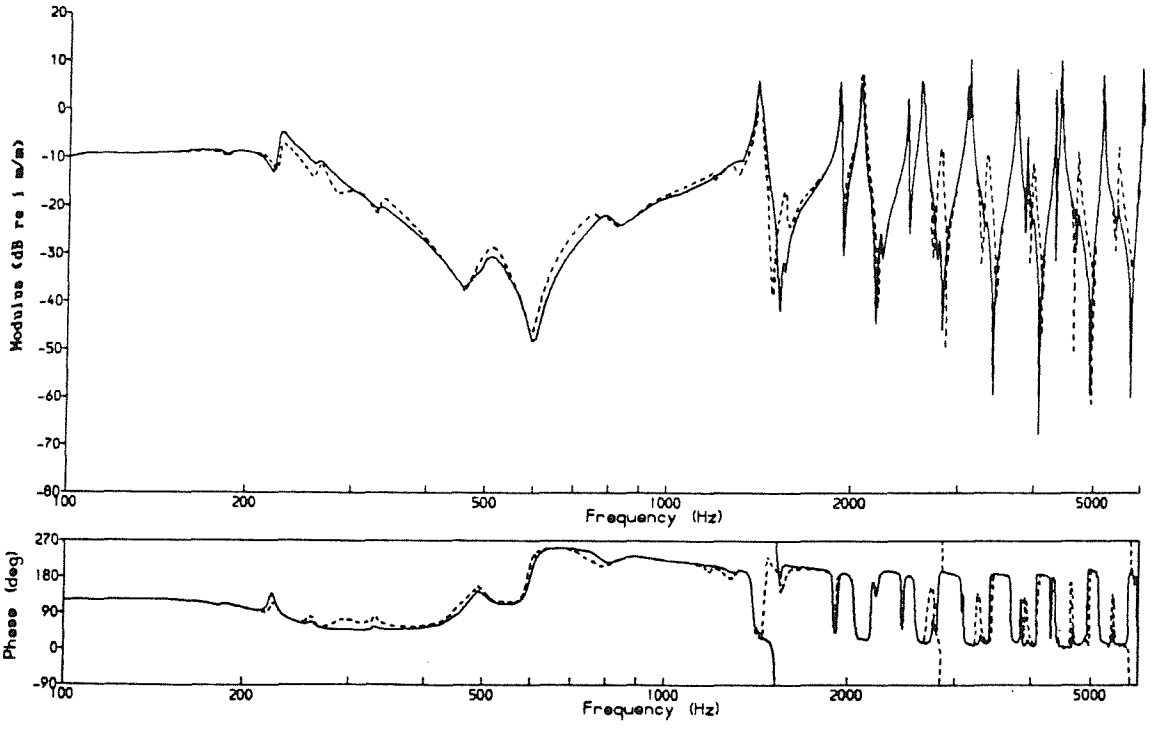

Figure 112 Vertical Responses using 2 Coupling Degrees of Freedom with a 15 mm Offset to the Contact Point: ——— on Rail, ····· on Wheel and Rail

(a) Lateral Rail Vibration Displacement for a Unit Roughness Input

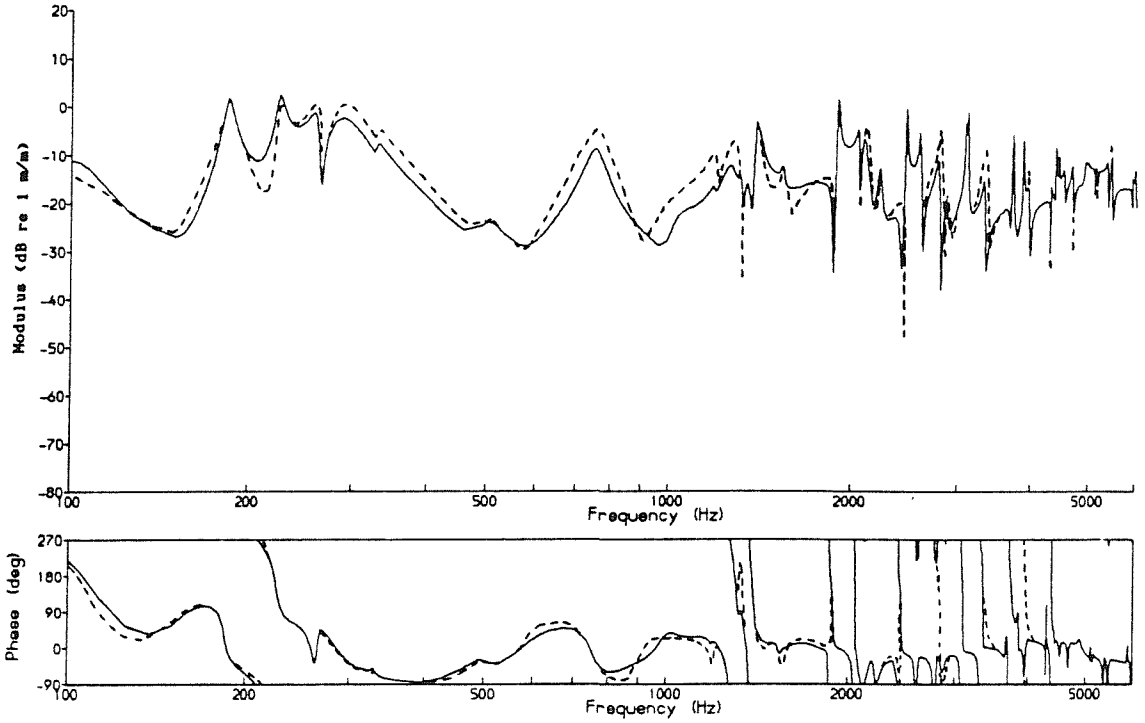

(b) Lateral Wheel Vibration Displacement for a Unit Roughness Input

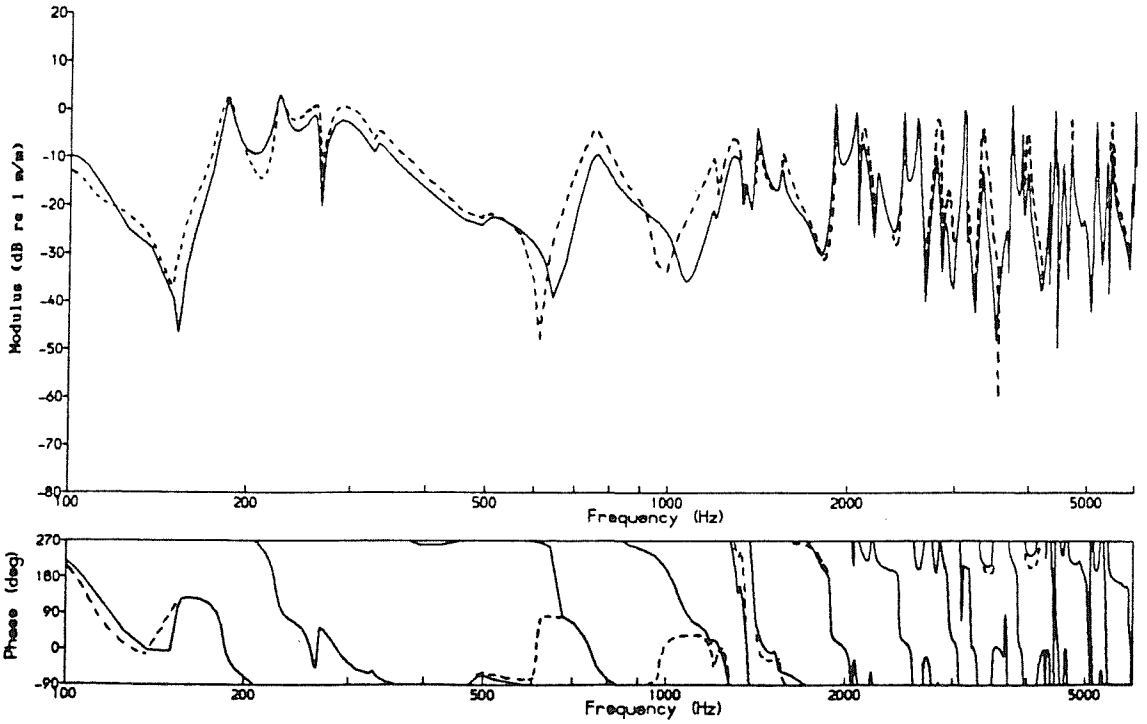

Figure 113 Lateral Responses using 2 Coupling Degrees of Freedom with a 15 mm Offset to the Contact Point: ——— on Rail, ····· on Wheel and Rail

Table 13 Changes in Contact Parameters due to Various Wheel and Rail Running Surface Radii

Radii of curvature (m)		Contact patch semi-axes (mm)		θ (deg) (from	Creep coefficients		
R_{12}	R_{22}	a	b	Table E1)	C_{22}	C_{23}	C_{33}
∞	0.3	6.12	4.20	106.1	1.669	0.782	0.359
-1.0	0.3	5.79	5.03	96.1	1.514	0.644	0.414
∞	0.6	5.48	5.95	86.4	1.394	0.543	0.482
∞	0.9	5.11	7.26	75.0	1.279	0.452	0.583
-1.0	0.6	4.64	9.26	61.5	1.168	0.369	0.763

7.3 INCLUSION OF ADDITIONAL COUPLING COORDINATES

7.3.1 Effect on Vertical and Lateral Responses

The model used until this point has two coupling degrees of freedom linking the wheel and rail: vertical and lateral. When extra degrees of freedom are included into the interaction model, the effect on the vertical and lateral responses is found to be negligible.

Figures 114 and 115 show the vertical and lateral responses based on the full 6 degrees of freedom in the interaction. These, and all subsequent results in this section, include the 15 mm offset to the lateral position of the contact on the rail, and hence a realistic level of rail lateral/vertical cross receptance. Comparing these results with the equivalent 2-degree-of-freedom results (Figures 112 and 113), they can be seen to be virtually identical.

From §3, it is not especially surprising that the vertical responses are not affected by other coordinates, as they were not greatly affected by the various lateral parameters, but it might have been expected that the lateral response might have been modified.

It may be recalled from §6, that it was expected that two of the coordinates, in particular (z_4 and z_5), would provide very little effective coupling between the wheel and rail, due to their relatively soft contact receptances (cf Figure 105). This appears to have been confirmed.

The following sections will look at the response in the other coordinates for this 6-degree-of-freedom interaction.

(a) Vertical Rail Vibration Displacement for a Unit Roughness Input

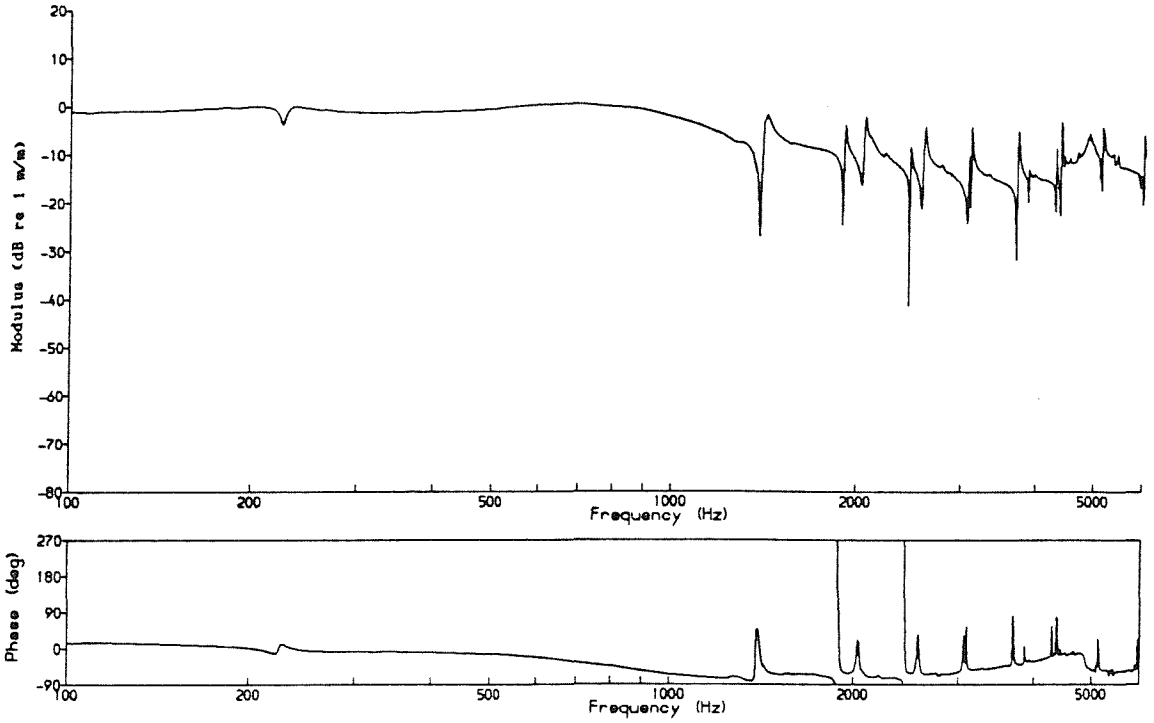

(b) Vertical Wheel Vibration Displacement for a Unit Roughness Input

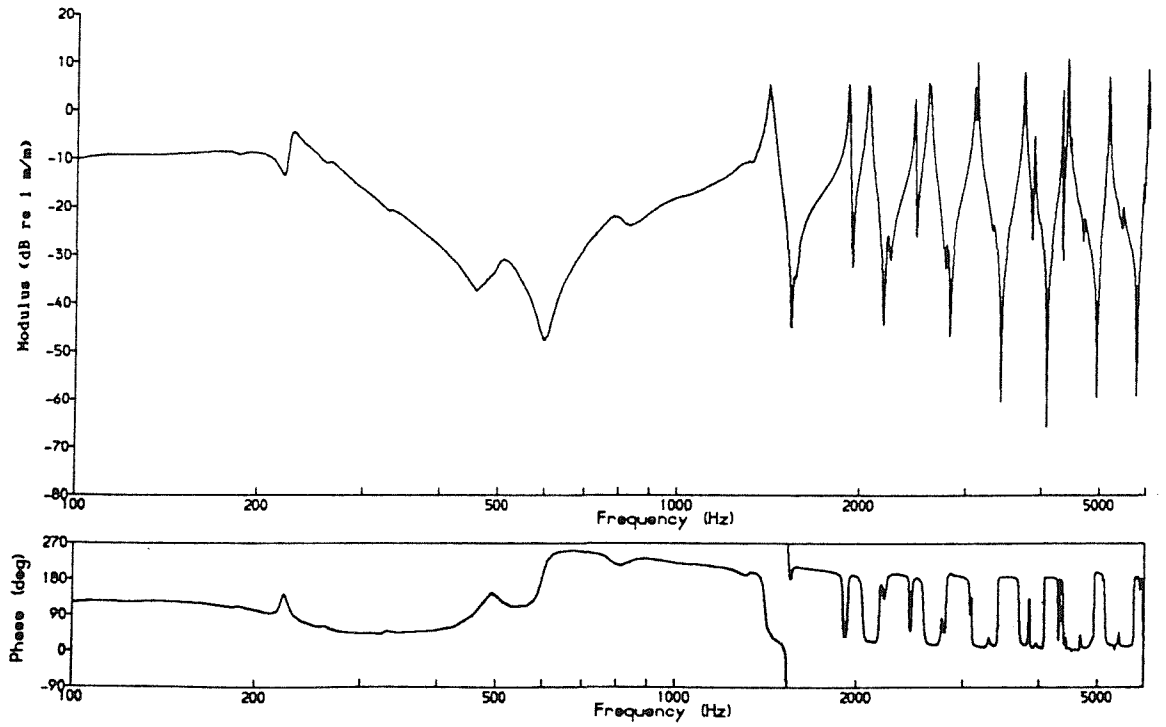

Figure 114 Vertical Responses using 6 Coupling Degrees of Freedom

(a) Lateral Rail Vibration Displacement for a Unit Roughness Input

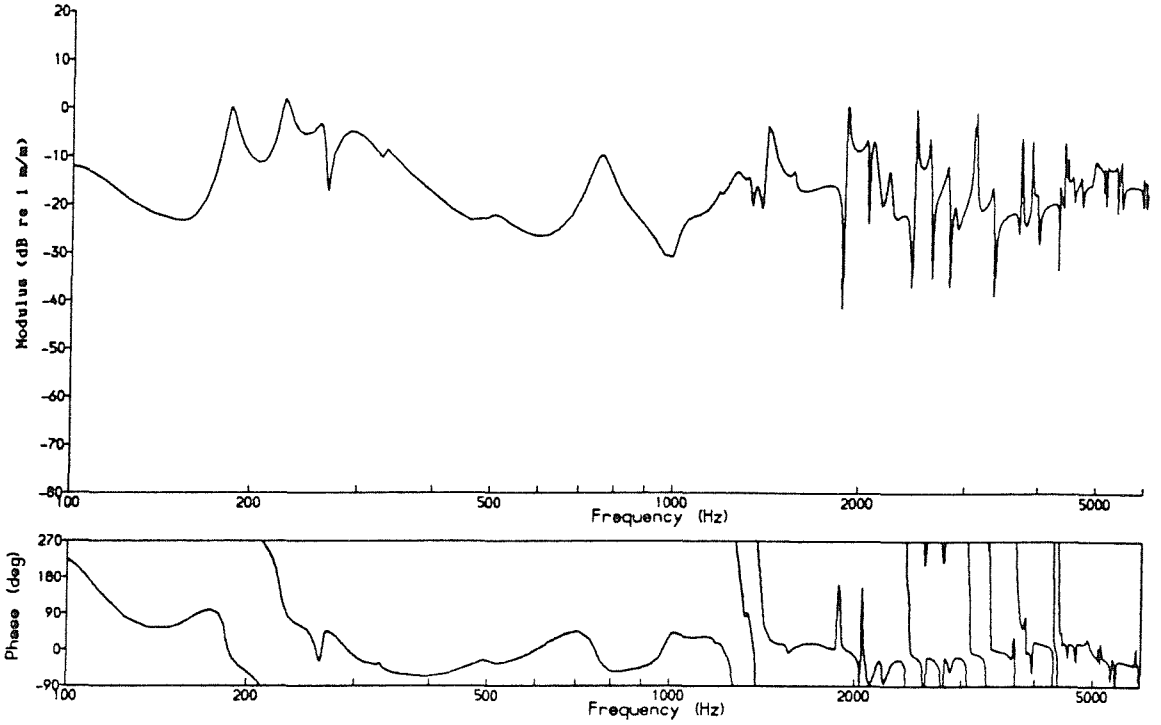

(b) Lateral Wheel Vibration Displacement for a Unit Roughness Input

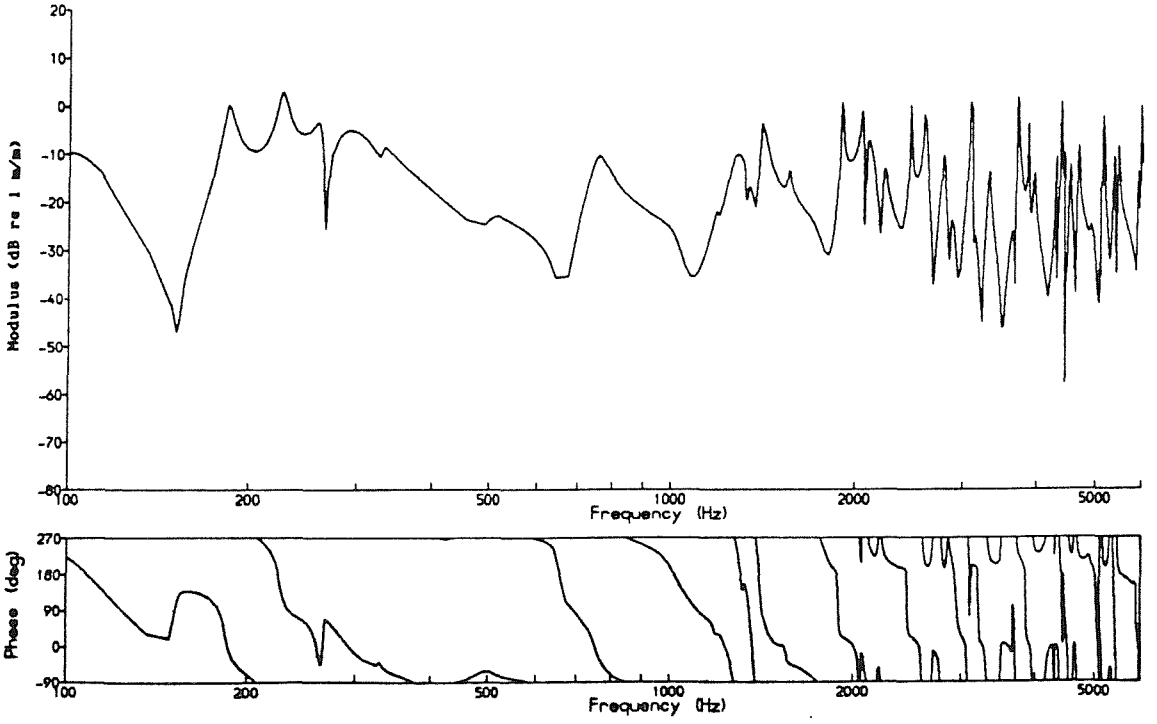

Figure 115 Lateral Responses using 6 Coupling Degrees of Freedom

Before looking at the response in other coordinate directions, however, it is worthwhile repeating the comparison with the 1/3 octave experimental data, which was given for the simple model in Figures 22 and 24.

The revised results are given in Figures 116 and 117. It can be seen that agreement is slightly improved in each case, except for the lateral rail vibration, where the rail cross receptance is an important parameter - the use of the 15 mm offset to introduce a non-zero cross receptance is perhaps inadequate. For the wheel, the response at the accelerometer positions gives better agreement with the measurements than that at the contact (as might be expected).

7.3.2 Rotation in the Lateral/Vertical Plane

The first additional coordinate to be considered is the 'twist' (z_4 in Figure 103), that is the rotation within the same plane as the vertical and lateral coordinates. Figure 118 shows these responses for the above 6-degree-of-freedom model. (Note that the responses for this and all rotational responses are shown as dB re 1 radian per 1 m roughness input, whereas the displacements are non-dimensional).

The link introduced between lateral motion at the contact z^C_2, and the P^W_4 moment (see §6.2.4) has no noticeable effect either.

7.3.3 Spin Rotation

The spin rotation (z_6 in Figure 103) is the rotation within the plane of the contact patch. The formulation of the creep forces implies that this degree of freedom is coupled with the lateral motion, which results in significant excitation of the response in this direction. Figure 119 shows the results for the spin vibration from the 6-degree-of-freedom interaction. The wheel response is dominated by large resonant peaks corresponding to each of the 0-nodal-circle modes.

It should be noted that the spin vibration corresponds to lateral vibration of the wheel tyre in a sin $n\theta$ pattern (ie with a node at the contact), where the lateral vibration (Figure 115) corresponds to the cos $n\theta$ component (ie with an anti-node at the contact). The spin vibration can be converted roughly to an equivalent anti-nodal lateral vibration, by taking account of the ratio of lateral to spin modal amplitudes for these 0-nodal-circle modes. Applying this, the estimated anti-nodal lateral vibration is shown in Figure 120 along

(a) Vertical Rail Vibration Displacement for a Unit Roughness Input

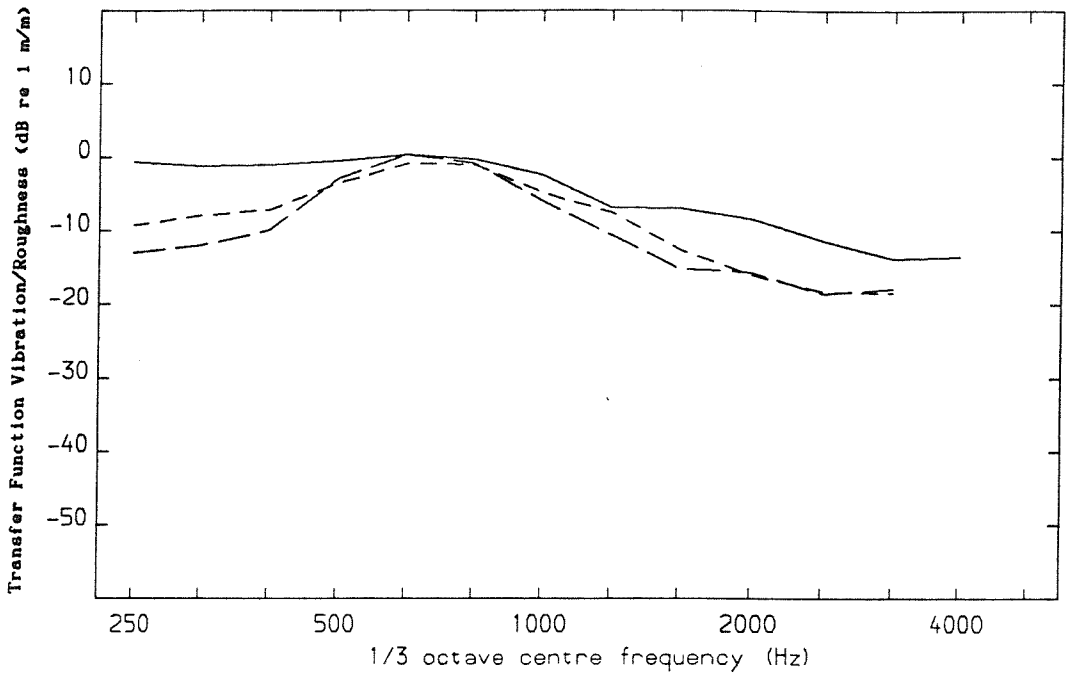

(b) Lateral Rail Vibration Displacement for a Unit Roughness Input

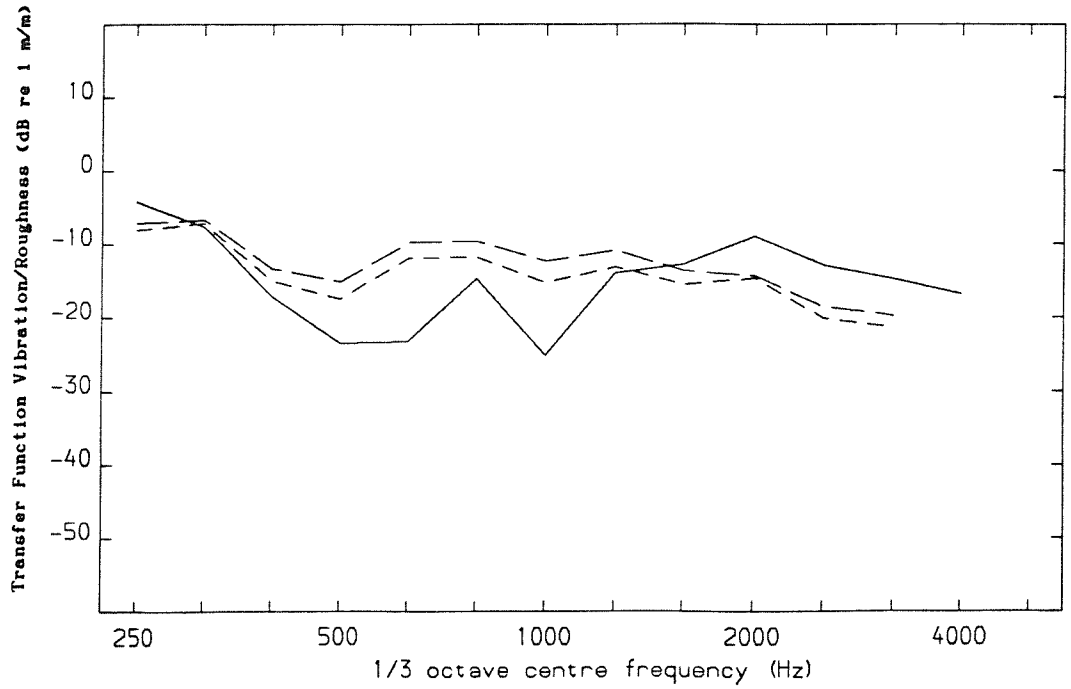

Figure 116 Comparison of Predicted Rail Vibration using 6 Coupling Degrees of Freedom (———) with Measurements at 160 km/h from Appendix A (— — Smooth Wheel, - - - Rough Wheel)

(a) Vertical Wheel Vibration Displacement for a Unit Roughness Input

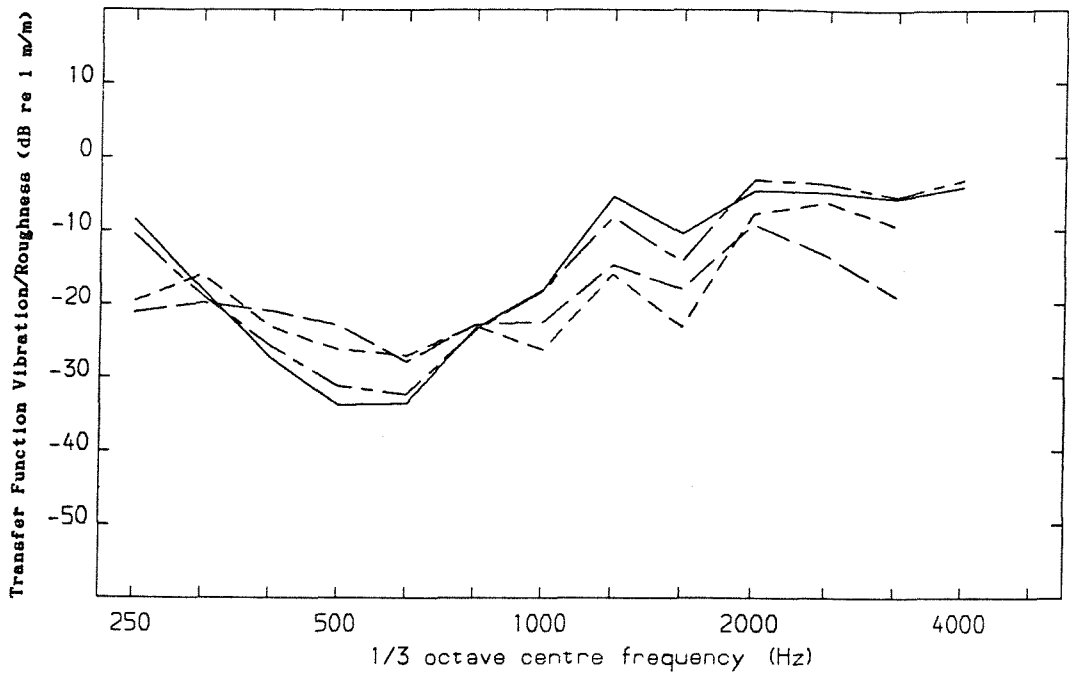

(b) Lateral Wheel Vibration Displacement for a Unit Roughness Input

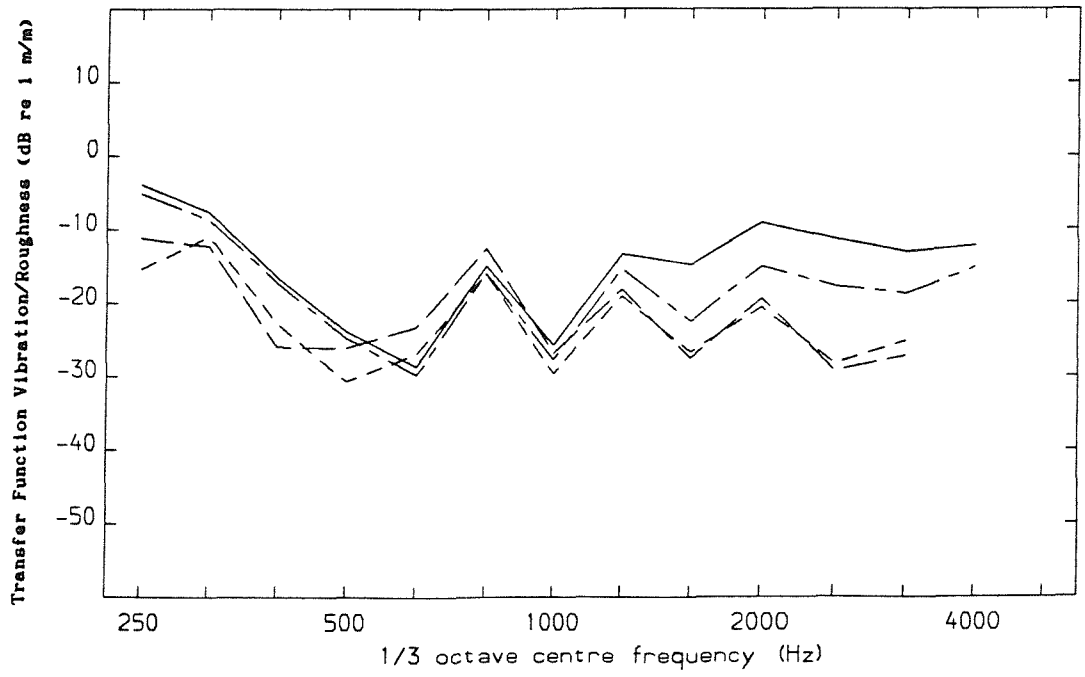

Figure 117 Comparison of Predicted Wheel Vibration using 6 Coupling Degrees of Freedom (——— Contact Point, —·— Accelerometer Positions) with Measurements at 160 km/h from Appendix A (— — Smooth Wheel, – – – Rough Wheel)

(a) Rail Twist Rotation for a Unit Roughness Input

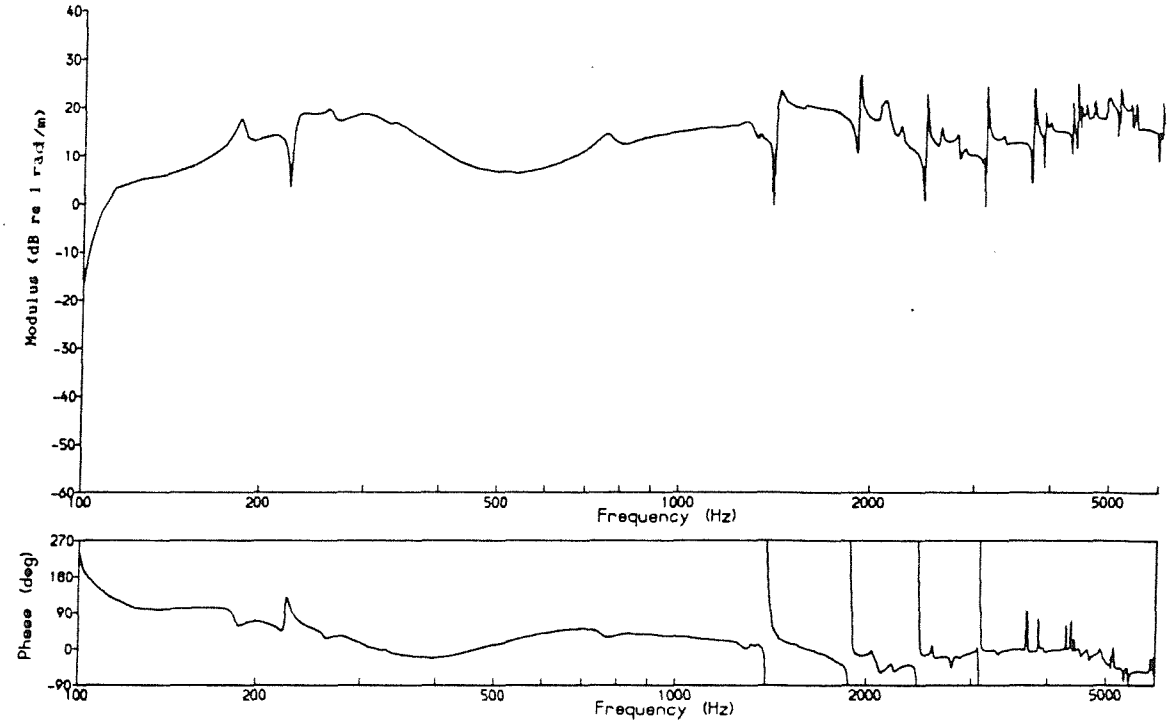

(b) Wheel Twist Rotation for a Unit Roughness Input

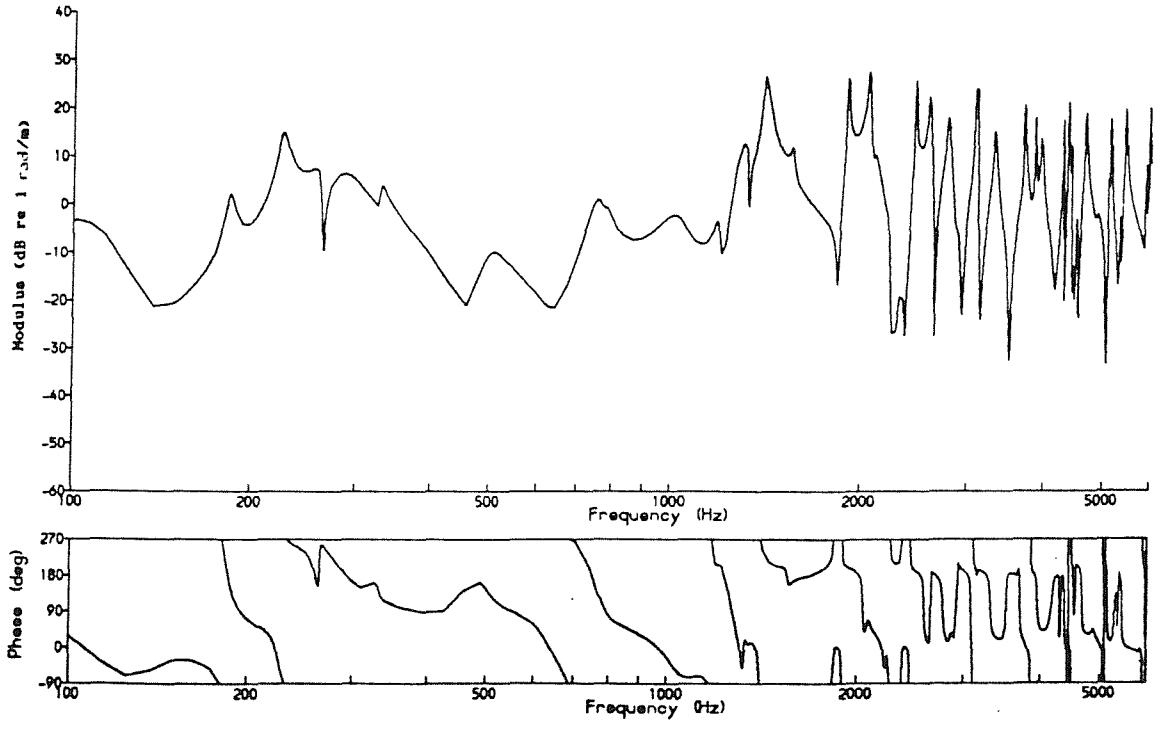

Figure 118 Twist (z_4) Responses using 6 Coupling Degrees of Freedom

(a) Rail Spin Rotation for a Unit Roughness Input

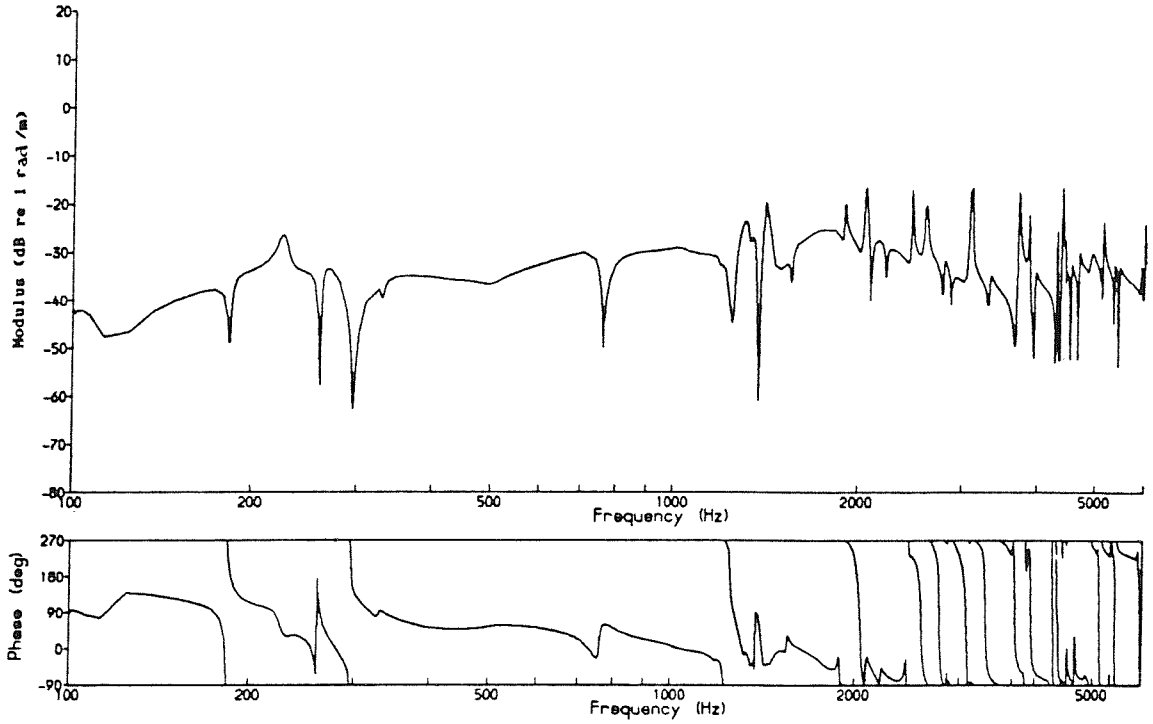

(b) Wheel Spin Rotation for a Unit Roughness Input

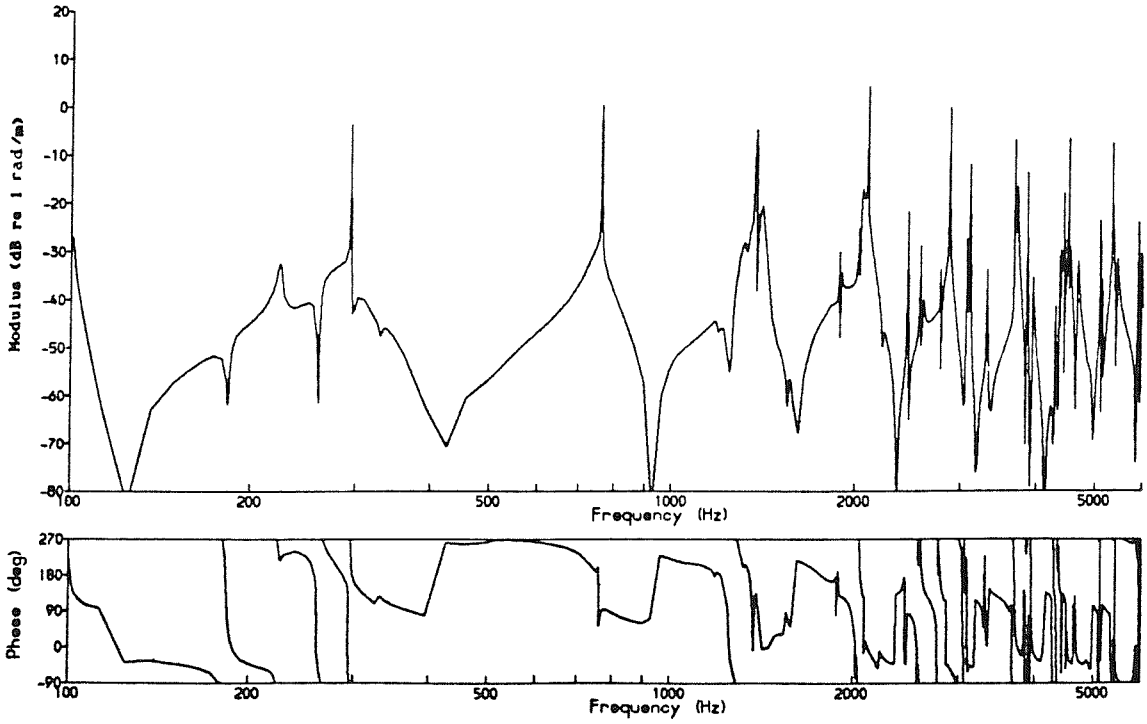

Figure 119 Spin (z_6) Responses using 6 Coupling Degrees of Freedom

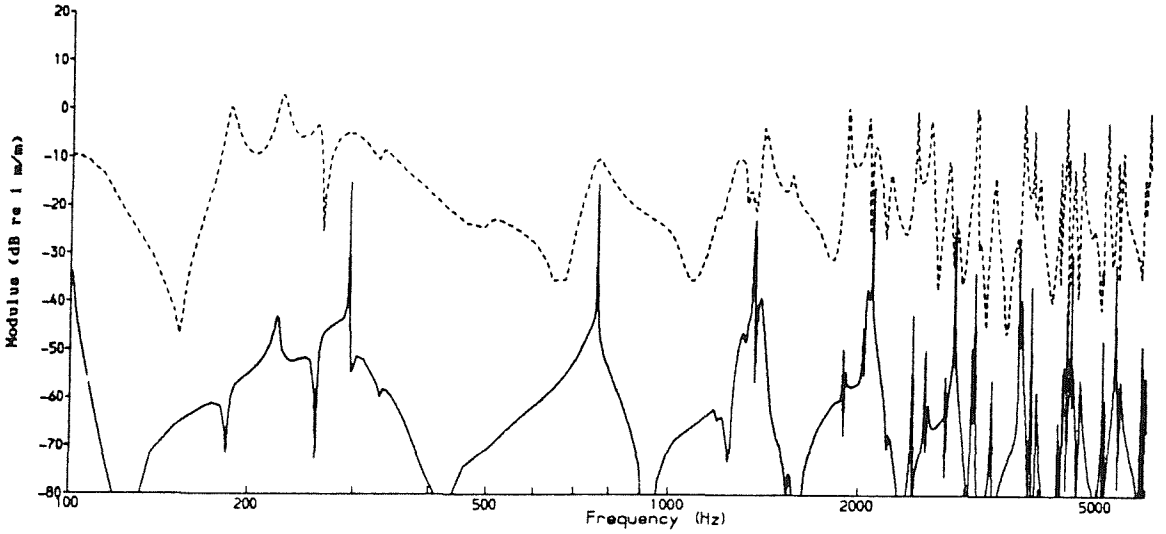

Figure 120 Equivalent Wheel Lateral Response due to Spin Response using 6 Coupling Degrees of Freedom (——— converted from z_6, ····· lateral from Figure 115)

with the lateral vibration at the contact (from Figure 115). It should be remembered that the different modes have different numbers of nodal diameters, and hence will have their anti-nodes at different positions around the wheel. Thus this estimate is only valid where it is dominated by a single mode (ie at the peaks), and the phase information (not shown) is useless.

The result is, in fact, slightly lower than the lateral vibration at the contact, even at the peaks.

Figure 121 shows the spin vibration when a steady lateral creepage of 0.001 is introduced, which increases the magnitude of the lower frequency peaks somewhat. More dramatic is the effect of a steady spin creepage of 0.1, shown in Figure 122, which increases the level of all of the peaks, particularly those at higher frequencies. The levels of the 0-nodal-circle peaks in the estimated equivalent lateral vibration, are listed for the various cases in Table 14.

(a) Rail Spin Rotation for a Unit Roughness Input

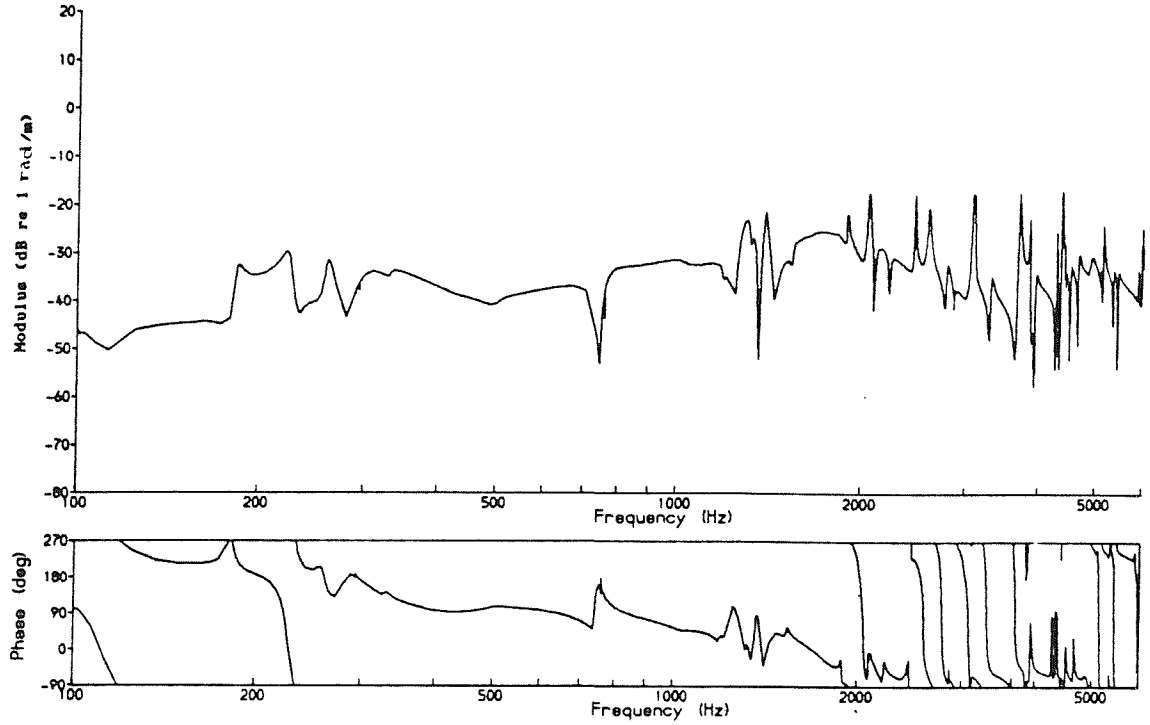

(b) Wheel Spin Rotation for a Unit Roughness Input

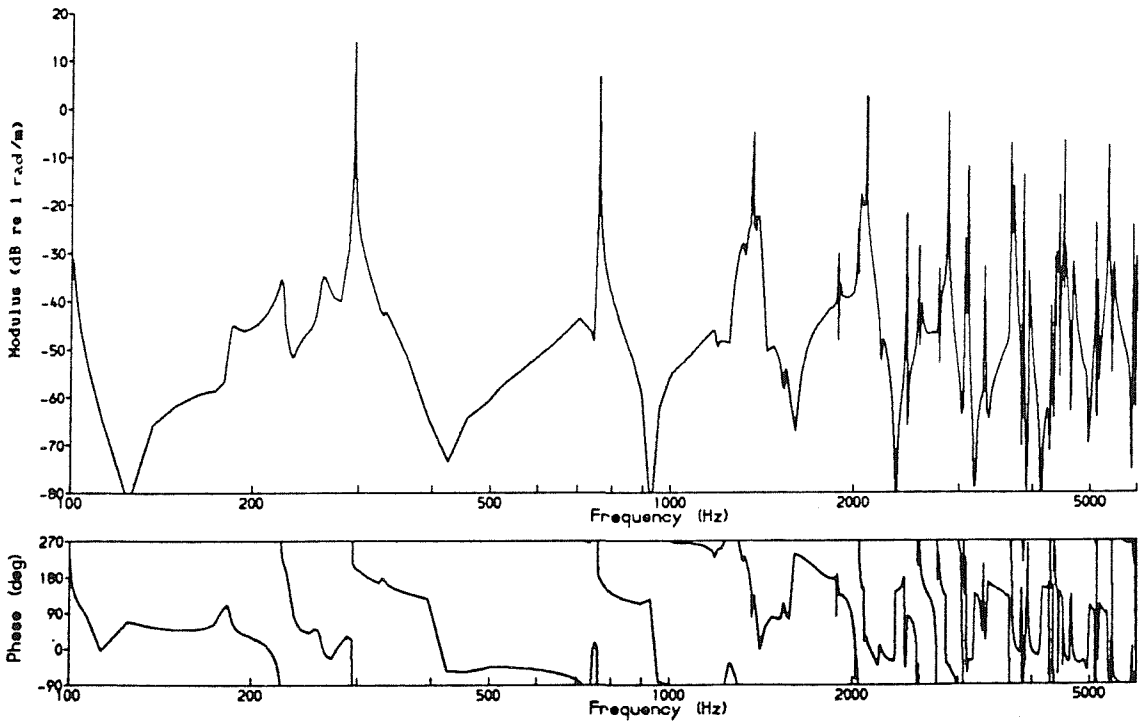

Figure 121 Spin (z_6) Responses using 6 Coupling Degrees of Freedom with Steady Lateral Creepage of .001

(a) Rail Spin Rotation for a Unit Roughness Input

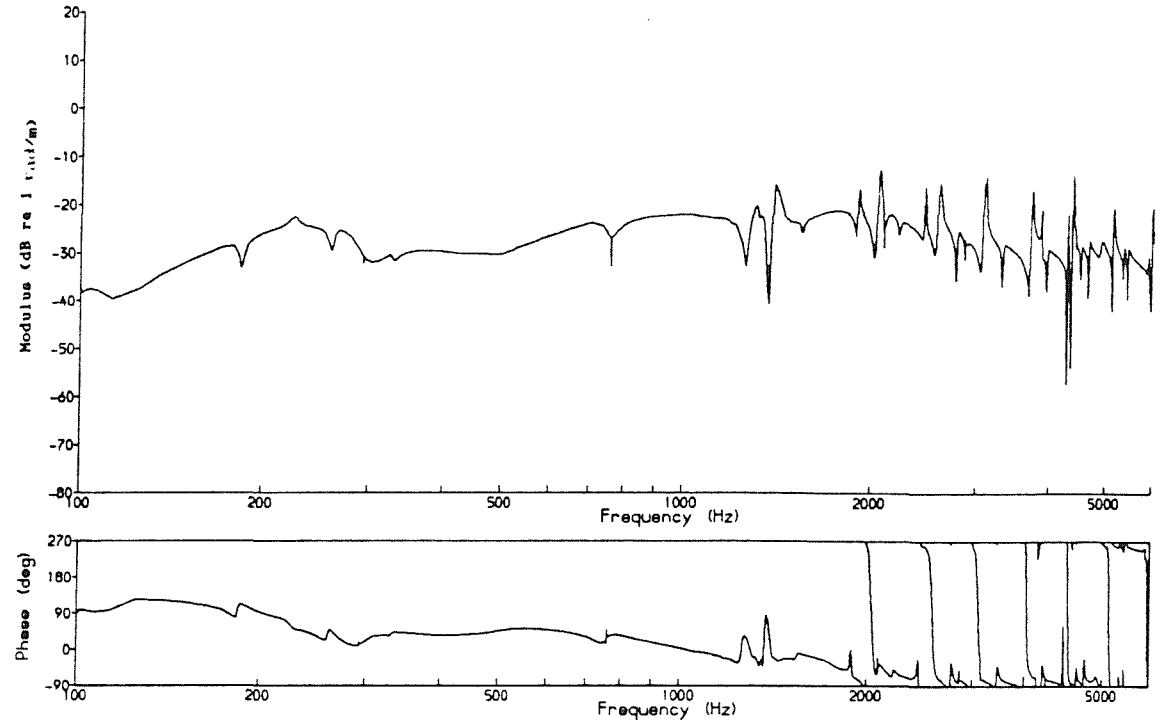

(b) Wheel Spin Rotation for a Unit Roughness Input

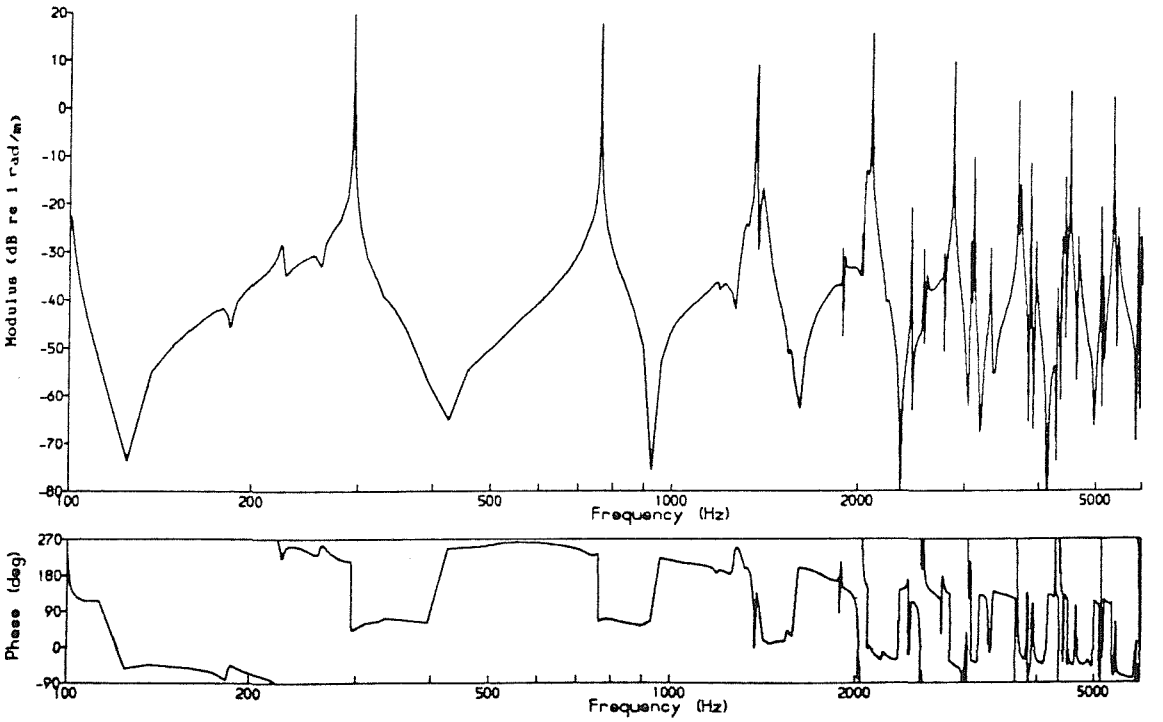

Figure 122 Spin (z_6) Responses using 6 Coupling Degrees of Freedom with Steady Spin Creepage of 0.1

Table 14 Estimated Amplitudes of Peaks in the Lateral Vibration Spectra at 0-nodal-circle Modes Resulting from Spin Vibration at the Contact Point (dB re 1 m/m)

Number of nodal diameters	Frequency (Hz)	No steady creepage (Figs 119/20)	$\bar{\gamma}_2$=0.001 (Fig 121)	$\bar{\omega}_3$=0.1 (Fig 122)
2	294	-15	3	8
3	760	-15	-9	2
4	1375	-23	-23	-9
5	2090	-16	-17	-4
6	2860	-21	-22	-12
7	3670	-29	-30	-21
8	4510	-30	-30	-20
9	5350	-32	-32	-22

Comparing these levels with lateral vibration spectra (Figure 115) it is clear that the lateral motion of the wheel excited by the spin moment will make a contribution to the overall lateral vibration of the rolling wheel, even if only at isolated frequencies. However, when considered in terms of 1/3 octave spectra, or overall levels, even this contribution would be small, as the peaks are very narrow.

This vibration pattern has been predicted with a node at the contact point. However, it has been based on a static wheel; rolling can be expected to modify this significantly, as coupling will then occur between the sin nθ and cos nθ components (given in §4 by the (non-zero) imaginary values of ε_{ij} in eg equation (66)). This will lead to greater coupling to the rail in the case of the sin nθ part, which for the static wheel appears to be relatively free.

The spin vibration of the rail is also related to lateral vibration with a node at the contact point. In this case, however (see Figures 119-122), the amplitudes are insignificant in comparison with the lateral vibration.

7.3.4 'Roll' Vibration Coordinate

The response in the z_5 (roll) coordinate, shown in Figure 123, is generally much lower than the z_6 response. This coordinate is related to the sin nθ component of the radial vibration in the same way that z_6 is related to the lateral vibration, but in this case it does not produce any significant contribution.

(a) Rail Roll Rotation for a Unit Roughness Input

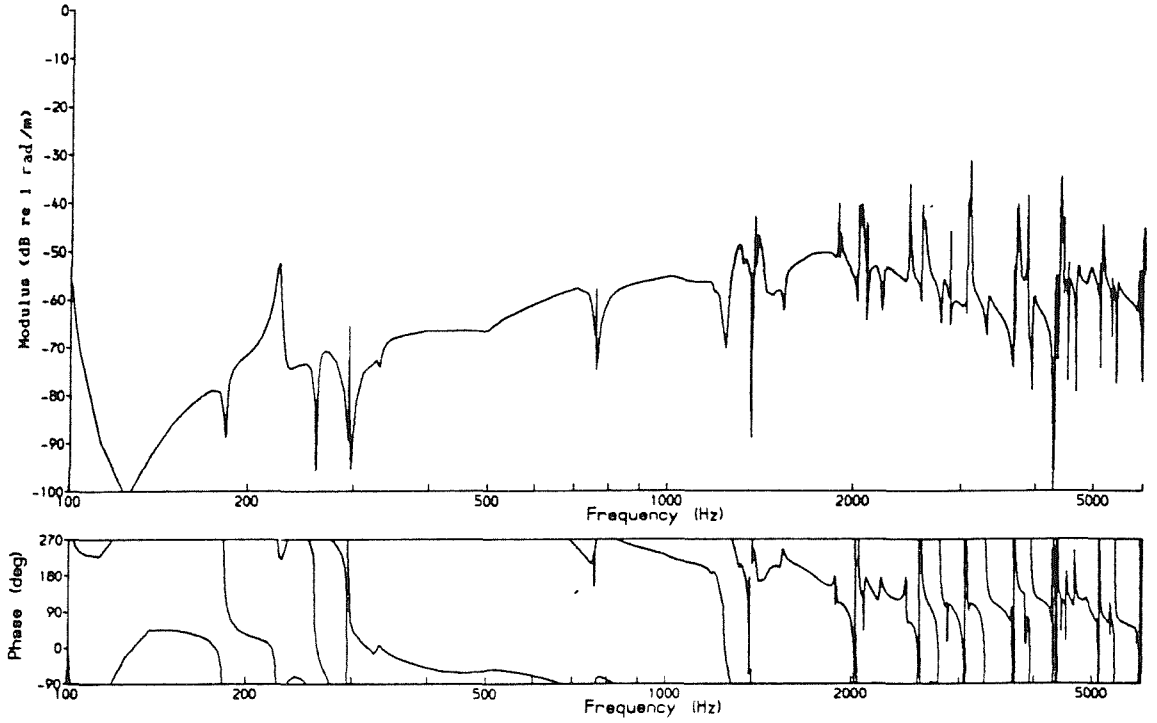

(b) Wheel Roll Rotation for a Unit Roughness Input

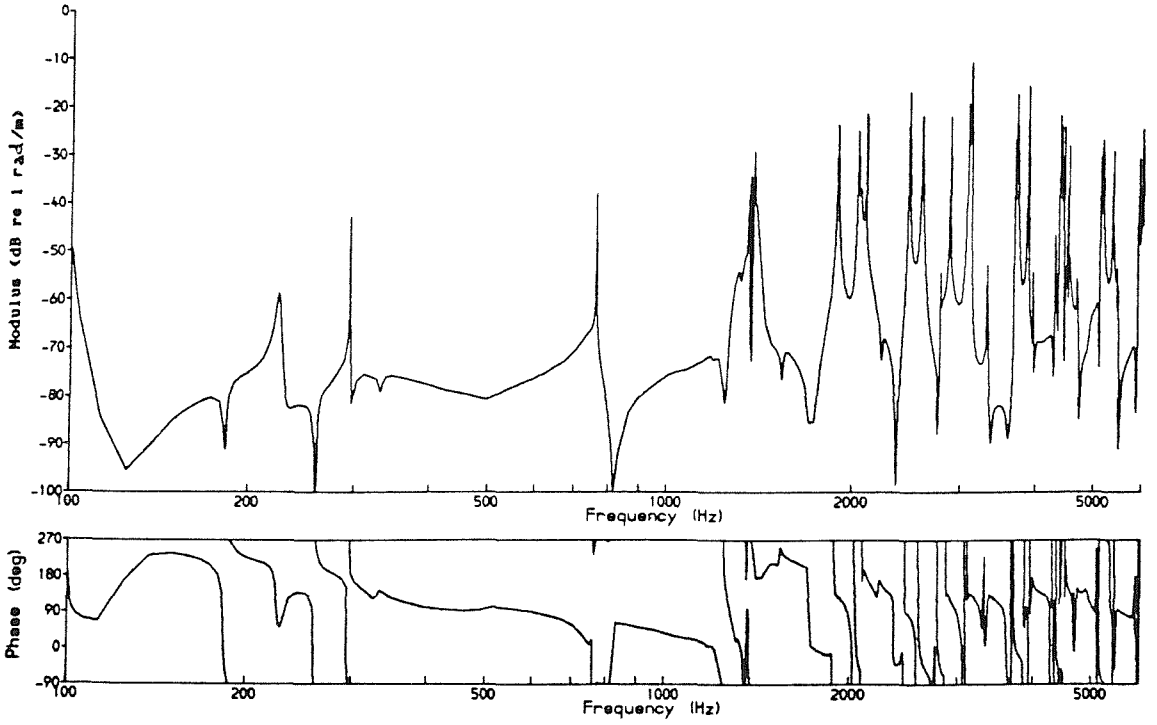

Figure 123 Roll (z_5) Responses using 6 Coupling Degrees of Freedom

7.3.5 Longitudinal Coordinate

The final coordinate to be considered is the displacement in the direction of travel (z_1). The results for this are shown in Figure 124. These also appear not to be particularly significant, being much less than the vertical and lateral responses.

If a steady longitudinal creepage is included, the longitudinal vibration is increased significantly, as shown in Figure 125 for a fairly high creepage of 0.003. The response in the spin and 'roll' coordinates is raised similarly (the spin response is also shown in Figure 125), but the response in vertical and lateral directions is still not noticeably affected. This indicates that the longitudinal direction is not strongly coupled with the latter coordinates. The wheel, rail and contact receptance matrices all contain very small, or zero, cross terms between the longitudinal direction and the lateral and vertical directions.

The longitudinal vibration is of little direct significance for noise radiation. However it is interesting to note that longitudinal waves propagate relatively unattenuated in the rail (see Figure 91). Thus at large distances from the wheel-rail contact (ahead of or behind the train), longitudinal waves will predominate. As these waves pass distinct sleepers, it can be expected that some of the vibration will be transformed into vertical waves (reflected and transmitted), which in turn will radiate noise. This could be postulated as a source of the propagation of rail vibration (and hence noise) over large distances in continuously welded rails, even if at low amplitudes. A test of this hypothesis would be provided by the prediction that such vibration should be greater when traction or braking (longitudinal creep) are present.

7.4 ADDITIONAL WHEEL EFFECTS

7.4.1 Inclusion of Wheel Rotation

Although the results for a rotating wheel in §4 used only 2 degrees of freedom, the mathematical derivation was quite general, and, in particular, allowed for the fact that some degrees of freedom (z_1, z_5 and z_6) correspond to the sin $n\theta$ distribution when the others (z_2, z_3 and z_4) correspond to cos $n\theta$. Results are therefore given here for the full 6 degrees of freedom at the contact, based on the mathematical derivation from §4. The detailed rail model is used, to obtain the necessary degrees of freedom. As in §4, the frequency step used in the

(a) Longitudinal Rail Vibration Displacement for Unit Roughness Input

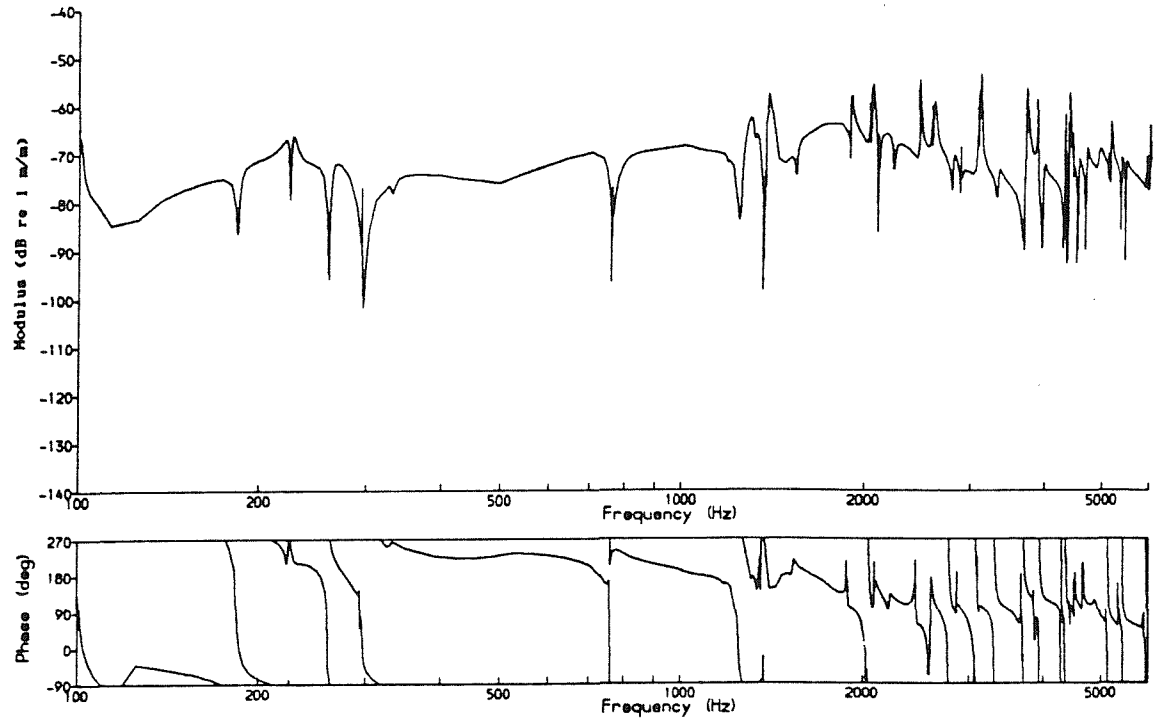

(b) Longitudinal Wheel Vibration Displacement for Unit Roughness Input

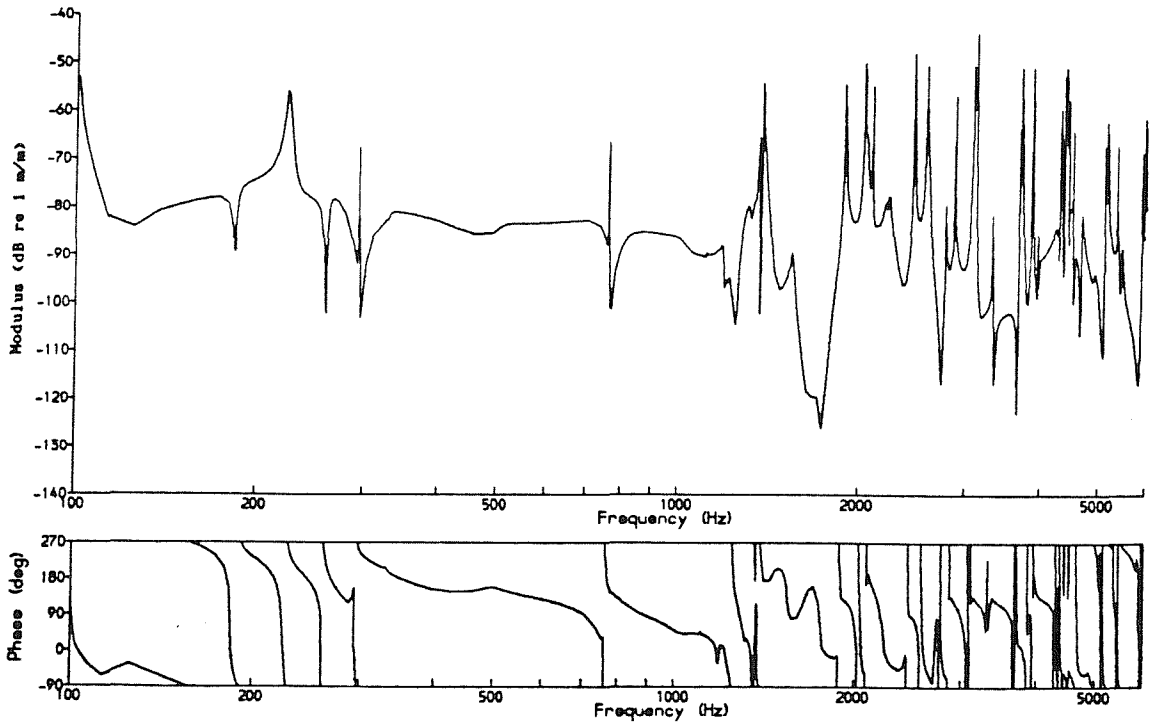

Figure 124 Longitudinal (z_1) Responses using 6 Coupling Degrees of Freedom

(a) Longitudinal Vibration Displacements for a Unit Roughness Input

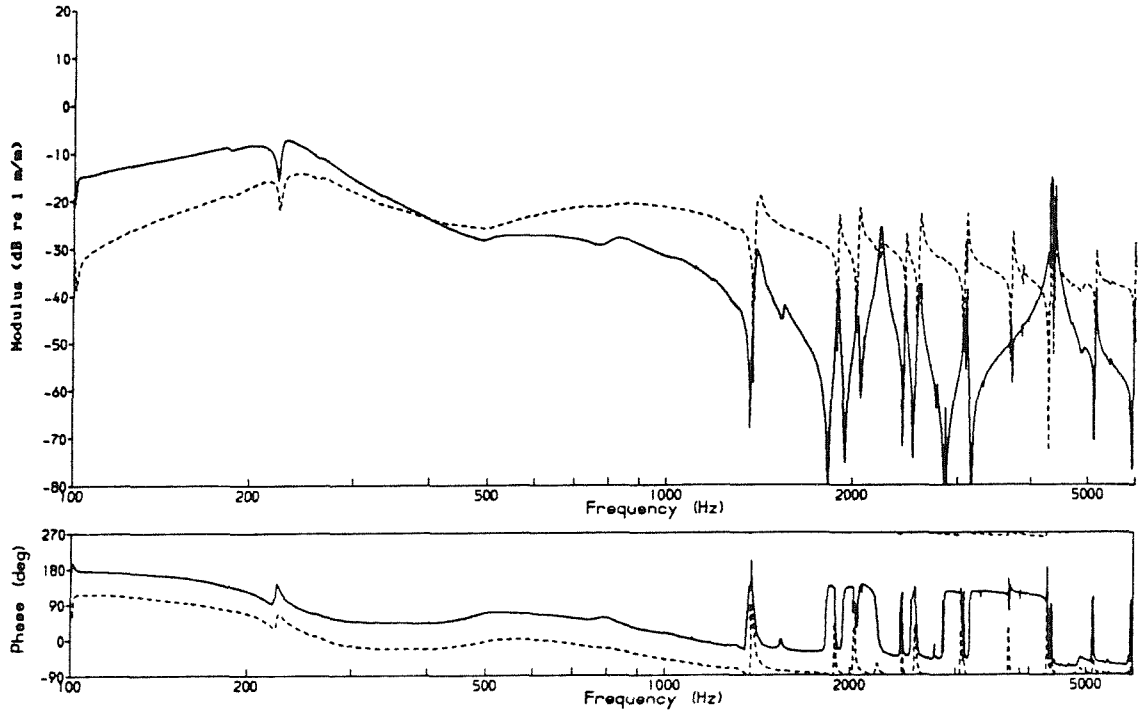

(b) Spin Rotations for a Unit Roughness Input

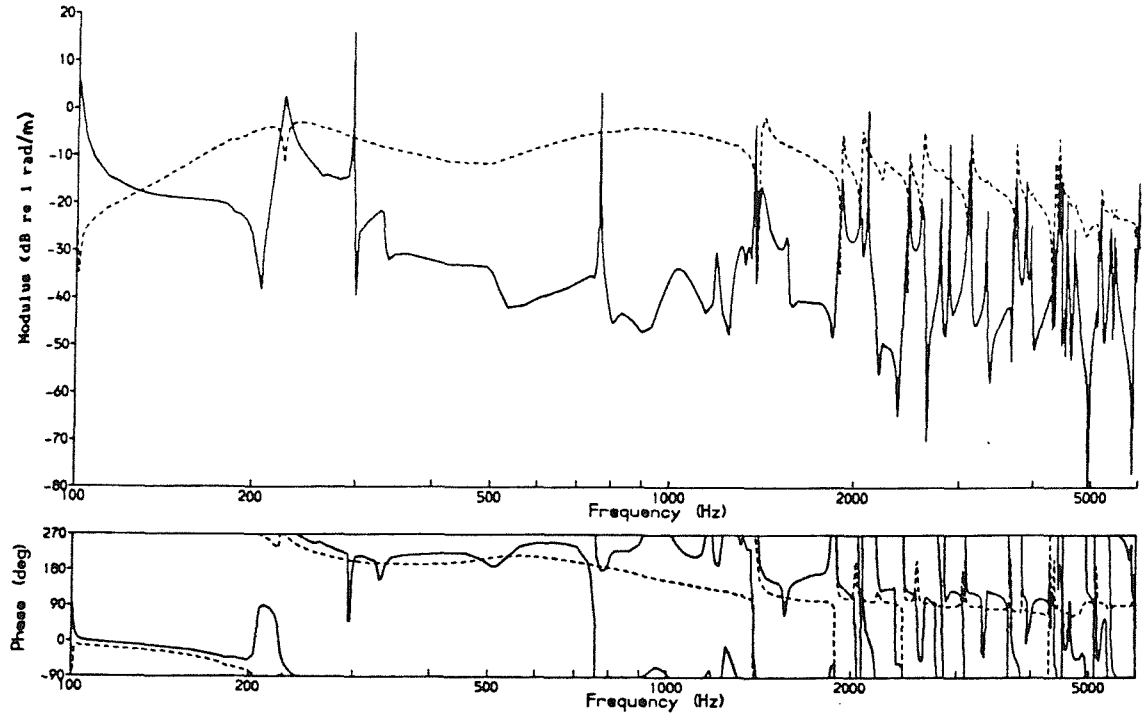

Figure 125 Effect of a Longitudinal Creepage of .003 based on 6 Coupling Degrees of Freedom (——— Wheel, ····· Rail)

calculation procedure is set to give finer resolution than for the static wheel calculations, a maximum change of 3 dB between adjacent wheel receptance points being specified.

Figure 126 shows the wheel web vibration, as seen from a frame of reference rotating with the wheel, for 3 train speeds. This web vibration is little different to that predicted in §4 (Figure 48), although larger low frequency components can be detected. These will be a consequence of the reduced rail receptances at low frequencies, for the detailed rail model, as noted in §7.2.2.

A slightly more significant change can be seen in the lateral tyre vibration, shown in Figure 127, particularly below about 1.5 kHz. Compared with measured results (Figure A6), this now gives slightly better agreement than was the case in §4. Previously, at 40 km/h, split peaks were seen at around 290 and 760 Hz (Figure 52), which became a broad hump at higher speeds. This feature is replaced by a single peak in each case (although it appears rather square), with lower levels of response in the troughs around 500 Hz and 1000 Hz, which accentuate the peaks. The larger low frequency component can again be seen.

The sharp peaks seen in the results of the spin vibration for the static wheel (Figures 119-122), are not seen at all in the rolling vibration. The receptances of the rolling wheel (§4) include coupling between the lateral and spin coordinates, which is not present in the static case; thus spin vibration is no longer unconstrained, as it appeared in Figures 119-122.

Comparisons of 1/3 octave results derived from the above spectra, and those taken from the measurements for 160 km/h (Appendix A), are given in Figure 128. Compared with the earlier results in Figure 24, and even those for the revised model in Figure 117 (static wheel), the predictions appear better, with good agreement at low frequencies. However, the predictions are still too great at high frequencies, particularly for the case of the lateral vibration of the tyre.

The reasons for this are unclear, although it is possible that inadequacies in the modal amplitudes derived from the finite elemene model (as used in equation (1)) at high frequencies could be responsible. These will be investigated below, briefly.

(a) 40 km/h

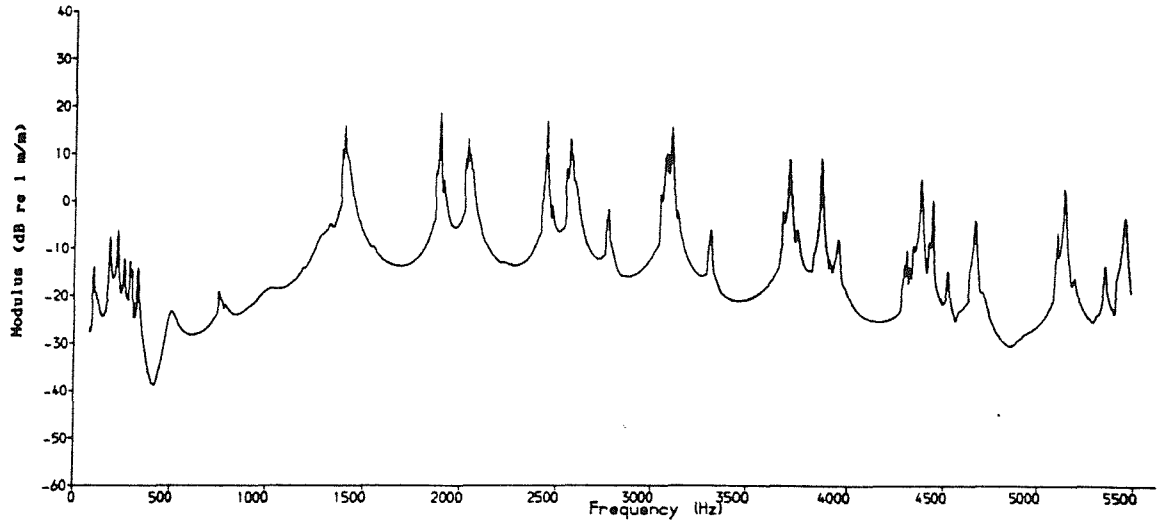

(b) 80 km/h

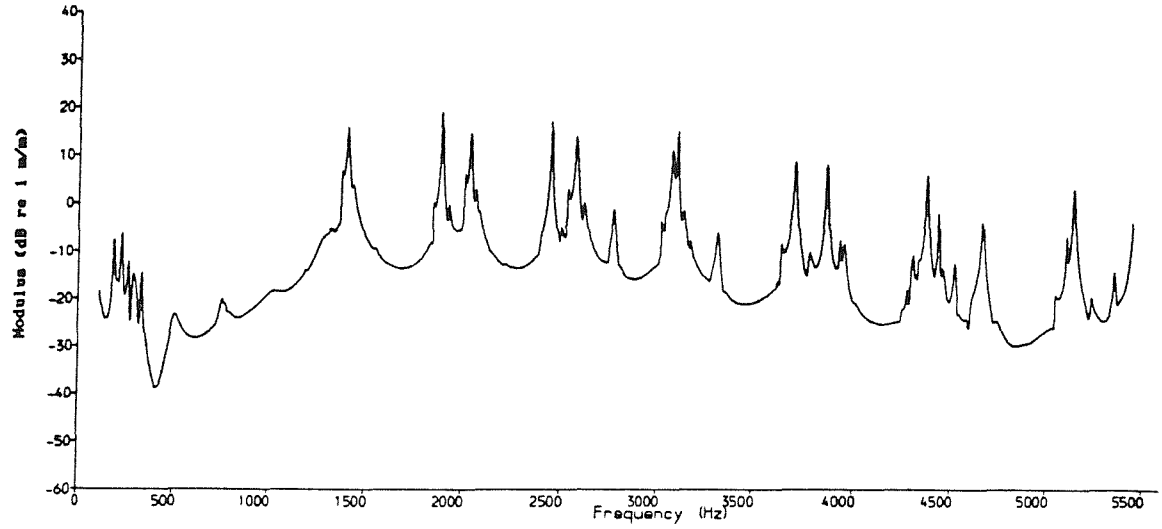

(c) 160 km/h

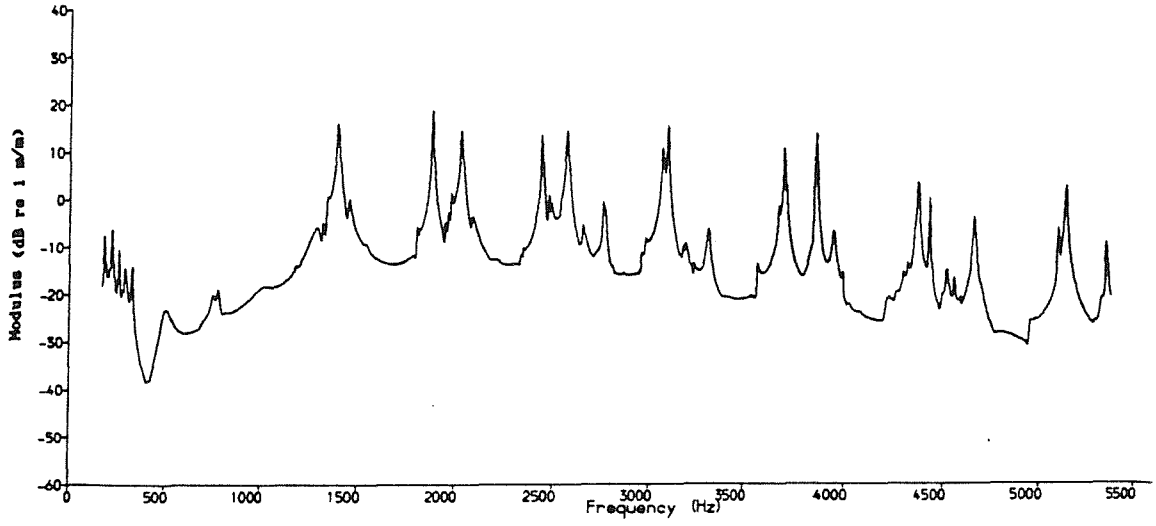

Figure 126 Predicted Wheel Web Axial Vibration (Displacement for a Unit Roughness Input) using 6 Coupling Degrees of Freedom

(a) 40 km/h

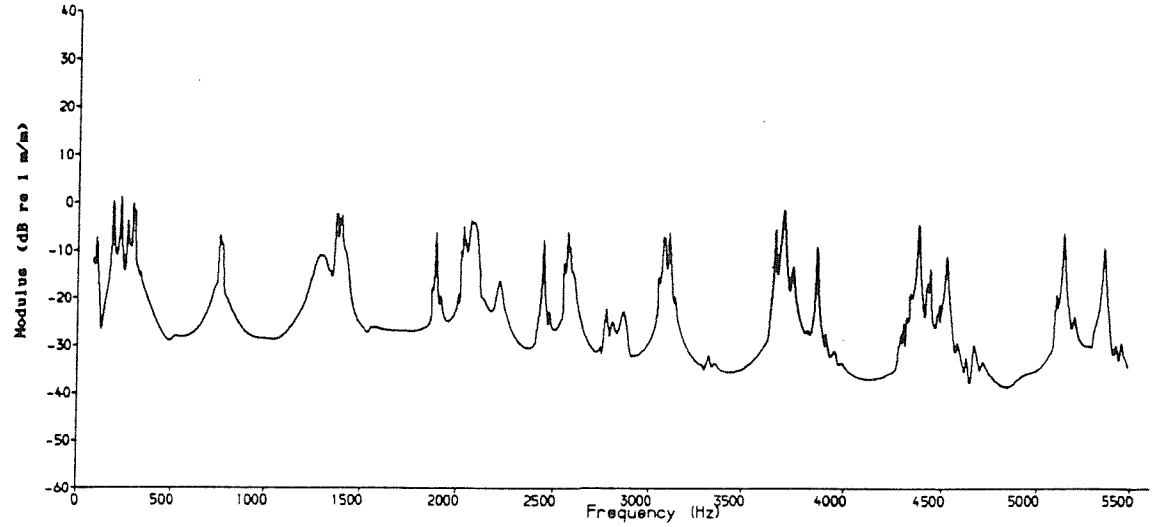

(b) 80 km/h

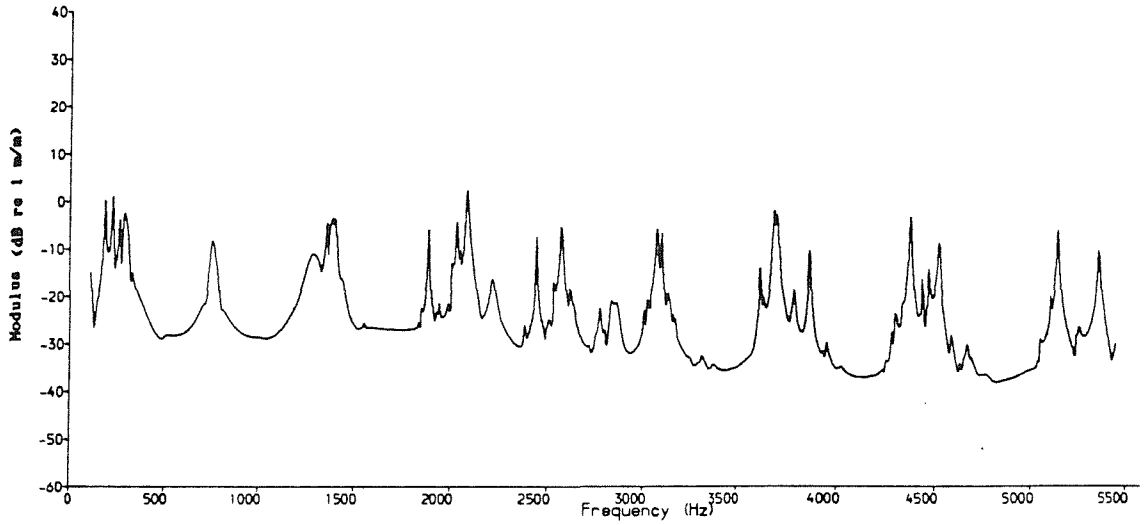

(c) 160 km/h

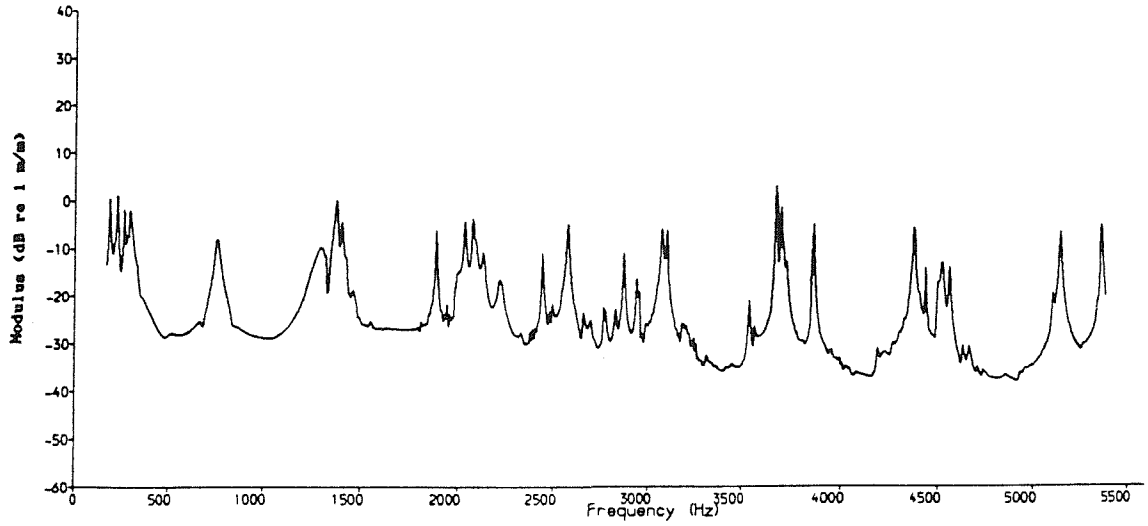

Figure 127 Predicted Wheel Tyre Axial Vibration (Displacement for a Unit Roughness Input) using 6 Coupling Degrees of Freedom

(a) Tyre Radial Vibration Displacement for a Unit Roughness Input

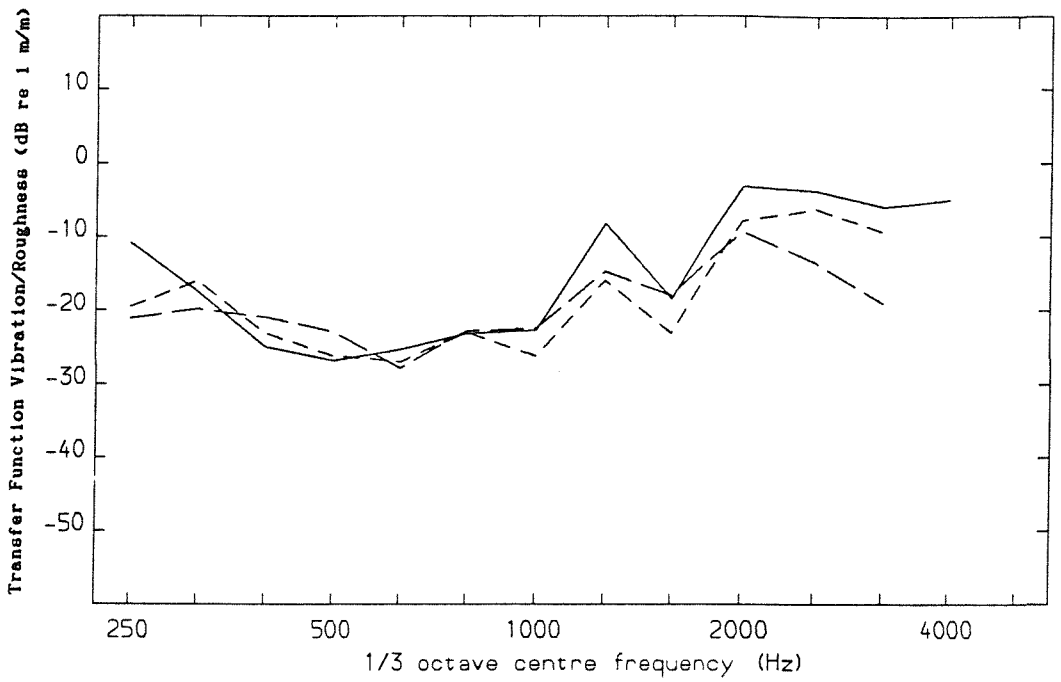

(b) Tyre Axial Vibration Displacement for a Unit Roughness Input

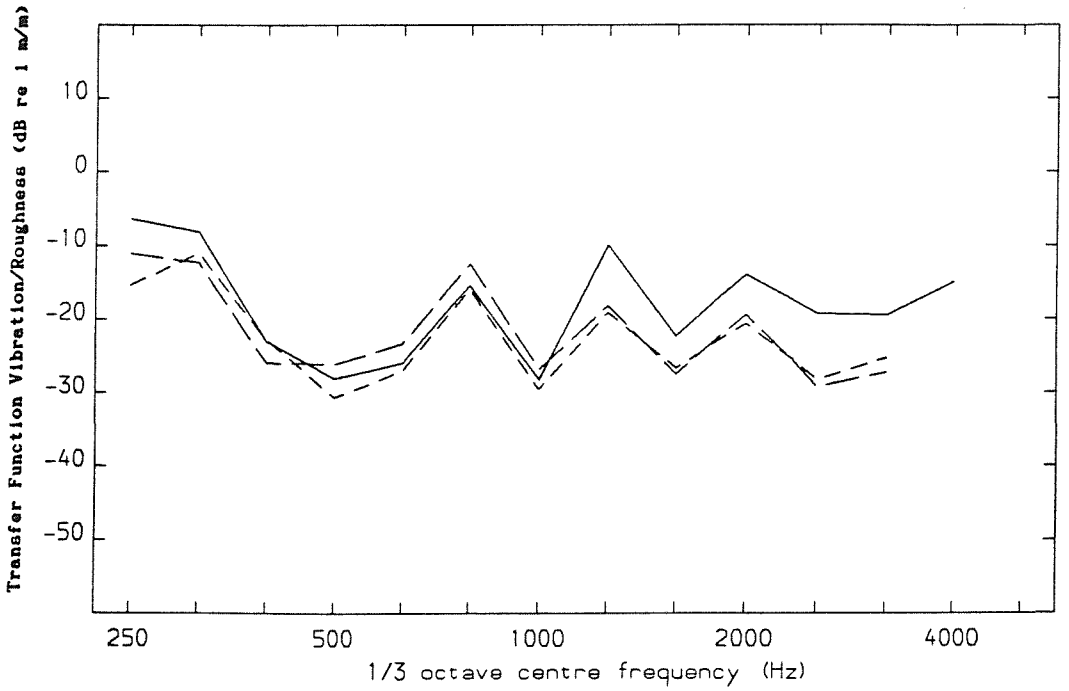

Figure 128 Comparisons of Predicted Rolling Wheel Vibration (———) with Measurements at 160 km/h from Appendix A (— — Smooth Wheel, - - - Rough Wheel)

Results based on just 2 linking coordinates (z_2 and z_3) are shown in Figure 129 for a train speed of 160 km/h. These are virtually the same as the 6-coordinate results shown in Figures 126 and 127; this is also the case for the other speeds. It can be concluded that, in terms of the rolling wheel vibration, these other 4 coordinates are actually superfluous, at least for these conditions. The differences between the current results and those of §4 are, therefore, not due to the inclusion of the extra degrees of freedom; they can only be due to the modified rail and contact receptances.

Inclusion of steady lateral or spin creepage makes little difference to the levels at resonances. It does, however, affect the off-resonance response below about 1 kHz, although only by 2-3 dB for a lateral creepage of 0.001, and even less for a spin creepage of 0.1.

7.4.2 Effects of Wheel Modal Parameters

The wheel receptances used throughout were derived in §2 from the plate-beam finite element model. They did not correspond precisely to those measured (Appendix C), particularly in the case of the cross receptance. The wheel modal parameters, from which the receptances are calculated, were the only parameters which were not varied in the parameter study of §3. Thus the effects of any errors in these has not yet been investigated.

For frequencies up to 5 kHz, the plate-beam finite element model predicted natural frequencies which were up to 12% higher than measured values. Unfortunately this suggests that the corresponding modeshapes are likely to be even less accurate, and for modes with nodes around the contact patch this could lead to quite large variations in receptances.

Looking at the rolling responses (in comparison with measurements), it would seem that the 1-nodal-circle modes, in particular, appear to have a response which is too great, in both the web and tyre axial responses, whereas the 0-nodal-circle modes appear to be excited too little in the tyre axial response, particularly at higher frequencies. If the former were excited less, and the latter slightly more, better agreement with the measurements may be achieved.

In order to assess this effect, adjusted modal parameters have been used. These have been derived roughly from the axisymmetric finite element model (which gave better agreement with measured natural frequencies), although modal masses had to be estimated by comparison

(a) Wheel Web Axial Vibration Displacement for a Unit Roughness Input

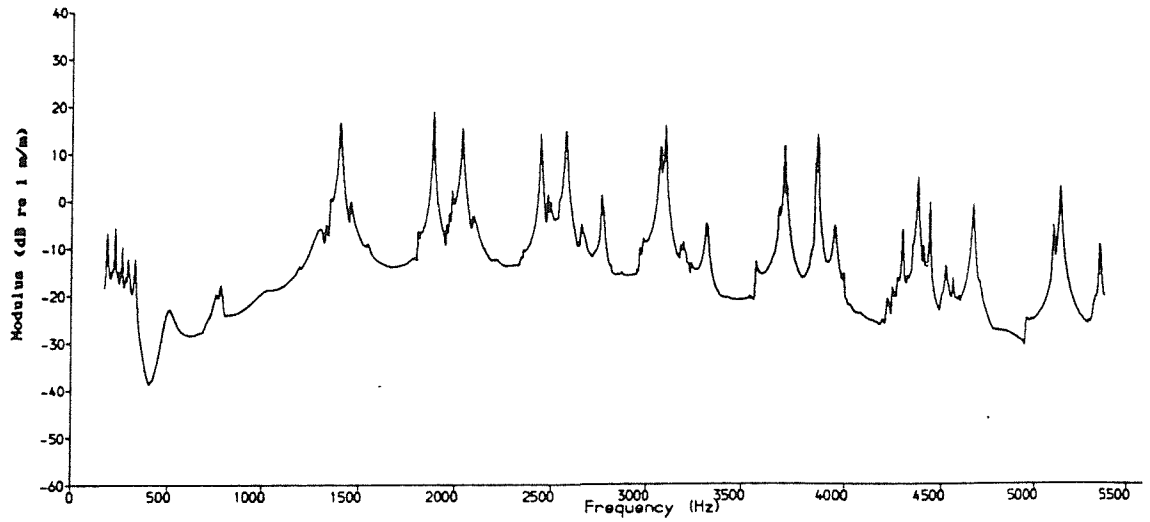

(b) Wheel Tyre Axial Vibration Displacement for a Unit Roughness Input

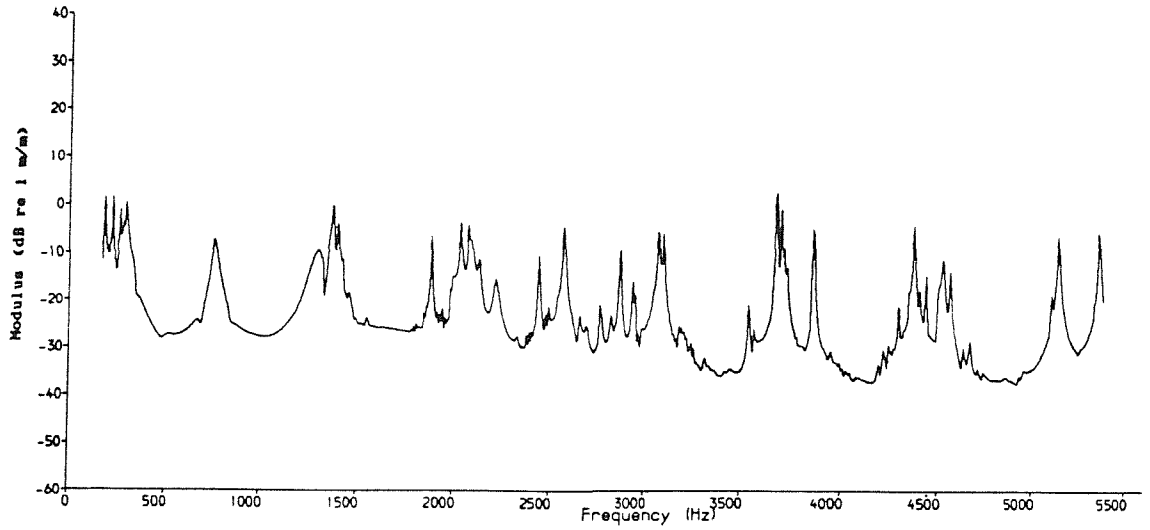

Figure 129 Wheel Rolling Responses using 2 Coupling Degrees of Freedom at 160 km/h

with the plate-beam model. From this analysis, it was found that the web response was reduced, above about 2 kHz, by up to 4 dB; the tyre axial response was influenced less. These results are promising, and suggest that more reliable modal data may give even better results. The modal data thus needs to be determined more accurately in future.

Throughout this thesis, only one type of wheel has been considered (Commonwealth) as experimental data are available for this wheel type. Alternative wheels would obviously produce a modified response. In particular, for a straight-webbed design of wheel (eg a BT10 type [54]), it may be expected that, although the vertical motion of the contact point will be excited as before, it will not result in large axial vibrations of the web. This is because the symmetry of a straight-webbed wheel means that the radial and axial motions are not coupled (as they are for a wheel with a curved web).

7.4.3 Effects of Wheel Damping

In §3 the effects of added wheel damping were considered for the 'static' wheel (see §3.4.4). For a rolling wheel, similar effects can be expected, since the same modes of vibration of the wheel appear in both cases. Once more, the damping ratios have been incresed in steps, to minimum levels in each case (ie all damping ratios smaller than the chosen level are raised, whilst higher values are unaltered). Values of .001, .003, .01, and .03 are used as before. These correspond roughly to 10 dB steps in the resonance amplitudes in the receptances.

Results are shown in Figure 130, in the same form as previously (Figure 45), ie the reduction in 1/3 octave response levels relative to the untreated case, for the three accelerometer positions used in Figure 128 (see Appendix A for their locations). It can be expected that the rail response will follow that found previously (Figure 45) - ie a small reduction for the lateral response, and virtually no effect on the vertical response.

Comparing the results in Figure 130 with those in Figure 45, the radial (and web axial) vibration shows a slightly larger reduction than the vertical wheel vibration did previously, whereas the tyre axial shows a slightly smaller reduction. All three positions now show similar reductions: there is little effect below 1 kHz; above this the first 10 dB step in damping (to .001) produces virtually no change, and each subsequent 10 dB step produces about 4 dB reduction in the 1/3 octave levels - this reduction increases slightly with frequency.

(a) Wheel Web Axial Vibration

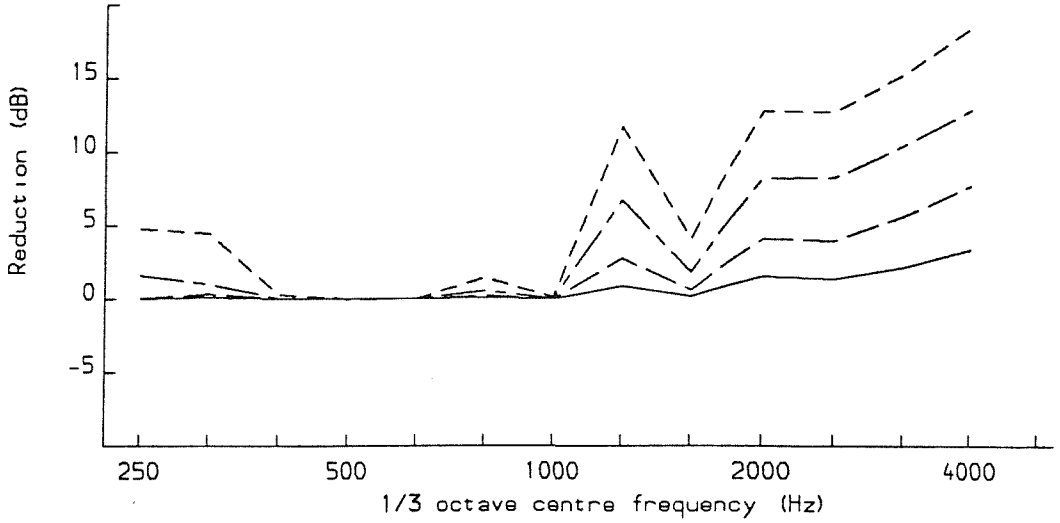

(b) Wheel Tyre Radial Vibration

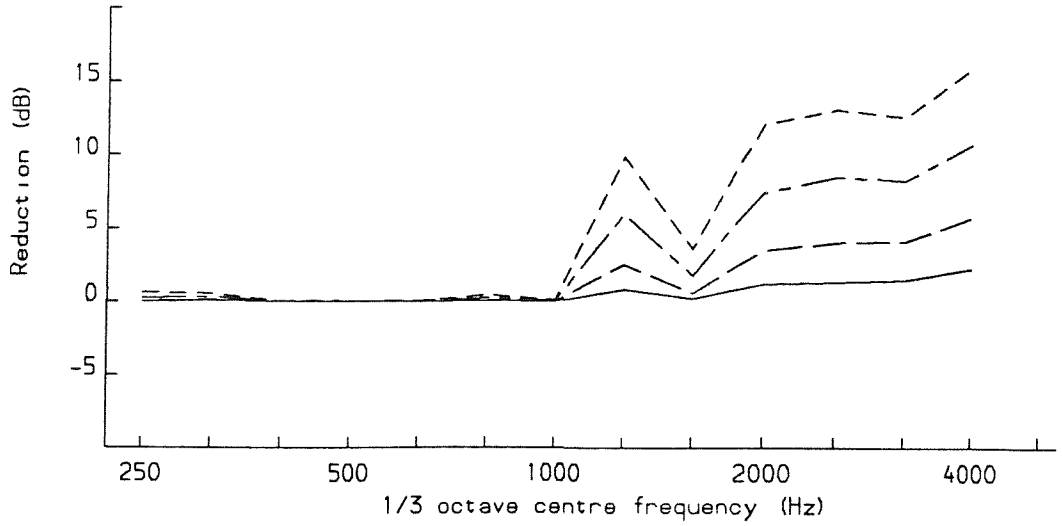

(c) Wheel Tyre Axial Vibration

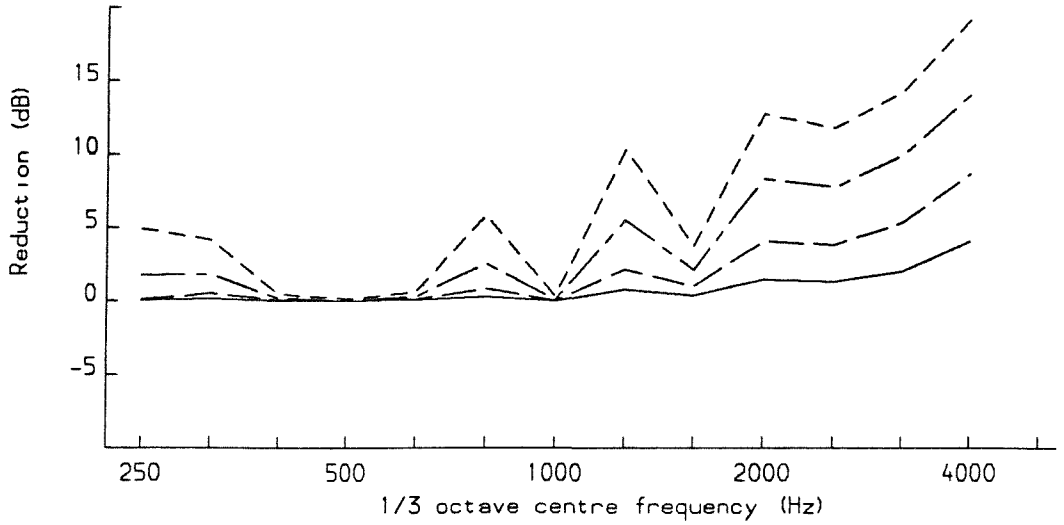

Figure 130 Reduction in Wheel Rolling Responses due to Added Damping

Minimum Damping Ratios: ——— .001, — — .003, —·—· .01, - - - .03

This implies that, when a wheel is rolling on the rail, it experiences a similar damping due to its coupling with the rail as it does when static on the rail. However, it should be remembered that the static wheel only experiences this damping for the cos nθ modes (which have an anti-node at the contact patch), whereas the sin nθ modes (with a node at the contact patch) are relatively unaffected and can be excited easily.

7.4.4 Inclusion of Coupling to Second Wheel

In §6.1.4, equations were derived to take account of the fact that a wheelset is actually excited through both of its wheels, and that a significant coupling could therefore occur through the axle. Results are predicted here for a 3-degree-of-freedom interaction (z_2, z_3 and z_4) at either wheel/rail interface, and with no offset to the contact point on the rail (ie no rail cross receptance).

The two components of vertical vibration are shown in Figure 131. It can be seen that the component generated at the same side as the excitation is much greater than that generated at the other side. The overall result is little different to that generated by a single wheel (Figure 114).

Figure 132 shows the two equivalent components of lateral vibration. In this case the two components are similar in magnitude to each other for frequencies up to around 1.5 kHz. Above this the transfer through the axle declines, even though all axle modes up to 5 kHz have been included into these results (in all previous results in §3 and §7 the axle modes above 1.5 kHz have been omitted). The total vibration displays very similar amplitudes to those predicted from the single wheel model, although at some of the troughs in the earlier results the levels are raised a little.

Hence, the inclusion of the second wheel, whilst introducing significant coupling through the axle for the case of the lateral responses, has little overall effect on the amplitudes or the character of the wheel or rail responses. It appears, therefore, that its neglect up to now has not been a serious omission.

(a) Components of Vertical Rail Vibration for a Unit Roughness Input

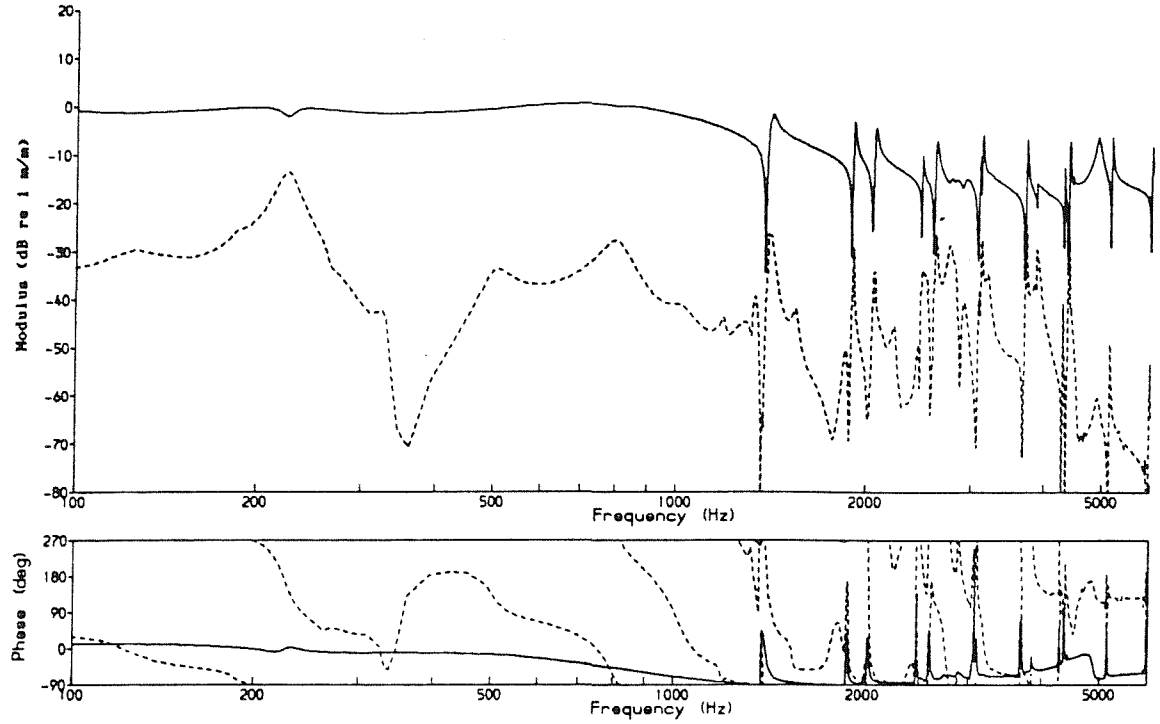

(b) Components of Vertical Wheel Vibration for a Unit Roughness Input

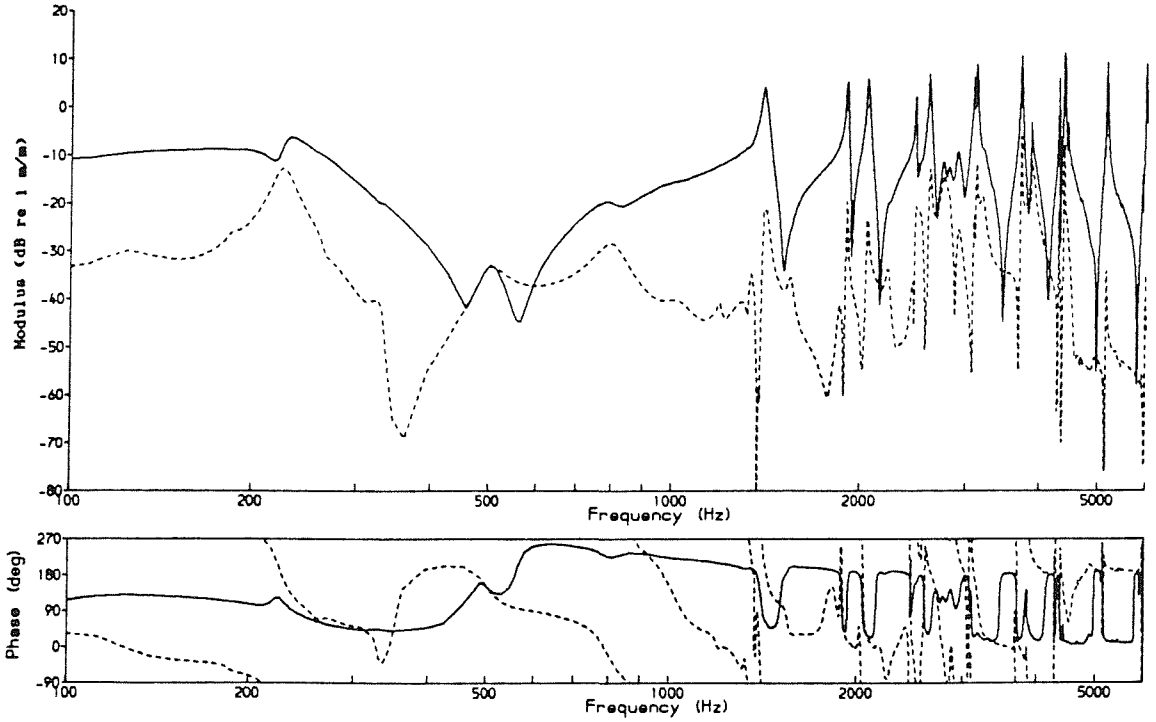

Figure 131 Effect of Coupling through Axle - Components of Vertical Vibration due to Excitation at Both Wheel-Rail Contacts (——— Near side, ····· Transfer through Axle)

(a) Components of Lateral Rail Vibration for a Unit Roughness Input

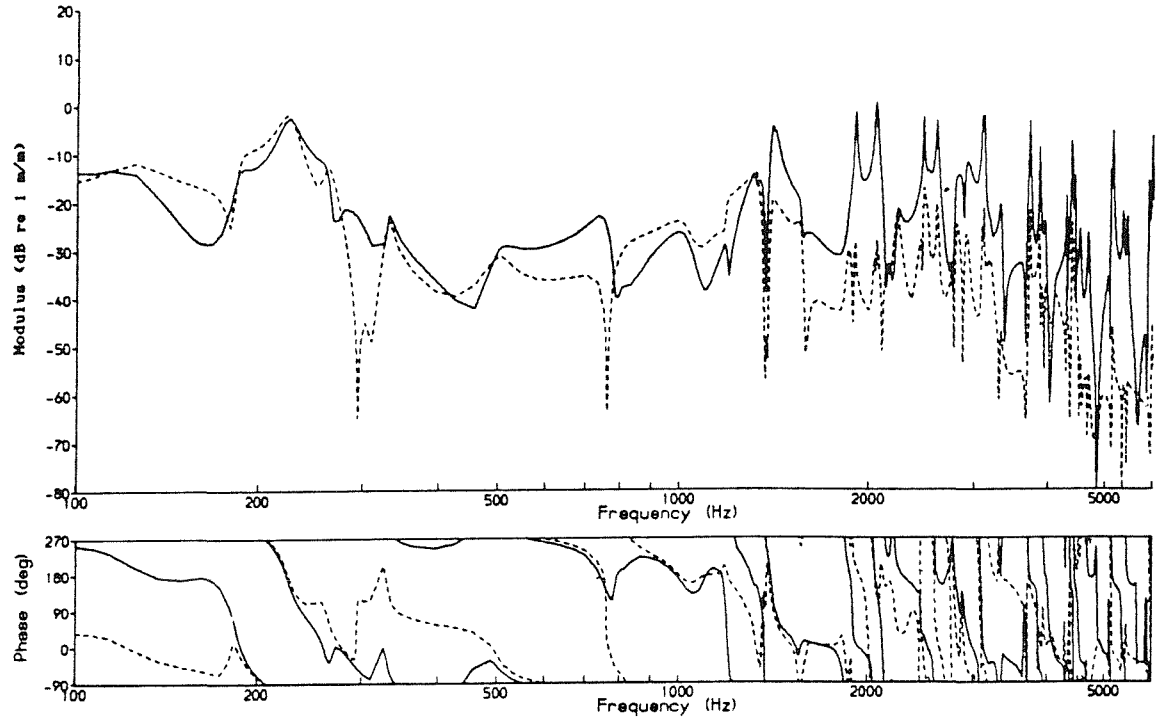

(b) Components of Lateral Wheel Vibration for a Unit Roughness Input

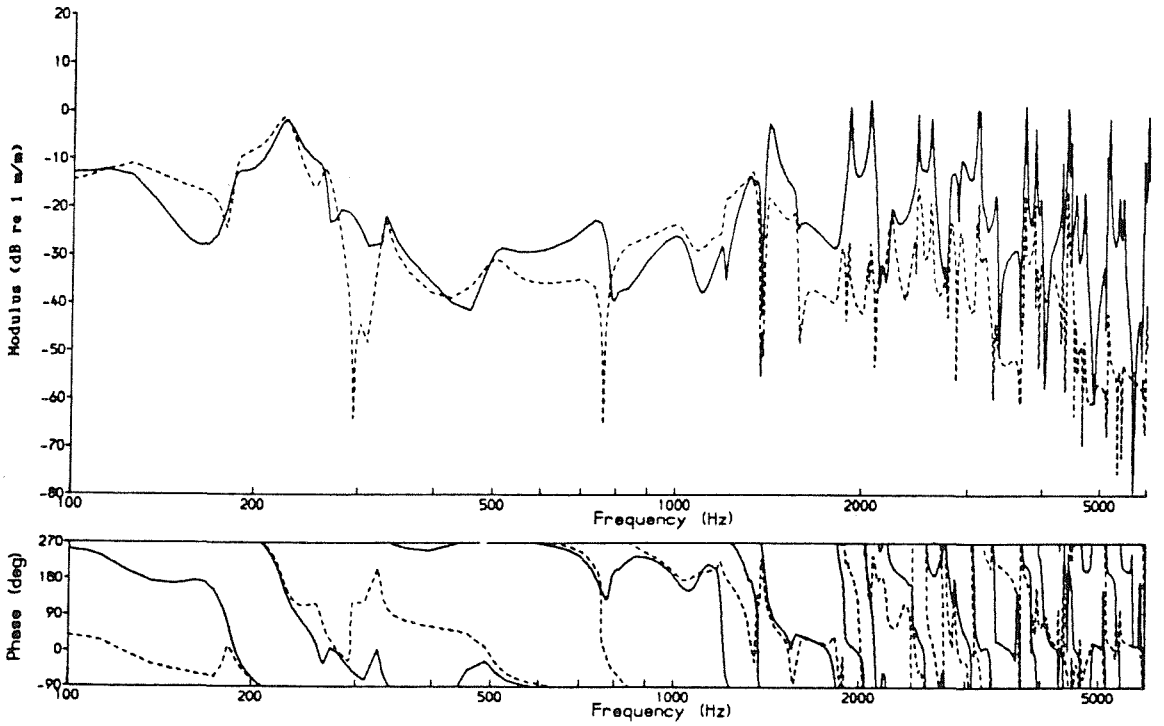

Figure 132 Effect of Coupling through Axle - Components of Lateral Vibration due to Excitation at Both Wheel-Rail Contacts

(——— Near side, ····· Transfer through Axle)

7.5 ALTERNATIVE FORCING MECHANISMS

7.5.1 Relative Force Input

So far, the predictions have all been based on a relative displacement input in the vertical direction, which has been taken to be the combined surface roughness. In §6.1, some alternative excitation inputs were discussed, and these will now be considered briefly. In this section, the simpler rail receptances will be used, to allow the response behaviour to be identified more clearly, and hence only 2 degrees of freedom will be included.

In §6.1.1, a relative displacement input {r} was shown to be equivalent to a relative force vector {P}. Thus for a relative force spectrum, it might be expected that the wheel and rail responses would maintain similar relative properties, although the overall magnitudes will be altered. It should be recalled (from §6.1.2) that, when a vertical relative force input is considered, the force vector should have (non-zero) components in all the other coordinate directions, determined from a zero relative displacement (constraint) in these directions. In this case, with 2 coupling degrees of freedom, a constraint is required only in the lateral coordinate.

Figure 133 shows the responses to a unit relative vertical force, which are therefore transfer functions in dB re 1 m/N. The vertical responses take almost the exact form of the vertical receptances. In the case of the rail, this is a straight line (see Figure 19), due to the use of the simple beam equations. The wheel response, by contrast, is very peaky. The *relative* magnitudes of the wheel and rail, however, take exactly the same form as for the relative displacement input (see Figure 106); at the wheel resonances the wheel now reaches a maximum, whereas previously the rail reached a minimum.

The lateral responses look quite similar in form to previously (Figure 107) and also to each other.

If the vertical force is introduced without the displacement constraints in the other coordinate directions, the results shown in Figure 134 are produced. The vertical responses take the exact form of the vertical receptances, and the lateral responses take the exact form of the cross receptances. This may deduced directly from equation (83) of §6.1.1.

(a) Vertical Wheel (———) and Rail (·····) Response

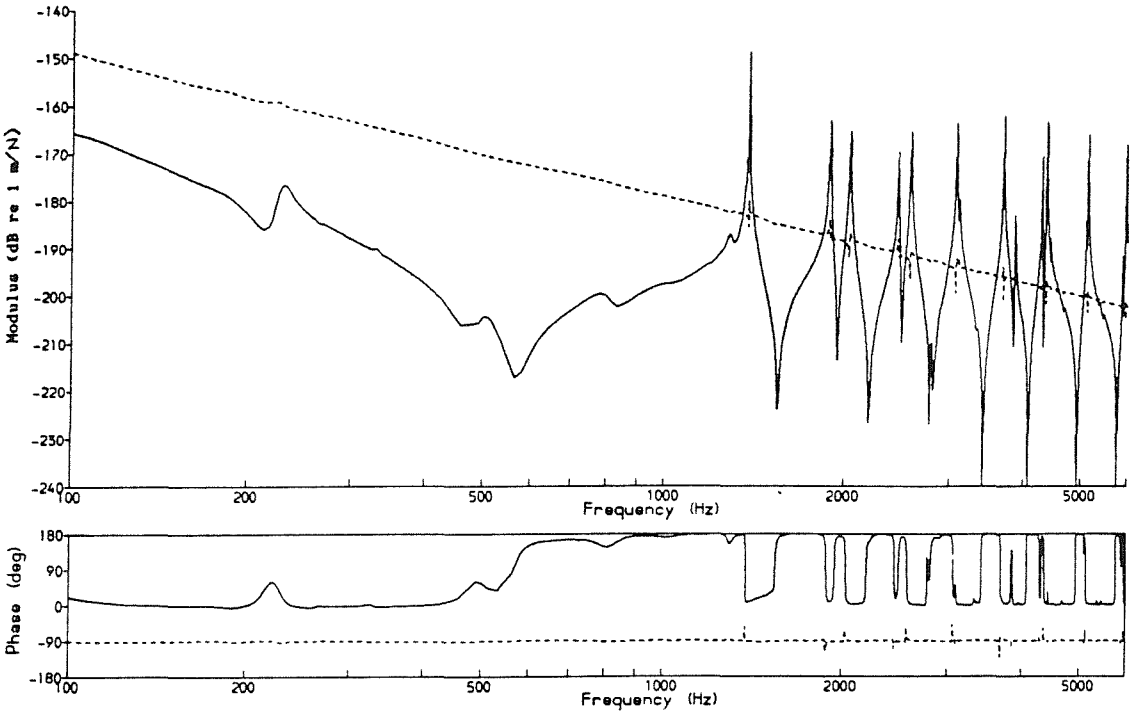

(b) Lateral Wheel (———) and Rail (·····) Response

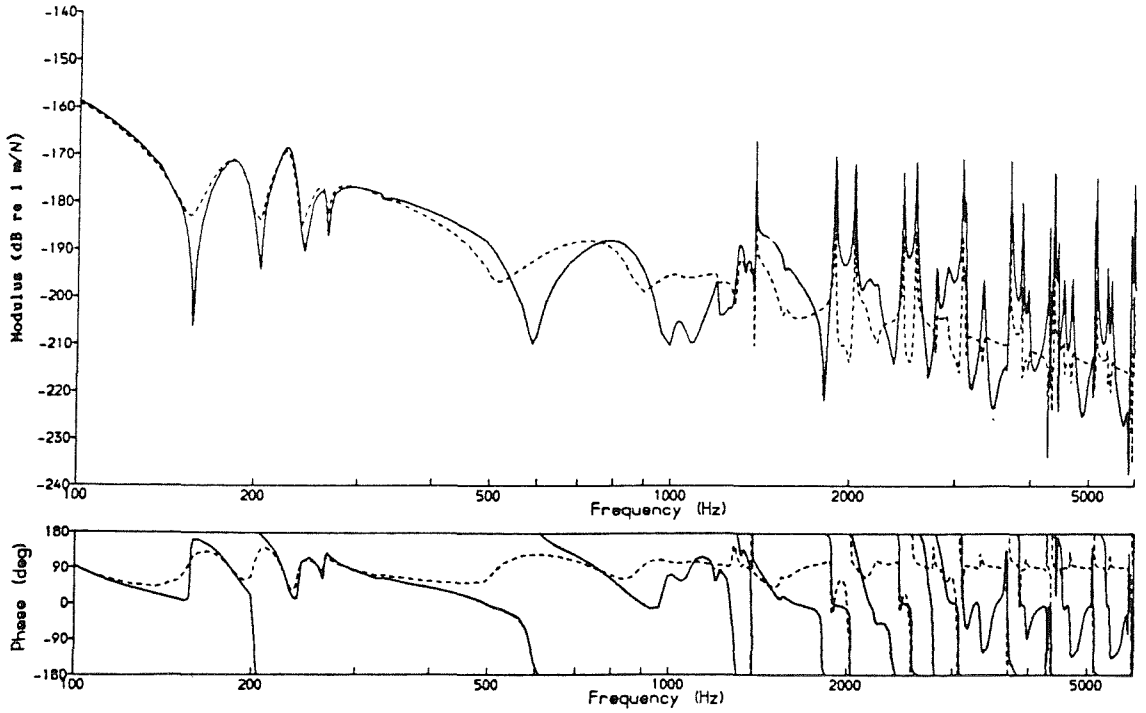

Figure 133 Wheel and Rail Vibration Displacement due to a Unit Vertical Relative Force Input with Lateral Coupling

(a) Vertical Wheel (———) and Rail (·····) Response

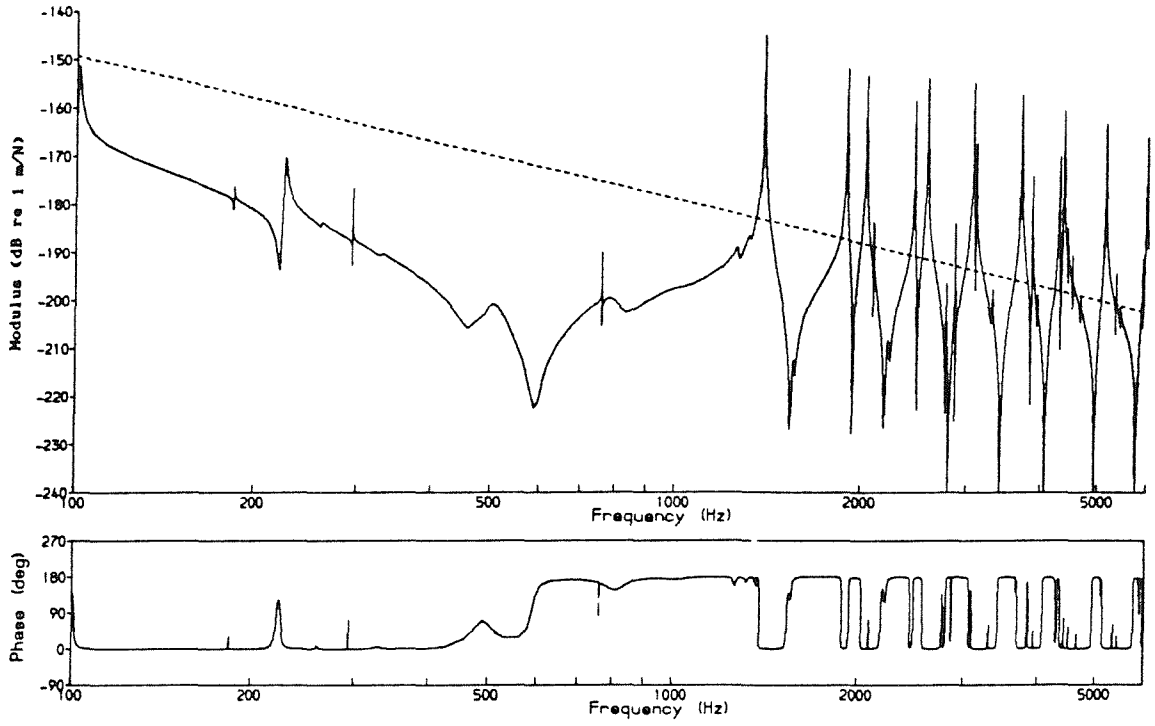

(b) Lateral Wheel (———) and Rail (·····) Response

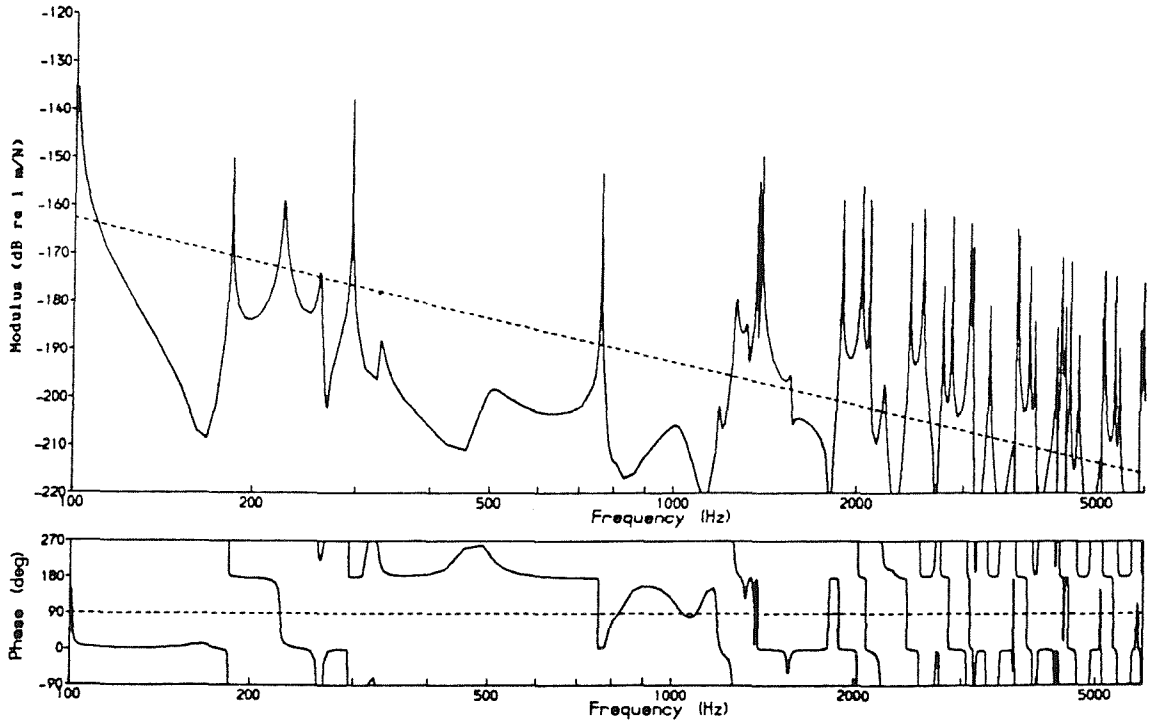

Figure 134 Wheel and Rail Vibration Displacement due to a Unit Vertical Relative Force Input without Lateral Coupling

The relative magnitudes of the wheel and rail vertical responses in this case, are similar to those for the solution based on interaction in the vertical coordinate alone (§3.4.1 from the relative displacement input), since in that case, as now, there is no wheel-rail coupling in the lateral direction. The lateral responses, however, are quite different from those obtained previously. This model effectively implies a decoupling of the wheel and rail, apart from the vertical direction - ie the lateral force was set to zero.

7.5.2 Absolute Inputs

The absolute displacement- and the absolute force-input models were derived in §6.1.3 to correspond to Feldmann's "series impedance model" [77]. By imposing a vertical displacement at the contact patch in this way (see Figure 100), both wheel and rail are forced to move in the same direction (apart from any extension/compression of the contact spring). This is in contrast to the relative displacement input model, where, to respond to a roughness asperity, the wheel moves upwards, the rail moves downwards, or the contact spring is compressed (see Figures 99 and 28); in practice a combination of these occurs.

In studying these absolute input models, the 2-degree-of-freedom model is again used, in combination with the simple rail model. Figure 135 shows the responses due to a vertical absolute displacement input of unit amplitude (ie the responses are agin non-dimensional, in dB re 1 m/m). These are quite different to the relative displacement results (Figures 106 and 107). The rail responses are completely featureless (because of the simple nature of the receptances used), whereas the wheel responses are much more resonant (with sharper peaks). In this respect the responses have a similar form to those due to a unit relative force (Figure 133).

The magnitude of the lateral rail response is much lower than for a relative displacement input; this does not correspond with measurements. The lateral wheel vibration is much greater, and its shape mirrors the lateral receptance rather than the cross receptance (see Figures 13 and 15). These results contain the 0-nodal-circle modes found in the experimental tyre response, but the very high predicted levels suggest that this model is unrealistic.

Figure 136 shows the equivalent results for a unit absolute force input. The vertical wheel response appears similar in form to that for

(a) Vertical Wheel (———) and Rail (·····) Response

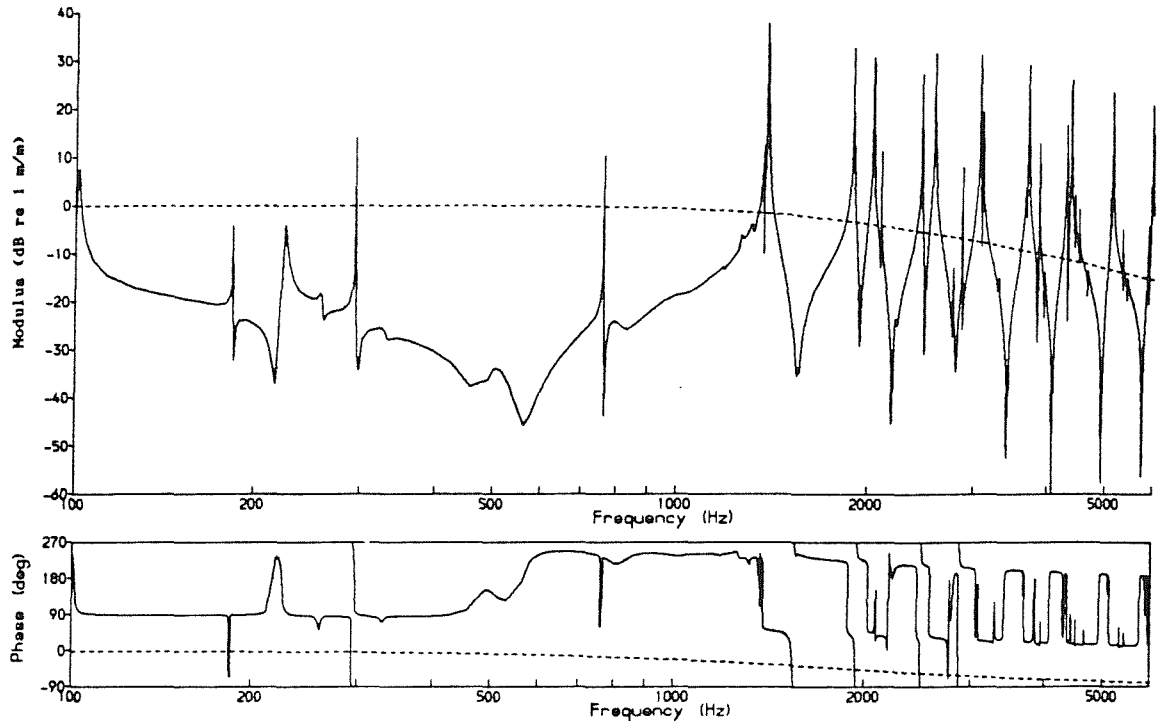

(b) Lateral Wheel (———) and Rail (·····) Response

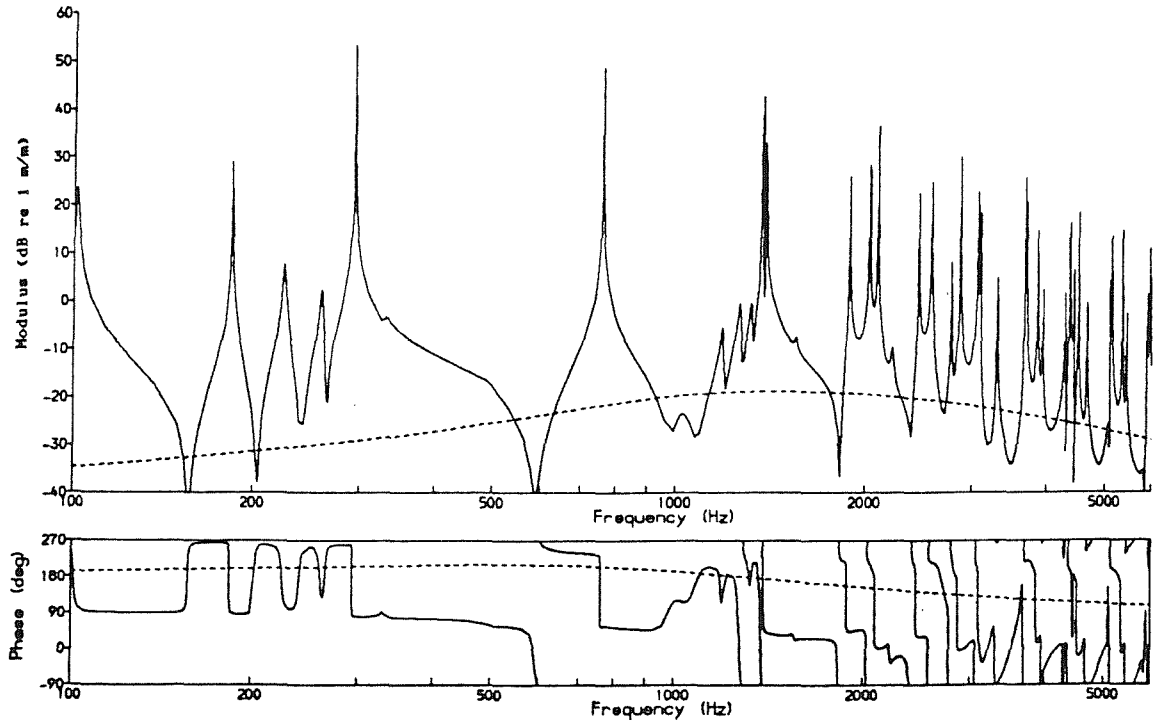

Figure 135 Wheel and Rail Vibration Displacement due to a Unit Vertical Absolute Displacement Input

(a) Vertical Wheel (———) and Rail (·····) Response

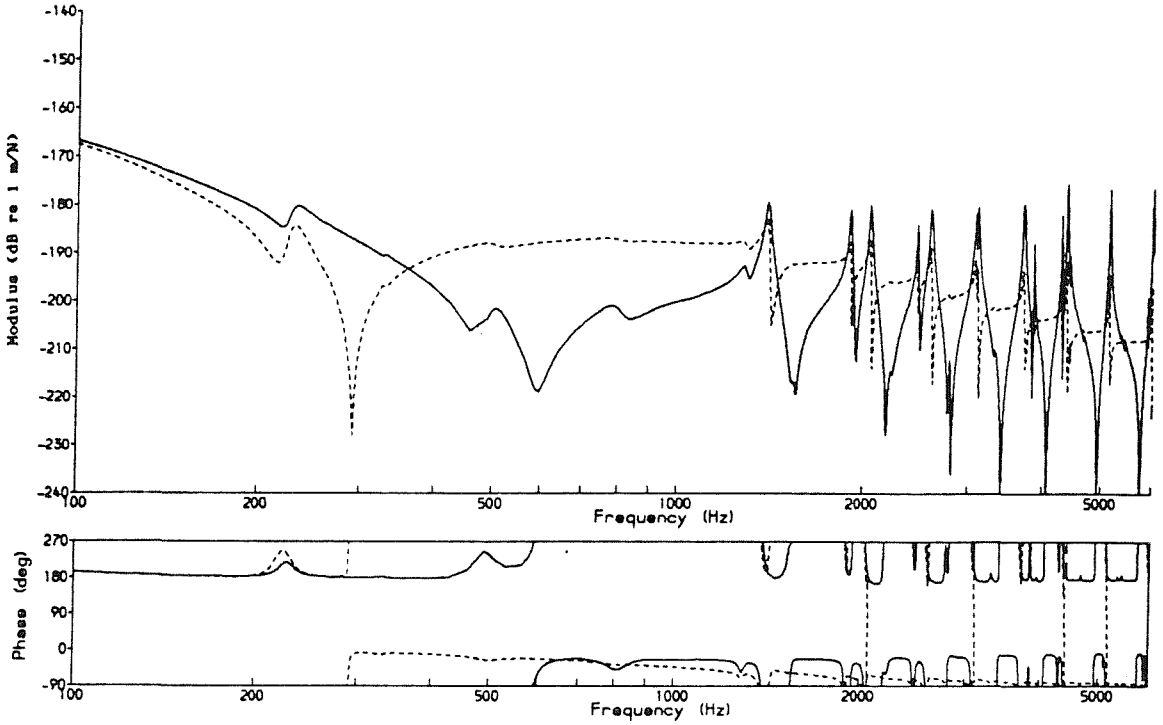

(b) Lateral Wheel (———) and Rail (·····) Response

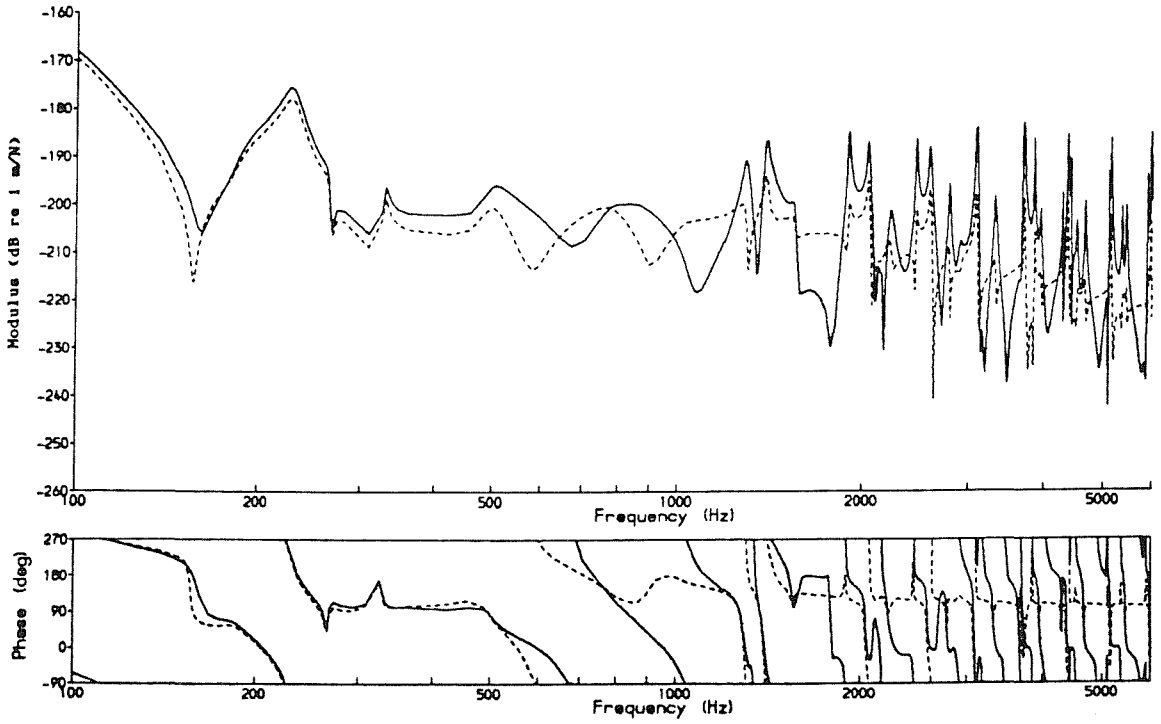

Figure 136 Wheel and Rail Vibration Displacement due to a Unit Vertical Absolute Force Input

the relative displacement input, with broad peaks just above the various wheel resonance frequencies over 1.3 kHz. However, the vertical rail response is altered slightly, so that the positions of its peaks and troughs are reversed (cf Figure 106). Unfortunately the analysis of measured rail vibration cannot resolve points of such fine detail, due to the transient nature of the signals.

At low frequencies the vertical rail vibration is predicted to be somewhat less than the wheel vibration, which is the opposite to that found for the relative displacement model (Figure 106). Once allowance was made for the decay with distance within the analysis length, reasonable agreement was achieved with measured results in that case (§3.3.1). Here, however, such allowance for the decay with distance results in a worsening of the agreement between the measurements and predictions in terms of the relative magnitude of the rail and wheel vibration. Feldmann [77] did not make such allowance for the effect of distance on the vibration of the track in his cylinder/beam test rig.

The lateral responses, as previously for the relative displacement model, contain no obvious wheel resonances. The wheel and rail responses appear very similar to each other.

The above has been based on an equal division of the contact receptances (ie α^{CR} and α^{CW} are both set to $\alpha^{C}/2$). Feldmann, however, used a division based on the relative magnitudes of the wheel and rail receptances (see §6.1.3). The equivalent results for such a division are shown in Figures 137 and 138. Whilst they show the same general trends as the above, some significant detail differences can be seen.

It is clear, then, that if the absolute displacement/force models were to be given further consideration, it would be important to determine the correct method of dividing the contact receptances. The localised nature of the contact stresses suggests that the simple division may be the more appropriate (ie the contact receptances should be independent of the behaviour of the remainder of the structures), but this is probably an over-simplification. In a sense, this arbitrary division gives the parallel impedance model an extra "degree of freedom" which may be altered in order to find a reasonable fit of the model to experimental data.

When compared with the experimental results (Appendix A), it would seem that the relative displacement model used in §3, and subsequently, gives a better form of results than any other formulation,

(a) Vertical Wheel (———) and Rail (·····) Response

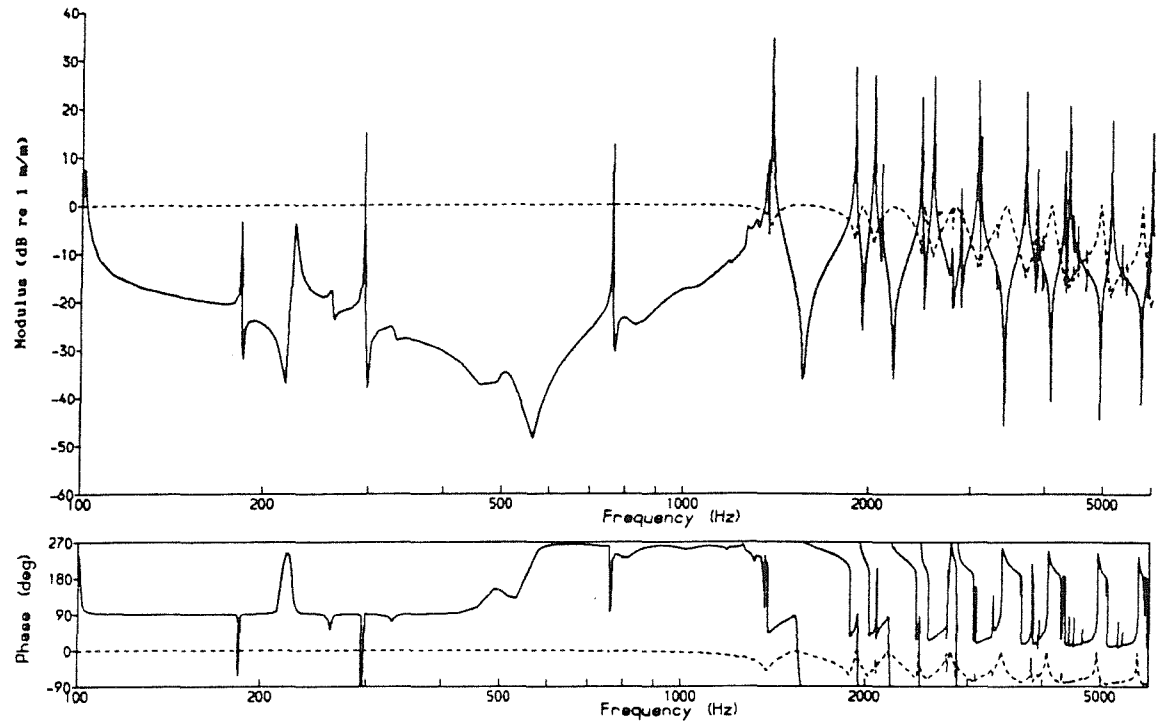

(b) Lateral Wheel (———) and Rail (·····) Response

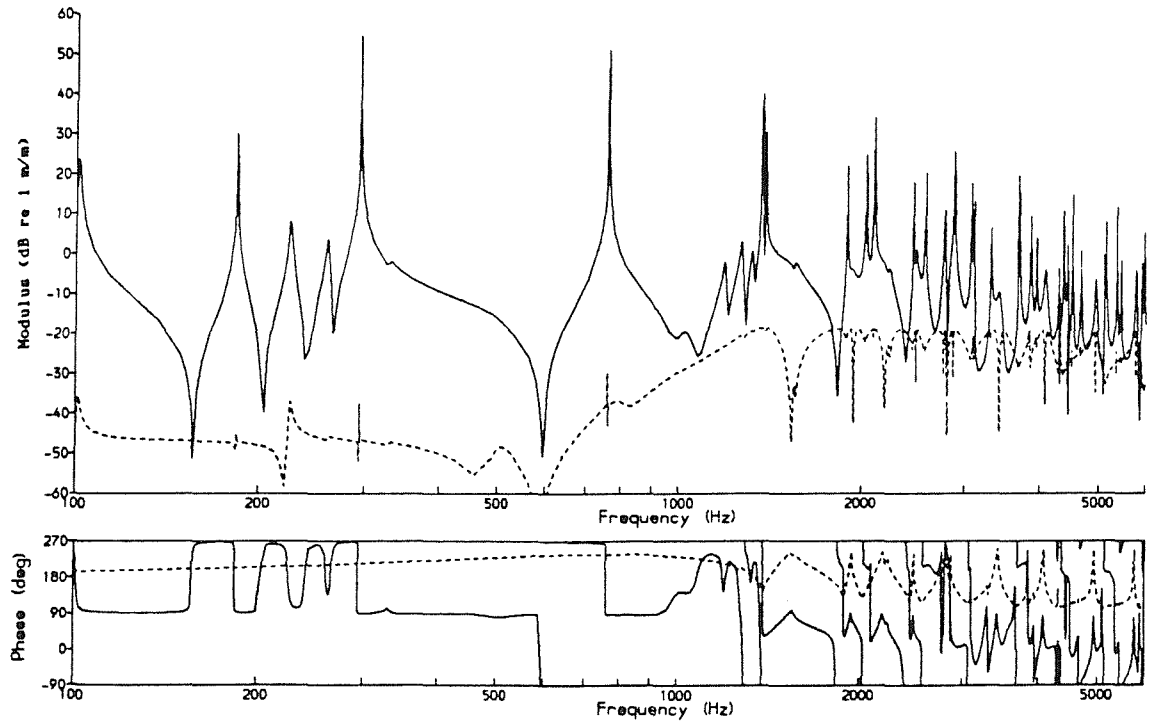

Figure 137 Wheel and Rail Vibration Displacement due to a Unit Vertical Absolute Displacement Input using Feldmann's Division of Contact Receptances

(a) Vertical Wheel (———) and Rail (·····) Response

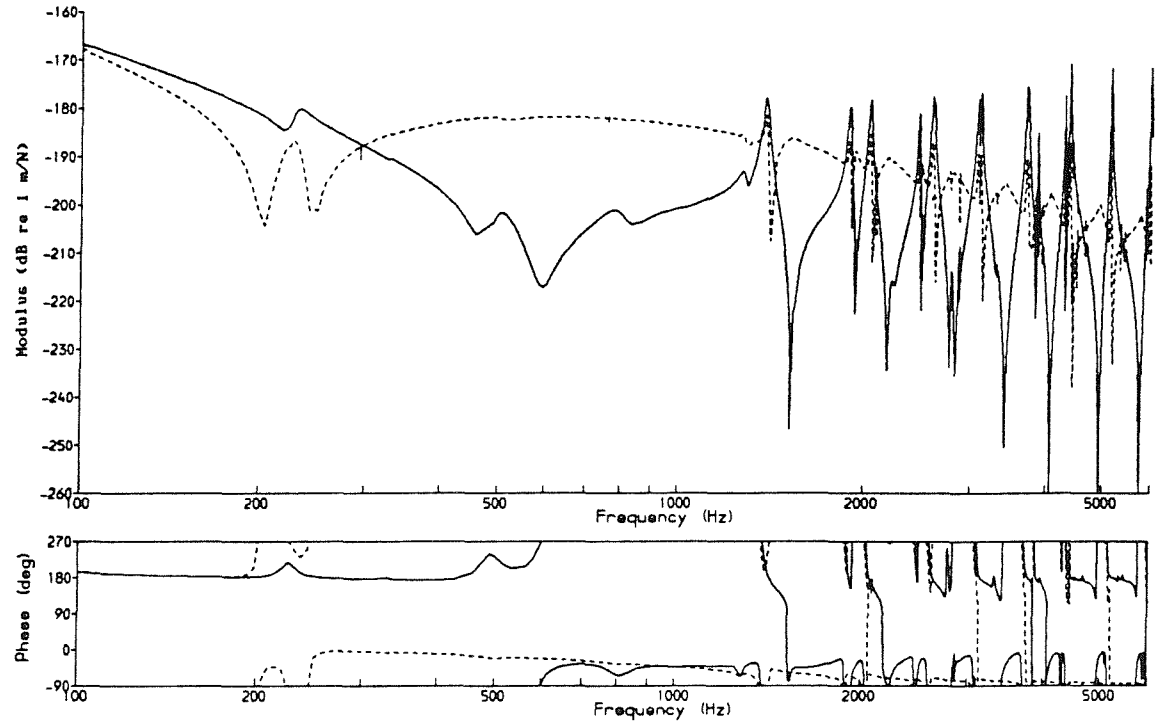

(b) Lateral Wheel (———) and Rail (·····) Response

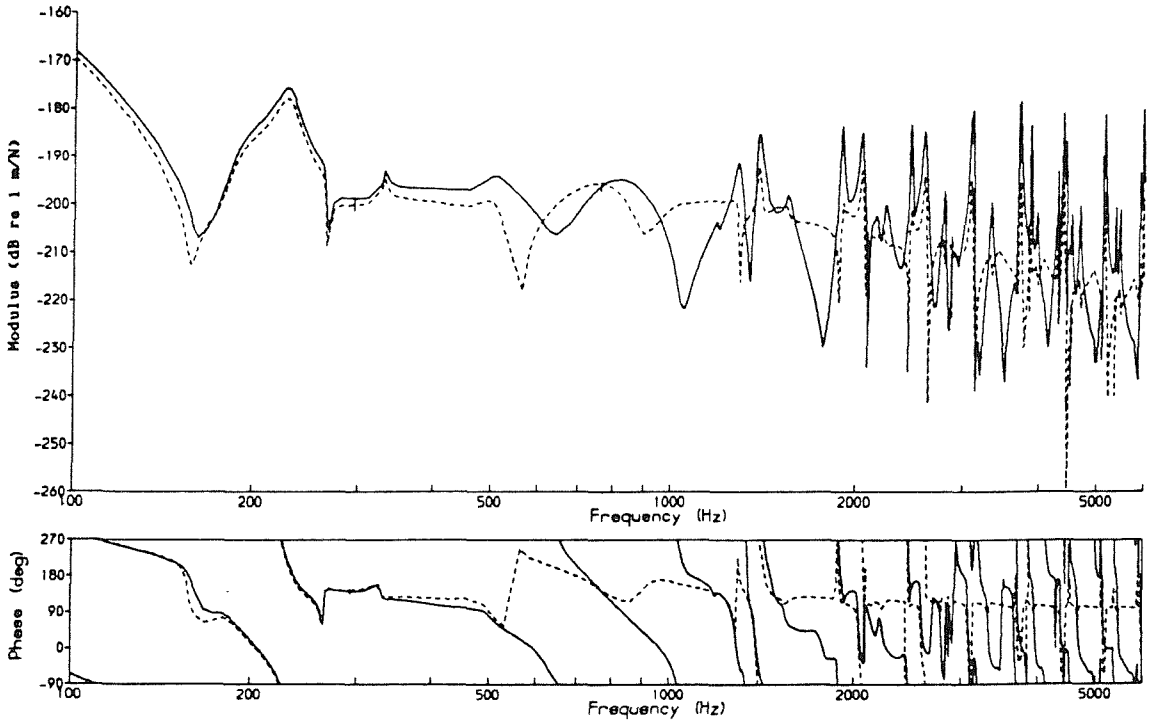

Figure 138 Wheel and Rail Vibration Displacement due to a Unit Vertical Absolute Force Input using Feldmann's Division of Contact Receptances

although the absolute force input appears similar in some respects. Feldmann [77] found that the latter (expressed as the "series impedance model") gave better agreement with the results from his cylinder-on-beam test rig. The reasons for this are not clear. However it should be noted that Feldmann looked only at the responses in the vertical direction, whereas the lateral vibrations appear less satisfactory in Figures 135-138.

From the current work, there seems to be no reason to pursue Feldmann's model for the wheel-rail case, as it seems inferior to the traditional "parallel impedance model". In any case, this relative displacement input model appears more realistic, as it is difficult to envisage a situation in which *the forces acting on the wheel and the rail are not equal and opposite*, even when an impulse is generated due to a roughness asperity (as in Feldmann).

Furthermore, the relative displacement input model has formed the basis of successful vehicle dynamics work (at lower frequencies) [83, 82].

7.5.3 "Wandering" Contact Patch

If the surface profile of the rail (or wheel) is such that the running line oscillates across the wheel and rail surfaces, an excitation of the system can occur, even if no vertical displacement is input. This lateral oscillation of the contact position generates a force input in the z_4 direction, as derived in §6.3.

Results are shown in Figure 139 for the vertical and lateral responses due a unit (1 Nm) moment input (ie in dB re 1 m/Nm). The lateral responses are generally greater than the vertical ones, particularly below 1 kHz. The form of the wheel responses appears somewhat different to that of the experimental results of Appendix A, although peaks still occur around wheel resonances particularly in the vertical response.

Unfortunately no measured data are available on the extent of this effect, but it is worthwhile making a rough estimate. It is conceivable that a peak-to-peak oscillation of up to 10 mm (roughly the width of the contact patch) could occur on a corrugated rail, where the roughness amplitude will be of the order of 100 μm peak-to-trough. This would then be equivalent (for a wheel load, P_o = 50000 N) to a moment input of $|P_4| = \varepsilon P_o$ = 500 Nm. In decibels, this means that a

(a) Vertical Wheel (———) and Rail (·····) Response

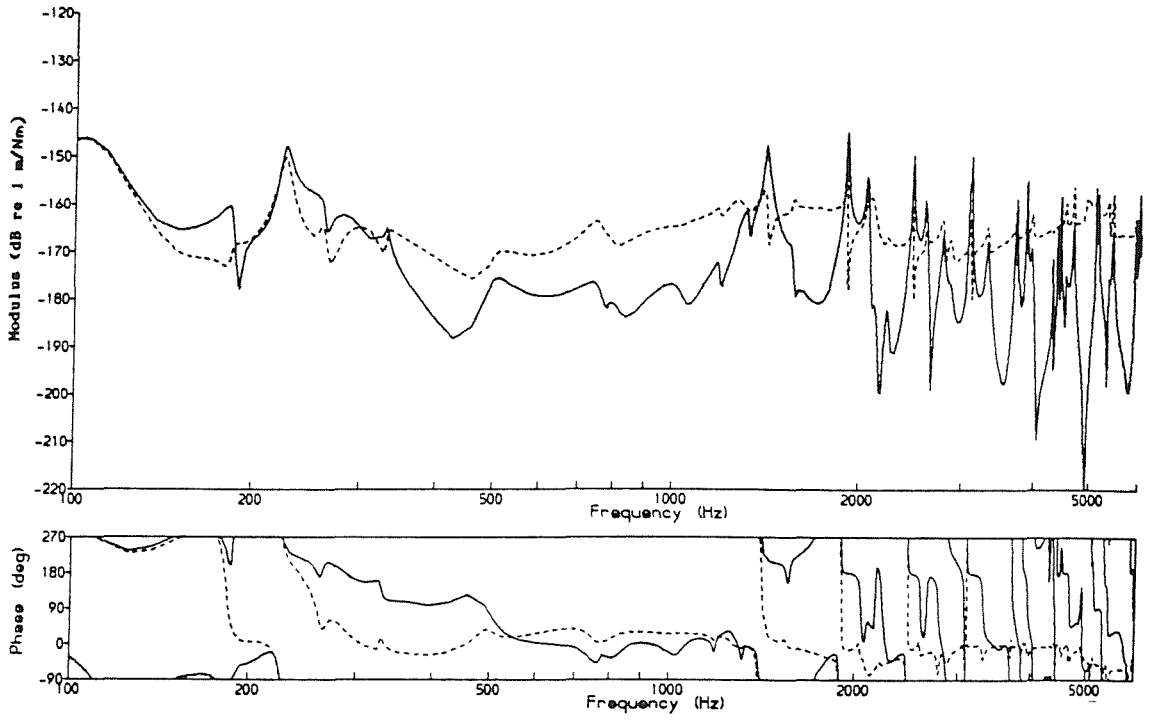

(b) Lateral Wheel (———) and Rail (·····) Response

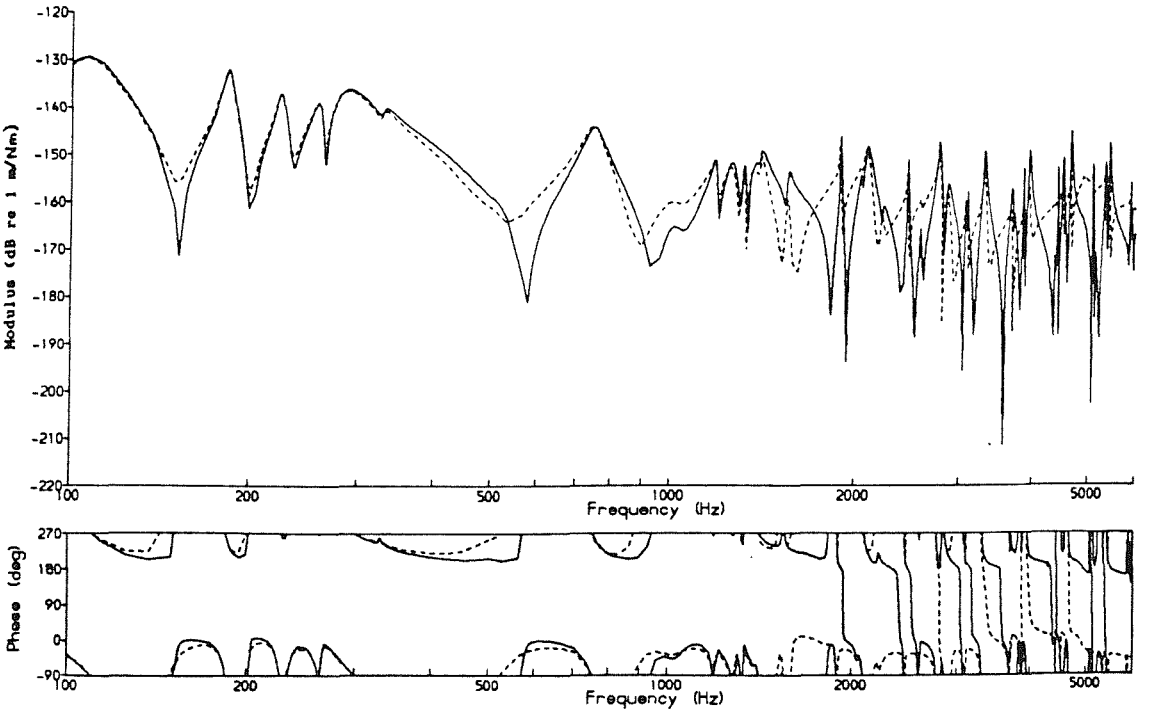

Figure 139 Wheel and Rail Vibration Displacement due to a Unit P_4 Moment Input

corrugation amplitude of -80 dB re 1 m could be equivalent to a moment input of 54 dB re 1 Nm.

Hence, to relate the current results to those predicted for a unit (0 dB) roughness input, an equivalent moment input could be as much as 134 dB re 1 Nm. The results of Figure 139 are for a 1 Nm input, so the addition of this factor to these results yields results which are comparable to the nominal 1 m roughness input. This gives lateral results as high as 0 dB (re 1 m/m) at low frequencies, and between -10 and -40 dB at higher frequencies, whereas the vertical responses are mostly between -20 and -50 dB. This means that this effect could be significant as an additional input to the system, although it is unlikely to be as great as direct roughness input.

Clearly, measured data would have to be collected before the full relevance of this source could be verified, which means that accurate maps of the rail (and wheel) surface in two dimensions are required, not simply a one-dimensional profile.

7.6 *CONCLUSIONS*

The use in the wheel-rail interaction model, of the more detailed rail and contact receptances, as derived in §5 and §6 respectively, led to very little change in the character of the responses. At low frequencies, the reduced rail receptances led to an increase in the wheel response, whereas at high frequencies, a higher rail receptance led to an increase in the rail response.

The rail cross receptance, which was found in §3 to determine the level of rail lateral response, was modelled in §5 by introducing, into the symmetrical model of the rail and its supports, a lateral offset to the position of the contact point on the rail. An offset of 15 mm was used to introduce a realistic level of rail cross receptance, but, unfortunately, it was found that the rail lateral response showed poorer agreement with measurements than with the simpler model of §3. In order to remedy this, more experimental data would be required of rail cross receptances (as a function of lateral position), and the model could be modified to take account of the non-zero cross receptance at the rail centre-line. It is also probable that allowance for the cone angle would modify the lateral response (cf Figure 43).

Inclusion of up to 6 degrees of freedom into the interaction model also makes very little difference to the vertical and lateral responses. Therefore, the conclusions reached in §3 about the effects

of changes to parameters, and the relative importance of the various parameters, are not altered.

Of these extra degrees of freedom, only the 'spin' vibration (rotation in the plane of the contact patch) has a significant level of response, and only then for the wheel. This consists of a strong modal response in the 0-nodal-circle modes. The spin response corresponds to lateral vibration with a node at the contact point, which is only weakly coupled to the rail.

This effect is not observed for the rotating wheel, however, due to the increased coupling to the rail, and the introduction of coupling between the cos $n\theta$ and sin $n\theta$ components of wheel vibration. It was, therefore, found that the inclusion of additional degrees of freedom into the prediction for the rolling wheel leads to little change in the response. An improvement was observed in the lateral vibration of the wheel tyre, although this appeared to be due, mainly, to the improved rail receptances at the lower frequencies. One-third octave results for the rolling wheel show quite good agreement with experimental results, but remain too high at the higher frequencies. The most likely reason for this is the inadequacy, at high frequencies, of the normal modes predicted by the finite element model.

Although steady creepages introduce a cross term into the contact receptances, the introduction of typical values had little effect on the response. As examples, a steady lateral creepage of 0.001 had only a slight effect on the lateral responses, whereas a spin creepage of 0.1 had negligible effect. The latter had a greater effect on the spin response, but this was still not seen for a rolling wheel. With a steady longitudinal creep (such as is present in traction or braking), the longitudinal responses were increased to a much more significant level. However, they do not have a direct influence on the radiated noise.

The introduction of coupling to the second wheel, through the axle, produces a significant component of vibration, particularly in the lateral direction. The overall vibration level, however, is little altered, and it appears that the neglect of this coupling is not a serious omission.

The absolute force/displacement input models (as used by Feldmann) have been considered, but appear inferior to the relative displacement model which has been used throughout the rest of the

study. Not only do they appear to be physically unjustified (they are contrary to Newton's third law), but their results do not appear to give as good agreement with measurements, particularly for the case of the lateral vibration. They have the added problem of the determination of a realistic method of dividing the contact receptances.

CHAPTER 8

DISCUSSION

8.1 COMPARISONS WITH EXPERIMENTS

8.1.1 Limitations of the Experimental Validation

Throughout this thesis, the experimental validation of the overall model has been based on measurements carried out in 1984 by BR and London Transport [23,24], as described in Appendix A. Of these, only half of the measurement conditions could be used for validation of the linear model - the corrugated track results had already been shown to be beyond the scope of the linear model [24]. This was due to large amplitudes of vibration in the contact zone, which result in a violation of the linearising assumptions used for the Hertzian contact spring.

When reduced to a non-dimensional form (vibration displacement divided by the roughness, taking into account the effects of contact filtering), some speed dependence could be seen in the remaining experimental results. In particular, the rail vertical vibration was found to increase at a greater rate than the effects of speed and roughness would indicate. There are two possible explanations for this, one or both of which may apply:

1) It is possible that these experimental data still contain anomalies or errors.

2) The model could be inadequate: there may be other inputs, apart from the roughness displacement-input, which have not been taken into account. This possibility will be considered briefly in §8.1.3 below.

For (1), the rail data, in particular, would seem to be prone to error due to their transient nature, and the consequent problem of ensuring that the correct time interval has been acquired.

It should be noted that the measured rail vibration consists of the sum of the vibrations generated by all of the wheels of the train. For the test train in question, these wheels were not all the same. Whilst the two test wheels were similar apart from their roughnesses (and all wheels on their bogies had similar wheels), those on adjacent coaches were disc-braked (and therefore smoother than the rough

instrumented wheel), and also had straight webs. The use of smooth wheels on the adjacent coaches was intended to minimise any interference in the vibration and noise signals resulting from wheels other than those on the test bogie in question.

The following points can be deduced from this:-

- Unfortunately, on *corrugated track* the advantage of using smooth wheels to minimise interference is lost, because, in this case, the rail roughness dominates in the excitation of each wheel. Consequently, the rail vibration due to each wheel will tend to be of a similar amplitude, and some of the rail vibration measured in the analysis interval will be due to these other wheels. This will be another cause of the greater rail response (relative to the surface roughness) found at the corrugated site in [24].

- The noise from disc-braked wheels has a higher speed exponent [10], probably resulting from the shape of their roughness spectra. This could introduce differences in the speed dependence of the various rail vibration signals, particularly for the smooth rail site, where the wheel roughness is more significant.

- The straight-webbed wheel-type used on the non-instrumented vehicles, could result in the lateral vibration being excited proportionately less than the vertical vibration (relative to the instrumented Commonwealth wheels). This could result in a greater increase with speed in the detected vertical rail vibration than lateral vibration, particularly at the corrugated site.

Thus the measured rail vibration spectra do not, in general, correspond to the vibration due to a single wheel, or even a single bogie. Much of the observed discrepancy can be explained from the above points, although much more detailed measurements would be required to offer a thorough quantitative explanation.

As well as the vibration, the roughness measurements have not been validated completely, although in comparison with other systems, the rail roughness system which was used in [23] appeared to give reasonable results down to the imposed wavelength limit of 14 mm [100]. Errors in roughness could be responsible for some of the speed effects seen in Appendix A, but not all of them, since each figure is different in this respect.

8.1.2 Recommendations for Further Validation

It is to be hoped that further validation experiments can be carried out at some time. The general (non-dimensionalised) form of the predictions given in this thesis should facilitate comparison with such experimental data, once allowance has been made for differences in wheel (and rail) receptances.

Detailed validation is particularly required of the dependence of the model on parameters such as the rail and wheel receptances, as discussed in §3.4. Experiments are needed which include significant variations in parameters, to assess the validity of this analysis.

The validity of the model, and in particular the formulation for a rolling wheel, may be checked by careful measurements of:-

- the differences (Δf) between the frequencies of the peaks in the response and the wheel natural frequencies, and any dependence on speed.
- the contra-rotating waves, particularly near wheel resonances, and their excitation by different roughness wavelengths.

In order to make more detailed comparisons between predicted and measured vibration, it would be preferable to investigate narrow-band spectra of the measured data rather than one-third octave spectra, although the potential frequency resolution is obviously limited by practical considerations for the rail, where the signal is transient. Also the decay of rail vibration with distance needs to be known for the test site under consideration.

8.1.3 Scope for Adapting the Theoretical Model

Comparisons with experimental results have indicated deficiencies in the roughness excitation hypothesis; whilst the measurements have been seen to contain inconsistencies, it is also possible that the model needs to be adapted to account for some of these features.

Residual speed dependence in the vibration divided by roughness was not explained in §3 by the introduction of a (speed-dependent) creep force damper. This was shown to have no effect on the vertical vibration, and very little effect on the lateral response. Some other possibilities could now be suggested from the results of §7.

As speed increases, the significance of impact excitation due to the entry of asperities into the contact patch is likely to increase.

These, whilst being generated by short wavelength phenomena, will produce a broad-band excitation. The amplitude of the response increases more sharply with speed than that due to the relative displacement input, whereas the spectral content moves towards higher frequencies more slowly than for the relative displacement input (as mentioned in §6.3.4 [77]). Although Feldmann introduced these impacts using the absolute force model, it is hard to see why the relative force input should not be more appropriate: impacts will act on both the wheel and rail equally, and in the opposite direction. However, from §7, it may be expected that a more resonant response will be generated (cf Figures 133 and 136).

It has been noted [24] that effects were found in the experimental data which suggested a breakdown in the linearity assumptions in the contact region for the case of the corrugated track site, and in §8.1.1 above, systematic differences due to interference from non-instrumented wheels have been noted. It is possible, nevertheless, that other factors were also present, which would result in a difference between the two measurement sites. For instance, the lateral motion of the contact patch due to roughness profile variations could have been different between the corrugated and non-corrugated sites. The rail response characteristics of the two sites could also have been different, particularly the decay with distance.

8.1.4 Nature of Force Spectra

During this study, it has been found that great care has been needed, in running the theoretical models, to ensure that the parameters input to the various programs correspond exactly.

This is especially true for the wheel response calculation, where the interaction forces are used as inputs. The wheel receptances are lightly damped and resonant in nature, whereas the responses are much less resonant (cf Figures 106 and 133). The forces, therefore, have minima, and/or carefully balanced vertical and lateral components, which control the response around the resonances. Thus, if the wheel receptances used in calculating the forces, and those used in determining the response to those forces, are not precisely the same, large and dramatic errors can occur, giving high resonance response levels.

This also has implications for experimental investigations of wheel-rail noise. For example, in [37], force spectra were estimated

from measurements and used to determine the response and noise, from the previously determined receptances and radiation characteristics. Because of the practical limits to the frequency resolution which could be achieved in such conditions, as well as the difficulty in matching the forces with estimated receptances, it is not surprising that in [37] excessive wheel vibration (and hence noise), was predicted due to sharp modal peaks.

It would appear, therefore, that whilst force spectra may be used as a link in the theoretical chain, attempts should not be made to extract wheel-rail forces from measurements.

8.2 IMPLICATIONS FOR NOISE RADIATION

Noise radiation modelling has not been a direct part of this thesis, as theoretical modelling of noise radiation from wheels and rails had previously been completed [33]. This has been summarised in Appendix B.

Ultimately, however, the aim of this research is to point to potential means of reducing rolling noise. Many parameter changes have been investigated, in terms of their effect on the interaction and response, some of which should be beneficial for noise reduction. In this section, the potential of some of these changes for noise reduction will be assessed, briefly. Others, which have been found to be ineffective in modifying the response, can be expected to have little effect on the radiated noise.

An example noise spectrum, along with a division into wheel and rail components, has been presented in Appendix B (Figure B7). This was based on the spectrum measured at 2 m from the braked wheel at the smooth rail site, at 160 km/h. The average wheel and rail components (taken from all conditions) are superimposed on this spectrum. These spectra will be used in this section to assess the effects of parameter changes on the individual noise components (wheel and rail) and on the total noise.

It should be noted that these average wheel and rail components result in levels of 101.4 dB(A) and 102.4 dB(A) for the wheel and rail respectively (ie the radiation from rail is greater than that from the wheel), whereas the actual results for these conditions (160 km/h, braked wheel, smooth rail) show that the wheel component is up to 1 dB

greater than the rail (see Figure B6). This discrepancy is within the level of experimental error.

First, however, the validity of the rail radiation predictions will be investigated, in the light of the theoretical understanding of the nature of the response.

8.2.1 Validity of Rail Radiation Calculations

As discussed in Appendix B, the wheel and rail radiation have been estimated from the same experiment used in this work for the validation of vibrational response. The rail radiation is, therefore, based implicitly on the noise received during 4.45 m of train pass-by, whereas the rail vibration decays (slowly), away from the excitation point, to infinity. Consequently, it is important to determine the proportion of the total noise which will be detected in the 4.45 m analysis length. Unfortunately, this depends on the decay rate of vibrations in the rail, which is not known for the test site in question.

As mentioned in §5, measurements of decay rates in similar track have produced values between 0.5 and 2 dB/m [70], which allows some estimate to be made.

Using the equations for the response of an Euler-Bernoulli beam (from Appendix D), the total vibration-squared in a damped infinite beam, excited at x=0, can be calculated by integrating from x=0 to ∞:-

$$E(\infty) = \int_0^\infty |w(x)|^2 \, dx = w_o^2 \int_0^\infty |-ie^{-i\bar{k}x} - e^{-\bar{k}x}|^2 \, dx \qquad \ldots(131)$$

where $\bar{k} \simeq k/(1+i\eta)$ is the complex wavenumber, and w_o is the amplitude of vibration at x=0. The two terms in the integral correspond to the damped propagating wave and the decaying near-field wave. From the results of §5 it would appear that these Euler-Bernoulli equations, whilst not precise, should give a reasonable first-order approximation to k and w(x) (compare Figures 57, 59 and 61a).

This result has then been compared with the equivalent integral from x=0 to 2.25 m, E(2.25). (This involves another approximation, since the integrals should strictly be considered over 1 m and 3.5 m (see §5) due to the presence of two wheels in the analysis interval).

Results for the ratio, $L_1 = E(\infty)/E(2.25)$, and for $L_2 = E(2.25)/w_o^2$ (equivalent to the differences of the two curves in Figure 97) are

Table 15 Effect of Rail Damping on Radiating Lengths

η	Frequency (Hz)	L_1 (dB)	L_2 (dB)	d_r (m)	Δ (dB/m)
0.5	500	0.21	0.21	1.10	5.3
	1000	0.08	-1.15	0.78	7.5
	2000	0.02	-2.60	0.55	10.6
	4000	0.002	-4.09	0.39	15.0
0.2	500	1.46	2.21	2.33	2.1
	1000	0.95	1.31	1.68	3.0
	2000	0.49	0.25	1.18	4.2
	4000	0.20	-0.99	0.83	6.0
0.1	500	3.30	3.08	4.34	1.1
	1000	2.54	2.50	3.19	1.5
	2000	1.71	1.81	2.25	2.1
	4000	1.03	0.96	1.58	3.0
0.05	500	5.66	3.56	8.36	0.53
	1000	4.75	3.18	6.21	0.75
	2000	3.67	2.75	4.38	1.1
	4000	2.66	2.23	3.09	1.5
0.02	500	9.23	3.87	20.4	0.21
	1000	8.22	3.62	15.3	0.30
	2000	6.96	3.37	10.8	0.42
	4000	5.72	3.10	7.62	0.60
0.01	500	12.10	3.97	40.5	0.11
	1000	11.05	3.77	30.3	0.15
	2000	9.73	3.59	21.5	0.21
	4000	8.40	3.41	15.2	0.30

Key:-

η = Damping loss factor

L_1 = 10 log (E(∞)/E(2.25)).

L_2 = 10 log (E(2.25)/w_o^2).

d_r = Effective semi-length, (given by equation (132)).

Δ = Decay rate in dB/m.

given in Table 15, for various values of loss factor. The beam equation has been used with parameters equivalent to lateral bending ($EI=0.97\times10^6$ Nm^2 and $\rho A=56$ kg/m, as in Appendix D). Also given in the table are the equivalent decay rates in dB/m, for comparison.

It can be seen that, for decay rates of 0.5, 1 and 2 dB/m, the integrated vibration up to 2.25 m is 6 dB, 3.6 dB and 1.8 dB (respectively) less than the integral to infinity. By symmetry, the same also applies for the negative direction ($x=-2.25$ to 0).

This suggests that the total noise from the rail could be, on average, about 3-4 dB higher than that which has been predicted in Appendix B from a 4.5 m analysis length. Consequently the wheel contribution may be slightly less important than it appeared, and the rail contribution slightly greater.

For the results from Figure B7 (160 km/h, braked wheel, smooth rail), it has already been noted that the wheel component should be 1 dB greater than the rail rather than the other way around. Applying this new correction means that the results are, in fact, quite close to those originally given in Figure B7, so for simplicity these will be used unaltered in the subsequent sections to assess wheel damping etc.

Also shown in Table 15 are the effective radiating lengths, d_r, of the rail for the various values of loss factor (d_r is actually half of the total length since only positive x have been considered). These are defined as the length of rail which would have to vibrate at an amplitude of w_o to give the same total mean-squared vibration $E(\infty)$ (and hence noise). They are given by

$$d_r = \frac{1}{w_o^2} \int_0^\infty |w(x)|^2 \, dx \qquad \ldots(132)$$

8.2.2 Wheel Damping

In §7.4.3, an assessment was made of the reduction in rolling wheel vibration, due to different levels of added wheel damping; results were shown in Figure 130. The damping ratios of the more lightly damped wheel modes were raised to .001, .003, .01 and .03 respectively. It may be recalled from §3 that a constrained layer damping treatment may be expected to achieve damping ratios of around 0.01 [99].

Since the wheel radiation has been found to be dominated by the web vibration (Appendix B), the wheel noise component should be reduced in direct proportion to the web vibration levels. Thus, the revised wheel noise component has been estimated by subtracting the reduction in the web vibration level achieved in Figure 130, from the level of the wheel component of noise in Figure B7.

Figure 140 shows the resulting wheel components, and the corresponding overall noise. The latter is based on an unaltered rail component. Although, in practice, the lateral rail vibration will be reduced slightly (see Figure 45), at the higher frequencies (where this applies) the rail radiation is produced mainly by the foot component. This vertical response of the foot, will correspond to both lateral and vertical waves, but that due to the vertical waves will tend to be greater. Therefore, since the vertical motion is not affected by wheel damping (Figure 45), it can be expected that the foot response will not be affected, and hence the noise is also not affected much.

The overall A-weighted noise levels from the spectra in Figure 140 are listed in Table 16, along with the overall reductions achieved. It can be seen that the wheel component is reduced by less than 1 dB(A) for the first (10 dB) step in damping, and by up to 3 dB(A) for each

Table 16 Changes in A-Weighted Noise Levels Due to Various Modifications to the Wheel and Rail Components (from Figures 140-143)

Case	Wheel Component		Rail Component		Total Noise	
	dB(A)	Δ	dB(A)	Δ	dB(A)	Δ
From measured spectrum	101.4	0	102.4	0	104.9	0
Wheel damping ζ=.001	100.5	0.9	102.4	0	104.5	0.4
ζ=.003	98.8	2.6	102.4	0	104.0	0.9
ζ=.01	96.0	5.4	102.4	0	103.3	1.6
ζ=.03	92.9	8.5	102.4	0	102.8	2.1
No wheel	-	-	102.4	0	102.4	2.5
Rail damping η=0.5	101.4	0	97.3	5.1	102.8	2.1
Half-height rail	101.4	0	100.4	2.0	103.9	1.0
Half-size rail	101.4	0	97.7	4.7	102.9	2.0
No rail	101.4	0	-	-	101.4	3.5

Note: Δ = (measured spectrum from first row) - (level in current case).

(a) Noise Components from the Wheel

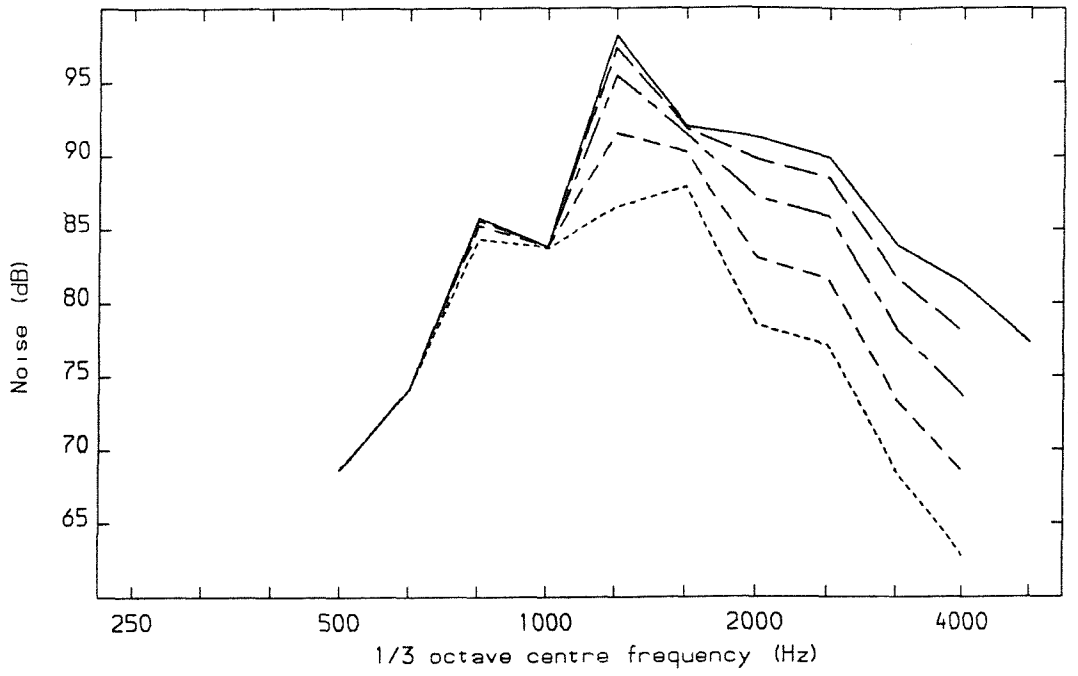

(b) Total Noise

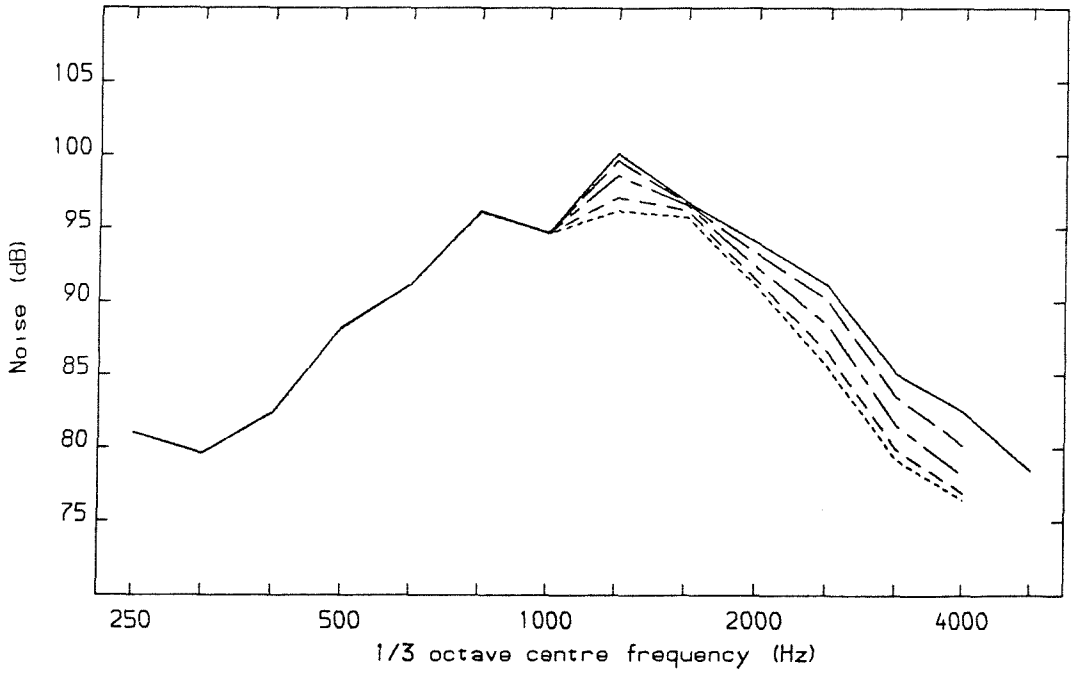

Figure 140 Effect of Added Wheel Damping on Noise Radiation:
——— Untreated, Minimum Damping Ratios of: — — .001, —·—· .003,
– – – .01, ····· .03

successive step. However, since the rail component has not been modified, the overall noise is reduced very little, and is limited to a total of 2.5 dB(A) reduction, if the wheel component could be eliminated altogether.

It is clear, then, that the wheel radiation can be reduced appreciably using a realistic level of damping, but the rail component also needs to be reduced to achieve more than about 2-3 dB(A) overall reduction.

The result for the highest wheel damping value (.03), shows a slight peak at 1.6 kHz, where the original spectrum showed a dip, since Figure 130 gave very little reduction for this band. This peak is obviously a false result, as the 1.6 kHz band contains no wheel resonances. However, due to the Doppler effect, the noise in this band will, in part, be radiated by resonances in adjacent 1/3 octave bands; therefore, in practice, the noise in this band should also have been reduced somewhat.

8.2.3 Rail Damping

The application of a damping treatment to the rail produces a reduction in the vibration propagating away from the excitation point, as discussed in §5, although the point receptances are virtually unaltered. Figure 97 showed the effect of damping on the average vibration over a 4.5 m length (simulating the vibration measurements described in Appendix A).

The rail radiation is derived from these average responses, using an analysis time corresponding to train motion over this distance, so a rough estimate of the potential reduction in noise from the rail can be produced, by forming the difference between the two curves in Figure 97.

Unfortunately, the rail radiation is based on an infinite line-type source, with a roughly constant level along it. Whilst this is a reasonable approximation for an untreated rail with a low decay with distance, it is not the case for a highly damped rail, where the vibration is much more localised, and may be approximated more closely by a point source.

However, it would seem that a reasonable prediction should ensue, given that:-

1) The radiation from a moving point source and that from a line source are equivalent. The equivalent line source which was used, is based on the mean-squared velocity over this length, so this gives roughly the correct equivalent source strength.

2) The motion of the point source is, of course, limited to the 4.5 m analysis length, but, particularly at the 2 m microphone position, the noise from the equivalent finite length line source (4.5 m) and that from an infinite line source are similar.

Figure 141 shows the estimated reduction in rail radiation for a rail loss factor of 0.5. This is produced by applying separate factors to the three rail components. Each is based on the difference between the average response in 4.5 m, without and with the damping treatment (Figure 97), for the respective motion.

It may be expected, as already noted, that the total noise from the rail in the untreated case will be somewhat greater than that received during the analysis interval (approximately 3 dB), whereas for the damped rail, where the noise source is localised, the noise measured would be close to the total rail noise component. Thus a correspondingly greater reduction in total noise from the rail should be achieved than is indicated in the figures.

Alternatively, the results shown correspond to a revised loss factor of 0.2. This can be deduced from the total mean-squared vibrations (from Table 15, given by the values of L_1+L_2) which are approximately 3 dB greater for $\eta=0.2$ than for $\eta=0.5$.

In contrast with the effect of wheel damping, the effect of rail damping is quite dissappointing. Even with these extremely high loss factors of 0.5 or 0.2, the reduction is quite small: 5 dB(A) from Table 16

As noted in §5, measurements of the effects of damping treatments on a length of rail have produced loss factors of around 0.03 [104]. From Table 15, it may be deduced that the reduction for a loss factor of 0.05 would be approximately 5 dB(A) less than for $\eta=0.2$. This implies that the untreated rail is roughly equivalent to a loss factor of 0.05; ie to a slightly higher loss factor than has been achieved (on a finite length) using a constrained layer treatment! It is clear from this that better damping treatments will need to be developed. The wheel, by contrast, gave reasonable reductions for a damping ratio of 0.01 (ie a loss factor of 0.02).

(a) Noise Components from the Rail

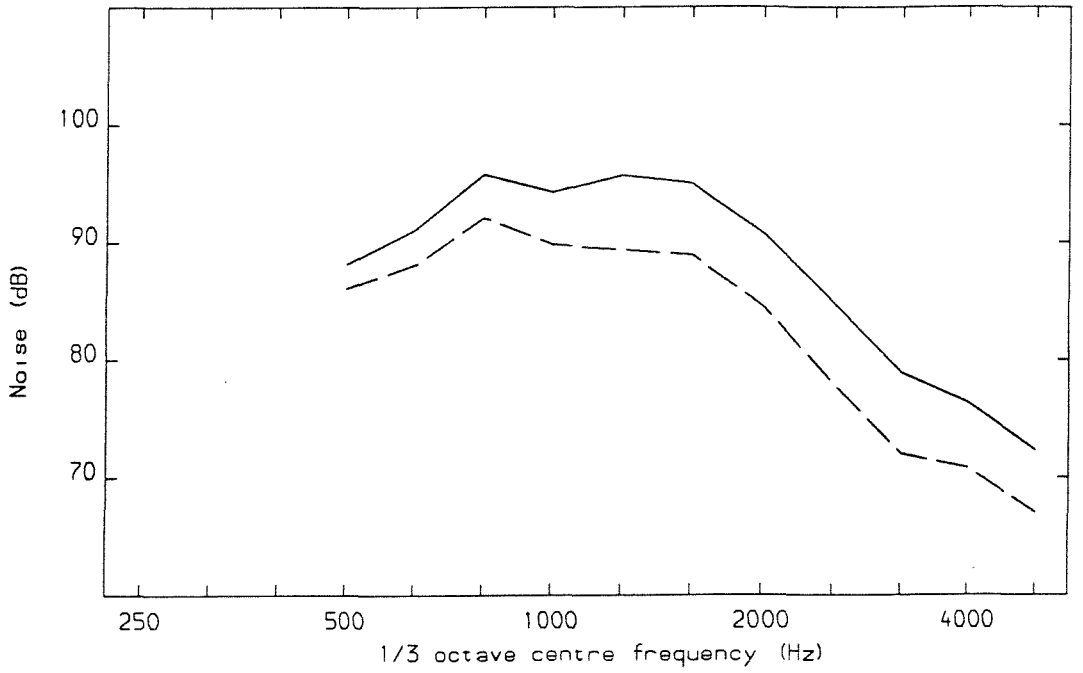

(b) Total Noise

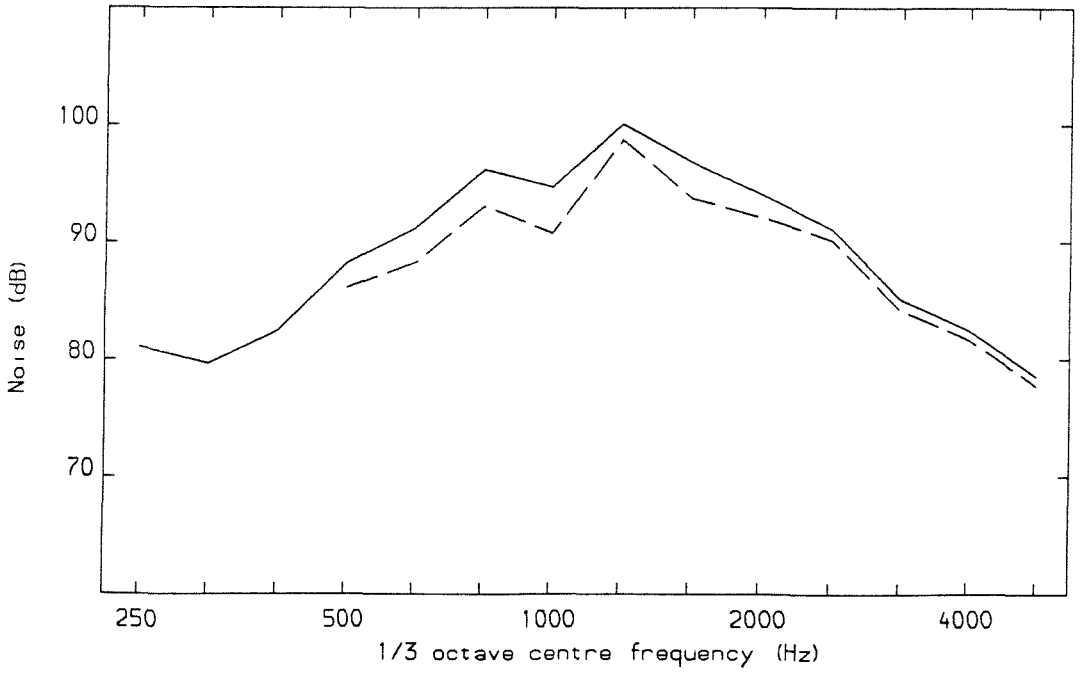

Figure 141 Effect of Added Rail Damping on Noise Radiation:
——— Untreated, — — Damping Loss Factor 0.5

8.2.4 Small Rail Sections

At low frequencies the wheel damping has no effect (Figure 140), and the rail damping has only a small potential effect (Figure 141), and a given damping loss factor is more difficult to achieve at low frequencies. It is, therefore, clear that the reduction of low frequency noise requires a more drastic solution; one possibility is a reduction in the size of the rail cross-section.

Figure 142 shows the sound radiation of a circular cylinder (from [115]), and the effect of reducing the size of the cylinder from 150 mm diameter (similar dimensions to a rail cross-section) to half that size. At high frequencies a reduction of 3 dB is achieved by the reduction in the radiating area, but at low frequencies the reduction is as much as 12 dB due to the raising of the critical frequency.

The difference between these two curves gives an indication of the reduction in the rail component of the noise due to a reduction in the size of the rail, whilst maintaining the response level. Figure 143 shows the results: in the upper figure only the lateral components are reduced (simulating the effect of halving the height), whereas in

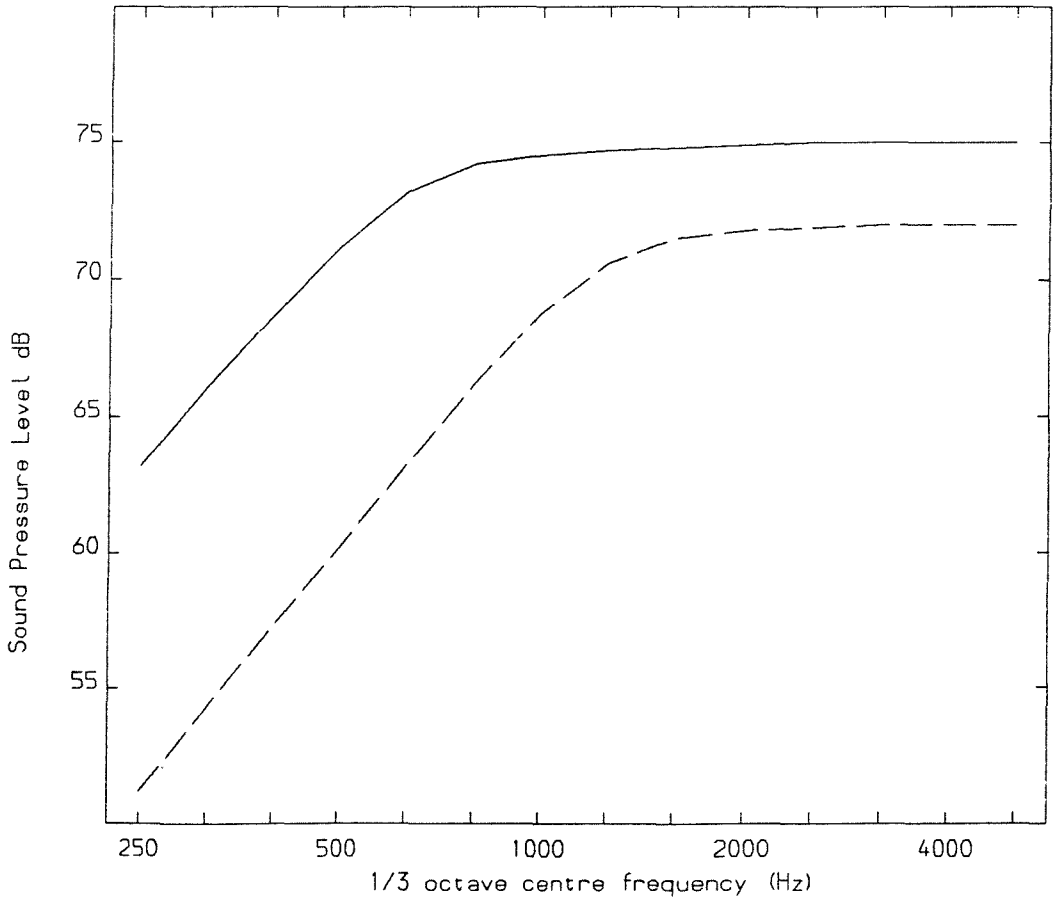

Figure 142 Sound Radiation at 1 m from Circular Cylinders Vibrating at 1 m/s; ——— 150 mm Diameter, — — 75 mm Diameter

(a) Half-Height Rail (Lateral Component Reduced)

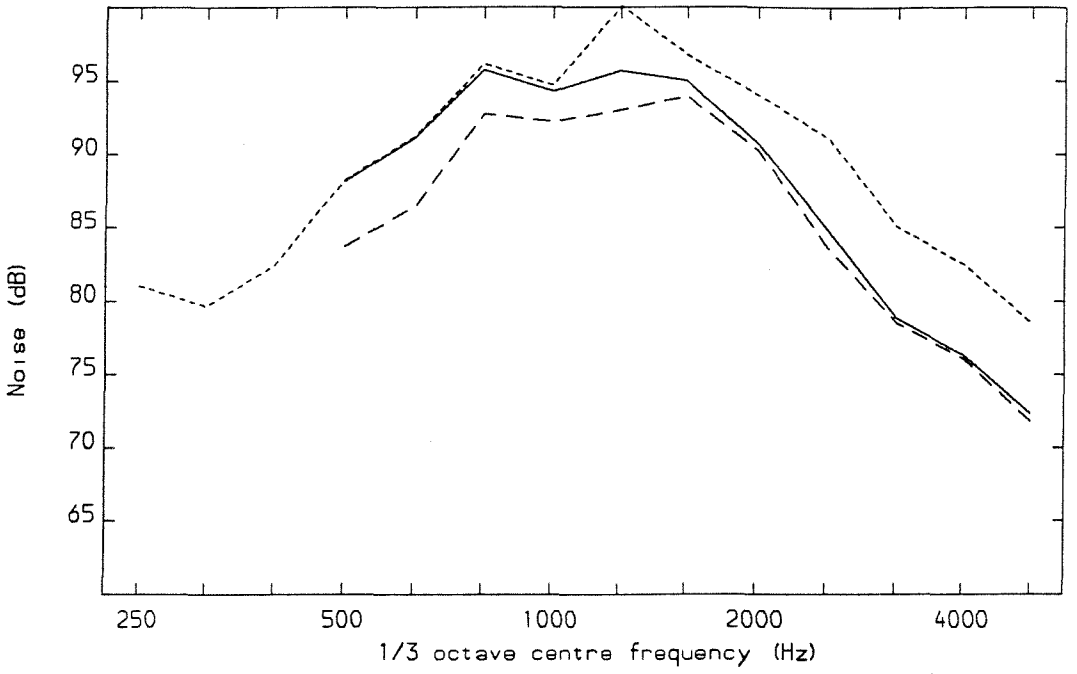

(b) Half-Size Rail (All Rail Components Reduced)

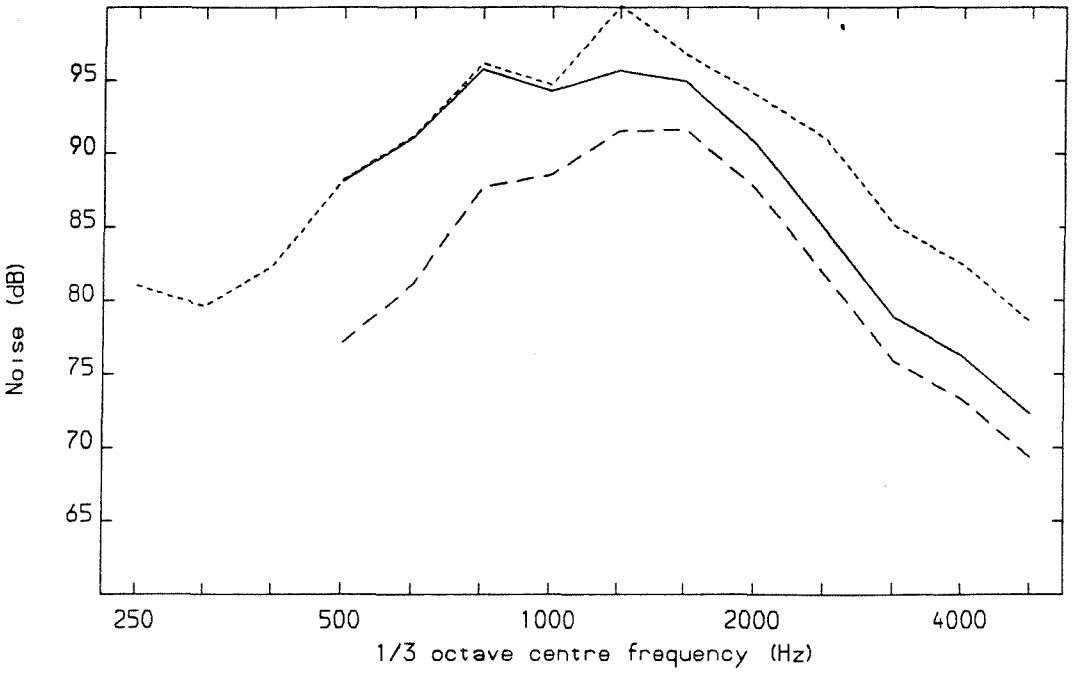

Figure 143 Effect of Reduced Rail Size on Noise Radiation:
····· Total Noise, ——— Noise Component from the Rail,
— — Noise Component from Small Rail

the lower figure the whole rail component is reduced (simulating the effect of halving the total cross-section). Overall levels from these curves (in dB(A)) are again listed in Table 16.

A change in the section of the rail would also change its response level, which has not been included in these figures. For a halving of height, the vertical bending stiffness will be reduced by a factor of approximately 8, and hence the receptance would be increased by about 5 dB.

The effect of this on the vertical responses was shown in Figure 32: at low frequencies (below about 1 kHz) the wheel response is reduced by 5 dB and the rail response is unchanged, whereas at higher frequencies the rail response is increased by 5 dB and the wheel response is unchanged. The lateral responses of both wheel and rail were found to follow the same pattern as the wheel vertical responses. Thus, overall, this suggests an improvement to the noise reduction shown in Figure 143 at low frequencies, but little change in the noise at high frequencies.

In combination with damping, which is more effective at high frequencies, a reduction in the size of the cross-section offers some hope of reducing the rail radiation across the entire frequency range.

However, the practical difficulties of reducing the rail cross-section, sufficiently to produce a noticeable effect, should not be underestimated.

8.2.5 Other Parameters

As seen in §3, changes in contact parameters (particularly vertical) lead to changes in the relative vibrations of the wheel and rail, but these parameters can not easily be influenced to a significant degree and must be ruled out for practical noise reduction.

Whilst the wheel radiation can be reduced by the use of damping, other measures could be used instead or as well. The use of a straight-webbed wheel has been mentioned as a possible means of reducing the lateral vibration (which radiates most of the noise) without needing to reduce the vertical vibration. The wheel may also be made smaller in order to increase its natural frequencies; it has been found [51] that a reduction in radius to around 0.37 m can raise the relevant natural frequencies of the wheel to about 4 kHz and over,

and hence they will be excited significantly less (due to the influence of the contact filter).

However the reduction of the noise radiation from the rail remains the biggest problem. Quite drastic solutions will be needed to reduce its vibration and/or radiation.

CHAPTER 9

SUMMARY AND CONCLUSIONS

9.1 BACKGROUND

The most comprehensive model of rolling noise generation previously available was that produced by Remington [15-21]. Although this had been found to have significant shortcomings, it has been possible to develop a more realistic model by using the same framework, but replacing and improving the various components.

The main thrust of this work has been in the development of much improved wheel and rail frequency response predictions, along with the corresponding contact receptances (representing the local deformations and relative motions in the contact zone) and more generalised interaction equations. The noise radiation aspects of the model had already been covered adequately elsewhere ([33] and Appendix B), and have not been developed further here, although reference has been made to the noise radiation implications of various parameter changes which may affect the vibration.

Work has been concentrated on a single type of wheel (the Commonwealth type) and a single type of track (type 113A flat-bottomed rail on concrete mono-bloc sleepers and ballast) on which validation measurements are available.

9.2 WHEEL RECEPTANCE PREDICTIONS

The vibration behaviour of a wheelset has been studied theoretically. Reasonable agreement was found between predictions of the natural frequencies and modeshapes using two different finite element idealisations. One (an axisymmetric model) has been used extensively before for natural frequency predictions of various wheel types, whereas the other (using plate and beam elements) has been developed for this study.

In both cases, these results also compared well with measured natural frequencies. Using the modal parameters derived from the second finite element model in a modal sum, the frequency response functions (radial, axial and cross) were predicted and appeared to give good agreement with experimental results. The modal damping had to be derived from measurements, although it is envisaged that predictions for a different wheel type could be based on these same values of

damping. The exact level of damping in these wheel modes was subsequently found not to be critical in the prediction of responses to wheel-rail interaction.

In the frequency range up to about 1600 Hz, it was found to be essential to include modes of vibration involving the axle into the modal sum, despite the fact that their damping was high and their modal amplitudes were relatively low.

The cross accelerance was found to be less accurate than the point accelerances, owing to the need to include the sign of the relevant modeshape parameters as well as their amplitudes. The presence of nodal circles near the excitation point in some modes causes particular difficulties in both measurements and predictions, as the modeshape parameters are consequently less accurate in relative terms.

Due to their low damping, the wheel receptances have a very large dynamic range. Although the predictions appeared reasonable, in practice errors of 5-10 dB would tend to be overlooked at this stage. With hindsight, it would seem that this has led to the acceptance of a level of error which is subsequently unsatisfactory, in terms of the response to the wheel-rail interaction.

Detail differences between wheelsets could also be significant; the validation of the wheel response modelling was based on a different wheel (of the same type) to that used in the rolling tests.

The receptances of the wheel in other degrees of freedom have been used from the same finite element model, although without experimental validation.

9.3 PREDICTIONS OF RAIL VIBRATION BEHAVIOUR

Almost all previous models of the vibration of a rail have been based on an infinite beam. In §5, periodic structure theory has been used successfully to model the vibration of an infinite rail beam, the cross-section being represented by matrices derived from finite elements (using plate and beam elements).

Wavenumber results for propagating waves were validated against results calculated using a finite element model of a length of rail with symmetry/anti-symmetry conditions at both ends (to simulate the infinite extent). Good agreement was also found with wavenumber results derived from experimental data. This idealisation of the rail

cross-section appeared to be reasonable, although its accuracy was limited by the use of 4-noded plate elements, particularly for the transition between web and foot. Three-dimensional solid elements could provide a better representation of this region, but were not available in the finite element package used.

For lateral excitation the cross-section was found to deform significantly above about 1500 Hz, as found experimentally. For vertical motion the foot response was progressively greater than that of the head for frequencies greater than about 1 kHz. This confirmed that the simple beam equations are not completely adequate to model the rail vibration at these higher frequencies.

Receptances have also been calculated using this periodic structure model, and results agreed closely with experimental data taken from the literature. At wave cut-on frequencies, strong resonance peaks were found, although the inclusion of damping reduced these significantly. The inclusion of the flexibility of the rail cross-section was seen to result in an increase of the receptances, particularly at high frequencies, and a change in the phase.

A detailed model of the sleepers was not required for the purposes of predicting the rail response, as they were found to be adequately represented by an equivalent mass and springs (representing the railpad and ballast stiffnesses). Above the bounce frequency (at around 90 Hz), the resilience of the pad was found to be the dominant element in the support. The inclusion of these mass-spring layers led to a reduction in the receptance at low frequencies. Above about 1 kHz, their only effect was to introduce damping, which resulted in a significant decay with distance along the rail, as found experimentally.

If damping were added to the rail, the receptances would not be significantly affected, but the decay of vibration with distance from the excitation point would be increased. Damping loss factors in excess of at least 0.01 (and probably 0.05) are required to have a noticeable effect.

Agreement with experimental results was good except at "pinned-pinned" frequencies, which the continuous model could not represent. However, the large degree of isolation offered by the railpads suggested that, at least for the values of pad stiffness considered, the

effects of the periodic supports should be limited to the region below 1 kHz, where existing models (eg [58-60]) are adequate.

9.4 DETAILED CONTACT EQUATIONS

In §6, the development of a general linear theory of wheel-rail interaction allowed the inclusion of any number of coupling degrees of freedom. Alternatives to the traditional relative displacement input were considered: a mutual force, an absolute displacement or an external force excitation. Equations were also presented taking into account the effects of coupling through the axle to the other wheel.

The relative motion in the contact region has been modelled by receptances in 6 degrees of freedom. These were presented, including the effects of the (linearised) Hertzian contact spring, and the creep force formulation with approximations for the frequency-dependence of the creep coefficients. The effects of steady creepages on the dynamic behaviour were also included (they were found to introduce coupling between the vertical and the lateral/spin and longitudinal directions).

The lateral movement of the contact patch was also considered, as an alternative form of excitation.

9.5 RESULTS OF INTERACTION MODEL

9.5.1 Initial Study

Using the overall theoretical framework of Remington, an initial theoretical model was presented in §3 for the generation of wheel and rail vibration from surface roughness. This included interaction between the wheel and the rail in two degrees of freedom (vertical and lateral) at the contact.

The wheel receptances were taken from the finite element study, but, at this stage, simplified models for the rail and contact receptances were used, those for the rail being based on Euler beam equations. These simplified models allowed parameter variations to be assessed more readily than more complex models, and a comprehensive parameter study was carried out at this stage. The range of rail receptances used covered the likely actual values.

A detailed study was carried out into this initial model, which showed it to be only partially successful.

The vertical responses were found to be determined principally by the vertical receptances of the wheel, rail and contact. The cross

receptances are important in determining the lateral response, which is unfortunate as they cannot be modelled to the same accuracy.

The surface roughnesses were confirmed as a major source of wheel and rail vibration, and hence of rolling noise; the response levels, expressed relative to the roughness, were of similar magnitudes to the measured results. At low frequencies the rail vertical vibration corresponded to the level of the roughness, the wheel vibration being much lower. The wheel vertical vibration rose sharply at around 1.25 kHz to exhibit a series of peaks, whereas the rail vibration gradually reduced with increasing frequency.

As well as the vertical vibration, the predicted lateral vibration of the wheel web contained peaks which corresponded roughly to modes known to be important in noise radiation (1-nodal-circle), also seen in measured spectra.

The damping of the wheel-rail coupled system appeared to be much greater than the damping of the free wheel, so that added wheel damping would have to be quite large to have any significant effect.

The peaks in the wheel web lateral and tyre vertical vibration occurred at frequencies which were slightly too high in relation to the corresponding resonance frequencies. This remained the case when the various parameters were altered within reasonable bounds.

It is important to note that the subtleties of the interaction have only been revealed by the use of detailed frequency resolution.

The lateral vibration of the wheel tyre was less well predicted; the 0-nodal-circle axial modes of vibration, found to predominate in measurements of the lateral vibration, were not excited in the predictions.

Experimental results indicated that, even when divided by the roughness, the vibration contained a slight speed dependence, particularly for the vertical vibration of the rail, but no such speed effects were found in the predictions. The creep force damper introduced one possibility for speed dependence, but this was found to have no significant effect on the vertical vibration, and only a limited efect on the lateral vibration.

9.5.2 Results Using the Full Interaction Model

In §7, inclusion into the wheel-rail interaction model, of the more detailed rail and contact receptances (as derived in §5 and §6

respectively), led to very little change in the character of the responses. The wheel response was raised slightly at low frequencies due to the reduced rail receptance, whereas at high frequencies the rail response was increased somewhat.

The rail cross receptance was included by introducing a 15 mm lateral offset to the position of the contact point on the rail. Whilst this gave a reasonable level of rail cross receptance, the shape of the response appeared to agree less well with measurements than the results for the simpler rail receptances used in §3. It is clear that more work, both experimental and theoretical, is required on both wheel and rail cross receptances, as their precise details are important in determining the respective lateral responses.

The inclusion of up to 6 degrees of freedom into the interaction model (rather than the 2 used initially) was found to make very little difference to the vertical and lateral responses. Therefore, the conclusions about the relative importance of the various parameters, reached in §3, were confirmed for the full interaction model.

Of these extra degrees of freedom, only the 'spin' vibration (rotation in the plane of the contact patch) has any significant response, and only then for the wheel. This consists of a strong modal response in the 0-nodal-circle modes. The spin response corresponds to lateral vibration with a node at the contact point (which is not strongly coupled to the rail for the non-rotating case).

Steady creepages introduce coupling, in the contact receptances, between the vertical and the longitudinal, lateral and spin coordinates. However, using typical values (a steady spin creepage of 0.1, or a lateral creepage of 0.001), it was found that these had very little effect on the lateral responses, although the former had a greater effect on the spin response. A steady longitudinal creep resulted in significant longitudinal vibration, but this is not of primary importance for the noise radiation.

The coupling to the second wheel through the axle was found to produce a significant component of vibration, particularly in the lateral direction. However the overall vibration level is little altered from the single wheel case, and it appears that the neglect of this coupling appears not to be a serious omission.

The absolute force/displacement input models have been considered, but appear inferior to the relative displacement model

which has been used throughout the rest of the study. They appear physically unjustified, and give poorer agreement with experimental results, particularly for the case of lateral vibration. They have the added problem of the determination of a realistic method of dividing the contact receptances.

9.6 INCLUSION OF WHEEL ROTATION

The effects of wheel rotation were derived mathematically, and included into the above model for wheel-rail interaction. The wheel receptances, as viewed from the contact point, have two peaks for each wheel mode (with $n \geq 1$) separated by $\pm n\Omega$ (where n is the number of nodal diameters in the mode and Ω is the rotational speed). To look at the vibration in a frame of reference rotating with the wheel it was necessary to study spectral densities. At a given response frequency, different modal components were found to be excited by different frequencies at the contact zone, resulting in an energy sum of the various components.

The representation of the wheel web response was improved by this, anti-resonance dips being eliminated. The major peaks in this motion were found to be located closer to the corresponding resonance frequencies than was the case for the model based on a static wheel, and were brought within the 10 Hz resolution of the experimental data. This apparent deficiency of the interaction model, found in §3, was therefore resolved.

When viewed in a non-rotating frame, the peaks were found to divide into two distinct peaks, corresponding to two contra-rotating waves. In the rotating frame, however, these two waves appear at the same frequency. The total motion of the wheel, when viewed from either a rotating or non-rotating frame, should contain no distinct node lines, since the phases of the two waves are randomly related. This feature appears to be confirmed in practice.

There remained a lack of any significant speed effect in the results (for a unit roughness), apart from a slight increase in peak frequency with speed. The lateral response of the tyre remained inadequate, although it was altered from the results based on the static wheel formulation. Use of more realistic rail receptances resulted in a slight improvement in this.

The inclusion of additional degrees of freedom at the contact into the prediction for the rolling wheel, led to little change in the

results. Even the spin degree of freedom, which had such large modal responses for the static wheel, had no noticeable effect on the rolling vibration. This is a result of the coupling (introduced by the rotation) between the cos nθ and sin nθ components of wheel vibration.

9.7 REASONS FOR REMAINING DISCREPANCIES WITH EXPERIMENTAL RESULTS

It is clear that there are systematic differences in the measurements of rail vibration. These arise from the interference, by the wheels of other vehicles in the train, in the rail vibration detected during measurements. These can introduce site- and speed-dependencies of the type which have been observed. There could also be differences between the rail or wheel responses for the various conditions which have not been taken into account.

The techniques for measuring the surface roughnesses of wheels and rails still need to be improved, and their results need further validation. The systems available also need development to allow the measurement of profile variations in the lateral direction as well as the longitudinal direction.

It is still possible that the model could be developed to take account of some discrepancies with measurements: eg account could be taken of non-linearities in the contact spring (and the creep force relations), and rotational inputs due to lateral movement of contact patch. However, better experimental validation would be required before these could be studied satisfactorily.

9.8 NOISE RADIATION IMPLICATIONS

The introduction of wheel damping leads to a reduction in the wheel component of noise, although much less than might be expected from the free wheel receptances. For damping ratios of around 0.01 (loss factors of around 0.02), such as could be achieved by a constrained layer treatment, the wheel component should be reduced by about 5 dB(A).

However, both the wheel and rail components must be reduced in order to achieve more than about 3 dB(A) overall reduction, and the rail radiation has been found to be less susceptible to added damping. A loss factor of 0.05 would have negligible effect, although a rather less practical loss factor of 0.2 should achieve about a 5 dB(A) reduction in rail component, by reducing the effective radiating length.

At low frequencies, neither wheel damping nor rail damping can be expected to reduce the noise, which is mainly due to lateral vibration of the rail. Only quite radical solutions, such as a reduction in the size of the rail cross-section, can be expected to achieve any reduction here.

9.9 RECOMMENDATIONS FOR FURTHER WORK

It is clear that further experimental validation of the model is required. In particular:

- Investigations could be carried out into the predicted difference between the peak frequencies in the wheel response and the corresponding resonance frequencies (Δf).
- The contra-rotating waves in the wheel could be identified.
- Effects of added wheel damping could be assessed by measuring the rolling response with various treatments added to the wheel (although allowance should also be made for the changes in mass/stiffness characteristics of the wheels).

Because the decay of vibration with distance along the rail depends strongly on the damping loss factors of the railpads, much better data on their damping properties, as a function of frequency, are required.

The source of the excitation for each mechanism considered consisted of undulations in the surface profile of the wheel and rail. Further experimental and analytical work is required in developing and validating the measurements of surface roughness, and in modifying these measurements to provide the correct inputs.

The effects of the periodic support offered to the rail by the sleepers have not been considered. Because the consequent time-varying receptances are not consistent with the linear nature of the model, it is not possible to take it into account fully except by a time-domain model. However it has been seen that the effect should be restricted to the region below 1 kHz where existing models (using simple beam equations) are valid.

Other effects which could be considered by such a time-domain model include the non-linearity of the Hertzian contact spring, particularly for higher amplitude vibrations [24], and the effects of roughness asperities which are shorter than the contact patch length.

REFERENCES

1 J.G.WALKER 1989 *Railway Gazette International, July 1989* 477-479. Technology tames the noise problem.

2 *Railway Gazette International, July 1989* 482-484. Tunnel link still interests the City.

3 BRITISH RAILWAYS BOARD 1989 *Noise and the Channel Tunnel Rail Link.* Series of public information leaflets issued by the Channel Tunnel Group: Paper A1, An Introduction; Paper A2, Technical Background to the Standard; Paper A3, The Prediction Method; Noise and the channel tunnel rail link - some explanatory notes.

4 C.G.STANWORTH 1977 *British Rail Research Technical Note TN PHYS 4.* Railway noise and the environment - a summary - 2nd edition.

5 P.NELSON (ed) 1987 *Transportation Noise Reference Book,* Butterworths.

6 S.PETERS 1974 *Journal of Sound and Vibration* 32, 87-99. The prediction of railway noise profiles.

7 P.J.REMINGTON 1987 *Journal of Sound and Vibration* 116, 339-353. Wheel/rail squeal and impact noise: What do we know? What don't we know? Where do we go from here?

8 B.HEMSWORTH 1988 *British Rail Research Technical Memorandum TM SAV 24.* Class 150 curve squeal: investigation of potential solutions.

9 G.M.PELL 1988 *British Rail Research Technical Memorandum TM MF 159.* The growth of corrugations in high speed straight track and their removal by grinding.

10 B.HEMSWORTH 1979 *Journal of Sound and Vibration* 66, 297-310. Recent developments in wheel/rail noise research.

11 B.HEMSWORTH 1977 *Internoise - Zurich* Noise barriers for fast passenger trains.

12 P.J.REMINGTON 1988 *Journal of Sound and Vibration* 120, 203-226. Wheel/rail rolling noise: What do we know? What don't we know? Where do we go from here?

13 D.J.THOMPSON, B.HEMSWORTH and D.J.WILLIAMS 1986 *British Rail Research Technical Report TR SAV 4.* Fundamental investigations of wheel/rail rolling noise from trailing vehicles on tangent track.

14 O.R.E. 1985 *Office for Research and Experiment of the International Union of Railways. Question C163 Railway Noise. Report No 5.* Wheel/rail contact noise - existing mathematical models and research prospects.

15 P.J.REMINGTON 1976 *Journal of Sound and Vibration* **46**, 359-380. Wheel/rail noise - Part I: Characterisation of the wheel/rail dynamic system.

16 M.J.RUDD 1976 *Journal of Sound and Vibration* **46**, 381-394. Wheel/rail noise - Part II: Wheel squeal.

17 I.L.VER, C.S.VENTRES and M.M.MYLES 1976 *Journal of Sound and Vibration* **46**, 395-417. Wheel/rail noise - Part III: Impact noise generation by wheel and rail discontinuities.

18 P.J.REMINGTON 1976 *Journal of Sound and Vibration* 46, 419-436. Wheel/rail noise - Part IV: Rolling noise.

19 A.G.GALAITSIS and E.K.BENDER 1976 *Journal of Sound and Vibration* **46**, 437-451. Wheel/rail noise - Part V: Measurement of wheel and rail roughness.

20 P.J.REMINGTON 1987 *Journal of the Acoustical Society of America* 81, 1805-1823. Wheel/rail rolling noise I: Theoretical analysis.

21 P.J.REMINGTON 1987 *Journal of the Acoustical Society of America* **81**, 1824-1832. Wheel/rail rolling noise II: Validation of the theory.

22 R.LYON 1973 *Lectures in Transportation Noise*, Grozier Publishing, Cambridge, MA, U.S.A.

23 O.R.E. 1986 *Office for Research and Experiment of the International Union of Railways. Question C163 Railway Noise. Report No 7.* Wheel/rail contact noise - comparative study between theoretical model and measured results.

24 O.R.E. 1987 *Office for Research and Experiment of the International Union of Railways. Question C163 Railway Noise. Report No 8.* Wheel/rail contact noise - further comparative analysis of noise vibration and roughness data.

25 1977 *Journal of Sound and Vibration* 51(3), Proceedings of the First Workshop on Railway and Tracked Transit System Noise, Derby, U.K., 1976

26 1979 *Journal of Sound and Vibration* 66(3), Proceedings of the Second Workshop on Railway and Tracked Transit System Noise, Lyon, France, 1978

27 1983 *Journal of Sound and Vibration* 87(2), Proceedings of the Third Workshop on Railway and Tracked Transit System Noise, Monument, Colorado, U.S.A., 1981

28 1988 *Journal of Sound and Vibration* 120(2). Proceedings of the Fourth International Workshop on Railway and Tracked Transit System Noise, Noordwijkerhout, Netherlands, 1985.

29 E.K.BENDER and P.J.REMINGTON 1974 *Journal of Sound and Vibration* 37, 321-334. The influence of rails on train noise.

30 S.PETERS, B.HEMSWORTH and B.WOODWARD 1974 *Journal of Sound and Vibration* 35, 146-150. Noise radiation by a railway rail.

31 E.RAQUET 1980 *Rail Engineering International*, March 1980, 13-14. Noise damped wheels for long distance rail traffic.

32 D.J.THOMPSON 1986 *British Rail Research Unpublished Memorandum.* Simplified models for predicting the acoustic radiation from vibrating wheels and rails†

33 D.J.THOMPSON 1988 *Journal of Sound and Vibration* 120, 275-280. Predictions of the acoustic radiation from vibrating wheels and rails.

34 P.WETTA, B.BEGUET and E.PARENT DE CURZON 1988 *Journal of Sound and Vibration* 120, 255-266. Experimental analysis of wheel/rail noise by nearfield acoustic imaging.

35 B.BARISKOW, W.F.KING III and E.PFIZENMAIER 1987 *Journal of Sound and Vibration* 118, 99-122. Wheel/rail noise generated by a high speed train investigated by a line array of microphones.

†: See also earlier Unpublished Memoranda: A model to predict the sound pressure radiated by a wheel as approximated by a disc set in an infinite baffle (1983); A theoretical comparison of various wheel radiation models (1983); Models for predicting the acoustic radiation from a rail, including the boundary element method (1985).

36 R.HEMELRIJK 1985 *Presented at the Fourth International Workshop on Railway and Tracked Transit System Noise, Noordwijkerhout, The Netherlands.* Sound intensity near a running bogie.

37 T ten WOLDE and C.J.M. van RUITEN 1983 *Journal of Sound and Vibration* 87, 147-160. Sources and mechanisms of wheel/rail noise: state-of-the-art and recent research.

38 H.M.FISCHER 1979 *Journal of Sound and Vibration* 66, 333-349. Noise generation by railroad coaches.

39 E.PARENT DE CURZON and B.BEGUET 1988 *Journal of Sound and Vibration* 120, 311-320. Study into sources of wagon noise; measurement of sound energy generated by vehicle bodies and running gear.

40 J.FELDMANN 1983 *Journal of Sound and Vibration* 87, 179-187. The noise behaviour of the wheel/rail system - some supplementary results.

41 S.L.GRASSIE, R.W.GREGORY and K.L.JOHNSON 1982 *Journal of Mechanical Engineering Science* 24, 103-111. The dynamic behaviour of railway wheelsets and track to high frequency vertical excitation.

42 S.SATO and H.MATSUHISA 1981 *Bulletin of Japanese Society of Mechanical Engineers* 24, No 191, 849-853. Wheel flexural vibration including the effects of shear deformation and rotary inertia.

43 H.ARAI 1978 *Internoise 78*, 767-770. Study on dynamic characteristics of wheel concerned with wheel/rail noise.

44 H.IRRETIER 1983 *Journal of Sound and Vibration* 87, 161-177. The natural and forced vibration of a wheel disc.

45 E.SCHNEIDER, K.POPP and H.IRRETIER 1988 *Journal of Sound and Vibration* 120, 227-244. Noise generation in railway wheels due to rail-wheel contact forces.

46 S.HARAN and R.D.FINCH 1983 *Journal of the Acoustical Society of America* 74, 1433-1439. Ring model of railway wheel vibrations.

47 B.HEMSWORTH 1983 *Journal of Sound and Vibration* 87, 189-194. Vibration of a rolling wheel - preliminary results.

48 P.HEISS 1986 Untersuchungen über das Körperschall- und Abstrahlverhalten eines Reisezugwagenrades. (Investigations into the

vibration and noise behaviour of a passenger coach wheel). Doctoral thesis, Technical University of Berlin.

49 N.G.LEE 1982 *British Rail Research Technical Memorandum TM EST 16.* Natural frequencies and vibrational modes of coach wheels using NEWPAC.

50 D.J.THOMPSON 1987 *British Rail Research Unpublished Memorandum.* Refinements of finite element predictions of the natural frequencies of wheelsets.

51 C.J.C.JONES and D.J.THOMPSON 1987 *British Rail Research Unpublished Memorandum.* The effects of wheel radius on the wheel's natural frequencies and implications for noise radiation.

52 G.G.HEWITT, D.J.THOMPSON and R.A.CLARK 1987 *British Rail Research Technical Memorandum TM EST 45.* Determination of natural frequencies and vibration amplitudes of a class 143 wheelset by theoretical and experimental methods.

53 B.N.PERRY 1981 *British Rail Research Unpublished Memorandum.* Resonant frequencies, modes of vibration and damping ratios for a Commonwealth wheelset.

54 P.G.DAVIES, N.D.SHERRATT, D.J.THOMPSON and C.E.WRIGHT 1987 *British Rail Research Technical Memorandum TM SAV 19.* Determination of resonant frequencies, modes of vibration and damping ratios for a BT10 wheelset with and without brake discs.

55 N.S.FERGUSON and R.G.WHITE 1984 *Proceedings of the 2nd International Conference on Recent Advances in Structural Dynamics, ISVR, Southampton.* Assessment of the generating mechanisms and characteristics of wheel/rail noise via a study of a rolling disc.

56 N.S.FERGUSON 1988 The vibration of rolling discs, PhD thesis, University of Southampton.

57 Y.HONDA, H.MATSUHISA and S.SATO 1985 *Journal of Sound and Vibration* **102**, 457-472. Modal response of a disk to a moving concentrated harmonic force.

58 S.L.GRASSIE, R.W.GREGORY, D.HARRISON and K.L.JOHNSON 1982 *Journal of Mechanical Engineering Science* **24**, 77-90. The dynamic response of railway track to high frequency vertical excitation.

59 S.L.GRASSIE, R.W.GREGORY and K.L.JOHNSON 1982 *Journal of Mechanical Engineering Science* 24, 91-95. The dynamic response of railway track to high frequency lateral excitation.

60 S.L.GRASSIE, R.W.GREGORY and K.L.JOHNSON 1982 *Journal of Mechanical Engineering Science* 24, 97-102. The dynamic response of railway track to high frequency longitudinal excitation.

61 S.J.COX and S.L.GRASSIE 1983 *Cambridge University Engineering Department Report CUED/C-Mech/TR27* A new dynamic model of railway track incorporating flexible sleepers.

62 S.L.GRASSIE and S.J.COX 1984 *Proceedings of I.Mech.E.,Series D.* The dynamic response of railway track with flexible sleepers to high frequency vertical excitation.

63 R.A.CLARK, P.A.DEAN, J.A.ELKINS and S.G.NEWTON 1982 *Journal of Mechanical Engineering Science* 24, 65-76. An investigation into the dynamic effects of railway vehicles running on corrugated track.

64 S.G.NEWTON and R.A.CLARK 1979 *Journal of Mechanical Engineering Science* 21, 287-297. An investigation into the dynamic effects on the track of wheelflats on railway vehicles.

65 M.L.MUNJAL and M.HECKL 1982 *Journal of Sound and Vibration* 81, 491-500. Vibration of a periodic rail-sleeper system excited by an oscillatory, stationary, transverse point force.

66 E.TASSILLY 1987 *Revue Générale des Chemins de Fer*, March 87, 45-54. Propagation des ondes de flexion dans la voie ferrée considérée comme un milieu périodique (Propagation of deflection waves in a railway track considered as a periodic structure).

67 E.TASSILLY 1987 *International Journal of Engineering Science* 25, 85-95. Propagation of bending waves in a periodic beam.

68 K.ONO and M.YAMADA 1989 *Journal of Sound and Vibration* 130, 269-297. Analysis of railway track vibration.

69 D.J.THOMPSON 1985 *British Rail Research Unpublished Memorandum.* Mickleover rail vibration experiment, Summer 1983 : Report 1 - Experimental procedure and preliminary results.

70 D.J.THOMPSON 1985 *British Rail Research Unpublished Memorandum.* Mickleover rail vibration experiment, Summer 1983 : Report 2 - Propagation of vibration away from excitation point.

71 D.J.THOMPSON 1985 *British Rail Research Unpublished Memorandum.* A finite element analysis of the modes of vibration of a rail cross-section.

72 W.SCHOLL 1984 *Proceedings of the 2nd International Conference on Recent Advances in Structural Dynamics, ISVR, Southampton.* Two theoretical models for wave propagation in rails.

73 W.SCHOLL 1982 *Acustica* **52**, 10-15. Schwingungsuntersuchungen an Eisenbahnschienen (Investigations into the vibrations of a railway rail)

74 P.RANGANATH NAYAK 1973 *Journal of Sound and Vibration* **28**, 277-293. Contact vibrations of a wheel on a rail.

75 A.SOOM and J.W.CHEN 1986 *Journal of Tribology* **108**, 123-127. Simulation of random surface roughness-induced contact vibrations at Hertzian contacts during steady sliding.

76 J.FELDMANN 1987 *Journal of Sound and Vibration* **116**, 527-543. A theoretical model for structure-borne excitation of a beam and a ring in rolling contact.

77 J.FELDMANN 1986 Ein Beitrag zur Klärung des Körperschall- und Impedanzverhaltens zweier Körper beim Rollen unter Berücksichtigung der Kontaktsteife und der Anregung (An attempt to explain the structure-borne noise and impedance behaviour of two bodies in rolling, taking account of the contact stiffness and excitation). Doctoral thesis, Technical University of Berlin.

78 M.HECKL, J.FELDMANN and W.SCHOLL. *Statusseminar.* Mechanismen der Schallentstehung beim Rad/Schiene System (Mechanisms of noise generation for the wheel/rail system).

79 M.L.MUNJAL and M.HECKL 1982 *Journal of Sound and Vibration* **81**, 477-489. Some mechanisms of excitation of a railway wheel.

80 J.J.KALKER 1979 *Vehicle System Dynamics* **8**, 317-358. Survey of wheel-rail rolling contact theory.

81 J.J.KALKER 1967 On the rolling contact of two elastic bodies in the presence of dry friction. Doctoral thesis, Technical University of Delft.

82 J.A.ELKINS and R.J.GOSTLING 1977 *Paper presented to the IUTAM Symposium, Vienna.* A general quasi-static curving theory for railway vehicles.

83 R.A.CLARK and B.M.EICKHOFF 1983 *British Rail Research Technical Memorandum TM DA 44.* Predicting the transient response of vehicles to track with known lateral and vertical alignments.

84 C.J.M.van RUITEN 1988 *Journal of Sound and Vibration* 120, 245-254. Mechanism of squeal noise generated by trams.

85 K.KNOTHE and A.GROSS-THEBING 1984 *Proceedings of the Institution of Mechanical Engineers* Vol 198C No 12, 167-173, High frequency contact mechanics: the derivation of frequency-dependent creep coefficient.

86 K.KNOTHE and A.GROSS-THEBING 1986 *Vehicle System Dynamics* 15, 133-153, Derivation of frequency dependent creep coefficients based on an elastic half-space model.

87 A.VALDIVIA 1987 The interaction between high frequency wheel-rail dynamics and irregular rail wear - a linear model. Doctoral thesis, Technical University of Berlin.

88 W.F.KING III 1977 *Journal of Sound and Vibration* 54, 361-378. On the role of aerodynamically generated sound in determining radiated noise levels of high speed trains.

89 W.F.KING III and E.PFIZENMAIER 1984 *DFVLR Report DFVLR-FB-84-27.* On the relative importance of aerodynamic and wheel/rail noise sources generated by railway trains.

90 A.J.MCLEOD and R.E.D.BISHOP 1965 *Mechanical Engineering Science Monograph* 1. The forced vibration of flat circular plates.

91 R.PERRIN, T.CHARNLEY and J.DePONT 1983 *Journal of Sound and Vibration* 90, 24-49. Normal modes of the modern English church bell.

92 R.J.GILBERT 1983 *British Rail Research Unpublished Memorandum,* Wheel/rail noise and vibration investigations : Instrumentation development and initial rolling tests on Laboratory coach 14 (WREN).

93 D.J.THOMPSON 1984 *British Rail Research Unpublished Memorandum,* A note on the radial and one-nodal circle modes of vibration of a Commonwealth wheelset.

94 K.P.ROBINSON, E.M.STROVER and R.J.M.DODD 1984 *British Rail Research Technical Note TN EMMA 15.* A user's guide to the NEWPAC program for structural analysis using the finite element method.

95 R.J.GUYAN 1965 *AIAA Journal* 3, 380. Reduction of stiffness and mass matrices.

96 R.J.ROARK *Formulas for Stress and Strain*, McGraw-Hill.

97 D.J.EWINS 1984 *Modal testing : theory and practice*, Research Studies Press.

98 R.D.MINDLIN 1949 *Journal of Applied Mechanics* 71, 259-268 Compliance of elastic bodies in contact.

99 C.J.C.JONES 1987 *British Rail Research Unpublished Memorandum.* A preliminary assessment of three wheel damping treatments using a fifth scale wheel.

100 O.R.E. 1988 *Office for Research and Experiment of the International Union of Railways. Question C163 Railway Noise. Report No 9.* Wheel/rail contact noise - an experimental comparison of various systems for measuring the rail roughness associated with train rolling noise.

101 L.MEIROVITCH 1986 *Elements of Vibration Analysis*, McGraw-Hill, second edition.

102 D.E.NEWLAND 1975 *An introduction to Random Vibrations and Spectral Analysis*, Longman.

103 D.J.THOMPSON 1985 *British Rail Research Unpublished Memorandum* . The modes of vibration and radiated noise from a cylindrical bar and a short length of rail.

104 P.G.DAVIES, N.D.SHERRATT and D.J.THOMPSON 1987 *British Rail Research Unpublished Memoranda.* The natural frequencies and damping ratios of a freely suspended short length of rail. The damping treatment of a short length of freely suspended rail: T.MAT PD4, with and without a constraining layer.

105 J.R.CHAPMAN, D.BUTLER and P.R.BRAZIER-SMITH 1985 *Journal of Sound and Vibration* 102, 563-577. An investigation of the dispersion law for I-section beams.

106 N.G.STEPHEN and P.J.WANG 1986 *Journal of Sound and Vibration* 109, 51-64. Web flexibility and I-beam torsional oscillation.

107 D.J.MEAD 1973 *Journal of Sound and Vibration* 27, 235-260. A general theory of harmonic wave propagation in linear periodic systems with multiple coupling.

108 D.J.MEAD 1975 *Journal of Sound and Vibration* **40**, 1-18. Wave propagation and natural modes in periodic systems I: Monocoupled systems.

109 D.J.MEAD 1975 *Journal of Sound and Vibration* **40**, 19-39. Wave propagation and natural modes in periodic systems II: Multicoupled systems.

110 R.M.ORRIS and M.PETYT 1974 *Journal of Sound and Vibration* **33**, 223-236. A finite element study of harmonic propagation in periodic structures.

111 L.CREMER, M.HECKL and E.E.UNGAR 1973 *Structure-borne Sound.* Berlin: Springer-Verlag.

112 C.J.M.van RUITEN 1979 Wiel/rail geluid (Wheel/rail noise), Dissertation, Technische Hogeschool Delft, Labatorium voor Technische Natuurkunde.

113 S.L.GRASSIE 1989 *Proceedings of the Institution of Mechanical Engineers* **203**, part F, 25-32. Resilient railpads: their dynamic behaviour in the laboratory and on track.

114 D.J.MEAD 1986 *Journal of Sound and Vibration* **104**, 9-27. A new method of analysing wave propagation in periodic structures; applications to periodic Timoshenko beams and stiffened plates.

115 P.M.MORSE 1948 *Vibration and Sound* McGraw-Hill.

116 D.J.THOMPSON 1987 *British Rail Research Unpublished Memorandum.* The measurement of wheel and rail roughness as part of ORE sponsored experiments conducted on BR.

117 D.J.THOMPSON 1987 *British Rail Research Unpublished Memorandum.* The effects of roughness condition and train speed on the rolling vibration levels of wheels and rails. 1: relative levels.

118 D.J.THOMPSON 1987 *British Rail Research Unpublished Memorandum.* The effects of roughness condition and train speed on the rolling vibration levels of wheels and rails. 2: overall levels.

119 H.M.FISCHER 1986 Der Einfluß von Oberflächenrauhigkeiten auf die Körperschallentstehung beim Rollen (The influence of surface roughness on the generation of vibration during rolling). Doctoral thesis, Technical University of Berlin.

120 D.J.WILLIAMS 1988 A study of the rolling vibrations of a type of railway wheel. MSc dissertation, University of Salford.

121 BRÜEL & KJAER 1978 *Piezoelectric accelerometer and vibration preamplifier handbook.*

122 G.B.WARBURTON 1976 *The Dynamical Behaviour of Structures,* Pergamon.

123 N.G.STEPHEN 1982 *Journal of Sound and Vibration* **80**, 578-582. The second frequency spectrum of Timoshenko beams.

124 S.P.TIMOSHENKO 1956 *Strength of Materials Part II: Advanced.* Van Nostrand Reinhold.

125 K.L.JOHNSON 1982 *Proceedings of I.Mech.E.* **196**, 363-378. One hundred years of Hertz contact.

126 S.P.TIMOSHENKO and J.N.GOODIER 1982 *Theory of Elasticity* 3rd edition. McGraw Hill.

127 F.W.CARTER 1926 *Proceedings of the Royal Society, Series A* 112, 151-157. On the action of a locomotive driving wheel.

128 NUMERICAL ALGORITHM GROUP 1987 *NAG Fortran Library Manual, Mark 12.*

129 R.FORD 1988 *School of Mechanical and Industrial Engineering, University of New South Wales, Acoustics and Vibration Group. Research Note AVG/RN881122-1.* Modal analysis of a concrete sleeper.

APPENDIX A

EXPERIMENTAL DATA: MEASUREMENTS AND ANALYSIS

A.1 EXPERIMENTAL DETAILS

A series of measurements of wheel-rail noise and vibration were carried out in 1984 jointly by BR and London Transport, under O.R.E. sponsorship [23,13]. The objective was to investigate the validity of the linear model of rolling noise developed by Remington [18,20], and in particular to look at the relationships between measured noise, wheel and rail vibration and combined surface roughness without implementing the theoretical model itself.

Experimental data from these measurements are used as a basis on which to judge the results from the theoretical models of wheel-rail interaction developed in this thesis.

Simultaneous measurements were taken of 10 channels of rail vibration, 6 of wheel vibration and 5 of noise (using both wayside and train-borne microphones). These measuring positions are shown in Figure A1. The instant at which the instrumented wheel passed over the trackside instrumentation position was recorded on both train-based and trackside measuring systems.

The measurements were carried out for a range of 4 train speeds (40, 80, 120 and 160 km/h), and for a combination of naturally occurring surface roughness conditions, which comprised a rough (cast-iron block tread-braked) wheel and a smooth (unbraked) wheel, and rough (corrugated) rail and smooth (uncorrugated) rail.

Analysis was carried out to produce one-third octave spectra of the various vibration and noise signals over the range 250 Hz to 5000 Hz. In each case a time interval was chosen which corresponded to a distance travelled by the train of 4.44 m (ie a different time interval for each speed). This was centred on the instant when the centre of the test bogie in question was over the rail measurement position. (Note that all wheels in each bogie had nominally similar condition).

Measurements were also taken of the surface roughnesses of the wheels and rails concerned [116]. For the rail, a trolley system was used, developed originally by Cambridge University, and now operated by Fracture Mechanics Unit, BR Research. This pulls along a seismic

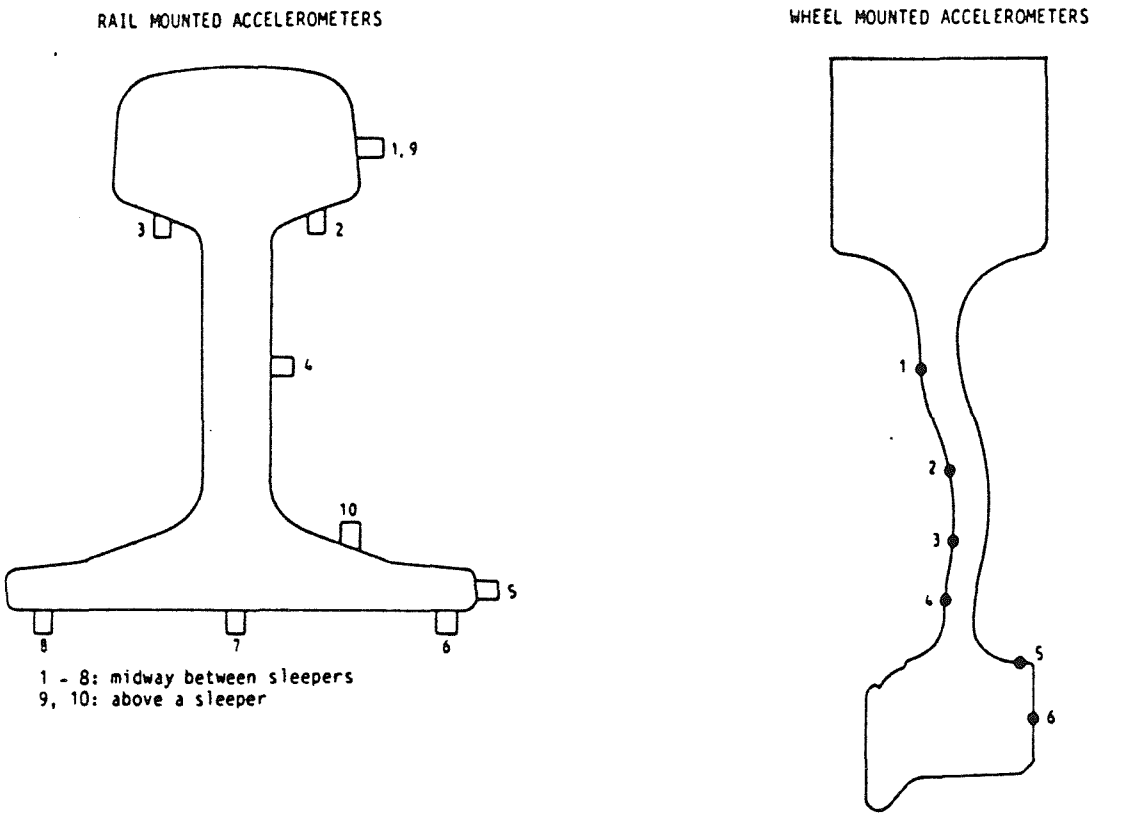

Figure A1 Transducer Locations

accelerometer which is mounted on a rubber pad on the rail. For the wheel, a system based on a displacement transducer (LVDT) was made available by French Railways (SNCF).

These measurements were also analysed into one-third octave spectra. Band centre wavelengths were selected to correspond to the 'preferred' centre frequencies when traversed at the various train speeds (using $f=V/\lambda$). Because of the limitations of the roughness measuring equipment (both wheel and rail), valid results are limited to a minimum wavelength band of 14 mm, ie a maximum frequency band of 3150 Hz at the highest speed (160 km/h), and proportionately lower at lower speeds.

A.2 COMPARATIVE ANALYSIS

Analysis was carried out using these one-third octave results to determine whether they were self-consistent [117], and to establish whether or not a linear model, such as Remington's, was appropriate over the range of conditions measured [118]. The ratio of vibration to roughness was formed for each measurement (by subtraction of dB levels), and the resultant transfer functions were compared for the various conditions. For a linear mechanism, these would be constant across the various test conditions, within the limits of experimental accuracy. However this was found not to be the case and it was concluded that the linear model could not adequately represent all test conditions [24].

By contrast, similar comparisons of vibration with noise spectra showed that a linear relationship did exist in this case. This has been confirmed by subsequent theoretical modelling of the noise radiation based on the same measurements [33] (cf Appendix B).

Clearly the validity of the comparison between roughness and vibration depends on the correct analysis of the surface roughness. Three sets of surface roughness spectra were used in the comparative analysis described above:-

(i) The profiles as measured by the roughness instruments were converted directly to one-third octave spectra. It was observed that pits in the surface of the wheel influenced results whereas the relatively large radius of the wheel prevents such pits from being monitored fully during rolling. This was not the case for the rail roughness data as the measuring instrument already included a mechanical filter which eliminated any such pits.

(ii) The wheel profiles were modified mathematically to take account of the effect of the relatively large radius of the wheel in sensing the surface. A similar method has been used by Fischer [119]. No modification was made to the rail roughness data, as the measuring system uses a fairly large radius probe which eliminates any such pits. In any case, these are less common in the rail surface. Spectra were then calculated as before.

(iii) A contact filter (as used by Remington [20]) was applied, as a frequency-domain correction to the spectra of (ii). This takes account of the finite length of the contact patch and is a separate effect from the analysis of (ii). (Initially a time domain correction was used for examples of the wheel roughness, and found to give results which were consistent with a frequency domain filter, which was then used in wider data analysis [116]).

The tests for linearity between vibration and roughness appeared more positive in each successive case, but even for (iii) the difference spectra were still not close enough to each other to imply a linear relation, as they had been in the case of the relation between vibration and noise. In particular, this analysis showed systematic differences between the results for the two rail roughness conditions and for the various train speeds.

Attempts were made to identify possible sources of such a non-linear relationship. These showed that the corrugated site conditions were definitely outside the scope of the linear model, because the vertical deflections in the contact patch were outside the range where a linear approximation for the Hertzian contact spring could be considered valid [118].

All of the above analysis is based on comparing relative levels between one measurement and another to test the hypothesis of linearity. The model of Remington had not been applied explicitly to any of the data, and the conclusions drawn apply not just to the specific model implemented by Remington, but to any similar linear model in which roughness is the sole input.

Although it had been demonstrated that the corrugated rail site represented a condition that was definitely outside the linear regime, it still remained a possibility that rolling over a relatively smooth rail could be represented by a linear model. The range of conditions

remaining is not sufficiently large, however, to justify further comparative analysis.

A.3 EXTRA ANALYSIS FOR THE CURRENT WORK

The conditions available from the smooth rail site consist of the two wheel roughnesses and 4 train speeds, with 2 or 3 runs for each of these test conditions. For each run 6 data channels on the wheel and 10 on the rail are available. In order to reduce the amount of data to be considered, averaging is carried out over the 2-3 runs for each condition, and only selected channels are considered. These are mainly those corresponding most closely to the vibration at the wheel-rail contact (ie channels 5 and 6 for the wheel, and channels 1 and 7 for rail), although some results for the wheel web (channel 2) will also be considered.

The results are presented in the form of vibration level minus roughness level, which is the opposite way around to that used in earlier work [118], but is a more logical presentation. Additionally the vibration is converted from acceleration to displacement using a frequency factor:-

$$\text{displacement amplitude} = \frac{\text{acceleration amplitude}}{(2\pi \text{ frequency})^2} \qquad \ldots(A1)$$

The result, displacement level minus roughness level, can then be compared directly with the predictions which are given in the form of a transfer function from roughness to vibration. A level of 0 dB for this transfer function spectrum would imply that the vibration corresponded to the same displacement amplitude as the roughness. The roughness used includes both the curvature analysis and the effects of the contact filter (ie (iii) in §A.2 above).

The results are shown in Figures A2 and A3 for the rail, for vertical vibration under the centre of the foot and lateral vibration of the head. Each figure contains results for all 4 speeds and for the two wheel conditions. Figures A4 and A5 contain the corresponding results for the wheel for radial and axial vibration of the tyre. These wheel and rail vibration measurement positions were selected as being the most representative of the vibration of the contact zone.

(a) Smooth Wheel, Smooth Rail

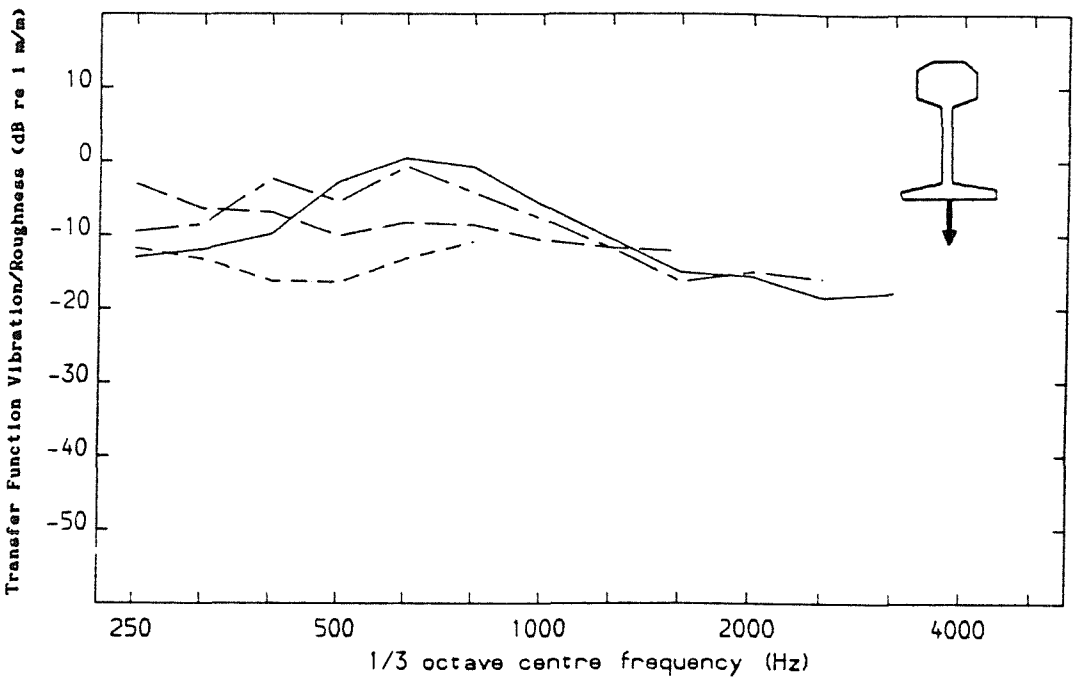

(b) Rough Wheel, Smooth Rail

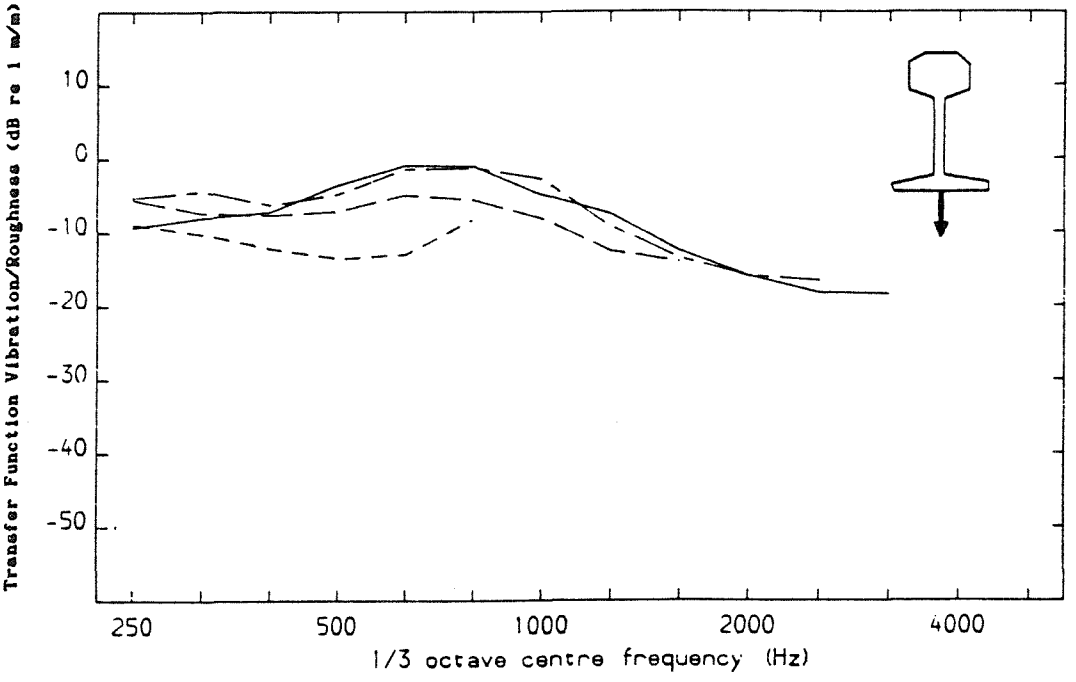

Figure A2 Experimental Results: Rail Foot Centre Vertical (Channel 7) Vibration Displacement/Roughness (– – – 40 km/h, — — 80 km/h, — · — 120 km/h, ——— 160 km/h)

(a) Smooth Wheel, Smooth Rail

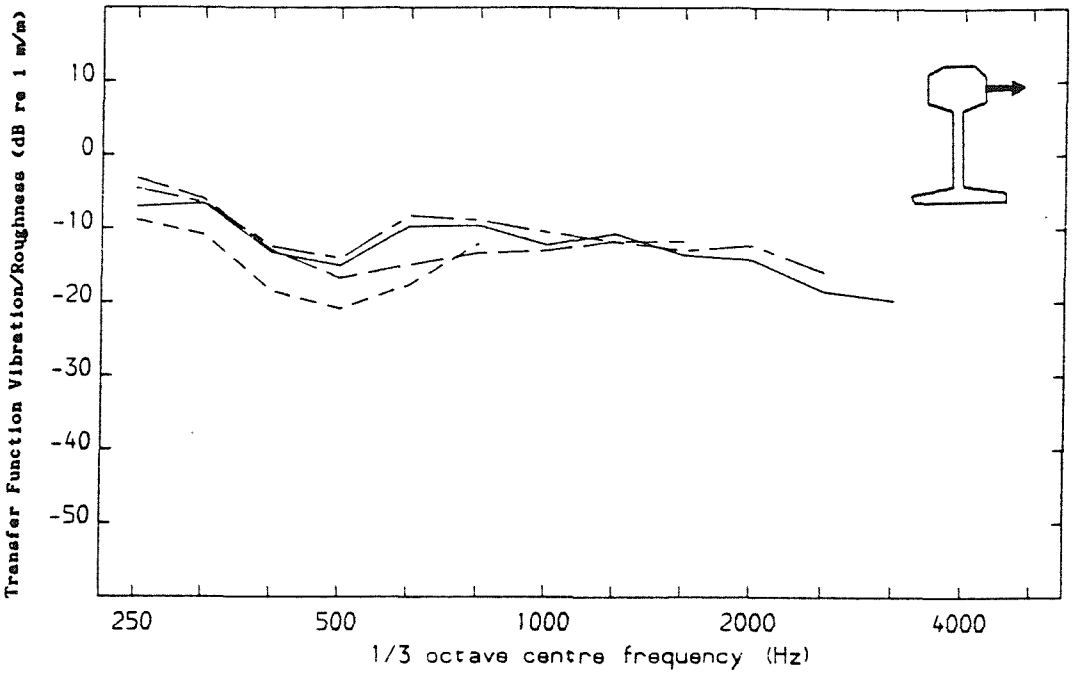

(b) Rough Wheel, Smooth Rail

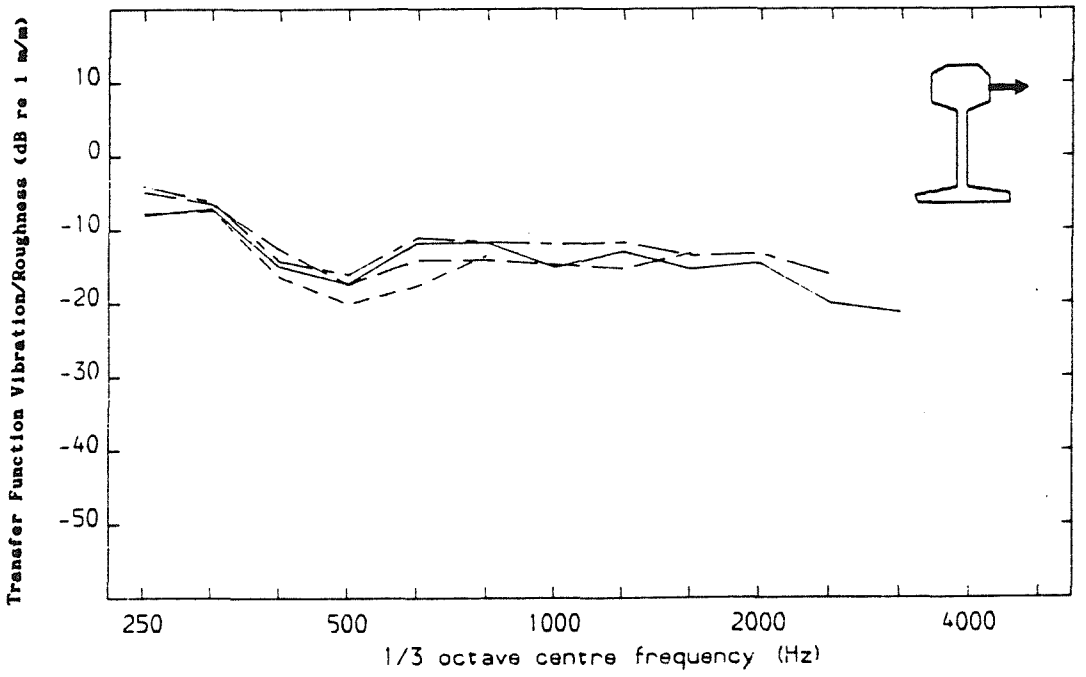

Figure A3 Experimental Results: Rail Head Lateral (Channel 1) Vibration Displacement/Roughness (– – – 40 km/h, — — 80 km/h, — · — 120 km/h, ——— 160 km/h)

(a) Smooth Wheel, Smooth Rail

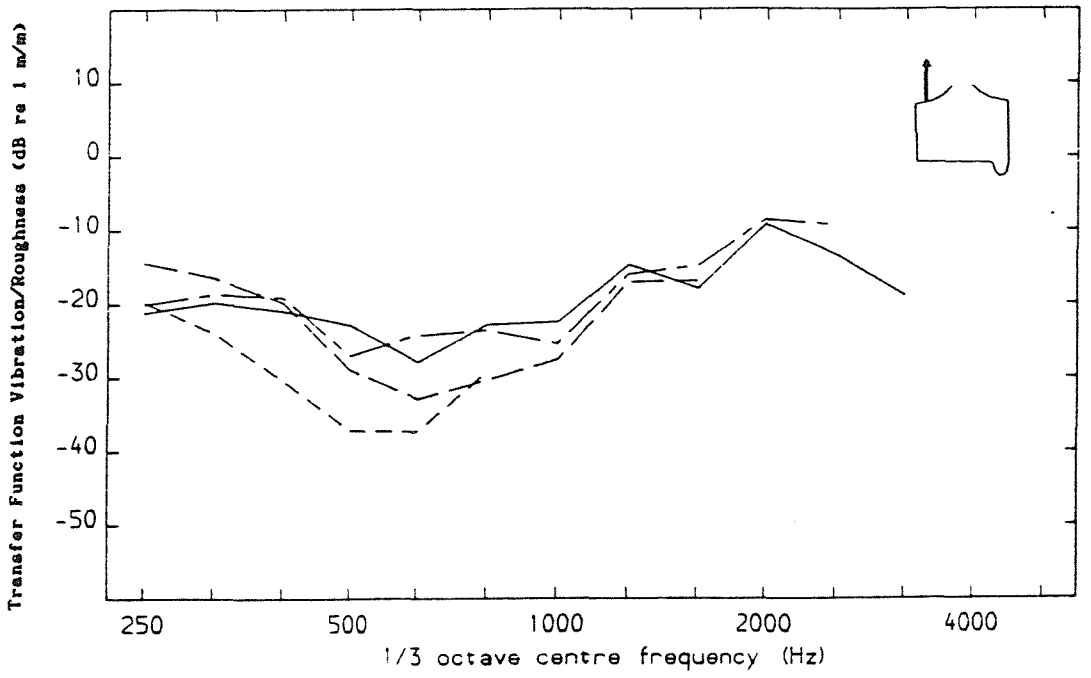

(b) Rough Wheel, Smooth Rail

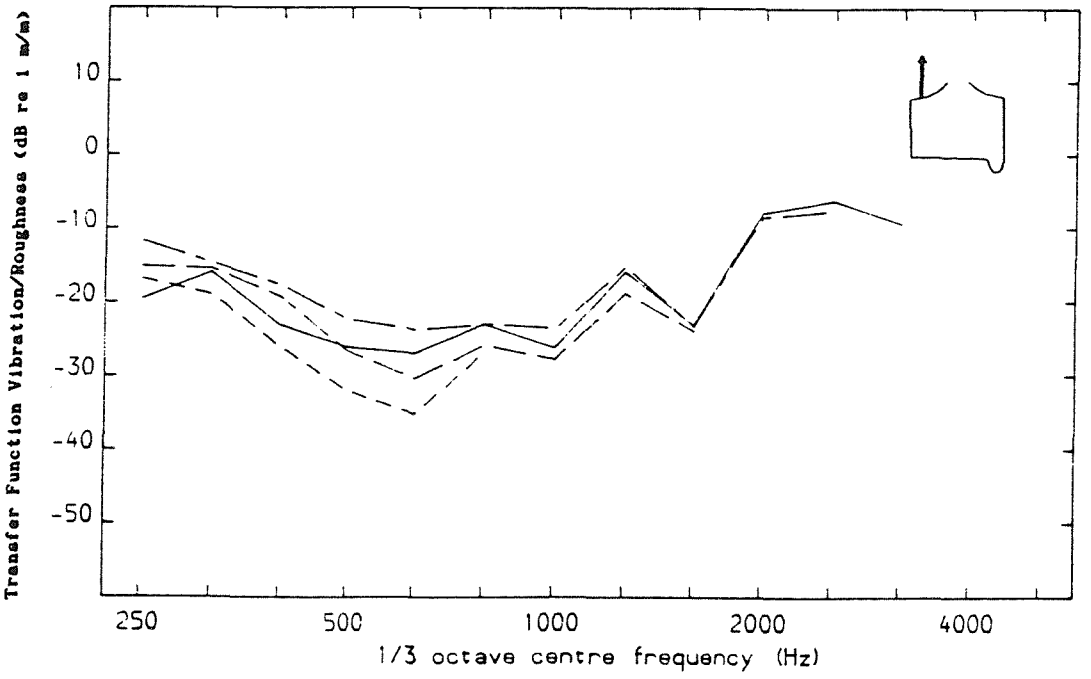

Figure A4 Experimental Results: Wheel Tyre Radial (Channel 5) Vibration Displacement/Roughness (– – – 40 km/h, — — 80 km/h, — · — 120 km/h, ——— 160 km/h)

(a) Smooth Wheel, Smooth Rail

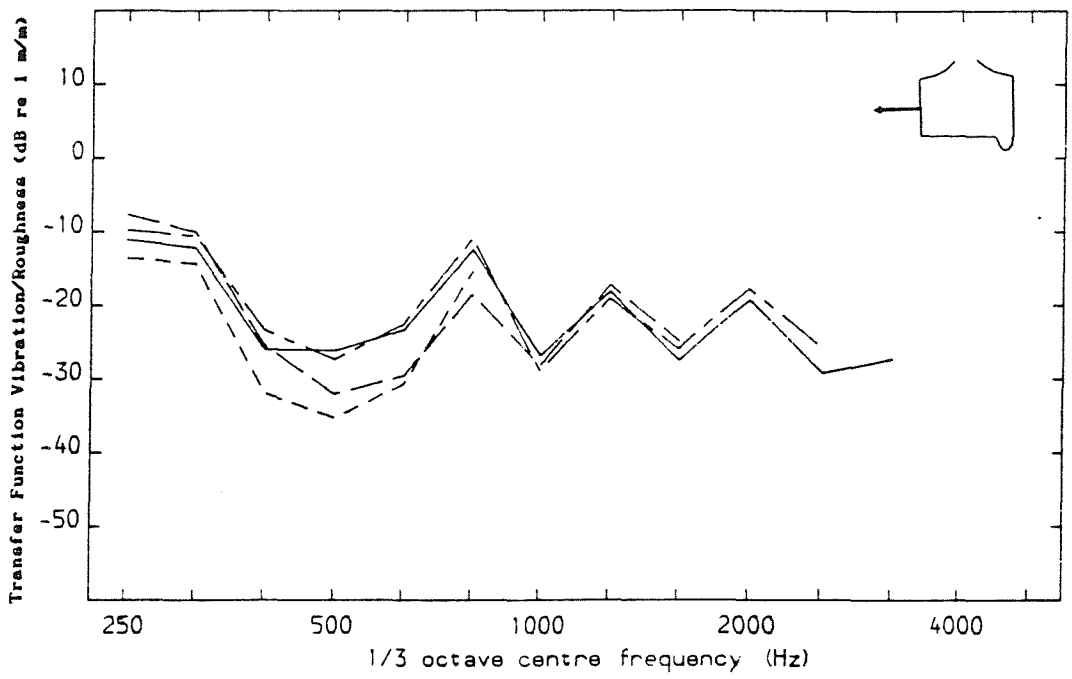

(b) Rough Wheel, Smooth Rail

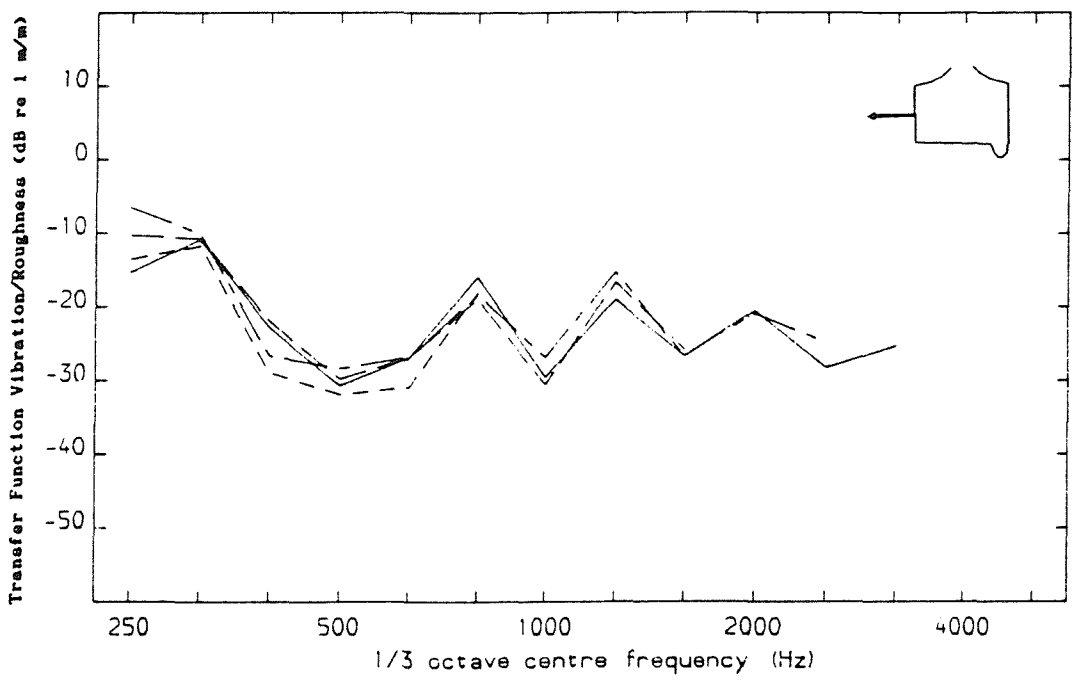

Figure A5 Experimental Results: Wheel Tyre Axial (Channel 6) Vibration Displacement/Roughness (– – – 40 km/h, — — 80 km/h, — · — 120 km/h, ——— 160 km/h)

The results are limited by the range of validity of the roughness measurements, which eliminates the results at higher frequencies, particularly for the lower speeds.

Presented in this form, these experimental results show that the vertical vibration of the rail (Figure A2) is of a similar amplitude to the roughness in the region of 800 Hz, and falls at higher and lower frequencies. The lateral vibration of the rail (Figure A3) is generally a little less than this. For the wheel, the radial vibration (Figure A4) is comparable to the roughness amplitude at high frequencies, whereas the axial tyre vibration (Figure A5) is generally lower. It is clear that the roughness is of an amplitude which is large enough to constitute a significant source of vibration, particularly in the vertical direction in which it acts.

It should be noted that Figure A2 in particular, the vertical vibration of the rail, contains significant speed dependence, whereas Remington's linear model contains no provision for such a speed dependence. Remington's experimental results also showed a speed dependence, although it was the reverse situation with an over-prediction at higher speeds.

Since the wheel vibration results are known to be resonant in nature [47], analysis is also required of wheel vibration as narrow-band spectra. Figure A6 contains these results for two positions: axial vibration on the tyre and axial vibration on the web. These are shown for one wheel condition only, but in each case showing all 4 speeds. These results are taken from a separate analysis [120] of the results of the same experiment as above ([13,23]). These have been analysed using a rectangular window (ie without a shaped window), which will tend to broaden the peaks. They have a frequency resolution of 10 Hz, and have been averaged over a considerable sample length.

These results are used to investigate the detailed shape of the predicted narrow-band spectra. It is not critical that the corresponding roughness has not been measured, since the rail roughness, which is larger than the wheel roughness for this case, will be a broad-band random signal. In particular it should be noted that a long time average has been used in the vibration measurements so that the corresponding roughness can be expected to have a relatively smooth spectral density. Thus, although the overall level will be determined by the roughness, the spectral detail will not be affected by it. This

(a) Web Axial Vibration (Channel 2)

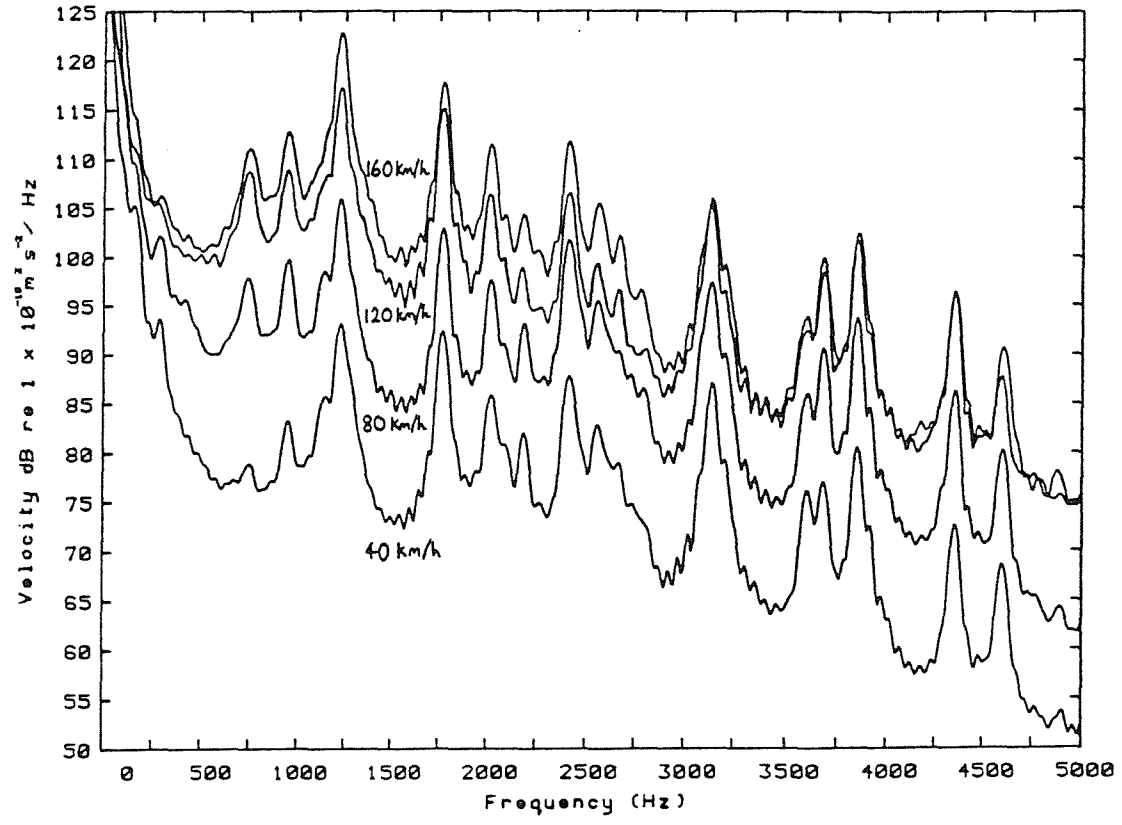

(b) Tyre Axial Vibration (Channel 6)

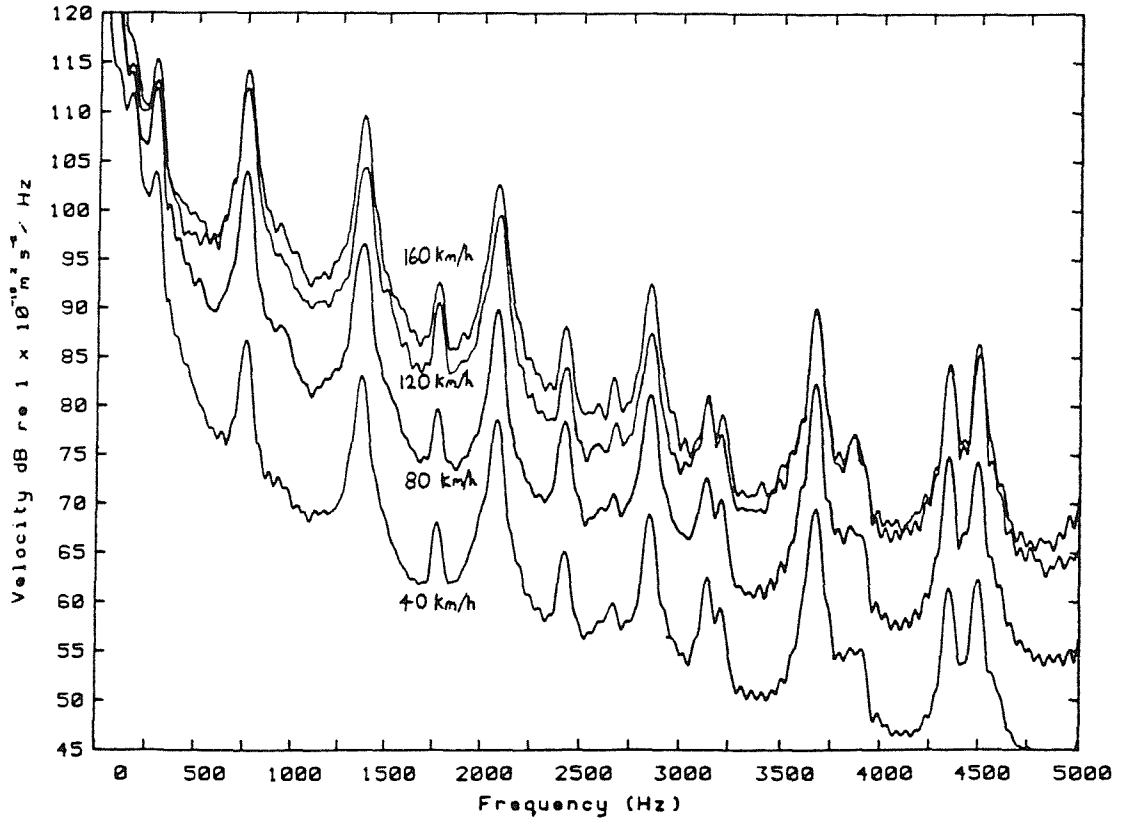

Figure A6 Measured Narrow-band Spectra of Wheel Vibration (Smooth Wheel, Smooth Rail) from [120]

would not be the case if the roughness were periodic or had sharp spectral components.

Figure A7 is a comparison between the rolling vibration spectrum, for axial vibration of the web at 160 km/h, and the response at this same position to a radial hammer excitation on the tyre (also from [120]). The latter has been analysed using an exponential window to truncate the ringing in the signal. This has the effect of introducing hypothetical damping, ie significantly reducing the height of the resonance peaks. This figure is included to show that the frequencies of peak response correspond to resonance frequencies of the free wheelset to within the bandwidth of the analysis.

The short analysis time interval available for the rail measurements means that such narrow-band analysis cannot be used for validating the predicted rail response.

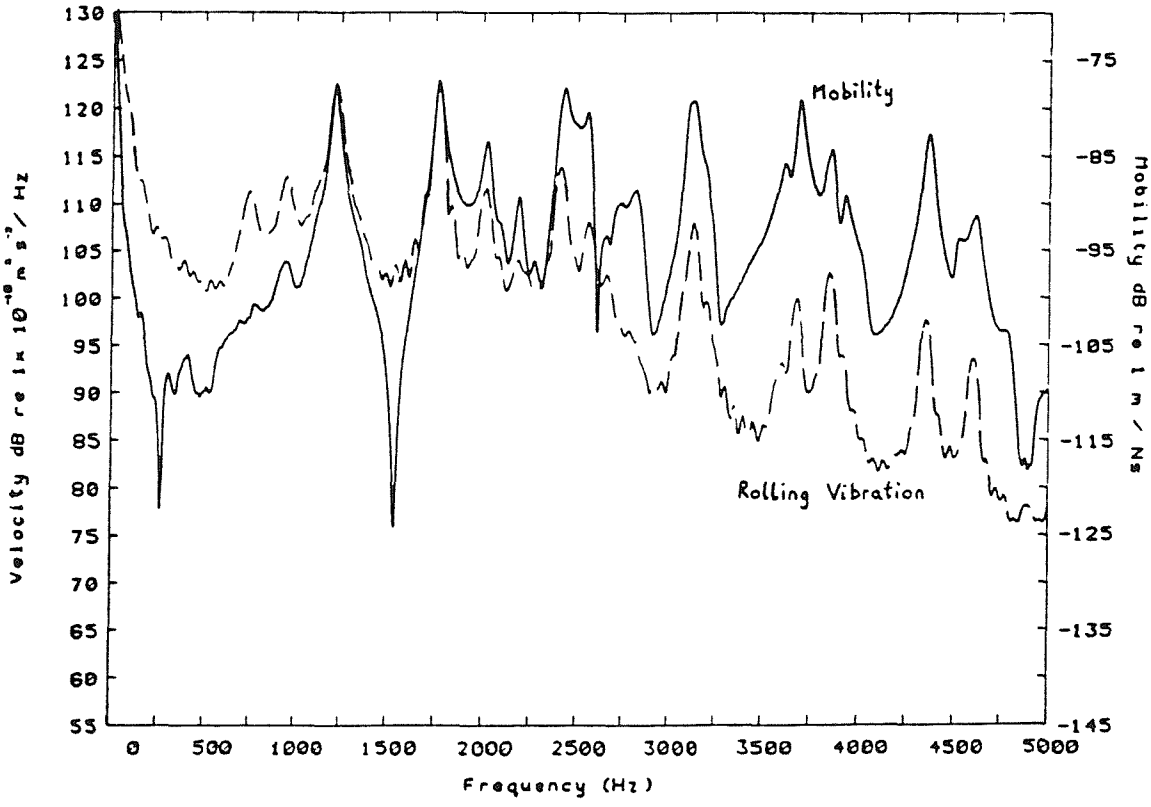

Figure A7 Measured Rolling Wheel Vibration (Web Axial) and Mobility of Static Wheel (Web Axial Response/Radial Force) from [120]

APPENDIX B

NOISE RADIATION MODELLING

B.1 INTRODUCTION

Wheel-rail noise is generally assumed to emanate from vibrations of the wheel and/or rail. Theoretical models have been developed to predict the noise radiation from a wheel and a rail, based on their respective vibrations. From these it should be possible, given estimates of the vibration levels, to determine whether these vibrations generate the noise, and to assess the relative importance of the wheels and the rails as sources of noise.

The experiment described in Appendix A consists of a series of simultaneous measurements of the vibration of a wheel and a rail, and of the overall sound radiated to the wayside. This covered a large range of measurement conditions (surface roughnesses and speeds). These measured vibration spectra have been used as inputs to the theoretical models, the corresponding measured noise providing a basis for assessment of their validity. This Appendix summarises this work, which has been published in [33].

B.2 WHEEL RADIATION MODEL

The wheel radiation model [32] is based on the Rayleigh integral for the radiation from a flat surface, in this case of circular shape, mounted in an infinite baffle. The following features are, therefore, ignored:-

- wheel cross-sectional shape (by assuming a flat surface)
- radiation from the radial vibration of the wheel
- any effects of wheel rotation
- effects of airflow (diffraction, turbulence etc)
- shielding and/or reflection from the bogie and vehicle body
- the Doppler effect (as the vehicle passes the measurement position)

The use of a formulation which is based on a baffled source, results in errors in the directivity pattern. At low frequencies the radiation efficiency, σ, is over-predicted, but above a critical frequency the radiation efficiency is approximately unity for both baffled and unbaffled cases. Thus, as long as details of the directivity are avoided, by taking a spatial average, the baffled

prediction should give valid results above this critical frequency. The critical frequency depends on the modeshape, but investigations for various modes of a Commonwealth wheel showed that $\sigma \simeq 1$ for all modes above 1 kHz [32]. Thus the model can be expected to give reasonable results above 1 kHz, but to over-predict the radiation slightly at lower frequencies.

As radial motion of the wheel is ignored, the vibration is estimated from the outputs from the 5 available axial accelerometers (shown in Figure B1). Of these, 4 were located on the wheel web at various radii, and the fifth was mounted on the tyre. The wheel surface is therefore divided into 5 concentric rings (shown in Figure B1), and a constant vibration level is assumed over each ring, the level corresponding to the respective accelerometer output (for the 1/3 octave band under consideration). The vibration of the hub and axle region is ignored.

Since average 1/3 octave spectra are used, details of the wheel response as a function of position are not known. Instead it is assumed that a constant level prevails over the entire ring (which would seem to be correct on average). The motions of each ring can be

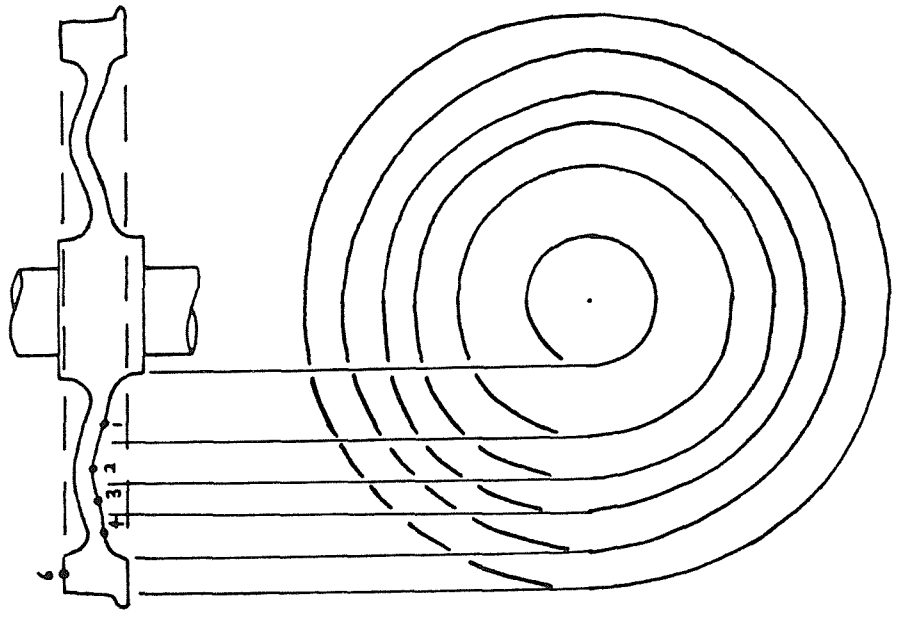

Figure B1 Wheel Radiation Model: Correspondence between Positions of Rings and Accelerometer Positions on the Wheel

assumed to be in phase with each other along any radial line, since this is the case for most of the motion in most of the dominant modes which make up the wheel vibration.

However the motion can not be assumed to be in-phase around the whole wheel, as, generally, the wheel vibrates in modes which contain a number of nodal diameters, and thus the vibrations of different parts of the wheel surface are out of phase. The resulting directivity pattern will have a minimum on the axis of symmetry, whereas an in-phase vibration distribution would have a maximum there. The radiation prediction has therefore been based on the results for n=2 and n=4 (depending on the frequency). For convenience, only even values of n are used as, for odd values of n a numerical integration is required. The values of n used (n=2 up to 1.6 kHz, and n=4 for 2 kHz and above) correspond roughly to the 1-nodal-circle modes present in these bands. However the precise value of n used matters much less than the fact that a non-zero value of n is used.

Although the prediction is based on the noise at an anti-node of the directivity due to the vibration at an anti-node of the modeshape, this is, nevertheless, equivalent to the required result, which is the r.m.s. average noise due to an r.m.s. average vibration level (in the circumferential direction).

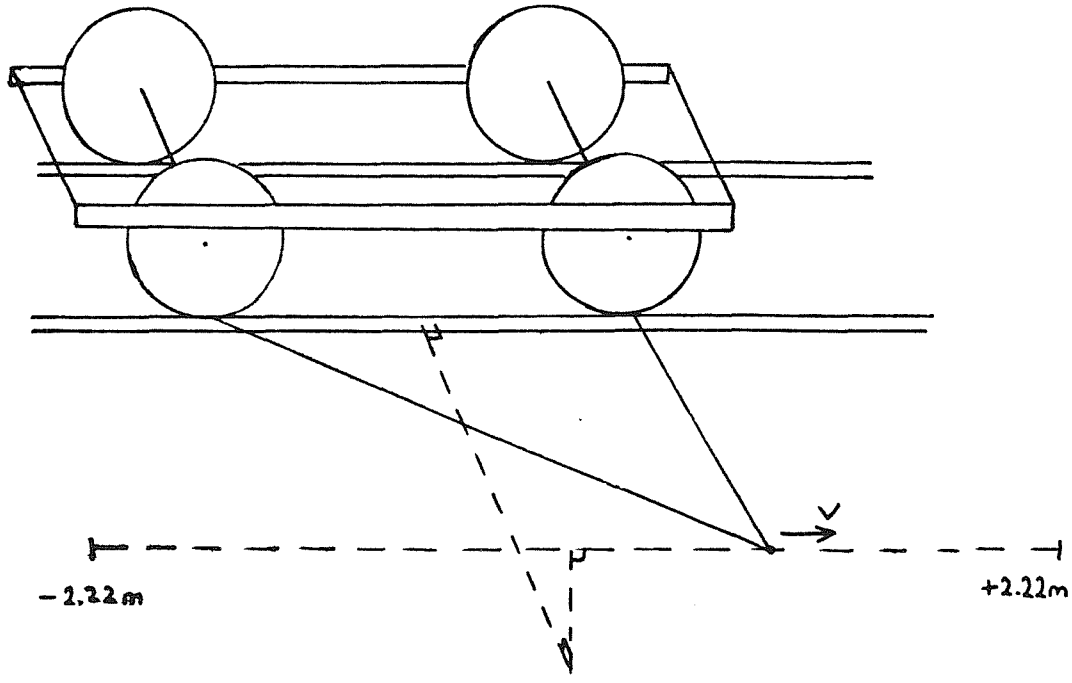

Figure B2 Wheel Radiation Model: Pass-by Averaging and the Addition of Various Wheel Components

The radiated sound is then averaged over the radiation directivity by integrating over the pass-by geometry, thus calculating the average sound level at the microphone position as the wheel moves past it (ignoring the Doppler effect), as shown in Figure B2.

In addition the sound radiated from all four wheels of the same bogie was calculated (as shown in Figure B2), as was the sound from the image sources of each of these wheels, as reflected in a rigid ground. These components of sound were all added incoherently (ie by adding energies); in the case of the reflected components this eliminates any interference effects due to path differences, but such details depend on the precise details of the ground geometry which are not known.

The overall noise was predicted for each of the three wayside microphone positions (shown in Figure A1), ie at 2, 5 and 7.5 m from the near rail.

As noted above, the Doppler effect has been ignored; this is necessary because the use of 1/3 octave spectra does not allow sufficient frequency resolution to determine how much leakage will occur between adjacent bands. However it should be borne in mind that the amount of the Doppler shift at 160 km/h corresponds to plus/minus half the width of a one-third octave band, so that it can be expected that a significant proportion of the radiated noise in a given band will come from vibration in adjacent frequency bands.

B.3 RAIL RADIATION MODEL

The rail radiation has been calculated in two stages. In the first stage a boundary element program has been used to calculate the radiation from a vibrating rail cross-section. This model is two-dimensional: the rail is assumed to be infinite, and the motion is assumed to be constant along this infinite length. The wavespeeds in the rail are much greater than the speed of sound in air, which means that the wavelength in the rail can be ignored.

The boundary element model requires a detailed knowledge of the vibration of the surface. Therefore the radiated sound was calculated only for three 'standard' motions, at the three wayside microphone positions. As for the wheel, the sound radiation from two rails (at different distances), and from their respective image sources was calculated, and these components were added incoherently. The 'standard' motions used were:-

- lateral vibration of the whole cross-section
- vertical vibration of the whole cross-section
- flapping of the rail foot (with no motion of the web or head)

Their radiation for a unit acceleration are shown in Figure B3, taking into account the addition of the components from the 2 rails and 2 image sources. In addition the radiation from torsion and web bending were considered, but were not included in the final model.

The second stage of the predictions uses the results from the first stage as one-third octave transfer functions between acceleration levels and radiated sound. In this program, the vibration levels from 5 accelerometers (lateral on the head, web and foot (channels 1, 4 and 5) and vertical under the foot end and centre (channels 6 and 7)) are used as inputs. These levels are based on an average over 4.45 m of train pass-by; the vibration will not be constant over this analysis interval, but the use of this average level in the prediction is probably appropriate, since it is based on an infinite line source.

The average lateral vibration spectrum is calculated from an average of the first three of these spectra. The whole-body vertical

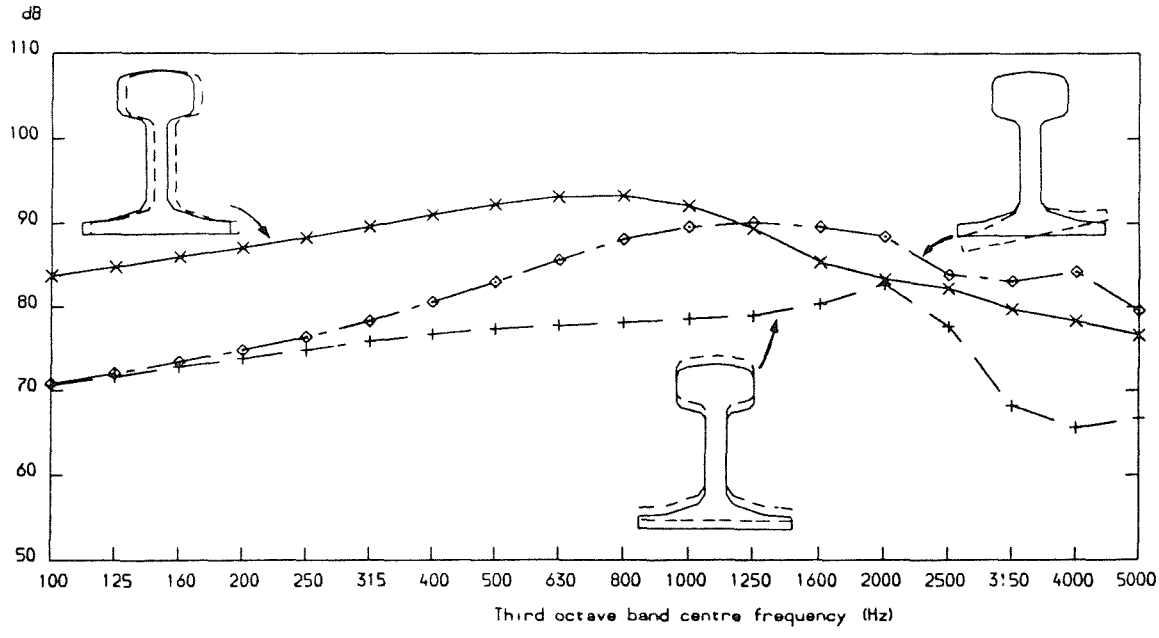

Figure B3 Rail Radiation Model: Transfer Functions from 'Standard' Motions. Sound Pressure Level (dB re 2×10^{-5} Nm^{-2}) due to 2 Rails and 2 Image Sources at 2 m from Near Rail (——— Lateral 3 ms^{-2}, — — Vertical 3 ms^{-2}, - - - Foot Flapping 15 ms^{-2})

vibration is taken directly from the foot centre signal, and the foot flapping component from the foot end signal. These three spectra are then modified by the respective transfer functions, and added (incoherently) to produce the predicted noise, at each of the three microphone positions.

B.4 ANALYSIS METHOD

These models of wheel and rail radiation have been applied to the measured spectra for each test run of the experiment. In each case, the predicted noise due to the wheel and the rail are combined using an incoherent sum, to give the total predited noise.

A total of 64 sets of data are generated, based on the 3 microphone positions (2 m, 5 m and 7.5 m from the nearest rail), 4 speeds (40, 80, 120 and 160 km/h), and 4 combinations of surface roughness (rough and smooth wheels with rough and smooth rails). Unfortunately, different numbers of runs (between 1 and 3) were available for the different conditions. The large range of the conditions which were covered by these measurements can be appreciated by the fact that the overall dB(A) levels of the measured noise covered a range of 45 dB. The spectral shapes also vary significantly.

For each set of data, the difference has been formed of the predicted noise spectrum minus the total measured noise spectrum (each in dB; thus the result is strictly a ratio). These difference spectra are then averaged over the various test conditions, to give overall mean and standard deviation spectra. If the mean is close to 0 dB, this indicates that the predicted noise is close to the measured noise. If it is much less than 0 the predicted noise is much lower than the measured noise, and vice versa. The size of the standard deviation is a measure of the consistency of the predictions.

B.5 RESULTS

The mean and standard deviation of the predicted total noise minus measured noise are shown in Figure B4. The standard deviations are about 2-3 dB between 630 Hz and 2500 Hz, indicating that the predictions are reasonably consistent for these frequencies. This level of agreement is remarkable given the range of levels and spectral shapes involved; it actually corresponds to the level of random error which has been identified between different measurements of the same parameters [117]. The results for these frequencies are within one

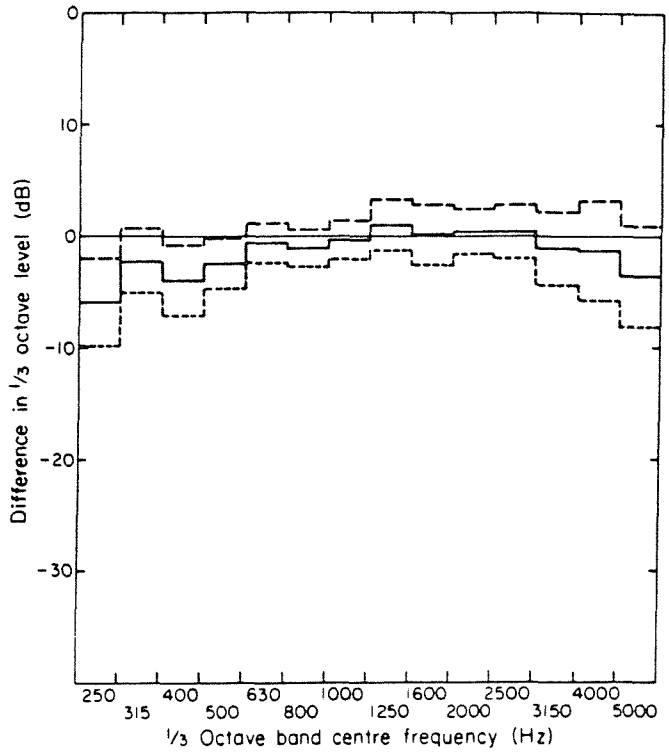

Figure B4 Predicted Total Noise from Wheel and Rail minus Total Measured Noise (——— Mean, - - - / — — Mean ± Standard Deviation)

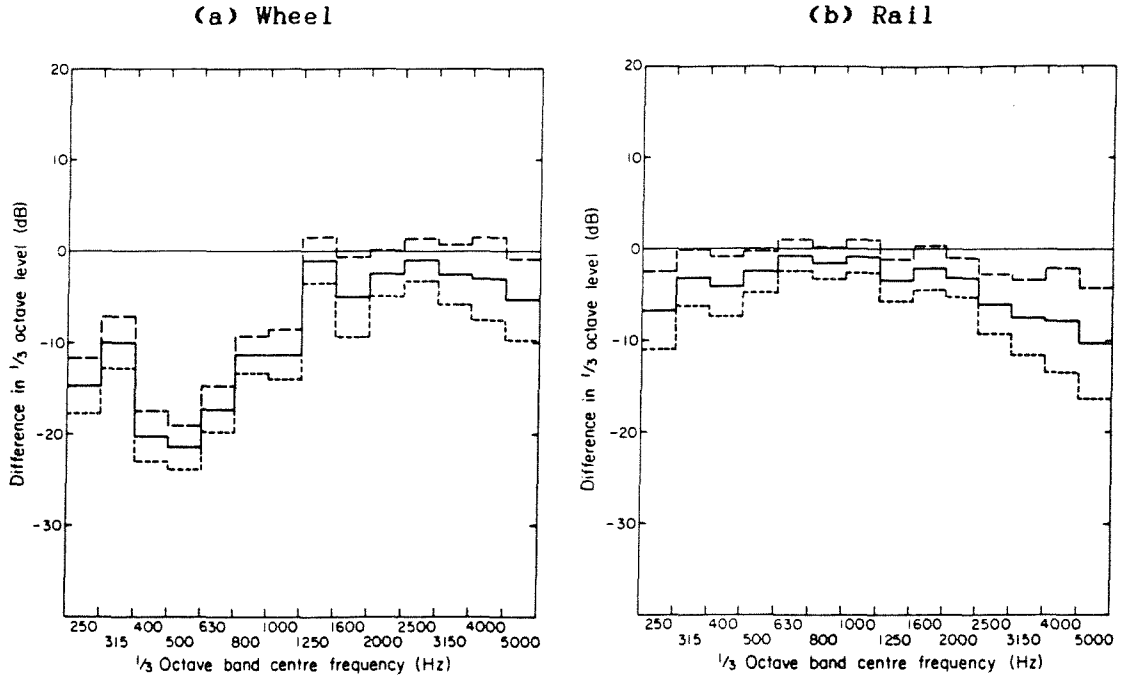

Figure B5 Predicted Noise Components from Wheel and Rail minus Total Measured Noise (——— Mean, - - - / — — Mean ± Standard Deviation)

standard deviation of 0 dB, indicating that the measured noise corresponds closely to the sum of the wheel and rail predictions.

For 500 Hz and below, and above 2500 Hz, the standard deviations are greater, and the mean predictions are lower, indicating deficiencies in the model, the presence of other sources, or noise contamination of the signals.

Figure B5 shows the equivalent results based on the predicted noise from the wheel and rail alone. The rail can be seen to be a major source across the whole frequency range, whereas the wheel is only a significant source in the region above 1250 Hz. Although the baffled radiator model for the wheel over-predicts at low frequencies, this corresponds to a region where the wheel radiation is not significant, so this approximation appears justified.

By considering the results for each speed, or each roughness condition, no significant dependencies on these parameters were found. However, it was found that the poor agreement at high frequencies could be attributed almost completely to low speed runs on the rougher track, where the spectrum shape slopes steeply downwards. Thus excessive measurement noise contamination can be expected at these high frequencies for this case. Similarly at low frequencies, greater deterioration in agreement occurs at high speeds and low roughnesses. This could be due to aerodynamic noise contamination of the signals; also at these low frequencies radiation from the vibration of the sleepers provides another potential source of noise.

The relative importance of the wheel and rail, for a given 1/3 octave band, was found to be virtually independent of roughness condition, train speed and microphone position (at least within the overall accuracy level of the measurements, which was roughly ±1-2 dB [117]). However, because of differences in the overall spectrum shape, the overall importance of these two sources does not remain constant. As speed increases, the relative importance of the wheel increases slightly, and that of the rail decreases slightly. These are approximated by the lines shown in Figure B6.

Whilst the use of differences between measured and predicted spectra is a useful tool in reducing the results to a non-dimensional form, it also results in a loss of information about the frequency content. In order to remedy this, an example noise spectrum will be presented. It is for 160 km/h, rough wheel, smooth rail, at the 2 m

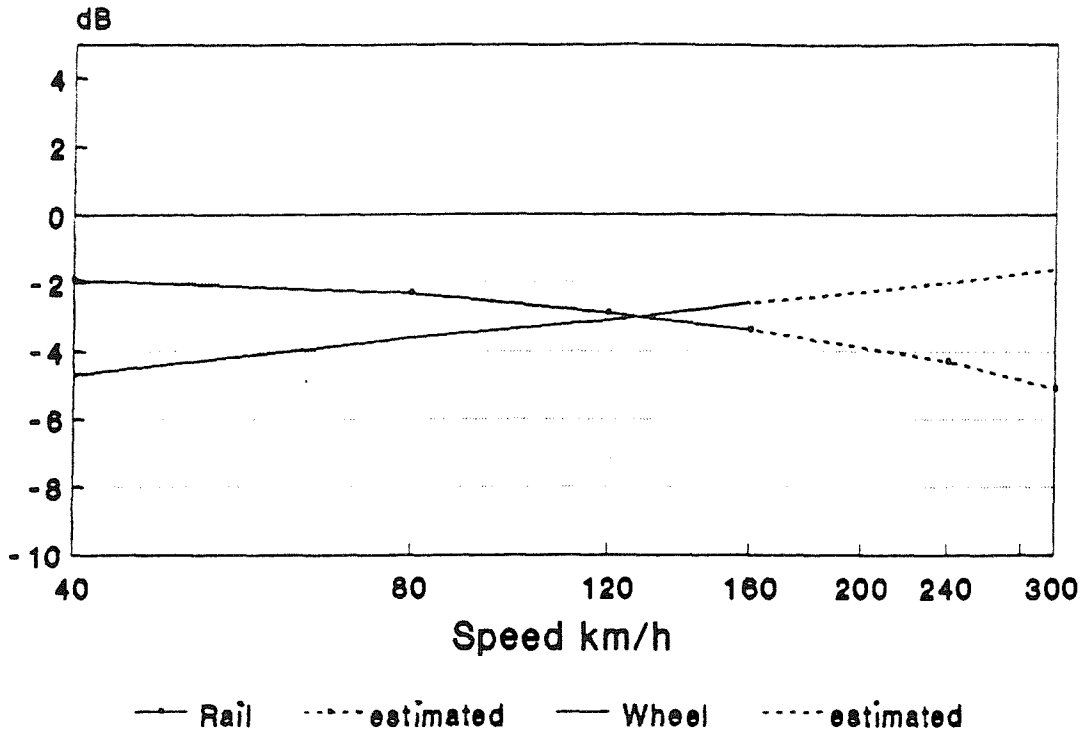

Figure B6 Predicted Overall Noise Components from Wheel and Rail as a Proportion of the Total Noise

microphone position, and is based on the average of 3 measurements. Figure B7 shows this result, along with the estimated wheel and rail components, taken from the average results of Figures B4 and B5. These results are only shown above 500 Hz, as for lower frequencies the total noise was not predicted by the sum of the wheel and rail components. This figure emphasises the importance in the spectrum of the region between 800 Hz and 2 kHz at high speeds. This is the region where the predictions gave the best agreement with the measurements.

For the rail, the proportions of noise radiated by the three components (lateral, vertical and foot flapping) are shown in Figure B8. These are shown as proportions of the overall rail component taken from Figure B7.

At lower frequencies (up to 1 kHz) the lateral vibration is the dominant radiator; although the vertical vibration is actually slightly greater, it radiates less effectively to the wayside because of its directivity. At higher frequencies deformation of the cross-section results in larger vibration of the foot vertically, and this becomes the most significant motion in radiation.

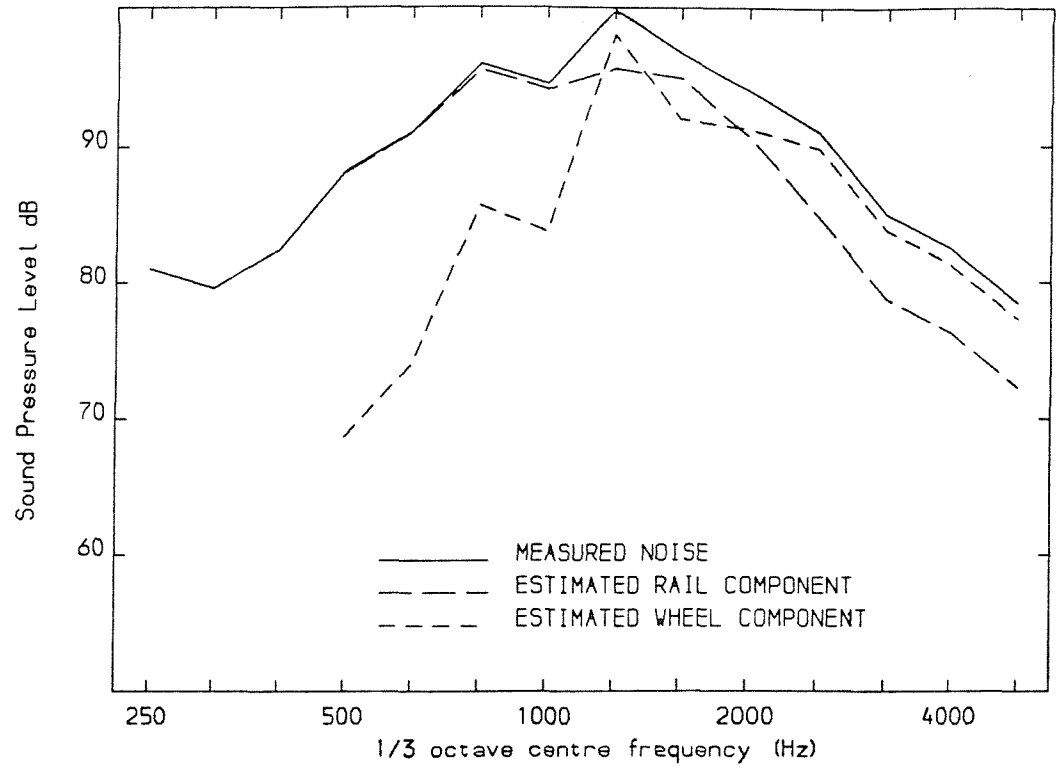

Figure B7 Average Proportions of Noise Radiated by Wheel and Rail shown Against 160 km/h Rough Wheel/Smooth Rail Spectrum at 2 m

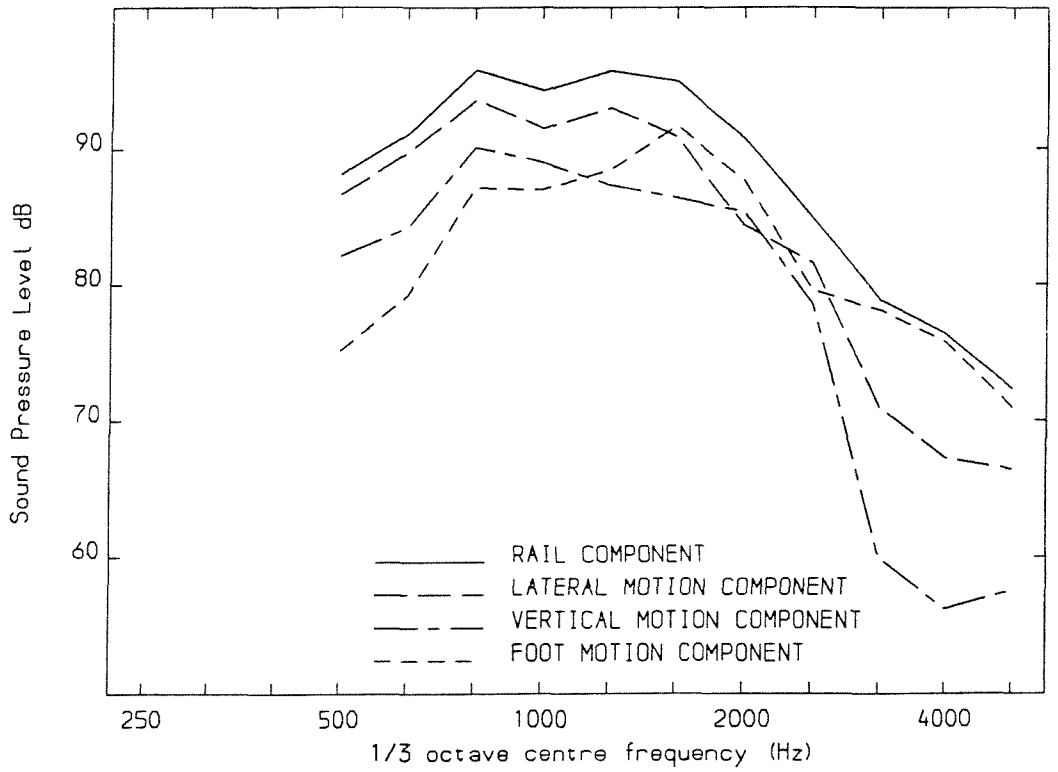

Figure B8 Proportions of Noise Radiated by Various Components of Rail Vibration for 160 km/h Rough Wheel/Smooth Rail at 2 m

In the frequency range in which the wheel radiation is dominant (above 1250 Hz), the wheel vibration is greatest on the web (see also [47]). This range also corresponds to the onset of 1-nodal-circle modes, in which the maximum vibration occurs on the web. These modes occur at around 1400 Hz, 1800 Hz, 2400 Hz, 3200 Hz, etc, with n=2, 3, 4, 5, etc nodal diameters. The radial modes have similar motion of the web, but occur at higher frequencies for this type of wheel.

The predictions are obviously only valid for the type of wheel on which measurements have been made. For a different wheel design, it can be expected that the frequency range in which the wheel radiates significantly will again begin at the lowest natural frequency of 1-nodal-circle modes. For example, a BR BT10-type wheel, which has a diameter of 0.91 m, has its first such mode at around 1900 Hz [54]; for a class 143 Pacer wheel (with diameter 0.80 m), the first radial mode occurs at 2300 Hz with the first 1-nodal-circle mode somewhat higher than this.

B.6 DISCUSSION

A number of simplifying assumptions have been used, which mean that the predictions are perhaps inadequate in a number of ways. The following should perhaps be listed:-

1) The use of the image source based on a rigid ground will produce a slight over-prediction, since the ground will be partially-absorbing. However at the fairly close distances used this effect should not be large.

2) The bogie will tend to shield parts of the wheels (especially those on the far side). This will be countered, to some extent, by reflections of the noise from the near wheels by the bogie.

3) The vertical motion of the rail is quite large, and, although it does not radiate significantly to the side, it will radiate effectively in a vertical direction. In turn this noise will tend to be reflected by the vehicle, and so it will add to the wayside noise.

4) The radiation from the radial motion of the wheel has been ignored, but it is of a similar magnitude to the web axial vibration, and the total area of the wheel tread ($2\pi \times 0.53 \times 0.125 = 0.42$ m^2) is almost half that of the front surface of the wheel ($\pi \times 0.53^2 = 0.88$ m^2), although the directivity will result in a smaller part of the sound being radiated to the wayside.

5) The analysis has been based on the noise measured (at 2, 5 and 7.5 m) during 4.45 m of train pass-by. It is implicitly assumed that the noise received during this time is representative of the overall noise, and in particular that the proportions of noise from the wheel and rail are representative. In practice, the wheel noise will tend to be confined to this analysis region, but the rail radiation will not. The total noise from the rail will be somewhat greater than that received during the analysis interval, due to the significant length of rail which radiates. Unfortunately this depends on the decay of vibration with distance in the rail, which is not available for the test sites used. Some consideration is given to the extent of this effect in §7 of this thesis.

6) Radiation from the sleepers has been ignored. In practice the sleepers vibrate at significant amplitudes below about 500 Hz, and since their radiating area is quite large, the radiated noise is not negligible for these low frequencies. Measurements of sleeper vibration, and a corresponding radiation model are therefore required to resolve the sources of low frequency noise.

APPENDIX C

MEASUREMENTS OF WHEELSET RESPONSE

C.1 PREVIOUS MEASUREMENTS

Measurements have previously been taken of a number of wheel types at BR Research [52-54]. These have concentrated on identifying the natural frequencies and modes of vibration.

The aim of the current theoretical work (§2) is to predict the frequency response functions (FRFs) of a wheelset. Measurements are required to validate these, and for the current purpose the previous experimental work is deficient in that the measurements aimed only to derive resonance properties. Whilst the off-resonance response can be calculated from the resonance properties, as will be shown, this relies on having a full set of resonances and accurate estimates of modal properties. The possibility that some of the axle-dominated modes (which are more heavily damped than the wheel modes) have been missed, means that reliable off-resonance response measurements are still needed. Thus the current experimental work concentrates on the FRFs of the wheelset.

C.2 MEASURING TECHNIQUES FOR FREQUENCY RESPONSE FUNCTIONS

Various methods are available for measuring FRFs [97]. Traditionally an electrodynamic shaker is used to excite the structure with either discrete sinusoidal inputs ("stepped-sine method") or at a slowly varying frequency ("slow sine sweep method"). The former has potential for great accuracy, but is laborious, and for the latter the light damping of a wheelset requires a very slow sweep rate, and a very high dynamic range in the instrumentation system.

Two-channel digital spectrum analysers can be used to measure the frequency spectra of the force and response simultaneously. The drive signal may be Gaussian random, or it may be transient, such as a rapid sweep ("chirp"). These allow a force to be input to the structure through a specific frequency range. An alternative source of force input is an instrumented hammer. This excites all frequencies roughly equally, up to a cutoff which is determined by force level, tip stiffness and hammer mass. On the other hand the excitation point may be varied with ease.

For a lightly damped structure, such as the wheelset, impact testing in conjunction with a spectrum analyser poses problems. The pulse excites a wide frequency range, but if the analyser is set to cover this range, insufficient frequency resolution results, particularly around the resonances. To increase the resolution, a longer sample is required, in which case the force signal becomes very susceptible to noise contamination.

The method which has been used for most of the current tests is based on random excitation using a vibrator. In order to increase frequency resolution, a narrow band random input has been used in conjunction with the zoom facility of the spectrum analyser, to give results over a series of narrow overlapping regions of frequency.

C.3 MEASUREMENTS OF FREQUENCY RESPONSE FUNCTIONS

Ideally measurements of the wheelset FRFs should be made with the wheelset in situ under a vehicle, or at least in its bogie. However this had to be ruled out because of practical difficulties. It was decided that it would be adequate to simulate the usual support experienced by the wheelset in its bogie by supporting the wheelset by its axleboxes. This was done by standing the axleboxes on wooden axlestands, which consist of sections of wooden railway sleepers bolted together. The exciter (an electrodynamic vibrator) was then positioned in its trunion, on the ground. Only one wheel was excited.

The vibrator was connected to a force transducer and a drilled and tapped pad which was glued to the wheel surface. The response of the wheel was measured using an accelerometer attached with a thin layer of beeswax (which should have a flat frequency response up to at least 10 kHz [121]. The wheelset was excited in each of two directions, radially and axially, in each case through the usual point of contact between the wheel and the rail. The response was measured radially and axially at equivalent positions, giving a total of four combinations - two point accelerances and two cross accelerances. By reciprocity the two cross accelerances should be identical.

Figure C1 shows the excitation and response positions diagrammatically. Because of the coning of the wheel running surface (an inclination of 1:20), the 'radial' direction for both excitation and response was not quite truly radial. The 'axial' direction, however, was truly axial.

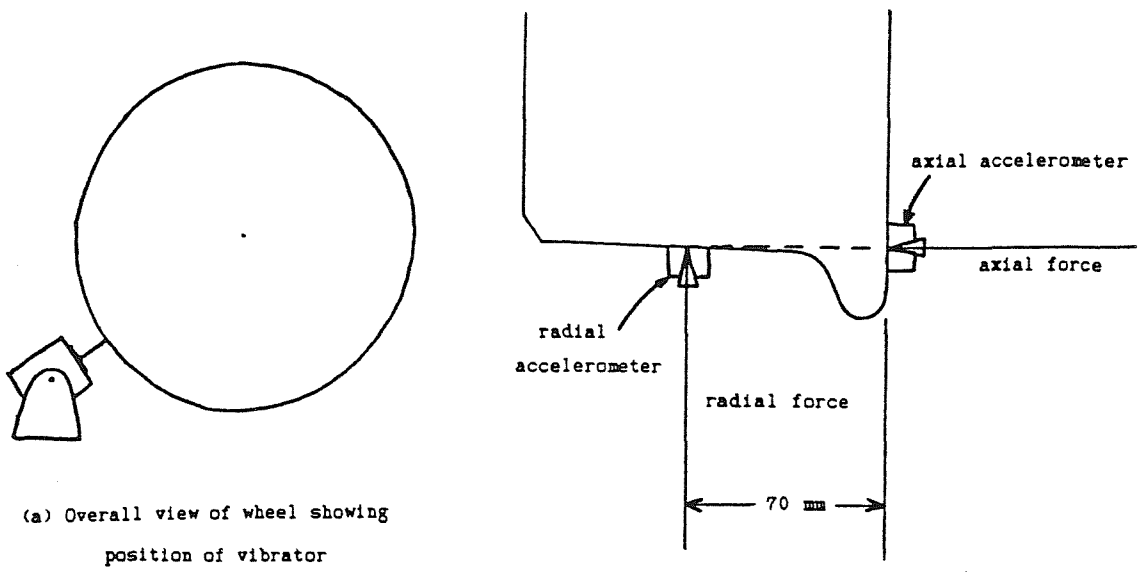

(a) Overall view of wheel showing position of vibrator

(b) Close-up view of wheel rim cross-section

Figure C1 Arrangement of Exciter and Accelerometers for Frequency Response Measurements of Wheelset

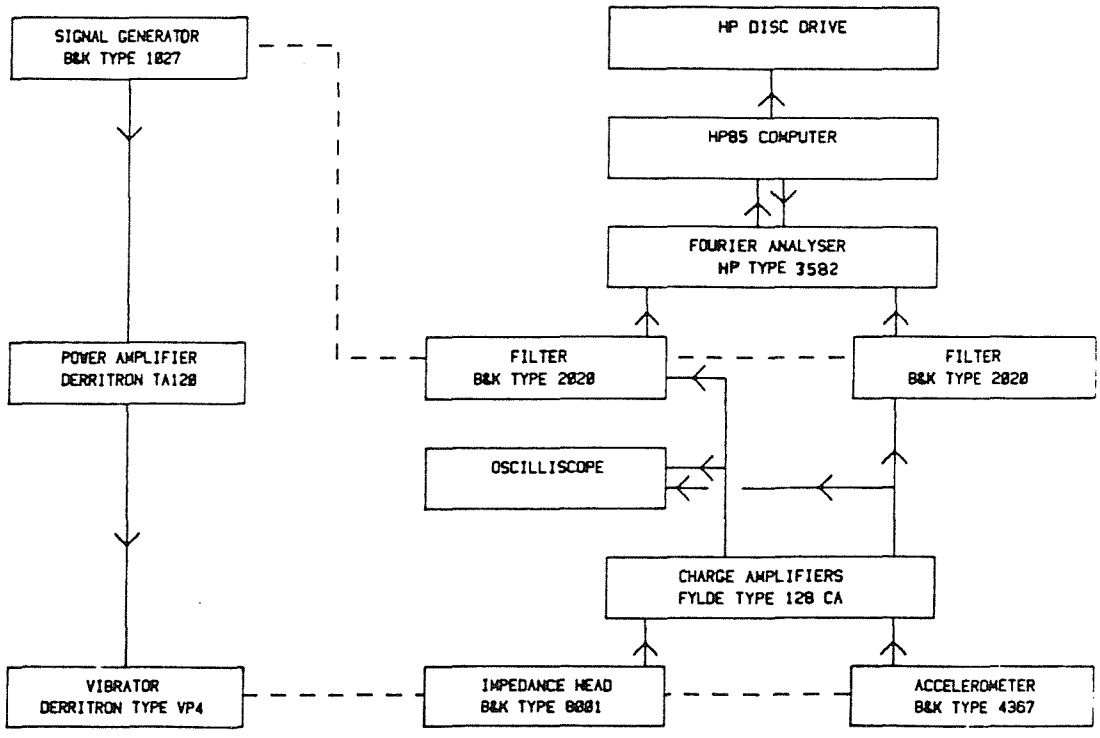

Figure C2 Instrumentation used for Measurements of Wheel Receptances

The instrumentation used is shown schematically in Figure C2. The excitation was a narrow band random signal generated by the sine/random generator. The force and response signals were filtered using matched heterodyne filters (so that their relative phase was not affected), before being analysed over a narrow frequency range by the spectrum analyser. The averaged spectra (64 samples) were stored on disc by the desktop computer.

The signal and filter bandwidths were set to the same range, as was the range of the spectrum analyser. The frequency ranges of these analyses were spaced to allow some overlap. At higher frequencies (above about 2.5 kHz) the frequency range of each measurement was increased from 100 Hz (0.8 Hz resolution) to 500 Hz (4 Hz resolution).

For each frequency band of excitation the settings of the vibrator input and the spectrum analyser sensitivities were optimised to give maximum signal-to-noise-ratio without overloading, before commencing analysis. In some cases, where doubts about the data occurred, duplicate measurements were made.

The coherence function was used to determine any areas where contamination of the data had occurred. Because of insufficient resolution (bias errors), the coherence is always low at lightly damped resonances when using a random input (see [97]). A much narrower bandwidth would be required to measure the response at resonances accurately. This was not done, since the object of the measurements was to establish the off-resonance response rather than the damping-controlled resonance levels.

Background noise tends to cause the coherence to drop at anti-resonances as well, but this was accepted as being inevitable, having attempted to reduce the problem by optimising settings. However at all other points (ie apart from resonances and anti-resonances) where the coherence dropped, the data have been eliminated from the final results. This is usually at the boundaries of the particular frequency bands under study.

The results of these measurements are shown in Figures C3-6 as FRFs plotted on a logarithmic frequency scale, in terms of their amplitude and phase. Figures C3 and C4 show the results for the two point accelerances. These both show the familiar features of point response functions. In particular the phase is restricted to the range 0-180° (except at some of the anti-resonances where both real and imaginary parts are very small). Figures C5 and C6 show the two measurements of cross accelerance. They are generally similar, but slight differences do exist between them (and within Figure C6 itself). These can probably be attributed to slight variations in the alignment of the vibrator and the accelerometer. The modes of vibration which have a nodal circle in the tyre region will be particularly sensitive to such variations.

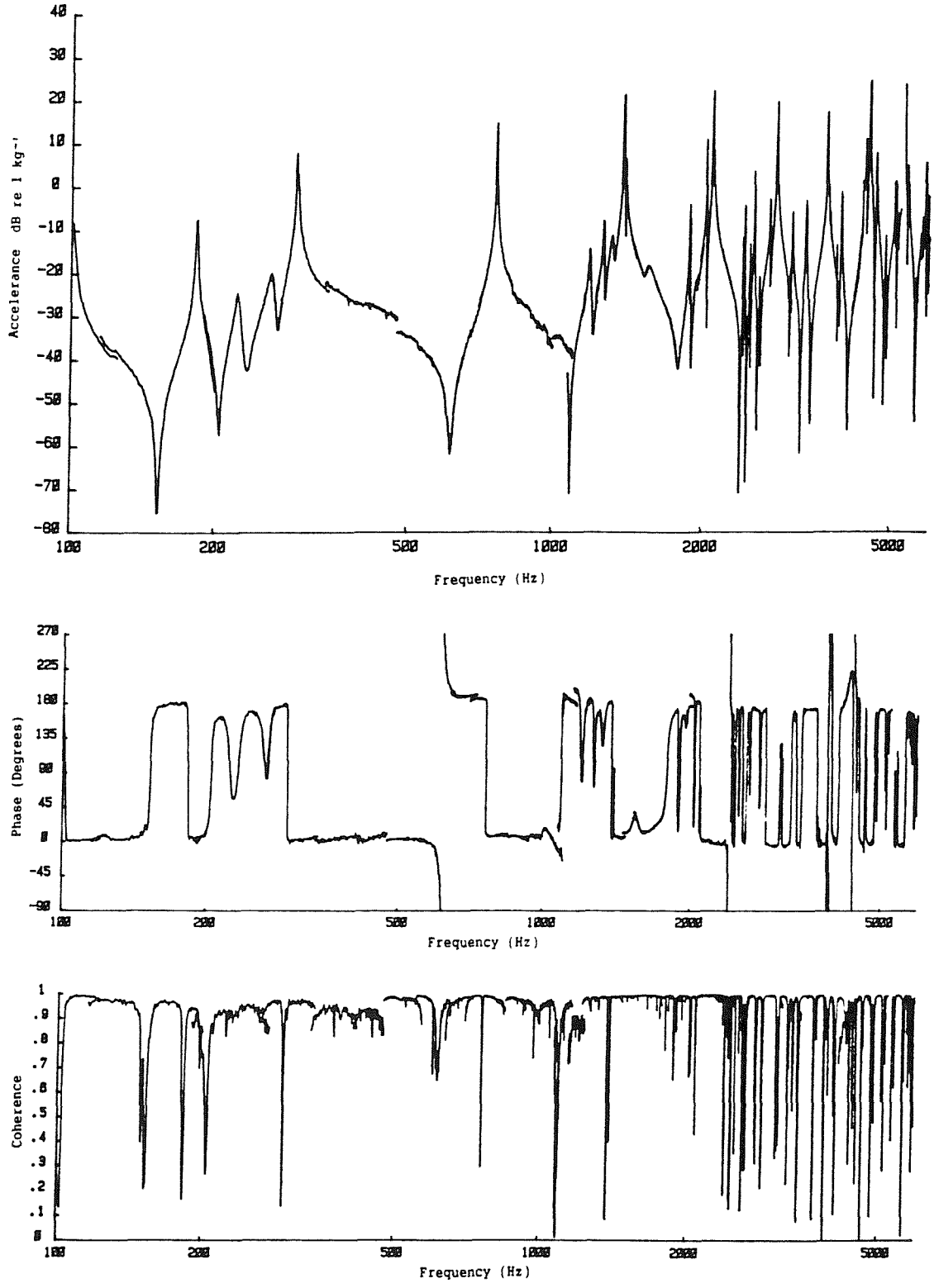

Figure C3 Measured Axial Point Accelerance Spectrum

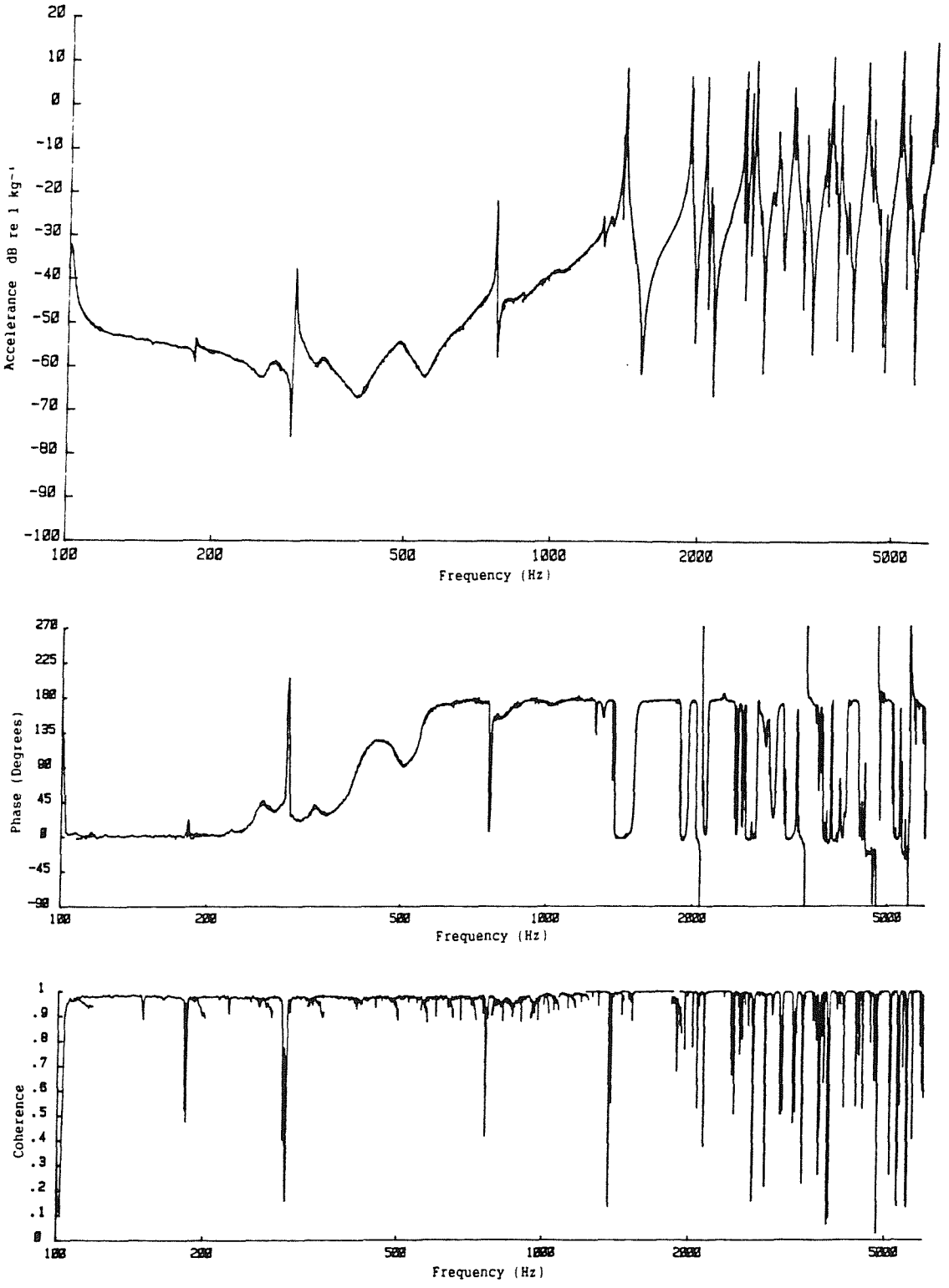

Figure C4 Measured Radial Point Accelerance Spectrum

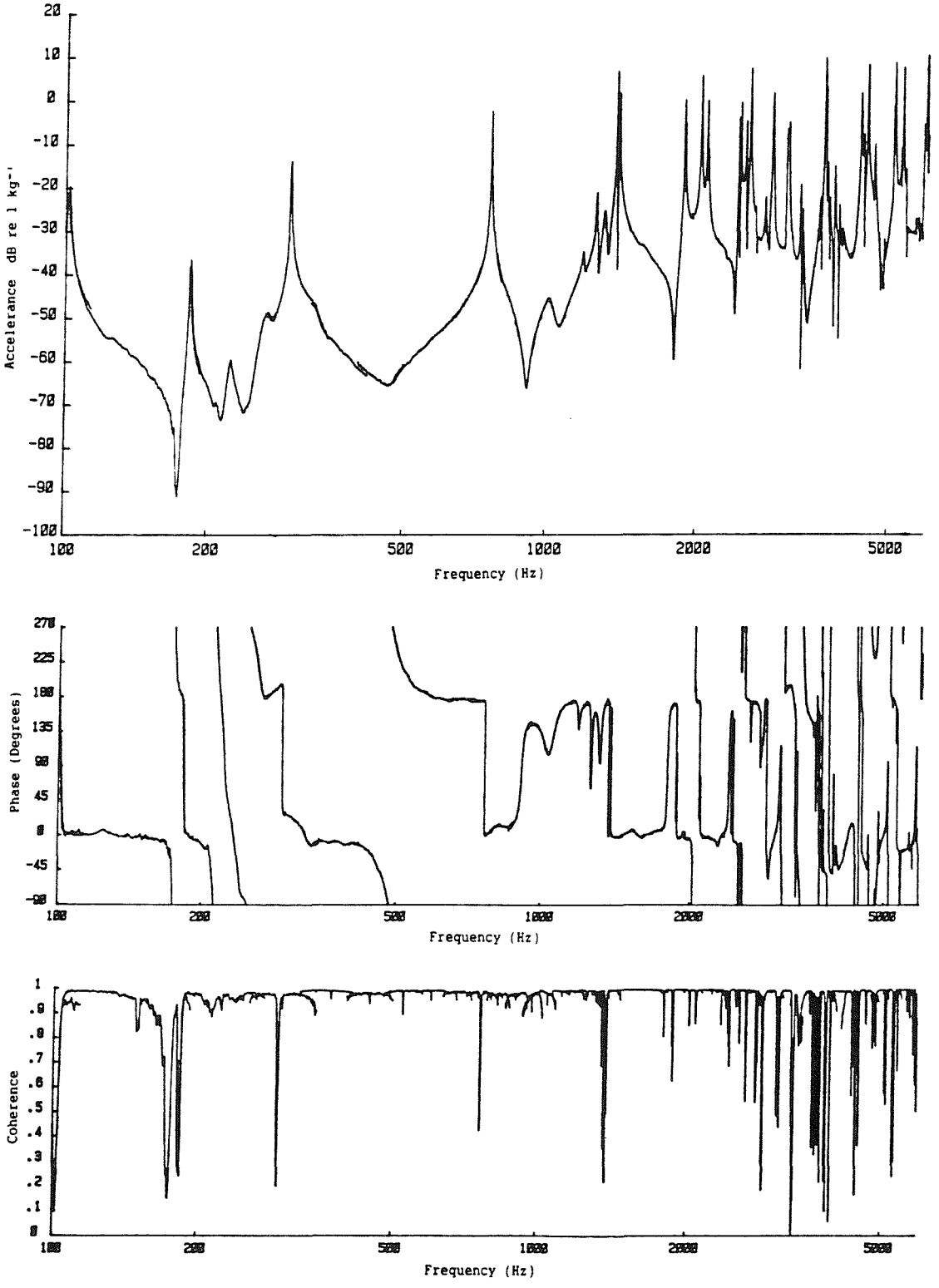

Figure C5 Measured Cross Accelerance Spectrum

(radial force, axial response)

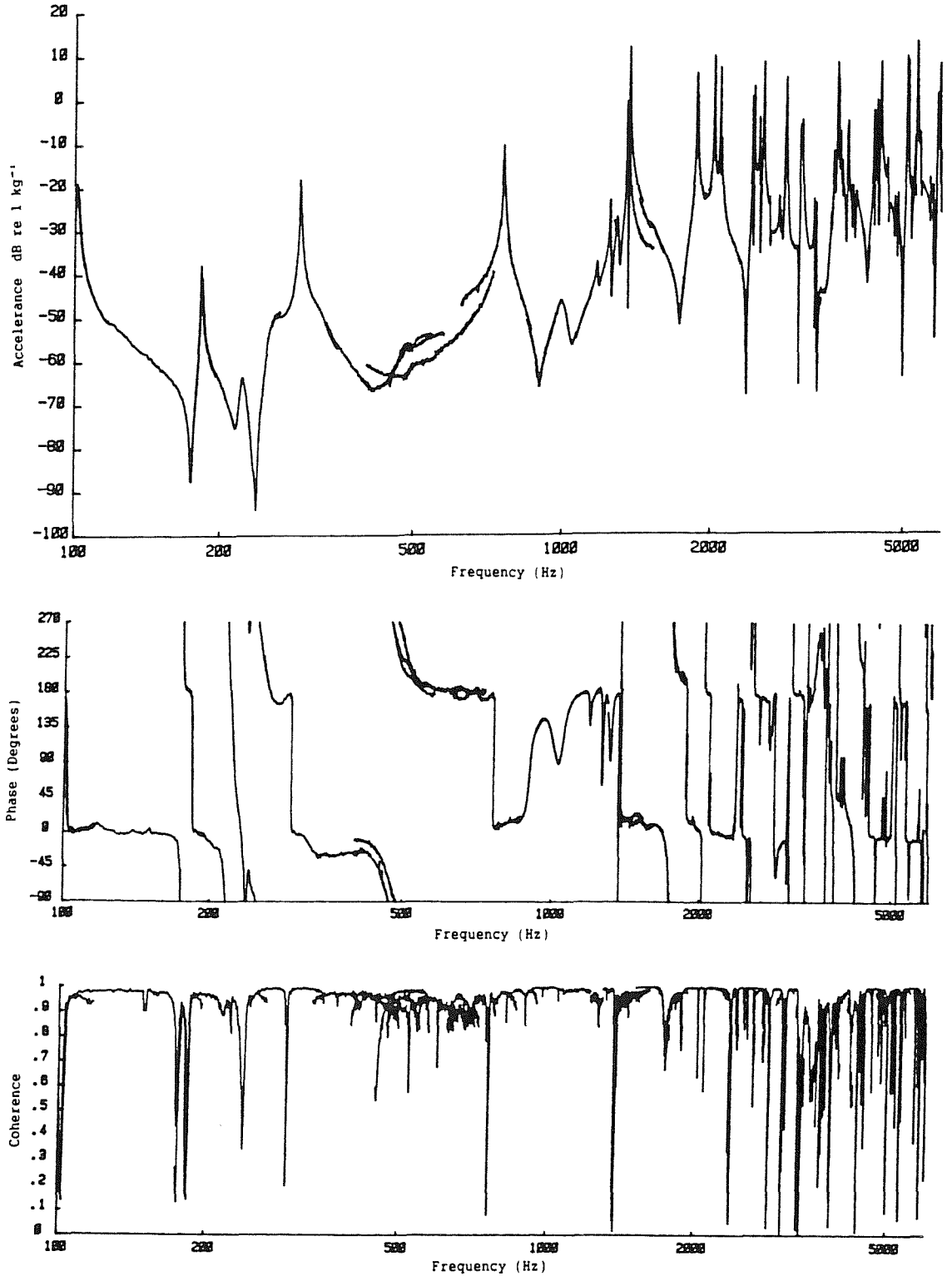

Figure C6 Measured Cross Accelerance Spectrum

(axial force, radial response)

C.4 MODESHAPE IDENTIFICATION

Modeshape identification was not intended to be a major part of the experiment, but investigation of nodal patterns was included because the wheelset investigated was not precisely that used by Perry [53], and some differences in the natural frequencies were found.

An instrumented hammer was used to excite the wheel for these measurements. An accelerometer was kept in a fixed position whilst the hammer was used to tap the wheel in various positions. The force signal itself was not monitored, but was used to trigger the spectrum analyser which was then used to measure the acceleration spectrum close to the resonance of interest (using a zoom analysis). When the force and/or the accelerometer was at a node of the mode under examination the peak in the spectrum disappeared. In this way node lines could be found quite quickly. The investigation concentrated on finding the number of nodal diameters, relying then on the original measurements for other details such as the number of nodal circles. Most of the modes up to 2100 Hz were covered.

The results are listed in Table C1, to the nearest 1 Hz. Several modes occur in close pairs with node lines fixed in the wheel

Table C1 Results of Modeshape Identification

Natural Frequency (Hz)	Number of nodal diameters	Proposed modeshape description	Result from [53]
184	0	Dishing	162
295	2	0-nodal-circle	288
296	2		
1196	1	radial	1139 *
1270	0	1-nodal-circle or radial ?	1265 *
1375	4	0-nodal-circle	1370
1390	2	1-nodal-circle	1214
1873	3	1-nodal-circle	1759
1880	3		
2026	2	radial	2012 *
2036	2		
2085	5	0-nodal-circle	2075
2089	5		

* : modeshape not described in [53]

structure. However the two modes at 1375 Hz and 1390 Hz were found to be quite different from each other, the first being the 4 nodal diameter mode, and the second the mode with 2 nodal diameters and one nodal circle. The latter frequency is significantly different from the result of Perry [53], who found this mode at 1214 Hz. This was the largest discrepancy between the two sets of results. The mode with one nodal circle and 3 nodal diameters was found here to be at 1873/1880 Hz as opposed to 1759 Hz previously, and higher one-nodal-circle modes were progressively closer to Perry's results. It appears that there are detail differences between the wheelset measured by Perry, and that

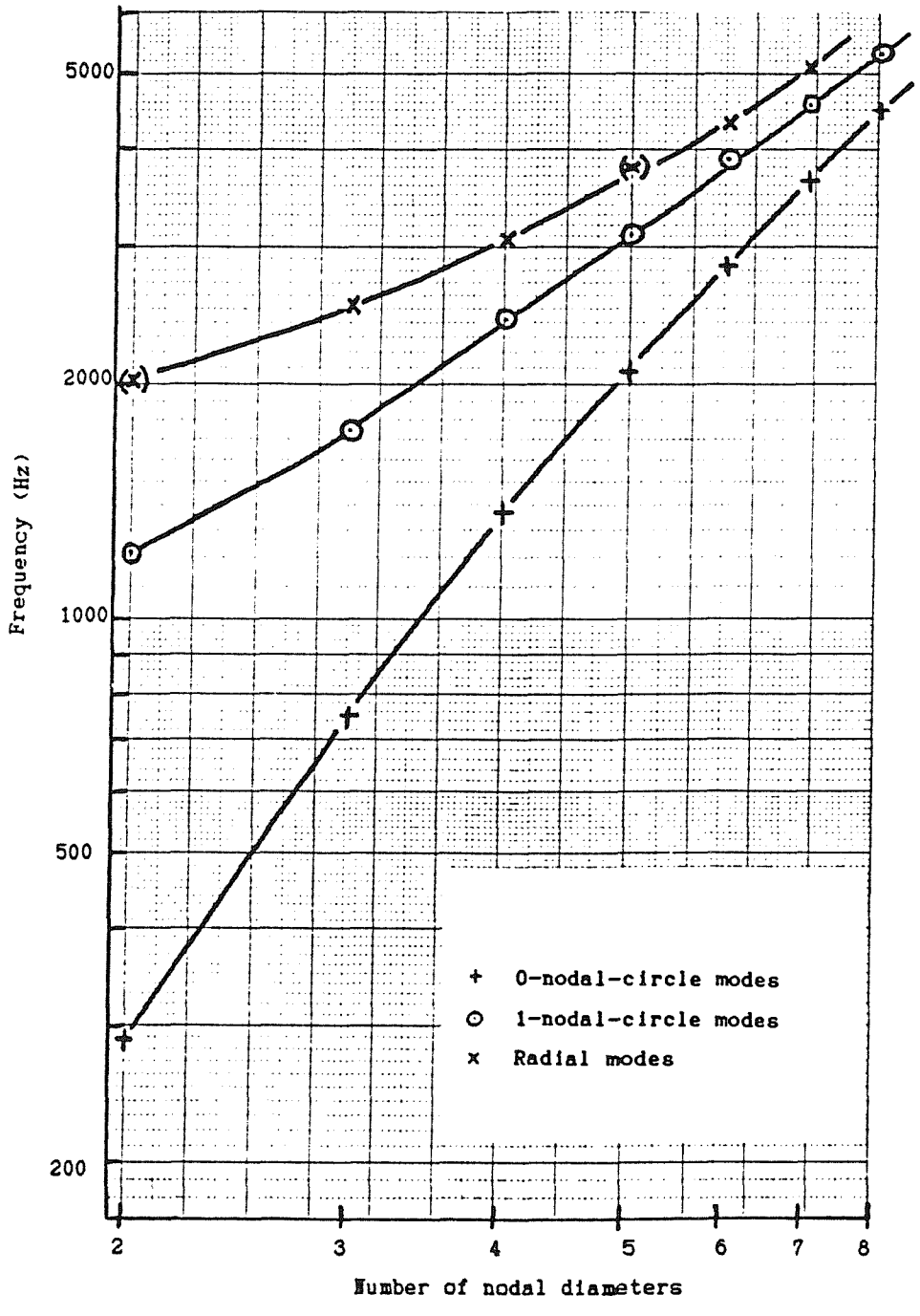

Figure C7 Natural Frequencies found Experimentally by Perry [53]

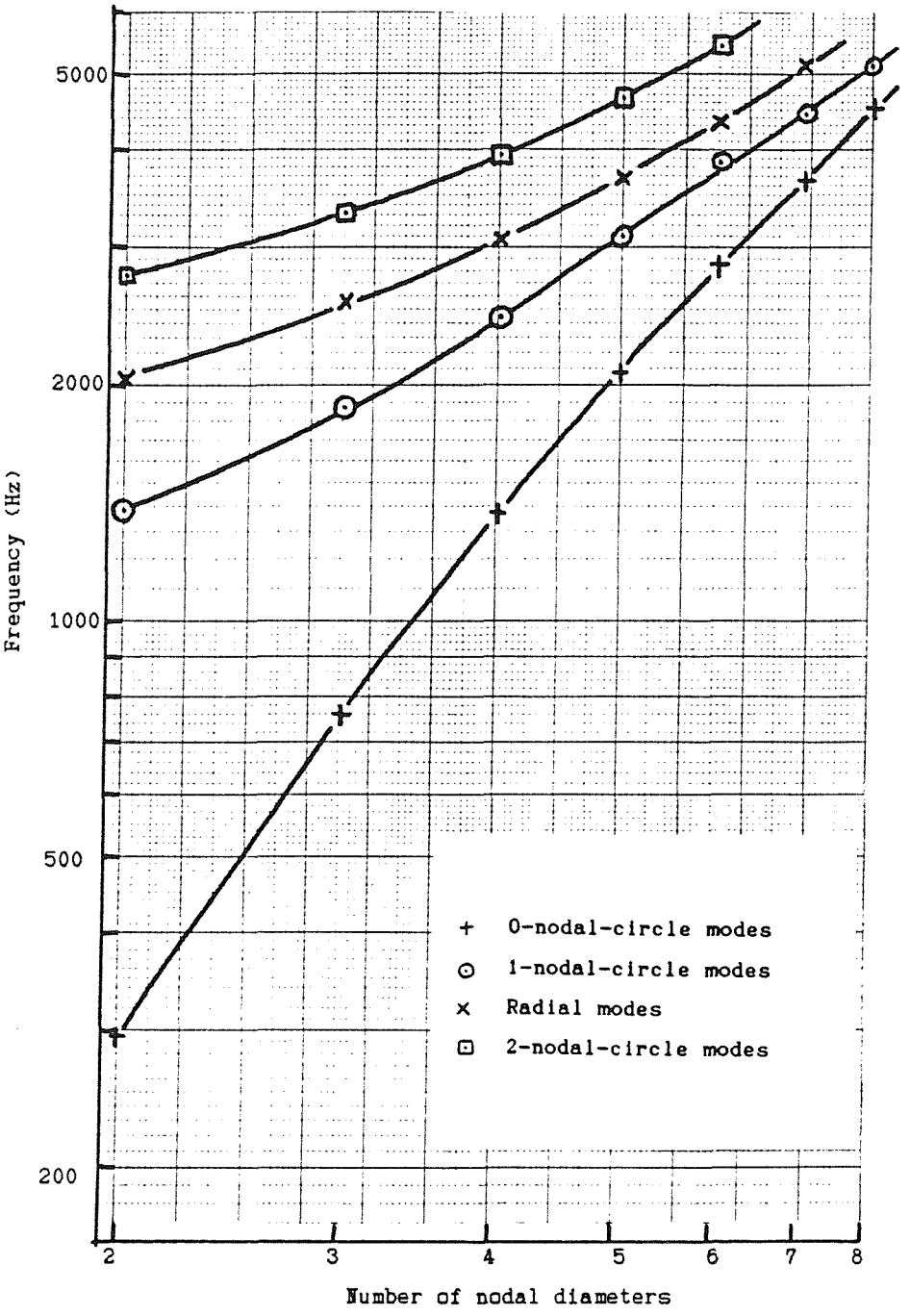

Figure C8 Natural Frequencies found in the Current Experiment

used here. A subsequent comparison of the resonance frequencies of the 4 wheels on one side of the laboratory coach has found that significant differences occurred between them [119].

The natural frequencies of modes found by Perry [53] have been plotted in Figure C7 against the number of nodal diameters on a logarithmic scale. Figure C8 shows the equivalent results derived from the current modeshape investigations, and at higher frequencies by comparing the peaks in the data of Figures C3-6. For example, the

major peaks in Figure C3 are identifiable as the nodal-diameter-only modes and those in Figure C4 as the radial modes. Apart from the first few one-nodal-circle modes (as discussed above) agreement between Figures C7 and C8 is good.

C.5 AXLE MODES AND EFFECTS OF SUPPORT

Modes of vibration involving the axle in bending or extension derive from sets of axle modes and sets of n=0 and n=1 wheel modes which are coupled together. Of these Perry identified only the first two axle bending modes and a dishing mode of the wheel.

The modes involving flexural motion of the axle were investigated by measuring the point accelerance of the axle at 3 positions using an instrumented hammer, accelerometer and the spectrum analyser. The natural frequencies of modes found in this way are listed in Table C2 to the nearest 10 Hz, along with information about the modeshape.

Usually in modal testing the structure under test is supported on soft springs, giving rise to 6 rigid body modes [97], all of which should be kept well below the frequency range of interest. The wooden blocks used for supporting the wheelset will be resilient and so will

Table C2 Natural Frequencies of Modes Measured on the Axle

Natural frequency (Hz)	Symmetric (S) or Antisymmetric (A)	Proposed modeshape description
30	S	Bounce suspension mode
55	S	Axle mode with 2 nodes
100	A	Axle mode with 3 nodes
220	S	1 nodal diameter
290	S	
510	S	Axle mode with 4 nodes
800	A	Axle mode with 5 nodes
1020	S	
1190	A	
1280	S	
1530	S	
1940	A	
2090	S	
2640	A	
2750	S	

act as springs, so at what frequencies do the various rigid body modes occur?

In Table C2 the vertical bounce mode appears at approximately 30 Hz. The pitching mode (vertical motion at each end being out of phase) can be expected to occur at a similar frequency since the wheelset mass is concentrated near the two ends (ie over the springs). Gross rolling motion has no stiffness associated with it because the wheelset was mounted in its bearings, although small amplitude motion will experience some stiffness, which is hard to quantify.

This leaves three modes which all depend on the transverse (bending or shear) stiffness of the supports, which since they are relatively tall, will be much less than the compressional stiffness. This implies that these 3 modes will occur well below 30 Hz.

When supported in a vehicle, the suspension mode occurs at about 5 Hz, which is quite a lot lower than the 30 Hz found with the blocks.

The first wheelset mode is found at 55 Hz. This will probably experience some coupling with the bounce mode, but the second wheelset mode at 100 Hz should be relatively free from this. Thus by restricting analysis to frequencies above 100 Hz, the supports should affect the results very little.

However one additional effect of the supports could be to modify the damping of modes which contain significant motion of the axleboxes. This means that is not possible to estimate accurately the modal damping of such modes, particularly at lower frequencies.

APPENDIX D

A REVIEW OF SIMPLE BEAM THEORIES

D.1 WAVE PROPAGATION IN AN INFINITE BEAM

D.1.1 Euler-Bernoulli Beam

The flexural vibration of a beam can be calculated using the Euler-Bernoulli equations (as used by Remington [15]), as long as the beam cross-section is much smaller than the wavelength of the motion [122,111]. This formulation assumes that plane sections remain plane and perpendicular to the deformed 'neutral axis'. For a beam of constant cross-sectional and material properties, and for free wave motion, the equation of motion is:-

$$EI \frac{\delta^4 w}{\delta x^4} + \rho A \frac{\delta^2 w}{\delta t^2} = 0 \qquad \ldots(D1)$$

where $w(x,t)$ is the transverse displacement at a distance x and time t, E is Young's modulus of the material, and ρ is its density, A is the area of the cross-section and I is its second moment of area about the neutral axis.

Assuming harmonic motion at an angular frequency ω, the above equation has four wave-type solutions, which together give the general solution:-

$$w(x,t) = A_1 e^{i\omega t+kx} + A_2 e^{i\omega t-kx} + A_3 e^{i(\omega t+kx)} + A_4 e^{i(\omega t-kx)} \qquad \ldots(D2)$$

where A_i are arbitrary constants and the wavenumber, k, is given by

$$k^4 = \frac{\rho A}{EI} \omega^2 \qquad \ldots(D3a)$$

The third and fourth terms in equation (D2) represent harmonic waves propagating in the negative and positive x directions respectively. The first two terms are exponential in space (although harmonic in time) and are referred to as 'near-field waves'. They only occur in the vicinity of discontinuities or external forces, decaying away from them.

The wavelength of the propagating waves is given by

$$\lambda = \frac{2\pi}{k} = \frac{2\pi}{\omega^{1/2}} \left(\frac{EI}{\rho A}\right)^{1/4} \qquad \ldots(D3b)$$

Figure D1 shows the relation between k and ω (the 'dispersion diagram'), using parameters which are typical of a rail in lateral bending.

D.1.2 Inclusion of Damping

Structural damping may be included, by changing the Young's modulus E, to $E(1+i\eta)$ in the above [111]. Then the wavenumber, k, is replaced by a complex quantity, $\bar{k}$, with $\bar{k}^4=k^4/(1+i\eta)$. For low damping ($\eta<<1$), this can be approximated by $\bar{k}\approx k(1-i\eta/4)$. The general solution is now given by

$$w(x,t) = A_1\, e^{i\omega t+\bar{k}x} + A_2\, e^{i\omega t-\bar{k}x} + A_3\, e^{i(\omega t+\bar{k}x)} + A_4\, e^{i(\omega t-\bar{k}x)} \qquad \ldots(D4)$$

so that the forward propagating wave A_4 contains an exponential term,

$$A_4\, e^{i(\omega t-\bar{k}x)} = A_4\, e^{i(\omega t-kx)}\, e^{-k\eta x/4} \qquad \ldots(D5)$$

which decays in the positive x direction. Similarly the backward propagating wave contains an exponential term which decays in the negative x direction. The decay is dependent on the imaginary part of $\bar{k}$, $k_I=k\eta/4$. Thus the decay of vibration along the beam, Δ, in dB/m is given by, [111],

$$\Delta = 20\, \log_{10}(e^{k_I}) = 8.686\, k_I = 2.172\, \eta k \qquad \ldots(D6)$$

This derives from the fact that the equation of motion (D1) is fourth order. By contrast the equation of motion for torsion is second order (see §D.3 below), as is that for longitudinal motion, so that the imaginary part of $\bar{k}$ is equal to $k\eta/2$ for these cases. (Note that Remington [20] mistakenly used $\Delta=8.686k\eta$ for bending waves).

D.1.3 Higher-Order Beam Theories

For thick beams (or high frequencies) the assumptions of the Euler-Bernoulli beam equations break down and further terms need to be included into the equations of motion to allow for cross-sectional deformation. A standard formulation is that of Timoshenko [122] which

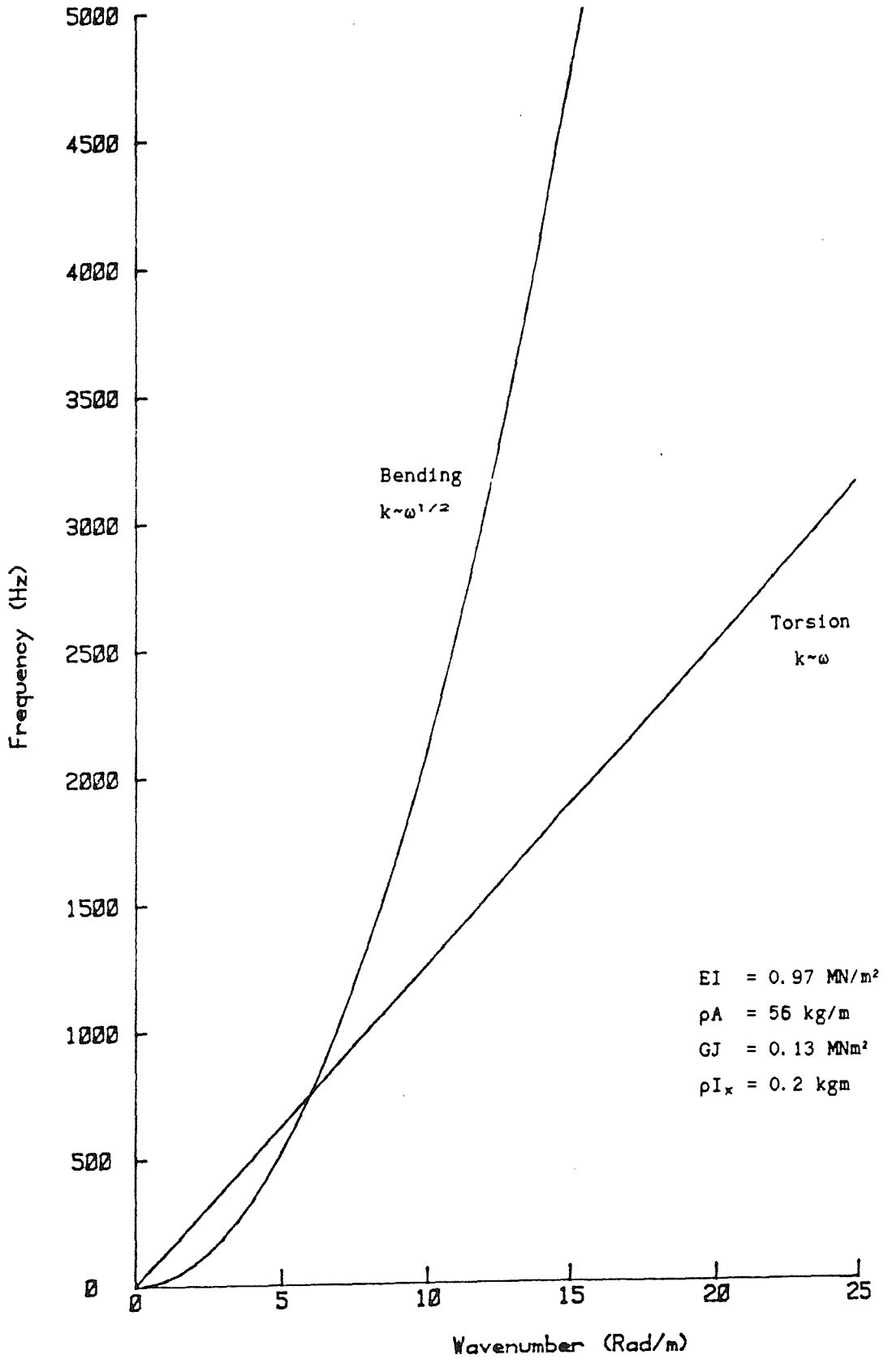

Figure D1 Dispersion Diagram for Uncoupled Euler Bending and St Venant Torsion

includes the effects of shear deformation and rotational inertia, and results in a pair of coupled differential equations.

The frequency/wavenumber equation results in two distinct propagating wave solutions in each direction at each frequency. However the higher order propagating wave is imprecise. It would require an even higher order equation to represent it accurately [123].

D.2 MODES OF VIBRATION OF A FINITE BEAM

For a finite beam, of length L, the above equation of motion applies in conjunction with the appropriate end conditions.

D.2.1 Simply Supported Beam

For a beam which is 'simply supported' (ie constrained from translation but not from rotation) at both of its ends, the constraints can be written as

$$\begin{aligned} &\text{displacement,} && w = 0 && \text{at } x=0 \text{ and } L \\ &\text{bending moment,} && EI\frac{\delta^2 w}{\delta x^2} = 0 && \text{at } x=0 \text{ and } L \end{aligned} \qquad \ldots(D7)$$

which lead to the solution, from equations (D2) and (D3),

$$w_n(x,t) = W_n \sin\left(\frac{n\pi x}{L}\right) e^{i\omega_n t} \qquad \omega_n = \frac{n^2\pi^2}{L^2}\left(\frac{EI}{\rho A}\right)^{1/2} \qquad \ldots(D8)$$

This modeshape can also be considered as the superposition of forward and backward travelling waves (the A_4 and A_3 terms in equation (D2)) with no near-field waves present. The natural frequencies correspond precisely to the frequencies given by equation (D3) for $k=n\pi/L$, ie wavelengths which are integer fractions of 2L. This is a consequence of the elimination of near-field waves from the solution, by the choice of boundary conditions.

D.2.2 Free-free Beam

For a beam which is totally unconstrained, the shear force and bending moment must vanish at both of its ends (for convenience now set to $x=\pm L/2$):-

$$\text{bending moment} \qquad EI \frac{\delta^2 w}{\delta x^2} = 0 \text{ at } x = \pm L/2$$

$$\text{shear force} \qquad EI \frac{\delta^3 w}{\delta x^3} = 0 \text{ at } x = \pm L/2 \qquad \ldots(D9)$$

This leads to a solution which includes near-field waves as well as propagating waves which can be written as:-

$$w_n(x) = B_1 \begin{matrix}\cosh \\ \sinh\end{matrix} k_n x + B_2 \begin{matrix}\cos \\ \sin\end{matrix} k_n x \quad \text{for} \begin{matrix}\text{symmetric} \\ \text{anti-symmetric}\end{matrix} \text{modes} \qquad \ldots(D10)$$

The natural frequencies, ω_n, are such that the wavenumbers, k_n, (cf equation (D3)) satisfy the equation:-

$$\cosh k_n L \quad \cos k_n L = 1 \qquad \ldots(D11)$$

which for higher modes leads to the approximate solution

$$\omega_n \simeq (n+\tfrac{1}{2})^2 \frac{\pi^2}{L^2} \left(\frac{EI}{\rho A} \right)^{1/2} \qquad \ldots(D12)$$

It should be noted that the wavelength is no longer simply related to L, as it was for the simply supported beam.

D.3 INCLUSION OF TORSION

D.3.1 Simple Torsion

The equation of motion relating to the simple torsion of a bar is,

$$GJ \frac{\delta^2 \theta}{\delta x^2} - \rho I_x \frac{\delta^2 \theta}{\delta t^2} = 0 \qquad \ldots(D13)$$

where $\theta(x,t)$ is the angular displacement at longitudinal coordinate x, and time t. G is the bulk modulus, ρ the density, and both J (torsion constant) and I_x (the polar moment of area) depend on the cross-section. For a circular cross-section J and I_x are equal.

The solution to equation (D13) is given by,

$$\theta(x,t) = (\theta_1 e^{-ikx} + \theta_2 e^{ikx}) e^{i\omega t} \qquad \ldots(D14)$$

where θ_i are (complex) constants, and k is the wavenumber, given by,

$$k = \omega \left(\frac{\rho I_x}{GJ} \right)^{1/2} \qquad \ldots(D15)$$

Figure D1 includes this curve for parameters which are typical of a rail cross-section in torsion.

D.3.2 Torsion Bending

For non-circular bars, in particular I-beams where the torsional stiffness is dependent on the bending stiffness of the upper and lower flanges, a second-order torsion theory has been developed [124]. The resultant motion is known as torsion-bending. For this, the equation of motion is

$$E\Gamma \frac{\delta^4\theta}{\delta x^4} - GJ \frac{\delta^2\theta}{\delta x^2} + \rho I_x \frac{\delta^2\theta}{\delta t^2} = 0 \qquad \ldots(D16)$$

where GJ is the torsional rigidity, as above, and $E\Gamma$ is the warping rigidity. This gives a wavenumber, k, which is related to the frequency, ω, by a quadratic in k^2:-

$$E\Gamma\, k^4 - GJ\, k^2 - \rho I_x\, \omega^2 = 0 \qquad \ldots(D17)$$

At low frequencies this may be approximated by the simple torsion result (equation (D15)), but at higher frequencies k depends on $\omega^{1/2}$, as in the case of the Euler-Bernoulli beam.

Figure D2 contains a curve of this with parameters typical of a rail cross-section, with the simple bending curve from Figure D1 shown for comparison.

D.3.3 Coupled Bending and Torsion

If the shear centre and the centroid of the beam cross-section coincide, the bending and torsion motions are uncoupled, and the above equations apply. However if these two points are not coincident, which is the case for a non-symmetric cross-section, the motions are coupled. Letting the distance between these two points be a, and the displacement at the centroid be w, the equations of motion can be shown to be,

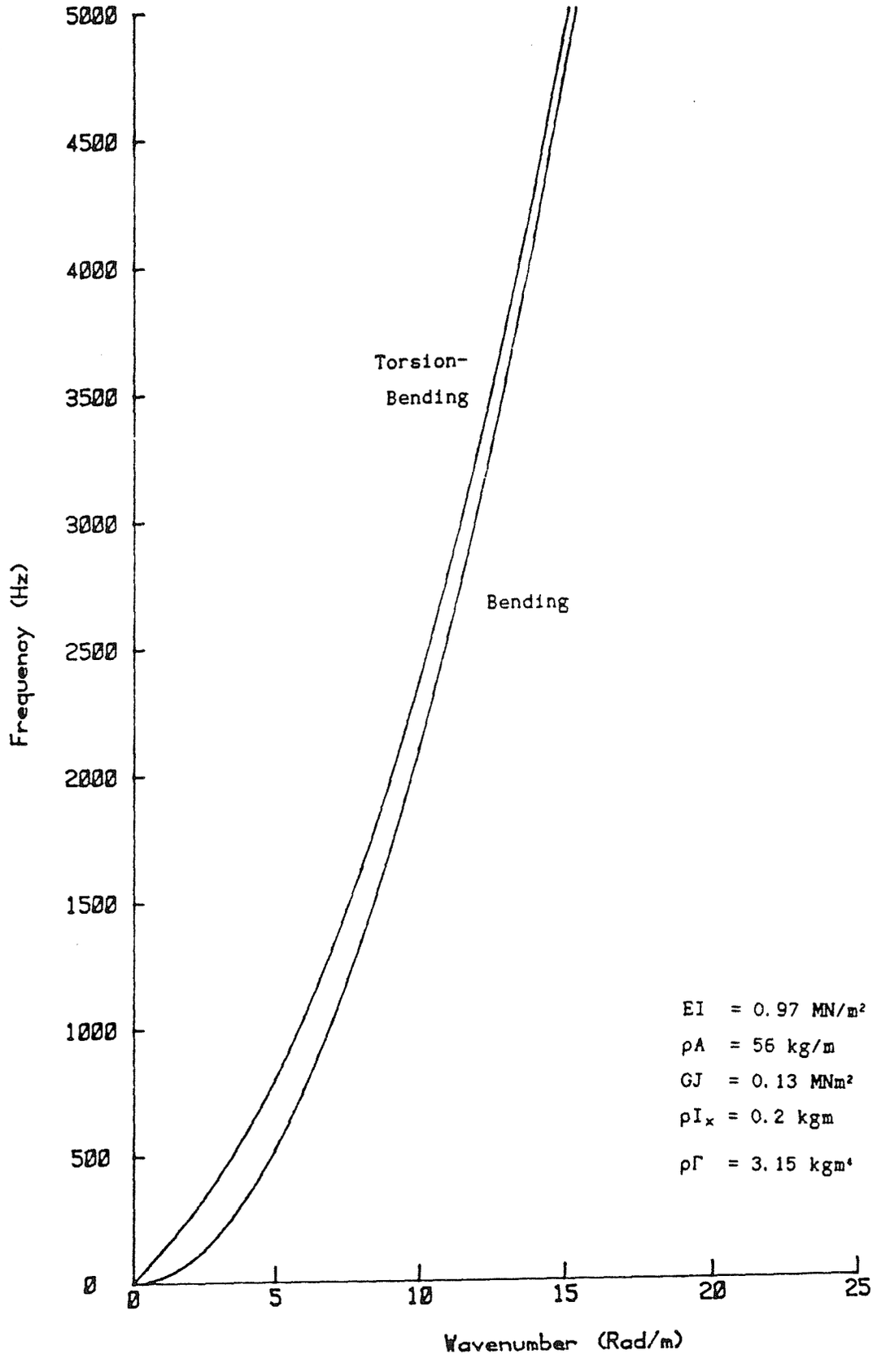

Figure D2 Dispersion Diagram for Uncoupled Euler Bending and Torsion-Bending

$$EI \frac{\partial^4 w}{\partial x^4} + EI\, a \frac{\partial^4 \theta}{\partial x^4} + \rho A \frac{\partial^2 w}{\partial t^2} = 0$$

$$GJ \frac{\partial^2 \theta}{\partial x^2} - EI\, a \frac{\partial^4 w}{\partial x^4} - a^2\, EI \frac{\partial^4 \theta}{\partial x^4} - \rho I_x \frac{\partial^2 \theta}{\partial t^2} = 0 \qquad \ldots(D18)$$

This coupled set of equations can be solved by assuming harmonic motion at frequency ω, and a spatial wavenumber k. The resulting equation relating ω and k is

$$\omega^4 - \omega^2 k^2 \left\{ \frac{GJ + a^2\, EI\, k^2}{\rho I_x} + \frac{EI}{\rho A} k^2 \right\} + \frac{EI}{\rho A} \frac{GJ}{\rho I_x} k^6 = 0 \qquad \ldots(D19)$$

This is a quadratic in ω^2, or a cubic in k^2, yielding two pairs of real wavenumbers and one pair of imaginary wavenumbers at each frequency, corresponding to two travelling waves and one near-field wave in each direction. One of the travelling waves will be predominantly bending, and the other will be predominantly torsion. Figure D3 shows results of the coupling resulting from an offset of 32 mm, which is typical of a rail cross-section, with other parameters as in Figure D1. Note that the cross-over of the two waves now disappears. Both waves contain some bending and some torsion, the proportion varying with frequency.

A similar equation can be derived for coupled bending and torsion-bending, yielding an equation which is quadratic in ω^2 and quartic in k^2. Results from this are shown in Figure D4.

D.4 FREQUENCY RESPONSE FUNCTIONS OF AN INFINITE BEAM

D.4.1 Free Beam

If an infinite Euler-Bernoulli beam is excited by a harmonic point force $Pe^{i\omega t}$ at $x=0$, the solution consists of propagating waves (forward for $x>0$ and backward for $x<0$) and near-field waves (one on each side of the origin, each decaying away from $x=0$). Each pair of waves is absent from the other side of the origin, because energy is assumed to be input only at $x=0$, and not at $x=\pm\infty$. Thus the solution can be written as:-

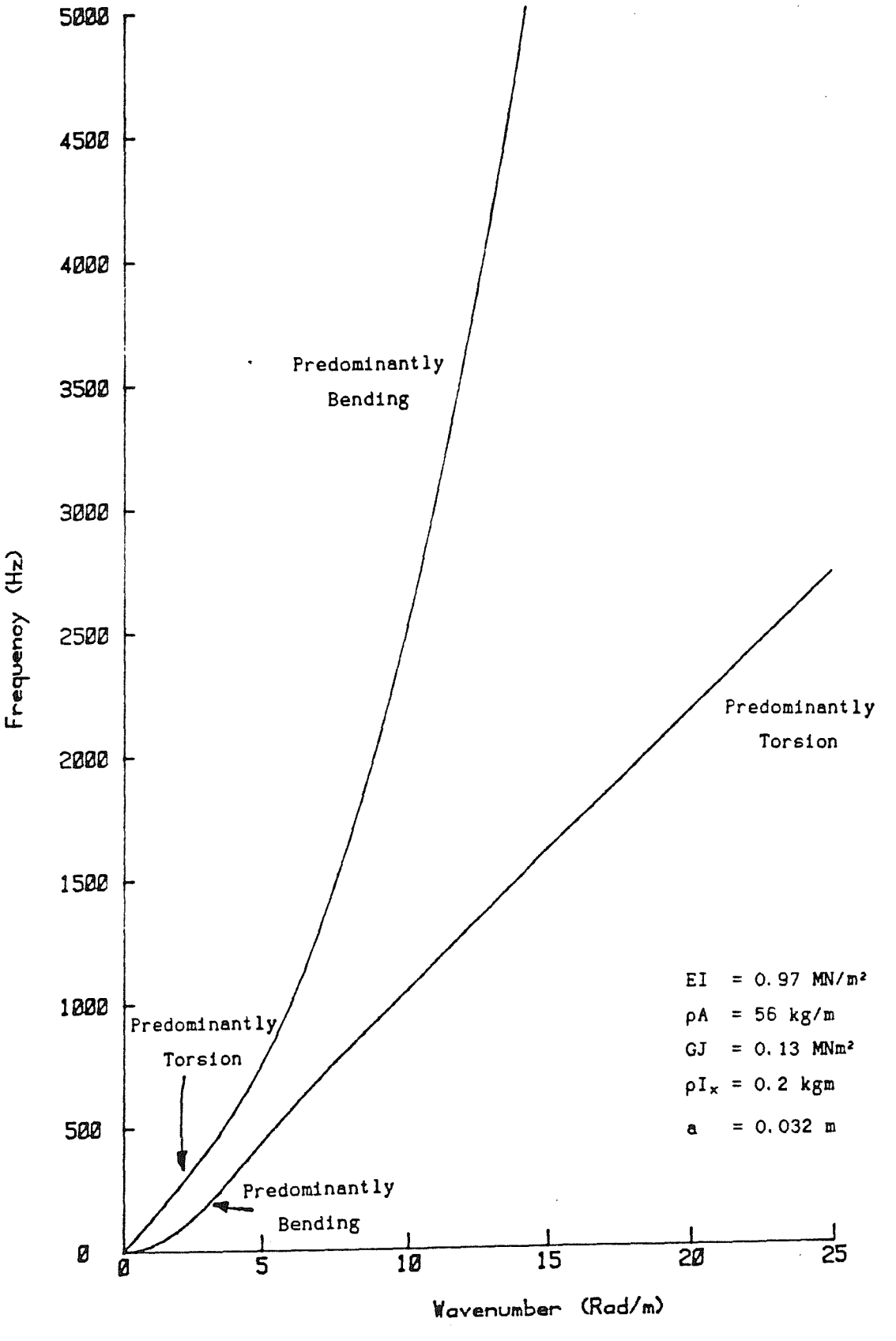

Figure D3 Dispersion Diagram for Coupled Euler Bending and St Venant Torsion

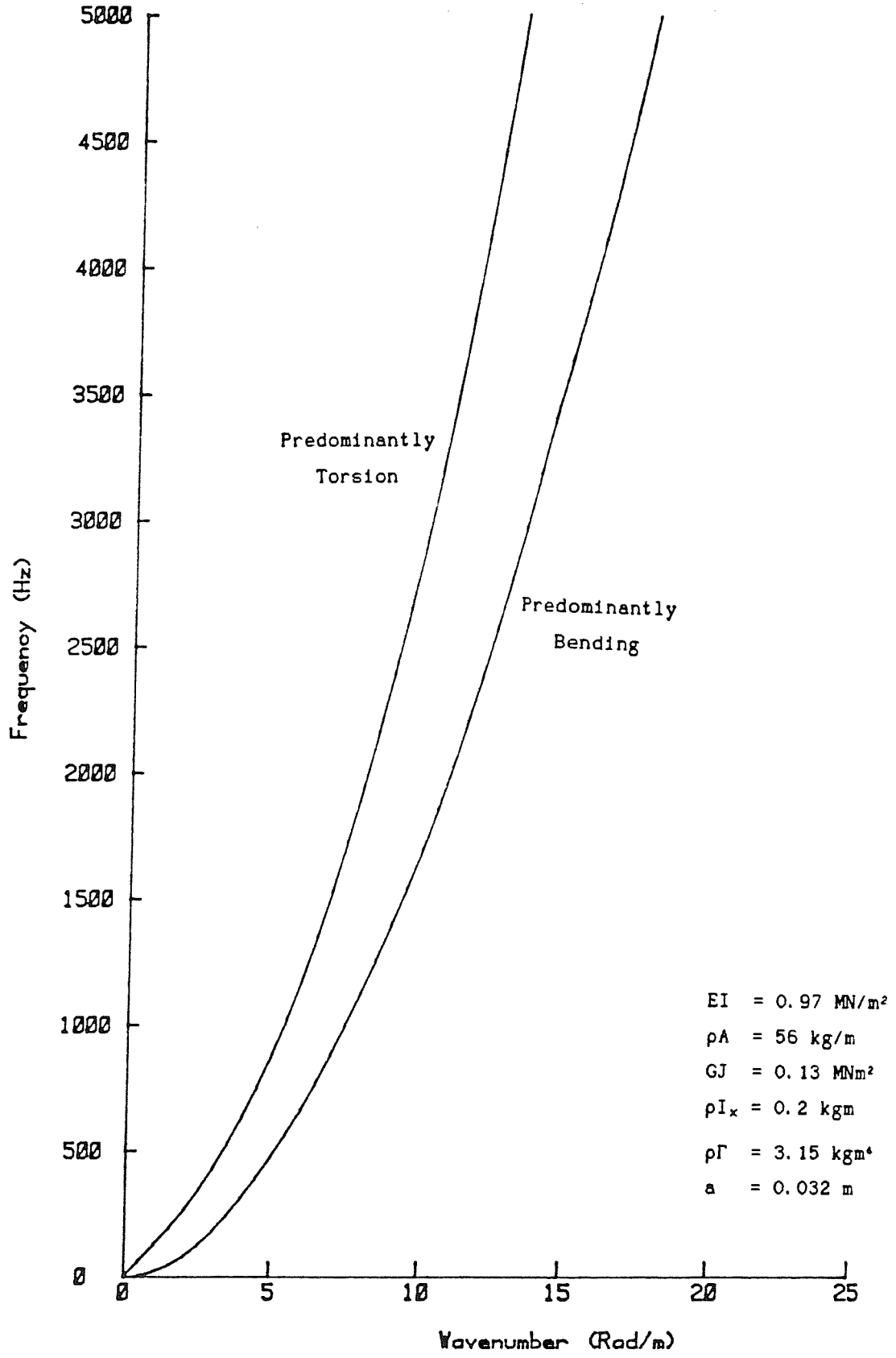

Figure D4 Dispersion Diagram for Coupled Euler Bending and Torsion-Bending

$$w_+(x) = A_2\ e^{-kx} + A_4\ e^{-ikx} \quad \text{for } x>0$$

$$w_-(x) = A_1\ e^{kx} + A_3\ e^{ikx} \quad \text{for } x<0 \qquad \ldots(D20)$$

By symmetry $A_1=A_3$ and $A_2=A_4$. The remaining two unknowns are found by boundary conditions relating the total shear force (allowing for sign conventions) at x=0 to P, and equating the gradients of w_+ and w_-

$$EI\ \frac{\delta^3 w_+}{\delta x^3}(0) - EI\ \frac{\delta^3 w_-}{\delta x^3}(0) = P \quad ; \quad \frac{\delta w_+}{\delta x}(0) - \frac{\delta w_-}{\delta x}(0) = 0 \qquad \ldots(D21)$$

This leads to the solution

$$w_+(x) = -\frac{iP}{4EIk^3}\ \left(e^{-ikx} - ie^{-kx} \right) \qquad \ldots(D22)$$

with $w_-(-x) = w_+(x)$. From this the receptance at x=0 can be derived as

$$\alpha(\omega) = \frac{w_+(0)}{P} = -\frac{(1+i)}{4EIk^3} = \frac{-(1+i)}{4\ (EI)^{1/4}\ (\rho A)^{3/4}\ \omega^{3/2}} \qquad \ldots(D23)$$

This has a phase of -135° and magnitude decreasing at 30 dB per decade of frequency.

D.4.2 Beam on Elastic Foundation

If the beam is resting on a continuous elastic support of stiffness K per unit length, the equation of motion (D1) is altered to

$$EI\ \frac{\delta^4 w}{\delta x^4} + \rho A\ \frac{\delta^2 w}{\delta t^2} + Kw = 0 \qquad \ldots(D24)$$

The solution is a similar wave motion to that of a free beam (equation (D2)) except that the wavenumbers are given by

$$k^4 = \frac{\rho A}{EI}\ (\omega^2 - \omega_o{}^2) \qquad \ldots(D25)$$

where $\omega_o{}^2=K/\rho A$. The boundary conditions in §D.4.1 (equations (D21)) apply here as well with the result that the receptance is given by

$$\alpha(\omega) = -\frac{(1+i)}{4EIk^3} = \frac{-(1+i)}{4\,(EI\,(\rho A)^3\,(\omega^2-\omega_o{}^2)^3)^{1/4}} \qquad \ldots(D26)$$

It should be noted that as the frequency $\omega \to \omega_o$ the receptance $|\alpha| \to \infty$. This corresponds to the bounce resonance of the whole rail on the elastic foundation.

D.4.3 Effect of Forward Velocity of Forcing Point

Suppose that a harmonic force $Pe^{i\omega t}$ is applied at the point $x=Vt$. It is convenient to transform to coordinates (ξ,t), where $\xi=x-Vt$, so that $\xi=0$ corresponds to the forcing point. Transforming equation (D1), gives

$$EI\frac{\delta^4 w}{\delta \xi^4} + \rho A\left(\frac{\delta}{\delta t} - V\frac{\delta}{\delta \xi}\right)^2 w = 0 \qquad \ldots(D27)$$

Assuming harmonic motion with a wavenumber k, gives the wavenumber-frequency equation:-

$$\frac{EI}{\rho A}k^4 + (Vk - i\omega)^2 = 0 \qquad \ldots(D28)$$

For $V^2 << \omega\left(\frac{EI}{\rho A}\right)^{1/2}$ this can be approximated as

$$k \simeq \pm\omega^{1/2}\left(\frac{\rho A}{EI}\right)^{1/4} + \frac{iV}{2}\left(\frac{\rho A}{EI}\right)^{1/2} \; ; \; k \simeq \pm i\omega^{1/2}\left(\frac{\rho A}{EI}\right)^{1/4} - \frac{iV}{2}\left(\frac{\rho A}{EI}\right)^{1/2} \qquad \ldots(D29)$$

Thus the wavenumbers for the propagating waves are raised and lowered by an amount proportional to the speed (raised for the wave travelling in the same direction as the force), whereas the near-field waves have a spatial harmonic component added to them. It may be noted that the additional terms are independent of frequency.

However for realistic speeds of travel these shifts are very small. For example, using the beam parameters from above and a speed V=44.4 m/s, the approximation is valid for frequencies above about 1 Hz, and the shift can be calculated as 0.076 rad/m. It is therefore reasonable to ignore the effects of movement of the forcing point along the rail, apart from any effects of the periodic support, which are beyond the scope of the current work.

APPENDIX E

WHEEL-RAIL CONTACT EQUATIONS

E.1 INTRODUCTION

The wheel and the rail are joined at curved surfaces, so that the contact occurs over a small area, known as the contact patch. The relations governing the coupling of the wheel and the rail, at least quasi-statically, are quite well known. This appendix summarises them with reference to the relevant literature.

The coordinate system used is shown in Figure E1. Relative motion between the wheel and rail, made up of local elastic deformations of each and of sliding in the plane of the contact patch, is expressed by the displacement vector $\{z^c\}$. This has three translation components and three corresponding rotational components, as shown in Figure E1.

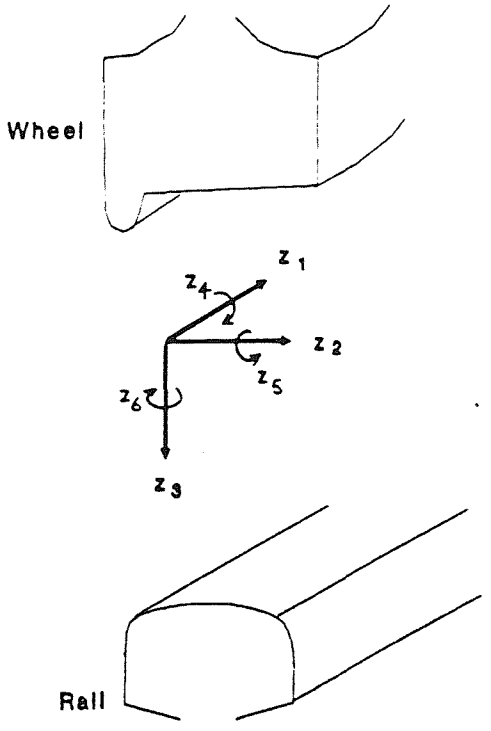

Figure E1 Coordinates at Wheel-Rail Contact

E.2 HERTZIAN CONTACT THEORY

E.2.1 Vertical Contact Stiffness

The local deformations of two bodies in contact act as a non-linear stiffness between them. For smooth regularly curved surfaces,

the vertical compression of the contact zone, z^{C_3}, is given by (see [77,20,125]),

$$z^{C_3} = \frac{\xi}{2}\left(\frac{9\ P_3{}^2}{16\ E^{*2}\ R_e}\right)^{1/3} \qquad \ldots(E1)$$

where E^* is the plain strain elastic modulus, $E^*=E/(1-\nu^2)$, and P_3 is the vertical load at the contact. ξ is a dimensionless quantity (values of which are given in Table E1) dependent on the radii of curvature R_{ij}, and hence the shape of the contact patch. R_e is an

Table E1 Contact parameters

θ	μ	σ	$g=\mu/\sigma$	$\xi/2$
30	2.731	0.493	5.54	0.727
35	2.397	0.530	4.52	0.775
40	2.136	0.567	3.77	0.817
45	1.926	0.604	3.19	0.855
50	1.754	0.641	2.74	0.887
55	1.611	0.678	2.38	0.913
60	1.486	0.717	2.09	0.938
65	1.378	0.759	1.816	0.957
70	1.284	0.802	1.601	0.972
75	1.202	0.846	1.421	0.985
80	1.128	0.893	1.263	0.993
85	1.061	0.944	1.124	0.998
90	1.0	1.0	1.0	1.0
95	0.944	1.061	0.890	0.998

Key:-

$\theta = \cos^{-1}\left(\frac{B-A}{A+B}\right)$ in degrees where A and B are functions of the radii of curvature of the two bodies in contact: for the wheel R_{11} is the radius and R_{12} is the radius of curvature of the profile, and for the rail $R_{21}=0$ and R_{22} is the radius of curvature of the profile.

$$A+B = \frac{1}{R_{11}} + \frac{1}{R_{12}} + \frac{1}{R_{21}} + \frac{1}{R_{22}} \qquad A-B = \frac{-1}{R_{11}} + \frac{1}{R_{12}} + \frac{-1}{R_{21}} + \frac{1}{R_{22}}$$

μ,σ = factors in semi-axes of contact patch along rail (a), and across rail (b) respectively, see equations (E4) (from [126,77])

g = aspect ratio of elliptical contact patch = $a/b = \mu/\sigma$

ξ = factor in contact stiffness, see equations (E1,E2) (from [20,77])

effective radius of curvature of the surfaces in contact, which for general curved surfaces is (see [77])

$$\frac{1}{R_e} = \frac{1}{2}\left\{ \frac{1}{R_{11}} + \frac{1}{R_{12}} + \frac{1}{R_{21}} + \frac{1}{R_{22}} \right\} \qquad \ldots(E2)$$

where the R_{ij}s are the principal radii of curvature of the two bodies as described in Table E1 (see also [126]). The special cases of two spheres ($1/R_e=1/R_1+1/R_2$) and two perpendicular cylinders ($1/R_e= 1/2R_1+1/2R_2$) can be derived from this.

A linearised Hertzian contact stiffness, k_H, may be calculated (for small displacements) as:

$$k_H = \frac{\delta P_3}{\delta z_{C_3}} = \frac{2}{\xi}\left(\frac{3\ E^{*2}\ R_e\ P_o}{2} \right)^{1/3} \qquad \ldots(E3)$$

where P_o is the static wheel load (ie the value of P_3 ignoring small quantities).

For smooth regular surfaces the contact patch is elliptical, with semi-axes represented by a and b (a being taken in the direction of travel, and b in the transverse direction). They can be calculated using (see [77,126]):

$$a = \mu\left(\frac{3\ P_o\ R_e}{2\ E^*} \right)^{1/3} \qquad b = \sigma\left(\frac{3\ P_o\ R_e}{2\ E^*} \right)^{1/3} \qquad \ldots(E4)$$

where μ and σ are also tabulated in Table E1. They depend on R_{ij}, in a manner similar to ξ.

E.2.2 Transverse Contact Stiffness

The contact between two static bodies has a transverse compliance which Mindlin [98] showed to be approximately the same as that for the vertical case, and this result is widely used (see §3 and for instance Grassie [41]). In fact the lateral compliance is slightly greater than the vertical compliance (a factor of x=1-1.2 being typical) as shown in Figure E2 taken from Mindlin [98]. This means that the lateral contact stiffness, k_T, is given by

$$k_T = \frac{1}{x} k_H \qquad \ldots(E5)$$

where k_H is the vertical Hertzian contact stiffness. The factor x depends on g=a/b, the aspect ratio of the contact patch. Figure E2 applies for the compliance in the longitudinal direction; for the lateral direction x(1/g) should be used. The linear approximation to k_H was defined in equation (E3), so that

$$k_T = \frac{2}{x(g)\,\xi}\left(\frac{3\,E^{*2}\,R_e\,P_o}{2}\right)^{1/3} \qquad \ldots(E6)$$

An analytical approximation may be used for x as follows

$$x \approx 1 + \frac{\nu}{1-\nu}\left\{\frac{1}{4} + \frac{1}{\pi}\tan^{-1}g\right\} \qquad \text{valid for } 0.2<g<5 \qquad \ldots(E7)$$

with $x \to 1$ as $g \to 0$ and $x \to \frac{1}{1-\nu}$ as $g \to \infty$

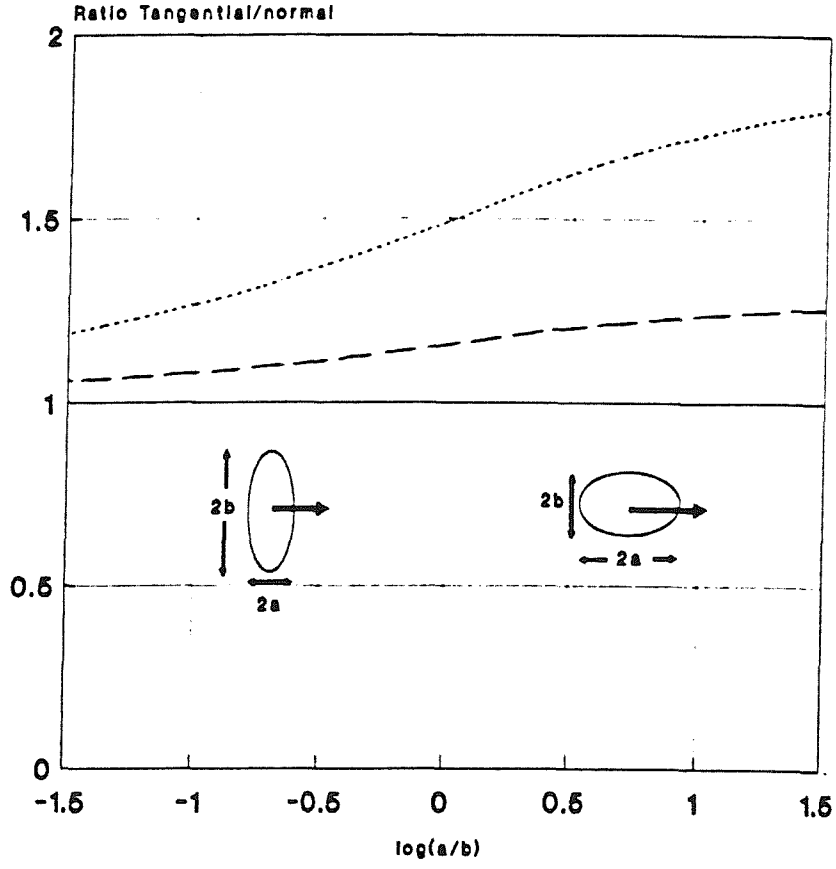

Figure E2 Ratio of Tangential to Normal Compliance (from Mindlin [98]) for Poisson's ratio: ———, ν=0; – – –, ν=0.25; ·····, ν=0.5.

E.3 KALKER'S ROLLING CONTACT THEORY

During rolling, a small relative motion occurs between the two rolling bodies, known as creepage. A corresponding force acts between the bodies, known as the creep force. This was first investigated by Carter [127] in relation to traction forces. The theory of creep forces was developed in detail by Kalker [80,81] using the assumption that the contact conditions change slowly in relation to the rolling velocity.

E.3.1 Longitudinal Creep Force

The simplest case is longitudinal creepage (in the direction of rolling), so although it has less relevance to noise generation than the lateral case, it will be considered first. For quasi-static rolling, Kalker gives the longitudinal contact force P_1 as

$$P_1 = f_{11}\,\gamma_1 \qquad \ldots(E8)$$

where the longitudinal creepage, γ_1, is defined by

$$\gamma_1 = \frac{\dot{z}c_1}{V} = \frac{VW_1 - VR_1}{V} \qquad \ldots(E9)$$

where $\dot{z}c_1$ is the relative longitudinal velocity at the contact, VW_1 and VR_1 are the velocities of the contact patch relative to the wheel and the rail respectively and $V=(VW_1+VR_1)/2$ is the mean rolling velocity. The coefficient f_{11} is given by

$$f_{11} = E\,ab\,C_{11} = E\,c^2\,C_{11} \qquad \ldots(E10a)$$

where E is Young's modulus, a and b are the semi-axis lengths of the (elliptical) contact patch given by equation (E4), $c=\sqrt{ab}$, and C_{11} is a creep coefficient tabulated by Kalker, and dependent on $g=a/b$, and on Poisson's ratio, ν. Equation (E10a) may be stated alternatively in terms of G, the shear modulus,

$$f_{11} = G\,ab\,C'_{11} \qquad \ldots(E10b)$$

In this case the values of C'_{11} differ from C_{11} by a factor depending only on Poisson's ratio, ν. In fact those values tabulated by Kalker in [81] relate to G, but the form relating to E will be used here.

E.3.2 Lateral Creep Force

The lateral creep force is similarly related to the lateral creepage, γ_2, but with an additional term, due to the spin creepage ω_3 (relative rotation about the normal to the contact surface).

$$P_2 = f_{22}\,\gamma_2 + f_{23}\,\omega_3 \qquad \ldots(E11)$$

where the lateral creepage, γ_2, is given by the relative lateral velocity between the wheel and rail, $\dot{z}c_2$, divided by the mean rolling velocity, V,

$$\gamma_2 = \frac{\dot{z}c_2}{V} = \frac{Vw_2 - Vr_2}{V} \qquad \ldots(E12)$$

and the spin creepage is given by

$$\omega_3 = \frac{\dot{z}c_6}{V} = \frac{\Omega w_3 - \Omega r_3}{V} \qquad \ldots(E13)$$

The coefficients f_{22} and f_{23} are given by:

$$f_{22} = E\,ab\,C_{22} = E\,c^2\,C_{22} \qquad \ldots(E14)$$

$$f_{23} = E\,(ab)^{3/2}\,C_{23} = E\,c^3\,C_{23} \qquad \ldots(E15)$$

where C_{22} and C_{23} are creep coefficients tabulated by Kalker [81].

E.3.3 Spin Moment

As well as the lateral creep force, the lateral and spin creepages generate a spin moment, P_6, which is given by:

$$P_6 = -f_{23}\,\gamma_2 + f_{33}\,\omega_3 \qquad \ldots(E16)$$

where f_{23} was given by equation (E15), and f_{33} is given by:

$$f_{33} = E\,(ab)^2\,C_{33} = E\,c^4\,C_{33} \qquad \ldots(E17)$$

It will be noted that equations (E13) and (E16) represent coupling between lateral and spin motions.

E.4 FREQUENCY-DEPENDENT CREEP COEFFICIENTS

The vertical contact receptance due to the localised stiffness can be expected to be unaffected by the rolling process as any inertial effects will be small. However for the lateral contact receptance some means must be found to combine the high frequency contact stiffness effects with the low frequency creep forces due to rolling. (In §3 this is done (with no direct justification) by simply adding the contact spring and creep force damper in series).

An alternative means of obtaining a lateral contact receptance is to retain the creep force formulation, but to make use of a frequency-dependent creep coefficient C^*_{22}, as derived by Knothe and Gross-Thebing [85,86] and Valdivia [87].

Knothe and Gross-Thebing modify the above equations (E8-17) for high frequencies by replacing C_{pq} by frequency-dependent creep coefficients C^*_{pq}. In order to derive these, the analysis of Kalker was repeated for harmonic motion, taking account of the variations of force across the contact patch and other high frequency effects, assuming throughout small creepages so that a linear (non-saturated) creep regime can be used.

The derivations involve numerical integration, and the final results are presented in terms of a plot of C^*_{pq}/C_{pq} in the complex plane. These functions depend on the non-dimensional parameter L/a, where $L=2\pi V/\omega$ is the wavelength of the force fluctuation and a is the semi-axis length of the contact patch in the direction of rolling. Examples are given in Figure E3.

It is clearly desirable to have available a simple expression for these frequency-dependent creep coefficients C^*_{pq}, rather than to use the complicated numerical integration of the contact forces of Knothe and Gross-Thebing. The following sections develop such approximate expressions for each C^*_{pq}.

E.4.1 Approximations to C^*_{11} and C^*_{22}

In Ref [86] Knothe and Gross-Thebing present a simplification for C^*_{11}/C_{11} and C^*_{22}/C_{22}, which consists of the first term of their series in each case. This is

$$\frac{C^*_{pp}}{C_{pp}} = \frac{k}{(k+i4\pi a/L)} \qquad \ldots(E18)$$

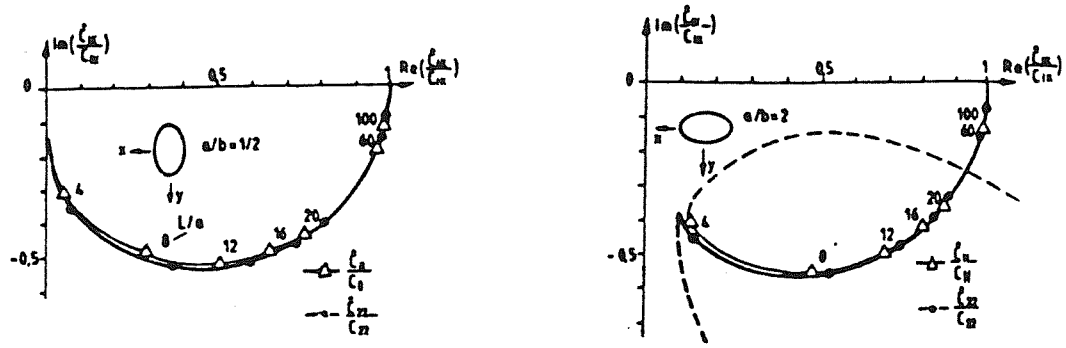

(a) Longitudinal and Lateral Coefficients C_{11} and C_{22}

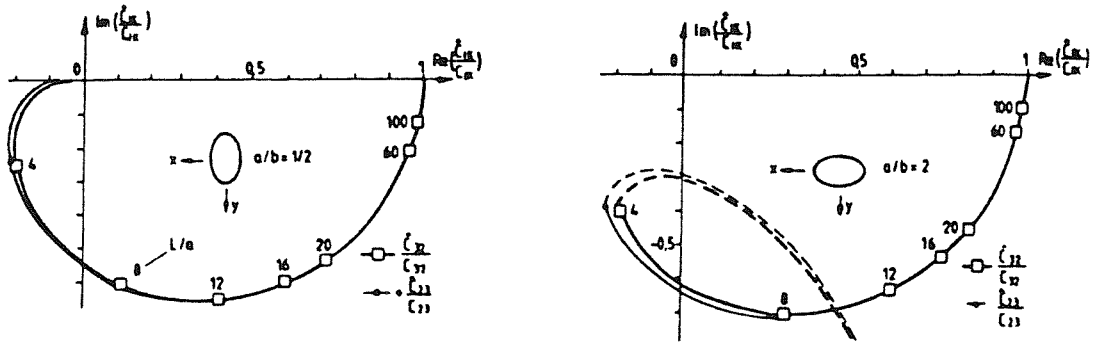

(b) Lateral/Spin Cross Coefficient C_{23}

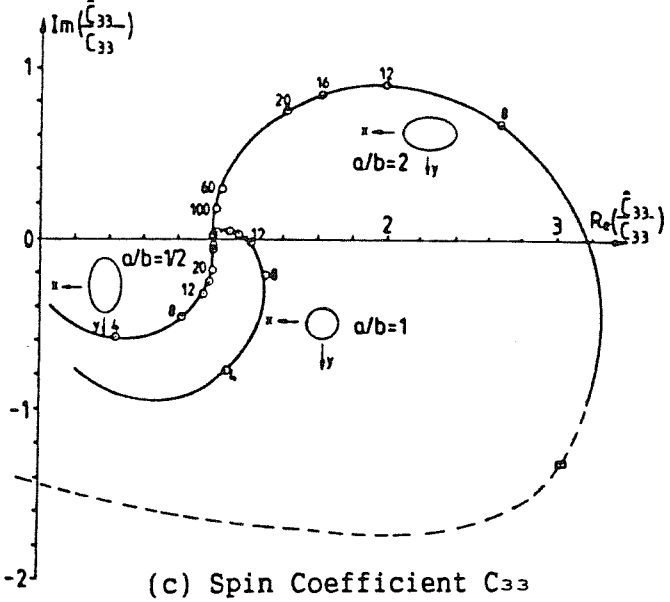

(c) Spin Coefficient C_{33}

Figure E3 Frequency-dependent Creep Coefficients (from Knothe [86])

where k=1.149 for C^*_{11} and 1.409 for C^*_{22} for a/b=0.5. These result in semi-circular curves which are quite similar to those shown in Figure E3. It will now be shown, however, that the model of a contact spring and a creep damper in series, which has been used in §3, is actually identical to the simplification given in equation (E18).

Given a lateral contact receptance consisting of a contact stiffness k_T, and a creep damper $C=f_{22}/V$, in series,

$$\alpha C_{22} = \frac{1}{k_T} + \frac{1}{i\omega C} = \frac{x}{k_H} + \frac{V}{i\omega E a b C_{22}} \qquad \ldots(E19)$$

this can be expressed as a modification to C_{22}, giving

$$\alpha C_{22} = \frac{V}{i\omega E a b C^*_{22}} \qquad \ldots(E20)$$

in which,

$$\frac{C^*_{22}}{C_{22}} = \frac{1}{C}\,\frac{1}{i\omega\,\alpha C_{22}} = \frac{1}{1 + i\omega C/k_T} \qquad \ldots(E21)$$

where $$\frac{\omega C}{k_T} = \frac{\omega\ E\ ab\ C_{22}\ x}{V\ k_H} = \pi\ (1-\nu^2)\ C_{22}\ x\xi\sigma\ \frac{a}{L} \qquad \ldots(E22)$$

and hence the only dependency on frequency is via the parameter L/a, and otherwise it depends only on Poisson's ratio ν (directly and via C_{22}) and on the shape of the contact patch, g, via C_{22}, x, ξ and σ.

The curve equivalent to Figure E3 always has a semicircular shape, the position of points for a given value of L/a depending on the other parameters according to equation (E22).

The above analysis applies equally to C^*_{11}. Using parameters equivalent to those used by Knothe (g=0.5, ν=0.25), deriving x from equation (E7) and ξ and σ from Table E1, gives k=0.948 for C^*_{11} and k=1.075 for C^*_{22}, which are a little lower than the values of 1.149 and 1.409 given by Knothe. For g=2, the values of k derived from above are 1.265 for C^*_{11} and 1.396 for C^*_{22}. The curves are compared with Knothe's exact values in Figure E4.

The equivalent lateral receptance, αC_{22}, is shown in Figure E5 in a non-dimensional form. They show the same form as in §3 - dominance by the creep force damper at low frequencies, and by the contact spring

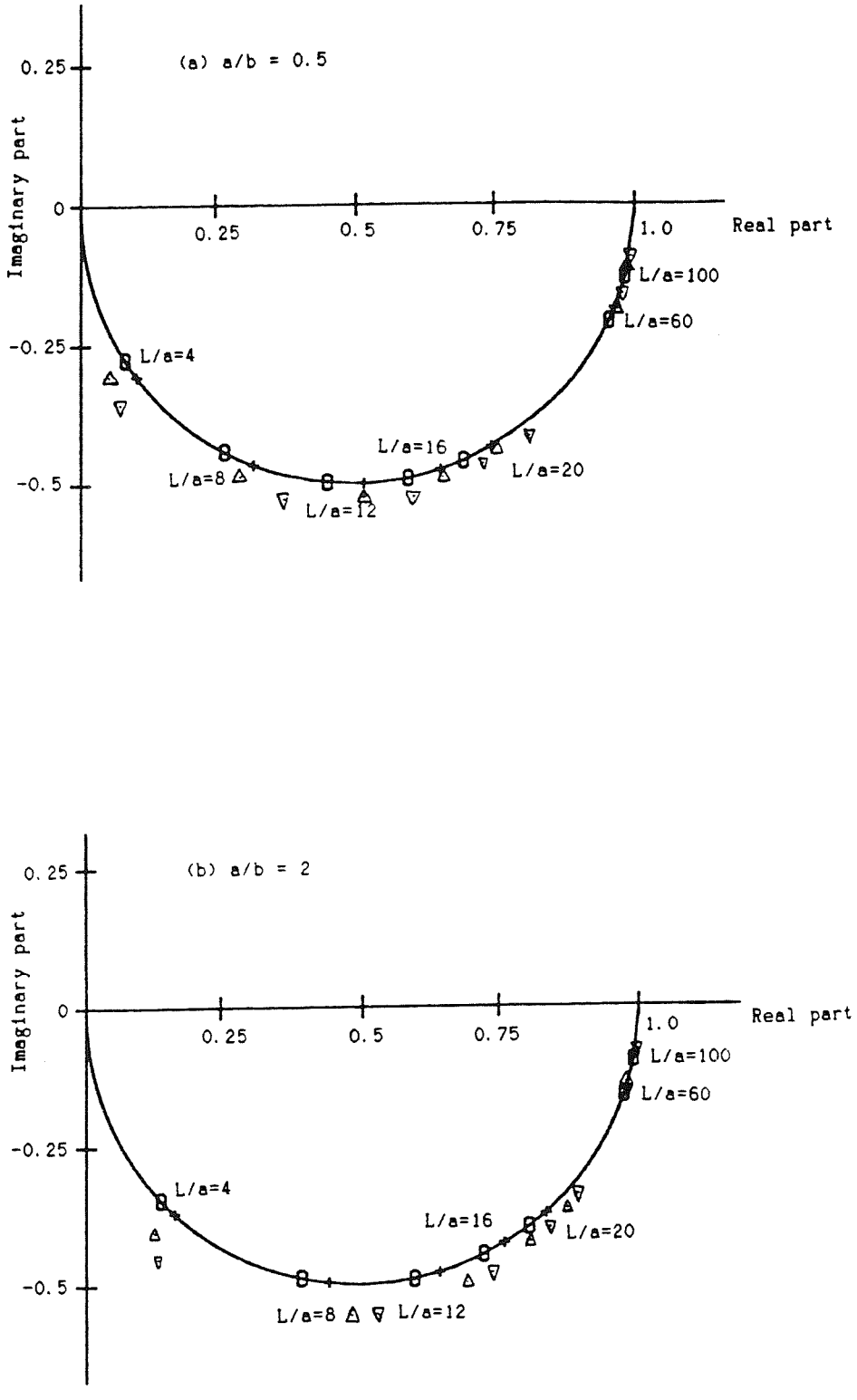

Figure E4 Frequency-dependent Creep Coefficients; Longitudinal: o estimate, Δ from Knothe [86]; Lateral: + estimate, ∇ from Knothe [86]

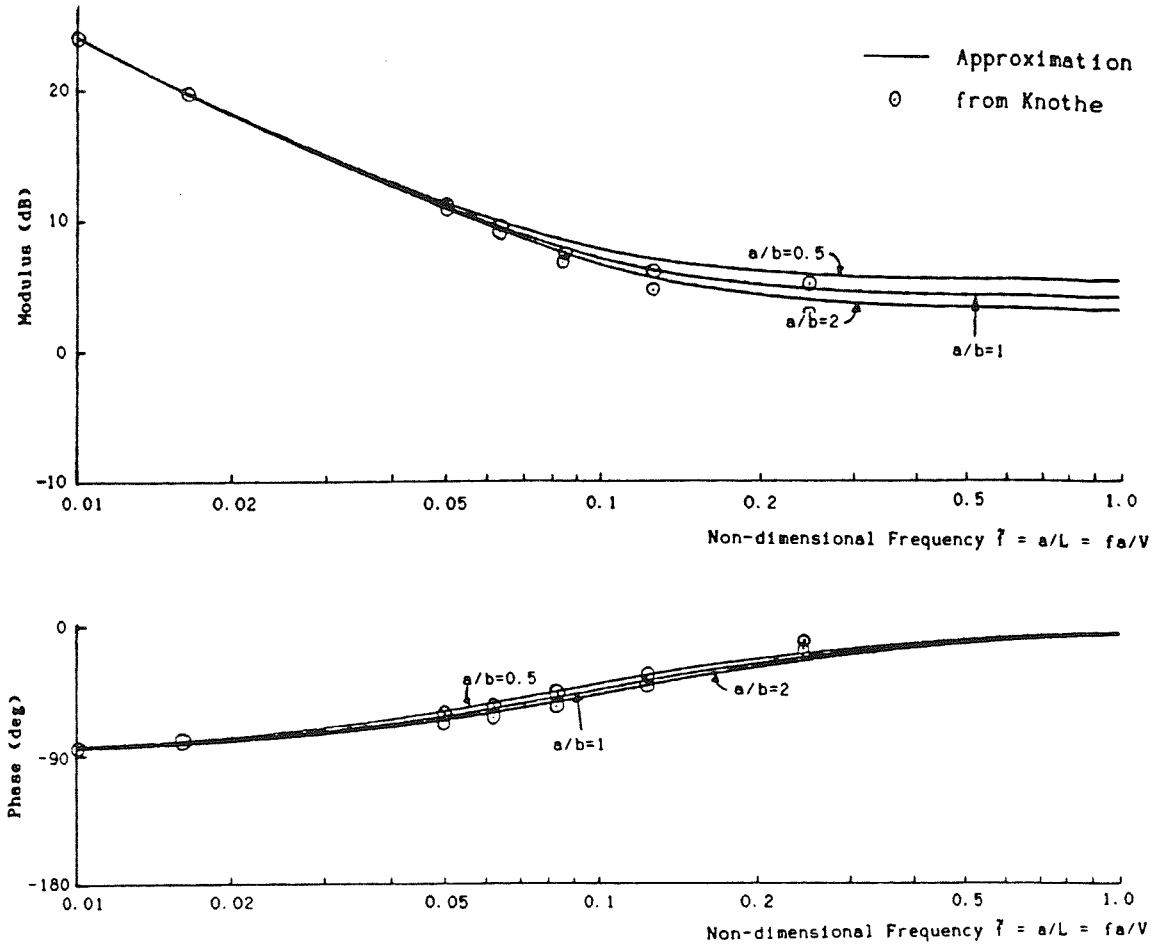

Figure E5 Non-dimensional Lateral Contact Receptance $\alpha = C_{22}L/2\pi i C^*_{22}a$

at high frequencies. Also shown are points derived from Knothe's curves of C^*_{22}/C_{22}.

E.4.2 Approximations to C^*_{23}

The curve for C^*_{23} in Figure E3 cannot reasonably be represented by the spring and damper in series of §E.4.1, since the curve crosses the imaginary axis before tending to zero. However a third term may be added to the denominator of equation (E18):-

$$\frac{C^*_{23}}{C_{23}} = \frac{\lambda^2}{(\lambda^2+i A\lambda-B)} \qquad \ldots(E23)$$

where $\lambda=L/a$, and the constants A and B, which may depend on g and ν as before, have to be determined. Fitting this to Knothe's values of C^*_{23}/C_{23}, gives $A = 17.6\ C_{23}/g$ and $B = 57.4\ C_{23}/g$, from which the curve in Figure E6 is derived. It can be seen that this gives a reasonable approximation. Figure E7 shows the equivalent receptance, αC_{23}, in non-dimensional form, along with points derived from Knothe's results.

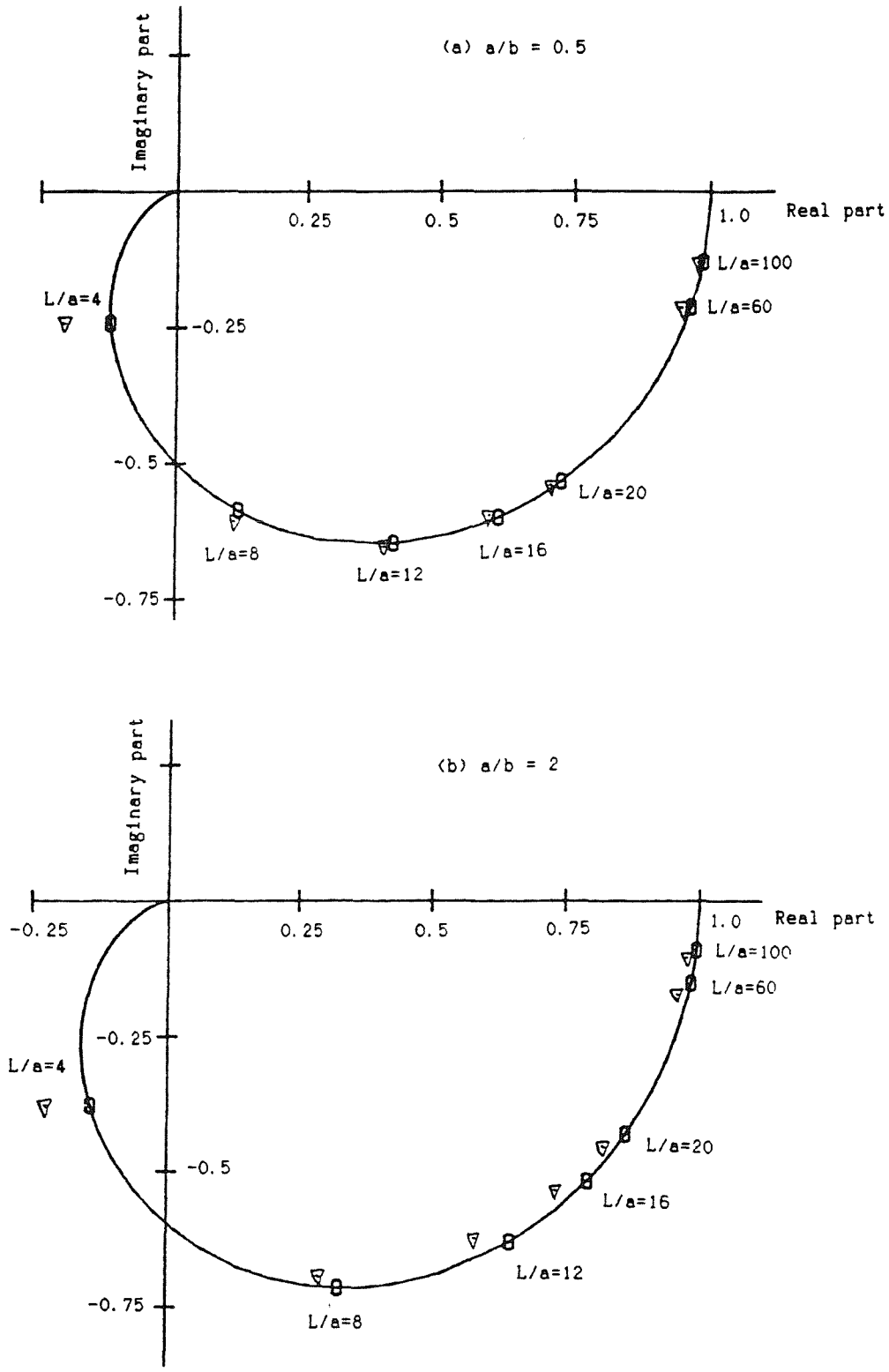

Figure E6 Frequency-dependent Lateral-Spin Cross Coefficients; o estimate, ∇ from Knothe [86]

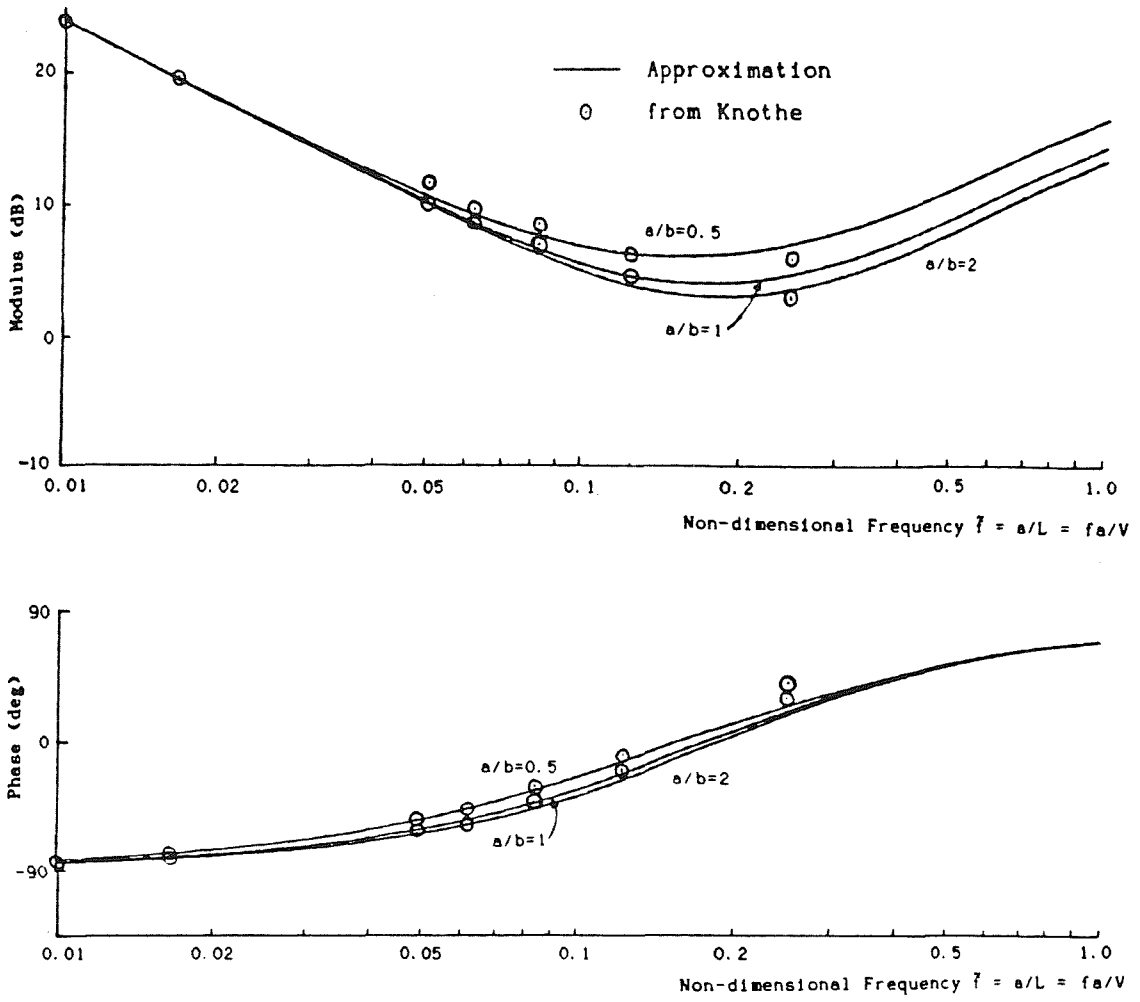

Figure E7 Non-dimensional Lateral-Spin Receptance $\mathfrak{C} = C_{23}L/2\pi i C^*_{23}a$

E.4.3 Approximations to C^*_{33}

From Figure E3 it can be seen that the frequency-dependent spin creep coefficient, C^*_{33}, is much less simple than C^*_{11}, C^*_{22} and C^*_{23}, as its form varies significantly with the aspect ratio of the contact patch ellipse, g.

In order to derive a readily usable approximation, it can be noted from Figure E3 that points for a given value of $\lambda=L/a$, and different values of g, lie in a straight line. Furthermore the ratio of the distances between g=0.5 to 1 and g=1 to 2 is always just under 1:3. It should therefore be possible to extrapolate back to a curve for g=0, and to do this a dependence of $g^{3/2}$ has been used (equivalent to a length ratio of 1:2.83), so that C^*_{33} can be written as:

$$\frac{C^*_{33}(g,\lambda)}{C_{33}} = \frac{T(\lambda)}{C_{33}} + \frac{S(\lambda)}{C_{33}} g^{3/2} \qquad \ldots(E24)$$

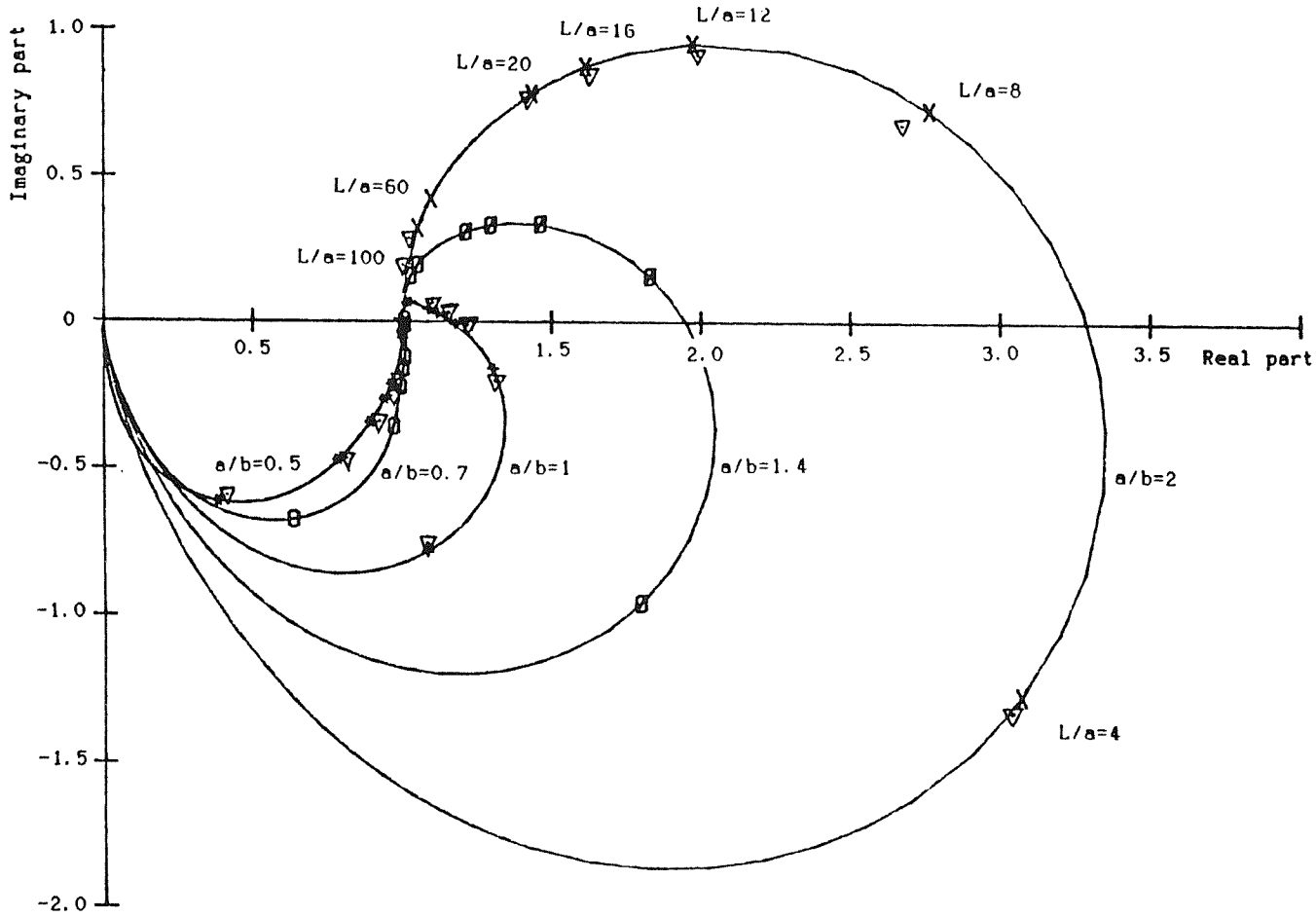

Figure E8 Frequency-dependent Spin Creep Coefficients;

***, O, +, Ø, ×, estimates; ∇ from Knothe [86]**

The resulting g=0 curve, $T(\lambda)$ was found to have the same form as C^*_{23}, so that only two parameters A and B are required to define it

$$\frac{T(\lambda)}{C_{33}} = \frac{\lambda^2}{(\lambda^2+iA\lambda-B)} \qquad \ldots(E25)$$

with the values of A and B found to be 7.7 and 16 respectively.

Finally the dependence on g needs to be defined, $S(\lambda)$ being a complex function of λ. It must be assumed that as $\lambda \to 0$, $S \to 0$ so that $C^*_{33} \to 0$ as for other frequency-dependent creep coefficients. The following function was found to give acceptable results, as shown in Figures E8 and E9, although it involved the choice of four constants.

$$\frac{S(\lambda)}{C_{33}} = \left(\frac{\lambda^2}{1+\lambda^2}\right)\left(\frac{\lambda}{(0.88+\lambda)} + (2 - 0.9\lambda^{1/2})i\right)^{-1} \qquad \ldots(E26)$$

The initial, rather arbitrary multiplier is required to ensure that $S \to 0$ as $\lambda \to 0$.

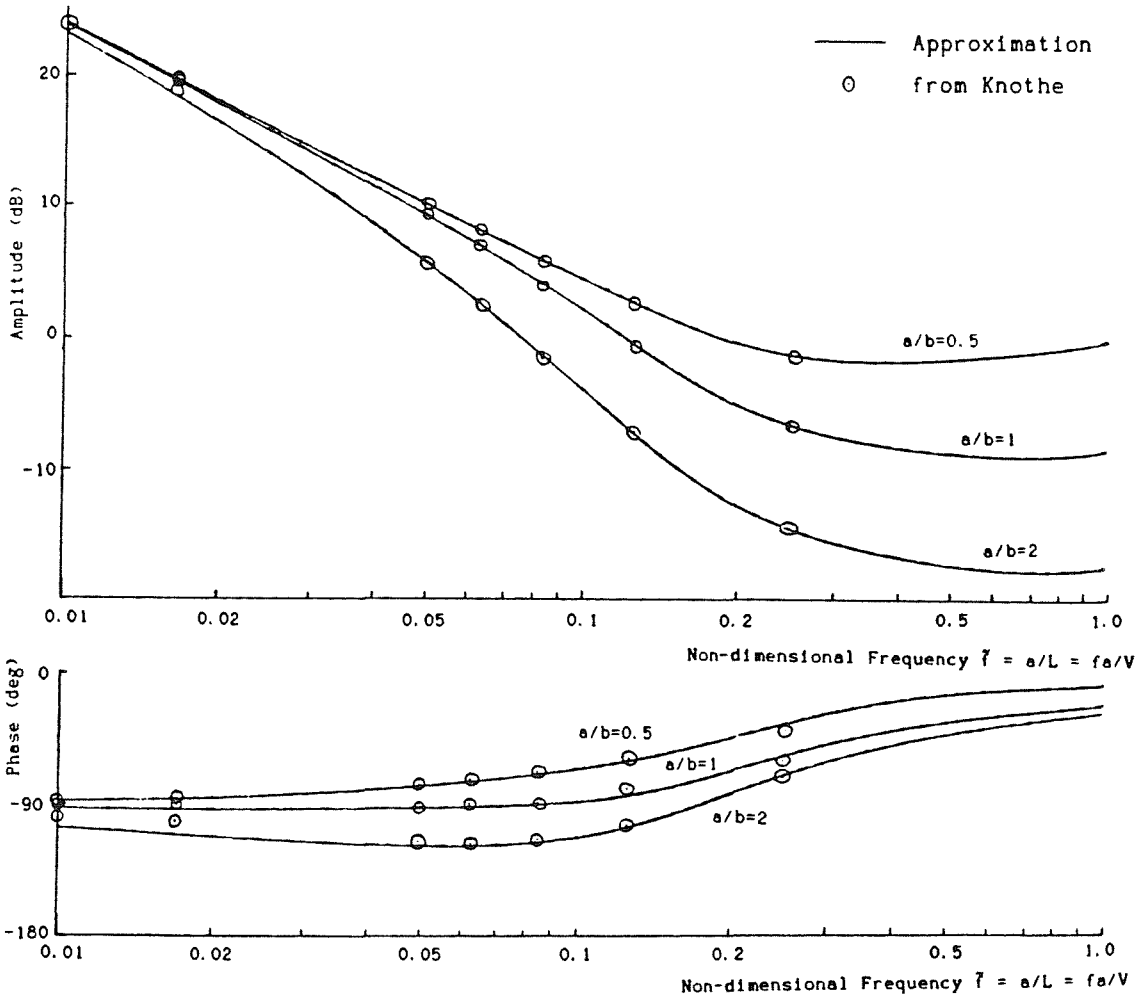

Figure E9 Non-dimensional Spin Contact Receptance $\bar{\alpha} = C_{33}L/2\pi i C^*_{33}a$

APPENDIX F

CALCULATION OF WAVENUMBERS AND RECEPTANCES FOR AN INFINITE BEAM USING PERIODIC STRUCTURE THEORY

F.1 WAVENUMBER CALCULATION

An infinite beam of constant cross-section, such as the rail, can be considered as a periodic structure of arbitrary period. Periodic structure theory [107-109] allows the motion of the infinite structure to be derived from the properties of a single element. This is generally carried out by deriving the allowable wavenumbers at a particular frequency. Hence the motion of the infinite rail can be derived in the frequency domain from the properties of a short length. From the wavenumber solution at a given frequency, it is possible to proceed to derive the receptances as well, by a superposition of the various wavetypes.

Considering an infinite structure, such as a beam, as a periodic structure of arbitrary period length L, the continuum of length L can be reduced to a set of N discrete degrees-of-freedom, $\{q\}$, using the standard techniques of the finite element method. The equations of motion can then be written in matrix form:-

$$([K] - \omega^2[M]) \{q\} = \{F\} \qquad \ldots(F1)$$

where [K] is the stiffness matrix and [M] is the mass matrix, both square matrices of dimension N. The vector $\{F\}$ consists of the forces applied at the N coordinate positions $\{q\}$.

Damping can also be introduced, either by a viscous damping matrix [C], which introduces a term $i\omega[C]$, or alternatively using structural damping, in which case [K] may be considered as a complex matrix. The latter is used here. For a constant damping loss factor, η, [K] is multiplied by the factor $(1+i\eta)$.

Following the method of Mead [107], the coordinates are now partitioned into 3 groups corresponding to those on the left-hand end of the element (common with the next element in the negative x direction), $\{q_l\}$, those on the right-hand end of the element $\{q_r\}$, and those internal to the element $\{q_i\}$. The forces are divided in a corresponding way, but for free wave motion it may be noted that the

only forces to act are at the boundaries between elements, so that $\{F_i\}=0$. Hence,

$$\{q\} = \begin{Bmatrix} q_l \\ \hline q_i \\ \hline q_r \end{Bmatrix} \qquad \{F\} = \begin{Bmatrix} F_l \\ \hline 0 \\ \hline F_r \end{Bmatrix} \qquad \ldots(F2)$$

The mass and stiffness matrices are partitioned correspondingly:-

$$[K] = \left[\begin{array}{c|c|c} K_{ll} & K_{li} & K_{lr} \\ \hline K_{il} & K_{ii} & K_{ir} \\ \hline K_{rl} & K_{ri} & K_{rr} \end{array}\right] \qquad [M] = \left[\begin{array}{c|c|c} M_{ll} & M_{li} & M_{lr} \\ \hline M_{il} & M_{ii} & M_{ir} \\ \hline M_{rl} & M_{ri} & M_{rr} \end{array}\right] \ldots(F3)$$

The equations can be further simplified by restricting consideration to the case of no internal coordinates. This is realistic only so long as the element is short enough, but since the length is arbitrary, it can be arranged that this is the case. It must be shown that all wavelengths are considerably greater than 2L. Then writing

$$[D] = (1+i\eta)\,[K] - \omega^2\,[M] \qquad \ldots(F4)$$

gives the partitioned equation:-

$$\left[\begin{array}{c|c} D_{ll} & D_{lr} \\ \hline D_{rl} & D_{rr} \end{array}\right] \begin{Bmatrix} q_l \\ \hline q_r \end{Bmatrix} = \begin{Bmatrix} F_l \\ \hline F_r \end{Bmatrix} \qquad \ldots(F5)$$

Free wave motion in a periodic structure is characterised by the displacements in one element being equal to the corresponding displacements in the adjacent element apart from a factor e^{μ}, where μ is known as the propagation constant. Taking this condition in conjunction with continuity of displacement across the boundaries between adjacent elements, and Newton's third law, gives [107]:-

$$\{q_r\} = e^{\mu}\,\{q_l\} \qquad \{F_r\} = -\,e^{\mu}\,\{F_l\} \qquad \ldots(F6)$$

$$\Rightarrow \quad e^{\mu}\left[\begin{array}{c|c} D_{ll} & D_{lr} \end{array}\right] \begin{Bmatrix} q_l \\ \hline q_r \end{Bmatrix} = e^{\mu}\,\{F_l\} = -\left[\begin{array}{c|c} D_{rl} & D_{rr} \end{array}\right] \begin{Bmatrix} q_l \\ \hline q_r \end{Bmatrix} \ldots(F7)$$

by eliminating $\{F_r\}$, and so,

$$\left(\left[\begin{array}{c|c} D_{rl} & D_{rr} \\ \hline 0 & I \end{array}\right] + e^{\mu} \left[\begin{array}{c|c} D_{ll} & D_{lr} \\ \hline -I & 0 \end{array}\right] \right) \begin{Bmatrix} q_l \\ \hline q_r \end{Bmatrix} = \{0\} \qquad \ldots(F8)$$

where [I] is the unit matrix, and [0] (or {0}) is the null matrix (or vector). This has the form of a standard eigenvalue problem $([A] + \lambda[B])\{\psi\} = \{0\}$, which can be solved using a standard computer routine.

If the structure is such that the periodic element is symmetric left-to-right (which is the case for an infinite beam), the solutions will occur in pairs. This means in practice that equivalent waves can travel in either direction. Hence if e^{μ} is an eigenvalue, $e^{-\mu}$ is also an eigenvalue.

Use can be made of this symmetry to give a more efficient eigenvalue problem - if N is now the number of degrees-of-freedom at one end of an element, equation (F8) has dimension 2N, whereas only N eigenvalues are required for waves travelling in one direction, and those travelling in the other direction can be derived from them.

Equations (F6) and (F7) can be reformulated as:-

$$\left(e^{\mu} [D_{lr}] + ([D_{ll}] + [D_{rr}]) + e^{-\mu} [D_{rl}] \right) \{q_l\} = 0 \quad \ldots(F9)$$

which is a quadratic eigenvalue problem, and hence less easy to solve directly than the simple eigenvalue problem of equation (F8).

In practice, as shown in Figure F1, since the structure is periodic along one of the three coordinate axes, the N coordinates (which consist of displacements and rotations at various positions on

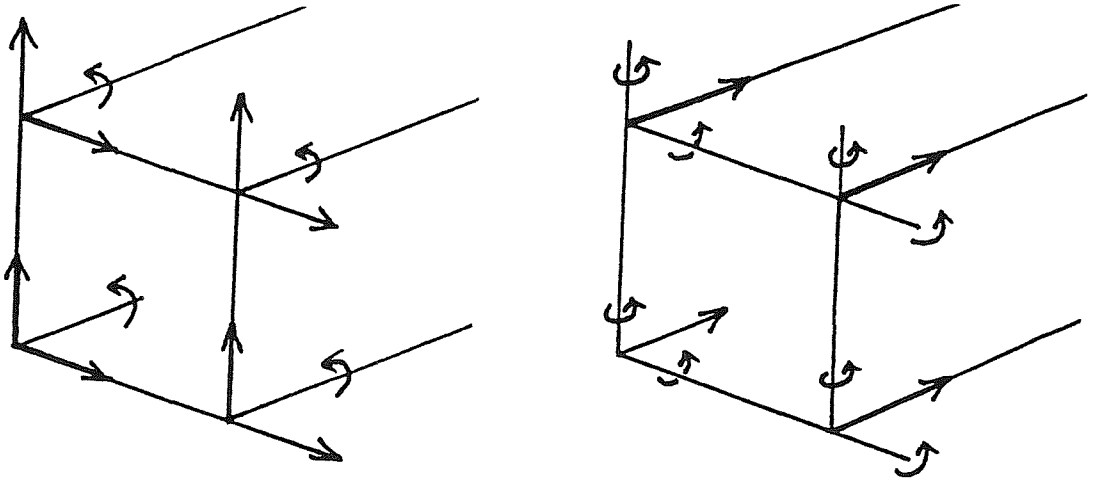

(a) Type S Coordinates (b) Type A Coordinates

Figure F1 Illustration of Type S and Type A Coordinates

the interface between adjacent periodic elements) can be separated into two distinct categories. Firstly those which would be allowed by a symmetric constraint at the interface but restrained by an anti-symmetric constraint are designated 'S'. Secondly those which would be allowed by an anti-symmetric constraint and restrained by a symmetric constraint are designated 'A'.

Making use of the structural symmetry of the element in the longitudinal direction, it can be noted that

$$D_{rrij} = \begin{cases} D_{llij} & \text{for i,j both type S} \\ -D_{llij} & \text{for i~type S, j~type A} \\ -D_{llij} & \text{for i~type A, j~type S} \\ D_{llij} & \text{for i,j both type A} \end{cases} \qquad \text{...(F10a)}$$

and similarly

$$D_{rlij} = \begin{cases} D_{lrij} & \text{for i,j both type S} \\ -D_{lrij} & \text{for i~type S, j~type A} \\ -D_{lrij} & \text{for i~type A, j~type S} \\ D_{lrij} & \text{for i,j both type A} \end{cases} \qquad \text{...(F10b)}$$

Hence, for i,j both type S or for i,j both type A:-

$$e^{\mu} D_{lrij} + D_{llij} + D_{rrij} + e^{-\mu} D_{rlij} = 2 (\cosh\mu D_{lrij} + D_{llij}) \quad \text{...(F11)}$$

whereas, for i~type S, j~type A, or for i~type A, j~type S:-

$$e^{\mu} D_{lrij} + D_{llij} + D_{rrij} + e^{-\mu} D_{rlij} = 2 \sinh\mu D_{lrij} \quad \text{...(F12)}$$

Hence writing $[X]=[D_{lr}]$ and $[Y]=[D_{ll}]$ and partitioning equation (F9) into types S and A, gives (dropping the factor of 2):-

$$\left[\begin{array}{c|c} \cosh\mu X^{SS} + Y^{SS} & \sinh\mu X^{SA} \\ \hline \sinh\mu X^{AS} & \cosh\mu X^{AA} + Y^{AA} \end{array}\right] \left\{\begin{array}{c} q^S \\ \hline q^A \end{array}\right\} = 0 \qquad \text{...(F13)}$$

Consider first the simple case $\sinh\mu=0$, => $\cosh\mu=\pm1$ (which only occurs for zero damping, $\eta=0$).

The case $\cosh\mu=1$ corresponds to a 'wave' with a displacement constant along the length, ie a zero wavenumber, or infinite wavelength. This therefore signifies the 'cut-on' of a given wave type - the frequency at which a wave passes from being a 'near-field' decaying wave to being a propagating wave.

By contrast, the case $\cosh\mu=-1$ corresponds to a reversal of sign from one element to the next, ie a wavelength of 2L. This wavelength would be too short for the idealisation used, and signifies the breakdown of the approximations used (wavelength >> element length). It is anticipated that such solutions would occur only at very high frequencies, and so they will be ignored here.

From the above, it emerges that two uncoupled sets of solutions exist:-

$$[\ Y^{SS} + X^{SS}\ ]\ \{q^S\} = 0 \qquad \text{with} \qquad \{q^A\} = 0$$

$$\text{and} \quad [\ Y^{AA} + X^{AA}\ ]\ \{q^A\} = 0 \qquad \text{with} \qquad \{q^S\} = 0 \qquad \ldots(F14)$$

Although these equations can be solved, it has been found to be simpler to avoid these frequencies, as infinite receptances ensue. Turning to the case $\sinh\mu\neq0$, equation (F13) can be rewritten as

$$\begin{bmatrix} \cosh\mu X^{SS} + Y^{SS} & X^{SA} \\ \hline \sinh^2\mu X^{AS} & \cosh\mu X^{AA} + Y^{AA} \end{bmatrix} \begin{Bmatrix} q^S \\ \hline \sinh\mu q^A \end{Bmatrix} = 0 \qquad \ldots(F15)$$

$$\Rightarrow \quad \begin{bmatrix} \cosh\mu X^{SS} + Y^{SS} & (\cosh\mu + 1)X^{SA} \\ \hline (\cosh\mu - 1)X^{AS} & \cosh\mu X^{AA} + Y^{AA} \end{bmatrix} \begin{Bmatrix} (\cosh\mu + 1)q^S \\ \hline \sinh\mu q^A \end{Bmatrix} = 0 \qquad \ldots(F16)$$

$$\Rightarrow \quad \left(\begin{bmatrix} Y^{SS} & X^{SA} \\ \hline -X^{AS} & Y^{AA} \end{bmatrix} + \cosh\mu\ [X] \right) \begin{Bmatrix} \bar{q}^S \\ \hline \bar{q}^A \end{Bmatrix} = 0 \qquad \ldots(F17)$$

where $$\bar{q}^S_i = (\cosh\mu + 1)q^S_i$$

$$\text{and} \qquad \bar{q}^A_i = \sinh\mu q^A_i. \qquad \ldots(F18)$$

This is now a standard N-value eigenvalue problem, with eigenvalues $\lambda = \cosh\mu$ and eigenvectors $\{\bar{q}\}$. This is solved using a computer routine from the NAG library [128].

The wavenumbers, k, given by $e^{-ikL}=e^{\mu}$, are then extracted using $k = i\mu/L = i\cosh^{-1}(\lambda)/L$, where it should be remembered that $\cosh^{-1}$ is here a function of a complex variable. For the particular cases of λ real, k is given by

$$\text{for } |\lambda|<1, \quad k = \begin{cases} (\cos^{-1}\lambda)/L & \text{for positive travelling waves } (x>0) \\ -(\cos^{-1}\lambda)/L & \text{for negative travelling waves } (x<0) \end{cases}$$

$$\text{for } |\lambda|>1, \quad k = \begin{cases} -i(\cosh^{-1}\lambda)/L & \text{for near-field waves } (x>0) \\ i(\cosh^{-1}\lambda)/L & \text{for near-field waves } (x<0) \end{cases}$$

Thus real wavenumbers, k, correspond to travelling waves and imaginary wavenumbers to decaying near-field 'waves'. Complex eigenvalues, λ, result in complex wavenumbers, corresponding to a decaying near-field wave with a harmonic spatial component.

In the same way, the 'waveshapes' $\{\psi\}_n$, the normalised displaced shapes corresponding to the various waves, can be identified as the displacement vectors $\{q\}$ arising in equations (F17) and (F18), on substitution of the appropriate wavenumber k_n. It should be noted that these 'waveshapes' are different for each frequency.

F.2 RECEPTANCES

Having calculated the free wave response, attention is now turned to the forced response, and in particular the point receptances of the infinite beam.

Consider a set of forces $\{F\}$ acting at the point x=0, at the boundary between two elements, labelled - and + and shown in Figure F2. For these elements it is possible to write down the continuity boundary conditions:-

$$\{q_r\}^{(-)} = \{q_l\}^{(+)} \qquad \ldots(F19)$$

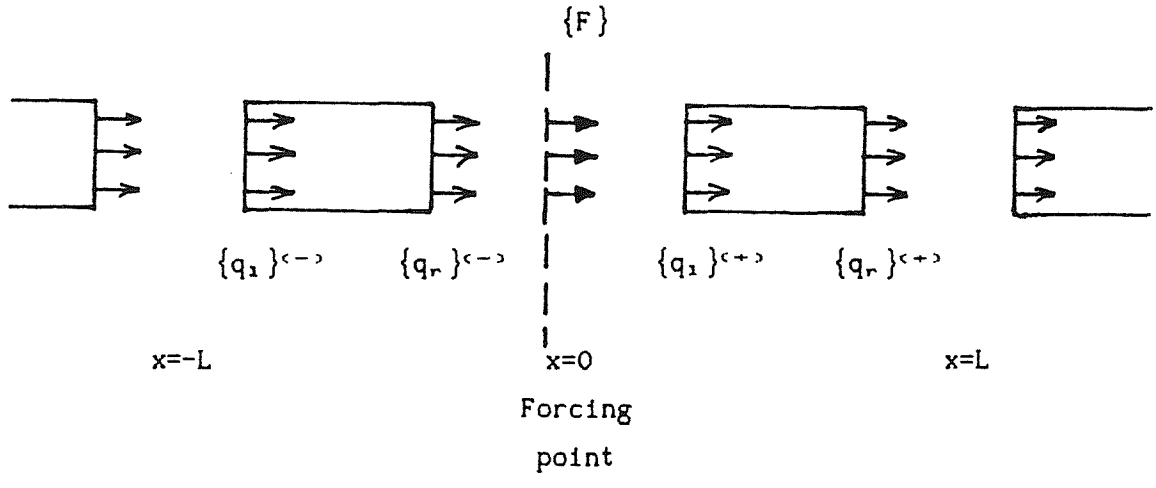

Figure F2 Periodic Elements either side of the Forcing Point

The motion in the right-hand beam ($0<x<\infty$) can be taken to be a superposition of the N waves with wavenumbers k_n and waveshapes ψ_{jn} as given in equations (F17) and (F18). Thus letting A_n be the generalised coordinate corresponding to the nth wavetype, the motion at coordinate position j is given by:-

$$q_j(x) = \sum_{n=1}^{N} A_n \psi_{jn} e^{-ik_n x} \qquad \text{for } x>0 \qquad \ldots(F20)$$

Similarly the motion in the left-hand beam ($-\infty<x<0$) can be taken to be a superposition of the N waves with wavenumbers $-k_n$ and waveshapes Ψ_{jn}, the latter being given by

$$\Psi^S_{jn} = \bar{q}^S_{jn}/(\cosh(-\mu_n) + 1) = \psi^S_{jn}$$

$$\text{and} \quad \Psi^A_{jn} = \bar{q}^A_{jn}/\sinh(-\mu_n) = -\psi^A_{jn} \qquad \ldots(F21)$$

Thus letting B_n be the generalised coordinate corresponding to the nth wavetype, the motion at coordinate position j is given by:-

$$q_j(x) = \sum_{n=1}^{N} B_n \Psi_{jn} e^{ik_n x} \qquad \text{for } x<0 \qquad \ldots(F22)$$

Hence equation (F19) can be written as

$$\sum_n A_n \{\psi\}_n = \sum_n B_n \{\Psi\}_n \qquad \ldots(F23a)$$

or in vector notation

$$[\psi]\{A\} = [\Psi]\{B\} \qquad \ldots(F23b)$$

Applying equation (F20) to the right-hand element (+):-

$$q^{(+)}_{1j} = \sum_n A_n \psi_{jn} \quad \Rightarrow \quad \{q_1\}^{(+)} = [\psi]\{A\} \qquad \ldots(F24a)$$

$$\text{and} \quad q^{(+)}_{rj} = \sum_n A_n \psi_{jn} e^{-ik_n L} \quad \Rightarrow \quad \{q_r\}^{(+)} = [\psi']\{A\} \qquad \ldots(F24b)$$

where $\psi'_{jn} = \psi_{jn} e^{-ik_n L}$.

Hence from the element equation (equation (F5)):-

$$\{F_1\}^{(+)} = ([D_{11}][\psi] + [D_{1r}][\psi'])\{A\} \qquad \ldots(F25)$$

Similarly for the left-hand element,

$$q_{ij}^{(-)} = \sum_n B_n \, \Phi_{jn} \, e^{ik_n(-L)} \quad \Rightarrow \quad \{q_l\}^{(-)} = [\Phi'] \, \{B\} \qquad \ldots(F26a)$$

where $\Phi'_{jn} = \Phi_{jn} \, e^{-ik_nL}$

and $$q_{rj}^{(-)} = \sum_n B_n \, \Phi_{jn} \quad \Rightarrow \quad \{q_r\}^{(-)} = [\Phi] \, \{B\} \qquad \ldots(F26b)$$

$$\Rightarrow \quad \{F_r\}^{(-)} = (\, [D_{rl}][\Phi'] + [D_{rr}][\Phi] \,) \, \{B\} \qquad \ldots(F27)$$

It may be noted from equation (F23) that $\{B\} = [\Phi]^{-1}[\psi]\{A\}$, and hence

$$\{F_r\}^{(-)} = (\, [D_{rl}][\Phi'][\Phi]^{-1}[\psi] + [D_{rr}][\psi] \,) \, \{A\} \qquad \ldots(F28)$$

$$\Rightarrow \quad \{F\} = \{F_l\}^{(+)} + \{F_r\}^{(-)}$$

$$= ([D_{ll}][\psi]+[D_{lr}][\psi']+[D_{rl}][\Phi'][\Phi]^{-1}[\psi]+[D_{rr}][\psi]) \, \{A\} \ldots(F29)$$

which is solved using a standard matrix inversion routine from the NAG library [128].

For the particular case of a point receptance, the force vector should be set to unity for the degree-of-freedom to be excited and zero for the remainder, the response vector at x=0, $\{q\} = [\psi]\{A\}$ then giving the point and cross receptances. It may be noted that ψ can be multiplied by an arbitrary factor, but this is not reflected in the result $\{q\}$ due to cancellation.

APPENDIX G

SLEEPER VIBRATIONS

G.1 PREVIOUS WORK

Dynamic models of the track which have included the sleepers have generally done so as masses (Grassie [58]) or as beams of constant thickness (Clark et al [63,64], Cox and Grassie [61]). However sleepers have a varying cross-section, as shown in Figure G1. The beam stiffness taken corresponded to that at the thinnest point (the centre).

Experimental work often considers the vibration of sleepers in the track. For ease of interpretation, the free vibration of a sleeper is preferable, and this has been carried out by Ford [129].

G.2 FINITE ELEMENT MODEL OF A SLEEPER

A finite element model of a typical (type F27) concrete sleeper (shown in Figure G1) has been set up using the NEWPAC program [94]. This consists of 16 beam elements representing the whole length. Account is taken of the profile variations along the length.

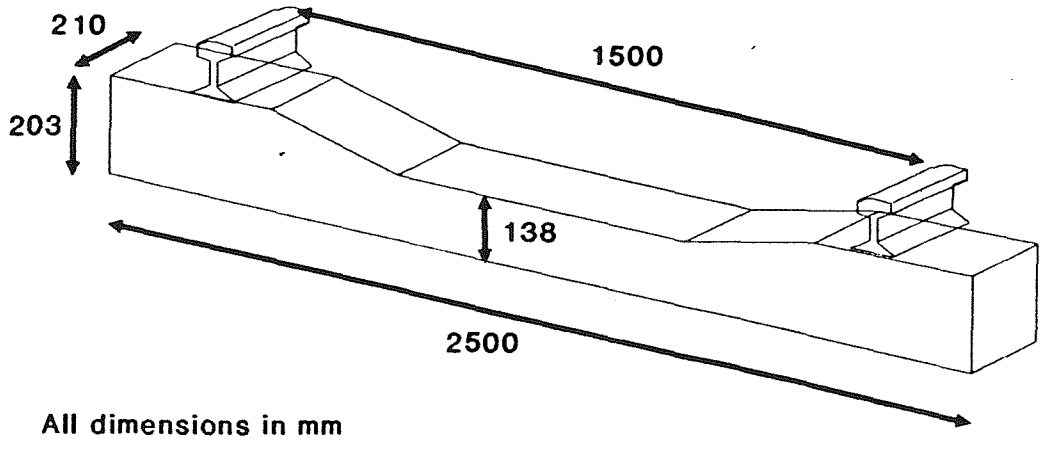

Figure G1 F27-type Concrete Sleeper

The density of the elements was arranged to give the correct total mass of 275 kg, and the Young's modulus was chosen to give the best agreement with natural frequencies measured on a similar sleeper [129] for vertical bending modes. The torsional modes do not agree so well, but this might be expected since the sleeper is not homogeneous (due to the reinforcing bars), and since the torsional parameters (J and I_x) cannot be adjusted separately in the NEWPAC program. The various natural frequencies are listed in Table G1.

Table G1 Natural frequencies of a concrete sleeper

		From finite element model		Measured (from [129])	
Type of Mode	Number of nodes	Natural frequency (Hz)	Damping ratio (%)	Natural frequency (Hz)	Damping ratio (%)
Vertical Bending	2	107	2.43	114	2.03
	3	350	0.82	344	0.89
	4	662	0.63	664	0.59
	5	975	0.52	1038	0.50
Torsional	1	474	0.66	404	1.00
	2	1390	0.56	997	0.63
Longitudinal	1	997	0.52		
Lateral Bending	2	178	1.45		
	3	530	0.62		
	4	972	0.52		

In order to calculate frequency responses of the sleeper, viscous damping was included, in the form $[C]=\alpha[M]+\beta[K]$, as required by the NEWPAC program. The values used were $\alpha=31.4$ and $\beta=8.67\times10^{-7}$ which produced damping ratios comparable to those measured in [129] (see Table G1).

The sleeper was next attached to a rail pad at the rail seat (750 *mm* from the centreline). The vertical pad stiffness of 250 MN/m was taken from Clark et al [63], and is also used by Cox and Grassie [61]. In practice the pad stiffnesses are both frequency-dependent, and load-dependent [113].

The transverse stiffnesses have been calculated from the vertical stiffnesses by noting that the shear modulus (G) should determine the

transverse stiffness, whereas the bulk modulus (K) should determine the vertical stiffness. These moduli are related by

$$G = \frac{3(1-2\nu)}{2(1+\nu)} K \qquad \ldots(G1)$$

where ν is Poisson's ratio, which tends to be relatively large for the visco-elastic materials used for rail pads. Using a (rather arbitrary) value of ν=.4 gives $G \simeq 0.2\ K$ and hence transverse stiffnesses of 50 MN/m. Grassie [59] uses a similar value of 34 MN/m for the lateral pad stiffness, derived from best fit to experimental data.

Rotational stiffnesses have been derived from these values using the geometry of the pad (which is approximately 200×150 mm). Damping values for the pad were based on the value given by Cox for the vertical damping (25.9 kNs/m), and for other directions the same proportion to the stiffnesses was maintained.

The sleeper was also attached to springs representing the ballast. The vertical ballast stiffness was also taken from Clark [63] and Cox [61] (40 MN/m per unit length of sleeper). The transverse ballast stiffnesses were derived from the vertical stiffnesses in the same way as for the pad, and using a factor of 0.9. This corresponds to ν=.15, which should not be too unreasonable for ballast. Damping for the ballast however was taken as 30 kNs/m per unit length of sleeper to correspond with Clark's data, whereas Cox used 40 kNs/m^2.

The frequency response of the sleeper excited through the rail pad in the various coordinate directions was calculated using the NEWPAC program, and the main results are shown in Figures G2-4.

G.3 SIMPLIFIED MODEL

It can be seen from the above that the sleeper modes do not appear strongly, except for the bounce frequencies at around 90 Hz. It therefore seems that it might be justifiable to replace the sleeper by a simplified model, representing the sleeper by an equivalent mass, on a stiffness foundation, and excited through a stiffness representing the railpad. At high frequencies the receptances are dominated by the pad stiffness, although they can be seen to roll off due to the dominance of the viscous damper over the stiffness element within the pad.

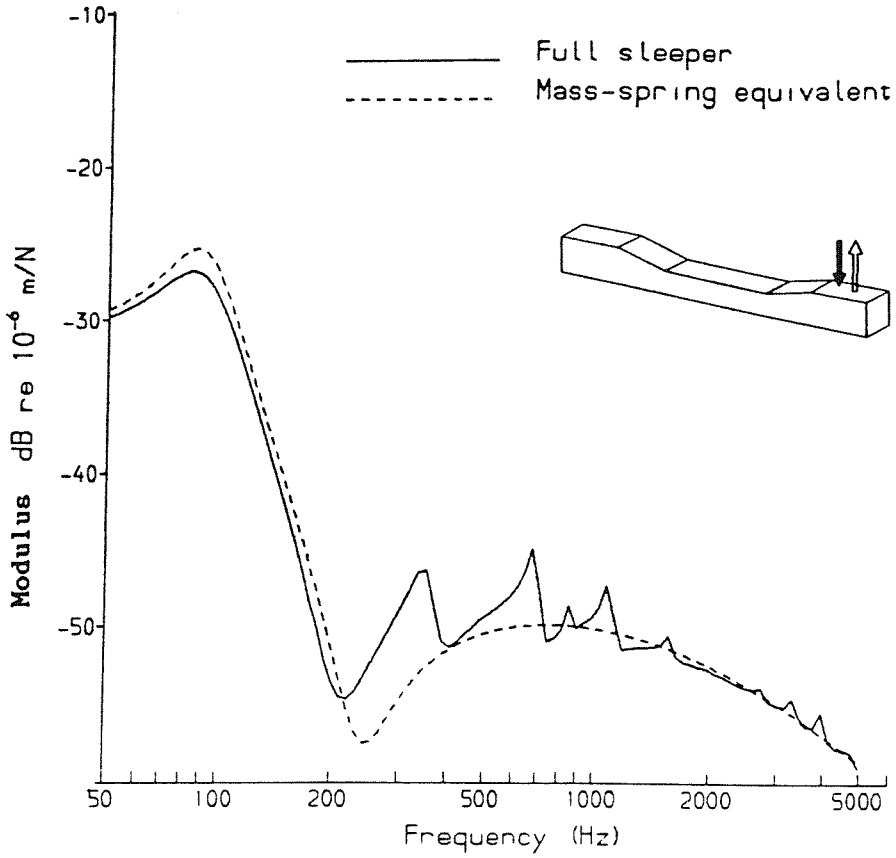

Figure G2 Vertical Receptance of Pad/Sleeper/Ballast

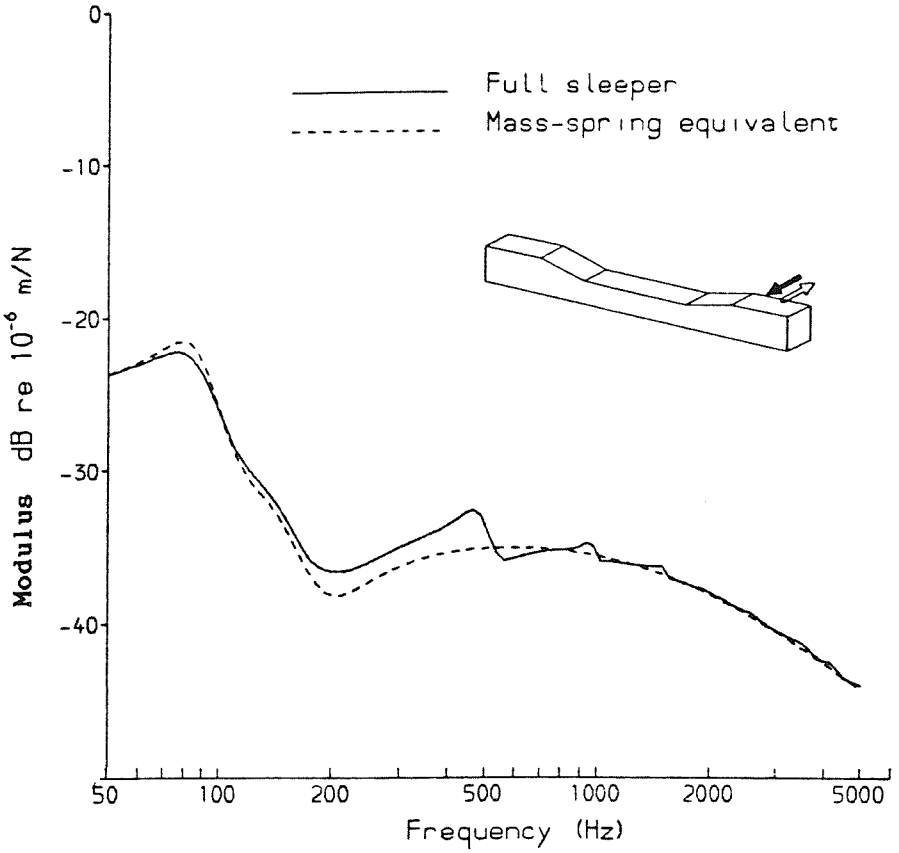

Figure G3 Transverse Receptance of Pad/Sleeper/Ballast (Direction Longitudinal to Rail)

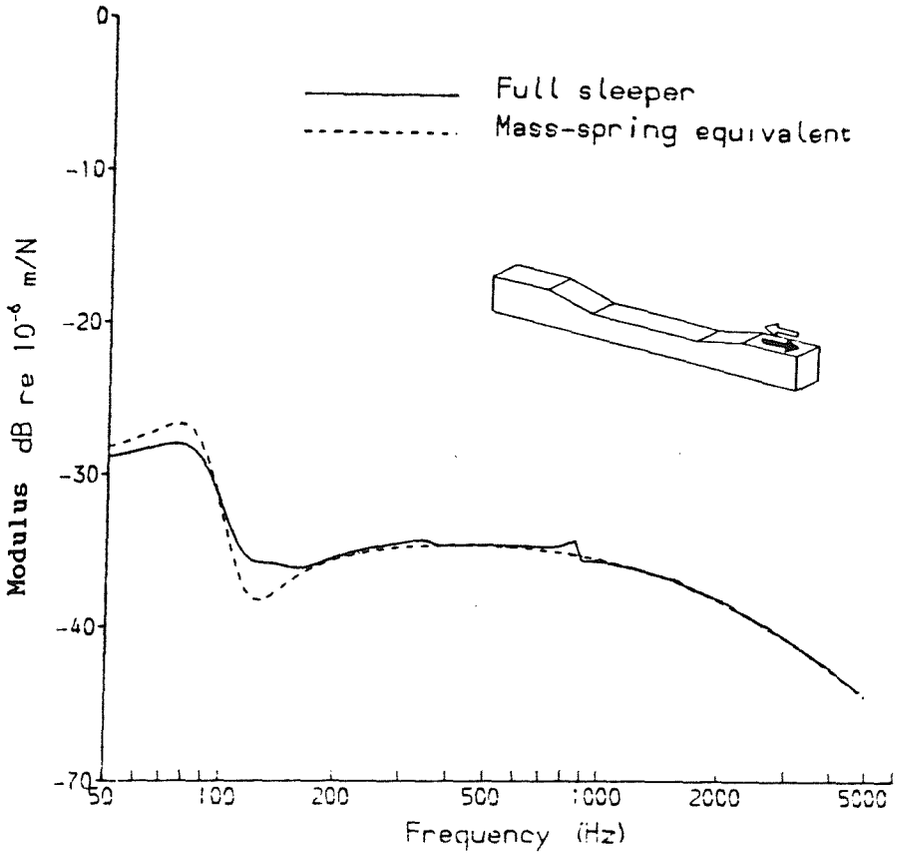

Figure G4 Longitudinal Receptance of Pad/Sleeper/Ballast (Direction Lateral to Rail)

Table G2 Values of parameters used for simplified model of pad/sleeper/ballast

	Vertical	Longitudinal to sleeper (across rail)	Lateral to sleeper (along rail)
Translations			
Pad stiffness (MN/m)	250	50	50
Pad damping (kNs/m)	25	5	5
Sleeper mass (kg)	129	258	129
Ballast stiffness (MN/m)	44	79.2	39.6
Ballast damping (kNs/m)	33	60	30
Rotations			
Pad stiffness (kNm/rad)	260	833	469
Pad damping (Nms/rad)	26	83.3	46.9
Sleeper inertia (kgm^2)	31.6	1.64	31.6
Ballast stiffness (MNm/rad)	10	1.31	10
Ballast damping (kNms/rad)	7.5	0.98	7.5

The results of such a simpified model are also shown in Figures G2-4. The values of the various parameters used are listed in Table G2, and were derived to give a best fit to the sleeper receptances.

The vertical, lateral and longitudinal point receptances can be seen to agree well. This justifies the neglect of sleeper bending, and the use of this simplified sleeper model, at least for the purposes of modelling of the rail response. Furthermore the details of the sleeper concerned are clearly relatively unimportant.

Angular receptances (not shown) were equally close to the results for the full sleeper, with the rotations about the vertical and lateral (along the rail) axes in particular showing only the resilience of the pad.

G.4 EFFECT OF COUPLING THROUGH SLEEPER

In the above simplified model, coupling between the two rails through the sleeper is necessarily omitted. This would clearly simplify the track model, if it is a valid assumption. In order to justify this, the transmission of forces through the sleeper were calculated using the above finite element model. By constraining the rail pad at one side and exciting with a force at the other side, a displacement in the constrained pad was generated. This was converted into a force using the stiffness of the pad.

Figures G5-7 shows the ratio of transmitted force to input force for the three coordinate directions. It is clear from this that the two rails are quite effectively isolated from each other at most frequencies, and particularly at higher frequencies. The exceptions are peaks of -5 dB at 350 Hz and 700 Hz in the vertical transmission (Figure G5), and a broad peak of -5 dB around 200 Hz in the transverse transmission (Figure G6).

The effectiveness at high frequencies is due to the isolation properties of the pad. At low frequencies the vertical and transverse forces are well isolated due to the close coincidence of the bounce modes (vertical and rocking).

Longitudinal motion of the sleeper (corresponding to lateral motion of the rail) contains only one rigid body mode of the sleeper, so that transmission is strong at low frequencies (Figure G7). However above 200 Hz, the ratio is below -20 dB, due to isolation by the pads.

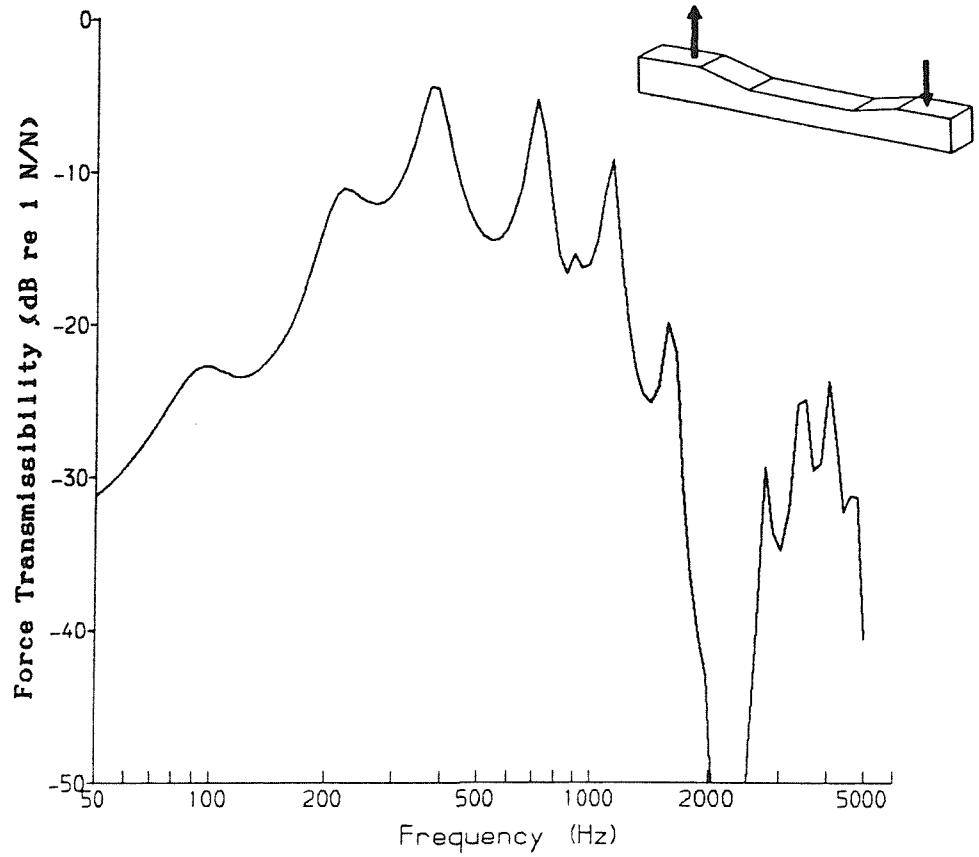

Figure G5 Vertical Transfer Function across Sleeper

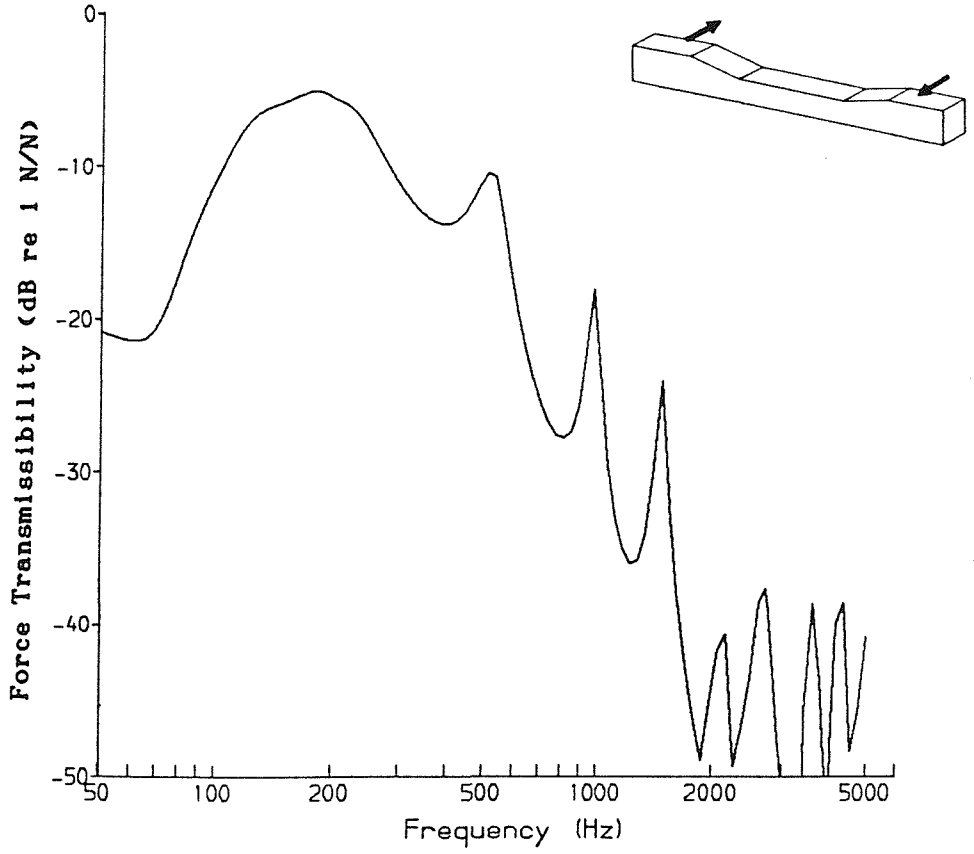

Figure G6 Transverse Transfer Function across Sleeper
(Direction Longitudinal to Rail)

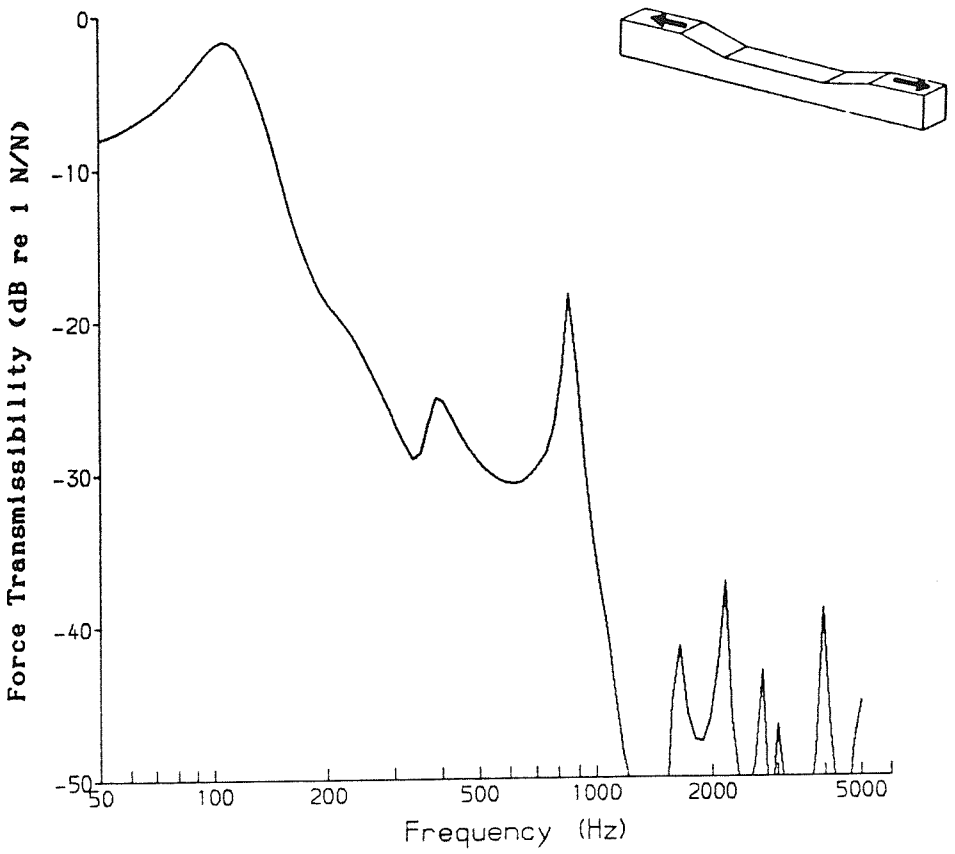

Figure G7 Longitudinal Transfer Function across Sleeper (Direction Lateral to Rail)